UNIVERSITY OF LILLE
Lille Graduate School of Biology and Health (n°446)
PhD in Neuroscience

SCREENING ALZHEIMER'S GENETIC RISK FACTORS AGAINST AMYLOID-BETA-INDUCED SYNAPTOTOXICITY

Carla GELLÉ

INSERM UMR1167: Risk factors and molecular determinants of aging-related disease
Team 3: Molecular determinants of Alzheimer's disease and relative disorders

Thesis defended on December 10th, 2025

CHAMI Mounia, PhD – *Reporter*
Team leader, CNRS UMR 7275, INSERM U1323, AlzPark team, Institute of Molecular and Cellular Pharmacology, Université- Côte d'Azur, Valbonne, France

HUMBERT Sandrine, PhD – *Reporter*
DR1, CNRS UMR 7225, INSERM U1127, Institut du Cerveau, Sorbonne Université, Hôpital de la Pitié-Salpêtrière, Paris, France

SELIMI Fekrije, PhD – *Reviewer*
DR2 CNRS, Centre of Interdisciplinary Research, Collège de France, Paris, France

SERGEANT Nicolas, PhD – *Reviewer and President of the jury*
INSERM UMRS 1172, Lille Neuroscience & Cognition, Univ. Lille, CHRU Lille, France

LAMBERT Jean-Charles, PhD – *Team leader*
Univ. Lille, Inserm, CHU Lille, Institut Pasteur de Lille, U1167 (RID-AGE), DISTALZ, Lille, France

SIEDLECKI-WULLICH Dolores, PhD – *Invited member*
Univ. Lille, Inserm, CHU Lille, Institut Pasteur de Lille, U1167 (RID-AGE), DISTALZ, Lille, France

KILINC Devrim, PhD – *Thesis director*
Univ. Lille, Inserm, CHU Lille, Institut Pasteur de Lille, U1167 (RID-AGE), DISTALZ, Lille, Fran

UNIVERSITE DE LILLE
École graduée Biologie et Sante de Lille (n°446)
Doctorat en Neuroscience

CARACTERISATION DES DETERMINANTS GENETIQUES DE LA MALADIE D'ALZHEIMER IMPLIQUES DANS LA TOXICITE SYNAPTIQUE

Carla GELLÉ

INSERM UMR1167: Facteurs de risques et déterminants moléculaires des maladies liées au vieillissement
Équipe 3 : Déterminants moléculaires de la maladie d'Alzheimer et syndromes apparentés

Thèse soutenue publiquement le 10 décembre 2025

CHAMI Mounia, PhD – *Rapportrice*
Directrice d'équipe, CNRS UMR 7275, INSERM U1323, équipe AlzPark, Institut de Pharmacologie Moléculaire et Cellulaire, Université- Côte d'Azur, Valbonne, France

HUMBERT Sandrine, PhD – *Rapportrice*
DR1, CNRS UMR 7225, INSERM U1127, Institut du Cerveau, Sorbonne Université, Hôpital de la Pitié-Salpêtrière, Paris, France

SELIMI Fekrije, PhD – *Examinatrice*
DR2 CNRS, Centre de Recherche Interdisciplinaire, Collège de France, Paris, France

SERGEANT Nicolas, PhD – *Examinateur et Président du jury*
INSERM UMRS 1172, Lille Neuroscience & Cognition, Univ. Lille, CHRU Lille, France

LAMBERT Jean-Charles, PhD – *Directeur d'unité*
Univ. Lille, Inserm, CHU Lille, Institut Pasteur de Lille, U1167 (RID-AGE), DISTALZ, Lille, France

SIEDLECKI-WULLICH Dolores, PhD – *Membre invité*
Univ. Lille, Inserm, CHU Lille, Institut Pasteur de Lille, U1167 (RID-AGE), DISTALZ, Lille, France

KILINC Devrim, PhD – *Directeur de thèse*
Univ. Lille, Inserm, CHU Lille, Institut Pasteur de Lille, U1167 (RID-AGE), DISTALZ, Lille, France

Acknowledgements

This thesis was made possible through a PhD fellowship co-funded by the **Institut Pasteur de Lille** and the **Region Hauts-de-France**, and through a 4th year PhD fellowship from **France Alzheimer** (*Soutien aux Jeunes Chercheurs* – AAP-JC-2024 #6473). Different aspects of this project were supported by microfabrication grants from the French **RENATECH network** (P-16-01891 and P-18-02737) and by an **Alzheimer's Association** Research Grant (AARG-22-926152).

I thank the **BiCel** imaging platform of the Institut de Biologie de Lille for microscopy resources, to **Sophie Salomé Desnoulez** and the **ARIADNE** platform for the access to the automated InCell microscope. A special mention to **Alexandre Vandeputte** for the specific training and his precious support for adapting the imaging to the microfluidic model. I also thank **Dr. Karine Blary** at the **IEMN** Lille for the fabrication of microfluidic masters. Thank you to **Dr. Pierre Yger** for his precious insight and help during the establishment of the synaptic connectivity functional readout. Finally, thank you to **PLETHA** for the care and maintenance of the animals used during this thesis.

I would like to address my deepest thanks to the jury: **Dr. Chami**, **Dr. Humbert**, **Dr. Selimi** and **Dr. Sergeant** for accepting to be part of my defence and to assess my work. A special thank you to my CSI members Dr. Selimi and **Dr. Blum** who have both been incredibly helpful and for their valuable insight concerning the technical challenges I faced.

Thank you to **Devrim** and **Dolo** for supervising my work. For supporting and encouraging me throughout this project. Thank you for the long meetings during which we were always arguing but as if we were a big family debating at Christmas dinner. Devrim, thank you for trusting me with this project and for your unfailing honestly. It truly helped me progress and evolve both professionally and personally. Thank you for spending all this time correcting my reports, helping me organising excel sheets and fixing MATLAB codes. And a special mention to you for diagnosing my dyslexia (I have now accepted it :P).

And thank you to Dolo, for co-supervising my work and being an amazing friend. Thank you for all this time spent on my manuscripts, writing paragraph-long comments for me to improve, for training me at the bench and always explaining why thing were done a certain way. Thank you for never giving up in explaining me anything even if I was making the mistake 5 times in a row. And thank you for all the beautiful memories we also made outside of the lab, during night outs at the bar or at the karaoke.

To **Nina**, without whom, my life in the lab would have a been way less fun! To all these late nights in the lab, to all these gossips that we so much liked to discuss and laugh about until our abs were sore. I will always cherish the moments we spent at the kine or Krav

Maga together, building on our bulldog reputations. Thank you for expanding my vocabulary and adding the verb 'nining' to it. To your crazy spontaneity, legendary clumsiness and devoted support during the difficult times.

To **Bruno**, thank you for giving more life to our office, for being my confident, for your sass and your love for gossips. Thank you for helping out during the numerous Ticketmaster ticket wars for securing shows of our favourite artists (that we almost all won by the way!). Even if your obsessions with lunch schedule is often killing me, you are one of my pillars in this lab.

To **Floriane**, thank you for our little gossip sessions during the culture and so many talks about trouble shooting that always ended up in us laughing a lot.

To **Pauline**, thank you for your kindness and unconditional help with the rats and the western blot advice. Thanks for trusting me into reading TOG, what a journey it has been!

To **Valentin**, thank you for your help with the rats. Thank you for the mutual support we were giving each other in these last months of thesis writing. I am glad everything went well for the both of us.

To **Morgane** for all the times I asked you to help me out with a Western blot, thank you so much, it would have been way more difficult and stressful without you. Thank you for being my smiling desk neighbour and sharing all the latest food deals with me.

To **Karine** for always being accessible, kind, and helpful with my last minute-orders and virus queries. You always helped me out when I needed it and I am very grateful for this.

To **Anne-Marie** for always helping when there was an issue with the animals. It was great to learn from you and to be part of the rat / mice team with you and Dolo.

To **Fernanda**, thank you for your sweetness, your smile and your kindness. Thank you for helping me with the microfluidics when I was writing my thesis!

To **Pol**, the king of gossips. Thank you for your sharp opinions and relaxed vibe, so needed in stressful periods.

To **Anais-Camille** for training me from scratch when I arrived in the lab.

To **Benjamin**, thank you for always helping with informatics issue and for never turning down a drink at the local bar.

To **Chloe** and **Erwan**, thank you both so much for your help with the rats and cultures when I did not yet have the certification.

To **Julie**, a very warm thank you for your unconditional support throughout difficult times. And thank you for sharing all the precious moments outside of the lab!

To **Julien**, thank you for the important role you played during the lentiviral construction design and ordering for the screening.

To **Pierre**, thank you for your wise advice, kindness and for the opportunity to include me in the BIN1 project.

To **Jean-Charles**, thank you for accepting me in the team and for your joyful attitude.

Et enfin, merci à ma famille, mes parents, mon frère, à mes amis en dehors du labo ainsi qu'à mon chéri Channavane d'avoir toujours été là dans les bons et moins bons moments de cette thèse. Pour votre soutien sans faille et vos précieux conseils, merci à vous.

Cette thèse est dédiée à ma grand-mère, partie bien trop tôt, qui était extrêmement fière de cette étape de ma vie.

« Long live all the mountains we moved,
I had the time of my life fighting dragons with you »
T.S.

Abstract

Synaptic dysfunction is one of the earliest and most predictive hallmarks of Alzheimer's disease (AD), preceding overt neurodegeneration and cognitive decline. While numerous genetic risk factors have been linked to AD, the molecular mechanisms through which they modulate synaptic vulnerability to amyloid-beta (Aβ) peptide remain largely unresolved. This thesis aimed to identify the genes that promote synaptic protection under Aβ-induced stress and to dissect the mechanisms by which such factors preserve synaptic structure and function.

To address this question, a multi-scale experimental pipeline was developed that combines gene screening, compartment-specific validation, and microelectrode array (MEA)-based functional analysis. Using a medium-throughput microfluidic screening co-culture system, a set of AD-associated genes was systematically tested for their ability to modulate synaptic connectivity in the presence of cell-secreted Aβ. Among the top candidates, *ARFRP1* (ADP-ribosylation factor-related protein 1) appeared to mitigate Aβ-induced synaptic loss, identifying it as a potential regulator of synaptic resilience. Subsequent validation experiments suggested that *ARFRP1* may function as a postsynaptic trafficking modulator that maintains AMPA-type glutamate receptor (AMPAR) dynamics under toxic conditions. Silencing *ARFRP1* reduced GluA1 intensity and phosphorylation at Ser845 residue –a modification leading to AMPAR internalisation and long-term depression (LTD)– while overexpression promoted a shift toward GluA1-enriched receptor composition associated with long-term potentiation (LTP)-like mechanisms and synaptic strengthening.

Compartment-specific manipulations using microfluidic devices demonstrated that *ARFRP1's* protective role may originate primarily from the postsynaptic compartment, where it could support the recycling and surface retention of AMPARs within dendritic spines. By stabilising endosome-Golgi trafficking and maintaining receptor availability at excitatory synapses, *ARFRP1* may counteract the Aβ-induced internalisation and degradation of AMPARs that typically drive Aβ-induced LTD-like processes.

Functional recordings from microfluidic-coupled MEAs provided complementary network-level evidence. Neurons overexpressing *ARFRP1* selectively in the postsynaptic chamber appeared to maintain network connectivity despite Aβ-induced hyperexcitability, suggesting that molecular stabilisation of postsynaptic trafficking translates into preserved communication across neuronal assemblies. This coordinated structural and functional protection supports a working model in which *ARFRP1* enhances synaptic resilience by preserving receptor trafficking homeostasis and maintaining the balance between synaptic pruning and strengthening.

Beyond its mechanistic findings, this thesis achieved significant methodological progress by establishing two complementary microfluidic-based platforms: (1) a co-culture screening device enabling medium-throughput assessment of gene expression modulation on synaptic connectivity, and (2) an integrated microfluidic-MEA hybrid system permitting compartment-specific genetic manipulation with simultaneous structural and electrophysiological readouts. These tools provide a versatile framework for studying gene-dependent mechanisms of synaptic regulation and dysfunction.

In summary, this work identifies *ARFRP1* as a potential trafficking regulator that might support AMPAR stability and synaptic resilience to Aβ-induced stress, while introducing advanced microfluidic approaches for multi-scale analysis of synaptic function. Together, these contributions advance our understanding of mechanisms underlying early synaptic vulnerability in AD models and open new experimental avenues for exploring molecular pathways that sustain synaptic integrity.

Key words: Microfluidic devices, high-content screening, co-culture, microelectrode array, ARFRP1, LTP, AMPAR

Résumé

La perte synaptique constitue l'un des premiers marqueurs prédictifs de la maladie d'Alzheimer (MA), précédant la neurodégénérescence et le déclin cognitif caractéristiques. Bien que de nombreux facteurs de risque génétiques aient été associés à la MA, les mécanismes moléculaires par lesquels ils modulent la vulnérabilité synaptique face à la bêta-amyloïde (Aβ) demeurent mal compris. Cette thèse visait à identifier les gènes capables de protéger les synapses du stress induit par Aβ et à élucider les mécanismes par lesquels ces facteurs préservent la structure et la fonction synaptiques. Pour répondre à cet objectif, une approche expérimentale multi-échelle a été développée, combinant un criblage en coculture microfluidique, des validations compartiment-spécifiques et des enregistrements fonctionnels sur réseaux neuronaux à l'aide de microélectrodes (MEA).

À l'aide d'un système de coculture microfluidique à moyen débit, un ensemble de facteur de risque associés à la MA a été testé de manière systématique pour leur capacité à moduler la connectivité synaptique en présence d'Aβ sécrété par des cellules. Parmi les candidats, *ARFRP1* (ADP-ribosylation factor-related protein 1) s'est distingué par sa capacité à atténuer la perte synaptique induite par Aβ, suggérant un rôle de régulateur potentiel de la résilience synaptique. Les expériences de validation suggèrent qu'*ARFRP1* agit comme un modulateur postsynaptique du trafic des récepteurs AMPA (AMPAR) sous conditions toxiques. L'inhibition *d'ARFRP1* réduit l'intensité et la phosphorylation de GluA1 sur le résidu Ser845 - une modification favorisant l'internalisation des AMPAR et la dépression à long terme (LTD) des synapses - tandis que sa surexpression induit un profil enrichi en GluA1, associé à des mécanismes de potentialisation à long terme et à un renforcement synaptique.

Les manipulations compartiment-spécifiques dans des dispositifs microfluidiques ont montré que l'effet protecteur *d'ARFRP1* provient principalement du compartiment postsynaptique, où il soutient potentiellement le recyclage et la rétention membranaire des AMPAR au sein des épines dendritiques. De ce fait, *ARFRP1* pourrait contrer

l'internalisation et la dégradation des AMPAR responsables des processus LTD-like induits par Aβ. Les enregistrements fonctionnels réalisés sur des MEA couplées à des microfluidiques ont apporté une confirmation au niveau du réseau : la surexpression postsynaptique d'*ARFRP1* semble maintenir la connectivité malgré l'hyperexcitabilité induite par l'Aβ, indiquant que la stabilisation des récepteurs postsynaptiques se traduit par une communication neuronale préservée. Cette protection structurale et fonctionnelle coordonnée soutient un modèle selon lequel *ARFRP1* renforce la résilience synaptique en préservant l'homéostasie du trafic des récepteurs et l'équilibre entre élagage et consolidation synaptiques.

Cette thèse a également permis des avancées méthodologiques majeures avec le développement de deux plateformes microfluidiques complémentaires : (1) un dispositif de criblage en coculture permettant une analyse à moyenne échelle des effets de modulation de l'expression génique sur les synapses, et (2) un système hybride microfluidique-MEA autorisant des manipulations compartiment-spécifiques couplées à des mesures structurales et électrophysiologiques. Ces outils constituent un cadre polyvalent pour l'étude des mécanismes de régulation synaptique dépendants des gènes. En conclusion, ce travail identifie *ARFRP1* comme un nouveau régulateur postsynaptique du trafic des AMPAR favorisant la stabilité et la résilience des synapses face au stress induit par Aβ, tout en introduisant des approches microfluidiques avancées pour l'analyse multi-échelle de la fonction synaptique. Ces contributions approfondissent la compréhension des défaillances synaptiques précoces dans la MA et ouvrent de nouvelles perspectives pour cibler les voies moléculaires soutenant l'intégrité synaptique.

Mots clés : dispositifs microfluidiques, dépistage à haut contenu, coculture, réseau de microélectrodes, ARFRP1, AMPAR

Lay Summaries (French & English)

Alzheimer's disease is the most common cause of dementia, affecting nearly 45 million people worldwide. In patients' brains, two hallmark proteins, beta-amyloid (Aβ) and Tau abnormally aggregate, becoming toxic to neurons. This thesis focuses on the effect of Aβ on synapses, the neuronal connections essential for brain communication. Large genetic studies have identified over 300 genes linked to the risk of developing Alzheimer's, although their roles remain unclear. Using innovative cell models and microfluidic devices, we assessed the impact of these genes on synapses. The goal is to identify protective genes that could become new therapeutic targets, improving our understanding of the disease and guiding future efforts to block Aβ toxicity and protect synapses.

La maladie d'Alzheimer est la cause la plus fréquente de démence et touche près de 45 millions de personnes dans le monde. Dans le cerveau des patients, deux protéines clés : la bêta amyloïde (Aβ) et Tau s'agrègent anormalement et deviennent toxique pour les neurones. Cette thèse s'intéresse à l'effet de l'Aβ sur les synapses, les connexions entre neurones indispensables à la communication cérébrale. De grandes études génétiques ont identifié plus de 300 gènes associés au risque de développer la maladie d'Alzheimer, sans que leur rôle ne soit clair. À l'aide de modèles cellulaires innovants et de dispositifs micro fluidiques, nous avons évalué l'impact de ces gènes sur la communication entre neurones. L'objectif est d'identifier des gènes protecteurs pouvant devenir de nouvelles cibles thérapeutiques, afin de mieux comprendre la maladie et, à terme, développer des traitements capables de bloquer la toxicité induite par l'Aβ et ainsi de protéger les synapses.

Articles and communication

The work presented in this thesis is currently being expanded into a dedicated research article, for which I will be the first author. The article will be structured to reflect the experimental and conceptual progression developed throughout this thesis. It will begin with an introduction positioning the study within the broader context of Alzheimer's disease (AD) genetics, synaptic vulnerability, and Aβ-induced synaptotoxicity. The first section will present the gene selection strategy and medium-throughput screening pipeline, outlining how AD-associated candidates were shortlisted and evaluated using the microfluidic co-culture system. This section will also summarise the screening outcomes and describe the identification of *ARFRP1* as a synaptoprotective hit, based on its ability to preserve synaptic connectivity in the presence of CHO-secreted Aβ.

The second section will detail the characterisation of *ARFRP1* modulation on glutamatergic synapses, integrating the structural and biochemical analyses performed in this thesis. This will include the effects of *ARFRP1* silencing and overexpression on AMPAR composition, subunit-specific phosphorylation states (e.g., GluA1-Ser845), and synaptic connectivity, as well as the impact of cLTP induction on these parameters. Together, these experiments will define *ARFRP1* as a postsynaptic trafficking regulator influencing LTP-related AMPAR dynamics and synaptic resilience.

The third section will present the functional validation of *ARFRP1's* protective effect against Aβ-induced synaptotoxicity using both CHO-APP conditioned medium and the microfluidic–MEA hybrid system, which enables compartment-specific manipulation combined with simultaneous structural and electrophysiological readouts. This will include the pre–post synaptic drive measurements and the demonstration that postsynaptic *ARFRP1* overexpression maintains functional connectivity despite Aβ-induced network hyperexcitability. The manuscript will conclude with a discussion integrating these findings into a unified model of *ARFRP1*-dependent synaptic protection.

In parallel, complementary experiments currently underway will reinforce and extend the scope of the article. These include: (1) testing whether *ARFRP1* influences LTP-associated AMPAR trafficking under Aβ exposure; and (2) exploring whether *ARFRP1* interacts with Rab11/Rab7-mediated endosomal trafficking pathways. These additional analyses aim to provide mechanistic depth to the proposed model and strengthen the overall conclusions of the study.

Together, these elements will form a cohesive and comprehensive manuscript that extends the thesis findings into a fully developed, publication-ready research article.

The work accomplished during this thesis also led to the following publications:

- Lambert, E.[†], Gelle, C.[†], Leclerc, V.[†], Freire-Regatillo, A.[†], Barois, N., Malfoi, T., Hermant, X., Demiautte, F., Lafont, F., Amouyel, P., Blary, K., Kuenen, S., Najdek, C., Versteken, P., Siedlecki-Wullich, D., Yger, P., Lambert, J.-C., Kilinc, D.*, Dourlen, P.* BIN1 expression in the presynaptic compartment leads to isoform-specific synaptotoxicity; bioRxiv 2025.08.11.669624; doi: 10.1101/2025.08.11.669624 (**in revision**)
  [†] Co-first authors
  * Co-corresponding authors

The study explores the impact of presynaptic *BIN1* expression on neuronal communication and synaptic stability. Using both *Drosophila* and rat neuron models, we show that over-expression of BIN1 isoform 1 (BIN1iso1) leads to pronounced synaptic loss and disrupts synaptic vesicle dynamics. In *Drosophila* photoreceptor and neuromuscular junction systems, electrophysiological recordings revealed early functional deficits accompanied by accumulation of abnormally large vesicles and altered bouton morphology. In rat primary neurons grown in microfluidic devices, only presynaptic over-expression of BIN1iso1 induced a reduction in synaptic connectivity, confirming the compartment-specific effect. Multi-electrode array recordings further demonstrated that BIN1iso1 over-expression decreases overall functional connection between pre- and postsynaptic neuronal populations without affecting network activity, indicating impaired synaptic communication at the circuit level. Together, these results show that presynaptic BIN1iso1 expression disrupts both the structural integrity and

functional output of neuronal networks, suggesting a role in early synaptic vulnerability relevant to AD.

I contributed to this project by developing a functional readout of synaptic connectivity tailored to the microfluidic–MEA platform and by performing the MEA experiments that supported the study's conclusions. This included preparing the MEA chips, establishing and maintaining primary neuronal cultures, executing electrophysiological recordings, and subsequent processing and analysis of the acquired datasets, as well as contributing to the writing of the resulting manuscript. Building on this foundational work, the same analytical approach was subsequently adapted and applied within the context of my thesis, as detailed later in the Results section. The established pipeline is described in Section 3.18. Combined with morphological synaptic puncta co-localisation readouts, I ensured the generation of a coherent multi-modal evaluation of synaptic function. Through optimisation of acquisition parameters, analysis thresholds, and experimental scheduling, this work resulted in a robust and reproducible functional synaptic connectivity assay that was essential both for the BIN1 study and for the experimental framework of this thesis.

- Lefebvre, C., Vreulx, A. C., Dumortier, C., Bégard, S., Gelle, C., Siedlecki-Wullich, D., Colin, M., Kilinc, D., & Halliez, S. (2024). Integration of Microfluidic Devices with Microelectrode Arrays to Functionally Assay Amyloid-β-Induced Synaptotoxicity. *ACS Biomaterials Science & Engineering*, *10*(3), 1856–1868. https://doi.org/10.1021/acsbiomaterials.3c00997

This study aims to develop a reliable and physiologically relevant model to investigate Aβ-induced synaptotoxicity, a central process in the progression of AD. Because synaptic loss closely correlates with cognitive decline, we sought a method capable of assessing functional synaptic integrity with precision. To achieve this, we integrated a tricompartment microfluidic device, allowing physical separation of neuronal compartments, with microelectrode arrays to measure neuronal communication. Primary cortical neurons formed synapses within the central chamber, which was selectively exposed to Aβ-containing conditioned media. Exposition to high Aβ levels led to a marked reduction in interchamber connectivity after 48 hours, despite preserved

neuronal activity within presynaptic and postsynaptic chambers. This indicates a specific impairment of synaptic function rather than general neuronal dysfunction. Overall, the study introduces a robust platform for evaluating Aβ-driven synaptic deficits and for testing candidate therapeutic strategies targeting synapse vulnerability.

I contributed to this project by performing the alignment and bonding of microfluidic devices onto 59-electrode MEA chips, ensuring precise positioning, secure sealing, and compatibility with downstream electrophysiological recordings. In addition, I was responsible for producing and characterising the Aβ-conditioned medium used in the study. This included preparing the necessary biological material, generating the conditioned medium under standardised conditions, and quantifying Aβ concentration using AlphaLISA.

In addition to the two projects described above, I also contributed to three studies through my involvement in all key stages of the primary neuronal culture workflow. My responsibilities included weekly animal care, coordination of mating, monitoring and replacing animals as needed, and performing the euthanasia and dissection of the relevant brain regions, as well as contributing to the preparation and routine maintenance of primary neuronal cultures.

- Coulon, A., Rabiller, F., Takalo, M., Roy, A., Martiskainen, H., Siedlecki-Wullich, D., Mendes, T., Lemeu, C., Carvalho, L.-I., Ehrardt, A., Melo de Farias, A. R., Hulsman, M., Najdek, C., Lannette-Weimann, N., Freire-Regatillo, A., Amouyel, P., Charbonnier, C., Dols-Icardo, O., Jeskanen, H., Willman, R.-M., Kuulasmaa, T., Kurki, M., Hardy, J., Wagner, R., Heikkinen, S., Holstege, H., Mäkinen, P., Nicolas, G., Mead, S., Wagner, M., Ramirez, A., Rauramaa, T., Palotie, A., Sims, R., Soininen, H., van Swieten, J., Williams, J., Bellenguez, C., Grenier-Boley, B., Gelle, C., Lambert, E., Ayral, A.-M., Demiautte, F., Costa, M. R., Deforges, S., Kilinc, D., Mulle, C., Chapuis, J., Hiltunen, M., Dumont, J., Lambert, J.-C. Neuronal downregulation of PLCG2 impairs synaptic function and elicits Alzheimer disease hallmarks; bioRxiv 2024.04.29.591575; doi: 10.1101/2024.04.29.591575 (**in revision**)

This study examines the role of the gene *PLCG2* in neuronal function and its implications for AD. Using high-content screening in rodent primary neurons and human-induced

neurons, we show that shRNA-mediated downregulation of *PLCG2* significantly impairs dendritic morphology, reduces synaptic activity, and increases levels of both Aβ and tau phosphorylation. The effects appear to involve the AKT/GSK3β signalling axis. The findings suggest that loss-of-function variants of *PLCG2* may elevate AD risk by inducing early synaptic dysfunction and accelerating hallmark neuropathology. We propose that maintaining adequate *PLCG2* expression in neurons could be protective, highlighting *PLCG2* as a potential target for early intervention in AD.

- Najdek, C., Walle, P., Flaig, A., Ayral, A. M., Demiautte, F., Coulon, A., Buiche, V., Neuro-CEB Brain Bank, Lambert, E., Amouyel, P., Gelle, C., Siedlecki-Wullich, D., Dumont, J., Kilinc, D., Eysert, F., Lambert, J. C., & Chapuis, J. (2025). Calpain and caspase regulate Aβ peptide production via cleavage of KINDLIN2 encoded by the AD-associated gene FERMT2. *Neurobiology of Aging*, *151*, 117–125. https://doi.org/10.1016/j.neurobiolaging.2025.04.009

This study identifies a new regulatory mechanism linking *FERMT2*, an AD–associated gene, to Aβ production. We show that KINDLIN2, the protein encoded by *FERMT2*, is cleaved by both calpain I and caspases. These proteolytic events separate the F0 and F1 domains of KINDLIN2, disrupting its normal role in modulating amyloid precursor protein (APP) processing. Loss of intact KINDLIN2 consequently alters APP cleavage dynamics and increases Aβ peptide production. By demonstrating that calpain- and caspase-dependent cleavage of KINDLIN2 negatively affects APP metabolism, we provide a mechanistic link between *FERMT2* genetic risk and amyloid pathology, highlighting KINDLIN2 stability as a potential therapeutic target in AD.

- Coulon, A., Siedlecki-Wullich, D., Najdek, C., Gelle, C., Ayral, A. M., Demiautte, F., Lambert, E., Vandeputte, A., Brodin, P., Mendes, T., Lambert, J. C., Kilinc, D., Dumont, J., & Chapuis, J. (2023). High-Content Screening of Synaptic Density Modulators in Primary Neuronal Cultures. *Current Protocols*, *3*(10), e904. https://doi.org/10.1002/cpz1.904

This technical paper describes a high-content screening approach to quantify synaptic density in primary hippocampal neurons following gene silencing. Using shRNA-mediated knockdown of AD–associated genes, we demonstrate that the high-throughput platform reliably identifies genetic modulators of synaptic connectivity. This method

provides a scalable tool for probing synaptic regulation and vulnerability in neurodegenerative contexts.

This work also led to the following communications:

- AAIC – Alzheimer's Association International Conference July 16-20th, 2023, Amsterdam, Netherlands
  Poster presentation: "Screening Alzheimer's genetic risk factor against Aβ-induced synaptotoxicity".

- Journée André Verbert – PhD Student Conference, November 13th, 2023, Université de Lille
  Poster presentation: "Screening Alzheimer's genetic risk factor against Aβ-induced synaptotoxicity".

- My thesis in 180 seconds – Institut Pasteur de Lille, October 10th, 2022
  Oral presentation: "Screening Alzheimer's genetic risk factor against Aβ-induced synaptotoxicity".

This work was recognised by the following prize:

- Prix Jeunes Chercheurs – France Alzheimer & Maladies Apparentées – 2024
  This prize supported the 4th year of my PhD.

Table of contents

List of figures

List of tables

List of abbreviations

ABCA7	ATP-binding cassette sub-family A member 7
ACSF	Artificial cerebrospinal fluid
AD	Alzheimer's disease
AICD	APP intracellular domain
AMPAR	α-amino-3-hydroxy-5-methyl-4-isoxazolepropionic acid (AMPA) receptor
APH1B	Aph-1B Gamma-Secretase Subunit
APOE	Apolipoprotein E
APP	Amyloid precursor protein
ARA-C	Cytosine arabinoside
ARFRP1	ADP-ribosylation factor-related protein 1
ARIA	Amyloid-related imaging abnormalities
ATP	Adenosine triphosphate
Aβ	Amyloid beta
Aβo	Amyloid beta oligomers
BCA	Bicinchoninic acid assay
BDNF	Brain-derived neurotrophic factor
BIN1	Bridging integrator 1
BSA	Bovine serum albumin
CaMKII	Calcium/calmodulin-dependent protein kinase II
cAMP	Cyclic adenosine monophosphate
CCNH	Cyclin H
CHO	Chinese hamster ovary
CIAO2A	Cytosolic iron-sulfur assembly component 2A
CLU	Clusterin
CM	Conditioned medium
CNPY4	Canopy FGF signalling regulator 4
CR1	Complement receptor 1
CREB	cAMP response element-binding protein
CSTF1	Cleavage stimulation factor subunit 1
CTF	C-terminal fragments
DAPI	4',6-diamidino-2-phenylindole
DIV	Days in vitro
DMEM	Dulbecco's Modified Eagle Medium
DNA	Deoxyribonucleic acid
E/LOADS	Early/Late-onset Alzheimer's disease
EAAT	Excitatory amino acid transporter
EADB	European Alzheimer's Disease Biobank
EDTA	Ethylenediaminetetraacetic acid

EGF	Epidermal growth factor
EPHA1	Ephrin type-A receptor 1
EPSP	Excitatory postsynaptic potential
FBS	Fetal bovine serum
FDA	Food and Drug Administration
FLII	Flightless I actin remodeling protein
FNBP4	Formin-binding protein 4
Fsk	Forskolin
GABA	γ-aminobutyric acid
GAPDH	Glyceraldehyde-3-phosphate dehydrogenase
GluA1 / GluA2	AMPA receptor subunits (glutamate receptor subunits A1 and A2)
GWAS	Genome-wide association study
HBEGF	Heparin-binding EGF-like growth factor
HBSS	Hank's Balanced Salt Solution
HCS	High content screening
HEPES	4-(2-hydroxyethyl)-1-piperazineethanesulfonic acid
HFS	High-frequency stimulation
HRP	Horseradish peroxidase
ICA1	Islet cell autoantigen 1
IF	Immunofluorescence
IPSP	Inhibitory postsynaptic potential
IQR	Interquartile range
KD	Knockdown
LDN	London APP mutation
LTD	Long-term depression
LTP	Long-term potentiation
MAD	Median absolute deviation
MAP2	Microtubule-associated protein 2
MAPK3	Mitogen-activated protein kinase 3
MCI	Mild cognitive impairment
MEA	Microelectrode array
MEM	Minimum Essential Medium
MOI	Multiplicity of infection
MOPS	3-(N-morpholino)propanesulfonic acid buffer
MTHFSD	Methenyltetrahydrofolate Synthetase Domain-containing protein
NBA	Neurobasal A
NFT	Neurofibrillary tangles
NMDAR	N-methyl-D-aspartate receptor (NMDA receptor)
NT	Non-targeting
OE	Overexpression

PBS	Phosphate-buffered saline
PDL	Poly-D-lysine
PDMS	Polydimethylsiloxane
PFA	Paraformaldehyde
PICALM	Phosphatidylinositol binding clathrin assembly protein
PKA	Protein kinase A
PKC	Protein kinase C
PPIB	Peptidylprolyl isomerase B
PSD	Postsynaptic density
PSD95	Postsynaptic density protein 95
PSEN1/2	Presenilin 1 and Presenilin 2
Rol	Rolipram
ROS	Reactive oxygen species
SAP25	Sin3A Associated Protein 25
sAPPα, sAPPβ	Soluble amyloid precursor protein α and, β fragments
SDS	Sodium dodecyl sulfate
SEM	Standard error of the mean
shRNA	Short hairpin RNA
SNP	Single nucleotide polymorphism
SORL1	Sortilin-related receptor 1
SRC	Proto-oncogene tyrosine-protein kinase Src
SYP	Synaptophysin
TBC1D20	TBC1 domain family member 20
TBS	Tris-buffered saline
TREM2	Triggering receptor expressed on myeloid cells 2
TRF2	Telomeric repeat-binding factor 2
WB	Western blot
WDR81	WD repeat domain 81
WT	Wild type
WWOX	WW domain-containing oxidoreductase
YWHAQ	Tyrosine 3-Monooxygenase/Tryptophan 5-Monooxygenase activation protein theta

1. INTRODUCTION

1.1 Alzheimer's disease

1.1.1 Disease presentation

Alzheimer's disease (AD) was first described in 1906 by the German physician and neuropathologist Alois Alzheimer. He studied a 51-year-old patient named Auguste Deter, who exhibited severe memory loss, confusion, and behavioural changes that were unusual for her age. After her death, Alzheimer examined her brain and reported a significant decrease in brain mass[1] along with other characteristic abnormalities that distinguished her condition from other known forms of dementia[2]. In modern terms, AD patients typically show a 20 to 25% reduction in cortical volume compared to healthy individuals. Hippocampal volume can also be decreased by up to 40% depending on disease stage[3]. Widened cortical sulci and gyral atrophy in the frontal and temporal cortices are usually observed while primary motor and somatosensory cortices are relatively spared[4]. Additionally, enlargement of the frontal and temporal horns of the lateral ventricles is common and reflects cortical atrophy[4]. Alongside this significant brain loss, Alzheimer found two microscopic brain lesions that were later recognised as the major pathological hallmarks of the disease: extracellular senile plaques (now known to be composed of amyloid-beta, Aβ), and intracellular neurofibrillary tangles (NFTs, later identified as aggregates of hyperphosphorylated Tau protein)[2] (Figure 1.1).

Initially, AD was considered a rare condition, often referred to as 'presenile dementia' because it was thought to primarily affect individuals under 65. However, during the 1970s and 1980s, researchers recognised that similar pathological changes also occurred in older patients, then referred to as senile dementia. Today, AD is the most common type of dementia and has a profound impact on society. In France in 2020, around 1.3 million individuals were affected, with more than 200,000 new cases every year[5]. Due to increasing life expectancy and demographic shift, the number of people living with AD is projected to double by 2050[6], placing immense economic pressure on healthcare systems, which already spend billions of euros annually on dementia care[7]. Additionally, millions of informal caregivers, often family members, provide unpaid support impacting workforce productivity and mental health[8]. These numbers

underscore the urgent need for effective interventions and societal preparedness to address the growing AD burden[9].

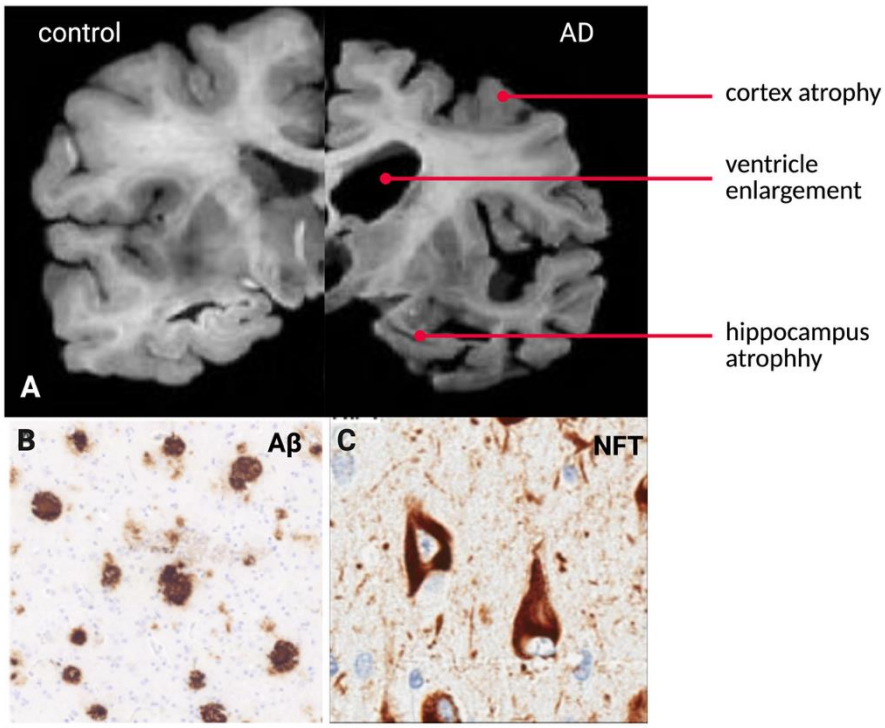

Figure 1.1. Pathological hallmarks of AD. (A) Post-mortem brain sections of healthy individuals and AD patients, highlighting the cortical atrophy observed in AD patients. (B, C) Immunohistochemistry of brain tissue from AD patients illustrating extracellular Aβ plaques (B), and intracellular NFTs (C). Adapted from Morales *et al.*, 2010 (panel A); Querol-Vilaseca *et al.*, 2019 (panel B); and Moloney *et al.*, 2021 (panel C)[10–12].

1.1.2 Clinical stages as a function of symptoms and biomarkers

AD is a slowly progressive neurodegenerative disease that causes irreversible memory loss, cognitive decline and language impairment, often described in three main clinical stages (Figure 1.2).

The preclinical phase is the earliest stage of AD and is characterised by the gradual accumulation of hallmark biomarkers in the absence of clinical symptoms[13–15]. Aβ peptides start to accumulate in the basal temporal and orbitofrontal neocortex while pre-tangled Tau develops first in the locus coeruleus and then spreads as NFTs to the entorhinal cortex[16,17]. This silent stage, that can last 10 to 20 years, has become a critical

focus for the development of disease-modifying therapies since significant neurodegeneration has often occurred by the time symptoms emerge[14,18].

The second clinical stage of AD is characterised by mild cognitive impairment (MCI) which involves deficits in memory, particularly episodic memory, and/or non-memory domains, such as executive tasks, including planning and organisation skills[19]. Additional neuropsychiatric symptoms such as depression or apathy may also emerge and are increasingly recognised as early indicators of underlying pathology[20]. At this stage, key biomarkers can be reliably detected[14,21] (e.g., positron emission tomography imaging detecting Aβ and Tau; and/or quantification of $A\beta_{1\text{-}42}$ and phosphorylated Tau proteins concentration in the cerebrospinal fluid), with Aβ spreading throughout the neocortex, hippocampal formation and amygdala while NFT pathology progresses from limbic cortex to association cortex[17,22]. Despite these changes, individuals in the MCI stage typically maintain functional independence and can still have a preserved quality of life[23].

The final stage of AD is the dementia phase, marked by significant cognitive decline that interferes with daily functioning. Clinical features include progressive memory loss, language impairment and often neuropsychiatric disorders like irritability or anxiety[14]. Although AD can be detected as early as the MCI stage, diagnosis is often made during the mild dementia stage when symptoms become more pronounced and begin to affect independence[14]. Diagnosis relies on a combination of neuropsychological assessments, neuroimaging and consideration of genetic and clinical history which also help to assess disease progression rate[24,25]. At this advanced stage, NFTs are typically widespread across most of the neocortex. As dementia progresses, many individuals require institutional care, particularly in the late stages, which are associated with loss of functional independence and severe cognitive impairment. At this point, patients often experience difficulties with eating, swallowing, walking, and other essential activities, necessitating constant medical care[26].

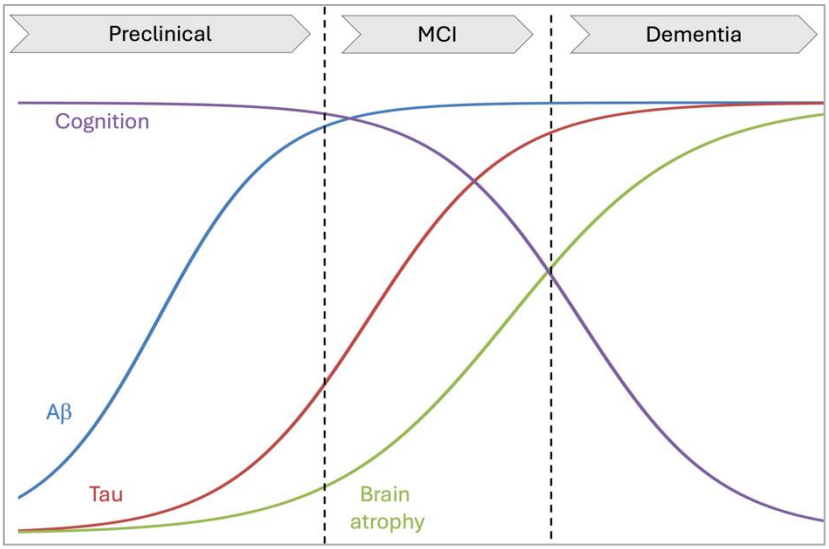

Figure 1.2. Temporal progression of AD hallmarks across to clinical stages. Schematic representation of the temporal evolution of Aβ (blue), Tau (red) and brain atrophy (green), in relation to cognitive decline (purple) across disease stages. Adapted from Kim *et al.*, 2021[27].

While clinical stages of AD are defined by symptomatic progression, biomarker dynamics follow their own temporal trajectory, with only partial overlap between the two. Among these biomarkers, Aβ and Tau accumulation exhibit distinct patterns of spatial and temporal spreading. While the progression of NFTs shows a stronger correlation with clinical stages of AD than Aβ deposition[28], several post-mortem studies have demonstrated that synaptic degeneration has the strongest correlation with cognitive deficits[29–32]. Although both Aβ and NFTs contribute to neuronal dysfunction and disease progression, this thesis focuses specifically on Aβ-induced synaptic toxicity. Given that Aβ is the earliest reliably detectable biomarker in AD, it is widely hypothesised to play a central role in disease pathogenesis. However, the molecular determinants that confer synaptic vulnerability or resilience to Aβ remain poorly understood, justifying the focus of this work.

1.1.3 The amyloid pathology

1.1.3.1 APP processing

APP is a type I transmembrane protein that can be proteolysed into various fragments, through several pathways, each generating metabolites that play distinct roles in the neuron (Figure 1.3). In the non-amyloidogenic pathway, APP is first cleaved by α-secretase, releasing sAPPα extracellularly and preventing the production of Aβ as the

cleavage site is located within the Aβ domain. sAPPα is generally considered neuroprotective against excitotoxicity[33] and is implicated in neurite outgrowth and synaptogenesis[34,35]. The remaining carboxyterminal fragment (CTF) is then cleaved by the γ-secretase, generating p3 and the APP intracellular domain (AICD). While p3 has no identified physiological role to date[36], AICD is a transcriptional regulator of apoptosis and cytoskeletal dynamics[37]. In physiological conditions, the non-amyloidogenic pathway represents the predominant pathway with *ca*. 90% of APP processing[38].

In the remaining cases, APP is processed through the amyloidogenic pathway, leading to the production of Aβ peptides[39]. Here, APP is first cleaved by β-secretase releasing a sAPPβ fragment, which is similar to sAPPα, but lacks the $A\beta_{1-16}$ region at its C-terminal end, and therefore does not retain the sAPPα-associated neuroprotective effect[40]. The remaining APP CTF is then cleaved by the γ-secretase, generating Aβ peptides of varying length (mainly $A\beta_{1-40}$ and $A\beta_{1-42}$) and an AICD fragment[39]. In AD, an imbalance between the amyloidogenic and non-amyloidogenic pathways, together with impaired clearance mechanisms, favours the accumulation of Aβ peptides, which aggregate into oligomers and eventually deposit as plaques[41].

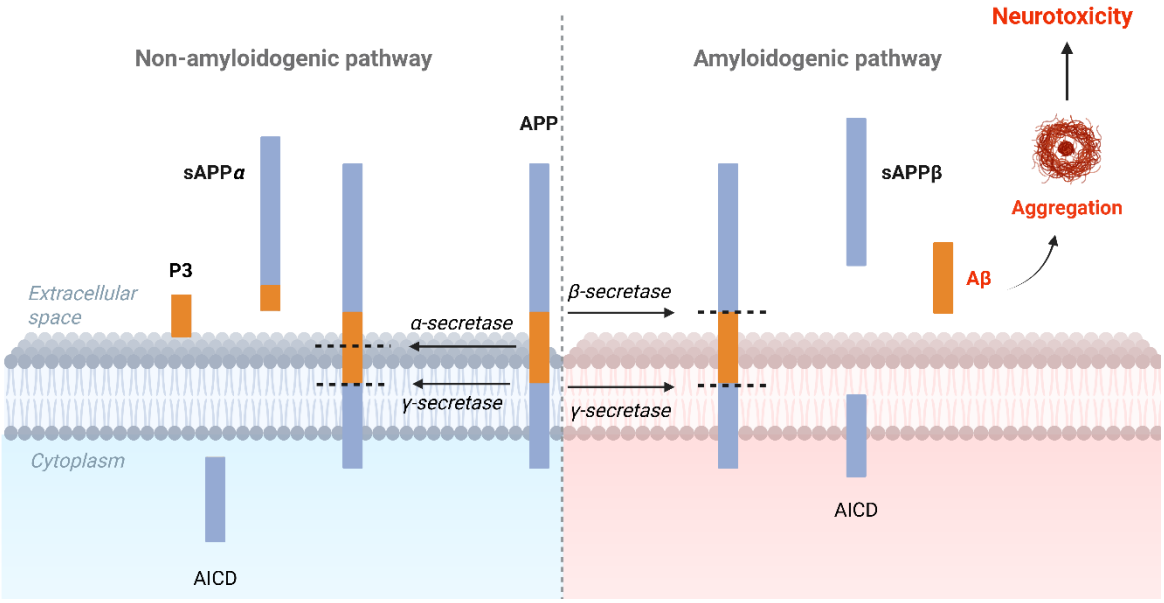

Figure 1.3. APP processing in the brain through non-amyloidogenic and amyloidogenic pathways, including the generated metabolites. Created in https://BioRender.com.

1.1.3.2 Aβ aggregation and toxicity

Once produced as soluble monomers, Aβ can adopt several different aggregation states, forming dimers, trimers, soluble oligomers, and protofibrils, before assembling into fibrils that deposit as plaques[42] (Figure 1.4). As monomers assemble into low molecular weight oligomers, their solubility decreases, promoting aggregation and contributing to enhanced toxicity[43]. Aβ peptides range from 37 to 43 amino acids and $Aβ_{1-40}$ is the most abundant type of Aβ peptide found in the healthy brain, while the relative concentration of $Aβ_{1-42}$ peptides is significantly increased in AD brains[44,45]. Characteristic fibrils and plaques that are observed in AD patient brains result from the accumulation of Aβ peptides and are enriched in $Aβ_{1-42}$, whose higher hydrophobicity compared to $Aβ_{1-40}$ promotes self-aggregation[46].

Soluble Aβ oligomers (Aβo) have been found in human brain extracts and can range from small assemblies such as dimers and trimers to higher-order species including dodecamers ($Aβ_{56}$)[47]. Among these, low molecular weight oligomers, particularly dimers and trimers, are established as the most toxic forms, and synaptic dysfunction correlates more strongly with Aβo than with plaque load[48]. Indeed, a study using patient brain extracts and hippocampal slice cultures suggested that Aβ dimers are the most potent form of Aβo to disrupt synaptic connections between neurons[49,50]. In parallel, higher molecular weight Aβo and insoluble fibrils are less acutely toxic and primarily contribute to the formation of plaques that could serve as Aβo reservoirs and indirectly sustain long-term toxicity[51,52]. Accumulation of Aβ, particularly in aggregated forms, also triggers chronic microglial activation resulting in sustained neuroinflammation, which further contributes to synaptic impairment[53–55].

Given that Aβo primarily target synapses, elucidating synaptic organisation and function is crucial to understanding their contribution to Aβo-associated deficits in learning and memory.

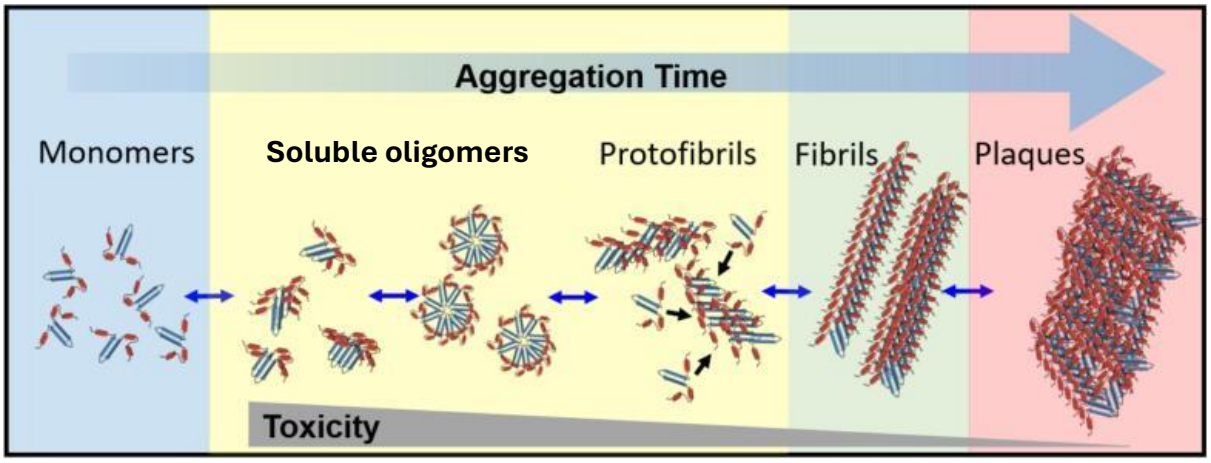

Figure 1.4. Aβ peptide oligomerisation and relative toxicity in AD. Aβ peptides can assemble into soluble oligomers that aggregate into protofibrils and fibrils to eventually form insoluble plaques. Low molecular weight oligomers are the most toxic forms of Aβ. Adapted from Dresser *et al.*, 2021[56].

1.2 Synapse vulnerability in AD

1.2.1 Synapse structure and function

Santiago Ramón y Cajal was the first scientist to propose that the brain is composed of individual cells, later called neurons. His work also suggested that neurons served as 'memory units' interconnected to form a dynamic network that could be modulated[57,58]. The connections between neurons were later named 'synapses' by Charles Scott Sherrington[59]. While early theories were initially dominated by the idea of purely electrical transmission, it is now established that most synapses rely on chemical transmission[58].

In the hippocampus, pyramidal neurons interconnected through excitatory glutamatergic synapses represent *ca*. 85 to 90% of the neuronal population, whereas inhibitory GABAergic interneurons account for the remaining 10 to 15%[60–64]. In the presynaptic terminal, vesicular glutamate transporters (VGLUTs) fill synaptic vesicles with neurotransmitters (e.g., glutamate in excitatory synapses) *via* an electrochemical gradient generated by the proton pump activity[65]. Vesicles then translocate and dock at the active zone of the presynaptic membrane, thereby becoming primed for release[66]. Upon stimulation, an action potential is generated at the axon initial segment and propagates along the axon to the presynaptic terminal[67,68]. There, membrane depolarisation triggers the opening of voltage-gated calcium channels, resulting in Ca^{2+}

influx that leads to the fusion and exocytosis of docked synaptic vesicles and the subsequent release of neurotransmitters into the synaptic cleft[69,70]. Emptied vesicles undergo endocytosis and are either recycled *via* endosomes or directly refilled with neurotransmitters[71].

In the synaptic cleft of excitatory synapses, glutamate binds to ionotropic receptors such as α-amino-3-hydroxy-5-methyl-4-isoxazole-propionic acid receptors (AMPARs) and N-methyl- D-aspartate receptors (NMDARs) located on dendritic spines[72,73]. Activation of these receptors induces excitatory postsynaptic potentials (EPSPs) which depolarises the postsynaptic membrane[74]. Conversely, inhibitory synapses generate inhibitory postsynaptic potentials (IPSPs) which hyperpolarise the postsynaptic membrane[75]. EPSPs and IPSPs are graded events and vary in amplitude and duration, depending on multiple factors including the amount of neurotransmitter released into the synaptic cleft and the availability and distribution of postsynaptic receptors[76–82]. Since a single postsynaptic neuron can receive input through multiple synapses, these potentials are summed to integrate all incoming signals. If the net depolarisation exceeds a threshold, the postsynaptic neuron generates an action potential; otherwise, it fails to fire an action potential[83,84]. Inhibitory inputs can prevent spiking by hyperpolarising the membrane or increasing conductance (shunting), thereby reducing excitatory drive.

For reliable signalling and to prevent excitotoxicity, neurotransmitters need to be quickly removed from the synaptic cleft[85]. In excitatory synapses, glutamate is cleared through excitatory amino acid transporters (EAAT1/GLAST and EAAT2/GLT-1) located on nearby astrocytes, which account for the majority of glutamate clearance[86]. Glutamate clearance is essential for synaptic health as inefficient clearance could cause postsynaptic receptors overstimulation, leading to excessive Ca^{2+} influx, oxidative stress and eventually neuronal death[87].

1.2.2 Synaptic plasticity

Synapses are fundamental units of neuronal communication and play a critical role in learning and memory. Throughout their lifespan, synapses undergo continuous structural

and functional remodelling in response to synaptic activity and experience-dependent stimuli, a process known as synaptic plasticity[88,89]. While long-term depression (LTD) weakens synaptic connections, long-term potentiation (LTP) strengthens them providing a bidirectional and dynamic balance essential for cognitive processing[90].

Synaptic response enhancement during LTP is tightly regulated by the number, localisation and properties of AMPA and NMDA receptors[91]. While AMPARs mediate rapid excitatory synaptic transmission, it is the activation of NMDARs that initiates the molecular cascade underlying LTP[92,93]. If presynaptic activity generates sufficient summed AMPAR-mediated EPSPs to induce a strong postsynaptic depolarisation, the voltage-dependent block of NMDARs by Mg^{2+} is removed, allowing substantial Ca^{2+} flow into the postsynaptic neuron[92,93]. This influx induces early-phase LTP (E-LTP) and activates several protein kinases like protein kinase A (PKA), protein kinase C (PKC) and calcium/calmodulin-dependent protein kinase II (CaMKII)[94–99]. These kinases then phosphorylate AMPARs at distinct sites, with PKA and CaMKII/PKC acting through complementary mechanisms that promote receptor recruitment and increase their conductance, amplifying the postsynaptic response[100–102]. While CaMKII is usually considered the central mediator of E-LTP by driving rapid phosphorylation and recruitment of AMPARs to the postsynaptic membrane, PKA also plays a prominent role in late-phase LTP (L-LTP) by promoting gene transcription and new protein synthesis required for long-term stabilisation of synaptic changes[98,103,104]. In this case, prolonged Ca^{2+} influx through NMDARs activates adenylyl cyclase, increasing cyclic adenosine monophosphate (cAMP) levels and subsequently activating PKA, which translocates to the nucleus to phosphorylate cAMP-responsive element-binding protein (CREB). Transcription of immediate early genes is then triggered, which directly reshapes synaptic structure (AMPARs recycling, dendritic remodelling, synaptogenesis) or serves as a transcriptional regulator required for synaptic strengthening[105–112]. Downstream of CREB phosphorylation, brain-derived neurotrophic factor (BDNF) and other transcription factors are also upregulated to sustain long-term synaptic changes and memory consolidation[113].

Overall, NMDAR-dependent LTP induces long-lasting synaptic changes by promoting (1) the recruitment and stabilisation of AMPARs at the postsynaptic membrane; (2) an enhanced synaptic response due to increased AMPAR-mediated currents; and (3) structural remodelling including dendritic spine enlargement and, under some conditions, synaptogenesis[92,93,114–116]. Indeed, several electron microscopy studies have established the correlation between spine size and synaptic AMPAR number[73,117,118]. Thus, the availability of AMPARs serves as a critical molecular switch governing the direction and persistence of synaptic plasticity.

Postsynaptic AMPARs are key players in the maintenance of L-LTP as the main kinases driving LTP have a downstream effect on AMPAR number, conductance or phosphorylation state[119] (Figure 1.5). AMPARs are tetrameric structures assembled from combinations of four different subunits (GluA1/2/3/4)[120]. The combination of these subunits defines the receptor properties such as ion permeability and agonist affinity[121,122]. In adult hippocampal neurons, the majority of AMPARs, *ca*. 80%, are composed of GluA1/GluA2 heterodimers, while the remaining AMPARs consist predominantly of GluA2/GluA3 heterodimers[123]. The C-terminal regions of AMPAR subunits are highly divergent and undergo post-translational modifications, such as phosphorylation/dephosphorylation, which are essential determinants of synaptic potentiation[119].

Indeed, AMPAR trafficking during synaptic potentiation is known to be regulated by the PKA-dependent phosphorylation of the Serine 845 (Ser845) residue of the GluA1 subunit, which promotes surface expression and availability[124–128]. In the absence of neuronal activity, AMPARs undergo constitutive recycling between the synaptic membrane and the cytosol, where they are either marked for degradation or reinserted into synapses[129,130]. However, during E-LTP, this recycling becomes more active and is routed through an endosomal pathway at extrasynaptic sites to enhance exocytosis and promote receptor insertion[128,131]. This also allows the synapse to have a pool of 'primed receptors' ready to be incorporated into the synaptic membrane[132]. Upon NMDARs activation, Ser845-phosphorylated extrasynaptic AMPARs diffuse to the synapse site to be integrated into the postsynaptic density (PSD)[131]. Anchored AMPAR receptors can also be

phosphorylated at the Serine 831 (Ser831) residue by CaMKII or PKC, which further enhances synaptic transmission by increasing receptor conductance *via* improving the coupling efficiency between glutamate binding and channel opening[94–96,99].

In contrast, long-term depression (LTD), typically triggered by low-frequency stimulation, leads to the internalisation and removal of AMPARs from the postsynaptic membrane, resulting in weakened synaptic transmission and potentially contributing to synapse elimination[90]. This occurs through dephosphorylation of GluA1 by the calcium-dependent phosphatase calcineurin[128,133,134] and/or phosphorylation of Serine 880 (Ser880) residue on the GluA2 subunit[135,136], which disrupts receptor anchoring to the PSD and thereby favours endocytosis[137,138].

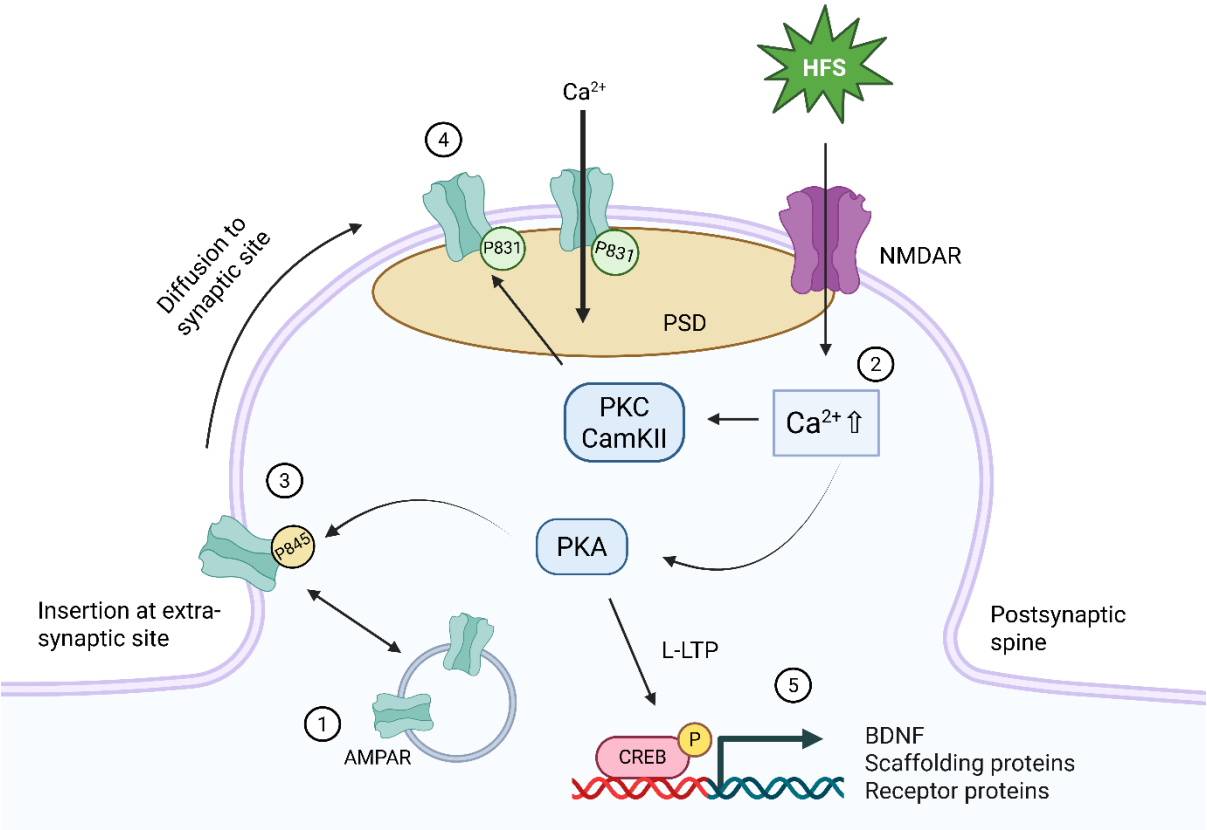

Figure 1.5. AMPARs trafficking during LTP. (1) In basal conditions, AMPARs are constantly inserted at extra-synaptic sites and recycled in endosomes. (2) Upon stimulation (i.e. HFS), NMDARs allow Ca^{2+} flow into the dendritic spine which induces E-LTP and activates several kinases. (3) PKA is first activated and phosphorylates Ser845 of the AMPAR-GluA1 subunit on the spine membrane, which then laterally diffuses to the synaptic site towards the PSD. (4) PKC and CaMKII then phosphorylate Ser831 residue to enhance receptor conductance and contribute to their anchoring to the PSD. (5) The resulting increase in Ca^{2+} influx also allows PKA to phosphorylate CREB, and initiate the transcription of several synaptic proteins, which is necessary for L-LTP induction and synaptic maintenance. Note that events 3, 4 and 5 happen simultaneously. Created in https://BioRender.com.

Synapses, which are essential for neuronal communication and the encoding of learning and memory, are also the earliest structures to be affected in AD[30,31]. Numerous proteomic and genomic analyses using samples from AD patients and transgenic mouse models have revealed early downregulation of critical genes for synaptic maintenance and function, encompassing multiple of signalling pathways including synaptic vesicle machinery, exocytosis and endocytosis, calcium binding and cytoskeletal dynamics[139–145]. Specifically, it has been shown that Aβo disrupts PKA-dependent AMPAR phosphorylation and trafficking, leading to synaptic plasticity impairment, a major feature of AD pathogenesis.

1.2.3 Aβo-induced synaptic dysfunction

Multiple studies have demonstrated that Aβo are highly detrimental for synapses where the number and volume of dendritic spines are often greatly reduced[29,146–148]. Consistently, levels of the presynaptic marker Synaptophysin (SYP) were reported to be decreased by 25%-55% in the hippocampus and neocortex of AD patients compared to healthy controls[149]. Notably, Aβo appear to bind preferentially to synaptic sites, with a particular affinity for the postsynaptic compartment. In cultured hippocampal neurons exposed to Aβo derived from synthetic preparations, AD brain extracts, or cerebrospinal fluid (CSF), the majority of Aβo puncta colocalise with PSD95, a key postsynaptic scaffolding protein[150,151]. This morphological observation was complemented by sub-fractionation and ELISA assays, reinforcing the association of Aβo to PSD, rather than to presynaptic active zones[152]. Prolonged exposure to Aβo induces major loss of PSD95[152,153] and abnormal spine morphology, including a temporary increase in the proportion of long, thin spines and a decrease in mushroom-shaped spines, which are characteristics of mature, stable spines[152]. Additionally, transient enlargement of synaptic boutons was observed as some dendritic spines become elongated, suggesting that Aβo may contribute to a maladaptive, transient compensatory response in synapses[152,154]. This aligns with the idea that early stages of synaptic dysfunction in AD involve an adaptive enlargement of presynaptic terminals[155].

This structural disruption extends beyond dendritic spines as neurite dystrophy can be found near Aβ plaques[154,156,157]. It remains unclear whether the accumulation of pathological peptides causes neurite swelling or if the malformed neurites promote plaque formation and expansion. It is most likely that the soluble $A\beta_{1\text{-}42}$ in the vicinity of the plaques increases the abundance of dystrophic neurites[156,158]. Amyloid pathology disrupts the balance between spine formation and elimination, ultimately leading to decreased spine density[159–161]. Both neurite dystrophy and spine loss may be attributed to disturbances in Ca^{2+} homeostasis –an essential regulator of dendritic development and synaptic plasticity[162,163]. In AD, dendrites located near plaques exhibit elevated intracellular Ca^{2+} levels, resulting in the reduction of glutamate receptors essential for synaptic plasticity and LTP[164].

Comparative transcriptomic studies across three different AD transgenic mouse models at two disease stages have revealed a strong concordance between transcriptional up- and down-regulation observed in human brains[139,145]. Upregulated genes include those involved in calcium homeostasis, kinase-mediated signalling, growth factor pathways, transcription regulation, oxidative stress defence, lysosomal function and inflammation. On the other hand, downregulated genes affect kinase and phosphatase signalling, ion channel proteins, metabolic and mitochondrial enzymes, transcription and translation, as well as synaptic vesicle transport. Particularly relevant to the synapse failure hypothesis, early downregulation of genes encoding postsynaptic NMDA and AMPA receptors, in addition to potassium and calcium channels were observed [139,165–167].

Aβo-induced synaptic toxicity is mainly induced by the increased postsynaptic intracellular Ca^{2+} levels through two separate mechanisms: disruption of the glutamate homeostasis and recruitment of extrasynaptic NMDARs. First, glutamate homeostasis is compromised due to impaired astrocytic glutamate uptake, notably *via* EAAT2 (GLT-1), the main astrocytic glutamate transporter, resulting in the sustained accumulation of extracellular glutamate within the synaptic cleft[168,169]. Concurrently, Aβo interacts with presynaptic calcium channels, altering their gating properties and causing abnormal rises in intracellular calcium[170]. This leads to excessive spontaneous neurotransmitter release followed by depletion of the readily releasable vesicle pool, thereby disturbing

the balance between spontaneous and evoked glutamate release and impairing reliable synaptic transmission[171,172]. Second, Aβo binds to cell-surface prion protein (PrP^C), recruiting Fyn kinase[173,174]. Fyn then phosphorylates extrasynaptic NMDARs containing the GluN2B subunit, enhancing receptor conductance and promoting its trafficking to the synaptic membrane[175]. Increased number and redistribution of NMDARs amplify Ca^{2+} influx upon glutamate activation[176,177]. Taken together, the reduced glutamate clearance and excess presynaptic release raise glutamate levels and set the stage for AMPA and NMDA receptors' overactivation and excitotoxicity, which is exacerbated by enhanced NMDARs surface retention [171,178–180].

The resulting excessive Ca^{2+} influx profoundly alters the balance of kinase, phosphatase and protease dynamics causing an initial increase in postsynaptic receptors activation followed by a synaptic desensitisation and internalisation eventually leading to synaptic depression[181] (Figure 1.6). Calcium-dependent proteases like calpains are activated and cleave cytoskeletal proteins and neurofilaments, disrupting dendritic spines and axon terminals[182]. Calpains also degrade key synaptic scaffold proteins that are essential for postsynaptic receptor anchoring, such as PSD95[183].

In parallel, phosphatases such as phosphatase 2A and calcineurin become overactive and dephosphorylate Ser845 on the AMPAR GluA1 subunit[166], while PKC phosphorylates Ser880 on GluA2[184]. Taken together, these post-translational modifications reduce receptor conductance and promote receptor internalisation, which decreases available AMPARs[185]. Calcineurin also dephosphorylates CREB, diminishing transcriptional support for synaptic proteins and spine maintenance[186]. As CREB directly regulates BDNF expression, its downregulation reduces activation of TrkB receptors on dendritic spines, impairing multiple downstream pathways required for synaptic strength and survival[187]. Moreover, Ca^{2+} overload disrupts mitochondrial function by impairing ATP synthesis and increasing reactive oxygen species (ROS) production, which further drives synaptic dysfunction[188]. Oxidative modifications damage glutamate receptors, transporters, mitochondria, and cytoskeletal proteins needed for spine integrity further amplifying the cycle of synaptic dysfunction[189].

In summary, Aβo-induced synapse dysfunction is largely driven by synaptic overstimulation and excitotoxicity which trigger endocytosis, ubiquitination and degradation of AMPARs and thereby weakens the postsynaptic response[166,190–192].

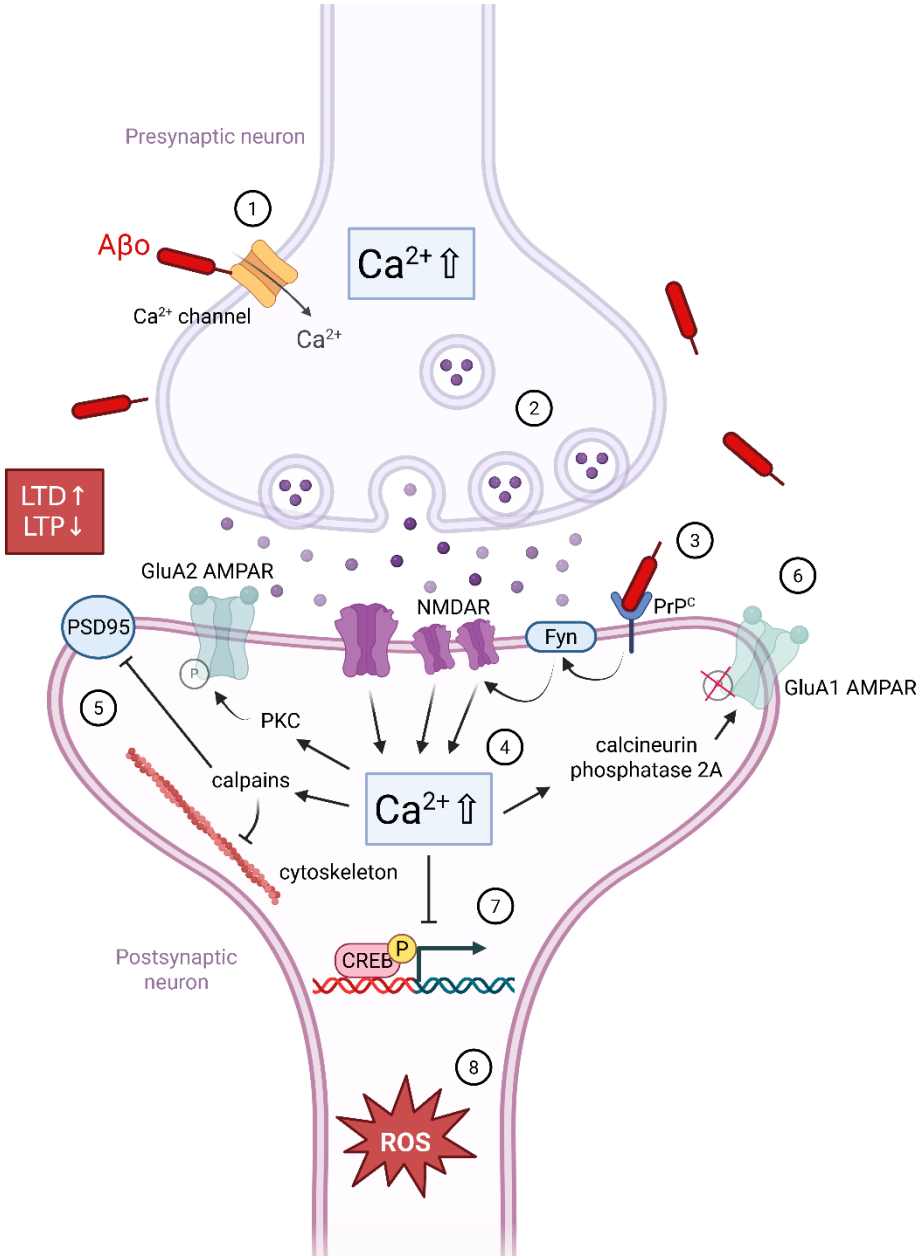

Figure 1.6. Aβo-induced synaptotoxicity. (1-4) Aβo induces excitotoxicity *via* multiple mechanisms. (1) Aβo modulates presynaptic voltage-gated Ca^{2+} channels, resulting in enhanced Ca^{2+} influx, (2) which increases the probability of presynaptic vesicle release, leading to elevated glutamate levels in the synaptic cleft. (3) Aβo interacts with PrP^C which activates Fyn and recruits additional NMDARs to the postsynaptic membrane. (4) NMDAR-driven Ca^{2+} influx rises intracellular Ca^{2+} levels. (5-8) Excitotoxicity decreases synaptic output and impairs synaptic transmission. (5) Spine structure is destabilised due to calpain-mediated cleavage of neurofilaments and PSD95. (6) AMPARs are internalised through dephosphorylation of GluA1 subunits and phosphorylation of GluA2 subunits. (7) CREB is dephosphorylated which inhibits the transcription of synaptic maintenance proteins. (8)

Mitochondrial respiration is impaired leading to the production of pro-inflammatory ROS. Adapted from Tzioras *et al.*, 2022[193]. Created in https://BioRender.com.

1.2.4 Therapeutic approaches targeting synaptic dysfunction and Aβ pathology

AD treatment includes a range of therapeutic strategies designed to alleviate symptoms, slow down disease progression, and target the underlying pathological processes. Until 2021, only four symptomatic treatments had received US Food and Drug Administration (FDA) approval, either aimed at facilitating synaptic transmission or alleviating Aβo-induced synaptic dysfunction. These drugs primarily offered temporary improvements in cognition and memory, without halting or reversing disease progression. Additionally, as the disease progresses, higher doses are often required, increasing the risk of secondary neuropsychiatric, cardiovascular and gastrointestinal side effects.

Among these, Donepezil, Galantamine and Rivastigmine – all acetylcholinesterase inhibitors – are prescribed for the mild to moderate stages of AD[194–196]. These agents work by inhibiting cholinesterase, thereby increasing the availability of acetylcholine in cholinergic synapses, enhancing synaptic transmission[197]. In contrast, Memantine, an uncompetitive NMDAR antagonist, is used to treat symptoms of moderate to severe forms of the disease[198]. Memantine preferentially blocks pathological NMDAR activation, reducing excessive Ca^{2+} influx and downstream neuronal loss, while sparing normal synaptic transmission.

In 2021, Aducanumab, the first disease-modifying treatment for AD, was approved by the FDA[199]. This selective monoclonal antibody targets aggregated Aβ species, including soluble oligomers and insoluble fibrils, facilitating clearance[200]. However, despite the significant reduction of Aβ in the brain at high doses, clinical benefits of Aducanumab were unclear, and treatment was associated with a substantial incidence of amyloid-related imaging abnormalities (ARIA), sparking major controversy about its safety and efficacy[201,202].

More recently, promising monoclonal amyloid immunotherapies have emerged that significantly reduce brain amyloid load. Indeed, Lecanemab and Donanemab have been

shown to slow cognitive decline by 27% and 35% respectively, compared to placebo[203,204]. Both drugs have been approved by both the FDA and the European Medicines Agency (EMA), but the latter approved the use of Donanemab only in *APOE*-ε4 heterozygotes or non-carriers[203–205].

Even though substantial advances have been made in AD treatment over the past decade, the available therapies are still unable to cure the disease, and only decelerate its progression at best. Given the complex and multifactorial nature of AD pathogenesis, combination therapies that target multiple molecular and cellular pathways will likely be essential to achieve meaningful clinical benefit. Maximising therapeutic efficacy will depend on early intervention, which in turn requires a more comprehensive understanding of the genetic and molecular mechanisms underlying disease risk and progression. Indeed, AD genetic studies have been essential for clarifying AD aetiology, revealing both rare, high-penetrance mutations that cause familial forms and common risk variants that influence susceptibility in the general population.

1.3 Genetics of AD: from risk factors to synapse pathology

1.3.1 Familial and sporadic forms

Despite the extensive knowledge of AD pathology, less than 1% of cases described in developed countries have a clear and definite cause and are associated with rare autosomal dominant mutations with Mendelian inheritance in three genes linked to the generation of Aβ peptides: *APP*, presenilin 1 (*PSEN1*) and presenilin 2 (*PSEN2*)[206–209]. These monogenic forms of the disease are termed familial AD (fAD), whereas the remaining vast majority of cases make up the so-called sporadic AD (sAD). fAD forms are typically characterised by an early age of onset (EOAD, often expressing itself before 55 years of age) and are associated with faster disease progression[210]. Mutations in *APP* linked to fAD are primarily concentrated around the γ-secretase cleavage site, with codon 717 representing a frequent mutational hotspot[206,211,212]. Valine-to-Isoleucine missense mutation (V717I), referred to as the London mutation (LDN), was one of the first described *APP* mutations associated with fAD[206]. This mutation promotes the production of longer $A\beta_{1\text{-}42}$ peptides, which are more prone to aggregation and neuronal toxicity[44].

Indeed, Aβ quantification in both *in vitro* and *in vivo* models showed that both cellular and transgenic mouse models carrying the LDN mutation display an increase in $A\beta_{1-42}/A\beta_{1-40}$ ratio, since $A\beta_{1-42}$ production is greatly enhanced[213–215]. In contrast, sAD forms usually present as a late-onset form of the disease (LOAD), which affects adults over 65 years with no familial aggregation[216].

AD is the most common type of dementia and is a multifactorial disease resulting from the combination of environmental and genetic risk factors[217]. Indeed, a recent study identified up to 14 modifiable risk factors for dementia regardless of APOE genetic status. Sedentary and unhealthy lifestyle habits including excessive alcohol consumption or smoking, history of head injury, and untreated, common, age-related comorbidities, such as diabetes, hypercholesterolemia, hypertension and depression, greatly increase the risk of developing age-related dementia[218] – including AD.

However, the greatest risk factor of AD remains age, followed by sex, as a recent meta-analyses reported that disease prevalence is significantly higher in women (*ca*. 7%) than in men (*ca*. 3%)[219]. Genetic background is also an essential factor influencing an individual's risk of developing AD, with genetic heritability estimated between 58% and 79%, as demonstrated by a twin study[217].

Further evidence for the role of genetic predisposition in AD risk is provided by the Apolipoprotein E (APOE) gene, which exists in three common allelic forms: ε2, ε3, and ε4. The ε4 allele significantly increases the risk of developing AD in a dose-dependent manner—heterozygous carriers (ε3/ε4) have an approximately 3-fold increased risk compared to non-carriers, whereas homozygous carriers (ε4/ε4) have up to a 12-fold increase[220]. Conversely, the ε2 allele appears to exert a protective effect, while ε3 is considered neutral with respect to disease risk[221]. Notably, around 40% of sporadic AD cases carry at least one ε4 allele, despite its relatively low frequency (*ca*. 15%) in the general population[222,223]. Identification of genetic risk factors is therefore essential for the early detection of individuals at risk and for the development of adequate preventive therapies. APOE was the only confirmed genetic risk factor for AD until 2009, when

genome-wide association studies (GWAS) became available and revolutionised the understanding of AD genetics.

1.3.2 Contributions of GWAS to our understanding of AD genetics

GWAS is a research approach used to identify genetic variants across the entire genome that are statistically associated with a specific phenotype (*i.e.*, AD in this case). This involves comparing the frequencies of single nucleotide polymorphisms (SNPs) between patient genomes and healthy individuals' genomes. Unlike previous technologies used for genetic variant identification, GWAS does not require preconceived functional hypotheses and rely on genome-wide SNP arrays to assess hundreds of thousands of SNPs at once. The first two GWAS for AD involved between 8,000- 10,000 individuals and identified 3 genomic *loci* within *CLU*, *CR1* and *PICALM* regions –in addition to *APOE*– that were associated with the risk of developing AD[224,225]. Several other GWAS were independently conducted after this, identifying many more risk *loci,* including *BIN1*[226], *SORL1*[227] and *TREM2*[228,229]. Finally, in 2022, the host laboratory published the most comprehensive list of genetic risk factors associated with AD to-date[230]. This meta-GWAS analysis contained almost 800,000 samples and had a stronger statistical power due to the inclusion of a new dataset from the European Alzheimer & Dementia Biobank (EADB) consortium and proxy cases (*i.e.*, individuals with at least one parent with dementia). In this study, a total of 75 risk *loci* (including 42 new ones), encompassing more than 350 genes, have been identified (Figure 1.7).

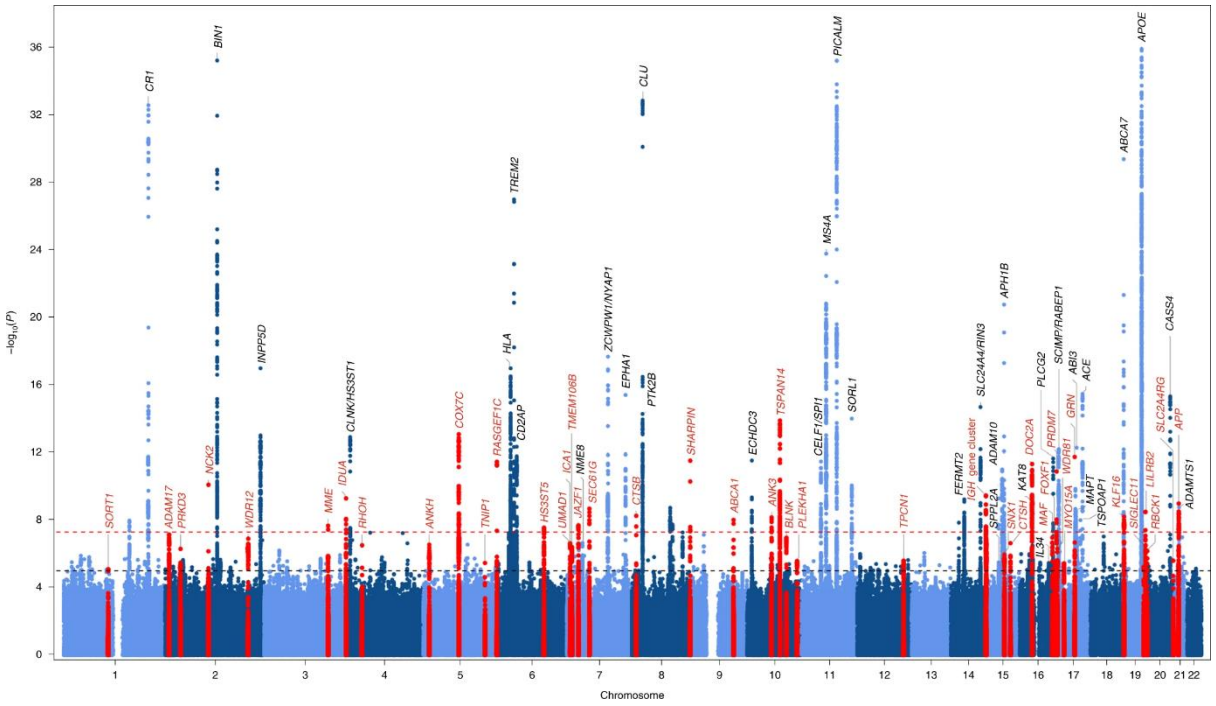

Figure 1.7. Genetic risk *loci* associated with the risk of developing AD. Manhattan plot displaying the genetic variants identified *via* GWAS according to their position along chromosomes (x-axis) and corresponding p-value (y-axis). The red and black dotted lines represent genome-wide ($p < 5\times10^{-8}$) and suggestive ($p < 1\times10^{-5}$) significance respectively. Newly identified *loci* are shown in red. For plotting purposes, p-value for APOE is shown at a lower value. From Bellenguez *et al.*, 2022[230].

1.3.3 From the amyloid cascade hypothesis to synapse-centred models

At least a third of the 75 risk *loci* contain genes that are directly associated with the amyloid pathology which re-emphasises the amyloid cascade hypothesis[230]. This hypothesis suggests that the accumulation of Aβ peptides drives AD development and acts upstream of other AD hallmarks. According to this hypothesis, abnormal processing of APP leads to the overproduction of Aβ while impaired clearance mechanisms further contribute to Aβ peptide accumulation resulting in plaque formations that trigger a series of downstream events, such as NFTs aggregation, neuroinflammation, synaptic dysfunction and eventually neuronal death[231] (Figure 1.8).

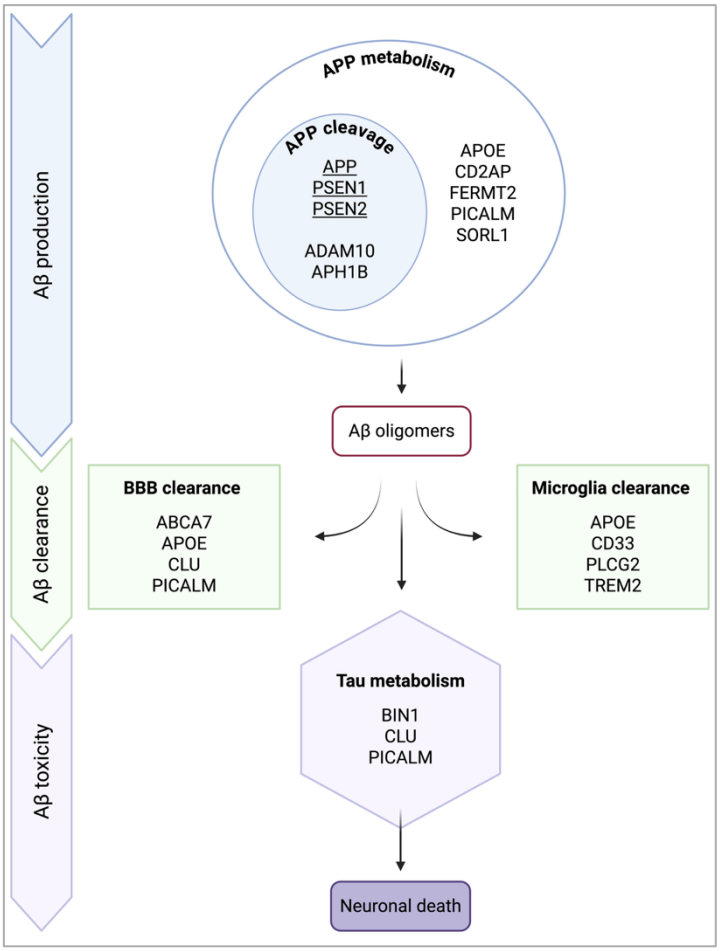

Figure 1.8. AD genetic risk factors involved in the amyloid cascade hypothesis. Numerous risk factors identified through GWAS modulate the amyloid pathology by influencing Aβ production, clearance or toxicity. Genes responsible for the familial forms of AD are underlined. Adapted from Dourlen *et al.*, 2019 [209]. Created in https://BioRender.com.

However, given the complex, multifactorial and polygenic nature of AD, a simple linear cause-effect model appears overly reductive. For instance, the severity of cognitive decline in AD patients does not correlate well with the Aβ deposition pattern[28]. This is underscored by the observation that many elderly individuals with substantial cerebral Aβ accumulation remain cognitively intact[232,233]. Moreover, transgenic mouse models engineered to overproduce Aβ through APP mutations or overexpression have reliably developed amyloid plaques but failed to recapitulate the core AD hallmarks such as NFTs and widespread neuronal loss, indicating that Aβ accumulation alone is not sufficient to drive the full pathological cascade[234].

Therefore, a more comprehensive and dynamic framework for understanding AD pathology has been proposed, in which dysfunction of the focal adhesion pathway has been suggested to play a key role in synaptic dysfunction[209] (Figure 1.9). Indeed, a considerable group of GWAS-identified risk genes, including *APP*, are involved in this pathway, which regulates actin remodelling, dendritic spine morphology, and synaptic stability[235,236]. This perspective highlights APP's physiological role in synaptic plasticity, beyond its role as a source of Aβ. In this model, synaptic dysfunction is considered the primary driver of AD pathology, aligning with the strong correlation between synaptic loss and cognitive decline observed in patients[28]. Importantly, synaptic failure may arise from a distinct set of factors, such as impaired APP metabolism, Aβ overproduction or reduced Aβ clearance, or Tau-mediated excitotoxicity, each capable of triggering the others, in a self-reinforcing cycle[209].

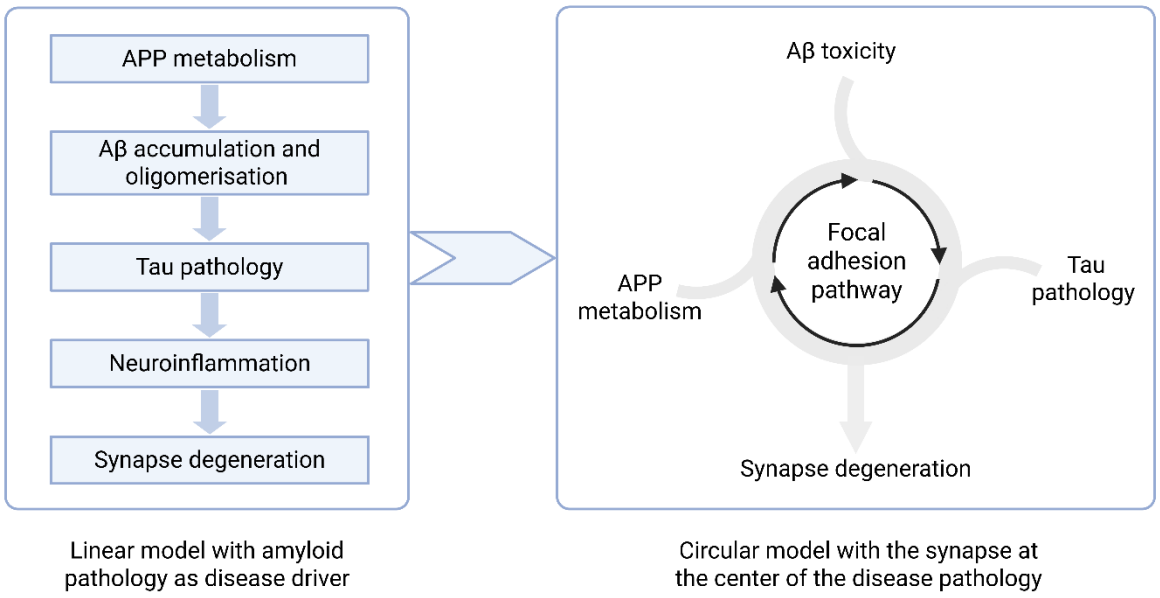

Figure 1.9. From the amyloid cascade hypothesis to a synapse-centred disease pathology. Adapted from Dourlen *et al.*, 2019 [209]. Created in https://BioRender.com.

Taken together, even if the amyloid cascade hypothesis is based on strong biochemical, genetic and histopathological evidence, it remains an incomplete model of AD as it fails to fully account for the complexity of sporadic forms. This is why an alternative circular, multi-entry model has been proposed, linking the different pathologies and hallmarks of AD to synapse degeneration and cognitive decline. In this thesis, I investigated the impact

of GWAS-defined genetic risk factors on synaptic dysfunction induced by Aβ through medium-throughput, high-content gene screening.

1.3.4 High-content screening approach for post-GWAS studies

The development of GWAS has substantially expanded the number of genes of interest for AD, which in turn requires new approaches to determine their contribution to disease mechanisms. The high-content screening (HCS) approach is a relevant and powerful strategy to systematically characterise the pathological functions of these genes[237]. HCS is an automated, microscopy-based technique that combines medium- or high-throughput screening with quantitative image analysis to assess multiple cellular parameters simultaneously. Unlike traditional assays that usually measure a single endpoint, HCS enables the extraction of multiparametric data such as cell morphology, protein localisation or organelle integrity, at the single-cell level across thousands of conditions. This makes HCS particularly powerful for functional genomics, drug discovery, and the systematic characterisation of gene functions in complex biological processes[238].

Therefore, the host laboratory conducted a high-content shRNA screen to investigate the potential role of previously GWAS-identified genetic risk factors in AD pathology, focusing particularly on synaptic effects[209,230,239]. This study generated a priority list of AD genetic risk factors whose knockdown leads to a significant beneficial or detrimental change in synapse density. Another study from the host laboratory defined synaptic connectivity as the proportion of co-localised pre- and postsynaptic puncta with greater overlap indicating more robust synapses and demonstrated that exposure of Aβo decreases synaptic connectivity[240]. Based on the hypothesis that the modulation of AD risk genes may be protective for synapses, the overall objective of this thesis is to further screen these risk factors in an AD-relevant *in vitro* model, by exposing synapses to Aβo, to uncover their potential contribution to disease mechanisms. Protective genes identified in this study will ultimately be considered as therapeutic targets in the future.

2. OBJECTIVES

Within this context, the overall aim of this thesis is to determine the role of AD genetic risk factors in Aβ-induced synaptic toxicity. My hypothesis is that modulating the expression levels of potential AD risk genes, whose knockdown impacts synaptic connectivity, may protect synapses from Aβ-induced impairment of synaptic structure and function. This thesis is divided into three aims:

- AIM 1: To identify genes that protect synapses against Aβ-induced synaptic dysfunction by screening the top 10% of AD risk genes whose silencing had the strongest impact on synaptic connectivity in the initial shRNA screen, through modulation of their expression in neurons co-cultured with Chinese hamster ovary (CHO) cells that actively secrete Aβ in microfluidic devices.

- AIM 2: To validate the protective effect of candidate genes identified in Aim 1 by assessing their ability to block Aβ-induced synaptic dysfunction, using high-resolution confocal microscopy in microfluidic devices and, whenever possible, *via* pharmacological inhibition of the gene product.

- AIM 3: To functionally characterise the validated hits using microelectrode arrays (MEAs) to assess network activity and plasticity-like responses, induced experimentally by high-frequency stimulation of presynaptic neurons or by chemical long-term potentiation (cLTP).

3. MATERIALS & METHODS

Composition of buffers in boldface are detailed in Table S2 in the Appendix.

3.1 Gene selection from the shRNA screening

The shRNA screen had been conducted in two parts, namely Screen #1 and Screen #2, each at two different MOIs (MOI = 2 and MOI = 4). The genes in Screen #1 originate from a list of 175 genes previously identified as potential risk factors for AD through GWAS[209]. Using the data from the Allen Brain Atlas Middle Temporal Gyrus Data Set ("Human MTG SMART-seq"; brain-map.org), only genes expressed in the brain had been selected. Non-coding genes and genes without any rat orthologues had been excluded, resulting in a total of 105 selected genes assessed in Screen #1. The genes in Screen #2 originate from a list of 31 *loci* encompassing 145 additional genes identified by the EADB consortium[230]. Due to budget restrictions, only genes with an average neural and/or astrocytic expression level (*i.e.*, the ratio of expression level of a gene compared to the total expression level of all the other genes in these cell types) greater than 0.1 had been selected. As for Screen #1, non-coding genes and genes without any rat orthologues had been excluded, resulting in a total of 93 genes assessed in Screen #2. A total of 198 genes (105 genes from Screen #1 and 93 genes from Screen #2) had thus been selected for this high-content shRNA screening (see Coulon *et al.*, 2024[241] for details).

As defined under Aim 1, the medium-throughput screen was based on the co-culture of primary neurons with CHO cells overexpressing APP. Previous work from the host lab determined that Aβo-induced synaptotoxicity in the co-culture model decreased the distance-based assignment of postsynaptic puncta to presynaptic puncta (*%SYP_assigned*), without impacting the density of presynaptic puncta (SYP density)[240]. For this reason, AD risk genes from the shRNA screen were shortlisted based on their impact on *%SYP_assigned*, with minimal impact on SYP density. The following criteria were defined: (i) SYP density should be within median ± 3 × median absolute deviations (MAD) and (ii) *%SYP_assigned* should be above or below the quadratic curve that passes through intersection of median ± 3 × MAD for *%SYP_assigned* and median ± 3 × MAD for SYP density and has its apex at ± 1.9 × MAD for *%SYP_assigned* (see Figure 4.2). The use of a quadratic curve instead of simple cut-off lines (as in the case for SYP density)

permitted us to keep the number of genes shortlisted within the range imposed by feasibility and cost constraints, while remaining objective.

3.2 Microfluidics preparation

Microfluidic devices used are summarised in Table S3 in the Appendix. Master patterns were fabricated at the Institute of Electronics, Microelectronics and Nanotechnology in Lille using two-step photolithography as previously described[242,243]. Master microfluidic devices were cast in polydimethylsiloxane (PDMS) *via* soft lithography. Master devices were then used to create reusable replicates made of polyglass 26/71 resin (Esprit Composite, France). These replicates were then used to generate copies of PDMS microfluidic devices for cell culture. The standard microfluidic design (referred to as the U-device) is composed of two 750-µm-wide, 3.6-mm-long neuronal chambers (named pre- and postsynaptic chambers) interconnected with a 300-µm-wide, 7.4-mm-long central chamber (the synaptic chamber) by two sets of parallel microchannels[240]. All three chambers are *ca*. 100-µm-high. 4-µm-high, 450-µm-long parallel microchannels that narrow from an entry width of 10 µm to an exit width of 3 µm connect the presynaptic chamber and the synaptic chamber. Parallel microchannels with identical height and width but shorter length (75-µm-long) connect the postsynaptic chamber to the synaptic chamber.

The co-culture version of the U-device is referred to as the X-device and contains two neuronal chambers interconnected to a central synaptic chamber, as well as an additional 8 mm^2 co-culture chamber, positioned on one end of the synaptic chamber (Table S3). The co-culture chamber was fluidically connected to the synaptic chamber *via* 4-µm-high, 10-µm-wide and 100-µm-long parallel microchannels. For the medium-throughput screening, a co-culture screening device (referred to as the D-device) was adapted from the X-device to reduce overall footprint. The D-device consists of two identical microfluidic units, each combining four X-devices into one microfluidic circuit. In this combined circuits, the co-culture chambers of the X-devices were replaced by a common, 14.2 mm^2 diamond-shaped co-culture chamber. This chamber was fluidically connected to the four synaptic chambers *via* parallel microchannels with similar

dimensions to the ones of the X-device (Figure 3.1).

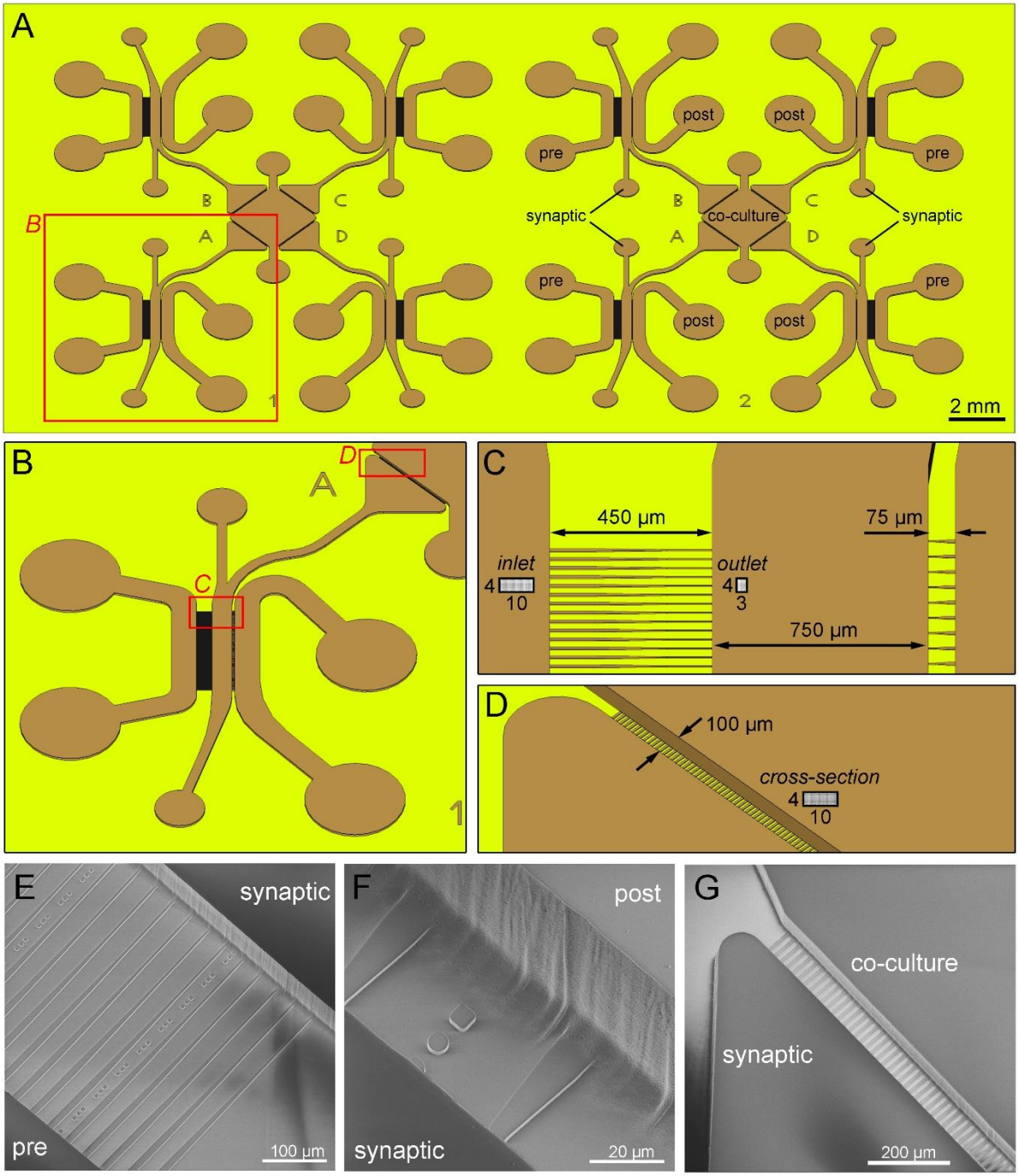

Figure 3.1. Design of the microfluidic co-culture system adapted for screening applications. (A) Microfluidic co-culture screening device (D-device) consists of two identical 4-in-1 X-devices, each comprising pre- and postsynaptic chambers interconnected to a central synaptic chamber which is further fluidically linked to a central, diamond-shaped co-culture chamber. (B) 2× magnification of the boxed area in panel A, showing the device layout with left, middle and right chambers corresponding to presynaptic, synaptic and postsynaptic chambers, respectively. (C) 10× magnification of the lower boxed area in panel B, illustrating the microchannels dimensions. (D) 8× magnification of the upper boxed area in panel B, showing the microchannels connecting the synaptic and the co-culture chambers. (E-G) Electron micrographs of the long (E), short (F) and co-culture chamber (G) microchannels.

Access wells were punched in the D-device at the extremities of the pre- and postsynaptic chambers using a Ø4-mm biopsy punch and of the synaptic and co-culture chambers using a Ø3-mm biopsy punch (Ted Pella, Inc., Redding, USA). The devices were washed with isopropanol before being permanently bonded onto 36 mm × 60 mm glass coverslips (260460-100, Ted Pella) using an O_2 plasma generator (Diener; Ebhausen, Germany). The devices were then sterilised under ultraviolet light (Light Progress; Anghiari, Italy) for 30 min, treated with 0.1 mg/ml poly-D-lysine (Sigma) overnight and rinsed with PBS.

3.3 Microfluidic device integration with MEAs

We used 256-electrode MEA chips (256MEA100/30iR-ITO-w/o, MultiChannel Systems, Reutlingen, Germany) where electrodes form a 16×16 Cartesian grid, except for the corners where the tips of large, triangular reference electrodes are positioned. As previously done for 60-electrode MEA chips[244], we adapted the U microfluidic device layout by adding a triangular chamber between the flow channels connecting synaptic and postsynaptic chambers to their respective medium reservoirs. This chamber corresponds to the tip of one reference electrode of the MEA chip such that the reference electrode is fluidically connected to the rest of the device. To minimise the effect of this reference electrode chamber on fluid flow in the aforementioned channels, we used sets of parallel microchannels (18-µm width; 7-µm separation) for the connections. These MEA-adapted microfluidic devices (called the V-device; Figure 3.2) were prepared in the same way as the U- and D-devices and align-bonded to MEA chips using O_2 plasma.

To position similar numbers of microelectrodes underneath pre- and postsynaptic chambers, we used a mechanical tool to precisely align the microfluidic device over the MEA chip[244]. Briefly, after O_2 plasma exposure, the MEA chip was placed on a manual stage allowing rotation and two-axis translation in the *xy*-plane (Newport; Irvine, CA). The microfluidic device was held above the MEA chip with a vacuum pen (Virtual Industries Inc.; Colorado Springs, CO) that was attached to manual *z*-axis translational stage. Using binoculars, the microfluidic device was then aligned with the MEA chip in a way that pre- and postsynaptic chambers were covered by *ca*. 50 electrodes each. The device was then

lowered onto the MEA chip until contact was established, and the integrated device was placed in a 70°C oven for 2 min to strengthen the bond. The MEA-integrated V-devices were placed in Ø100 mm polystyrene Petri dishes and sterilised and coated in the same way as other microfluidic devices. A Ø35-mm Petri dish containing sterile Milli-Q water was placed next to the MEA chips to minimise evaporation.

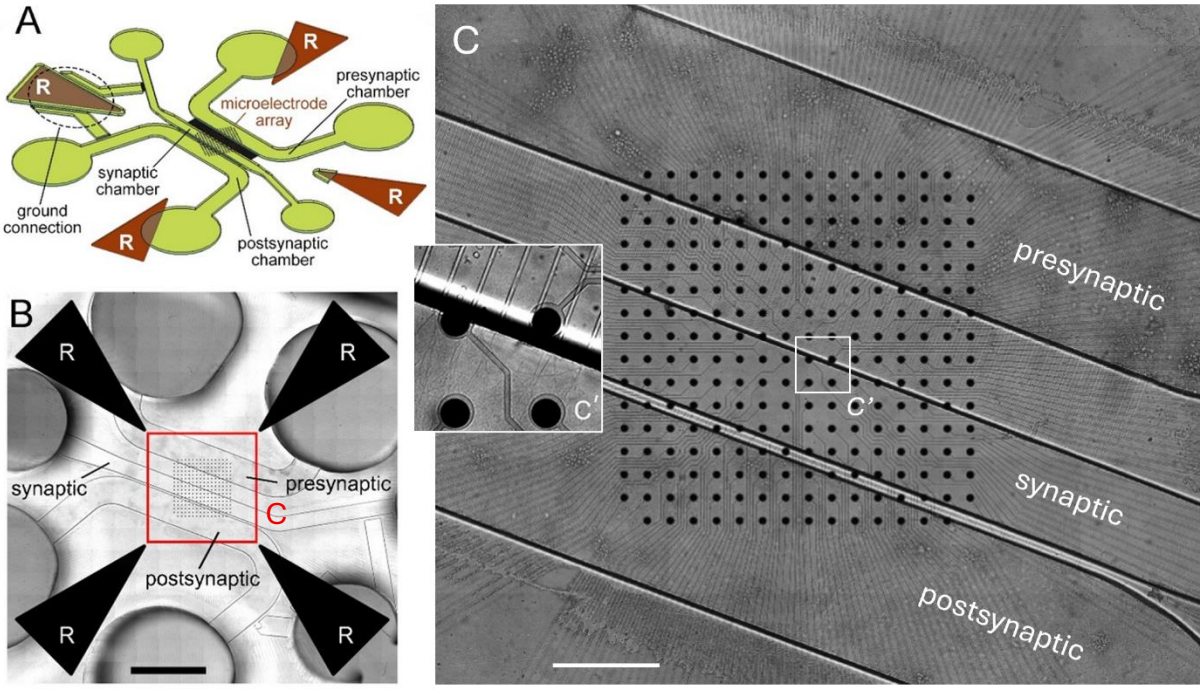

Figure 3.2. Microfluidic integration with MEA. (A) Cartoon showing the overlay of a V-device and the 256-electrode MEA layout. Reference electrodes are marked with 'R'. (B) Mosaic image of the MEA-integrated V-device seeded with rat hippocampal neurons. Scale bar = 2 mm. (C) Boxed area in panel C at higher magnification showing the distribution of electrodes across pre- and postsynaptic chambers (*i.e.*, *ca*. 50 electrodes per chamber). Scale bar = 500 µm. (C') Zoomed area is 3.4× magnified and showing axons from the presynaptic chamber exiting the "long" microchannels. Adapted from Lefebvre et *al.*, 2024[244].

3.4 CHO cells transfection and maintenance

CHO-K1 (CCL61, ATCC) were transfected with pcDNA4 vectors containing hAPP695WT or hAPP695LDN to generate stable line of CHO cells overexpressing the wild-type form of APP (CHO-APP-WT) or the APP variant carrying the LDN mutation (CHO-APP-LDN). The plasmid construct was a kind gift of Frédéric Checler's laboratory[243]. Plasmids were amplified using chemically competent *E. coli* One Shot Stbl3 (C737303, Invitrogen) according to manufacturer's instructions. Following recovery, 200 µL of the transformation mixture was plated on Lennox L Broth (LB) Agar (37 g/L, 22700025,

Invitrogen) plates supplemented with 50 µg/mL ampicillin and left overnight at 37°C. The following day isolated colonies were inoculated into 100 mL of LB Broth (12780029, Invitrogen) containing 50 µg/ml ampicillin and left overnight at 37°C with 200 rpm agitation. Plasmid DNA was then extracted using Nucleobond Xtra Midi (740410.100, Marcherey-Nagel) high copy protocol according to manufacturer's instructions.

In parallel, CHO cell lines were grown in 75 cm^2 tissue culture flasks (353136, Corning) in **CHO growth medium** until 80% confluence, at which point the cells were washed with PBS and incubated with 0.05% Trypsin (25300-054, Gibco) for 3 min at 37°C. Trypsinisation was then inhibited with CHO growth medium, and cells were resuspended, counted using a haemacytometer and 100,000 cells were seeded in fresh flasks. Cells were then stably transfected with 6 µg of cDNA construct using Lipofectamine 2000 (11668019, ThermoFisher) according to supplier's instructions. Clones were then selected using 250 µg/mL Zeocin (Invitrogen). Isolated colonies were then picked, and clones were grown in individual wells to be later characterised.

3.5 CHO-clone characterisation

When clones reached confluency, cells were lysed in ice-cold **lysis buffer** and immunoblotted to quantify APP protein levels. Clones with the highest APP expression were chosen to produce conditioned media (CM) to investigate Aβ production. Concentration of total amyloid ($Aβ_{1-X}$) was then quantified using AlphaLISA (AL288C, Revvity) according to manufacturer's recommendations. When necessary, samples were diluted in the dilution buffer provided with the kit to remain within the linear range of the standard curve. The APP-LDN clone was chosen for its pronounced increase in total Aβ levels compared to the APP-WT clone.

3.6 Primary culture

Culture media and supplements were purchased from ThermoFisher unless specified otherwise. Primary neurons were obtained from P0 (postnatal day 0) rats as previously described[245]. Cortices and hippocampi were isolated and washed with ice-cold **dissection medium** and treated with 2.5% Trypsin at 37°C for 10 min. The trypsin was

then inactivated using **MEM/FBS medium** supplemented with DNase (0.08 mg/mL; DN25-100MG, Sigma) for 1 min to minimise cell clumping, followed by 3 washes with MEM/FBS medium. The cells were then dissociated in **NBA culture medium** before being centrifuged at 200× *g* for 8 min to remove debris. Cells were then resuspended in culture medium and counted. Cortical cells were then plated in **poly-D-lysine** (PDL) pre-coated plates or dishes for immunoblotting or synaptic fractionation, respectively. Cell seeding densities for cortical cultures are given in Table 3.1.

Table 3.1. Cortical cell seeding densities in multi-well plates and Petri dishes.

	Ø10-cm dishes	12-well plates	24-well plates
Cells per dish / well	1.0×10^7	2.5×10^5	1.9×10^5
Cell density (cells/cm^2)	1.3×10^5	6.6×10^4	1×10^5

Hippocampal cells were concentrated at 2.5×10^7 cells/mL and seeded both in the pre- and postsynaptic chambers (5.0×10^4 cells per chamber). Culture medium was half replaced the next day to remove cellular debris and replenish nutrients. Water supplemented with 0.1% ethylenediaminetetraacetic acid (EDTA), to limit bacterial growth, was added to the Petri dishes containing microfluidic devices to minimise evaporation. At DIV4, neurons were treated with 1.5 µM cytosine arabinoside (Ara-C; C1768-100MG; Sigma Aldrich) to limit astrocyte proliferation. All neuronal cultures were maintained in a humidified tissue culture incubator (Panasonic; Osaka, Japan) at 37°C and 5% CO_2 for up to 21 days and medium was half replaced every week.

3.7 Neuron / CHO cell co-cultures

CHO cells (1.0×10^4 cells per chamber) were seeded in the co-culture chamber of the D-device and maintained in CHO growth medium two to three days prior to neuron seeding to ensure uniform cell distribution in the whole co-culture chamber. Primary neurons were then plated in the pre- and postsynaptic chambers as described previously for monocultures and maintained in **CHO-NBA medium**, allowing chronic exposure of the synaptic network to physiologically secreted Aβ forms. Media in the reservoirs of the presynaptic, postsynaptic and synaptic chambers were half replaced every week, while medium in reservoirs of the co-culture chamber was replaced fully twice a week. Co-cultures were maintained at 37°C and 5% CO_2 for up to 21 days.

3.8 Lentiviral transduction

Plasmid design and subsequent virus production was outsourced to Vector Builder (Chicago, IL, USA). When plasmid glycerol stock was readily available from other sources, lentiviral production was outsourced to VECT'UB (Bordeaux, France). Vectors were designed according to the plasmid diagram shown in Figure 3.3.

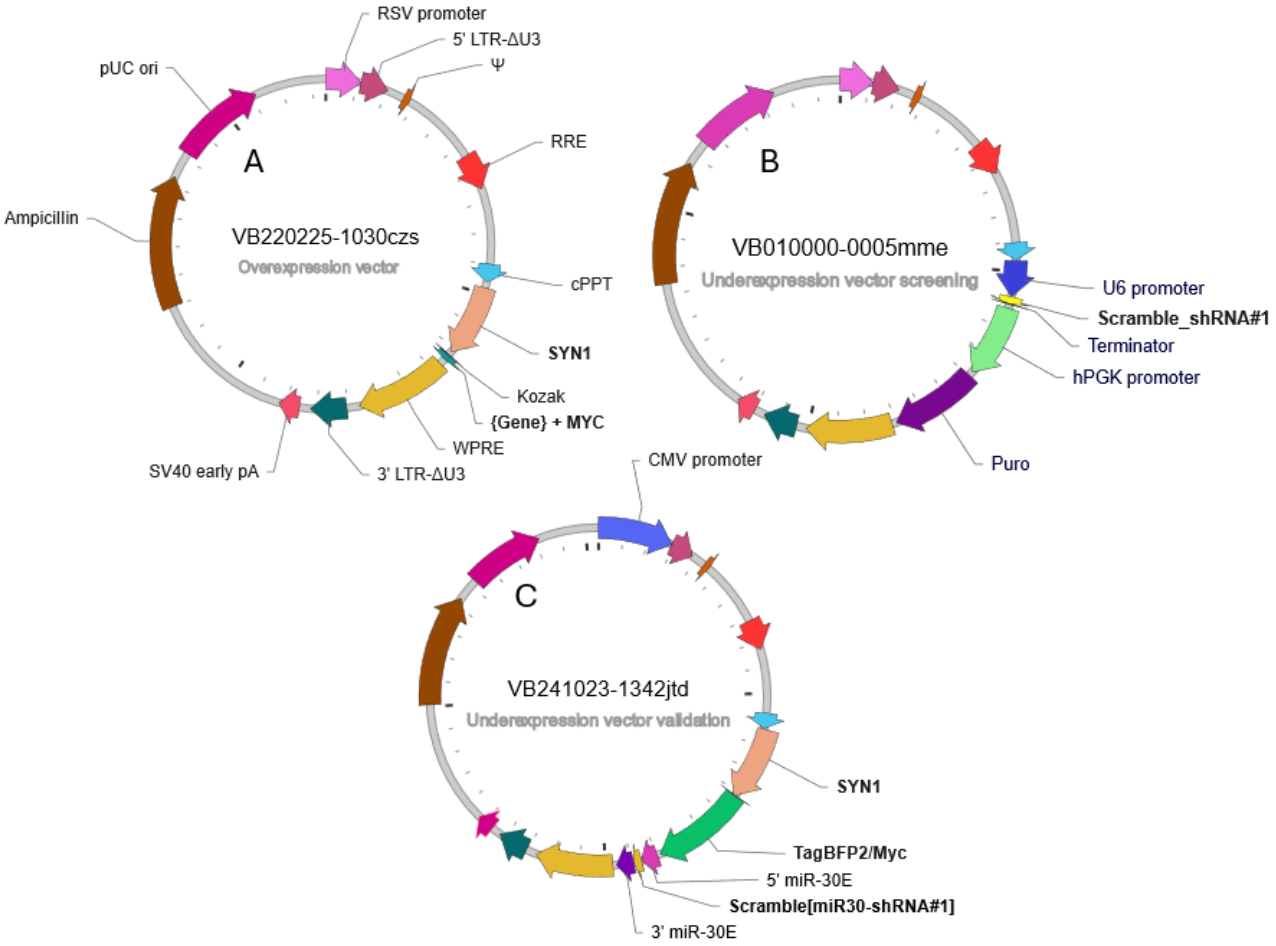

Figure 3.3. Representative lentiviral vector construction. (A) Overexpression vector with Synapsin1 (Syn1) promotor and Myc tag fused to the protein of interest. (B) Knockdown vector with U6 promotor used in the previous HCS[241]. (C) Knockdown vector with Syn1 promotor and BFP2/Myc tag used in the hit validation experiments.

At DIV7, neurons in microfluidic devices and well plates were transduced as previously described[246]. The transduction was performed at optimal MOI (ranging from MOI 0.5 to 10) depending on the virus construct. Optimal MOI was determined as the lowest MOI that significantly increased target protein expression without causing evident axonal degeneration. Lentiviral particles were diluted in pre-warmed appropriate medium – *i.e.*,

CHO-NBA for co-cultures and NBA for well plates and other microfluidic experiments. Viral particles were first diluted in fresh culture medium to prepare a 5× viral suspension. For transduction, this suspension was added to both well-plates and microfluidic devices at 1:4 ratio. Neurons were incubated with viral particles for 6 h and then the wells were topped up with the remaining collected medium.

In microfluidic devices, to prevent viral particles from diffusing into the co-culture chamber or to the non-transduced neuron chamber, a hydrostatic pressure gradient was imposed across the microchannels that connect the chamber intended for transduction and the adjacent synaptic chambers. To this end, media from pre- post- and synaptic wells were collected and pooled in a common tube. A total of 25, 15 and 20 µL of the collected media were returned to non-transduced, synaptic, and transduced chambers, respectively. Medium from the co-culture chamber was discarded to avoid cross-contamination of CHO cell secretion to neuronal chambers and 25 µL of fresh CHO-NBA was added to each well. It should be noted that, due to *ca*. 2-fold difference in the surface area between the reservoirs of synaptic and neuronal chambers, 15 µL medium volume in a synaptic well corresponds to a greater medium height (and thus greater hydrostatic pressure) than that of 20 µL medium volume in a neuronal well.

3.9 Conditioned media generation and exposure to neurons

CHO-APP-WT and CHO-APP-LDN cells were plated in Ø10-cm Petri dish (353003, Corning) and maintained in CHO growth medium. At 80% confluency, CHO-growth medium was replaced with CHO-NBA medium and collected 48 h later. CM was centrifuged at 3000× *g* at 4°C for 10 min to remove cell debris. The supernatant was then concentrated 50-fold using a 3-kDa spin column (Amicon ultra, UFC900324, Merck) by centrifugation at 3000× *g* at 4°C for 1 h. Total protein concentration was measured using Pierce BCA protein assay kit (23225, ThermoFisher). Total Aβ concentration was then quantified using AlphaLISA Aβ-1X kit (AL288C, Revvity) after adjusting for total protein mass among different samples. CM was then aliquoted in microcentrifuge tubes to avoid freeze/thaw cycles between experiments and kept at -80°C for until use. Several Aβ toxicity paradigms were applied on neurons differing in CM Aβ concentration and

treatment duration and frequency (Table 3.2).

Table 3.2. Experimental paradigms for Aβ treatment using CHO-APP CM.

Paradigm #	$Aβ_{1-X}$ concentration	Duration	Treatment frequency
1	60 nM	6 days	Every 24h
2	120 nM	3 days	
3	500 nM	24 hours	One-time

On the first treatment day, *i.e.*, DIV15; DIV18 or DIV20 for 60 nM; 120 nM or 500 nM treatments, respectively, aliquots of both CHO-APP-WT and CHO-APP-LDN CM were thawed on ice and vortexed for 30 s immediately before use. NBA medium from the synaptic chambers was collected and pooled into a common tube. The CM was then diluted in the collected NBA medium to reach the desired final $Aβ_{1-X}$ concentration. A total of 30 µL of diluted CM was added back into each synaptic chamber.

As demonstrated previously in the host laboratory, the half-life of endogenously secreted Aβ is about 24 hours[240]. Therefore, paradigms 1 and 2 required Aβ replenishment every 24 h to maximise treatment effectiveness and reduce fluctuations in Aβ concentration. Cultures were then maintained until fixation at DIV21.

3.10 Synaptic stimulation

For both cLTP and cLTD induction, NBA medium was replaced with pre-warmed complete artificial cerebrospinal fluid (ACSF) containing $MgCl_2$ for 30 min to stabilise baseline ionic conditions and minimise variability in basal phosphorylation levels. At resting membrane potential, extracellular Mg^{2+} blocks the NMDAR channel pore in a voltage-dependent manner, thereby preventing Ca2+ influx. cLTP and cLTD were then induced with distinct compounds.

3.10.1 cLTP induction

cLTP was induced by treating the cells for 10 min with forskolin (FSK; 50 µM in DMSO; 1099, Tocris) and rolipram (Rol; 0.1 µM in DMSO; 0905, Tocris) in Mg^{2+}-free ACSF, to remove the voltage-dependent block of NMDARs and facilitate permissive calcium

signalling, although the primary induction mechanism relies on cAMP/PKA activation. cLTP treatment was then replaced with complete ACSF for the 50-min-long recovery period prior to cell lysis or cell fixation, to allow stabilisation of downstream signalling and receptor trafficking before analysis[247]. While FSK directly activates adenylyl cyclase, the enzyme that converts ATP to cAMP, Rol inhibits phosphodiesterase-4, an enzyme that breaks down cAMP. When used together, these two drugs produce a strong and sustained elevation of cAMP levels, leading to robust PKA-mediated phosphorylation of the Ser845 residue of the GluA1 subunit[127,248–250]. DMSO in Mg^{2+}-free ACSF was used as vehicle. For microfluidic devices, FSK/Rol or DMSO solutions were introduced selectively to the postsynaptic chamber, while presynaptic and synaptic chambers were treated with vehicle.

3.10.2 cLTD induction

cLTD was induced by treating the cells for 5 min with N-methyl-D-aspartic acid (NMDA; 50 µM in H_2O; M3262-25MG, Merck) and Glycine (Gly; 10 µM in H_2O; G8790, Sigma) in Mg^{2+}-free ACSF. The resulting moderate and transient elevation of intracellular calcium levels through the NMDAR channels is widely interpreted to preferentially engage the calcineurin/PP1 phosphatase cascade rather than kinase pathways leading to the dephosphorylation of AMPAR subunits and endocytosis of surface AMPARs, a hallmark of LTD[251,252]. Following treatment, cells rapidly returned to complete ACSF for a 15-min-long recovery period prior to cell lysis. This brief NMDA/Gly pulse is widely used to reproduce an NMDA-dependant cLTD in neuronal cultures without inducing excitotoxicity, allowing the detection of early phosphorylation changes and subsequent AMPAR trafficking events by Western blot[253].

3.11 Synaptic fractionation

To verify the presence of ARFRP1 in pre- and postsynaptic compartments, we performed subcellular fractionation as previously described[254]. All steps were done on ice. At DIV14, cortical neurons were resuspended and scraped from the culture dish in a **neutral buffer**, which preserves organelle integrity, and centrifuged at 1000× *g* for 10 min to remove nuclei and cellular debris. The resulting supernatant was centrifuged at a higher

speed (12,000× *g* for 20 min) to eliminate the cytosolic fraction, leaving a pellet enriched in synaptic components. This pellet was then resuspended in an **EDTA buffer** and centrifuged twice at 12,000× *g* for 20 min to minimise residual cytosolic contamination. The washed pellet was subsequently reconstituted in a **HEPES-Triton buffer** and was gently agitated at 4°C for 1 h, and centrifuged at 12,000× *g* for 20 min. The resulting supernatant represented the non-PSD fraction (Triton-soluble). The remaining pellet was finally resuspended in a **denaturation buffer** containing a combination of detergents that promote protein denaturation, thereby solubilising the highly crosslinked PSD. After agitation at 4°C for 1 h and centrifugation at 12,000× *g* for 15 min, the supernatant was collected as the PSD fraction (Triton-insoluble).

3.12 Immunoblotting

Cell lysates were first sonicated at 80% amplitude (FB120EUK-220, ThermoFisher) for 15 s before being centrifuged at 10,000× *g* at 4°C for 10 min to remove cellular debris. Total protein concentration of the supernatant was quantified using Pierce BCA protein assay kit (23225, ThermoFisher). Lysates were mixed with 4× LDS sample buffer (Novex; ThermoFisher) and 10× reducing agent (Novex), then heated at 95°C for 10 min to denature proteins.

A total of 8 µg of protein was loaded into 1.0-mm-thick, 12-well or 1.5-mm-thick, 15-well, 4-12% Bis-Tris precast NuPage gel (Novex; ThermoFisher) along with 5 µl of molecular weight marker (Novex Sharp pre-stained protein standard). The gel was run with 3-(N-Morpholino) propanesulfonic acid running buffer (MOPS) at 120 V constant voltage for 1 h and transferred to a 0.22-µm nitrocellulose membrane using the Trans-Blot Turbo transfer system (BioRad, Hercules, CA, USA) using mixed molecular-weight method (1.3 A and 25 V for 7 min). Protein transfer was then checked with Ponceau S before being washed with H_2O. Membranes were blocked with 5% non-fat dry milk diluted in **Tris-buffered saline** (TBS) at RT for 1 h to prevent non-specific antibody binding and then washed three times with TBS containing 0.1% Tween20 (TBS-T). All membranes were cut at the 60 kDa marker, allowing simultaneous incubation of antibodies: the upper portion of the membrane was probed for the protein of interest, while the lower portion was

incubated with the antibody against the protein used as loading control (e.g., β-actin). Primary antibodies were diluted in the appropriate buffer (see Tables S4 in Appendix) and incubated overnight at 4°C. The next day, membranes were washed three times with TBS-T and incubated with horseradish peroxidase (HRP)-conjugated secondary antibodies in TBS containing 5% non-fat dry milk for 1 h at RT (see Tables S5 in Appendix). After three final TBS-T washes, membranes were developed by chemiluminescence (Luminata Classico, EMD Merck Millipore) and imaged with Amersham Imager 600 (GE Healthcare, Mississauga, Canada). Band intensities were quantified by densitometric analysis using ImageJ software (National Institutes of Health, Bethesda, Maryland, USA).

3.13 Immunofluorescence

Cells in microfluidic devices were fixed in 4% PFA as previously described and permeabilised in 0.3% Triton X-100 in PBS for 5 min. After blocking non-specific antibody-binding sites in 5% normal donkey serum in PBS, samples were incubated overnight at 4°C with the primary antibodies diluted in PBS (see Tables S4 in Appendix). Cells were then rinsed with PBS, incubated with the secondary antibodies at RT for 2 h and rinsed twice more in PBS (see Tables S5 in Appendix). Devices were mounted with 90% glycerol (G5516-1L, Sigma) and kept at 4°C, protected from light, for short term imaging. Due to host-species mismatch, a pre-conjugated synaptophysin (101011c2; Synaptic System) antibody was used when staining cultures in D-devices by incubation at RT for 2 h after incubation with secondary antibodies.

3.14 Imaging and image processing

For the medium-throughput screening, microfluidic devices were imaged using the automated IN Cell Analyzer 6000 with a 60× objective in the confocal mode at 5 different z-levels, taking a mosaic of 64 fields per synaptic chamber in four different wavelengths (405 nm, 488 nm, 594 nm and 647 nm) to image Tau, SYP, Homer and PSD95 respectively. Up to four screening devices could be imaged at once by fitting four coverslips into a custom coverslip holder with the same outer dimensions of a standard multi-well plate (Figure 3.4). Maximum intensity projections of each stack were generated for synaptic connectivity quantification. Then, unwanted areas from each field (e.g., microchannels,

astrocytes or neuronal cell bodies that crossed through the microchannels) were masked out using a custom ImageJ macro, before importing masked images into the Columbus software (Revvity, USA) for quantitative image analysis.

For other experiments, microfluidic devices were imaged using a spinning disk confocal microscope (Nikon XLightV3, Crest Optics) equipped with a 60× 1.42 NA oil-immersion objective. Five images per microfluidic device were acquired in the synaptic chamber close to the short microchannels, where dendrites extending from the postsynaptic chamber are found. *Z*-stacks with 0.2 µm step were taken at several emission wavelengths (405 nm, 488 nm, 594 nm and 647nm). Images were then deconvolved using Huygens Professional (Scientific Volume Imaging B.V., Hilversum, Netherlands) to enhance signal-to-noise ratio. Then, signals in each channel were segmented into distinct volumes using the "surfaces" tool of the Imaris software (Bitplane, Zurich, Switzerland) in batch mode, allowing for the detection of puncta using identical parameters across all images to ensure unbiased quantification.

3.15 Synaptic readouts

3.15.1 Synaptic connectivity

As described, pre- and postsynaptic puncta were defined using Columbus and Imaris software, by analysing SYP and Homer signals, respectively. The generated data, *i.e.*, the coordinates and other properties of all puncta, were then analysed using custom MATLAB codes (MathWorks, Natick, Massachusetts, USA), which assigned postsynaptic puncta to presynaptic puncta based on their relative proximity[240]. Briefly, each Homer1 spot was assigned to the nearest SYP spot within a fixed cut-off distance (Figure 3.5A). The distance cut-off was chosen to ensure that the percentage of SYP spots with at least one Homer1 spot assigned (*%SYP_assigned*) remains in the linear range of the curve, *i.e.*, before *%SYP_assigned vs.* distance cut-off curve reaches saturation (Figure 3.5B). Unless mentioned otherwise, a distance cut-off of 0.8 µm was used.

Similarly, PSD95 assignment to SYP puncta was also assessed exclusively during screening as it is one of the most studied postsynaptic scaffold proteins and plays an essential role in synapse integrity *via* the anchoring of AMPARs to the post-synaptic

membrane[255]. Therefore, any differences in synaptic connectivity between SYP assignment by Homer and SYP assignment by PSD95 in our screen could shed further light on the underlying mechanisms of Aβ-induced synaptotoxicity.

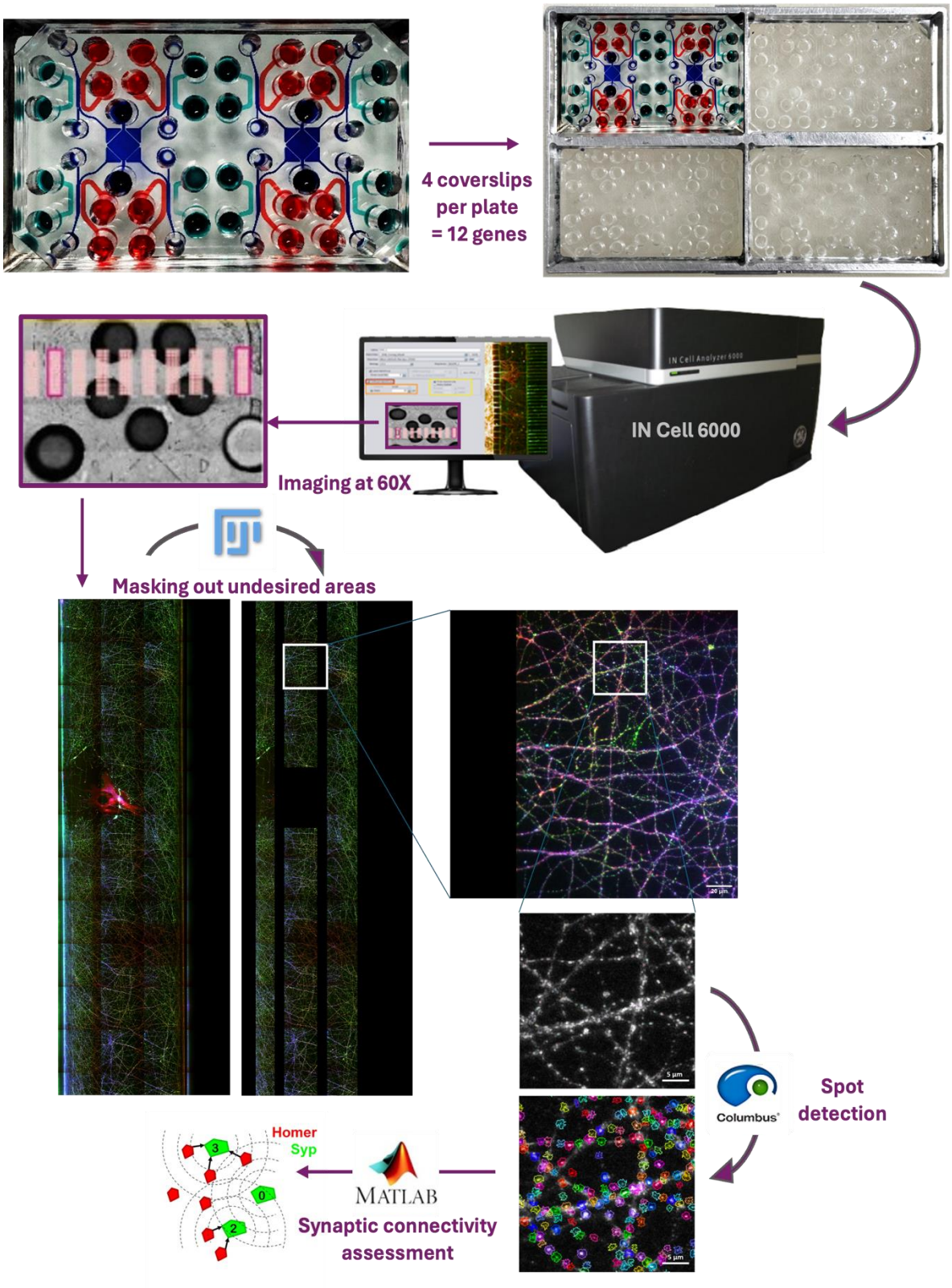

Figure 3.4. Medium-throughput screening overview. Four coverslips containing four D-devices were placed on a custom-made coverslip holder, allowing the screening of up to 12 genes in the same imaging session. Presynaptic and postsynaptic chambers are coloured labelled with green and red dyes, respectively, while CHO chambers that are fluidically connected to the synaptic chambers are coloured blue. Synaptic chambers are then imaged using the IN Cell 6000 automated microscope as a mosaic of 64 fields. Unwanted areas (*i.e.*, cell bodies, astrocytes, microchannels) are masked out using a custom ImageJ macro. Synaptic puncta are then detected in Columbus before synaptic assignment using a custom MATLAB code.

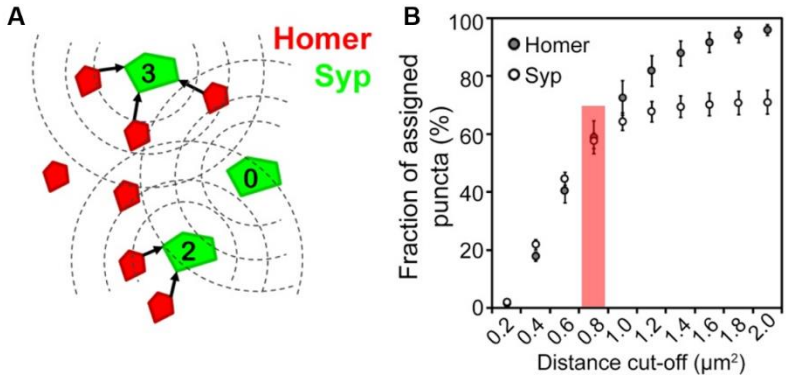

Figure 3.5. Proximity assignment of postsynaptic puncta (Homer1) to presynaptic puncta (SYP). (A) Visual representation of the assignment of Homer1 to SYP spots. (B) Fraction of assigned puncta as a function of distance cut-off. Highlighted in red is the chosen cut-off distance, close to the end of the linear segment, before %*SYP_assigned* reaches a plateau.

3.15.2 Synaptic density

Synaptic density and synaptic connectivity were assessed based on the same datasets, after pre- and postsynaptic puncta detection and assignment. Basically, %*SYP_assigned* was multiplied by the total number of detected SYP spots to obtain an integrated measure of synapse number. To account for differences in the density of the neural network, this value was then normalised to the network integrated density, calculated as the total fluorescence intensity of the neuronal network over the entire network area. The resulting metric, referred to as synaptic density, reflects the abundance of assigned presynaptic sites (synapses) relative to network size.

3.16 AMPAR subunit phosphorylation analysis

Similarly to the quantification of pre- and postsynaptic markers, GluA1 and GluA2 subunits of AMPARs (both total and phosphorylated forms) were segmented using Imaris software. The generated data included the volume, position and intensity of each detected spot and were analysed using a custom MATLAB code to quantify the number and total intensity of AMPAR subunits. Mean signal intensity of detected spots was then calculated by dividing the total spot intensity by the number of detected spots for each image. Separately, the number of spots was assessed and normalised to total Homer1 spot intensity to account for the local variation of the synaptic network.

3.17 MEA recordings

At DIV19, the spontaneous neuronal activity in each MEA chip was recorded using a MEA2100-System equipped with a single 256-channel head stage and an integrated temperature controller (MultiChannel Systems, Reutlingen, Germany). First, the head stage was preheated to 37°C. A plastic ring with ethylene-propylene membrane was placed over the microfluidic device to ensure sterility during transport and recordings. The MEA chip was placed on the head stage and left there for 5 min for the neurons to adjust to the new environment. Spontaneous activity was recorded from all channels (microelectrodes) for 5 min at 25 kHz sampling rate. After this baseline recording, the MEA chips were treated with CHO-APP-WT or CHO-APP-LDN CM as previously described (Section 3.8). A second recording was performed 24 h later to assess the impact of CM on network-level synaptic connectivity. The recordings were exported into .h5 format for further analysis. For each MEA-integrated microfluidic device, a chip map was manually generated to identify the electrodes corresponding to pre- and postsynaptic chambers.

3.18 MEA analysis

This methodology is adapted from Lambert *et al.*, 2025[256].

3.18.1 Spike sorting

The extracellular recordings were analysed using SpikeInterface[257], and the SpyKING CIRCUS 2 spike sorting pipelines, conceived as an extension of our spike sorting

toolbox[258]. Briefly, the spike sorting procedure to extract the single unit activities started with a preprocessing step, as follows: bandpass filter (frequency [150Hz, 7kHz]), then a common median reference filter (to remove shared fluctuations across channels) before whitening (to remove shared noise across channels). Then, negative threshold crossings are detected, aligned, and a subset is projected into a lower dimensional space *via* Principal Components (see[258] for details). Density-based clustering is then launched on these projected spikes to detect the templates, *i.e.*, the motifs regularly occurring in the data. Once the dictionary of templates is constructed, a proper orthogonal matching pursuit algorithm[259] reconstructs the signal as a linear sum of these templates to identify all the spike times. After spike sorting, only the putative units with a refractory period violation < 0.1 and a signal-to-noise ratio > 2 were kept as valid neurons.

3.18.2 Unit positions

The putative positions of the units kept after spike sorting are estimated from the extracellular templates, assuming that units could be considered as monopoles (Figure 3.6A and 3.6B)[260,261]. All the units that would be found within the presynaptic chamber (according to the chip map) are labelled as belonging to the *pre* population, while those found within the postsynaptic chamber are labelled as *post*. Note that while all electrodes were analysed simultaneously during the spike sorting process (to make use of spatiotemporal information to disambiguate sources), very few units were found between the two chambers, in accordance with the experimental setup. The *pre-post-drive* readout was previously established to be independent of the number of units detected[256]. MEA chips showing more than a 5-fold difference between pre- and postsynaptic unit numbers were excluded.

3.18.3 Drive between *pre* and *post* populations

To assess the directionality of the functional connectivity between pairs of units, we defined a metric called the *pre-post-drive* that measures to what extent the units in the *pre* population are leading the activity of the units in the *post* population. The assumption behind such a metric is that assuming monosynaptic, direct connections between *pre* and *post* neurons, an increase in activity in the *post* population following spikes emitted by the *pre* population should be observed. To quantify this functional effect, for each pair

of unit *i* belonging to the *pre* population and of unit *j* belonging to the *post* population, we measured the cross-correlogram $CC_{i_{pre},j_{post}}(t)$ of their spiking activity with a given time bin $T_{bin} = 2\ ms$ and during a time window $T_{window} = 20\ ms$. The *drive* $\Phi(i_{pre}, j_{post})$ was then computed as the ratio of the integral of $CC_{i_{pre},j_{post}}(t)$ for positive times (*i.e.*, how much the activity of i_{pre} drives the one of j_{post}) divided by the integral of $CC_{i_{pre},j_{post}}(t)$ for negative times (*i.e.*, how much the activity of j_{post} drives the one of i_{pre}). If the two units were firing independently, as Poisson-like sources, then $\Phi(i_{pre}, j_{post})$ should be close to 1. If, on the other hand, $\Phi(i_{pre}, j_{post})$ is larger than 1, it means that, on average, spikes of i_{pre} is more likely to precede the ones in j_{post} (Figure 3.6C). Such an asymmetry in the cross-correlogram is often used to infer putative directional connectivity [262]. Then, at the population level, the *drive* between *pre* and *post* populations is simply obtained as $\Phi(pre, post) = mean_{i \in pre, j \in post} \Phi(i_{pre}, i_{post})$.

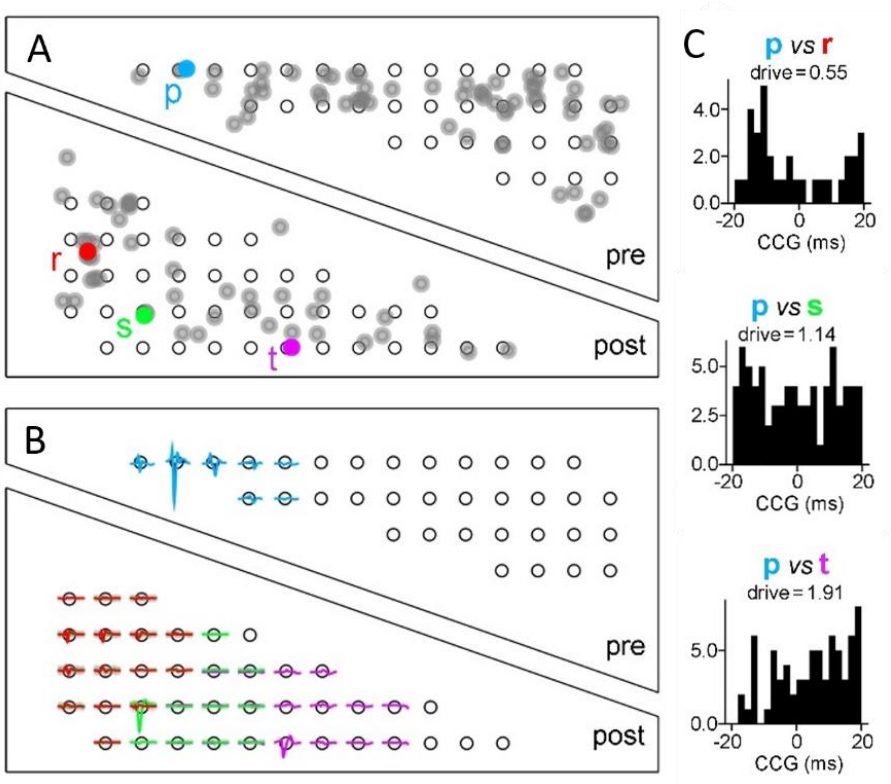

Figure 3.6. Analysis of MEA recordings and definition of *pre-post drive*. (A) A representative map of units identified through the spike-sorting algorithm (grey). One presynaptic unit and three postsynaptic units are color-coded for demonstration purposes. (B) Spike waveform patterns corresponding to these four color-coded units. (C) Cross-correlograms and the calculated *pre-post-drive* parameters for the three pre-post unit pairs that can be formed using these four units. Adapted from Lambert *et al.*, 2025[256].

3.19 Statistical analysis

Outliers were detected using several approaches depending on the dataset. For experiments with a small sample size and wide data range (e.g. Western blotting quantification), values exceeding 1.5 × the interquartile range above the 75th percentile or below the 25th percentile were excluded (hereafter referred to as the interquartile range - IQR- method of exclusion). For experiments with larger sample size (e.g. microfluidics datasets), outliers were defined as values outside the interval defined by the median ± η × median absolute deviation (MAD). The scaling factor η was adjusted according to the overall data range: the broader the range, the smaller the η value, resulting in a more stringent outlier detection.

For the screening experiments, the fraction of SYP spots assigned by at least one Homer1 spot (or by at least one PSD95 spot) were first calculated in the MOCK control groups, *i.e.*, neurons transduced with the MOCK vector and co-cultured with CHO cells overexpressing APP-WT or APP-LDN (MOCK-APP^{WT} and MOCK-APP^{LDN} groups). This confirmed that co-culturing primary neurons with CHO-APP-LDN cells significantly reduced synaptic connectivity. For each D-device, *%SYP_assigned* was normalised to the mean *%SYP_assigned* of the control group (MOCK-APP^{WT}) and processed as follows: (i) within the MOCK-APP^{WT} group, any value outside the interval defined by the median ± 2 × MAD was considered an outlier and excluded; (ii) within the MOCK-APP^{LDN} group, any normalised value greater than 0.85 was excluded, as the effect of CHO-APP-LDN co-culture was considered toxic only when synaptic connectivity was decreased by at least 15% based on previously described APP-LDN effect[240]; (iii) if a device from the MOCK control group (MOCK-APP^{WT} or MOCK-APP^{LDN}) was excluded, all genes linked to the excluded control were also excluded from the analysis. Once all experimental data were subjected to this process, all devices in the MOCK-APP^{WT} control group were pooled to identify outliers (outside the median ± 2 × MAD interval). *%SYP_assigned* values obtained for different conditions (AD risk gene knockdown or overexpression) in each experiment were then normalised to the mean *%SYP_assigned* of the MOCK-APP^{WT} control group of that particular experiment.

For the assessment of *ARFRP1* compartmental protective effect against synaptotoxicity induced by CHO-APP-LDN CM exposure, due to the wide range of values, normalised "per field" data (as opposed to "per synaptic chamber" data) from all five experiments were pooled and any values falling outside of the interval defined as the median ± 2× MAD were excluded. Then, for each device, a mean *%SYP_assigned* value was calculated using the remaining "per field" data. Finally, device means from all five experiments were pooled and a second, less stringent, outlier check (median ± 3× MAD) was applied to exclude any extreme values.

Normality was first assessed using the Shapiro-Wilk test. When data deviated from normal (or Gaussian) distribution ($p<0.05$), they were analysed using the non-parametric Kruskal-Wallis test, followed by Dunn's *post-hoc* correction for pairwise comparisons. For normally distributed datasets, the difference between the equality of variances of each experimental group was then assessed using Brown-Forsythe's test. Datasets with significant differences in variances were then analysed using Welch's ANOVA with Tamhane's T2 *post-hoc* test. For normally distributed data with equal variances, one-way ANOVA followed by Dunnett's *post-hoc* test was performed. Data with only two experimental groups were analysed using parametric unpaired t-test or non-parametric Mann-Whitney U-test.

Each microfluidic device was considered an independent experimental unit (n), as the devices were seeded, treated, and imaged separately. Neuronal cultures were prepared from pooled wild-type animals using identical protocols and reagents, minimising biological variability across preparations. Indeed, variability between devices is expected to be greater than that between neuronal preparations due to the inter-device heterogeneity in microenvironmental factors such as local cell density, neuronal maturation, or microchannels geometry. In addition, one microfluidic device relies on the analysis of five distinct fields, which serve as technical replicates to account for intra-device variability and ensures that the reported value accurately represents the overall cellular behaviour within each device. Experiments were conducted with at least three independent neuronal preparations (N). Device numbers (n) and number of cultures (N) are indicated in the corresponding figure legends.

4. RESULTS & DISCUSSION

4.1 AIM 1: Screening top AD risk factors against Aβ-induced synaptotoxicity

The first aim of this project was to evaluate the impact of AD risk factor expression levels on synaptic connectivity *via* medium-throughput screening using microfluidic co-cultures. To fulfil this aim, we first selected the AD risk genes that showed the strongest impact on synaptic connectivity, based on the previous high-content shRNA screening results (Section 4.1.1), then designed and tested the necessary lentiviral constructs (Section 4.1.2) and conducted a medium-throughput screening to assess Aβ-induced loss of synaptic connectivity (Section 4.1.3).

4.1.1 Gene selection based on previous shRNA screening results

A total of 198 brain-expressed AD risk genes were selected for a high-content shRNA screening (see Section 3.1 for gene selection criteria) which was conducted in two parts (Screen #1 and Screen #2) and at two different MOIs (MOI2 and MOI4)[239]. This screen aimed to evaluate the effect of gene knockdown on synaptic connectivity, assessed through the assignment of postsynaptic to presynaptic puncta (refer to Section 3.15.1 for details). Plotting the effects of 198 shRNA on *%SYP_assigned* after normalising them to the effect of the non-targeting shRNA (shNT) revealed considerable differences between Screen #1 and Screen #2 in terms of median effect size and variance (Figure 4.1, Table 4.1). We therefore selected genes separately from each screen, as pooling the datasets could bias the gene selection. We also observed that some genes significantly reduced *%SYP_assigned* at MOI2, but were deemed toxic at MOI4 (*i.e.*, induced a significant decrease in total network area compared to control conditions), while other genes had a significant impact only at MOI4. To be as objective as possible in our gene selection process, we integrated the data obtained at MOI2 and MOI4 by using a synthetic variable called MOImix, a computed MOI that accounts for the effect of the silencing of the common control gene *SYP* (shSYP) at MOI2 relative to MOI4, according to the following formula:

$$log_2\,(shRNA|_{MOImix}) = \left[\frac{log_2\,(shRNA|_{MOI2}) + log_2\,(shRNA|_{MOI4}) \times ratio}{2}\right],$$

where "ratio" is defined as $(1 - shSYP|_{MOI2})\ /\ (1 - shSYP|_{MOI4})$.

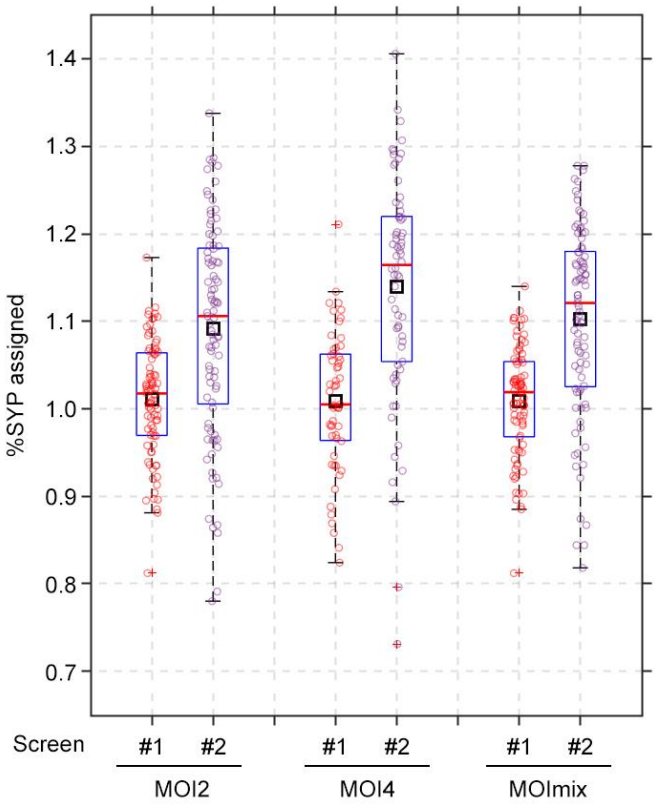

Figure 4.1. Distribution of shRNA effect on synaptic connectivity. Previous high-content screening results were reanalysed to show the effect of gene silencing on synaptic connectivity *(%SYP_assigned*). Individual data points indicate mean effect size for each shRNA, normalised by the mean *%SYP_assigned* value in control wells that received non-targeting shRNA. The MOImix dataset was defined to pool the screens conducted at MOI2 and MOI4, based on the effect of shRNA against *Syp* gene, which was included in both screens. In box plots, red lines indicate sample median and black squared indicate sample mean. N=4 independent cultures for each screen. Number of non-cytotoxic shRNAs and the quartile information are provided in Table 4.1.

The aim of our screening was to assess the potential synaptoprotective effects of these risk genes under pathological conditions using cell-secreted Aβ to disrupt synapses. It was previously demonstrated that the Aβ peptides secreted by CHO-APP-LDN cells decrease *%SYP_assigned* and Homer1 density without impacting SYP density[240]. It was also shown that *%SYP_assigned* is a more sensitive read-out than Homer1 density for detecting subtle effects on synaptic connectivity[240]. We therefore aimed to shortlist the genes that had a strong impact on *%SYP_assigned* and a minimal impact on SYP density, when knockdown in rat hippocampal neurons. Figure 4.2 shows *%SYP_assigned vs*. SYP density plots for the two screens using the criteria defined in Section 3.1. Here, all genes that satisfied the criteria for MOImix were labelled, but, among them, only those that also satisfied the same criteria based on experimental data obtained at MOI2 or at MOI4 were eventually shortlisted. This corresponds to a total of 24 genes: 18 genes that are

detrimental to synapses when knockdown and 6 genes that promote synaptic connectivity when knockdown (Figure 4.2).

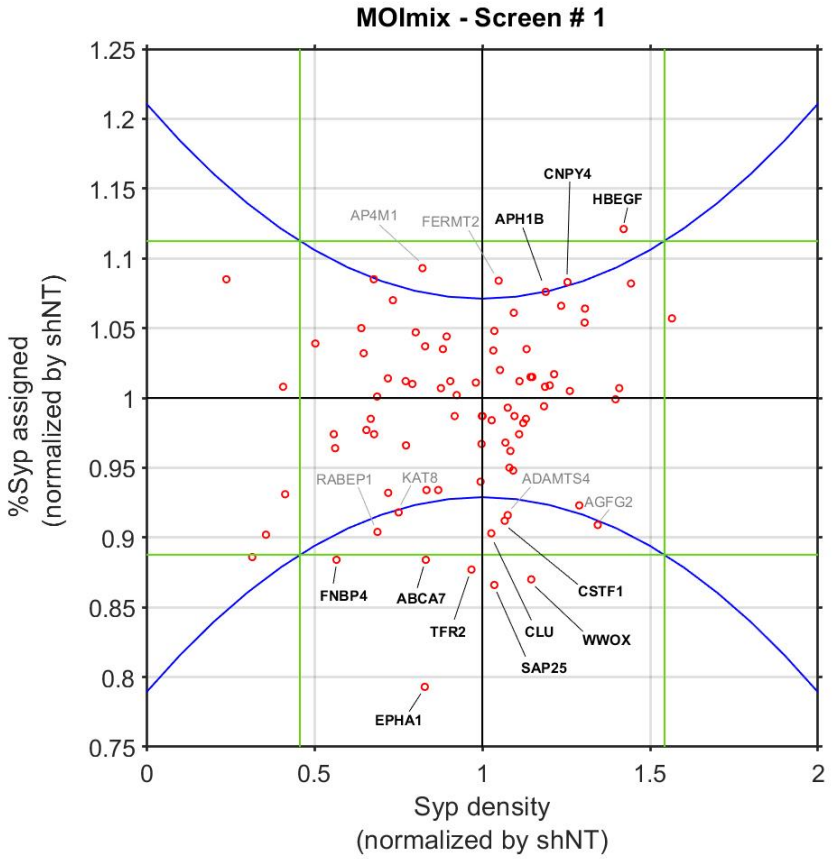

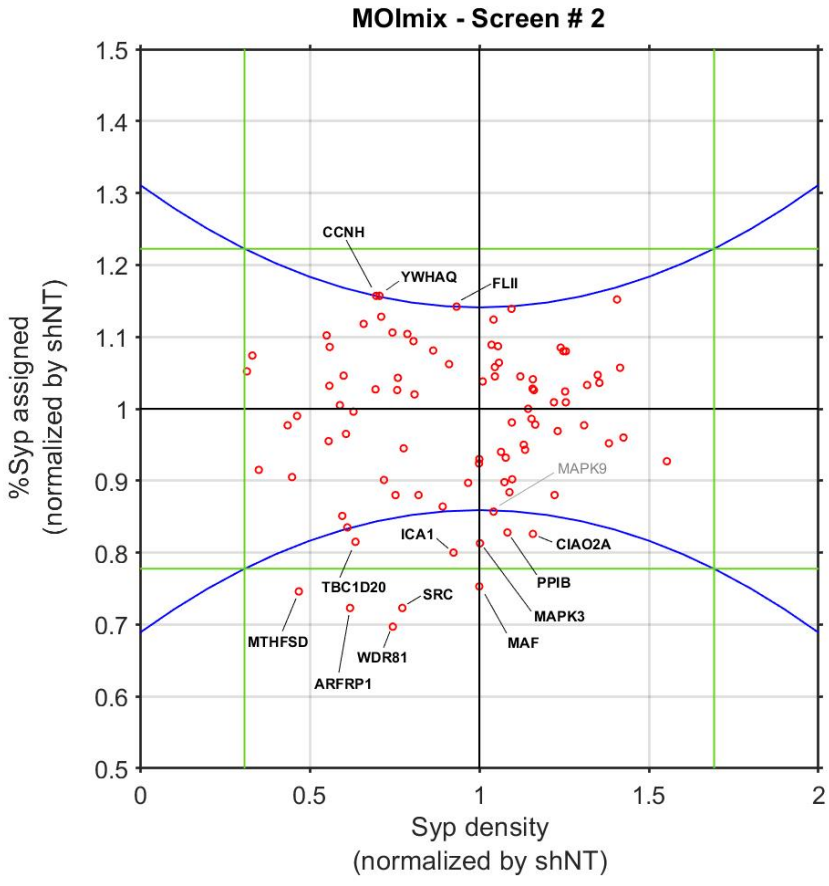

Figure 4.2. *%SYP_assigned vs*. SYP density plot for the shortlisting of genes. MOImix data from the previous high-content screening were plotted separately for Screen #1 and Screen #2, after translating the median effect size to 1 for better visualisation. Vertical and horizontal green lines indicate median ± 3 × MAD. Blue curves show quadratic fits intersecting the green lines with apexes at median ± 1.9 × MAD for *%SYP_assigned*. Genes showing SYP densities within the range of median ± 3 × MAD and *%SYP_assigned* values above or below the quadratic curve were shortlisted if they also met these criteria in either MOI2 or MOI4 datasets (black labels). Genes that satisfied the criteria only for MOImix but not for MOI2 or MOI4 were not shortlisted (grey labels).

Table 4.1. Gene numbers and quartile information for the shRNA effect on synaptic connectivity as a function of MOI (see Figure 4.1).

	MOI2		**MOI4**		**MOImix**	
	Screen #1	Screen #2	Screen #1	Screen #2	Screen #1	Screen #2
# genes	85	89	55	66	85	89
min	0.812	0.780	0.824	0.731	0.812	0.818
Q1	0.970	1.007	0.965	1.058	0.969	1.026
median	1.017	1.106	1.005	1.164	1.019	1.121
Q3	1.063	1.183	1.062	1.220	1.054	1.179
max	1.173	1.338	1.211	1.406	1.140	1.278

4.1.2 Optimisation of lentiviral gene expression for genes detrimental to synapses

As described, 18 genes that were detrimental to synapses when knocked down were shortlisted. Because Aim 1 sought to test whether their overexpression could counteract Aβ-induced synaptotoxicity, these genes were overexpressed in rat hippocampal neurons *via* lentiviral transduction (refer to Section 3.8 for virus constructions). We could not obtain a lentiviral vector for *ABCA7* as the cDNA is exceptionally large, exceeding the packaging limit of lentiviral particles. For the remaining 17 genes, expression levels were qualitatively evaluated in rat cortical neurons at varying MOIs *via* Western blotting. Myc-tags fused to each protein of interest were used to determine target protein levels, while GAPDH, a housekeeping protein, served as loading control. For each virus, the optimal MOI was defined empirically as the lowest MOI that induced sufficient protein overexpression while maintaining normal cell morphology and overall culture integrity. Gene overexpression was successful for 14 out of 17 genes (Figure 4.3). For the remaining three genes, Myc-tag signal was weak for *ICA1* and *MAF*, despite using very high MOIs, and undetectable for *WDR81* (Figure 4.3). This likely resulted from the large size of the

WDR81 cDNA, which may have hindered efficient lentiviral packaging. These genes were excluded from the screening.

The MOIs for shRNAs targeting the 6 genes that were knocked-down (*APH1B*, *HBEGF*, *CNPY4*, *CCNH*, *FLII* and *YWHAQ*) were already optimised in the previous shRNA screening[241]. The final list of genes to be screened, along with their respective validated MOIs is shown in Table 4.2.

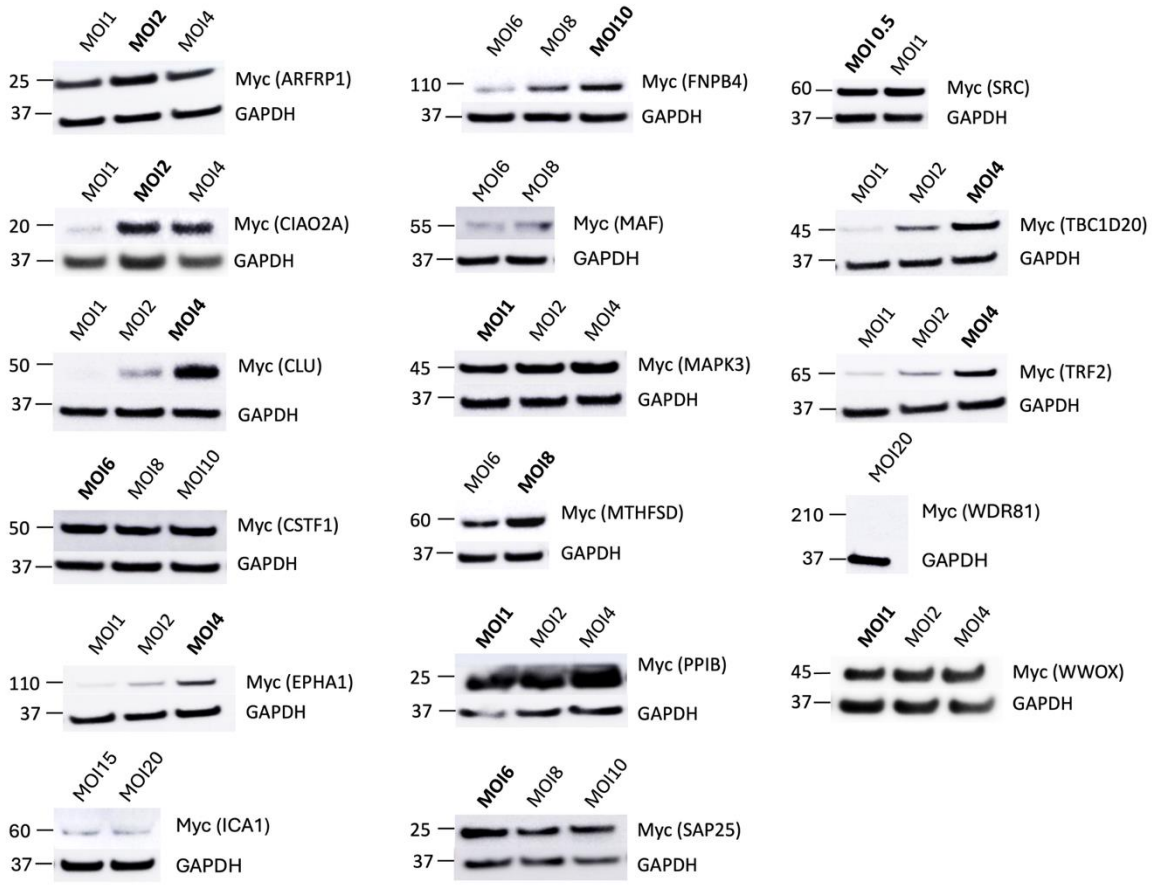

Figure 4.3. MOI optimisation for the lentiviral transduction of overexpression constructs. Immunoblots show Myc-tag expression levels as a read-out for target gene expression. GAPDH was used as a loading control. Considering the strong expression of Myg-tag for Src, MOI was decreased. Chosen MOIs are shown in boldface. N=1. Myc-Tag abundance was weak for ICA1 and MAF vectors despite using very high MOIs and undetectable for WDR81 vector.

Table 4.2. List of genes selected for the medium-throughput screening, with the corresponding type of genetic modulation and used MOI. OE = overexpression; KD = knockdown.

Gene	Modulation	MOI
APH1B	KD	2
ARFRP1	OE	2
CCNH	KD	2
CIAO2A	OE	2
CLU	OE	4
CNPY4	KD	2
CSTF1	OE	6
EPHA1	OE	4
FLII	KD	2
FNBP4	OE	10

Gene	Modulation	MOI
HBEGF	KD	2
MAPK3	OE	1
MTHFSD	OE	8
PPIB	OE	1
SAP25	OE	6
SRC	OE	0.5
TBC1D20	OE	4
TRF2	OE	4
WWOX	OE	1
YWHAQ	KD	2

4.1.3 Medium-throughput screening against Aβ-induced synaptic dysfunction

While these AD risk genes impact synaptic connectivity when knocked-down, they may not be directly implicated in amyloid pathology. Therefore, an additional screening was performed to identify their involvement in Aβ-induced synaptotoxicity by exposing them to CHO cell-secreted Aβo using microfluidic co-culture devices (refer to Section 3.14 for screening methodology overview). The number of genes to be screened (20) made it very difficult to use the individual co-culture device (X-device) where Aβ-induced synaptotoxicity due to CHO-APP-LDN co-culture was first demonstrated[240], as long microscopy times emerged as the major experimental bottleneck. To benefit from a high-throughput imager optimised for rapid, automated scanning of multi-well plates, we generated a new microfluidic layout (D-device). Four standard X-devices were integrated into one single device into which one shared co-culture chamber connects to four distinct synaptic chambers, thereby decreasing the overall footprint (see Section 3.2 for details). This design permitted us to screen three different genes in both control (CHO-APP-WT) and toxicity (CHO-APP-LDN) conditions per device (Figure 4.4) and up to 12 genes across four D-devices in a single automated microscopy session.

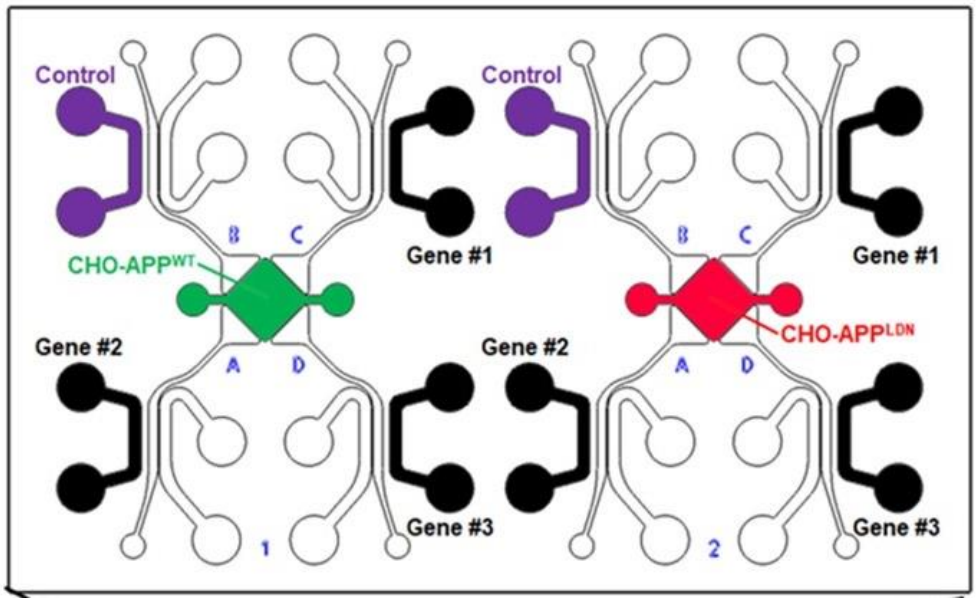

Figure 4.4. Experimental design of the medium-throughput screening. Three genes can be screened simultaneously under control and toxic conditions using a single D-device. Here, gene expression is highlighted only in presynaptic chambers (black shading) for demonstration purposes.

As a prerequisite for interpreting synaptic effects, we first validated Aβ secretion profiles across devices by quantifying total Aβ levels *via* AlphaLISA in media collected from the co-culture chambers. Pooled $Aβ_{1-X}$ Alpha counts were used to calculate global mean and standard deviation (SD), enabling identification of devices with aberrant Aβ secretion patterns. Only experiments in which CHO-APP-LDN cultures secreted significantly higher Aβ than CHO-APP-WT were retained for further analysis (Table 4.3). All experiments met this criterion, except for experiment #7. This particular experiment included less coverslips from the start, and after outlier exclusions, only 3 data points remained per group, preventing Mann-Whitney test from reaching significance. Therefore, this experiment was retained for further analysis.

Table 4.3. $A\beta_{1-X}$ Alpha counts in culture media collected from CHO-APP-WT and CHO-APP-LDN chambers. D-devices with CHO-APP-WT medium $A\beta_{1-X}$ Alpha count higher than median + 4 × MAD or with CHO-APP-LDN medium $A\beta_{1-X}$ Alpha count lower than median – 4 × MAD were excluded. For each CHO genotype, data show the number of quantified medium samples collected from a single CHO chamber (referred to as coverslip), the mean values per experiment with corresponding SD and the associated p-value (Mann-Whitney test, M-W). Non-significant result is highlighted in red.

Experiment #	APP-WT			APP-LDN			M-W p-value
	coverslip #	α counts	SD	coverslip#	α counts	SD	
1	6	2778	1588	6	147110	61262	0.0022
2	3	894	200	5	184076	104152	0.0357
3	5	918	209	6	206685	86531	0.0043
4	5	445	31	8	89321	33081	0.0016
5	5	1945	1011	5	76346	24756	0.0079
6	4	983	772	5	87770	3638	0.0159
7	3	704	98	3	139984	20694	0.1
8	4	815	560	5	48792	6368	0.0159
9	6	592	368	6	20195	11749	0.0022
10	3	696	433	5	33228	12837	0.0357
11	3	273	95	6	14228	12904	0.0005

Screening data were analysed for the potential synaptoprotective effect of each AD risk gene using experimental sets in which the toxic effect of the CHO-APP-LDN co-culture was validated (Figure 4.5). However, due to lower-than-expected synaptotoxicity of the CHO-APP-LDN co-culture, most genes could not be evaluated with a sufficient high number of independent experiments to permit robust statistical testing. After data exclusion (described in Section 3.19), only two genes were tested in three independent cultures, 14 genes were assessed in two experimental replicates while four genes were tested in a single culture. Despite these limitations, it appeared that PSD95 assignment to SYP puncta as a read-out was comparable to those obtained with Homer1 assignment to SYP puncta. Therefore, we report assignment by Homer1 in the subsequent results.

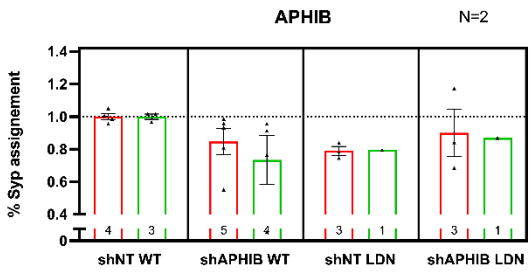

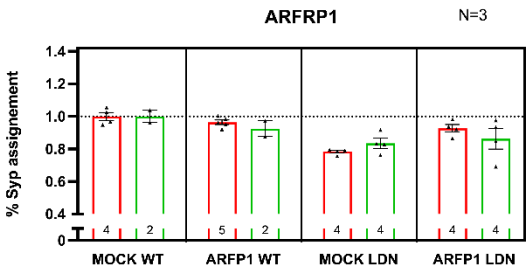

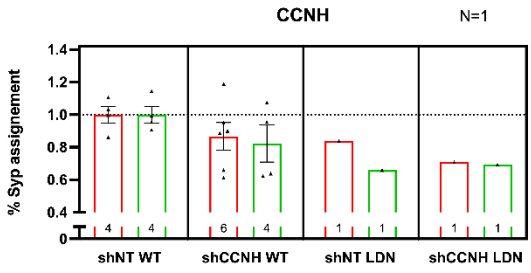

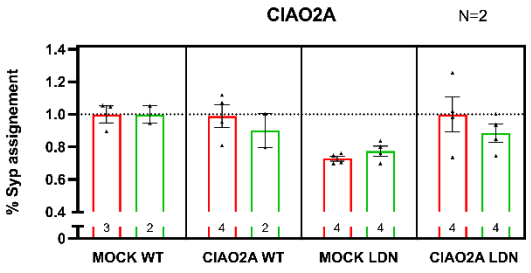

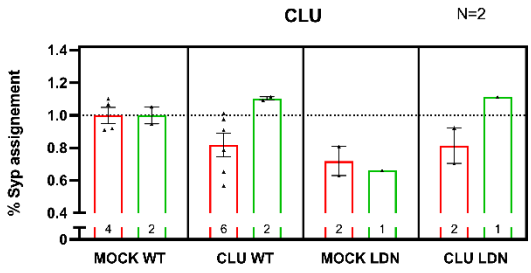

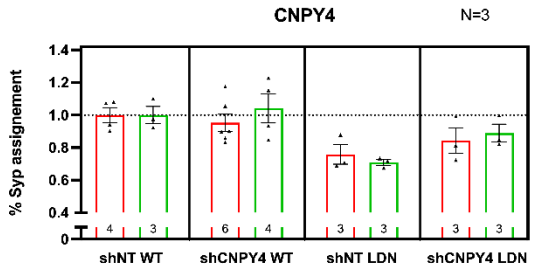

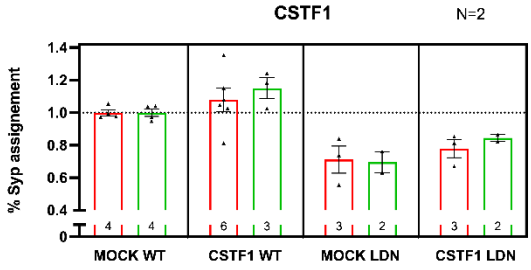

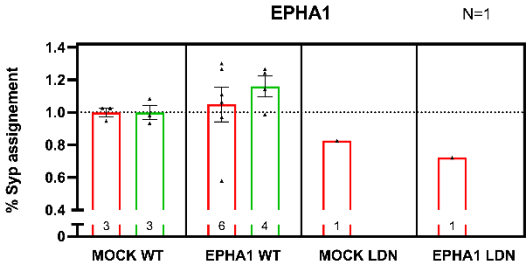

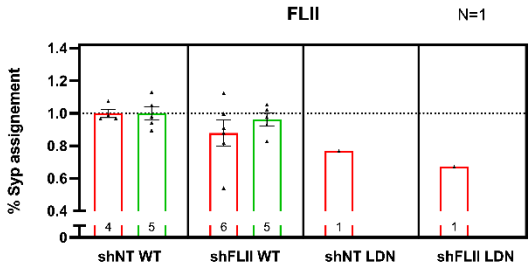

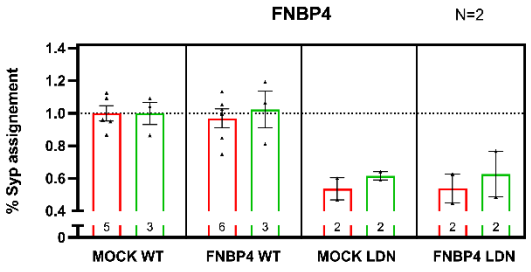

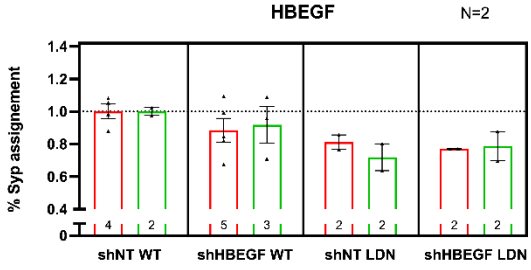

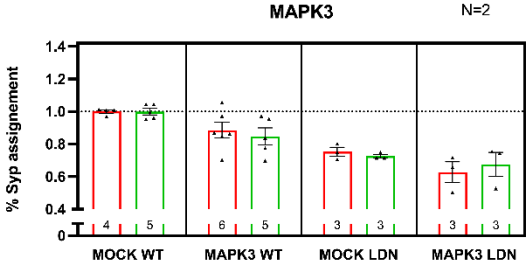

⇨ Continued on the next page

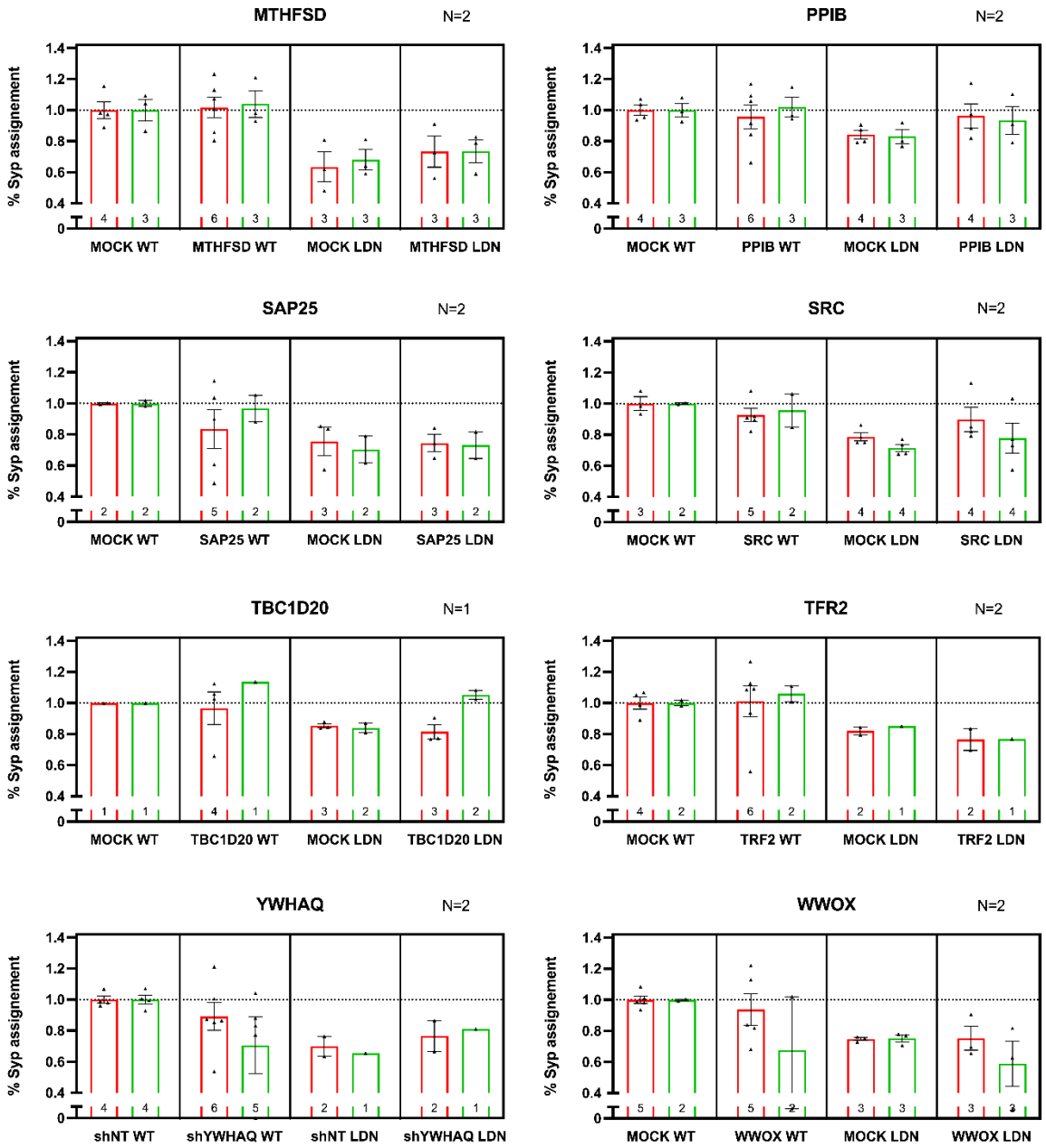

Figure 4.5. Medium-throughput screening of AD risk factors against Aβ-induced synaptic dysfunction. For each target gene, the percentage of SYP assigned by either Homer1 (red) or PSD95 (green) is reported for CHO-APP-WT (WT) and CHO-APP-LDN (LDN) co-cultures with or without genetic modulation. Each data point represents one microfluidic device (n; given on the bars) obtained from 1-3 independent cultures (N; shown next to the gene name). Data are normalised against the mean of the MOCK-APP^{WT} group and displayed as mean ± SEM.

Among the screened genes, only *ARFRP1* and *CNPY4* had three independent experimental replicates, allowing for statistical testing. Analyses using Welch's ANOVA, followed by Tamhane's T2 multiple comparison test, revealed no significant differences for *CNPY4*, suggesting no detectable effect on synaptic connectivity (Figure 4.5). In contrast, *ARFRP1* showed a clear pattern consistent with a synaptoprotective effect (shown in Figure 4.6 after normalisation with MOCK-APP^{WT} and statistical analysis). In the

MOCK-APP-LDN group, a significant reduction in synaptic connectivity was observed compared with MOCK-APP-WT (0.78±0.009; $p<0.01$), confirming the expected Aβ-induced synaptotoxicity. When *ARFRP1* was overexpressed in neurons co-cultured with CHO-APP-LDN cells, synaptic connectivity increased from 0.78±0.009 to 0.96±0.04, showing a trend towards recovery ($p=0.06$). In addition, no significant difference was observed between MOCK-APP-WT and ARFRP1-APP^{LDN} groups ($p>0.05$), indicating that the toxic effect associated with CHO-APP-LDN cells is abolished under these conditions.

These observations suggest that *ARFRP1* overexpression may counteract Aβ-induced synaptic loss. Importantly, *ARFRP1* overexpression did not alter baseline connectivity in the CHO–APP–WT condition (0.96±0.09; $p>0.05$), indicating that its effect is specific to the toxic Aβ context rather than general synaptic strengthening. Although replication was limited for the other genes, *CIAO2A* also appeared to partially restore synaptic connectivity under CHO-APP–LDN conditions (0.73±0.02 to 1.00±0.11), with no effect under control conditions (0.99±0.07; shown in Figure 4.6 after normalisation with MOCK-APP^{WT}). This trend points to *CIAO2A* as another potential protective candidate against Aβ-induced synaptic dysfunction.

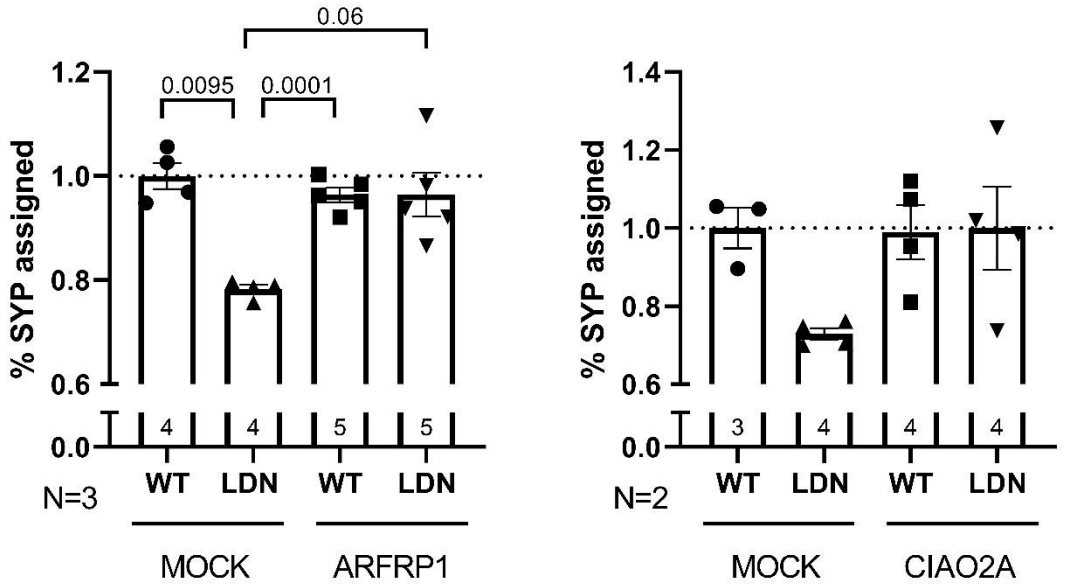

Figure 4.6. Identification of *ARFRP1* and *CIAO2A* as potential screening hit genes. Impact of *ARFRP1* (left) and *CIAO2A* (right) overexpression in neurons co-cultured with CHO-APP-WT (WT) or CHO-APP-LDN (LDN) cells. Each data point represents the mean assignment of SYP by Homer1 for one microfluidic device normalised by the mean of the control group (MOCK-APP^{WT}). The dotted lines (y=1) indicate the baseline. Device number (n) is reported per condition within each data bar. Number of independent cultures (N) is provided for each gene. Data represented as mean ± SEM. Welch's ANOVA test with Tamhane's T2 multiple comparisons test.

Overall, the proportion of coverslips with successful synaptotoxicity induced by co-culture with CHO-APP-LDN was low, despite the reproducible Aβ secretion (as measured *via* AlphaLISA in the medium collected from the co-culture chamber; Table 4.3) across the several sets. We observed that both CHO cell lines began to show stress signs in CHO-NBA co-culture medium, as evidenced by pronounced cell clustering, where CHO-APP-WT cells appeared to be more strongly affected (Figure S1 in the Appendix). Therefore, stressed CHO-APP-WT cells could have induced some form of synaptotoxicity, independently of secreted Aβ, leading to decreased synaptic connectivity in the control condition, hence reducing the expected detrimental effect of the experimental group (CHO-APP-LDN). We conducted further tests to mitigate this technical issue, namely the impact of experimental timeline, on CHO cells viability with the aim of optimising overall culture conditions (see Section A in the Appendix). A new stable CHO cell line was also established to attempt to solve cell viability issues (see Section B in the Appendix). Unfortunately, we were unable to overcome these problems and decided to use CHO-APP-LDN CM in the remaining experiments, in which CM from CHO-APP-WT served as the toxicity control condition. Indeed, during a previous collaboration, we had shown that exposing neurons to CHO-APP-LDN CM caused a detrimental effect on the firing synchronicity in mouse embryonic cortical neurons[244].

Even though we could not assess the impact of all genes on Aβ-induced synaptic dysfunction, two potential protective genes were identified in the screening: *ARFRP1* and *CIAO2A*. *CIAO2A* (Cytosolic Iron-Sulfur Assembly Component 2A) is involved in iron-sulphur cluster biogenesis and has been linked to cellular redox regulation and iron metabolism, process known to influence oxidative stress in AD pathology[263,264]. However, given its indirect relationship to synaptic trafficking mechanisms, *CIAO2A* was not pursued further in this study. Its contribution remains nonetheless relevant, and future assays focusing on redox balance or mitochondrial function could help determine whether *CIAO2A* affects synaptic resilience through metabolic pathways. In contrast *ARFRP1* (ADP-ribosylation factor Related Protein) plays a direct role in vesicular trafficking, including trans-Golgi network (TGN)-to-plasma membrane and endosome-to-TGN transport[265–267]. Since both synaptic stability and plasticity depend critically on presynaptic vesicle cycling and postsynaptic receptor trafficking[268], *ARFRP1* represents a

mechanistically relevant target. Given its function and the host laboratory's expertise and tools, we selected *ARFRP1* for further investigation.

We therefore hypothesised that the protective effect of *ARFRP1* overexpression against Aβ toxicity could either be postsynaptic, through modulation of postsynaptic receptors availability and recycling, or presynaptic, *via* effects on vesicle processing[269–273]. Thus, studying *ARFRP1* could offer a new mechanistic window into how Aβ toxicity translates into synaptic failure, a defining feature of AD progression.

4.2 AIM 2: Validation of synaptoprotective effects of *ARFRP1*, identified in the screening

The second aim of the project was to validate the potential synaptoprotective effects of *ARFRP1* using high-resolution confocal microscopy. We also investigated the physiological role of *ARFRP1* at the synapse to gain further mechanistic insight.

4.2.1 Synaptoprotective effect validation using CHO-APP conditioned medium

In order to confirm the potential protective effect observed during the screening, we used CM from CHO-APP-WT and CHO-APP-LDN cells as a model of Aβ-induced stress (refer to Section 3.9). Briefly, after 48 h of incubation, CM was collected and concentrated, and secreted Aβ levels were quantified using AlphaLISA. Subsequently, we tested three treatment paradigms varying in $A\beta_{1-X}$ concentration and exposure duration and frequency (see Table 3.2) to establish the most reproducible model of synaptic connectivity impairment. In a collaborative study using microfluidic devices coupled with MEA recordings, 85 nM Aβ treatment for 48 h markedly impaired inter-chamber connectivity (*i.e.*, synaptic connections between pre- and postsynaptic neurons)[244]. Based on these findings, we adopted comparable paradigms to evaluate Aβ-induced synaptotoxicity under different exposure regimes. The three different paradigms, 60 nM for 6 days (from DIV14 to DIV21), 120 nM for 3 days (from DIV17 to DIV21), and 500 nM for 24 h (from DIV20 to DIV21), were designed to encompass both chronic, low-dose, and acute, high-dose Aβ exposure conditions. In the acute model, treatment was initiated at a later developmental stage, when neuronal networks are denser and more stable compared to the stage at which chronic treatment began[274]. These differences in network maturation are therefore

expected to introduce variability in both the extent and the nature of Aβ-induced synaptic alterations [274]. We therefore chose to assess both synaptic connectivity and synaptic density, as the latter readout is indicative of structural synapse abundance, providing complementary information to synaptic connectivity by revealing whether observed changes arise from structural remodelling or functional pairing modulation.

ARFRP1 overexpression was assessed in parallel, given that the mechanisms underlying Aβ-induced toxicity can vary depending on the exposure paradigm and neuronal network maturity. Consequently, the molecular pathways through which *ARFRP1* may exert its synaptoprotective effect could also differ between paradigms, potentially leading to distinct effects on synaptic readouts. Although paradigms 1 and 2 (60 nM and 120 nM) did not induce any detrimental effect on synaptic density or on synaptic connectivity, some minor, yet statistically significant changes were detected for the MOCK-APP^{LDN} condition in paradigm 1. However, given the small magnitude of these changes and the absence of a clear toxic phenotype, these paradigms were not further considered for Aβ-induced synaptic impairment analysis.

Only paradigm 3, a non-physiological, acute high-dose Aβ treatment (500 nM for 24 h), induced a significant and reproducible decrease in synaptic density (0.73±0.04; $p<0.001$), without a parallel reduction in synaptic connectivity (0.95±0.02; $p>0.05$), in neurons treated with CM from CHO-APP-LDN cells compared to CM from CHO-APP-WT. Under these conditions, *ARFRP1* overexpression did not prevent the observed decrease in synaptic density (0.74±0.05; $p<0.01$; Figure 4.7), indicating that its previously observed protective effect could not be confirmed in this acute exposure model.

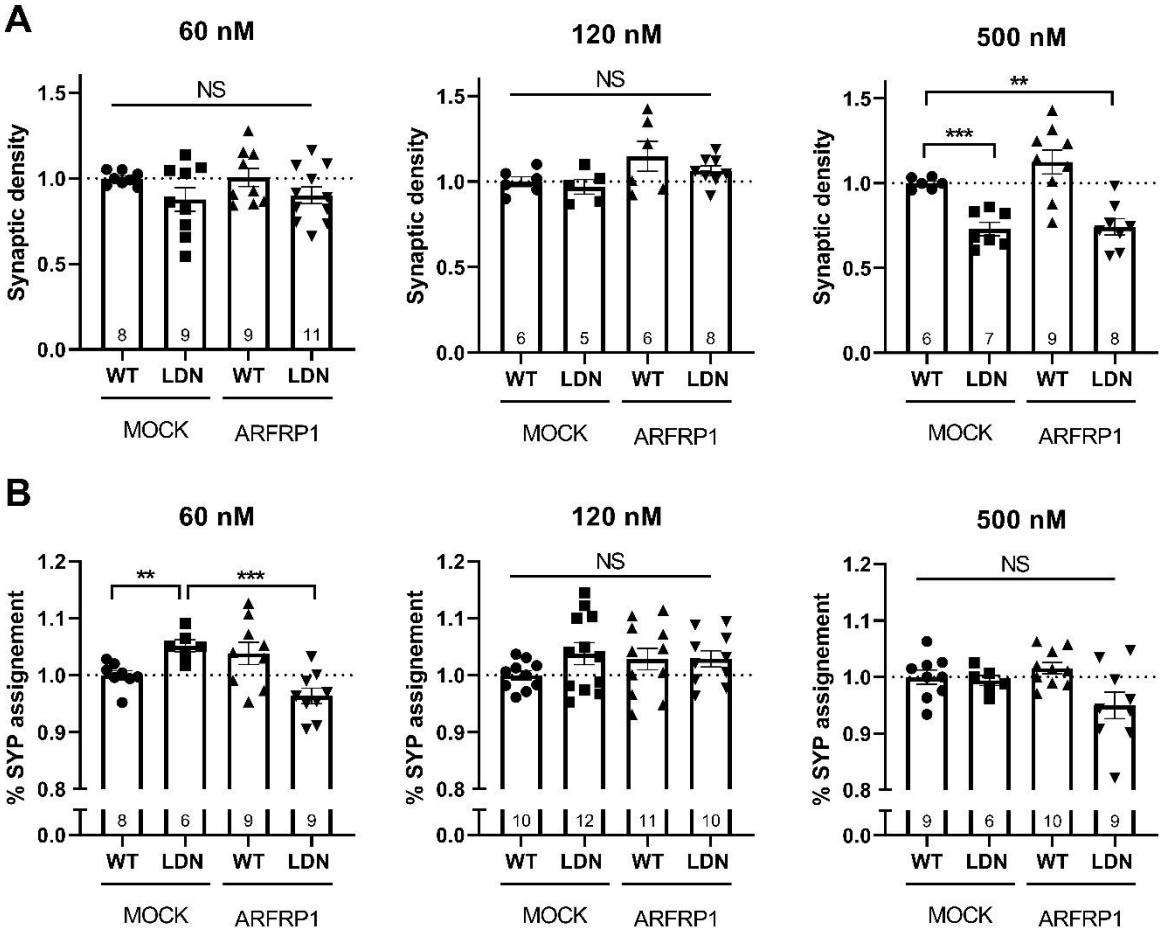

Figure 4.7. Conditioned medium paradigms and *ARFRP1* overexpression effects on synapses. Effect of 60 nM, 120 nM and 500 nM Aβ of CM from CHO-APP-LDN cells on (A) synaptic density and (B) synaptic connectivity. Each data point represents one microfluidic device, obtained from N=4 independent cultures. The dotted lines (y=1) indicate the baseline. Device numbers (n) are given per condition. Data represented as mean ± SEM. Values outside of the median ± 3× MAD interval were excluded. Welch's ANOVA followed by Tamhane T2 multiple comparison test. **p<0.01; ***p<0.001.

4.2.2 The physiological role of ARFRP1 at the synapse

4.2.2.1 ARFRP1 modulation impact on synaptic connectivity

To further understand the role of *ARFRP1* at the synapse we first assessed the impact of gene expression modulation (silencing and overexpression) in neurons in the presence or absence of cLTP induction. Therefore, we designed and optimised an shRNA lentivirus to selectively knockdown *ARFRP1* expression in neurons (Supplementary Figure S7). To overexpress the gene, we re-used the lentivirus obtained for the medium-throughput screening. We detected no significant effect of *ARFRP1* modulation on synaptic connectivity, regardless of cLTP induction (Figure 4.8).

Similarly, cLTP treatment alone did not significantly alter synaptic connectivity in control groups. This could be explained by a limited sensitivity of the readout on E-LTP phase. By contrast, structural changes associated with L-LTP typically emerge on longer time scale (>2-3 h post induction), when an increase in postsynaptic puncta and consequently a possible increase in synaptic connectivity would be expected during this later window[275]. These results differ from the well-plate-based shRNA screening previously conducted, where silencing *ARFRP1* decreased synaptic connectivity by 22%. Biologically, this discrepancy could stem from differences in the developmental stage and in the experimental context. In the screening assay, *ARFRP1* silencing was initiated at DIV1 under the control of a strong, ubiquitous U6 promoter, leading to broad knockdown in both neurons and astrocytes during an early period of neuronal polarisation, neurite extension, and synapse formation [276,277]. In contrast, in our microfluidic experiments, gene modulation occurred later (DIV7) in neuronal cultures that had already established a basic network architecture. Consequently, *ARFRP1* knockdown at this stage would be less likely to interfere with initial synaptogenesis and may instead affect processes associated with synaptic maturation, receptor trafficking, or activity-dependent remodelling. Furthermore, microfluidic systems differ from plate cultures in their spatial organisation and local environment as they impose directional connectivity and limit medium exchange. These conditions may buffer subtle developmental perturbations detectable in bulk cultures while emphasising compartment-specific and functional aspects of synaptic regulation.

Taken together, these findings suggest that *ARFRP1* may be dispensable for baseline synapse formation in more mature networks but could become critical under conditions of elevated trafficking demand or cellular stress, such as during cLTP induction or Aβ exposure, when it could modulate presynaptic vesicle release and/or postsynaptic receptor dynamics and contribute to synaptic resilience.

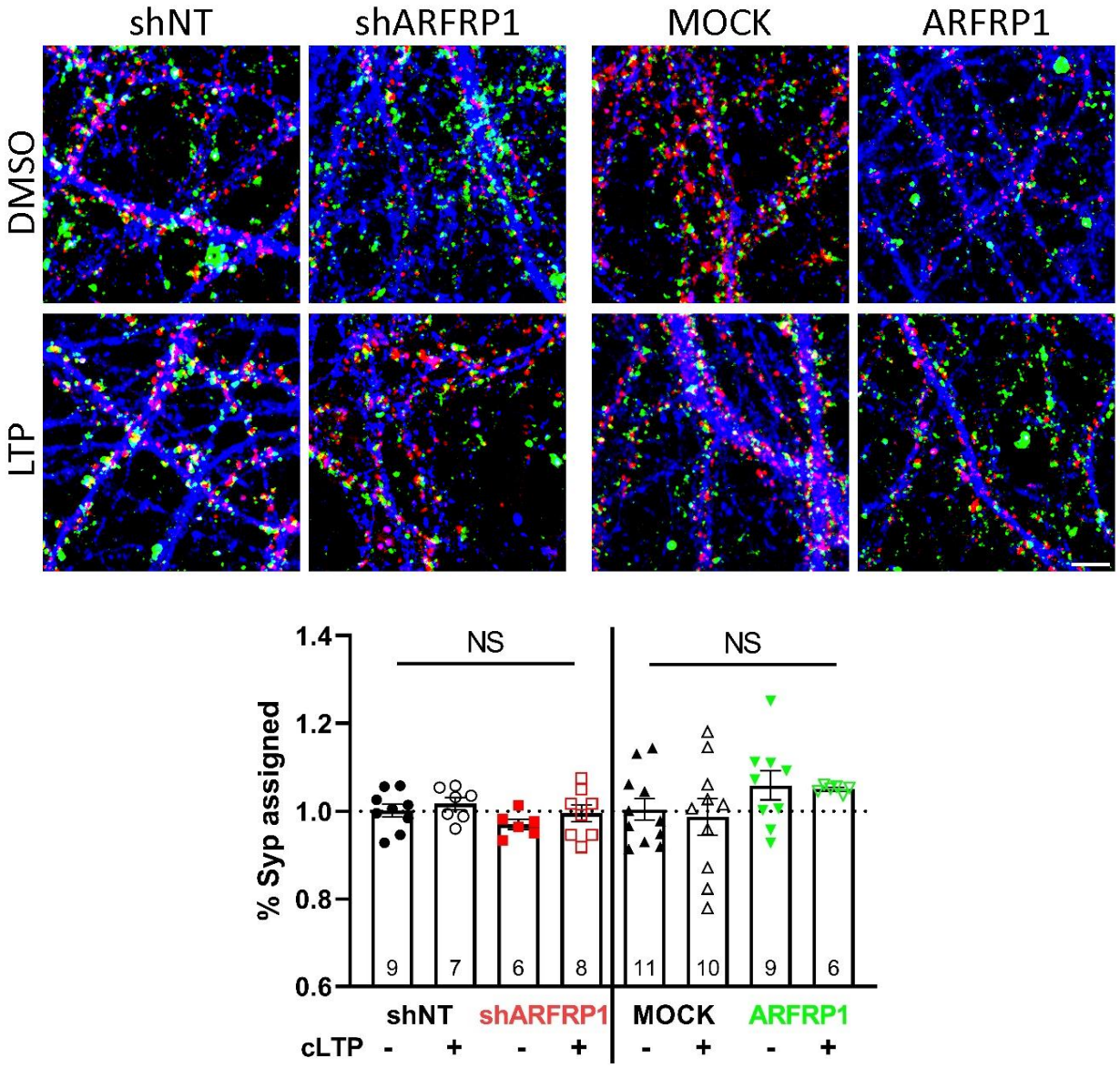

Figure 4.8. Impact of *ARFRP1* modulation on synaptic connectivity. Representative images (top) of the synaptic chamber at DIV21 showing SYP (green), Homer1 (red) and Tubulin (blue) immunostaining. Scale bar = 5 µm. Quantification of synaptic connectivity (bottom). Each data point represents device mean of *%SYP_assigned* of all images taken. Error bars show standard error. The dotted line (y=1) indicates the baseline. Device number (n) is reported per condition. Data obtained from N=3 independent cultures. Values outside of the median ± 3× MAD interval were excluded. Welch's ANOVA followed by Tamhane T2 multiple comparison test (separate tests for knock-down and over-expression). NS = not significant.

4.2.2.2 ARFRP1 modulation effect on postsynaptic receptors

As *ARFRP1* regulates secretory and endosomal pathways, we hypothesised that its potential synaptoprotective effect might modulate AMPAR dynamics – either by altering surface delivery and recycling or by promoting local dendritic retention. Given that Aβ toxicity has been shown to disrupt AMPAR trafficking[166], these pathways represent a

plausible point of convergence between *ARFRP1* function and Aβ-induced synaptic dysfunction. To explore this possibility, we measured total and phosphorylated forms of AMPARs subunits GluA1 and GluA2 by Western blotting (Figure 4.9) and examined dendritic labelling by immunofluorescence in microfluidic cultures after cLTP induction (Figures 4.10 and 4.11).

Analysis of lysates from primary cortical cultures (Figure 4.9) confirmed successful cLTP induction, evidenced by a robust increase in GluA1 phosphorylation across both control groups ($p<0.05$ for both shNT and MOCK) and experimental groups ($p<0.05$ for shARFRP1; $p<0.01$ for ARFRP1). However, *ARFRP1* modulation did not significantly alter total or phosphorylated GluA1 levels under basal or LTP conditions. cLTP also significantly reduced total GluA2 levels in MOCK and ARFRP1 groups (0.72±0.03; $p<0.05$ and 0.77±0.14; $p<0.05$ respectively) but not in shNT. Although Kruskal-Wallis indicated an overall effect within the shARFRP1 group on GluA2 levels, Dunn's *post-hoc* analysis did not reveal a specific pairwise difference. Finally, neither genetic modulation nor cLTP treatment affected phosphorylated GluA2 abundance. The ratio of pGluA1 to total GluA1 was significantly higher following cLTP in all experimental groups ($p<0.05$) whereas pGluA2/GluA2 ratio remained unchanged across conditions.

We observed some discrepancies in the effect of cLTP on GluA2 levels between control groups. Indeed, cLTP reduced GluA2 levels in MOCK control condition (0.71±0.03; $p<0.05$) but not in shNT (0.89±0.12; $p<0.99$). This variation is unexpected since total GluA2 protein typically remains stable during the early phases of LTP induction[278]. These differences are likely related to vector-specific factors rather than genuine biological variability. The shNT vector relies on the miRNA/shRNA backbone, engaging the endogenous RNA-interference machinery and potentially producing a mild transcriptional load, whereas the MOCK vector lacks this cassette and could therefore display a divergent phenotype[279]. Moreover, the MOCK vector was transduced at a higher MOI (MOI2) compared to the shNT vector (MOI1). Although elevated viral load can in principle trigger some innate immune signalling, this MOCK inconsistency was only observed once in all our experiments, so any potential adverse effect of MOI difference should be considered with caution[280].

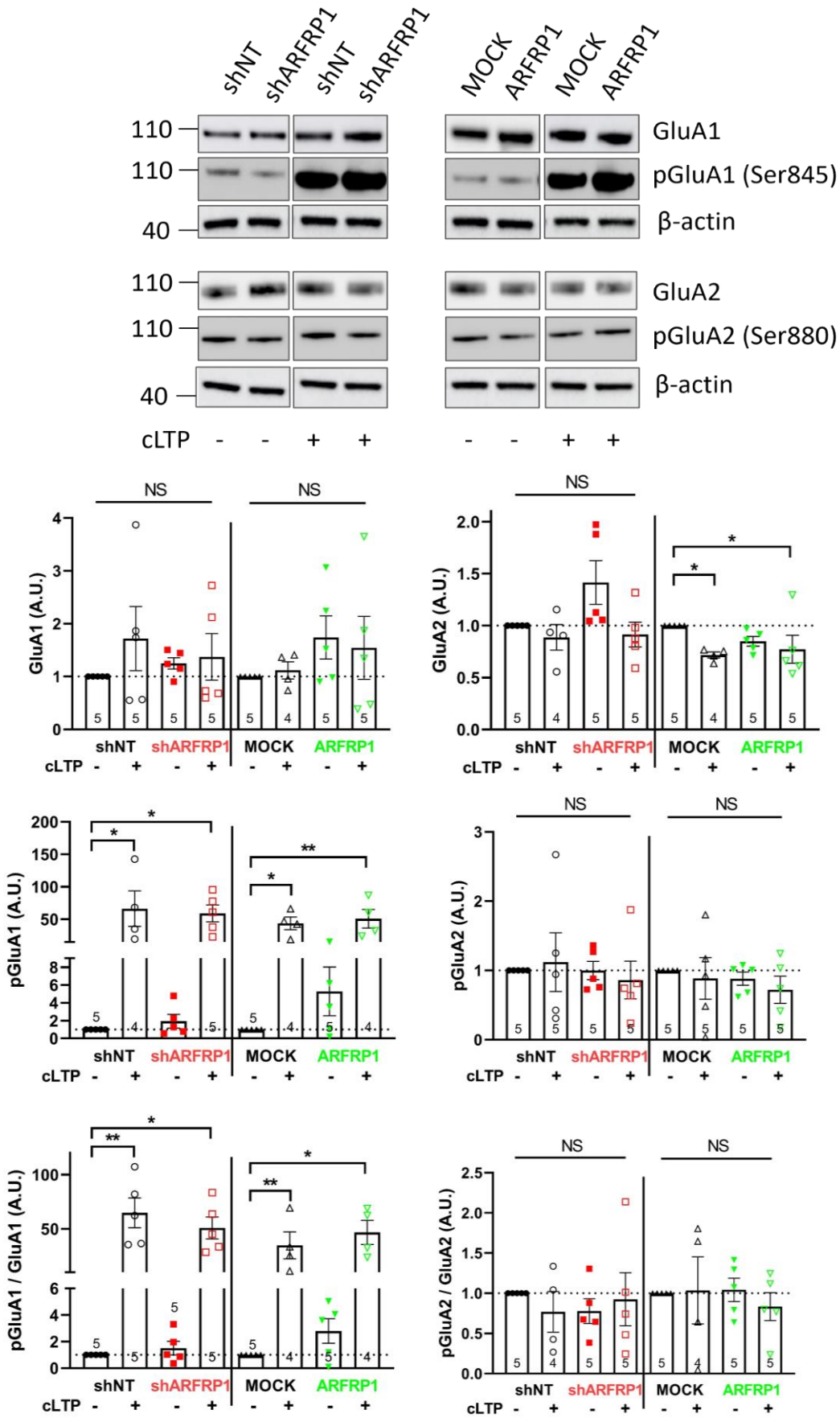
shNT
shARFRP1
shNT
shARFRP1
MOCK
ARFRP1
MOCK
ARFRP1
110
110
40
GluA1
pGluA1 (Ser845)
β-actin
110
110
40
GluA2
pGluA2 (Ser880)
β-actin
cLTP - - + + - - + +
GluA1 (A.U.)
GluA2 (A.U.)
pGluA1 (A.U.)
pGluA2 (A.U.)
pGluA1 / GluA1 (A.U.)
pGluA2 / GluA2 (A.U.)
NS
shNT
shARFRP1
MOCK
ARFRP1

Figure 4.9. *ARFRP1* modulation effect on AMPARs subunits phosphorylation in cortical neurons. Representative immunoblots and quantification of AMPAR subunits and their phosphorylated forms in primary cortical neurons. Neurons were stimulated with FSK and Rol to induce cLTP or treated with DMSO vehicle control. Values were normalised within vector family: shRNA conditions were normalised with shNT/DMSO mean; overexpression conditions were normalised with MOCK/DMSO mean. The dotted lines (y=1) indicate the baseline. N=5 independent cultures. Data are presented as mean ± SEM where each data point correspond to an independent culture. Outliers were excluded using the IQR method. Kruskal-Wallis followed by Dunn's multiple comparison test. *p<0.05; **p<0.001; NS = not significant.

Overall, the data validated cLTP induction but did not support *ARFRP1*-dependent-changes in AMPAR subunits. However, because Western blotting reflects bulk protein abundance in cortical population averaged across all cell types (*i.e.*, neurons and astrocytes) and subcellular compartments, potential synapse-restricted alterations in AMPARs distribution could have been masked. To resolve such compartment-specific effects with higher spatial precision, we next used hippocampal neurons in microfluidic devices combined with immunofluorescence analysis to selectively examine dendritic and synaptic localisation of AMPARs. It allows the investigation of whether *ARFRP1* modulates the trafficking and retention of GluA1- and GluA2-containing AMPARs in a neuronal population inherently susceptible to Aβ-driven plasticity defects. Thus, using hippocampal neurons provides both mechanistic specificity and translational value in understanding how *ARFRP1* contributes to synaptic resilience in the AD context.

Indeed, hippocampal neurons differ from cortical neurons in their AMPAR subunit composition, trafficking dynamics, and plasticity profiles, features that are directly relevant to AD-related synaptic mechanisms[126,281,282]. Hippocampal networks exhibit a higher proportion of GluA1-containing AMPARs and display pronounced activity-dependent insertion and removal of these receptors during LTP and LTD respectively – processes that are highly sensitive to Aβ-induced disruption[283]. In contrast, cortical neurons generally maintain more stable AMPAR populations with less dynamic subunit turnover, reflecting their predominant role in long-term information storage rather than rapid synaptic remodelling[283]. Given that Aβ oligomers preferentially impair LTP and facilitate LTD in hippocampal circuits, the hippocampal microfluidic model provides a particularly relevant framework to assess *ARFRP1* function[119,158].

As described in Section 3.10.1, neurons were transduced at DIV7, and cLTP was induced at DIV21 selectively in the postsynaptic chamber. Cells were then aldehyde-fixed and both total and phosphorylated forms of AMPAR subunits were immunolabelled (Figures 4.10 and 4.11). *ARFRP1* silencing significantly reduced GluA1 mean spot intensity under both basal (0.69±0.07; $p<0.05$) and cLTP conditions (0.66±0.10; $p<0.01$). pGluA1 mean spot intensity was also reduced in basal conditions (0.82±0.02; $p<0.0001$), whereas no significant changes were observed in GluA2 or pGluA2 mean spot intensity ($p>0.05$ for both read-outs). Such reductions in GluA1 and in its phosphorylated form suggest enhanced receptor internalisation and reduced synaptic incorporation, consistent with a shift towards LTD-like mechanisms that may weaken synaptic transmission[126]. Conversely, *ARFRP1* overexpression significantly increased GluA1 intensity after cLTP (1.70±0.24; $p<0.05$) and was close to significance in basal conditions (1.69±0.26; $p=0.07$), suggesting moderate effects under basal conditions. *ARFRP1* overexpression also led to a significant decrease in GluA2 mean spot intensity in both basal and LTP conditions (0.72±0.04 and 0.76±0.06, respectively) but had no impact on pGluA1 or pGluA2 readouts ($p<0.05$ for both read-outs). This pattern of GluA1 enrichment and GluA2 reduction indicates a shift towards mechanisms supporting E-LTP expression and enhanced synaptic plasticity dynamics[126,129].

Regarding cLTP effects, pGluA1 mean spot intensity showed an close-to-significance increase in the MOCK condition (1.48±0.17; $p=0.0503$) and a significant increase in the *ARFRP1*-overexpresion group (1.48±0.15; $p<0.05$), while no significant change was detected in the shNT condition, possibly explained by the strong variation in the data. We also observed a significant decrease in GluA1 mean intensity after cLTP induction in shNT (0.53±0.05; $p=0.001$) while the MOCK group was not affected. Although both constructs are designed as controls, the miR20-based shRNA cassette introduces additional cellular demands such as transcriptional load, and regulatory interactions absent in the MOCK vector. This could lead to subtle off-target and/or mild toxic effects induced by the non-targeting shRNA[279]. However, since this effect was only observed in a single readout and did not consistently impact other parameters, it is unlikely to reflect genuine endogenous toxicity and does not compromise the validity of the shNT construct as an experimental control.

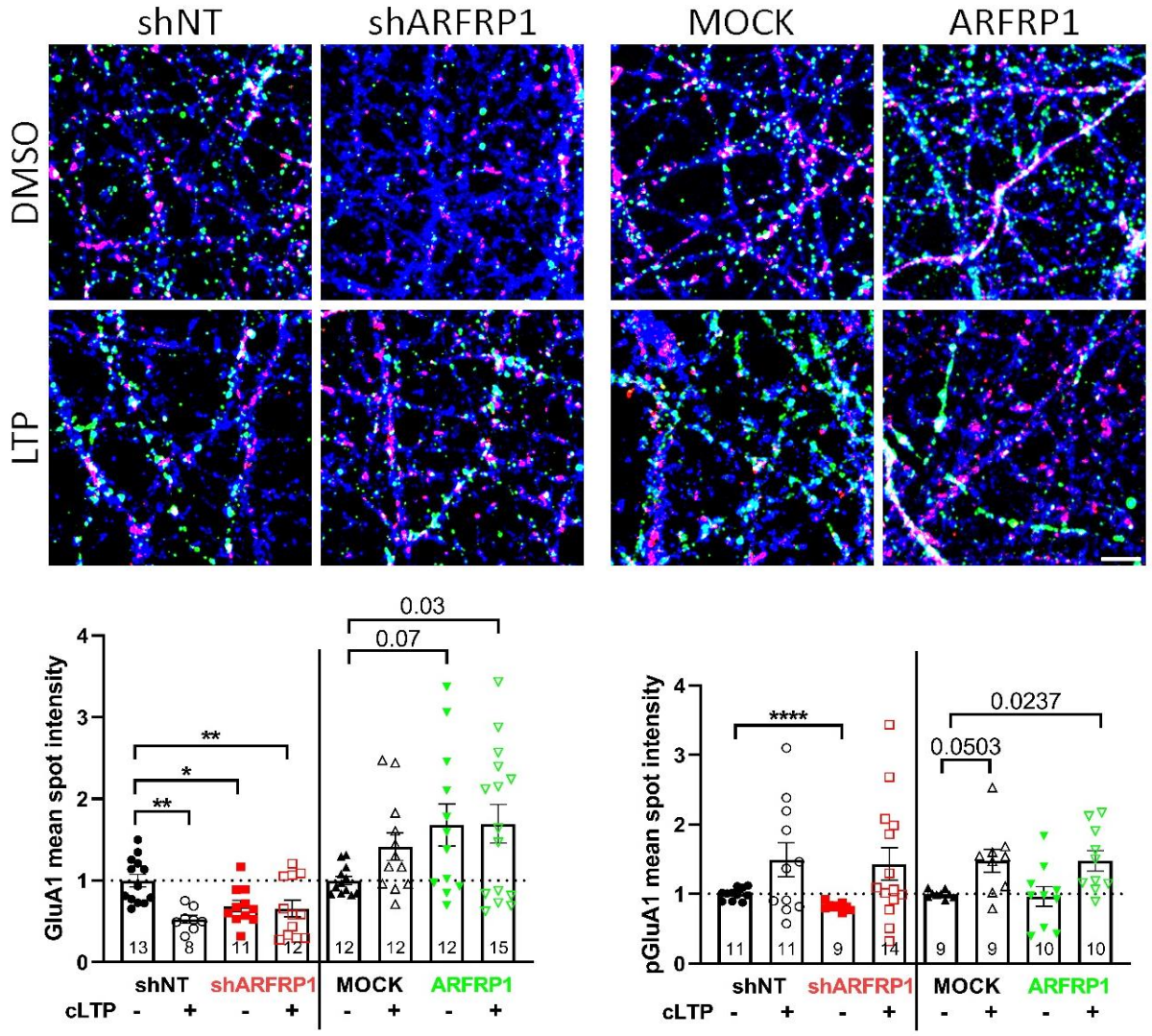

Figure 4.10. *ARFRP1* modulation affects the phosphorylation of the GluA1 subunit of AMPAR in hippocampal neurons in microfluidics. Representative images (top) of the neuronal network acquired from the synaptic chamber showing total GluA1 (red), pGluA1 (green) and tubulin (blue). Scale bar = 5 µm. Quantification of fluorescence intensity (bottom) for the given conditions. Values were normalised within vector family: shRNA conditions were normalised with shNT/DMSO mean; overexpression conditions were normalised with MOCK/DMSO mean. The dotted lines (y=1) indicate the baseline. Device number (n) is reported per condition. N=5 independent cultures. Data are presented as mean ± SEM where each data point correspond to an independent culture. Values outside of the median ± 2.5 × MAD interval were excluded. Welch's ANOVA followed by Tamhane T2 multiple comparison test. *p<0.05; **p<0.01; ****p<0.0001; NS = not significant.

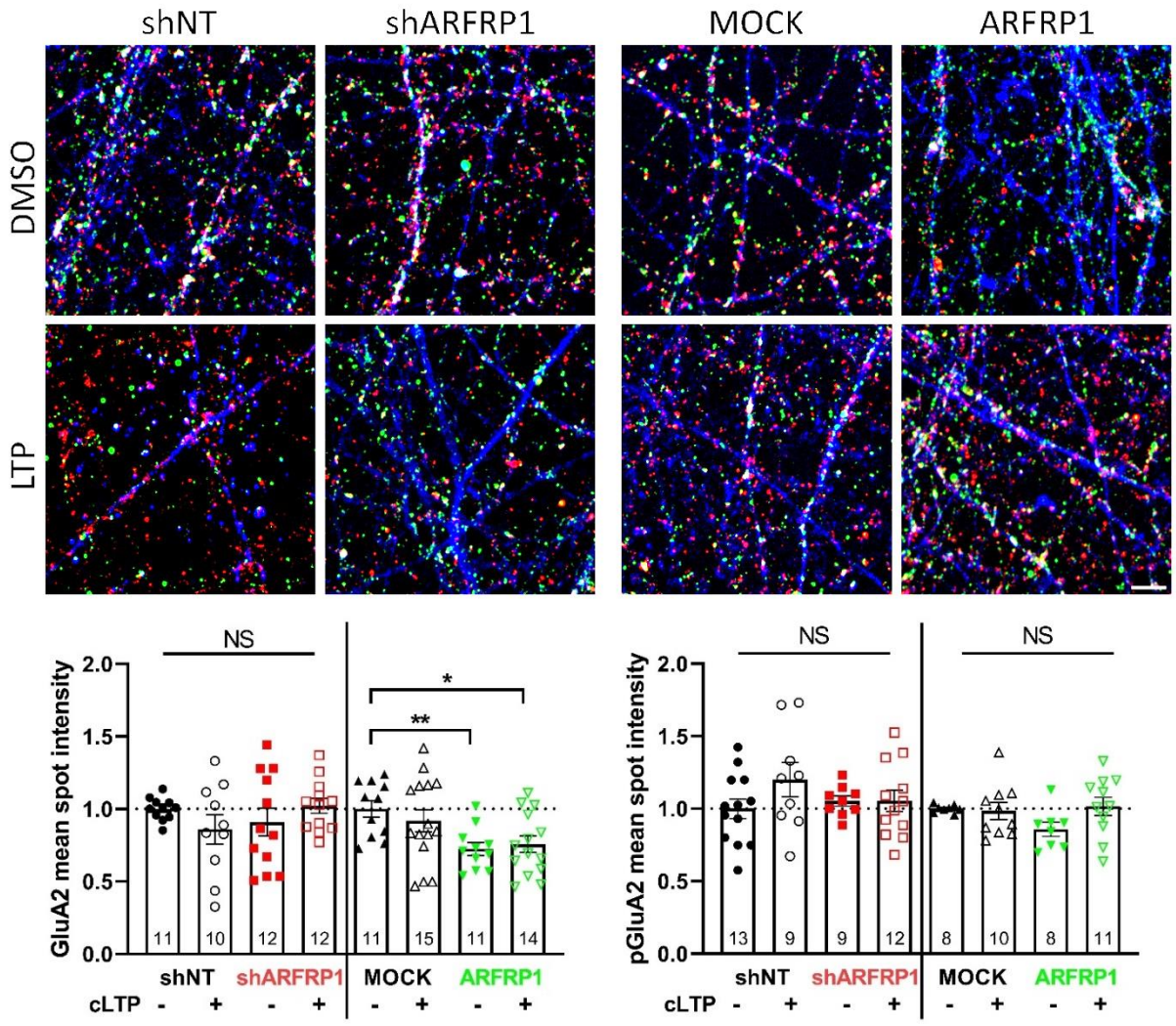

Figure 4.11. *ARFRP1* modulation affects the phosphorylation of the GluA2 subunit of AMPAR in hippocampal neurons in microfluidics. Representative images (top) of the neuronal network acquired from the synaptic chamber showing total GluA2 (red), pGluA2 (green) and tubulin (blue). Scale bar = 5 µm. Quantification of fluorescence intensity (bottom) for the given conditions. Values were normalised within vector family: shRNA conditions were normalised with shNT/DMSO mean; overexpression conditions were normalised with MOCK/DMSO mean. The dotted lines (y=1) indicate the baseline. Device number (n) is reported per condition. N=5 independent cultures. Data are presented as mean ± SEM where each data point correspond to an independent culture. Values outside of the median ± 2.5 × MAD interval were excluded. Welch's ANOVA followed by Tamhane T2 multiple comparison test. *p<0.05; **p<0.01; NS = not significant.

Together, these results suggest that *ARFRP1* differentially regulates AMPAR subunit composition in ways that may modulate synapses toward either LTD-like or LTP-like states, thereby shaping their susceptibility to Aβ-induced synaptic dysfunction. Silencing *ARFRP1* significantly reduced GluA1 and pGluA1 mean spot intensity, consistent with a shift toward an LTD-like molecular profile[284]. Since GluA1 and its phosphorylation are critical for AMPAR insertion and synaptic potentiation, these reductions are likely to

impair synaptic signalling by limiting GluA1-enriched receptor availability and activity-dependent signalling[285]. Such a state may also render synapses more vulnerable to Aβ, which preferentially exploits LTD-associated pathways to promote AMPARs internalisation and synaptic weakening. In contrast, *ARFRP1* overexpression significantly decreased GluA2 and tended to increase GluA1, producing a more GluA1-rich, LTP-like receptor profile that might be beneficial for strengthening synaptic connections[114]. This configuration can stabilise AMPARs at postsynaptic sites and counteract Aβ-driven receptor loss, explaining why *ARFRP1* overexpression could preserve synaptic connectivity in the chronic CHO-APP-LDN co-culture model. However, under acute high-dose Aβ exposure, the same GluA1-enriched, GluA2-depeleted composition likely increases the fraction of calcium-permeable AMPARs, enhancing excitotoxic risk and limiting the protective capacity of *ARFRP1*[79]. Altogether, these findings suggest that *ARFRP1* could modulate synaptic vulnerability to Aβ in a context-dependent manner: protective under chronic-low dose Aβ exposure by maintaining AMPARs trafficking and synaptic stability, but less effective when acute, high-dose Aβ treatment overwhelms calcium homeostasis.

To further elucidate the mechanisms underlying *ARFRP1*-mediated protection, we aimed (i) to assess its subcellular localisation within the synaptic compartment, and (ii) to selectively express *ARFRP1* in pre- and/or postsynaptic neurons in the presence of Aβ, to determine whether its effects arise primarily from modulation of presynaptic trafficking or postsynaptic AMPAR regulation.

4.2.3 ARFRP1 compartmental protective role

4.2.3.1 Synaptic localisation of ARFRP1

The localisation of ARFRP1 protein at the synapse was assessed by Western blotting after synaptic fractionation of cortical neurons following cLTP or cLTD induction (Figure 4.12). As expected, PSD95 was predominantly detected in the PSD fraction, while SYP was present in the non-PSD fraction, confirming successful compartmental separation. A minor PSD95 signal was also observed in the non-PSD fraction, which reflects limited post-to-presynaptic contamination. Finally, ARFRP1 was strongly enriched in the non-PSD fraction, which suggests that ARFRP1 is not tightly associated or stably cross-linked

with the postsynaptic density under basal conditions. However, this does not exclude the potential postsynaptic expression of the protein. Rather, these results suggest that ARFRP1 is present within synaptic compartments but is not firmly retained within the PSD scaffold at rest.

Synaptic stimulation did not noticeably affect the distribution of PSD95 or SYP across fractions, which is expected. In contrast, LTD induction appeared to increase the amount of ARFRP1 detected in the PSD fraction. Because Aβ-induced synaptic depression shares key molecular features with LTD, particularly AMPAR internalisation, this redistribution suggests that ARFRP1 may be recruited to the PSD under conditions of synaptic weakening.

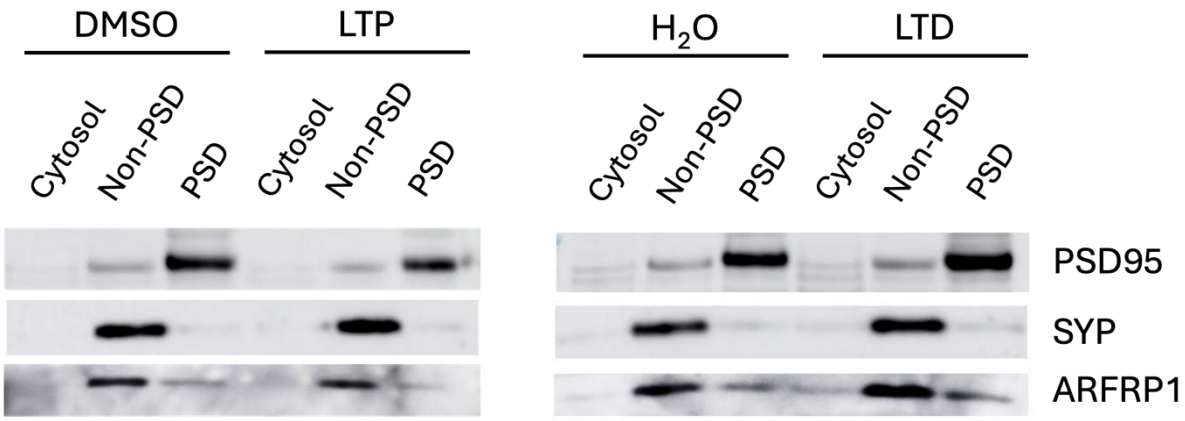

Figure 4.12. Synaptic localisation of ARFRP1. Immunoblot of cytosolic, non-PSD and PSD fractions showing PSD95 and SYP as post and presynaptic control proteins, respectively, and ARFRP1 after LTP and LTD induction with respective DMSO or H_2O vehicle controls.

Combined with previous results showing that ARFRP1 overexpression in both compartments modulated postsynaptic AMPAR subunits and appeared to limit synaptic vulnerability from Aβ-induced toxicity, this observation is consistent with a postsynaptic protective mechanism, in which *ARFRP1* may contribute to AMPAR trafficking and retention, enhancing GluA1-rich receptors availability and counteracting Aβ-induced receptor internalisation, thus preserving synaptic responsiveness and connectivity. Nevertheless, a distinct presynaptic contribution cannot be excluded: *ARFRP1* may also sustain endosomal and secretory trafficking at the presynaptic terminal, thereby maintaining vesicle recycling and neurotransmitter release, which would indirectly stabilise postsynaptic activity and receptor composition. These mechanisms are not mutually exclusive; indeed, presynaptic maintenance of activity could synergise with

postsynaptic AMPAR regulation to confer dual protection. To disentangle these possibilities, compartment-specific modulation of *ARFRP1* is required to determine the relative contribution of presynaptic *versus* postsynaptic processes to the potential synaptoprotective effect.

4.2.3.2 Compartmental effect of ARFRP1 against Aβ

In order to assess the potential protective mechanism against Aβ-induced synaptic dysfunction, we transduced microfluidic devices with MOCK control vector or *ARFRP1* selectively in the presynaptic, in the postsynaptic or in both compartments. At DIV21, the synaptic chamber was treated with CM from CHO-APP-WT or CHO-APP-LDN cells and synaptic density and connectivity were assessed (Figure 4.13).

Under basal conditions (without Aβ exposure), *ARFRP1* overexpression alone induced compartment-specific effects. Dual (pre- and postsynaptic) transduction decreased synaptic connectivity (0.88±0.03; $p<0.05$) without altering synaptic density (1.04±0.08; $p>0.99$), consistent with postsynaptic functional impairment. Presynaptic *ARFRP1* overexpression reduced synaptic density (0.79±0.08; $p<0.01$) without affecting connectivity (0.93±0.04; $p>0.05$), suggesting structural presynaptic loss. Conversely, postsynaptic *ARFRP1* overexpression decreased synaptic density (0.70±0.03; $p<0.0001$) but significantly increased connectivity (1.09±0.01; $p<0.01$), indicating fewer presynaptic terminals but enhanced alignment or retention of postsynaptic puncta – a pattern consistent with selective synaptic strengthening [286–288].

After treatment with CHO-APP-LDN CM, synaptic alterations were evident in all control (MOCK) configurations. In cultures transduced with the MOCK vector in both chambers, Aβ exposure led to a reduction in synaptic connectivity (0.87±0.03; $p<0.01$), while synaptic density remained stable (1.01±0.10; $p>0.99$). This pattern suggests a decrease in the number of functional synapses, likely reflecting postsynaptic receptors impairment rather than presynaptic loss. In cultures with MOCK transduced only in the presynaptic chamber, CHO-APP-LDN CM significantly reduced both synaptic density (0.72±0.04; $p<0.0001$) and connectivity (0.77±0.04; $p<0.001$), indicating a global synaptotoxic effect involving both pre- and postsynaptic compartments. Conversely, in cultures with MOCK

transduction only in the postsynaptic chamber, Aβ treatment decreased synaptic density (0.73±0.04; $p<0.001$) without affecting connectivity (0.89±0.04; $p=0.33$), suggesting a primarily presynaptic alteration, such as reduced bouton density or impaired axonal integrity.

When *ARFRP1* was overexpressed in the presence of Aβ, its effects were compartment dependent. *ARFRP1* overexpression in both chambers or selectively in the presynaptic chamber, showed no protection against Aβ-induced dysfunction for either synaptic density (0.61±0.09; $p<0.05$ and 0.67±0.02; $p<0.0001$ respectively) or connectivity (0.70±0.02; $p<0.0001$ and 0.75±0.03; $p<0.0001$ respectively). *ARFRP1* overexpression in both compartments also exacerbated Aβ-induced detrimental effects ($p<0.05$ for synaptic density; $p<0.001$ for synaptic connectivity). This effect likely reflects a loss of compartmental balance, as simultaneous modulation of presynaptic and postsynaptic trafficking could disrupt the coordination between vesicle release and receptor recycling. Given that the applied Aβ treatment paradigm represents a non-physiological, high-dose paradigm likely to saturate trafficking pathways, additional *ARFRP1* activity may have further overloaded the system, thereby amplifying synaptic dysfunction rather than preventing it. In contrast, postsynaptic *ARFRP1* overexpression maintained both parameters at levels comparable to the MOCK-WT group (0.94±0.10; $p=0.99$ for density and 0.92±0.06; $p>0.05$ for connectivity), suggesting that postsynaptic *ARFRP1* expression may mitigate Aβ-induced synaptic vulnerability.

These findings are consistent with a context-dependent role for *ARFRP1* in synaptic regulation and highlight how the temporal pattern of Aβ exposure critically shapes synaptic outcomes. Indeed, *ARFRP1* presynaptic overexpression did not rescue Aβ induced impairment, while *ARFRP1* postsynaptic overexpression showed no significant protection but a mild tendency to preserve synaptic connectivity. In our earlier CHO co-culture model, neurons were exposed to a chronic, low-level release of Aβ from the onset of development, a condition that better mimics the gradual accumulation occurring in the early stages of AD[289]. Under such circumstances, synapses may engage slower homeostatic mechanisms, including AMPAR trafficking and recycling[128,290], which could allow *ARFRP1* to support vesicle trafficking and/or receptor delivery, thereby contributing to long-term synaptic stability.

In contrast, the present experiments involved acute, high-dose Aβ exposure of mature networks, a setting known to trigger rapid AMPAR removal and dendritic spine loss within minutes to hours[166,291]. Such swift receptor internalisation and structural disassembly likely outpace the trafficking and membrane-stabilising processes possibly influenced by *ARFRP1*, limiting its protective potential. This interpretation aligns with evidence that acute Aβ exposure provokes immediate synaptic depression through NMDA-dependent signalling[292,293], whereas chronic and lower concentrations may allow compensatory plasticity and gradual remodelling. Nevertheless, *ARFRP1* postsynaptic overexpression effect on synaptic readout is consistent with postsynaptic structure stabilisation and synapse strengthening, further reinforcing its potential role in maintaining synapses under stress conditions.

Together, these considerations suggest that *ARFRP1* could acts primarily as a developmental or maintenance factor, potentially capable of counteracting the slow synaptic erosion caused by long-term Aβ stress, but largely ineffective against the rapid synaptic dysfunction elicited by late-stage, high-concentration of Aβ. To test this hypothesis in a functional manner, we combined MEA chips with microfluidic devices to selectively transduce postsynaptic neurons to investigate network function connectivity before and after Aβ treatment.

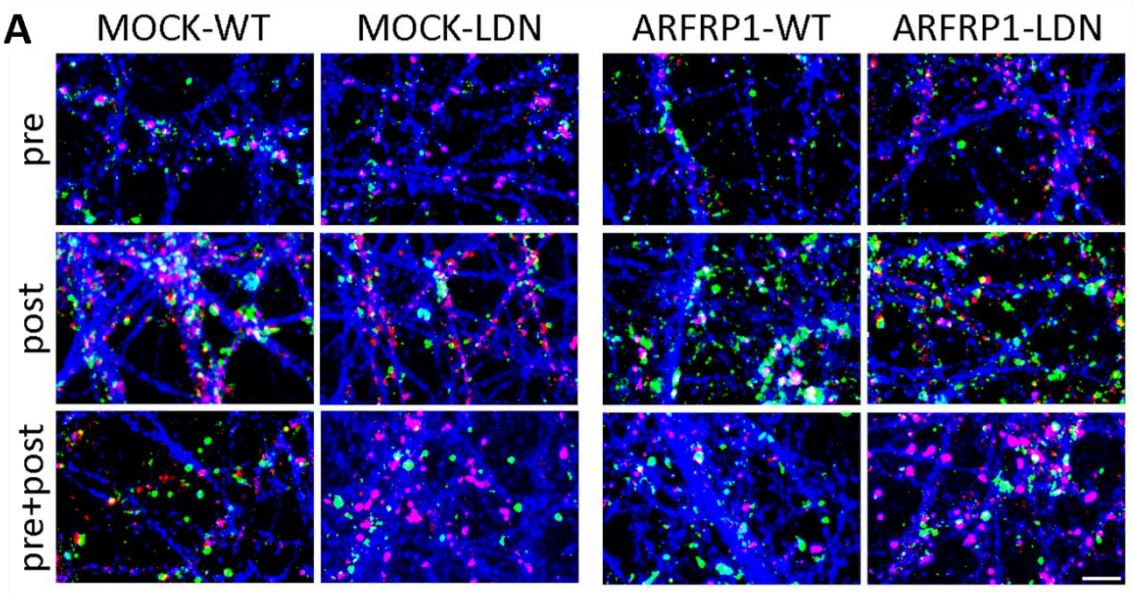

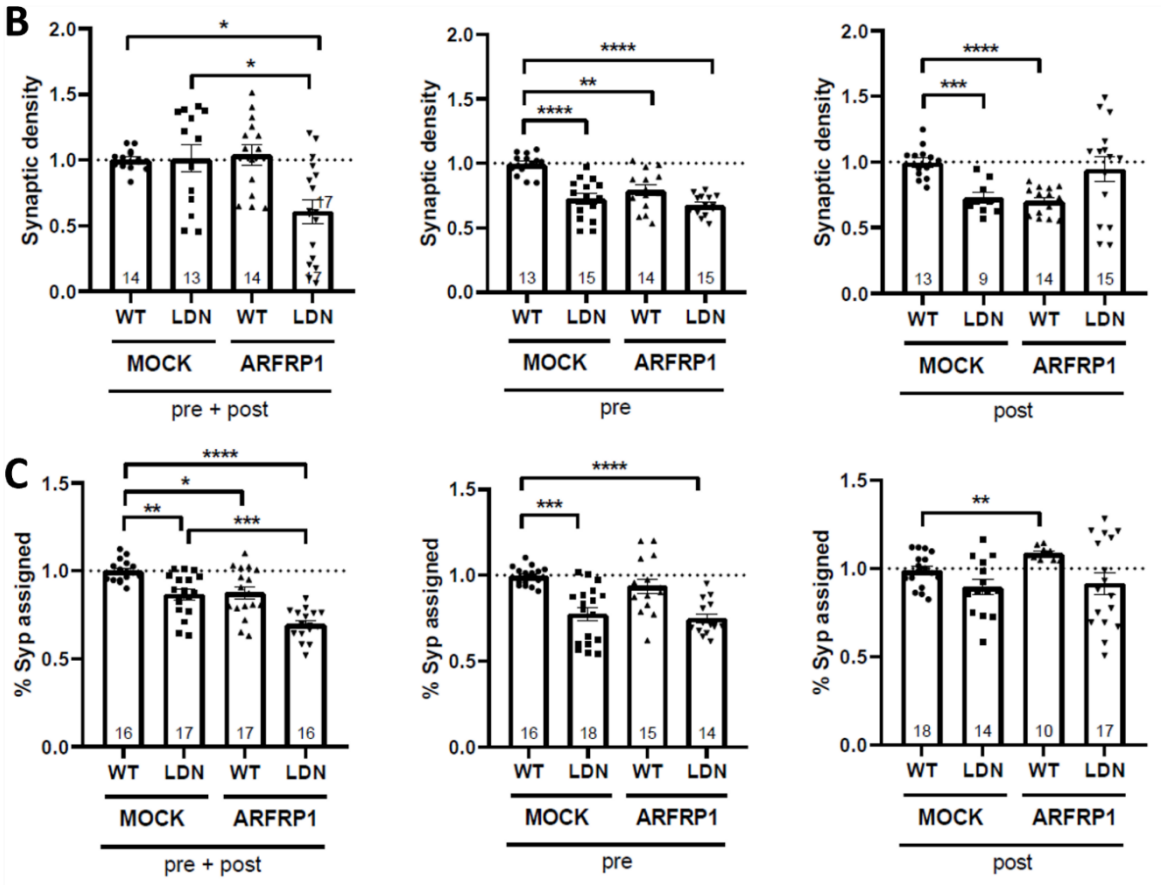

Figure 4.13. Compartment-specific effect of *ARFRP1* overexpression on Aβ-induced synaptotoxicity. (A) Representative images of the neuronal network acquired from the synaptic chamber showing total Homer1 (red), SYP (green) and tubulin (blue). Scale bar = 5 µm. (B-C) Quantification of synaptic density (B) and connectivity (C) in neurons transduced with MOCK or *ARFRP1* in both pre- and postsynaptic chambers (left), presynaptic chamber only (middle), or postsynaptic chamber only (right) and exposed to CHO-APP-WT (WT) or CHO-APP-LDN (LDN) CM. Data were normalised against the mean of the MOCK-APP^{WT} group. The dotted lines (y=1) indicate the baseline. Device number (n) is reported per condition. N=5 independent cultures. Data are presented as mean ± SEM where each data point correspond to an independent culture. Welch's ANOVA followed by Tamhane T2 multiple comparison test. *p<0.05; **p<0.01; ***p<0.001; ****p<0.0001.

4.3 AIM 3: Functional characterisation of the validated genes using MEAs

In the last aim of this project, we sought to assess the functional impact of *ARFRP1* and Aβ toxicity using microfluidic devices integrated with MEA chips. To achieve this, we developed a readout for functional synaptic connectivity called *pre-post-drive* (see Sections 3.17 and 3.18 for more details). This analytical framework was previously developed and optimised in the context of a parallel project, resulting in a manuscript currently under peer review, on which I am co–first author[256] (see Appendix, section D for the complete article manuscript). In this work, *BIN1* – the second strongest genetic risk factor for AD after *APOE*[230] – was investigated for its synaptic function and isoform-

specific toxicity. In *Drosophila*, BIN1iso1 expression (brain specific isoform) produced isoform-specific synaptic defects, including impaired transmission in photoreceptor neurons and altered neuromuscular junction morphology, highlighting a toxic gain-of-function that is not shared by BIN1iso8 (muscle specific) or BIN1iso9 (ubiquitous). Extending these findings to a mammalian context, microfluidic culture systems revealed that BIN1iso1 is specifically toxic when expressed presynaptically, leading to reduced synaptic connectivity. To directly assess the functional consequences of this structural loss, microfluidic devices were integrated with MEAs, enabling live readout of network-level synaptic communication.

We performed 40 MEA recordings from seven independent neuronal cultures (14 MOCK, 15 BIN1iso1, 11 BIN1iso9; presynaptic expression only). Five devices showed no detectable presynaptic units meeting the quality criteria and five more were excluded as outliers based on post:pre unit ratio (Supplementary Figure S8). The remaining datasets (12 MOCK, 8 BIN1iso1, 10 BIN1iso9) were used to evaluate functional connectivity. *Pre-post-drive* showed no correlation with the number of detected units in either chamber, confirming that it reflects network-level connectivity independently of unit count (Supplementary Figure S9). BIN1iso1 presynaptic overexpression significantly reduced *pre-post-drive* (0.94±0.06) value compared to control (1.35±0.11; $p<0.05$) and BIN1iso8 (1.35±0.02; $p<0.05$) expressing neurons, reflecting a loss of directional transmission from presynaptic to postsynaptic neurons (Figure 4.14A). Despite BIN1iso1 being expressed exclusively presynaptically, we also observed fewer postsynaptic units meeting quality criteria (4.71±0.87 for BIN1iso1; 14.27±2.63, $p<0.05$ for control; 17.86±2.82, $p<0.01$ for BIN1iso8), consistent with decreased synaptic connectivity between compartments (Figure 4.14B). Notably, firing rate and spike amplitude were unaffected, suggesting that BIN1iso1 alters synaptic communication rather than intrinsic neuronal excitability (Figures 4.14C and 4.14D). In summary, MEA-based activity analysis confirms that presynaptic BIN1iso1 expression impairs synaptic communication at the network scale, offering functional validation of the synaptic defects identified morphologically in both *Drosophila* and rat systems.

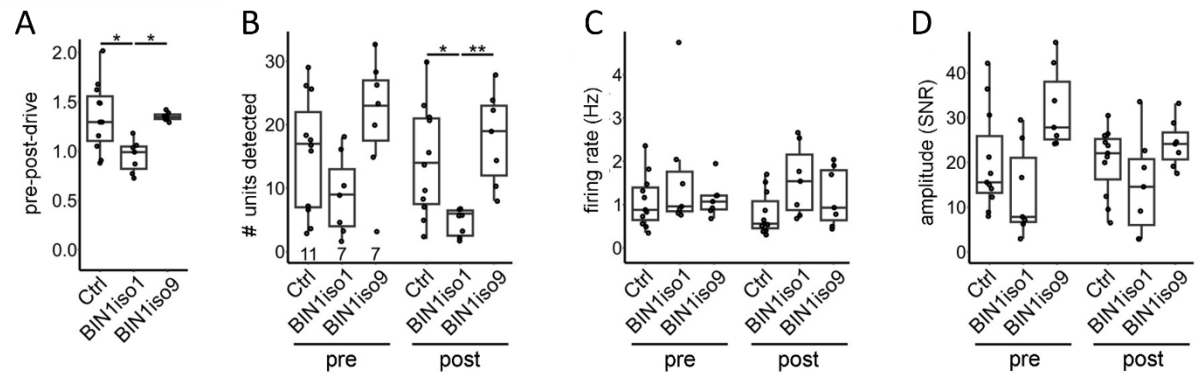

Figure 4.14. Presynaptic overexpression of BIN1iso1 perturbs the network-level connectivity in hippocampal neurons. *Pre-post-drive* (A), number of detected units meeting quality criteria (B), mean firing rate for these units (C) and mean amplitude for these units (D) as a function of BIN1 isoform (or Mock vector) expression in the presynaptic chamber. In box plots, data points refer to individual devices. N=6 independent cultures. Kruskal–Wallis ANOVA with Tukey-Kramer correction. * $p<0.05$; ** $p<0.005$.

Building on this established MEA–microfluidic framework, we used the same approach to investigate *ARFRP1* and Aβ-related synaptotoxicity, enabling direct comparison of their impact on neuronal connectivity and synapse function. Briefly, neurons were seeded in the microfluidic device coupled to the MEA and transduced at DIV7 in the postsynaptic chamber. At DIV19, a first recording was made as baseline before 500 nM Aβ treatment for 24 h. A second recording was performed at the end of this period to assess the combined impact of *ARFRP1* expression and Aβ treatment on synaptic *pre-post-drive*, an optimised readout for functional synaptic connectivity (see Sections 3.17 and 3.18 for more details)[256].

We first assessed the effect of *ARFRP1* overexpression on the pre-post-drive and unit properties under basal conditions (*i.e.*, prior to Aβ treatment; Figure 4.15). Overexpression of *ARFRP1* in the postsynaptic compartment did not significantly affect *pre-post-drive* (0.95±0.04; $p>0.05$; Figure 4.15.A). Similarly, spike amplitude (signal to noise ratio; SNR) was not altered (1.17±0.09; $p>0.05$ for presynaptic units and 0.84±0.11; $p>0.05$ for postsynaptic units; Figure 4.15.C). However, the firing rate of transduced postsynaptic units was significantly reduced (0.56±0.11; $p<0.01$; Figure 4.15.B), whereas presynaptic unit firing rate remained unchanged (1.09±0.11; $p>0.05$; Figure 4.15.B).

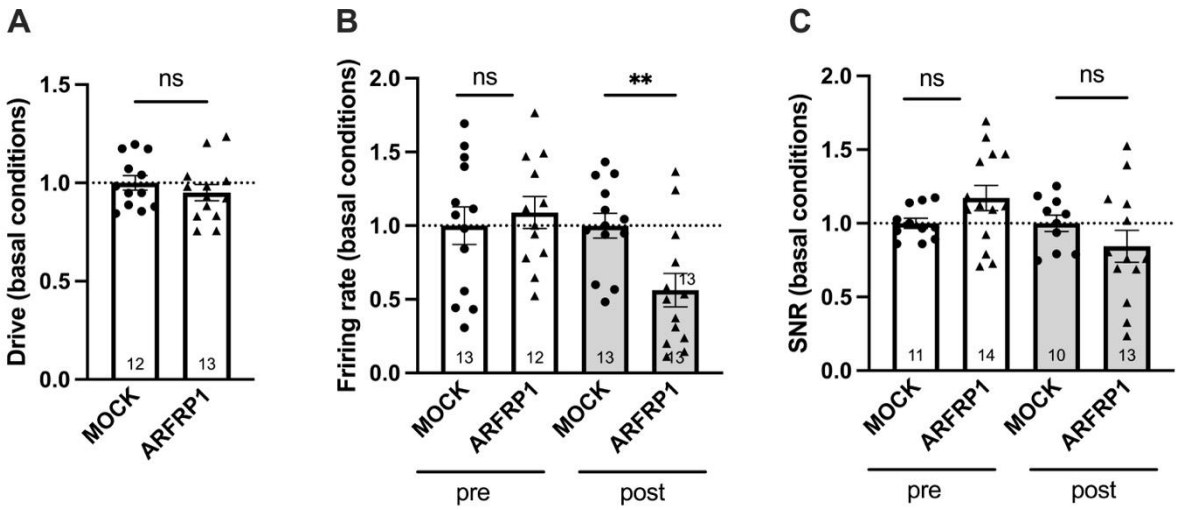

Figure 4.15. *ARFRP1* overexpression impact on synaptic drive in basal conditions using microfluidics-coupled MEAs. Effect of *ARFRP1* overexpression in basal conditions on (A) synaptic drive, (B) firing rate and (C) spike amplitude of presynaptic (white bars) and postsynaptic (grey bars) units. Device number is reported per condition within each data bar. Data normalised against the mean of the MOCK control group. Values outside of the median ± 2 × MAD interval were excluded. The dotted line indicates the reference value of y=1. N=4 independent cultures. Data displayed as mean ± SEM. MEA chip number (n) is reported per condition. Unpaired t-test. *p<0.05; **p<0.01; ns = non-significant.

We then evaluated the protective impact of *ARFRP1* on these same parameters following Aβ exposure. Figure 4.16 illustrates the fold change of each readout after treatment with Aβ. Exposure to CHO-APP-LDN CM significantly reduced *pre-post-drive* compared to the control group (0.75±0.06; p<0.05 for MOCK-APP^{LDN}). In contrast, *ARFRP1* overexpression attenuated this reduction, suggesting a partial rescue of the synaptic connectivity readout (0.90±0.05; p>0.05 for ARFRP1-APP^{LDN}). Notably, *ARFRP1* overexpression alone also significantly decreased *pre-post-drive* (0.71±0.06; p<0,05 for ARFRP1-MOCK^{WT}; Figure 4.16A). Treatment with CHO-APP-LDN CM also significantly increased the firing rate of postsynaptic units when compared to the control group (2.94±0.32-fold; p<0.01 for MOCK-APP^{LDN} units; Figure 4.16B). Although a similar trend was observed in *ARFRP1*-overexpressing units, this effect did not reach statistical significance, likely due to the variability in the data distribution (5.53±1.70-fold; p=0.11 for ARFRP1-APP^{LDN} units; Figure 4.16B). Interestingly, *ARFRP1* overexpression alone significantly increased postsynaptic units firing rate (3.28±0.52-fold for ARFRP1-APP^{WT}). Finally, spike amplitude (SNR) was largely unaffected by either *ARFRP1* overexpression or Aβ treatment (Figure 4.16C).

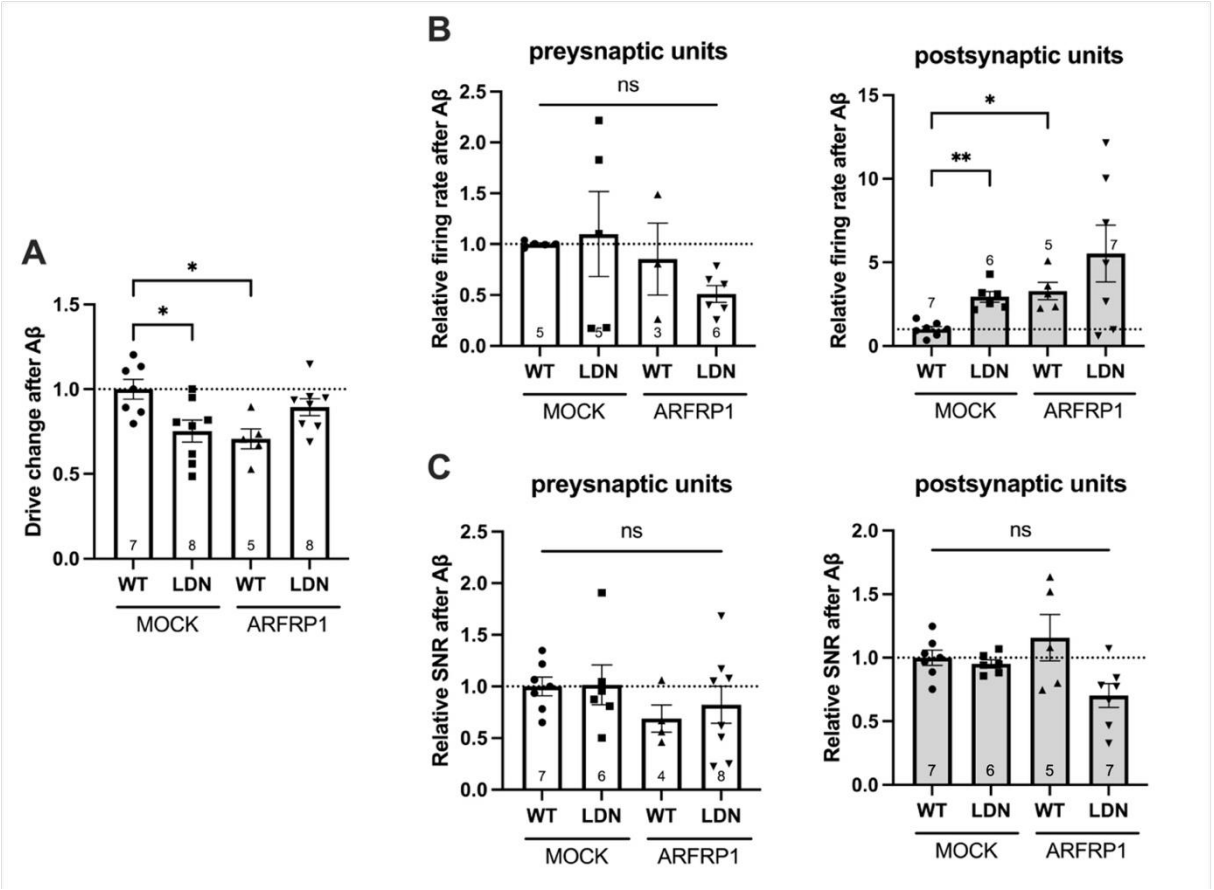

Figure 4.16. *ARFRP1* overexpression impact on synaptic drive after Aβ treatment using microfluidics-coupled MEAs. Effect of *ARFRP1* overexpression after Aβ treatment on (A) synaptic drive, (B) firing rate and (C) spike amplitude of presynaptic (white bars) and postsynaptic (grey bars) units. Device number is reported per condition within each data bar. Data normalised against the mean of the MOCK-APP^{WT} control group. Values outside of the median ± 3 × MAD interval were excluded. The dotted line indicates a reference value of y=1. N=4 independent cultures. Data displayed as mean ± SEM. MEA chip number (n) is reported per condition. Welch's ANOVA followed by Tamhane T2 multiple comparison test. *p<0.05; **p<0.01; ns = non-significant.

The presented data showed that units firing rate is significantly increased after CHO-APP-LDN treatment, which is consistent with previous reports that high concentrations of Aβ (hundreds of nanomolar) induce neuronal hyperactivity[294]. Indeed, Aβ (particularly $Aβ_{1-42}$-rich oligomers) within minutes, initially depresses synaptic transmission by reducing available postsynaptic receptors at the synapse which in turn reduces synaptic transmission and neuronal firing[295]. However, over the course of several hours to one day, neurons can undergo intrinsic compensatory changes such as lowered action-potential threshold, reduced afterhyperpolarisation, and altered membrane conductance that enhance excitability[296]. At an elevated concentration or longer exposure, these compensatory adjustments can become excessive, resulting in increased firing rate and bursting. In parallel, Aβ-mediated weakening of interneuron function disrupts

excitation/inhibition balance, further driving network hyperactivity and irregular firing patters that can manifest in bursts and eventually lead to epileptic discharges over several days of exposure[295,297]. Because recordings were performed after 24 h of Aβ exposure, the observed increase in firing rate likely reflects this later compensatory hyperexcitable phase rather than the initial depression phase described in acute paradigms. While Aβ primarily affected firing dynamics, its impact on circuit-level connectivity required further evaluation.

Interestingly, *ARFRP1* overexpression does not seem to prevent the CHO-APP-LDN CM-induced increase in neuronal firing but showed a tendency to restore *pre-post-drive* which was otherwise decreased with CHO-APP-LDN CM treatment. *Pre-post-drive* is a readout relying on the temporal synchronicity of firing activity between the pre- and postsynaptic chambers and thus represents a circuit-level property, rather than a mere reflection of firing frequency. Despite a 5-fold increase in the firing rate of the ARFRP1-APP^{LDN} group compared to MOCK-APP^{WT} group of postsynaptic units, these groups exhibited comparable *pre-post-drive* values. This highlights that the *pre-post-drive* metric captures coordinated cross-chamber activity independently of spike frequency and that *ARFRP1* overexpression may help preserve network synchrony despite Aβ-induced hyperexcitability.

Notable discrepancies were observed regarding the effect of *ARFRP1* overexpression alone on *pre-post-drive* and postsynaptic unit firing rate when comparing basal conditions to post CHO-APP-WT treatment. Specifically, *ARFRP1* overexpression did not affect *pre-post-drive* under basal conditions, whereas it significantly reduced this parameter following exposure to CHO-APP-WT CM. Similarly, *ARFRP1* overexpression significantly decreased postsynaptic unit firing rate in basal conditions, while a significant increase was observed after CHO-APP-WT CM exposure. These opposing effects suggest that CM derived from APP-WT cells may exert intrinsic biological activity independent of Aβ overproduction, potentially influencing neuronal excitability or synaptic dynamics. Therefore, to evaluate the direct impact of *ARFRP1* prior to Aβ exposure, we focused primarily on the results obtained under basal conditions.

The reduction in postsynaptic firing rate observed upon *ARFRP1* overexpression, in the absence of changes in spike amplitude or *pre–post-drive*, suggests that *ARFRP1* does not impair synaptic connectivity or action potential generation *per se*, but rather modulates neuronal excitability. The preserved spike amplitude indicates intact membrane integrity and sodium channel–dependent spike generation[298], while the unchanged *pre–post-drive*, combined with previous morphological synaptic assignment results (Section 4.2.2.1) argue against synaptic disconnection or loss of functional coupling between compartments[299]. Interestingly, the concomitant increase in postsynaptic AMPA receptor levels further supports the notion that synaptic structure and receptor availability are maintained or even enhanced. Together, these results are consistent with a model in which *ARFRP1* reduces intrinsic excitability while promoting postsynaptic receptor accumulation, potentially reflecting a homeostatic compensatory mechanism aimed at stabilizing network activity. Rather than inducing synaptotoxic effects, *ARFRP1* overexpression therefore appears to modulate the functional state of the postsynaptic neuron without compromising synaptic integrity.

Together with our previous results, these findings are compatible with a working hypothesis where *ARFRP1* could modulate postsynaptic receptor trafficking and contribute to maintaining synaptic function under Aβ-induced stress. Acute, high-dose Aβ exposure appears to transiently increase neuronal firing while disrupting functional connectivity between synapses across the network. Under these conditions, *ARFRP1* overexpression seems to stabilise postsynaptic receptor composition and preserve network coordination. These results are therefore consistent with the possibility that *ARFRP1* acts as a postsynaptic trafficking regulator that helps limit Aβ-driven synaptic disorganisation.

5. IMPLICATIONS & PERSPECTIVES

5.1 Integrative overview and link to research aim

The central objective of this thesis was to identify AD genetic risk factors that could prevent Aβ-induced toxicity to synapses. Based on a previous high-content shRNA screening that had identified genes impacting synaptic density, this work aimed to identify those genes that are capable of protecting synapses when exposed to Aβ. To address this, a multi-scale experimental strategy was developed: a medium-throughput microfluidic co-culture system for gene screening, followed by compartment-specific validation of promising candidates and, finally, functional evaluation of network dynamics using microfluidic-coupled MEAs.

This integrative pipeline identified *ARFRP1* as a potential modulator of synaptic resilience. Although the observed protective effects were moderate and dependent on the toxicity paradigms, they were consistent across morphological and electrophysiological readouts, suggesting a context-dependent but tentative role of *ARFRP1* in maintaining synaptic function under pathological stress.

In parallel, this work established two complementary technical models that together advance the study of synaptic mechanisms in AD. The first model is a microfluidic co-culture screening platform designed for medium-throughput identification of gene-dependent modulation of synaptic connectivity under Aβ exposure. This system combines directional synaptic compartmentalisation and high-content imaging enabling systematic and physiologically relevant evaluation of candidate protective factors. The second model is an integrated microfluidic-MEA hybrid setup, optimised for compartment-specific manipulation while providing immunocytochemical and electrophysiological readouts. Despite variability and culture limitations, these two models constitute a meaningful methodological advance and represent a solid step toward reproducible, compartmentalised assays bridging molecular and functional levels in AD research. Beyond experimental value, these platforms also hold translational potential for screening small molecular that modulate *ARFRP1* function or AMPAR trafficking, particularly when combined with human iPSC-derived neuronal models.

5.2 Interpretation of findings: from genetic screening to synaptic resilience

The progression of this project, from gene screening to mechanistic characterisation, offers an integrated view of how receptor trafficking processes can shape synaptic vulnerability to Aβ-induced toxicity. The medium-throughput microfluidic screen provided the first layer of insight by revealing that modulating the expression of certain AD risk genes can affect Aβ-induced decrease in synaptic connectivity. Among the top candidates, *ARFRP1*, a relatively uncharacterised gene appeared to preserve the proportion of assigned presynaptic and postsynaptic puncta, indicating a potential stabilising effect on mature synapses.

Subsequent validations using CM from CHO-APP cells further supported the possibility that *ARFRP1* might modulate synaptic vulnerability or resilience against Aβ-induced dysfunction. Our findings are consistent with *ARFRP1* acting as a potential postsynaptic AMPAR modulator as silencing *ARFRP1* reduced both GluA1 intensity and GluA1 phosphorylation at Ser845, changes known to impair AMPAR insertion and favour LTD-like depression state in synapses. Conversely, *ARFRP1* overexpression decreased GluA2 with a strong trend toward increased GluA1, a profile associated with Ca^{2+}-permeable AMPARs and E-LTP[114]. Although transient enrichment of Ca^{2+}-permeable AMPARs could also increase Ca^{2+} load and vulnerability under Aβ exposure, the net outcome likely depends on local buffering and temporal dynamics. These effects suggest that *ARFRP1* can promote a synaptic environment biased toward potentiation. Compartment-specific manipulations in microfluidic devices further suggested that *ARFRP1*'s potential protective role appears to originate predominantly from the postsynaptic side, where its overexpression may reduce synaptic vulnerability to Aβ exposure, whereas presynaptic modulation alone did not confer synaptic protection. However, a presynaptic contribution cannot be excluded.

Functional recordings using MEAs further reinforced the potential role of *ARFRP1* at the postsynaptic membrane in the regulation of synaptic receptor trafficking and postsynaptic protein organisation. Overexpressing *ARFRP1* selectively in the postsynaptic chamber appeared to stabilise *pre-post-drive* without preventing the Aβ-

induced hyperactivity, suggesting that *ARFRP1* could maintain network synchronicity despite Aβ-induced stress. This is further supported by the structural data previously described that showed a potential beneficial effect of *ARFRP1* on synaptic connectivity and density in the presence of Aβ.

Together, these converging observations support a model in which *ARFRP1* could act as a trafficking regulator that sustains receptor availability, spine integrity and synaptic communication during pathological stress. Although the observed rescue effects did not reach statistical significance, the consistent trends observed across several experimental paradigms highlight *ARFRP1* as a credible candidate for further investigation.

Beyond *ARFRP1*, this thesis underscores the value of combining compartmentalised models with functional assays to bridge the gap between gene-level modulation and emergent circuit behaviour. The modest but reproducible effects observed across different readouts reflect the multifactorial nature of AD pathology, where subtle changes in trafficking or signalling cascades may collectively determine synaptic resilience or vulnerability.

5.3 Model limitations and experimental constraints

5.3.1 CHO cells for modelling AD

CHO cells remain the most widely used mammalian host for the industrial production of therapeutic proteins and other biological compounds. Their dominance stems from several key advantages: (i) the ability to perform complex post-translational modifications, including proper protein folding and human-compatible glycosylation, which are essential for the bioactivity and safety of many biopharmaceuticals; (ii) regulatory acceptance, as CHO-derived products have a long record of safety in clinical use; and (iii) stability of transfection and robust growth in suspension with adaptability to serum-free, chemically defined media that facilitate large-scale production[300]. In the context of AD, CHO cells have been widely used to produce organic Aβ peptides using mutant APP (typically Indiana, Swedish and London mutations) all leading to an

increased Aβ production[206,301,302]. It is also important to note that CHO cells express the full complexity of mammalian secretase, yielding human-like Aβ species. As a result, CM typically contains a mixture of monomers and low molecular weight oligomers, which is biologically relevant. Finally, many studies reported the use of CHO-APP lines paired with primary neuronal cultures or brain slices to study synaptotoxicity, dendritic spine loss or electrophysiological changes caused by endogenously produced Aβ [177,302–306].

However, CHO cells also present limitations. They are genetically heterogeneous, prone to genomic instability and can accumulate mutations or epigenetic changes over long passages, leading to variable productivity and product quality[307,308]. Their metabolism differs from that of neurons or other primary cells, which may complicate their use as co-culture partners in disease models. Such variability in CHO cells viability and secretory capacities can confound the interpretation of neuronal responses, making it difficult to distinguish genuine Aβ-driven toxicity from secondary effects arising from CHO cells stress or degeneration. These constraints were particularly evident in our co-culture experiments, where CHO cells exhibited poor viability in NBA medium and in the microfluidic format. Despite supplementation with HT additives and L-proline, which are not present in standard NBA medium, CHO cells progressively clustered and died. Indeed, NBA was optimised for primary neurons and lacks several nutrients and growth factors required by CHO cells, such as higher concentrations of amino acids and serum-derived factors[309]. Partial replacement of CHO-NBA with DMEM alleviated some stress but did not fully rescue viability, highlighting the intrinsic incompatibility of this medium with CHO cell metabolism.

CM from CHO cells expressing human APP is typically collected after 12 to 24 h in serum-free medium and applied directly to neuronal preparations as a source of endogenously processed Aβ. In the literature, primary hippocampal neuron cultures are usually treated with 25-100 % CM for 16 to 48 h, which delivers low-picomolar to sub-nanomolar $Aβ_{1-42}$ equivalents (*ca*. 50-500 pM) and slightly higher $Aβ_{1-40}$, concentrations sufficient to induce dendritic spine loss, AMPAR internalisation, and LTP deficits[177,303,304]. Acute hippocampal slices perfused with fresh CM typically receive 0.5-2 nM $Aβ_{1-42}$ for 1-3 h to impair LTP[49], while *in vivo* infusion studies using concentrated CM rarely exceed *ca*. 100 nM total Aβ[310].

Against this backdrop, the *ca*. 500 nM total Aβ used in our experiments is two to three orders of magnitude higher than physiological levels, placing it within the "high-dose acute" range commonly employed with synthetic Aβ to ensure strong and rapid toxicity. Such a supraphysiological dose is expected to produce more robust synaptic impairment, but may also engage mechanisms such as nonspecific aggregation or membrane disruption-that are not prominent at the picomolar to low-nanomolar levels, which are thought to prevail in early AD. This approach likely overestimates physiological toxicity and may explain the lack of clear protective effect observed in more physiological assays. Future work using lower, more physiological Aβ concentrations and prolonged exposure paradigms will be valuable to assess whether *ARFRP1*'s potential protective role is maintained under more disease-relevant conditions.

Overall, this finding illustrates both the strength and limitations of CHO-APP systems as models for Aβ toxicity. While they remain highly valuable for generating endogenously processed and physiologically relevant Aβ species, their metabolic incompatibility with neuronal culture conditions limits their sustainability as long term co-culture partners. Consequently, CHO-APP lines are best suited as Aβ-producing sources for CM-based paradigms, rather than stable long-term co-culture partners. This methodological insight emphasises the importance of developing more compatible human-derived cellular systems for sustained modelling of Aβ neuron interactions.

5.3.2 Limitations of microfluidic models

A key limitation of using microfluidic devices is the inherent variability at multiple stages of the workflow. Variability could arise from cell seeding as using small volumes ranging from 1.6 to 2 µL may lead to differences in cell density. This, in turn, can influence both the efficiency of viral transduction and the effect of subsequent treatments. Additional variability comes from the development of the neuronal network within the microfluidic chambers, which can differ both within and between devices.

Imaging introduces further challenges, as it can be difficult to consistently locate regions with well-defined dendrites while avoiding cell bodies or astrocytes that sometimes

cross the microchannels. These imaging inconsistencies also complicate automated batch analysis. Although several approaches are applied to minimise these factors like using ARA-C to limit to limit glial overgrowth and preserve the neuronal composition of the network, or device tracking to ensure consistency in the use of microfluidic replicas, many factors remain difficult to fully control. Importantly, statistical analysis of data obtained from microfluidic cultures is improved markedly when data are normalised and analysed at the device level rather than at the neuronal preparation level. Indeed, each device functions as a relatively independent microenvironment, where subtle differences in local cell density, microchannel geometry or neuronal maturation introduce variability despite identical manipulation across devices. Consequently, device-level normalisation not only tends to reflect true experimental replication and improves robustness but also strengthens the precision and interpretability of functional and structural read-outs in microfluidic assays.

As a consequence, a relatively large number of independent experiments are often required to obtain reliable results. Nevertheless, despite its complexity, this model represents a powerful and unique approach, enabling the investigation of synaptic compartment-specific mechanisms that cannot be addressed with conventional models. Importantly, when significant effects are observed, the results can be regarded as particularly robust as the microfluidic approach offers greater sensitivity and precision in detecting sometimes subtle but biologically meaningful changes in synaptic functions.

5.4 *ARFRP1* as a regulator of AMPAR trafficking and synaptic vulnerability: a proposed working model

The present findings suggest that *ARFRP1* functions as a postsynaptic modulator of receptor trafficking and synaptic stability. *ARFRP1* belongs to the ADP-ribosylation factor (ARF) family of small GTPases involved in vesicular transport between the trans-Golgi network and endosomal compartments. Through this function, *ARFRP1* is strategically positioned to influence the recycling and surface expression of key synaptic proteins such as AMPARs.

AMPAR trafficking is a highly dynamic process that underlies both synaptic potentiation and depression[247]. Following activation, AMPARs undergo constant cycles of endocytosis, recycling, and reinsertion into the postsynaptic membrane, a balance that determines synaptic strength and plasticity[282]. This recycling relies heavily on the coordinated activity of endosomal Rab GTPases, which regulate discrete trafficking steps. Rab5 mediates early endosomal internalisation of AMPARs during LTD induction, Rab7 controls transport to late endosomes and degradation, whereas Rab11 governs recycling to the plasma membrane and receptor reinsertion during LTP[272,273,311,312]. Disruption of these cascades by Aβ oligomers has been shown to trigger excessive AMPAR endocytosis and loss of surface receptors, leading to dendritic spine retraction and synaptic weakening[166].

Given its established role in endosome-to-Golgi transport, *ARFRP1* may act upstream or in concert with Rab-dependent trafficking cascades to maintain the correct balance between AMPAR internalisation and recycling. Under Aβ exposure, enhanced or preserved *ARFRP1* activity could help sustain receptor recycling and surface delivery, counteracting the pathological shift toward receptor degradation. In this model, *ARFRP1* could serve as a molecular safeguard that sustains AMPAR availability at excitatory synapses, thereby maintaining functional transmission and protecting against Aβ-induced synaptic depression.

Importantly, this trafficking-centric interpretation in agreement within the broader genetic landscape of AD, as many of the risk *loci* identified by GWAS encode proteins involved in endosomal, vesicular or synaptic trafficking pathways. For instance, isoform 1of *BIN1*, a strong genetic risk factor for late-onset AD, has recently been shown in a neuron-specific context to impair early endosome dynamics and presynaptic function[256,313]. Likewise, *PICALM* encodes a clathrin-adaptor protein central to clathrin-mediated endocytosis and has been directly implicated in neuronal and microglial trafficking and homeostasis processes in AD[314]. By positioning *ARFRP1* alongside *BIN1* and *PICALM*, we thus propose that *ARFRP1* may represent one more node in a convergent trafficking network that modulates synaptic vulnerability in AD. If *ARFRP1* indeed supports endosomal-Golgi routing or recycling of AMPAR-containing vesicles, its

modulation would influence synaptic resilience in the face of Aβ-induces stress, just as isoform-specific alterations in *BIN1* or loss of *PICALM* function may predispose synapses to degeneration. Framing our findings in this context enhances their translational relevance, suggesting that *ARFRP1* may represent one additional component of the wider endosomal trafficking system that collectively shapes synaptic resilience in AD.

Beyond receptor recycling, *ARFRP1*-dependent trafficking may also modulate local EPSP-spike threshold and postsynaptic excitability. Indeed, previous studies have shown that endosomal and Golgi pathways regulate the membrane delivery of voltage-gated channels and postsynaptic scaffolds that set the integrative threshold of dendritic spines[315,316] . By stabilising these trafficking routes, *ARFRP1* could enhance postsynaptic responsiveness to presynaptic input without necessarily altering presynaptic release probability. In doing so, *ARFRP1* would potentially optimise synaptic efficiency rather than increase overall firing rate *per se*, a possibility consistent with, but not directly demonstrated by, the observed preservation of connectivity despite Aβ-induced hyperexcitability.

Together, these findings support a working model in which *ARFRP1* participates in endosomal and Golgi trafficking pathways that regulate AMPAR recycling and postsynaptic organisation. By preserving receptor homeostasis and structural integrity of dendritic spines under pathological stress, *ARFRP1* enhances synaptic resilience and mitigates Aβ-induced synaptic vulnerability. This conceptual framework links vesicular trafficking to synaptic protection and highlights *ARFRP1* as a promising molecular target for future mechanistic exploration.

5.5 Perspectives and future directions

Several directions arise from this work.

From a mechanistic perspective, direct visualisation of AMPAR recycling using live-cell imaging under *ARFRP1* manipulation would provide causal evidence for its trafficking

role. Co-localisation studies with Rab5, Rab7, or Rab11 markers could map the endosomal stages influenced by *ARFRP1*, while biochemical assays could identify interacting partners within the Golgi-endosome continuum. Expanding the MEA analysis using cLTP or chronic Aβ paradigms would help determine whether *ARFRP1* also contributes to sustained functional plasticity rather than only baseline stability.

From a modelling perspective, using human-compatible APP-expressing cell lines such as HEK293-APP or neuroblastoma-derived APP-expressing cells could offer better compatibility with neuronal culture conditions while maintaining human-like Aβ processing[317–319]. More recently, human iPSC-derived neurons or astrocytes carrying familial AD mutations have emerged as robust and physiologically relevant sources of endogenous Aβ[213,320,321]. These cells could be co-cultured with WT neurons to model paracrine toxicity while preserving long-term viability and intercellular signalling. When combined with microfluidic devices, such systems would allow compartmentalised, chronic, and physiologically relevant modelling of Aβ effects, bridging the gap between reductionist CHO-based assays and complex human neuronal networks.

From a translational standpoint, *ARFRP1* and its trafficking network may represent emerging candidates for therapeutic modulation. Small molecules or peptides enhancing *ARFRP1* activity or other targets involved in the protective mechanism could be screened using the optimised platform, providing a rapid functional readout of synaptic protection. Parallel studies in human neuronal cultures carrying AD-associated variants could test whether *ARFRP1* expression correlates with differential vulnerability to Aβ.

5.6 Technical significance and broader impact

Beyond its biological insights, this thesis delivers substantial methodological value.

The development of a microfluidic co-culture screening system is highly significant from a technical standpoint. Microfluidic platforms enable precise spatial and temporal control of cell-cell interactions, allowing the separation of neuronal and non-neuronal

compartments while permitting diffusion of soluble factors such as Aβ. This setup closely mimics physiological microenvironments, reduces reagent consumption, and supports medium-throughput screening under defined conditions. Importantly, even with limitations in CHO cell compatibility, the microfluidic design provides a versatile framework adaptable to alternative Aβ-secreting cell types or engineered neuronal-glial configurations, enhancing reproducibility and translational relevance of neurodegenerative disease models.

The integration of microfluidics with MEAs provides a versatile and scalable platform for analysing compartment-specific gene function across morphological, biochemical, and electrophysiological dimensions. This dual-readout system enables a level of spatial and functional precision rarely achieved in conventional *in-vitro* models. Its ability to manipulate and record pre- and postsynaptic compartments independently makes it particularly suited to study synaptic asymmetry and directional signalling, features that are central to AD pathology.

Although the protective effects observed here are modest, they were obtained in a physiologically constrained environment closely resembling neuronal microcircuits. Such realism comes with variability but also with translational value. The microfluidic-MEA setup, now optimised and validated, offers a strong foundation for future studies exploring genetic, pharmacological, or environmental modulators of synaptic function.

6. CONCLUSION

This thesis aimed to identify AD genetic risk factors capable of protecting synapses from Aβ-induced synaptotoxicity. Using a multi-scale experimental pipeline combining microfluidic co-culture screening, compartment-specific validation, and electrophysiological assessment with microfluidic-MEA devices, the study identified *ARFRP1* as a potential modulator of synaptic resilience. Although its protective effects were moderate, they were consistent across morphological and functional assays, suggesting a context-dependent but meaningful role in maintaining synaptic integrity.

Mechanistically, *ARFRP1* appears to regulate AMPARs trafficking and postsynaptic stability through its function in endosomal and Golgi-mediated transport. By influencing receptor recycling and surface expression, *ARFRP1* may help sustain excitatory transmission and counteract Aβ-induced synaptic weakening.

Beyond biological findings, this work provides key technical advances, including a medium-throughput microfluidic screening system and an integrated microfluidic-MEA model, both enabling compartmentalised and functionally relevant studies of synaptic mechanisms. These tools bridge molecular and network-level analyses, offering scalable, physiologically relevant models for AD research.

Future directions include live-cell imaging of AMPAR dynamics, mapping *ARFRP1's* interaction with Rab GTPases, and extending analyses to human iPSC-derived models for improved translational relevance. Ultimately, *ARFRP1* and its trafficking network emerge as promising targets for therapeutic exploration, while the developed platforms establish a robust foundation for investigating gene-dependent modulation of synaptic vulnerability in neurodegenerative diseases.

APPENDIX

Overall, the Appendices A and B presented here document the technical challenges encountered with CHO-APP models and the corresponding methodological refinements implemented throughout this study, supporting the robustness and reproducibility of the main findings.

A. Endogenous toxicity of CHO cells

During the screening experiments, several coverslips had to be excluded from the analysis as CHO-APP-LDN co-cultures did not consistently display the typical reduction in synaptic connectivity, despite reproducible Aβ secretion measured by AlphaLISA. Indeed, signs of cellular stress, such as clustering and increased cell death, were observed in both CHO cell lines from DIV7 onwards, with CHO-APP-WT cultures showing a more pronounced effect (Figure S1).

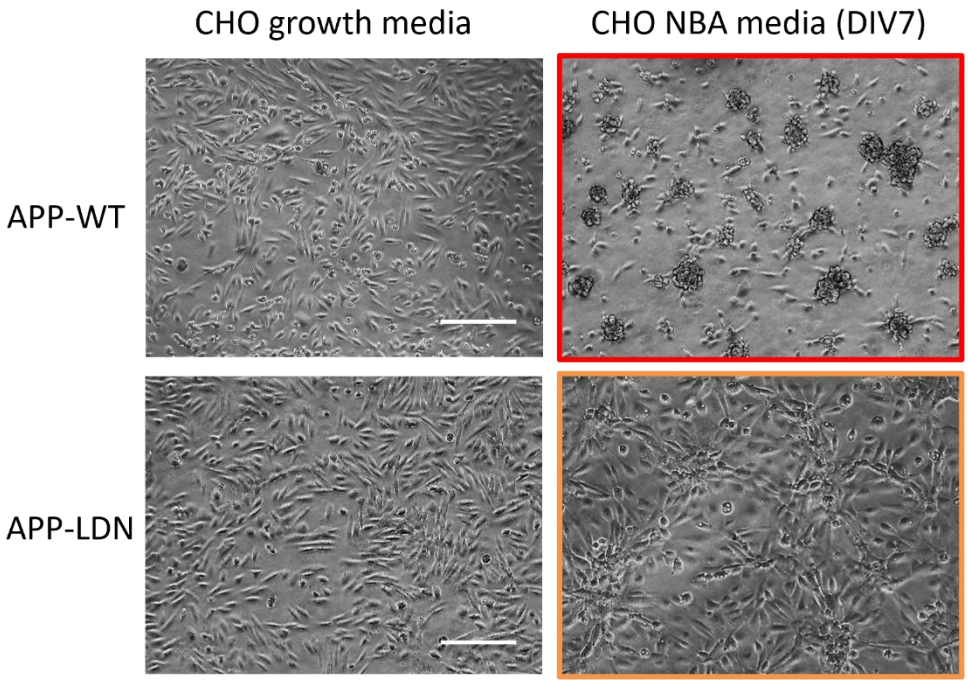

Figure S1. Stressed CHO-APP cells in co-culture media. Phase contrast images of CHO-APP cells in CHO growth media (before neuron seeding) and in CHO-NBA media (7 days after neuron seeding). Red frames indicate cell death; orange frames indicate clustering. Scale bar = 200 µm.

We therefore hypothesised that CHO-APP-WT cells could reduce synaptic connectivity independently of Aβ, thereby depressing the control baseline. To address this, neurons were seeded in the screening D-device and co-cultured with either no CHO cells; CHO-APP-WT; or CHO-APP-LDN (Figure S2). It seemed that co-culture with both CHO-APP-WT and CHO-APP-LDN was toxic for the synapses, as synaptic connectivity (0.72±0.07 and 0.65±0.05, respectively) and network intensity (0.78±0.02 and 0.73±0.03, respectively) were greatly reduced compared to neurons in monoculture. Although based on a single experiment, these results are consistent with what we observed during screening experiment which is a lower-than expected toxicity effect induced by the CHO-APP-LDN co-cultures due to a toxic effect of the CHO-APP-WT control cells.

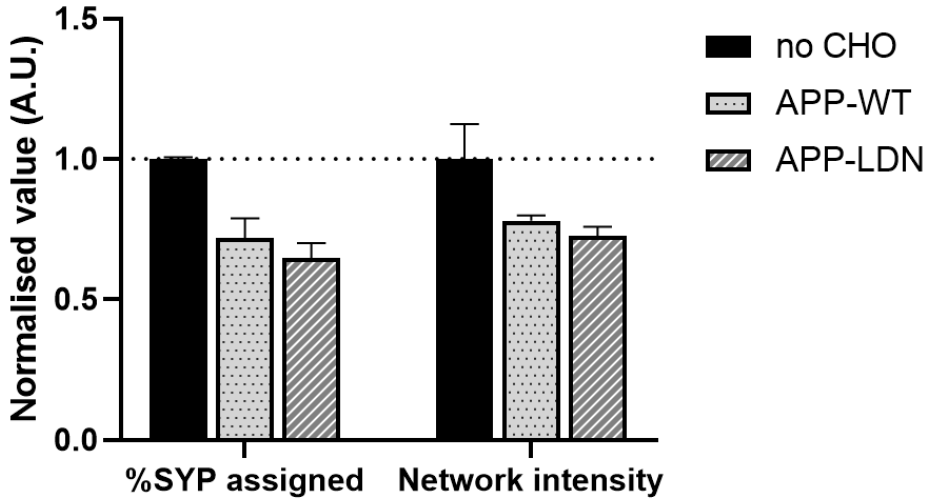

Figure S2. Impact of CHO-APP-WT and CHO-APP-LDN on synapses and neural network. Mean synaptic connectivity and network intensity were normalised to the no-CHO control condition. Data are displayed as mean ± SD. N =1 (3 devices per condition).

Collectively, all previous results suggested that CHO-NBA compromises CHO cell viability. To mitigate media switch stress, a gradual transition from growth medium to CHO-NBA co-culture medium was implemented. In earlier experiments, CHO cells were seeded in the screening microfluidic device 3 days before neurons and maintained in DMEM supplemented with FBS growth medium until neuron seeding, at which point the growth medium was completely replaced with CHO-NBA. To reduce potential stress on CHO cells, we hypothesised that a progressive shift from growth medium to CHO-NBA might be beneficial (Figure S3). Despite this adjustment, CHO-APP-WT cells continued to exhibit clustering and degeneration from DIV6 onwards, whereas CHO- APP-LDN cells

showed similar changes at later time points. In addition, synaptic connectivity seemed greatly decreased in neurons co-cultured with CHO cells in both genotypes (0.78±0.04 for APP-WT and 0.73±0.03 for APP-LDN), indicating that improved perfusion did not rescue viability or function.

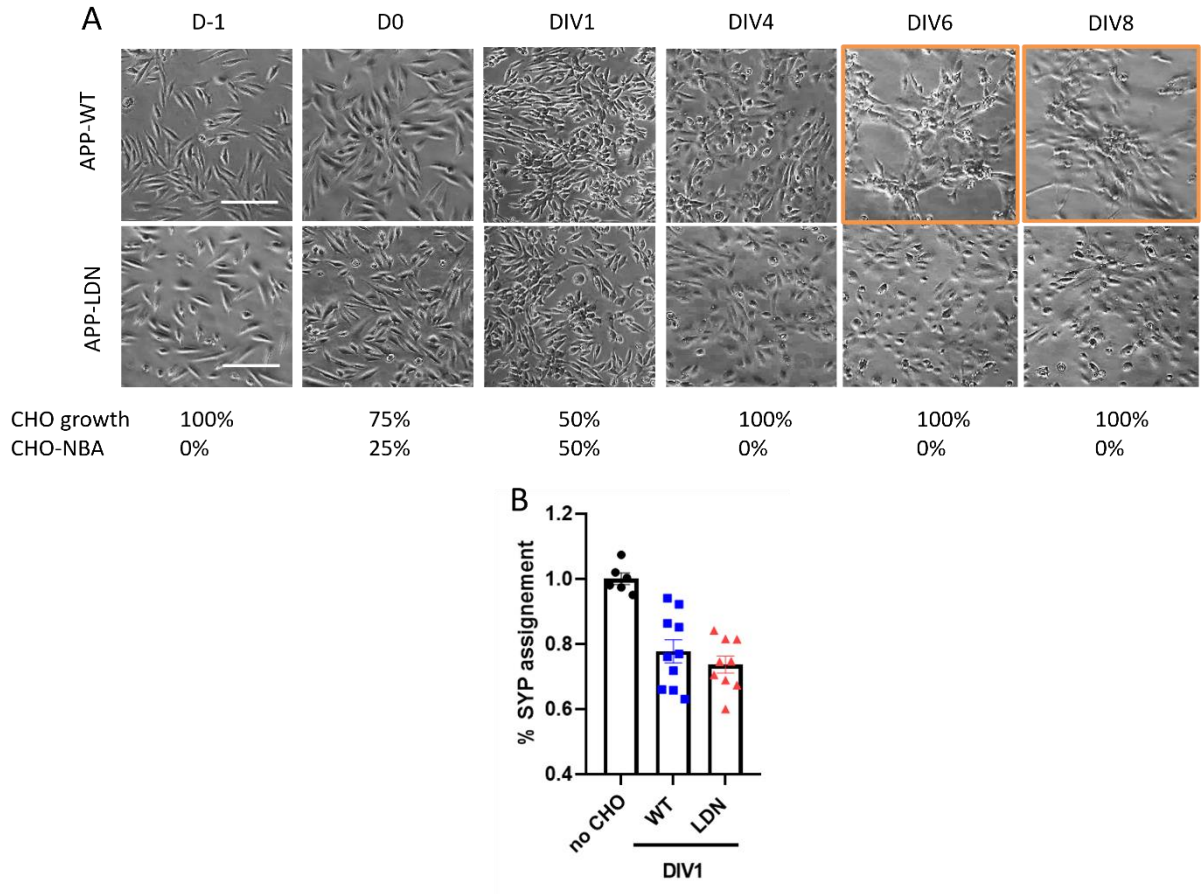

Figure S3. Synaptotoxicity of CHO cells co-culture after progressive media change. (A) representative phase contrast images of CHO cells in the CHO chamber from the day prior to neuron seeding to DIV8 with the respective proportions of CHO growth and CHO-NBA media. Orange-boxed images show cellular stress with clustering. Scale bars = 100 µm. (B) %SYP_assigned in co-culture microfluidic devices (D-devices) with neurons co-cultured without CHO cells (no CHO) or with CHO-APP-WT (WT) or CHO-APP-LDN (LDN) cells seeded at DIV1 with progressive media shift from CHO growth medium to CHO-NBA medium. N=2. Each data point represents one microfluidic device. Data were normalised to the no CHO condition and displayed as mean ± SEM.

An alternative approach involved seeding neurons first and to introduce CHO cells at DIV14, based on the observation that CHO cells appeared to remain stable for about one week. Neurons were subsequently fixed at DIV21, as in previous experiments. Under these conditions, CHO cells exhibited signs of stress three days post-seeding and began to degenerate from DIV19 onward (Figure S4A). As expected, synaptic connectivity was

decreased in neurons co-cultured with CHO-APP-WT cells (0.81±0.08), while the effect of CHO-APP-LDN cells was less pronounced (0.90±0.12). However, considering cellular morphology, it is likely that any apparent toxicity arose from stress-related factors released by degenerating CHO cells rather than from secreted Aβ (Figure S4B).

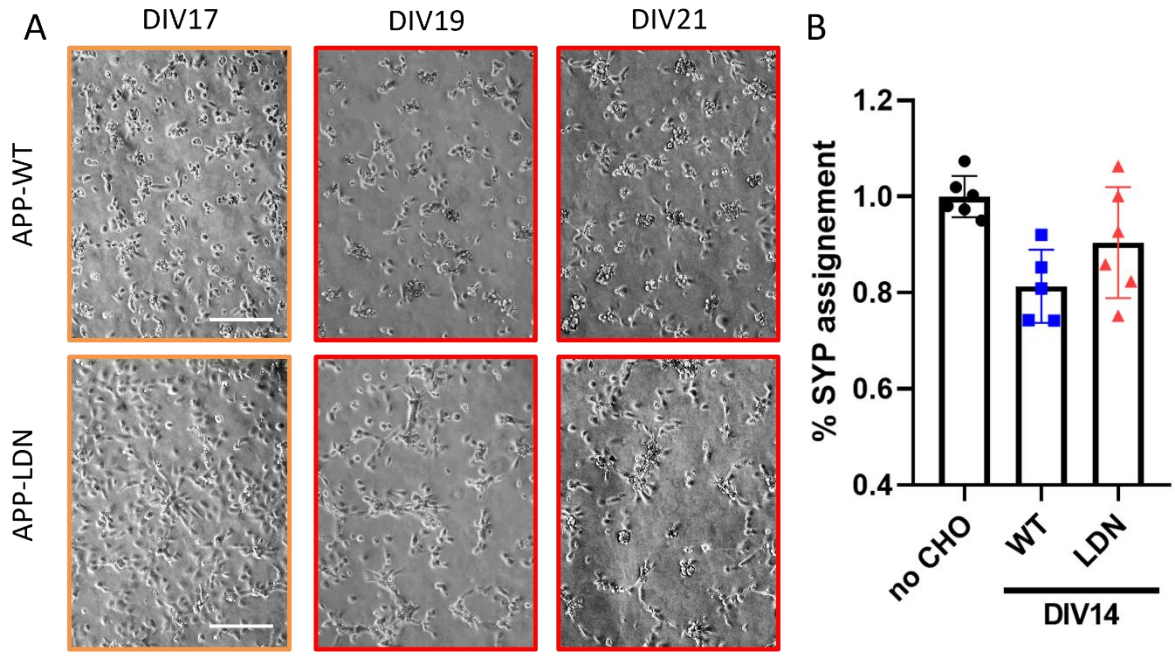

Figure S4. Synaptotoxicity of CHO cells co-cultures seeded at DIV14. (A) Representative phase contrast images of CHO cells in the CHO chamber after seeding at DIV14 and maintenance in CHO-NBA. Orange-boxed images show cellular stress with clustering and red-boxed images show cellular death. Scale bar = 200 µm. (B) %SYP_assigned in co-culture microfluidic devices (D-devices) with neurons co-cultured without CHO cells (no CHO) or with CHO-APP-WT (WT) or CHO-APP-LDN (LDN) cells seeded at DIV1 with progressive media shift from CHO growth medium to CHO-NBA medium. N=1. Each data point represents one microfluidic device. Data were normalised to the no CHO condition and displayed as mean ± SD.

In summary, co-culture with CHO-APP-WT cells appeared to consistently reduce synaptic connectivity by *ca.* 20%, irrespective of the time point at which the CHO cells were introduced. Moreover, CHO cells did not remain viable for more than 5 days in CHO-NBA medium. Collectively, these findings indicate an inherent synaptotoxicity associated with CHO-APP-WT cultures and could account for the reduced dynamic range observed during screening experiments. Consequently, new CHO-APP cell lines were generated (See Appendix B), as repeated efforts to improve cell viability proved unsuccessful. This approach was designed to minimise potential effects of passage history and to provide a fresh starting population for subsequent experiments.

B. Generation of CHO-APP cell lines and final media tests

To generate new CHO-APP lines, the plasmids previously used for CHO line production were kindly provided by our collaborators as dried DNA spots on filter paper. Following bacterial transformation, plasmid DNA was amplified, purified and transfected into naïve CHO-K1 cells. A total of 24 antibiotic-resistant clones per genotype were isolated, and cell lysates were analysed by Western blotting to screen for APP expression levels. Lysates from original CHO-APP lines used in prior experiments were included as reference control in each gel (Figure S5). Clone selection was guided by total APP protein level and APP banding profile, with both genotypes displaying the characteristic doublet around 110 kDa. For CHO-APP-LDN cells, the blotting profiles were consistent across clones, and those with the highest APP expression were selected for further analysis (Figure S5B). In contrast, CHO-APP-WT clones exhibited greater variability in banding patterns and relative intensities; therefore, clones with high APP expression but distinct banding profiles were selected for subsequent characterisation (Figure S5A).

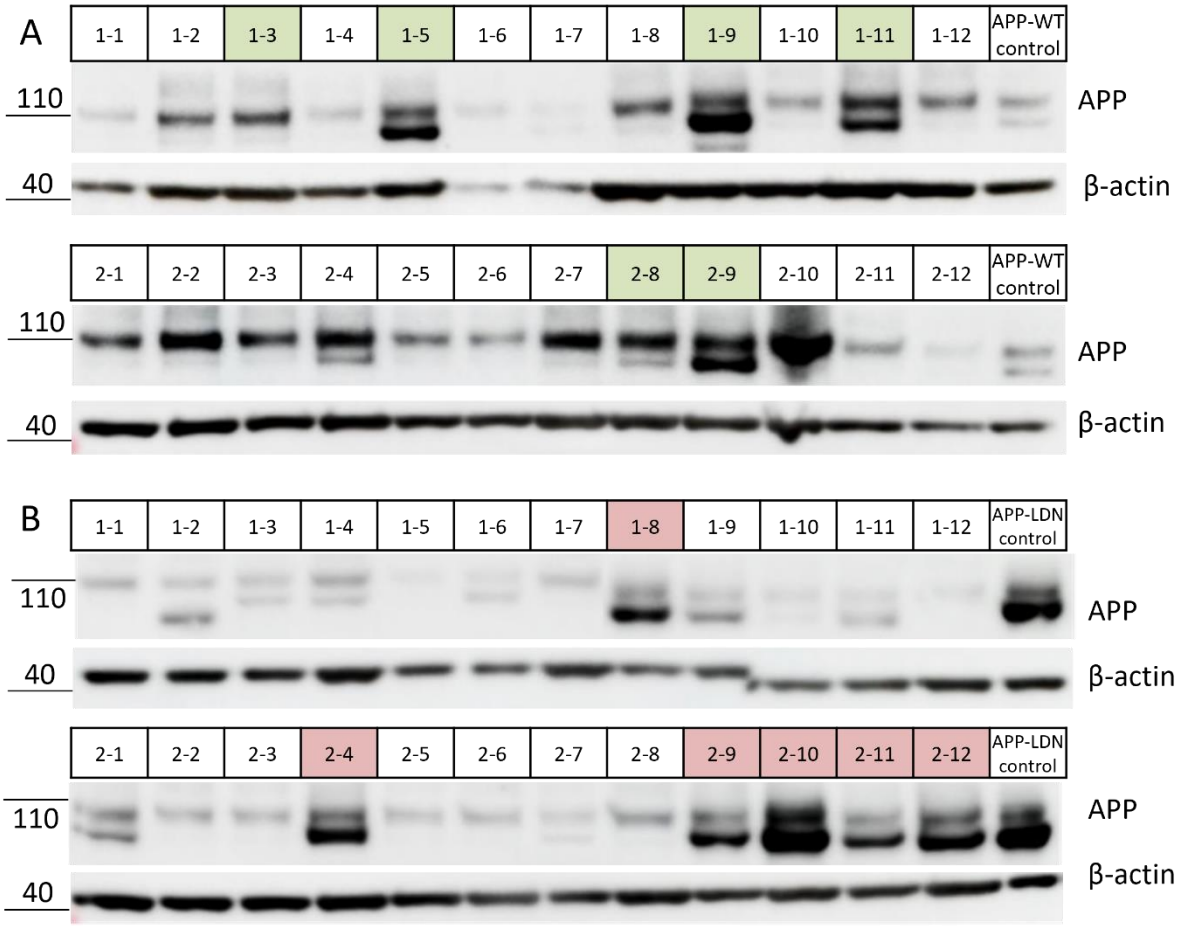

Figure S5. Immunoblot showing APP expression of the different antibiotics-resistant clones for stable CHO-APP-WT and CHO-APP-LDN lines production. Expression of APP and β-actin of the (A) CHO-APP-WT clones and (B) CHO-APP-LDN clones. N=1. Selected clones are highlighted in green and red for CHO-APP-WT and CHO-APP-LDN cell lines respectively. Molecular weight for each band is displayed on the left of the panel.

In most samples, two distinct protein bands were detected by the APP antibody. The upper band likely corresponds to the heavily N- and O-glycosylated, mature form of APP (mAPP), while the lower band represents the immature form of APP (imAPP), primarily N-glycosylated[322–324]. CHO-APP-WT cells displayed comparable or slightly higher levels of mAPP, while CHO-APP-LDN cells were dominated by the imAPP form[306,325]. This observation is consistent with previous reports indicating that the APP-LDN mutation impairs endoplasmic reticulum-to-Golgi trafficking, resulting in slower APP maturation and reduced delivery of mature APP to the cell surface[306,326]. The selected clones were subsequently cultured in well plates and CM was collected to quantify total secreted Aβ ($Aβ_{1-X}$) using AlphaLISA assay (Table S1).

Table S1. AlphaLISA measurement of total Aβ ($Aβ_{1-X}$) in CM from selected clones. Aβ concentrations are displayed in nM for 8 µg/µL of total protein. N=1, ND = non-detectable.

Clone	$Aβ_{1-X}$	Clone	$Aβ_{1-X}$
WT 1-3	ND	**LDN 1-8**	7.149
WT 1-5	1.408	**LDN 2-4**	1.343
WT 1-9	1.167	**LDN 2-9**	2.685
WT 1-11	0.615	**LDN 2-10**	0.366
WT 2-8	0.039	**LDN 2-11**	1.804
WT 2-9	0.412	**LDN 2-12**	2.362

Among the wild-type clones, WT2-8 was selected due to its low level of secreted Aβ and a similar protein band profile to the control sample. In contrast, LDN1-8 was chosen from the APP-LDN clones as it exhibited higher Aβ secretion concentrations, making it the most suitable model for studying Aβ-associated toxicity. The newly generated CHO lines were then seeded into the D-device and maintained in CHO growth medium, followed by a gradual transition to CHO-NBA medium as previously described. However, CHO cell viability on CHO-NBA was not improved under these conditions. CHO-APP-WT cells

exhibited early clustering and degeneration while CHO-APP-LDN cells also developed signs of cellular stress at later stages (Figure S6).

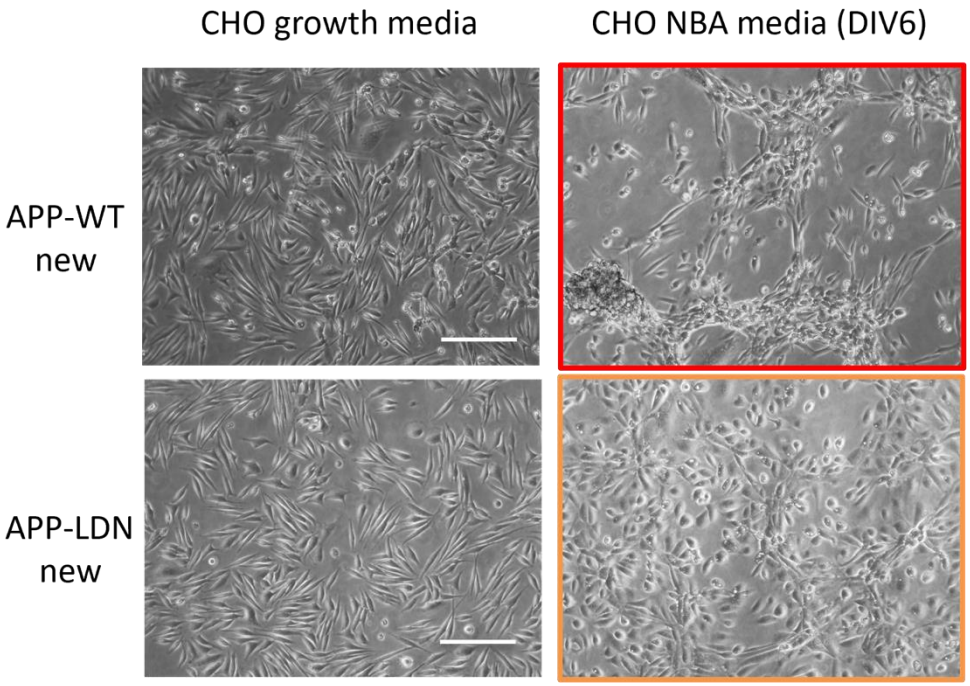

Figure S6. Impact of CHO-NBA media on newly established CHO-APP lines. Representative phase contrast images of new CHO-APP cells in CHO growth media and in CHO-NBA media, 6 days after a gradual medium switch. Images with a red or orange frame respectively indicate cell death and cell clustering. Scale bar = 200 µm.

Despite our extensive efforts to resolve the co-culture viability issues through multiple optimisation strategies, including experimental timing and generating new cell lines, CHO-APP-WT cells continued to exhibit clustering and cells death within one week of co-culture, suggesting a potential construct-related issue, although this could not be confirmed. Consequently, we decided to discontinue the co-culture approach and instead adopted the use of conditioned medium, which allowed us to maintain neuronal health while still assessing the effects of CHO cell secretions.

C. Additional supplementary figure and tables

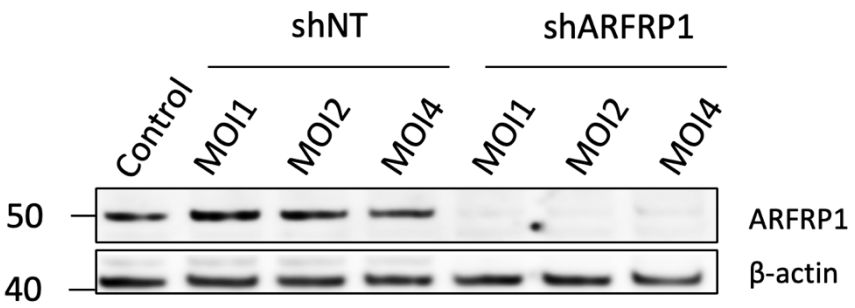

Figure S7. MOI test of shNT and shARFRP1 virus. Immunoblot of cortical cell lysate non transduced (control) or transduced with shNT and shARFRP1 virus at different MOIs (1, 2 and 4). ARFRP1 protein presence was assessed along with β-actin as a loading control. N=1.

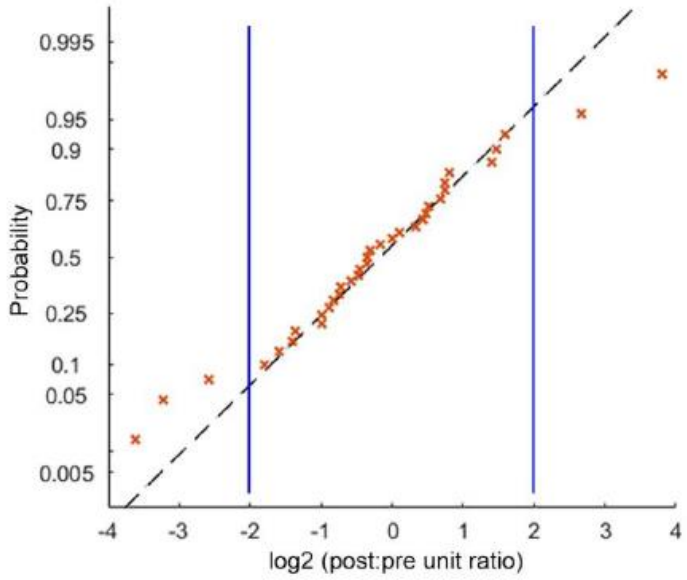

Figure S8. Probability plot comparing the distribution of the fold differences between unit numbers detected in presynaptic and postsynaptic chambers to the normal distribution. Each point indicates one MEA-integrated microfluidic device, in which the spike sorting algorithm detected at least one unit in both chambers (n = 35 devices from 7 independent cultures). Dashed line passes through the lower and upper quartiles. Solid lines indicate the limits for 4-fold difference in unit numbers and correspond to the exclusion criteria used for this dataset (|*z*-score| = 1.5).

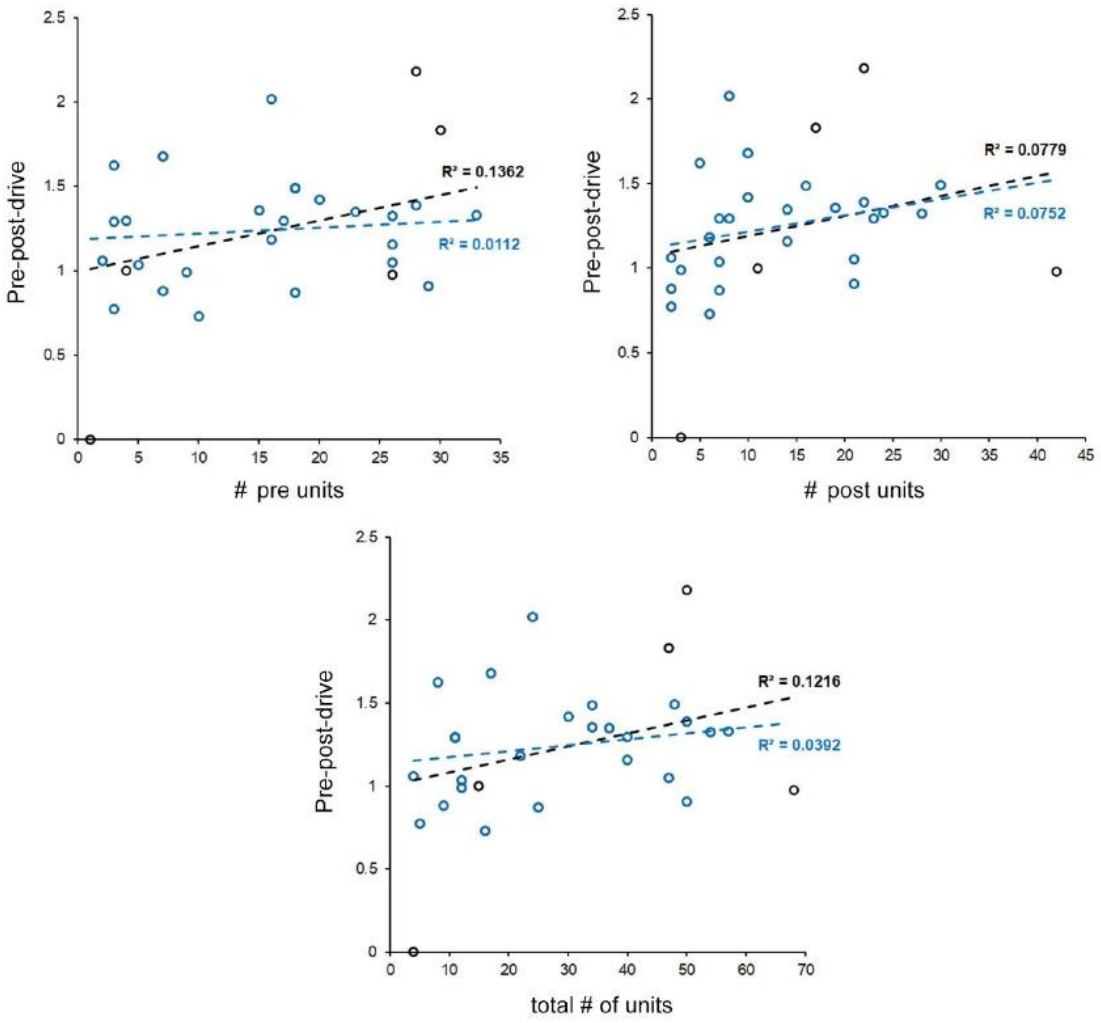

Figure S9. Correlation between detected unit numbers and *pre-post-drive*. Each point indicates one MEA-integrated microfluidic device within the normal distribution of fold differences in unit numbers (n = 30 devices from 7 independent cultures). Outlier data points (black dots) were included for clarity. Dashed lines show the least-squares fits before (black) and after (blue) outlier exclusion.

This section provides detailed buffer formulations, device schematics, and antibody lists used throughout the experiments.

Table S2. Buffers composition

Compound	Concentration	Reference	Supplier
Dissection buffer			
HBSS	1X	14185045	ThermoFisher
HEPES	10 mM	15630056	ThermoFisher
Sodium pyruvate	1 mM	11360039	ThermoFisher
Penicillin/Streptomycin	25 U/mL	15070063	ThermoFisher
MEM/FBS			

MEM (no glutamine)	1X	21090022	ThermoFisher
D-Glucose	3%	G8270	Sigma
Penicillin/Streptomycin	25 U/mL	15070063	ThermoFisher
GlutaMax	1%	35050038	ThermoFisher
MEM vitamins	0.80%	11120037	ThermoFisher
FBS	10%	10270106	ThermoFisher
NBA culture medium			
Neurobasal A	1X	10888022	ThermoFisher
GlutaMax	1%	35050038	ThermoFisher
B27	2%	17504001	ThermoFisher
CHO growth			
DMEM/F-12	1X	21331020	ThermoFisher
FBS	10%	10270106	ThermoFisher
HT supplement	1X	41065012	ThermoFisher
Penicillin/Streptomycin	500 U/mL	15070063	ThermoFisher
L-proline	600 µM	P0380	Sigma Aldrich
L-glutamine	2 mM	25030081	ThermoFisher
CHO-NBA			
NBA (no phenol)	1X	12349015	ThermoFisher
HT supplement	1X	41065012	ThermoFisher
Penicillin/Streptomycin	25 U/mL	15070063	ThermoFisher
L-proline	600 µM	P0380	Sigma Aldrich
Coating solution			
Boric acid	50 mM	B9645	Sigma Aldrich
Sodium tetraborate	12.5 mM	229946	Merck
PDL	0.1 mg/mL	P6407 5MG	Sigma Aldrich
pH 8.5			
Lysis buffer			
Tris	50 mM	T1503	Sigma Aldrich
Sodium chloride	150 mM	1112-A	Euromedex
Nonidet P-40	1%	18896	Sigma Aldrich
SDS	1%	27923.238	VWR
Sodium orthovanadate	1 mM	56508	Sigma Aldrich
Sodium deoxycholate	0.50%	D6750	Sigma Aldrich
Protease inhibitor	1X	469312400	Roche
Phosphatase inhibitor	1X	4906845001	Roche
pH 7.4			
TBS			
Tris	20 mM	T15 03	Sigma Aldrich
Sodium chloride	150 mM	1112-A	Euromedex
pH 7.4			
Complete ACSF			
Sodium chloride	125 mM	1112-A	Euromedex
Potassium chloride	2.5 mM	4933	Merck
Magnesium chloride	1 mM	M8266	Sigma Aldrich
Calcium chloride	2 mM	433381	Carlo Erba
D-glucose	33 mM	G8270	Sigma Aldrich
HEPES	25 mM	15630056	ThermoFisher
pH 7.3			

Synaptic fractionation: neutral buffer			
Sucrose	0.32 M	200-301-A	Euromedex
HEPES	10 mM	15630056	ThermoFisher
Protease inhibitor	1X	469312400	Roche
Phosphatase inhibitor	1X	4906845001	Roche
pH 7.4			
Synaptic fractionation: EDTA buffer			
HEPES	4 mM	15630056	ThermoFisher
EDTA	1 mM	EU0007-C	Euromedex
pH 7.4			
Synaptic fractionation: HEPES-Triton buffer			
HEPES	20 mM	15630056	ThermoFisher
Sodium chloride	100 mM	1112-A	Euromedex
Triton X-100	0.50%	T8787-250ML	Sigma Aldrich
pH 7.2			
Synaptic fractionation: denaturation buffer			
HEPES	20 mM	15630056	ThermoFisher
Sodium chloride	0.15 mM	1112-A	Euromedex
Triton X-100	1%	T8787-250ML	Sigma Aldrich
Deoxycholic acid	1%	700247P-10MG	Sigma Aldrich
SDS	1%	27923.238	VWR
pH 7.5			

Table S3. Microfluidic devices design overview.

Device type	Code	Design description	Illustration
Standard	U	3 chambers: presynaptic (pre), postsynaptic (post), and synaptic (syn)	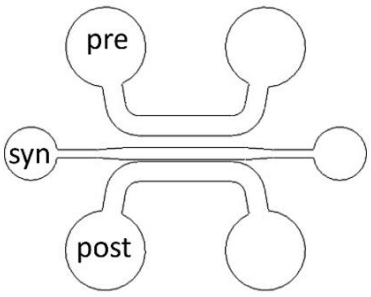
Co-culture	X	Same as **U**, plus an extra chamber for CHO cells co-culture (CHO)	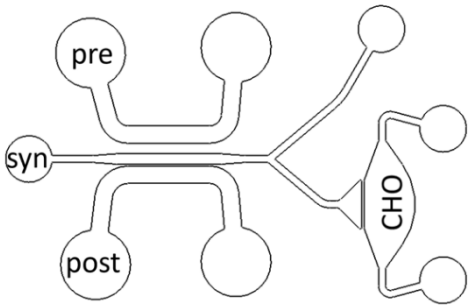

Screening	D	Two sets of four **X** devices combined into one unit	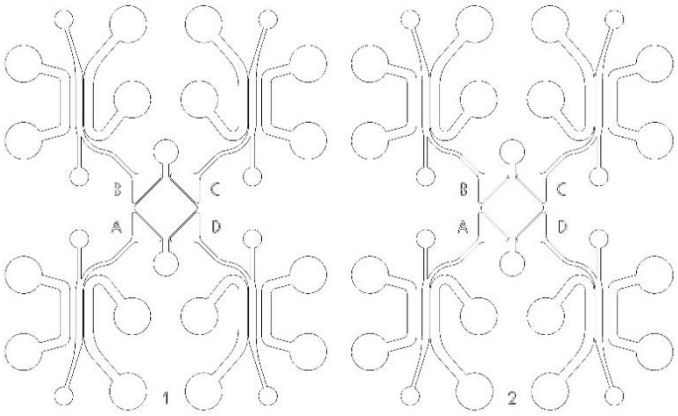
MEA	V	Same as **U**, plus an extra well for the MEA reference electrode (ref)	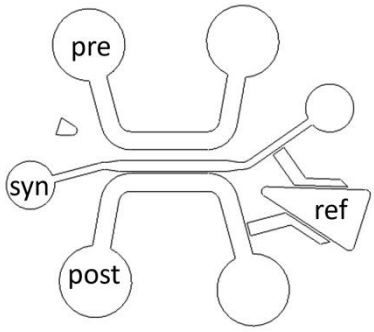

Table S4. Primary antibodies used for immunoblotting (WB) and immunofluorescence (IF).

Primary antibodies						
Target	**Host**	**Dilution buffer**	**Dilution**	**Supplier**	**Antibody reference**	**Method used**
β-actin	Mouse	TBS	1/15,000	Sigma Aldrich	A1978	WB
APP clone 22C11	Mouse	TBS	1/1,000	Sigma Aldrich	MAB348	WB
ARFRP1	Rabbit	TBS	1/1,000	Invitrogen	120267	WB
GluA1	Rabbit	TBS	1/1,000	Sigma Aldrich	AB1504	WB
GluA2	Rabbit	TBS	1/5,000	Abcam	206293	WB
pSer845-GluA1	Rabbit	PBS for IF, TBST-T for WB	1/100 for IF; 1/1,000 for WB	Cell signalling	8084	WB; IF
pSer880-GluA2	Rabbit	PBS for IF; TBS +1% BSA	1/400 for IF; 1/500 for WB	Thermo-Fisher	5359R	WB; IF
PSD95	Guinea pig	PBS for IF; TBS for WB	1/300 for IF1/1,000 for WB	Synaptic System	124014	WB; IF

Synaptophysin	Chicken	TBS	1/1,000	Synaptic System	101006	WB
GluA1	Rabbit	PBS	1/300	Clini-Science	Ab02178	IF
GluA2	Guinea pig	PBS	1/200	Synaptic System	182105	IF
Homer1	Chicken	PBS	1/300	Synaptic system	160006	IF
Synaptophysin	Guinea pig	PBS	1/300	Synaptic system	101004	IF
Synaptophysin oyster 488	N/A	PBS	1/150	Synaptic system	101011 c2	IF
Tau	Rabbit	PBS	1/400	Synaptic system	314003	IF
Tubulin-β3	Mouse	PBS	1/400	Millipore	MAB1637	IF

Table S5. Secondary antibodies used for immunoblotting (WB) and immunofluorescence (IF).

Secondary antibodies (Jackson ImmunoResearch)					
Fluorophore	**Host**	**Dilution buffer**	**Dilution**	**Antibody reference**	**Method used**
HRP	Goat anti-Rabbit	5% non-fat milk in TBS	1/10,000	111-035-003	WB
HRP	Goat anti-Mouse	5% non-fat milk in TBS	1/5,000	115-035-003	WB
HRP	Goat anti-Guinea pig	5% non-fat milk in TBS	1/5,000	106-035-003	WB
Alexa Fluor® 488	Donkey anti-Guinea pig	PBS	1/400	706-545-148	IF
Alexa Fluor® 488	Donkey anti-Chicken	PBS	1/400	703-545-155	IF
Alexa Fluor® 594	Donkey anti-Guinea pig	PBS	1/400	706-585-148	IF
Alexa Fluor® 594	Donkey anti-Chicken	PBS	1/400	703-585-155	IF
Alexa Fluor® 647	Donkey anti-Guinea pig	PBS	1/400	706-605-148	IF
Alexa Fluor® 647	Donkey anti-Rabbit	PBS	1/400	711-605-152	IF
Cy™3	Donkey anti-Rat	PBS	1/400	712-165-153	IF
DyLight™ 405	Donkey anti-Mouse	PBS	1/400	715-475-151	IF
DyLight™ 405	Donkey anti-Rabbit	PBS	1/400	711-475-152	IF

D. Articles

BIN1 expression in the presynaptic compartment leads to isoform-specific synaptotoxicity

Erwan Lambert[1†‡], Carla Gelle[1†], Valentin Leclerc[1†], Alejandra Freire-Regatillo[1†], Nicolas Barois[2,3], Tommy Malfoi[1], Xavier Hermant[1], Florie Demiautte[1], Frank Lafont[3], Philippe Amouyel[1], Karine Blary[4], Sabine Kuenen[5,6], Chloé Najdek[1], Patrik Versteken[5,6], Dolores Siedlecki-Wullich[1], Pierre Yger[7], Jean-Charles Lambert[1], Devrim Kilinc[1]*, Pierre Dourlen[1]*

[1] Université de Lille, Inserm, CHU Lille, Institut Pasteur de Lille, U1167 – RID – AGE – Facteurs de risque et déterminants moléculaires liés au vieillissement, Lille, France
[2] Université de Lille, CNRS, Inserm, CHU Lille, Institut Pasteur de Lille, UAR CNRS 2014 - US Inserm 41 - PLBS, Lille, France.
[3] University of Lille, CNRS, Inserm, CHU Lille, Institut Pasteur Lille, U1019-UMR 9017-CIIL-Center for Infection and Immunity of Lille, Lille, France.
[4] Univ. Lille, CNRS, Centrale Lille, Univ. Polytechnique Hauts-de-France, UMR 8520 - IEMN - Institut d'Electronique de Microélectronique et de Nanotechnologie, F-59000 Lille, France
[5] VIB Center for Brain and Disease Research, KU Leuven, Leuven, Belgium
[6] Department of Neurosciences, Leuven Brain Institute, KU Leuven, Leuven, Belgium
[7] Lille Neurosciences & Cognition (lilNCog) – U1172 (INSERM, Lille), Univ Lille, CHU Lille 59045 Lille, France

[†] Equal contribution
[‡] Present address: Donders Center for Neuroscience, Department of Molecular Neurobiology, Radboud University, Nijmegen, the Netherlands
* Address for correspondence: devrim.kilinc@pasteur-lille.fr; pierre.dourlen@pasteur-lille.fr

Abstract

Alzheimer's disease (AD) is characterized by a strong genetic predisposition and by an early loss of synaptic connectivity that strongly correlates with cognitive deficit. Some genetic determinants could contribute to synapse frailty toward AD pathology. However, the role of genetic determinants in AD pathogenesis remains poorly understood at the synaptic level. Here, we show that the expression of an isoform of the major AD susceptibility gene BIN1 in the presynaptic compartment results in synaptic loss. Using electrophysiology, we observed an early loss of synaptic transmission upon BIN1 isoform 1 (BIN1iso1) expression in *Drosophila* retinal photoreceptor neurons. This was not observed for the other human BIN1 isoforms tested, isoform 8 and isoform 9. Structural analysis of photoreceptor neuron synapses shows a strong accumulation of abnormally large vesicles in the presynaptic compartment, reminiscent of this same isoform-induced endosome defects in cell bodies. In addition, the expression of BIN1iso1 in motoneurons of the *Drosophila* neuromuscular junction alters the morphology of synaptic boutons, with a greater number and a smaller size of synaptic boutons, and the appearance of satellite boutons. As opposed to endosomal defects in cell body, modulating the Rab11 recycling endosome regulator did not prevent BIN1iso1 synaptotoxicity. To test if synaptic deficits are conserved in a mammalian model and to assert a presynaptic vs postsynaptic role for BIN1, we used rat primary neurons cultured in microfluidic devices that restrict gene expression modulation in particular neuron populations. We found a loss of synaptic connectivity only when expressing BIN1iso1 in the presynaptic compartment, which was confirmed by microelectrode array analysis. Together, our results suggest that BIN1 expression in the presynaptic terminal, but not the postsynaptic terminal leads to an isoform-specific, deleterious effect on synaptic integrity. BIN1 synaptotoxicity could contribute to the synapse loss observed early in AD. This supports the idea that genetic determinants could make synapses prone to failure in AD.

Keywords

Alzheimer's disease, BIN1 isoforms, synapse, *Drosophila*, primary neuronal culture, Rab11, electroretinography, MEA

Introduction

Alzheimer Disease (AD) is the most frequent neurodegenerative disease and cause of dementia worldwide. Besides the two pathognomonic protein aggregates, the extracellular senile plaques composed of amyloid-β peptide (Aβ) and the intracellular neurofibrillary tangles composed of phosphorylated tau, AD is characterized by progressive synaptic and neuronal losses. The synaptic loss strongly correlates with cognitive decline making synapse loss a central element of AD pathogenesis (DeKosky & Scheff, 1990; Mecca et al., 2022; Terry et al., 1991).

In addition, AD is considered to have a strong genetic component. Even in multifactorial cases, which represent the vast majority of AD forms, the heritability is estimated to reach 60-80% (Gatz et al., 2006). Recent advances in genetic studies have identified up to 76 genomic loci associated with the disease (Bellenguez et al., 2022). Genes responsible for the genetic signals in these loci are implicated somehow in the etiology of the disease. Therefore, some of them are likely involved in synapse loss. Accordingly, a genetically driven synaptic failure hypothesis has been raised for the disease (Dourlen

et al., 2019). However, the potential synaptic roles of many AD risk genes are yet to be characterized. It is the case for *BIN1*, which is the susceptibility gene with the strongest association with AD after *APOE* (Bellenguez et al., 2022).

BIN1 has various functions in membrane trafficking, cytoskeleton regulation, DNA repair, cell cycle progression, and apoptosis (Dourlen et al., 2025; Prokic et al., 2014). *BIN1* is expressed in many organs, mainly in muscle and in the brain (Butler et al., 1997). In the brain, it is expressed mostly in oligodendrocytes, microglia and neurons (Adams et al., 2016; De Rossi et al., 2016; Marques-Coelho et al., 2021). *BIN1* has more than 10 isoforms. Some are ubiquituous, like BIN1 isoform 9 (BIN1iso9) and others are brain- or muscle-specific, like BIN1 isoform 1 (BIN1iso1) or BIN1 isoform 8 (BIN1iso8) respectively (Butler et al., 1997; Dourlen et al., 2025). In the brain, BIN1iso1 and BIN1iso9 are the most expressed (Crotti et al., 2019; Taga et al., 2020) and BIN1iso1 is considered neuron-specific (De Rossi et al., 2016).

BIN1 has been identified as a member of the Amphiphysin family of proteins and therefore involved in the regulation of endocytosis and the endolysosomal pathway (Butler et al., 1997; Ramjaun et al., 1997; Tsutsui et al., 1997; Wigge et al., 1997). Also named AMPH2, BIN1 shows sequence similarity with AMPH, a neuronal protein highly enriched in synaptic terminals and involved in synaptic vesicle endocytosis (David et al., 1996; Lichte et al., 1992; Shupliakov et al., 1997). BIN1 interacts with many components involved in clathrin-mediated endocytosis, namely dynamin, synaptojanin, AP-2, clathrin and endophilin (Drake & Traub, 2001; Leprince et al., 1997; McMahon et al., 1997; Micheva et al., 1997; Ramjaun et al., 1997). Furthermore, BIN1 has been visualized to be recruited to clathrin-coated pits in the sequence of events when the neck of the endocytic vesicle is formed just before vesicle scission (Taylor et al., 2012). BIN1 also contributes to fast endophilin-mediated endocytosis, a process regulating axonal growth *in vitro* in mouse hippocampal neurons (Ferreira et al., 2021). In Neuro2a cells, BIN1iso1 expression increases transferrin uptake (Ellis et al., 2012). However, in primary embryonic rat neurons, BIN1iso1 inhibits clathrin-mediated endocytosis resulting in smaller endosomes (Calafate et al., 2016). In human induced neurons, gain and loss of BIN1iso1 increases and decreases respectively the size of early endosomes (Lambert et al., 2022). This effect of BIN1iso1 overexpression is conserved when expressed in *Drosophila* neurons and leads to neurodegeneration, which can be prevented upon inhibition of the early endosome regulator Rab5 and upon activation of the recycling endosome regulator Rab11 (Lambert et al., 2022). Of note, regulation of the endosome size is of interest for AD as endosomal enlargement is one of the first AD pathological hallmark (Cataldo et al., 1997, 2000).

Intracellular trafficking is crucial for synapses; in the presynaptic compartment it ensures the correct generation and release of synaptic vesicles and in the postsynaptic compartment it is required for the correct recycling of neurotransmitter receptors. From *Drosophila* to mammals, BIN1 is localized at synapses (Leventis et al., 2001; Ramjaun et al., 1997; Zelhof et al., 2001). Whether it is localized more in the presynaptic compartment or in the postsynaptic compartment depends on the experimental model and study (De Rossi et al., 2020; Schürmann et al., 2020). At the functional level, in the postsynaptic compartment, *BIN1* has been shown to regulate the recycling of AMPA receptors at the plasma membrane *in vitro* (Schürmann et al., 2020). In the presynaptic compartment, loss of *BIN1* has been shown to regulate presynaptic vesicular release in hippocampal excitatory synapses *in vivo* (De

Rossi et al., 2020). Therefore, the role of BIN1 at the synapse remains poorly understood and it is essential to address this question if we aim at better understanding its role in AD pathogenesis.

For this purpose, we investigated the synaptic role and potential toxicity of human BIN1iso1, BIN1iso8 and BIN1iso9. We used the highly tractable *in vivo* model *Drosophila*, in which human BIN1 functions are conserved. This is exemplified by human BIN1 being able to rescue the locomotor deficits of endogenous *Drosophila* BIN1 mutants (called Amphiphysin) (Lambert et al., 2022). We first analyzed the synaptotoxicity of human BIN1 isoforms expression in the retina photoreceptor neurons. We confirmed our results in third instar larval glutamatergic neuromuscular junction (NMJ), a synaptic reference model in *Drosophila* (Menon et al., 2013). We further tested the toxicity of BIN1iso1 and BIN1iso9 in rat primary neuronal cultures using microfluidic devices and multielectrode (MEA) arrays, which enabled us to assess pre- and postsynaptic roles of BIN1 in synaptic structure and transmission in the mammalian context.

Material and Methods

Drosophila genetics

Flies were raised on a standard medium (Nutri-fly BF, Genesee Scientific, San Diego, CA, USA) at 25°C under a 12h/12h day/night cycle. The UAS-BIN1iso1, UAS-BIN1iso9, UAS-BIN1iso8, UAS-dAmphA and rh1-Gal4 lines were described previously (Dourlen et al., 2012; Lambert et al., 2022). Other stocks were obtained from the Bloomington *Drosophila* Stock Center (BDSC, Bloomington, IN, USA): UAS-Luciferase (#35788), UAS-mCD8::GFP (#27400), UAS-GFP (#35786), UAS-Rab11::GFP (#8506), Nsyb-Gal4 (#42714).

Western blotting

Drosophila heads (10 heads per condition) were dissected and crushed in 30µL of NuPAGE LDS buffer (NP0008, NuPAGE, Novex, Life Technologies) supplemented with reducing agent (NP0009, NuPAGE, Novex, Life Technologies). Samples were centrifuged (8500g, 10min, 4°C) and the supernatants were stored at -80°C. Once thawed, they were denatured by heating for 10 minutes at 85°C, then plated and separated on a 4-12% bis-tris acrylamide gel (NuPAGE, Novex, Life Technologies) in 1X MOPS buffer (NP0001-02, NuPAGE, Novex, Life Technologies). Samples were transferred to nitrocellulose membrane (NuPAGE, Novex, Life Technologies) using the Biorad Trans-Blot transfer system kit (Biorad) according to the supplier's technical recommendations (7 min, 2.5A, 25V). The quality of migration and transfer was checked by staining with Ponceau Red 0.2% (Sigma).

Membranes were incubated for 1h at room temperature in 1X TNT (Tris 0.15M, Nacl 1.5M, Tween20 0.5%) supplemented with 5% skimmed milk powder to block aspecific sites, and labeled with primary antibody in SuperBlock Tween 20 blocking buffer (37563, Thermo Scientific) overnight at 4°C. This incubation was followed by three 10-minute rinses with 1X TNT to remove aspecifically bound antibodies. The membrane was then incubated with the secondary antibody for 2 hours, followed by 3 further 10-minute rinses with 1X TNT to remove excess of secondary antibodies. The antibodies used

were: anti-BIN1 primary antibodies (BIN1 99D, 05-449, Merck Millipore, RRID:AB_309738, 1/2500, BIN1 ab27796, abcam, RRID:AB_725699, 1/1000), anti-α-tubulin primary antibody (α-tubulin DM1A, T9026, Sigma, RRID: AB_477593, 1/5000), anti-actin primary antibody (Sigma-Aldrich Cat# A2066, RRID:AB_476693), anti-GFP primary antibody (anti-GFP, G1544, Sigma, RRID:AB_439690, 1/4000) and HRP-conjugated secondary antibodies (Jackson ImmunoResearch, anti-mouse 115-035-003, RRID:AB_10015289 and anti-rabbit 111-035-003, RRID:AB_2313567, 1/10000). Immunoreactivity was revealed by incubation with ECL (WBLUC0500, Immobilon Classico Western HRP Substrate, Millipore) and the chemiluminescence imaged with the Amersham Imager 600 camera (GE lifesciences, GE Healthcare, USA). Relative quantification was performed using Fiji software.

Electroretinography

Electroretinograms (ERGs) were recorded in flies immobilized on a glass microscope slide using liquid Pritt glue. For the recordings, glass pipettes (borosilicate, 1.5 mm outer diameter; Hilgenberg) were filled with 3M NaCl and placed in the thorax, as a reference, and over the fly's eye, lightly penetrating the cornea for the recordings. Responses to a repetitive light stimulus (1 s) given by a green light-emitting diode were recorded using AxoScope 10.5 software and analyzed using Clampfit 10.5 software (Molecular Devices). Recordings were amplified using a Warner DP311 AC/DC amplifier (Warner Instruments) and digitized using MiniDigi 1A (Molecular Devices). Raw data traces were analyzed with Igor Pro 6.36 (Wavemetrics).

Electron microscopy

Electron microscopy was performed as described previously (Lambert et al., 2022). After dissection, *Drosophila* eyes were fixed in 1% glutaraldehyde, 4% paraformaldehyde, 0.1M sodium cacodylate buffer (pH 6.8) 30 min at room temperature and then overnight at 4°C. After washing, eyes were post-fixed in 1% OsO4 and 1.5% potassium ferricyanide for 1h, then with 1% uranyl acetate for 45 min, both in distilled water at room temperature in the dark. After washing, they were dehydrated with successive ethanol solutions. Eyes were infiltrated with epoxy resin (EMbed 812 from EMS) and were mounted in resin into silicone embedding molds. Polymerization was performed at 60°C for 2 days. Ultrathin sections of 70-80 nm thickness were observed on formvar-coated grid with a Hitachi H7500 TEM (Milexia, France), and images were acquired with a 1 Mpixel digital camera from AMT (Milexia, France).

NMJ dissection and immunostaining

Third instar larvae were placed on a Petri dish coated with sylgard, a bicomponent silicone (Sylgard™ 184 Elastomer Base, Dow Corning), in a drop of cold Schneider's medium (Schneider's *Drosophila* Medium (1X), 21720-024, Gibco), to prevent the larvae from drying out and to stun them, making the work easier. The larvae were then pinned between the posterior spiracles and at the level of the pharyngeal apparatus, dorsal side up. Using dissecting scissors, we cut the dorsal cuticle along the anteroposterior axis in-between the two dorsal tracheal trunks to open larvae. We performed two additional horizontal incisions at the level of anterior and posterior spiracles. The muscular walls were deployed on either side of the vertical section to reveal the interior. We then removed the internal organs. Once the dissection was complete, we replaced the Schneider medium with 100 µL of 4% PFA fixation solution (Electron Microscopy Sciences, 15712) in 1x PBS (70011-036, Gibco) per larva for 20

minutes. We then performed three 10-minute washes with PBT (PBS 1x with 0.1% Triton-X100, AppliChem A4975). Saturation was carried out with 5% NGS (Normal Goat Serum, Jackson ImmunoResearch, 005-000-121) in PBT for 30 minutes. Primary antibodies were deposited overnight at 4°C in PBT 0.1% NGS 5%. The following antibodies were used: anti-HRP488 (123-545-021, Jackson ImmunoResearch, RRID:AB_2338965, 1/400), anti-Disc Large (Dlg 4F3, DSHB, RRID:AB_ 528203, 1/250), anti-Bruchpilot (nc82, DSHB, RRID:AB_2314866, 1/250) and anti-BIN1 (99D, Merck Millipore, RRID:AB_309738, 1/250). The following day, we performed three 10-minute washes with 0.1% PBT. Following this, we incubate the larvae with secondary antibodies in PBT 0.1% NGS 5%, 2 hours at room temperature: phalloidin (anti-F-actin Alexa 555, A34055, ThermoFisher Scientific), Alexa 633 Goat anti-mouse (A21052, Life Technology, RRID:AB_ 2535719) and Dye Light 405 Donkey anti-rabbit (711-475-152, Jackson ImmunoResearch, RRID:AB_ 2340616). We then performed three 10-minute washes with 0.1% PBT followed by a rinse with 90% glycerol in 1X PBS. NMJs were imaged with a Gataca Systems disk spinning microscope (Gataca Systems, France) equipped with a Yokogawa CSU-W1 head (Yokogawa, Japan), a Prime95B camera (Photometrics, Teledyne Technologies Inc., USA) and a Ti-2 inverted stand (Nikon, Japan). To quantitatively analyze NMJs, we manually delineated each synaptic bouton (including satellite boutons if present) one by one using FIJI (NIH, Bethesda, MD) and measured their area. These values were statistically analyzed using R software.

Microfluidic device preparation

Microfluidics masters were fabricated at the Institute of Electronics, Microelectronics and Nanotechnology, Lille, France using two-step photolithography as previously described (Blasiak et al., 2015). For synaptic connectivity analysis, we used a three-chamber design where the side chambers house neuronal cell bodies, and the central (or synaptic) chamber houses neurites arriving from the side chambers and the synaptic connections they form (Kilinc et al., 2020). The device consists of a 450-µm-wide central channel flanked by two 750-µm-wide side channels. All three channels are *ca.* 100 µm high. The left side channel (termed presynaptic) and the central channel (termed synaptic) are interconnected via 4-mm-high, 450-mm-long parallel microchannels that narrow from an entry width of 10 µm to an exit width of 3 µm. The right-side channel (termed postsynaptic) and the synaptic chamber are also interconnected via parallel microchannels with identical dimensions, except that they were 75-µm-long. 4-mm-high polydimethysiloxane pads were replica molded. Access wells were punched at the termini of the synaptic chamber and of the side channels using 3-mm and 4-mm biopsy punches (Harris Unicore), respectively. The devices were permanently bonded to 24 × 50 mm glass coverslips (Menzel) via O_2 plasma (Diener, Ebhausen, Germany). Prior to cell culture, the devices were sterilized under ultraviolet light (Light Progress, Anghiari, Italy) for 20 min, treated with 0.1 mg/mL poly-D-lysine (Sigma) for at least 2 h, followed by 20 µg/mL laminin (Sigma) treatment for 2 h. The devices were then washed once with PBS prior to neuron seeding.

Primary neuron culture

Culture media and supplements were purchased from Thermo Fisher unless specified otherwise. Primary neurons were obtained from P0 (post-natal day 0) rats according to established procedures (Sartori et al., 2019). The hippocampi were isolated from the cortex and washed with ice cold dissection medium (Hanks' balanced salt solution supplemented with HEPES, 1% sodium pyruvate, and 0.5% penicillin/streptomycin) and treated with 2.5% Trypsin at 37°C for 10 min. The trypsin was then

inactivated using an MEM/FBS medium (Minimum Essential Media supplemented with 10% heat inactivated fetal bovine serum, 1% GlutaMAX, 3% D-glucose (Sigma), 0.8% Minimum Essential Media vitamins and 0.5% Pen/Strep) and incubated with 5 mg/mL DNase (Sigma) for 1 min followed by 3 washes with MEM/FBS medium. The cells were then dissociated in culture medium (Neurobasal A, supplemented with 1% GlutaMAX and 2% B_{27} neural supplement with antioxidants) before being centrifuged at 200 ×*g* for 8 min. Cells were then resuspended in culture medium, counted and plated at 100,000 cells/cm^2 density in the pre- and post-synaptic chambers. The next day, the medium in reservoirs was replaced with fresh culture medium. The 0.1% ethylenediaminetetraacetic acid (in H_2O) was added to the Petri dishes containing microfluidic devices to minimize evaporation. The cultures were maintained in a tissue culture incubator (Panasonic; Osaka, Japan) at 37°C and 5% CO_2 for up to 21 days.

BIN1 isoform overexpression

Overexpression constructs were obtained from Gene Art (Thermo Fisher) based on pLenti6.3/Ubc/V5-DEST A244 backbone vectors with a CMV promoter (Life Technologies, Carlsbad, CA): BIN1iso1 (NM_009668), BIN1 isoform 9 (NM_139349), and an overexpression control vector (Mock). On day 7 *in vitro* (DIV7), neurons in the pre-synaptic or post-synaptic chambers were transduced as previously described (Eysert et al., 2021). To avoid the transduction of neurons in the opposite chamber, a hydrostatic pressure gradient is formed across the microchannels separating the synaptic chamber and the target cell chamber. Lentiviral particles were diluted in pre-warmed culture medium containing 2 µg/mL Polybrene (hexadimethrine bromide; Sigma). Media from all wells were collected in a common tube. A total of 20, 15 and 25 µL of the collected medium were added to the reservoirs of the target cell chamber, synaptic chamber and opposite cell chamber, respectively. Cells were transduced at a multiplicity of infection (MOI) of 2 by adding 10 µL of virus suspension to one of the wells of the target cell chamber. Neurons were incubated with viral particles for 6 h before the wells were topped-up with the remaining collected medium. In a separate experiment, cells in the pre- and postsynaptic chambers were transduced with lentiviral vectors encoding LifeAct-Ruby (pLenti.PGK.LifeAct-Ruby.W; RRID:Addgene_51009) and LifeAct-GFP (pLenti.PGK.LifeAct-GFP.W; RRID:Addgene_51010), respectively, to demonstrate that viral transductions were restricted to the intended cell chamber.

Immunocytochemistry of primary neurons

To quantify synaptic connectivity, we fixed the neurons on DIV14 in 4% paraformaldehyde (PFA) for 15 min, washed 3× with PBS, and permeabilized for 5 min with 0.3% Triton X-100. Cells were incubated with 5% normal donkey serum for 2 h at RT before overnight incubation with the following primary antibodies: BIN1 (Millipore Cat# 05-449, RRID: AB_309738), Homer1 (Synaptic Systems Cat# 160 004, RRID: AB_10549720), MAP2 (Synaptic Systems Cat# 188 006, RRID: AB_2619881). The cells were then washed 3× with PBS and incubated with the following secondary antibodies raised in donkey: AlexaFluor-conjugated AffiniPure Fragment 405, 594, or 647 (Jackson ImmunoResearch). The cells were then washed 3× with PBS and incubated with a Cy2-tagged monoclonal antibody against Synaptophysin 1 (Synaptic Systems Cat# 101 011C2, RRID: AB_10890165).

Microscopy and synaptic connectivity analysis

Microfluidic devices were imaged using a Zeiss LSM880 confocal microscope, equipped with a 63× 1.4-NA objective. Images were analyzed with Imaris software (Bitplane, Zürich, Switzerland) by reconstructing Synaptophysin I and Homer puncta in 3D. The volume and position information of all puncta were processed using a custom Matlab (MathWorks, Natick, MA) program. This program assigns each postsynaptic spot to the nearest presynaptic spot (within a distance threshold of 1 µm) and calculates the number of such assignments for all presynaptic puncta. The percentage of presynaptic spots assigned by at least one postsynaptic spot was systematically used as a readout for synaptic connectivity (Kilinc et al 2020).

Microfluidic device integration to MEAs

We used 256-electrode MEA chips (256MEA100/30iR-ITO-w/o, MultiChannel Systems, Reutlingen, Germany) where electrodes form a 16×16 Cartesian grid, except for the corners where the tips of large, triangular reference electrodes are positioned. As previously done for 60-electrode MEA chips (Lefebvre et al., 2024), we adapted the microfluidic device layout by adding a triangular chamber between the flow channels connecting synaptic and postsynaptic chambers to their respective medium reservoirs. This chamber matches the tip of one reference electrode such that the reference electrode is fluidically connected to the rest of the device. To minimize the effect of this reference electrode chamber on fluid flow in the aforementioned channels, we used sets of parallel microchannels (18 µm width; 7 µm separation) for the connections. MEA-adapted microfluidic devices were prepared in the same way as the regular microfluidic devices and align-bonded to MEA chips using O_2 plasma.

To position similar numbers of microelectrodes underneath pre- and postsynaptic chambers, we use a mechanical tool to precisely align the microfluidic device over the MEA chip (Lefebvre et al., 2024). Briefly, after O_2 plasma exposure, the MEA chip was placed on a manual stage allowing rotation and two-axis translation in the *xy*-plane (Newport; Irvine, CA). The microfluidic device was held above the MEA chip with a vacuum pen (Virtual Industries Inc.; Colorado Springs, CO) that was attached to manual *z*-axis translational stage. Using binoculars, the microfluidic device was then aligned with the MEA chip in a way that pre- and postsynaptic chamber were covered by *ca.* 50 electrodes each. The device was then lowered onto the MEA chip until contact was established, and the integrated device was kept at 70°C for 2 min to strengthen the bond. The MEA-integrated microfluidic devices were placed in 100 mm polystyrene Petri dishes and sterilized and coated in the same way as the regular microfluidic devices. A 35 mm Petri dish containing sterile milliQ water was placed next to the MEA chips to minimize evaporation.

MEA recordings

At DIV19, the spontaneous neuronal activity in each MEA chip was recorded using a MEA2100-System equipped with a single 256-channel headstage and an integrated temperature controller (MultiChannel Systems, Reutlingen, Germany). First, the headstage was preheated to 37°C. A plastic ring with ethylene-propylene membrane was placed over the microfluidic device to ensure sterility during transport and recordings. The MEA chip was brought on the headstage and left there for 5 min for the neurons to adjust to the new environment. Spontaneous activity was recorded from all channels for 5 min at 25 kHz sampling rate. The recordings were exported to .h5 files for further

analysis. For each MEA-integrated microfluidic device, a chip map was generated that lists the electrodes corresponding to pre- and post-synaptic chambers.

MEA analysis

Spike Sorting. The extracellular recordings were analyzed using SpikeInterface (Buccino et al., 2020), and the SpyKING CIRCUS 2 spike sorting pipelines, conceived as an extension of our spike sorting toolbox (Yger et al., 2018). Briefly, the spike sorting procedure to extract the single unit activities starts with a preprocessing step, as follows: bandpass filter (frequency [150Hz, 7kHz]), then a common median reference filter (to remove shared fluctuations across channels) before whitening (to remove shared noise across channels). Then, negative threshold crossings are detected, aligned, and a subset is projected into a lower dimensional space via Principal Components (see (Yger et al., 2018) for details). Density-based clustering is then launched on these projected spikes to detect the templates, *i.e.*, the motifs regularly occurring in the data. Once the dictionary of templates is constructed, a proper orthogonal matching pursuit algorithm (Tropp & Gilbert, 2007) reconstructs the signal as a linear sum of these templates to identify all the spike times. After spike sorting, only the putative units with a refractory period violation less than 0.1 and a signal-to-noise ratio more than 2 were kept as valid neurons.

Position of the units. The putative positions of the units kept after spike sorting are estimated from the extracellular templates, assuming that units could be considered as monopoles (Scopin et al., 2024; Varol et al., 2021). All the units that would be found within the presynaptic chamber are labeled as belonging to the *pre* population, while those found within the postsynaptic chamber are labeled as *post*. Note that while all electrodes were analyzed simultaneously during the spike sorting process (to make use of spatiotemporal information to disambiguate sources), very few units were found between the two chambers, in accordance with the experimental setup. We analyzed the ratio of *post* units to *pre* units to identify potentially abnormal devices. To this end, we used Matlab (Mathworks, Natick, MA) to generate a probability plot for normal distribution, using detected unit numbers for all devices (Supplementary figure 5). Based on this plot, devices with |*z*-score| > 1.5 were considered outside the normally distributed post:pre unit number ratio and discarded from further analysis. Note that this threshold corresponds to $\left|\log_2 \frac{\#post}{\#pre}\right| > 2$, *i.e.*, a maximum of 4-fold difference in unit numbers between the two chambers was allowed.

Drive between *pre* and *post* populations. To assess the directionality of the functional connectivity between pairs of units, we defined a metric called the *pre-post-drive* that measures to what extent the units in the *pre* population are leading the activity of the units in the *post* population. The assumption behind such a metric is that assuming monosynaptic, direct connections between *pre* and *post* neurons, one must see an increase in activity in the *post* population following spikes emitted by the *pre* population. To do so, for each pair of unit *i* belonging to the *pre* population and of unit *j* belonging to the *post* population, we measured the cross-correlogram $CC_{i_{pre},j_{post}}(t)$ of their spiking activity with a given time bin $T_{bin} = 2\,ms$ and during a time window $T_{window} = 20\,ms$. The *drive* $\Phi(i_{pre},j_{post})$ was then computed as the ratio of the integral of $CC_{i_{pre},j_{post}}(t)$ for positive times (*i.e.*, how much the activity of i_{pre} drives the one of j_{post}) divided by the integral of $CC_{i_{pre},j_{post}}(t)$ for negative times (*i.e.*, how much the activity of j_{post} drives the one of i_{pre}). If the two units were firing independently, as

Poisson sources, then $\Phi(i_{pre}, j_{post})$ should be close to 1. If, on the other hand, $\Phi(i_{pre}, j_{post})$ is larger than 1, it means that, on average, spikes of i_{pre} is more likely to precede the ones in j_{post}. Such an asymmetry in the cross-correlogram is often used to infer putative directional connectivity (Aertsen & Gerstein, 1985). Then, at the population level, the *drive* between *pre* and *post* populations is simply obtained as $\Phi(pre, post) = mean_{i \in pre, j \in post} \Phi(i_{pre}, i_{post})$. Data points beyond median ± 3 median absolute deviations (MAD) were deemed as outliers and excluded from subsequent statistical analysis.

Statistical analysis

Statistical information is available in the figure legends. Two-tailed statistical tests were used. Hypothesis testing was performed with the Kruskal Wallis test followed by a Mann-Whitney comparison, or by a post-hoc Dunn multiple comparison test (Holm method), or with Tukey-Kramer corrections. Statistical analyses were performed using Matlab (Mathworks, Natick, MA), R 3.6.0 (R Core Team (2019). R: A language and environment for statistical computing, R Foundation for Statistical Computing, Vienna, Austria. URL https://www.R-project.org/), especially with the FSA package (Ogle et al., 2023), and RStudio 1.2.1335. For box plots, the middle segment, lower and upper hinges represent the median, first quartile and third quartile respectively. The upper whisker extends from the upper hinge to the largest value within 1.5 x IQR of the hinge (where IQR is the interquartile range, or the distance between the first and third quartiles). The lower whisker extends from the lower hinge to the smallest value located at a maximum of 1.5 * IQR from the hinge. Differences with a *p*-value <0.05 were considered significant.

Results

BIN1iso1 altered synaptic transmission of adult photoreceptor neurons in *Drosophila*

To assess the effect of BIN1 isoforms on synaptic transmission, we investigated the electrophysiological response of *Drosophila* photoreceptor neurons expressing BIN1 isoforms upon light illumination. Flies expressed BIN1iso1, BIN1iso8, BIN1iso9, dAmphisoA (the longest endogenous BIN1 isoform) and Luciferase (used as a control) in the outer photoreceptor neurons at day2, day8-9 and day15-16 after birth. The expression was driven by a Rh1 promoter, active just before birth, after photoreceptor neuron development, and by the Gal4/UAS system (Brand & Perrimon, 1993). We checked BIN1 isoforms and dAmphisoA protein expression by western blot using two antibodies. The UAS constructs are inserted in the same genomic location and therefore exhibit similar expression (Lambert et al., 2022). All the constructs were expressed as expected (Supplementary figure 1). The ab27796 antibody cross-reacted partially with dAmphisoA whereas the 99D antibody did not detect dAmphisoA and more strongly detected BIN1iso1. On these flies, we performed electroretinograms (ERGs). Upon a 1 sec-long orange light stimulation, retinas usually exhibit a depolarization and two transient currents, called the ON transient and the OFF transient, at the initiation and termination of the light stimulation respectively (Figure 1A). The ON and OFF transients reflect the synaptic transmission activity of the photoreceptor neurons at the level of the lamina, the outermost part of the optic lobe. On day 2, we did not observe any alteration of the electrophysiological activity whatever the BIN1 isoforms. This indicated that all photoreceptor neurons were normal at birth. On day 8-9, we observed a significant reduction of the amplitude of the ON and OFF transients specifically for flies

expressing BIN1iso1 (Figure 1A, B). On day 15-16, the amplitude of all electrophysiological parameters, the ON and OFF transients and the depolarization, were strongly reduced for retinas expressing BIN1iso1 (Figure 1A, B). It was not observed for retinas expressing BIN1iso8, BINiso9 and dAmphisoA. The amplitude of the OFF transient was even slightly increased in these conditions. The loss of all electrophysiological parameters on day 15-16 for BIN1iso1 likely reflected neurodegeneration and loss of the photoreceptor neurons that have been shown in these flies (Lambert et al., 2022). The loss of the ON and OFF transients on day 8-9, observed here, showed in addition that BIN1iso1 expression altered synaptic transmission before neurodegeneration.

To understand the isoform-specificity of the result, we wondered whether all BIN1 isoforms were localized at the photoreceptor neuron axon synaptic terminals in the lamina. By immunofluorescence in 1-day-old whole-mount *Drosophila* retina, we observed that BIN1iso1, BIN1iso9 and to a lesser extent BIN1iso8 were all localized to the synaptic terminals (Figure 1C). This remained true in 7-day-old flies. Therefore, BIN1iso1 synaptotoxicity did not originate from an aberrant localization of this isoform at the synaptic terminals. In addition, we observed in 7-day-old flies a strong accumulation of vesicles in the presynaptic terminals for the BIN1iso1 condition. Some of these vesicles were very big, even bigger than the size of synaptic terminals (Figure 1C, arrows). We further analyzed the synaptic terminal structure using electron microscopy (Figure 1D). We confirmed the presence of abnormal giant vesicles. These vesicles had a single membrane and did not have any specific content. We could see mitochondria and capitate projections as in the control. Finally, we observed some degenerating synaptic terminals (Supplementary figure 2). Overall, the vesicles, observed in the synaptic terminals, perfectly corresponded to the ones exhibiting endosomal markers, described in photoreceptor neuron cell bodies (Lambert et al., 2022). Therefore, they likely originate from a defect in intracellular trafficking and are responsible for the synaptic transmission defects and synaptic terminal degeneration.

BIN1iso1 altered *Drosophila* larval neuromuscular junction

We wanted to further assess the role of BIN1 isoforms on synapse integrity and tested the effect of their expression in third instar larval type Ib neuromuscular junctions (NMJ). It is a large glutamatergic synapse between a motor neuron and a muscle cell. Expression of BIN1 isoforms and dAmphisoA was performed thanks to a Nsyb driver. We checked the expression of the protein by western blot in adult head originating from the larvae, as the Nsyb driver remains active in adulthood, and observed similar results as in the eye with the rh1 driver (Supplementary figure 3). For each larva, we observed the same NMJ, located on muscle cells 6/7 in abdominal segment A2. We labelled the actin cytoskeleton (Phalloidin), the neuron-specific horseradish peroxidase (HRP) epitope and Disc large (Dlg), the orthologue of PSD95, to visualize muscles, motor neuron axon terminals and postsynaptic compartments respectively (Figure 2A).

In larvae expressing luciferase (used as a control), BIN1iso8, BIN1iso9 and dAmphisoA, the innervation pattern appeared to be normal, with large, well-rounded, well-contoured Ib-type synaptic boutons and a stereotyped branching pattern (Figure 2A). It indicates that these isoforms did not impact NMJ morphology. In contrast, BIN1iso1-expressing synaptic boutons looked shredded, clustered in places, and their contours were not as sharp and defined as the control boutons. When quantifying the boutons, it translated in a significantly higher number (~225 boutons per NMJ versus ~150 for the control) of smaller boutons (~1.75 µm² versus ~2.5 µm² for the control) in the BIN1iso1-expressing

condition (Figure 2B). In addition, in this condition, we were able to see a significantly higher number of satellite boutons (~40 satellite boutons per NMJ compared with ~10 for the control), *i.e.*, boutons budding off from a bouton present in the axis of the branch, or boutons budding off from neuronal connections between two boutons. We did not observe any significant change when summing all individual bouton areas (cumulative area), nor when quantifying the number of active zones using a bruchpilot (brp) staining (Figure 2C, D). Active zones are synaptic vesicle-rich compartments in the presynaptic boutons, where precisely orchestrated molecular interactions control the fusion of synaptic vesicles with the presynaptic membrane. It indicates that despite the strong NMJ morphological alterations, the total size of the NMJ remained constant between conditions. Thanks to a BIN1 staining, we could detect BIN1iso1, BIN1iso9 and to a lesser extent BIN1iso8 in the motor neuron terminals and synaptic boutons (Figure 2A, C), indicating that the specificity of BIN1iso1 synaptotoxicity does not result from a different addressing of BIN1 isoforms in motor neurons.

Rab11 expression did not prevent BIN1iso1-induced morphological changes of the *Drosophila* larval neuromuscular junction

It is known in the PR neuron model, that BIN1iso1 leads to degeneration via a defect in early endosome trafficking, and that the activation of recycling endosomes via Rab11 alleviates the neurodegeneration (Lambert et al., 2022). Because in this work, BIN1iso1-associated synaptotoxicity exhibited endosomal-like vesicles and because the intracellular trafficking is crucial for synaptic function, we hypothesized that BIN1iso1 synaptotoxicity could also originate from an intracellular trafficking defect. To test this hypothesis, we expressed the recycling endosome regulator Rab11 and assessed if it was possible to restore the BIN1iso1-induced phenotype of NMJs to a wild-type appearance.

Wild-type NMJs exhibited normal morphology with round, well-defined synaptic boutons (Figure 3A). Expression of BIN1iso1 resulted again in NMJs featuring a higher number of smaller synaptic boutons, with a higher number of satellite boutons (Figure 3A, B). Overexpression of Rab11 alone did not affect the morphology of synaptic neurons but significantly decreased the number of synaptic boutons (Figure 3A, B). In this background, overexpression of BIN1iso1 still increased the number of synaptic and satellite boutons, although without changing the mean area of single boutons, and the increase in synaptic bouton number was significantly lower than in the control background (Figure 3A, B). This indicated that Rab11 overexpression did not clearly prevent the effect of BIN1iso1 on NMJs and suggested more an additive effect rather than an epistatic one between the overexpression of BIN1iso1 and Rab11. We checked that the staining of BIN1was similar between the BIN1iso1 alone and the BIN1iso1+Rab11 conditions, which we confirmed by western blot (Supplementary figure 4). Overall, these results suggested that BIN1iso1 synaptotoxicity is rather independent of Rab11-controlled endosomal trafficking.

BIN1iso1 is toxic for rodent synapses only when expressed in the presynaptic compartment

We next sought to determine if the isoform-specific effect of BIN1iso1 on synapses could be replicated in a mammalian system. To this end, we cultured rat hippocampal neurons in custom-design, three-chamber microfluidic devices that fluidically isolate synapses from their cell bodies and permit

modulation of gene expression exclusively in pre- or postsynaptic chambers (Kilinc et al., 2020). By employing two sets of parallel microchannels of different length to connect presynaptic and postsynaptic chambers to the (central) synaptic chamber (Figure 4A), these devices ensure that the synaptic chamber receives dendrites only from the postsynaptic chamber and contains 83.2±6.1% of all synaptic connections between pre- and postsynaptic chambers (Kilinc et al., 2020). We plated primary neuron cultures in pre- and postsynaptic chambers and transduced them on DIV7 with lentiviruses encoding for human BIN1iso1, BIN1iso9 or a scrambled control vector (Mock), either in the presynaptic or in the postsynaptic chamber. At DIV14, we fixed the cultures and immunostained them against BIN1, somatodendritic marker MAP2, presynaptic marker Synaptophysin and postsynaptic marker Homer (Figure 4B). We applied our distance-based synaptic connectivity analysis workflow, which assigns each postsynaptic puncta to the nearest presynaptic puncta within a distance threshold (Eysert et al., 2021; Kilinc et al., 2020; Saha et al., 2024). Overexpression of BIN1iso1 –but not BIN1iso9– in the presynaptic chamber –but not in the postsynaptic chamber– induced synaptotoxicity in mature hippocampal neurons as evidenced by a decrease in the fraction of presynaptic spots assigned by at least one postsynaptic spot (Figure 4C). This corroborates our findings in *Drosophila* NMJ that BIN1 induces isoform-specific perturbations at the presynaptic compartment.

Presynaptic BIN1iso1 overexpression decreases network-level functional connectivity

Analysis of synaptic connectivity by immunofluorescence provides inherently limited information on the functionality of the neuronal network. We therefore assessed network-level synaptic connectivity in three-chamber microfluidic devices integrated to MEA chips (Figure 5A-C) – based on the experimental model we recently developed in the context of Aβ-induced synaptotoxicity (Lefebvre et al., 2024). We analyzed the spiking activity via an established spike sorting algorithm (Yger et al., 2018), which identifies putative units based on their spatiotemporal firing patterns and calculated the cross-correlation for each unit pair that can be formed between units in the pre- and postsynaptic chambers (Figure 5D-F). As a measure for functional connectivity, we defined a *pre-post-drive* parameter by taking the ratio of right-hand-side integral to left-hand-side integral of the cross-correlation histogram for each such unit pair (Figure 5G) (see Materials and Methods for details).

We made a total of 40 recordings (14 Mock, 15 BIN1iso1, 11 BIN1iso9, expressed only in the presynaptic chamber) using primary neuronal cultures from 7 independent cultures. For 5 devices (1 Mock and 4 BIN1iso1) the algorithm was not able to identify any units in the presynaptic chamber (that passed the defined quality criteria). In addition, we discarded a total of 5 recordings (1 Mock, 3 BIN1iso1, 1 BIN1iso9) as they fell outside the normal distribution of post:pre unit number ratio (Supplementary figure 5). For the remaining recordings (12 Mock, 8 BIN1iso1, 10 BIN1iso9), we first assessed whether the number of units detected by the spike sorting algorithm correlated with *pre-post-drive*. When all conditions were pooled, the pre-post-drive parameter did not correlate with the number of units detected in the presynaptic chamber (R^2 = 0.136), number of units detected in the postsynaptic chamber (R^2 = 0.078) or with the total number of units detected (R^2 = 0.122) (Supplementary figure 6). This finding suggests that the *pre-post-drive* parameter can be used as a read-out for network-level connectivity, independently of the number of units detected in the microfluidic device.

We then compared the experimental groups in terms of detected unit numbers and pre-post-drive. To this end, we first plotted pre-post-drive as a function of numbers of detected units in each chamber (Figure 5H). For clarity, we included in this plot the outlier data points as defined by median ± 3×MAD pre-post-drive (1 Mock, 1 BIN1iso1, 3 BIN1iso9). Interestingly, the pre-post-drive was significantly lower in the BIN1iso1 group compared to the Mock and BIN1iso9 groups (Figure 5I). In fact, for the BIN1iso1 condition, the pre-post-drive parameter was very close to 1, indicating that the presynaptic chamber was no longer driving the postsynaptic chamber, in contrast with the other conditions. The number of units in the postsynaptic chamber was also lower for the BIN1iso1 group when compared to Mock and BIN1iso9 groups despite the fact that the overexpression was restricted to the presynaptic chamber (Figure 5J). This suggests that the postsynaptic activity is (in part) driven by the pre-to-post synaptic connections, which are perturbed by the expression of BIN1iso1 in the presynaptic chamber. The number of units in the presynaptic chamber was also decreased, but this is not reflected in Figure 5J due to the exclusion of 4 out of 15 devices with no presynaptic units, as this precludes cross-correlation analysis. Finally, despite these detrimental functional changes caused by BIN1iso1, neither the mean firing rate (Figure 5K) nor amplitude (signal-to-noise ratio) (Figure 5L) were affected. In summary, the MEA results based on the spontaneous activity of live neurons recapitulate our microscopy-based findings and confirm that presynaptic BIN1iso1 overexpression leads to a loss of network-level synaptic connectivity.

Discussion

Our findings demonstrate that the overexpression of BIN1iso1 induces synaptic dysfunction both morphologically and functionally across invertebrate and vertebrate models. In *Drosophila* photoreceptor neurons, BIN1iso1 impaired synaptic transmission prior to the complete loss of electrophysiological response, suggesting that synaptic dysfunction is an early and possibly primary event in BIN1-mediated toxicity. Notably, this effect was specific to isoform 1, as neither BIN1iso9 nor BIN1iso8 recapitulated the phenotype. Morphologically, BIN1iso1 expression resulted in an altered NMJ architecture characterized by an increased number of synaptic boutons, many of which were smaller in size and appeared as satellite boutons. This structural remodeling was accompanied in the photoreceptor synaptic terminals by an accumulation of endosome-like vesicles, pointing to a disruption of vesicular trafficking. These vesicles were reminiscent of the ones seen in cell bodies of degenerating photoreceptors, which could be rescued by gain-of-function of Rab11, a key regulator of recycling endosomes. In this work, we found that overexpression of Rab11 only partially rescued in an additive manner the synaptic defects caused by BIN1iso1, suggesting a slightly different mechanism at the synaptic level. We then extended our observations to mammalian models using rat hippocampal neurons. BIN1iso1 overexpression in the presynaptic compartment significantly reduced synaptic density, while postsynaptic expression had no detectable effect. This presynaptic specificity was again isoform-dependent, as BIN1iso9 expression did not affect synaptic density. Functionally, presynaptic BIN1iso1 expression led to disrupted synaptic transmission and altered network activity, further highlighting a conserved and isoform-specific synaptotoxic effect.

We showed in this work an early synapse toxicity for BIN1iso1. Because synapses are known to be affected early in AD and their loss correlates with cognitive decline, BIN1, a risk gene for the disease, may contribute to this process (DeKosky & Scheff, 1990; Mecca et al., 2022; Terry et al., 1991). This is

supported by some variants of BIN1, associated with AD and shown to increase the expression of BIN1iso1 (Chapuis et al., 2013). Other evidence suggests that BIN1 expression decreases in the later stages of AD (Marques-Coelho et al., 2021; Saha et al., 2024). This could be due to the death of high-expressing neurons, leaving only low-expressing neurons. Alternatively, the decline in BIN1 expression may be causal in disease progression. In this context, therapeutic strategies aimed at increasing BIN1 activity need to be carefully controlled to avoid exacerbating neurotoxicity due to BIN1iso1 overexpression, as demonstrated in our study.

Importantly, our results not only reveal structural synaptic loss upon BIN1iso1 expression but also demonstrate functional consequences on synaptic transmission. In *Drosophila*, thanks to ERGs, we showed an early progressive loss of synaptic transmission between photoreceptor neurons and the optic lobe. In rat primary neuronal cultures, we used MEA technology to assess neuronal activity. A key advantage of using this technology is its ability to measure neuronal activity directly, without relying on indirect calcium or glutamate sensors for example. For all these recordings, changes in signal frequency and amplitude can result from alterations in either intrinsic neuronal excitability or synaptic transmission, making it challenging to distinguish between the two. One way to disentangle these effects is by analyzing network synchronicity, which has been used as an indirect measure of synaptic transmission. This way, BIN1 knockout iPSC-derived neurons were shown to be defective in functional synaptic connectivity (Saha et al., 2024). To go further, in this work, we combined MEA with microfluidic compartmentalization to directly assess functional connectivity within a defined network of pre- and postsynaptic neuron populations. While we did not observe changes in firing rate or spike amplitude in the presynaptic chamber where BIN1iso1 was overexpressed, we did detect a clear reduction in functional connectivity as the pre-to-post synaptic drive was close to 1 upon BIN1iso1 expression. We did not observe the same result with BIN1iso9, reinforcing the isoform-specific effect. The absence of effect on the firing rate or spike amplitude contrasts with previous reports showing hyperexcitability with increased spike frequency upon BIN1 overexpression (Voskobiynyk et al., 2020). This may be explained by differences in the maturity of the neurons at the time of transduction and analysis. More broadly, our findings further support BIN1's role as a modulator of synaptic transmission and network dynamics.

Our results consistently point to a presynaptic-specific role for BIN1iso1. BIN1 has been shown to be predominantly localized in the pre- and post-synaptic compartments in rat primary neuronal cells and mouse brain (De Rossi et al., 2020; Schürmann et al., 2020). In both the *Drosophila* photoreceptor model and the larval NMJ model, BIN1iso1 was tested presynaptically. We further confirmed this compartment-specific effect using a microfluidic device allowing for precise control of protein expression in rat primary neuron cultures. This system revealed a clear reduction in synaptic density when BIN1iso1 was expressed presynaptically, but not postsynaptically. This is in accordance with a role of BIN1 in regulating presynaptic synaptic vesicle release probability seen in conditional knockout mouse brain (De Rossi et al., 2020), and with a presynaptic role of BIN1 in the synaptic vesicle endocytic cycle in inhibitory synapses of mouse primary neuronal cultures (Barata et al., 2025). A postsynaptic role has also been reported in the exocytosis of GluA1 AMPA receptor subunit (Schürmann et al., 2020). These observations suggest that BIN1 may have distinct, context-dependent functions on both sides of the synapse.

Mechanistically, the synaptic toxicity of BIN1iso1 appears to be linked to disruptions in endo-lysosomal trafficking. Indeed, BIN1iso1 expression led to the accumulation of endosome-like large vesicular structures in the terminals of photoreceptor neurons, as observed via immunofluorescence and electron microscopy. In addition, the synaptic overgrowth phenotypes, especially the formation of satellite boutons at the larval NMJ, have been reported in mutants affecting endocytosis, such as *endophilin, synaptojanin, dynamin, AP180, synaptotagmin* and *σ2-adaptin* (Choudhury et al., 2016; Dickman et al., 2006). These morphological changes are thought to arise from defective intracellular trafficking of signaling molecules from the BMP pathway that regulate synaptic growth (O'Connor-Giles et al., 2008). In addition, BIN1iso1-induced photoreceptor degeneration was previously linked to trafficking defects and could be suppressed by modulating Rab5 or Rab11 activity (Lambert et al., 2022), both key regulators of early and recycling endosomes. In the present study, overexpression of Rab11 only partially rescued in an additive manner the synaptic overgrowth phenotype induced by BIN1iso1, suggesting mechanistic divergence between the soma and presynaptic terminals. Similarly, Rab11 overexpression has been shown to mitigate synaptic toxicity in *Drosophila* models of Parkinson's disease involving *Parkin* and *PINK1* (Rai et al., 2023), yet it does not rescue overgrowth phenotypes in *AP-2* loss-of-function *Drosophila* models (Choudhury et al., 2022). The existence of different mechanisms in subcellular compartments in mammals may also explain why BIN1 loss-of-function has been associated with both smaller and bigger Rab5-positive endosomes in rodent primary neurons (Barata et al., 2025; Calafate et al., 2016). Of note, we also observed that Rab11 overexpression alone reduced bouton number at the *Drosophila* NMJ, a novel finding consistent with previously reported increases in bouton number in Rab11 loss-of-function mutants (Khodosh et al., 2006). The endo-lysosomal dysregulation by BIN1 is of interest for AD as endo-lysosomal defects are considered potentially causal in AD (Nixon et al 2024). BIN1 is known to interact with many components of this system, such as RIN3, another AD genetic risk factor (Dourlen et al., 2025; Kajiho et al., 2003; Shen et al., 2020). Together, these data further support a role for BIN1iso1 in regulating synaptic architecture via intracellular endo-lysosomal trafficking pathways.

Altogether, our data establish BIN1iso1 as a potent modifier of synaptic integrity, at structural and functional levels. The early synaptic alterations, the accumulation of endosomal vesicles, and the isoform and compartment specificity of BIN1iso1 toxicity provide novel insights into the molecular mechanisms by which BIN1 may contribute to neurodegeneration. These findings are particularly relevant given the genetic association of BIN1 with Alzheimer's disease and suggest that isoform-specific targeting could represent a therapeutic strategy.

Acknowledgements

The authors would like to acknowledge the BioImaging Center Lille (BICeL) and la PLateforme d'Expérimentation et de Haute Technologie Animale (PLEHTA), both part of Plateformes Lilloises en Biologie et Santé (PLBS) - UAR 2014 - US 41), for microscopy maintenance and animal housing, respectively. pLenti.PGK.LifeAct-Ruby.W and pLenti.PGK.LifeAct-GFP.W were gifts from Rusty Lansford (Addgene plasmid # 51009; http://n2t.net/addgene:51009; RRID:Addgene_51009 and Addgene plasmid # 51010; http://n2t.net/addgene:51010; RRID:Addgene_51010). The authors thank the vectorology service of the University of Bordeaux for lentiviral packaging. The 4F3 and nc82 antibodies developed by Goodman, C. (University of California, Berkeley) and Buchner, E. (Universitaetsklinikim Wuerzburg) were obtained from the Developmental Studies Hybridoma Bank, created by the NICHD

of the NIH and maintained at The University of Iowa, Department of Biology, Iowa City, IA 52242. Stocks obtained from the Bloomington *Drosophila* Stock Center (NIH P40OD018537) were used in this study.

This work was supported by the Joint Programme– Neurodegenerative Disease Research (JPND; 3DMiniBrain), by France Alzheimer (#328 ADhesion, #1999 BIN1DROSO), by Fondation Vaincre Alzheimer (LECMA Grant The BIN1-Tau neurotoxic link in *Drosophila*), by ANR (TAUFUNALZ project, ANR-23-CE14-0064), by the LabEx (Laboratory of Excellence) DISTALZ (Development of Innovative Strategies for a Transdisciplinary approach to Alzheimer's disease ANR-11-LABX-01), by the Région Hauts-de-France Regional Council and by an Alzheimer's Association Grant (AARG-22-926152). CG was supported by a fellowship from FranceAlzheimer (Soutien aux jeunes chercheurs – AAP JC 2024 – #6473). This work has been partially undertaken with the support of IEMN CMNF facilities and supported by the French Renatech network.

Conflicts of interest:

None.

Availability of data and material

Data and material from the current study are available from the corresponding authors upon request.

References

Adams, S. L., Tilton, K., Kozubek, J. A., Seshadri, S., & Delalle, I. (2016). Subcellular Changes in Bridging Integrator 1 Protein Expression in the Cerebral Cortex During the Progression of Alzheimer Disease Pathology. *Journal of Neuropathology and Experimental Neurology*, *75*(8), 779–790. https://doi.org/10.1093/jnen/nlw056

Aertsen, A. M. H. J., & Gerstein, G. L. (1985). Evaluation of neuronal connectivity: Sensitivity of cross-correlation. *Brain Research*, *340*(2), 341–354. https://doi.org/10.1016/0006-8993(85)90931-X

Barata, M. A., Perdigão, C., Ramalho, J., Gomes, E. R., & Guimas Almeida, C. (2025). Alzheimer's genetic risk factor Bin1 controls synapse vesicle exo-endocytosis in inhibitory synapses. *Cell Reports*, *44*(8). https://doi.org/10.1016/j.celrep.2025.116005

Bellenguez, C., Küçükali, F., Jansen, I. E., Kleineidam, L., Moreno-Grau, S., Amin, N., Naj, A. C., Campos-Martin, R., Grenier-Boley, B., Andrade, V., Holmans, P. A., Boland, A., Damotte, V., van der Lee, S. J., Costa, M. R., Kuulasmaa, T., Yang, Q., de Rojas, I., Bis, J. C., … Lambert, J. C. (2022). New insights into the genetic etiology of Alzheimer's disease and related dementias. *Nature Genetics*, *54*(4), 412–436. https://doi.org/10.1038/s41588-022-01024-z

Blasiak, A., Lee, G. U., & Kilinc, D. (2015). Neuron Subpopulations with Different Elongation Rates and DCC Dynamics Exhibit Distinct Responses to Isolated Netrin-1 Treatment. *ACS Chemical Neuroscience*, *6*(9), 1578–1590. https://doi.org/10.1021/acschemneuro.5b00142

Brand, A. H., & Perrimon, N. (1993). Targeted gene expression as a means of altering cell fates and generating dominant phenotypes. *Development (Cambridge, England)*, *118*(2), 401–415. http://www.ncbi.nlm.nih.gov/pubmed/8223268

Buccino, A. P., Hurwitz, C. L., Garcia, S., Magland, J., Siegle, J. H., Hurwitz, R., & Hennig, M. H. (2020). Spikeinterface, a unified framework for spike sorting. *ELife*, *9*, 1–24. https://doi.org/10.7554/eLife.61834

Butler, M. H., David, C., Ochoa, G. C., Freyberg, Z., Daniell, L., Grabs, D., Cremona, O., & De Camilli, P. (1997). Amphiphysin II (SH3p9; BIN1), a member of the amphiphysin/Rvs family, is concentrated in the cortical cytomatrix of axon initial segments and nodes of ranvier in brain and around T tubules in skeletal muscle. *Journal of Cell Biology*, *137*(6), 1355–1367. https://doi.org/10.1083/jcb.137.6.1355

Calafate, S., Flavin, W., Verstreken, P., & Moechars, D. (2016). Loss of Bin1 Promotes the Propagation of Tau Pathology. *Cell Reports*, *17*(4), 931–940. https://doi.org/10.1016/j.celrep.2016.09.063

Cataldo, A. M., Barnett, J. L., Pieroni, C., & Nixon, R. A. (1997). Increased neuronal endocytosis and protease delivery to early endosomes in sporadic Alzheimer's disease: neuropathologic evidence for a mechanism of increased beta-amyloidogenesis. *The Journal of Neuroscience : The Official Journal of the Society for Neuroscience*, *17*(16), 6142–6151. http://www.ncbi.nlm.nih.gov/pubmed/9236226

Cataldo, A. M., Peterhoff, C. M., Troncoso, J. C., Gomez-Isla, T., Hyman, B. T., & Nixon, R. A. (2000). Endocytic pathway abnormalities precede amyloid beta deposition in sporadic Alzheimer's disease and Down syndrome: differential effects of APOE genotype and presenilin mutations. *The American Journal of Pathology*, *157*(1), 277–286. http://www.ncbi.nlm.nih.gov/pubmed/10880397

Chapuis, J., Hansmannel, F., Gistelinck, M., Mounier, A., Van Cauwenberghe, C., Kolen, K. V, Geller, F., Sottejeau, Y., Harold, D., Dourlen, P., Grenier-Boley, B., Kamatani, Y., Delepine, B., Demiautte, F., Zelenika, D., Zommer, N., Hamdane, M., Bellenguez, C., Dartigues, J.-F., … Lambert, J.-C. (2013). Increased expression of BIN1 mediates Alzheimer genetic risk by modulating tau pathology. *Molecular Psychiatry*, *18*(11), 1225–1234. https://doi.org/10.1038/mp.2013.1

Choudhury, S. D., Dwivedi, M. K., Pippadpally, S., Patnaik, A., Mishra, S., Padinjat, R., & Kumar, V. (2022). AP2 Regulates Thickveins Trafficking to Attenuate NMJ Growth Signaling in *Drosophila*. *ENeuro*, *9*(5). https://doi.org/10.1523/ENEURO.0044-22.2022

Choudhury, S. D., Mushtaq, Z., Reddy-Alla, S., Balakrishnan, S. S., Thakur, R. S., Krishnan, K. S., Raghu, P., Ramaswami, M., & Kumar, V. (2016). σ2-Adaptin facilitates basal synaptic transmission and is required for regenerating endo-exo cycling pool under high-frequency nerve stimulation in *Drosophila*. *Genetics*, *203*(1), 369–385. https://doi.org/10.1534/genetics.115.183863

Crotti, A., Sait, H. R., McAvoy, K. M., Estrada, K., Ergun, A., Szak, S., Marsh, G., Jandreski, L., Peterson, M., Reynolds, T. L., Dalkilic-Liddle, I., Cameron, A., Cahir-McFarland, E., & Ransohoff, R. M. (2019). BIN1 favors the spreading of Tau via extracellular vesicles. *Scientific Reports*, *9*(1), 9477. https://doi.org/10.1038/s41598-019-45676-0

David, C., McPherson, P. S., Mundigl, O., & De Camilli, P. (1996). A role of amphiphysin in synaptic vesicle endocytosis suggested by its binding to dynamin in nerve terminals. *Proceedings of the National Academy of Sciences of the United States of America*, *93*(1), 331–335. https://doi.org/10.1073/pnas.93.1.331

DeKosky, S. T., & Scheff, S. W. (1990). Synapse loss in frontal cortex biopsies in Alzheimer's disease: Correlation with cognitive severity. *Annals of Neurology*, *27*(5), 457–464. https://doi.org/10.1002/ana.410270502

De Rossi, P., Buggia-Prévot, V., Clayton, B. L. L., Vasquez, J. B., van Sanford, C., Andrew, R. J., Lesnick, R., Botté, A., Deyts, C., Salem, S., Rao, E., Rice, R. C., Parent, A., Kar, S., Popko, B., Pytel, P., Estus, S., & Thinakaran, G. (2016). Predominant expression of Alzheimer's disease-associated BIN1 in mature oligodendrocytes and localization to white matter tracts. *Molecular Neurodegeneration*, *11*(1), 59. https://doi.org/10.1186/s13024-016-0124-1

De Rossi, P., Nomura, T., Andrew, R. J., Masse, N. Y., Sampathkumar, V., Musial, T. F., Sudwarts, A., Recupero, A. J., Le Metayer, T., Hansen, M. T., Shim, H. N., Krause, S. V., Freedman, D. J., Bindokas, V. P., Kasthuri, N., Nicholson, D. A., Contractor, A., & Thinakaran, G. (2020). Neuronal BIN1 Regulates Presynaptic Neurotransmitter Release and Memory Consolidation. *Cell Reports*, *30*(10), 3520-3535.e7. https://doi.org/10.1016/j.celrep.2020.02.026

Dickman, D. K., Lu, Z., Meinertzhagen, I. A., & Schwarz, T. L. (2006). Altered synaptic development and active zone spacing in endocytosis mutants. *Current Biology*, *16*(6), 591–598. https://doi.org/10.1016/j.cub.2006.02.058

Dourlen, P., Bertin, B., Chatelain, G., Robin, M., Napoletano, F., Roux, M. J., & Mollereau, B. (2012). *Drosophila* fatty acid transport protein regulates rhodopsin-1 metabolism and is required for photoreceptor neuron survival. *PLoS Genetics*, *8*(7), e1002833. https://doi.org/10.1371/journal.pgen.1002833

Dourlen, P., Kilinc, D., Landrieu, I., Chapuis, J., & Lambert, J. C. (2025). BIN1 and Alzheimer's disease: the tau connection. In *Trends in Neurosciences* (Vol. 48, Issue 5, pp. 349–361). Elsevier Ltd. https://doi.org/10.1016/j.tins.2025.03.004

Dourlen, P., Kilinc, D., Malmanche, N., Chapuis, J., & Lambert, J.-C. (2019). The new genetic landscape of Alzheimer's disease: from amyloid cascade to genetically driven synaptic failure hypothesis? *Acta Neuropathologica*, *138*(2), 221–236. https://doi.org/10.1007/s00401-019-02004-0

Drake, M. T., & Traub, L. M. (2001). Interaction of Two Structurally Distinct Sequence Types with the Clathrin Terminal Domain β-Propeller. *Journal of Biological Chemistry*, *276*(31), 28700–28709. https://doi.org/10.1074/jbc.M104226200

Ellis, J. D., Barrios-Rodiles, M., Colak, R., Irimia, M., Kim, T., Calarco, J. A., Wang, X., Pan, Q., O'Hanlon, D., Kim, P. M., Wrana, J. L., & Blencowe, B. J. (2012). Tissue-specific alternative splicing remodels protein-protein interaction networks. *Molecular Cell*, *46*(6), 884–892. https://doi.org/10.1016/j.molcel.2012.05.037

Eysert, F., Coulon, A., Boscher, E., Vreulx, A. C., Flaig, A., Mendes, T., Hughes, S., Grenier-Boley, B., Hanoulle, X., Demiautte, F., Bauer, C., Marttinen, M., Takalo, M., Amouyel, P., Desai, S., Pike, I., Hiltunen, M., Chécler, F., Farinelli, M., … Chapuis, J. (2021). Alzheimer's genetic risk factor FERMT2 (Kindlin-2) controls axonal growth and synaptic plasticity in an APP-dependent manner. *Molecular Psychiatry*, *26*(10), 5592–5607. https://doi.org/10.1038/s41380-020-00926-w

Ferreira, A. P. A., Casamento, A., Carrillo Roas, S., Halff, E. F., Panambalana, J., Subramaniam, S., Schützenhofer, K., Chan Wah Hak, L., McGourty, K., Thalassinos, K., Kittler, J. T., Martinvalet, D., & Boucrot, E. (2021). Cdk5 and GSK3β inhibit fast endophilin-mediated endocytosis. *Nature Communications*, *12*(1). https://doi.org/10.1038/s41467-021-22603-4

Gatz, M., Reynolds, C. A., Fratiglioni, L., Johansson, B., Mortimer, J. A., Berg, S., Fiske, A., & Pedersen, N. L. (2006). Role of genes and environments for explaining Alzheimer disease. *Archives of General Psychiatry*, *63*(2), 168–174. https://doi.org/10.1001/archpsyc.63.2.168

Kajiho, H., Saito, K., Tsujita, K., Kontani, K., Araki, Y., Kurosu, H., & Katada, T. (2003). RIN3: A novel Rab5 GEF interacting with amphiphysin II involved in the early endocytic pathway. In *Journal of Cell Science* (Vol. 116, Issue 20, pp. 4159–4168). J Cell Sci. https://doi.org/10.1242/jcs.00718

Khodosh, R., Augsburger, A., Schwarz, T. L., & Garrity, P. A. (2006). Bchs, a BEACH domain protein, antagonizes Rab11 in synapse morphogenesis and other developmental events. *Development*, *133*(23), 4655–4665. https://doi.org/10.1242/dev.02650

Kilinc, D., Vreulx, A.-C., Mendes, T., Flaig, A., Marques-Coelho, D., Verschoore, M., Demiautte, F., Amouyel, P., Eysert, F., Dourlen, P., Chapuis, J., Costa, M. R., Malmanche, N., Checler, F., & Lambert, J.-C. (2020). Pyk2 overexpression in postsynaptic neurons blocks amyloid β1–42-induced synaptotoxicity in microfluidic co-cultures. *Brain Communications*, *2*(2). https://doi.org/10.1093/braincomms/fcaa139

Lambert, E., Saha, O., Soares Landeira, B., Melo de Farias, A. R., Hermant, X., Carrier, A., Pelletier, A., Gadaut, J., Davoine, L., Dupont, C., Amouyel, P., Bonnefond, A., Lafont, F., Abdelfettah, F., Verstreken, P., Chapuis, J., Barois, N., Delahaye, F., Dermaut, B., … Dourlen, P. (2022). The Alzheimer susceptibility gene BIN1 induces isoform-dependent neurotoxicity through early endosome defects. *Acta Neuropathologica Communications*, *10*(1). https://doi.org/10.1186/s40478-021-01285-5

Lefebvre, C., Vreulx, A. C., Dumortier, C., Bégard, S., Gelle, C., Siedlecki-Wullich, D., Colin, M., Kilinc, D., & Halliez, S. (2024). Integration of Microfluidic Devices with Microelectrode Arrays to Functionally Assay Amyloid-β-Induced Synaptotoxicity. *ACS Biomaterials Science and Engineering*, *10*(3), 1856–1868. https://doi.org/10.1021/acsbiomaterials.3c00997

Leprince, C., Romero, F., Cussac, D., Vayssiere, B., Berger, R., Tavitian, A., & Camonis, J. H. (1997). A new member of the amphiphysin family connecting endocytosis and signal transduction pathways. *The Journal of Biological Chemistry*, *272*(24), 15101–15105. http://www.ncbi.nlm.nih.gov/pubmed/9182529

Leventis, P. A., Chow, B. M., Stewart, B. A., Iyengar, B., Campos, A. R., & Boulianne, G. L. (2001). *Drosophila* Amphiphysin is a post-synaptic protein required for normal locomotion but not endocytosis. *Traffic (Copenhagen, Denmark)*, *2*(11), 839–850. http://www.ncbi.nlm.nih.gov/pubmed/11733051

Lichte, B., Veh, R. W., Meyer, H. E., & Kilimann, M. W. (1992). Amphiphysin, a novel protein associated with synaptic vesicles. *The EMBO Journal*, *11*(7), 2521–2530. https://doi.org/10.1002/j.1460-2075.1992.tb05317.x

Marques-Coelho, D., Iohan, L. da C. C., Melo de Farias, A. R., Flaig, A., Letournel, F., Martin-Négrier, M. L., Chapon, F., Faisant, M., Godfraind, C., Maurage, C. A., Deramecourt, V., Duchesne, M., Meyronnet, D., Streichenberger, N., de Paula, A. M., Rigau, V., Vandenbos-Burel, F., Duyckaerts, C., Seilhean, D., … Costa, M. R. (2021). Differential transcript usage unravels gene expression alterations in Alzheimer's disease human brains. *Npj Aging and Mechanisms of Disease*, *7*(1). https://doi.org/10.1038/s41514-020-00052-5

McMahon, H. T., Wigge, P., & Smith, C. (1997). Clathrin interacts specifically with amphiphysin and is displaced by dynamin. *FEBS Letters*, *413*(2), 319–322. https://doi.org/10.1016/S0014-5793(97)00928-9

Mecca, A. P., O'Dell, R. S., Sharp, E. S., Banks, E. R., Bartlett, H. H., Zhao, W., Lipior, S., Diepenbrock, N. G., Chen, M. K., Naganawa, M., Toyonaga, T., Nabulsi, N. B., Vander Wyk, B. C., Arnsten, A. F. T., Huang, Y., Carson, R. E., & van Dyck, C. H. (2022). Synaptic density and cognitive performance in Alzheimer's disease: A PET imaging study with [11C]UCB-J. *Alzheimer's and Dementia*, *18*(12), 2527–2536. https://doi.org/10.1002/alz.12582

Menon, K. P., Carrillo, R. A., & Zinn, K. (2013). Development and plasticity of the *Drosophila* larval neuromuscular junction. In *Wiley interdisciplinary reviews. Developmental biology* (Vol. 2, Issue 5, pp. 647–670). Wiley Interdiscip Rev Dev Biol. https://doi.org/10.1002/wdev.108

Micheva, K. D., Kay, B. K., & McPherson, P. S. (1997). Synaptojanin forms two separate complexes in the nerve terminal. Interactions with endophilin and amphiphysin. *The Journal of Biological Chemistry*, *272*(43), 27239–27245. http://www.ncbi.nlm.nih.gov/pubmed/9341169

O'Connor-Giles, K. M., Ho, L. L., & Ganetzky, B. (2008). Nervous Wreck Interacts with Thickveins and the Endocytic Machinery to Attenuate Retrograde BMP Signaling during Synaptic Growth. *Neuron*, *58*(4), 507–518. https://doi.org/10.1016/j.neuron.2008.03.007

Ogle, D. H., Doll, J. C., Wheeler, A. P., & Dinno, A. (2023). *FSA: Simple Fisheries Stock Assessment Methods.* https://fishr-core-team.github.io/FSA/authors.html#citation

Prokic, I., Cowling, B. S., & Laporte, J. (2014). Amphiphysin 2 (BIN1) in physiology and diseases. *Journal of Molecular Medicine*, *92*(5), 453–463. https://doi.org/10.1007/s00109-014-1138-1

Rai, P., Ratnaparkhi, A., & Kumar Roy, J. (2023). Rab11 rescues muscle degeneration and synaptic morphology in the park13/+ Parkinson model of *Drosophila* melanogaster. *Brain Research*, *1816*. https://doi.org/10.1016/j.brainres.2023.148442

Ramjaun, A. R., Micheva, K. D., Bouchelet, I., & McPherson, P. S. (1997). Identification and characterization of a nerve terminal-enriched amphiphysin isoform. *Journal of Biological Chemistry*, *272*(26), 16700–16706. https://doi.org/10.1074/jbc.272.26.16700

Saha, O., Melo de Farias, A. R., Pelletier, A., Siedlecki-Wullich, D., Landeira, B. S., Gadaut, J., Carrier, A., Vreulx, A. C., Guyot, K., Shen, Y., Bonnefond, A., Amouyel, P., TCW, J., Kilinc, D., Queiroz, C. M., Delahaye, F., Lambert, J. C., & Costa, M. R. (2024). The Alzheimer's disease risk gene BIN1 regulates activity-dependent gene expression in human-induced glutamatergic neurons. *Molecular Psychiatry*, *29*(9). https://doi.org/10.1038/s41380-024-02502-y

Sartori, M., Mendes, T., Desai, S., Lasorsa, A., Herledan, A., Malmanche, N., Mäkinen, P., Marttinen, M., Malki, I., Chapuis, J., Flaig, A., Vreulx, A.-C., Ciancia, M., Amouyel, P., Leroux, F., Déprez, B., Cantrelle, F.-X., Maréchal, D., Pradier, L., … Lambert, J.-C. (2019). BIN1 recovers tauopathy-induced long-term memory deficits in mice and interacts with Tau through Thr348 phosphorylation. *Acta Neuropathologica*, *138*(4), 631–652. https://doi.org/10.1007/s00401-019-02017-9

Schürmann, B., Bermingham, D. P., Kopeikina, K. J., Myczek, K., Yoon, S., Horan, K. E., Kelly, C. J., Martin-de-Saavedra, M. D., Forrest, M. P., Fawcett-Patel, J. M., Smith, K. R., Gao, R., Bach, A., Burette, A. C., Rappoport, J. Z., Weinberg, R. J., Martina, M., & Penzes, P. (2020). A novel role for the late-onset Alzheimer's disease (LOAD)-associated protein Bin1 in regulating postsynaptic trafficking and glutamatergic signaling. *Molecular Psychiatry*, *25*(9), 2000–2016. https://doi.org/10.1038/s41380-019-0407-3

Scopin, M., Spampinato, G. L. B., Marre, O., Garcia, S., & Yger, P. (2024). Localization of neurons from extracellular footprints. *Journal of Neuroscience Methods*, *412*. https://doi.org/10.1016/j.jneumeth.2024.110297

Shen, R., Zhao, X., He, L., Ding, Y., Xu, W., Lin, S., Fang, S., Yang, W., Sung, K., Spencer, B., Rissman, R. A., Lei, M., Ding, J., & Wu, C. (2020). Upregulation of RIN3 induces endosomal dysfunction in Alzheimer's disease. *Translational Neurodegeneration*, *9*(1). https://doi.org/10.1186/s40035-020-00206-1

Shupliakov, O., Löw, P., Grabs, D., Gad, H., Chen, H., David, C., Takei, K., De Camilli, P., & Brodin, L. (1997). Synaptic vesicle endocytosis impaired by disruption of dynamin-SH3 domain interactions. *Science*, *276*(5310), 259–263. https://doi.org/10.1126/science.276.5310.259

Taga, M., Petyuk, V. A., White, C., Marsh, G., Ma, Y., Klein, H. U., Connor, S. M., Kroshilina, A., Yung, C. J., Khairallah, A., Olah, M., Schneider, J., Karhohs, K., Carpenter, A. E., Ransohoff, R., Bennett, D. A., Crotti, A., Bradshaw, E. M., & De Jager, P. L. (2020). BIN1 protein isoforms are differentially expressed in astrocytes, neurons, and microglia: neuronal and astrocyte BIN1 are implicated in tau pathology. *Molecular Neurodegeneration*, *15*(1). https://doi.org/10.1186/s13024-020-00387-3

Taylor, M. J., Lampe, M., & Merrifield, C. J. (2012). A feedback loop between dynamin and actin recruitment during clathrin-mediated endocytosis. *PLoS Biology*, *10*(4). https://doi.org/10.1371/journal.pbio.1001302

Terry, R. D., Masliah, E., Salmon, D. P., Butters, N., Deteresa, R., Hill, R., Hansen, L. A., & Katzman, R. (1991). Physical Basis of Cognitive Alterations in Alzheimer's Disease : Synapse Loss Is the Major Correlate of Cognitive Impairment. *Annals of Neurology*, *30*(4), 572–580.

Tropp, J. A., & Gilbert, A. C. (2007). Signal recovery from random measurements via orthogonal matching pursuit. *IEEE Transactions on Information Theory*, *53*(12), 4655–4666. https://doi.org/10.1109/TIT.2007.909108

Tsutsui, K., Maeda, Y., Tsutsui, K., Seki, S., & Tokunaga, A. (1997). cDNA cloning of a novel amphiphysin isoform and tissue specific expression of its multiple splice variants. *Biochemical and Biophysical Research Communications*, *236*(1), 178–183. https://doi.org/10.1006/bbrc.1997.6927

Varol, E., Boussard, J., Dethe, N., Winter, O., Urai, A., Churchland, A., Steinmetz, N., & Paninski, L. (2021). Decentralized motion inference and registration of neuropixel data. *ICASSP, IEEE International Conference on Acoustics, Speech and Signal Processing - Proceedings*, *2021-June*, 1085–1089. https://doi.org/10.1109/ICASSP39728.2021.9414145

Voskobiynyk, Y., Roth, J. R., Cochran, J. N., Rush, T., Carullo, N. V. N., Mesina, J. S., Waqas, M., Vollmer, R. M., Day, J. J., McMahon, L. L., & Roberson, E. D. (2020). Alzheimer's disease risk gene BIN1 induces Tau-dependent network hyperexcitability. *ELife*, *9*, 1–25. https://doi.org/10.7554/eLife.57354

Wigge, P., Köhler, K., Vallis, Y., Doyle, C. A., Owen, D., Hunt, S. P., & McMahon, H. T. (1997). Amphiphysin heterodimers: potential role in clathrin-mediated endocytosis. *Molecular Biology of the Cell*, *8*(10), 2003–2015. http://www.ncbi.nlm.nih.gov/pubmed/9348539

Yger, P., Spampinato, G. L. B., Esposito, E., Lefebvre, B., Deny, S., Gardella, C., Stimberg, M., Jetter, F., Zeck, G., Picaud, S., Duebel, J., & Marre, O. (2018). A spike sorting toolbox for up to thousands of electrodes validated with ground truth recordings in vitro and in vivo. *ELife*, *7*. https://doi.org/10.7554/eLife.34518

Zelhof, A. C., Bao, H., Hardy, R. W., Razzaq, A., Zhang, B., & Doe, C. Q. (2001). *Drosophila* Amphiphysin is implicated in protein localization and membrane morphogenesis but not in synaptic vesicle endocytosis. *Development (Cambridge, England)*, *128*(24), 5005–5015. http://www.ncbi.nlm.nih.gov/pubmed/11748137

Figure legends

Figure1: BIN1iso1 disrupted synaptic transmission of *Drosophila* photoreceptor neurons with age. **A.** Electroretinograms of *Drosophila* expressing BIN1iso1, BIN1iso8, BIN1iso9, dAmphisoA and Luciferase (control) under a rh1 driver at day 2, day 8-9 and day 15-16. Specifically, for BIN1iso1, we observed a loss of ON and OFF transients (magenta arrows) at day 8-9 followed by a loss of all electrophysiological parameters, (depolarization, ON and OFF transients, magenta arrows) at day 15-16. **B.** Quantification of the depolarization and ON and OFF transients (Kruskal-Wallis ANOVA followed by Wilcoxon rank-sum test). **C.** Immunofluorescence of the synaptic extremities of photoreceptor neurons expressing BIN1iso1, BIN1iso8, BIN1iso9, dAmphisoA and Luciferase (as a control) under a rh1 driver at day 1 and day 7. BIN1 staining shows the localization of BIN1iso1, BIN1iso9 and BIN1iso8 at the presynaptic terminal at day 1 and day 7. The neuron-specific plasma membrane Na/K ATPase and the actin staining are used to label these structures. At day 7, presynaptic extremities of BIN1iso1-expressing photoreceptor neurons accumulate big vesicles (arrows). **D.** Electron microscopy analysis of synaptic terminals of photoreceptor neurons expressing Luciferase and BIN1iso1 at day 15. Six synaptic terminals (cyan dotted lines) are gathered into a lamina cartridge (yellow dotted lines). Expression of BIN1iso1 resulted in the presence of giant vesicles (*, magenta dotted lines).

Figure 2: BIN1iso1 caused morphological alterations in *Drosophila* NMJs without affecting the number of active zones. **A.** Immunofluorescence of NMJs from 3rd instar larvae expressing BIN1iso1, BIN1iso8, BIN1iso9 and dAmphisoA and Luciferase (control) in motoneurons with the Nsyb promoter. HRP, Dlg and actin labeling are used to label motor neuron terminals, postsynaptic compartments and muscle cells, respectively. Arrowheads show satellite boutons. **B.** Quantification of NMJ morphometric parameters: the number of boutons per NMJ, the mean area of single bouton per NMJ, the cumulative area of all boutons per NMJ and the number of satellite boutons per NMJ. The number of NMJ analyzed per condition are indicated at the bottom of the top left graph. Data were analyzed with a non-parametric Kruskal Wallis test followed by post-hoc Dunn's multiple comparison test (Holm method, * $p<0.05$, ** $p<0.01$, *** $p<1.10^{-3}$, **** $p<1.10^{-4}$, ***** $p<1.10^{-5}$, ****** $p<1.10^{-6}$). **C.** Immunofluorescence of NMJs from 3rd instar larvae expressing BIN1iso1, BIN1iso8, BIN1iso9 and dAmphA and Luciferase (control) in motoneurons with the Nsyb promoter. HRP, Brp and actin labeling are used to label the motor neuron terminals, active zones and muscle cells, respectively. Arrowheads show satellite boutons. **D.** Quantification of the number of active zones. Numbers at the bottom of the graph indicate the number of quantified NMJs. Non-parametric Kruskal Wallis analysis did not show any statistically significant difference between conditions.

Figure 3: Rab11 did not prevent BIN1iso1-induced morphological defects at the larval NMJs. **A.** Immunofluorescence of NMJ from 3rd instar larvae expressing BIN1iso1 and/or Rab11 in motoneurons (Nsyb driver). mCD8::GFP and luciferase are used as controls respectively for Rab11::GFP and BIN1iso1. HRP, Dlg and actin labeling are used to label motor neuron terminals, post-synaptic compartments and muscle cells respectively. **B.** Quantification of NMJ morphometric parameters: the number of boutons per NMJ, the mean area of single bouton per NMJ, the cumulative area of all boutons per NMJ and the number of satellite boutons per NMJ. The number of NMJ analyzed per condition are indicated at the bottom of the top left graph. Data were analyzed with a non-parametric Kruskal Wallis test followed by post-hoc Dunn multiple comparison test (Holm method, * $p < 0.05$, ** $p < 0.01$, **** $p<1.10^{-4}$, ****** $p<1.10^{-6}$).

Figure 4: Presynaptic overexpression of BIN1iso1 induces synaptotoxicity in hippocampal neurons. **A.** Scheme of the custom-design, three-chamber microfluidic devices used to culture primary rat hippocampal neurons. Scale bar = 2 mm. **B.** Representative images of the synaptic network at DIV14. Overexpression of Mock (control), BIN1iso1 or BIN1iso9 vectors in the pre- or postsynaptic neuron chamber is indicated in the left schemes (scale bars = 5 µm). **C.** Quantification of Synaptophysin (Syp) and Homer spot densities and the fraction of Syp spots assigned by at least one Homer spot, as a measure for synaptic connectivity between the two neuronal populations. In box plots, data points correspond to device means. Fraction of Syp assigned was normalized by the mean of the control group. N = 3 independent cultures each for presynaptic and postsynaptic expression. Kruskal–Wallis ANOVA with Tukey-Kramer correction. * $p < 0.05$. N/S: not significant. a.u.: arbitrary units.

Figure 5: Presynaptic overexpression of BIN1iso1 perturbs the network-level connectivity in hippocampal neurons. **A.** Schematics of the three-chamber microfluidic device integrated with a 256-electrode MEA. Reference electrodes are marked with "R". **B.** Mosaic image of the MEA-integrated microfluidic device housing rat hippocampal neurons. Cells in the pre- and postsynaptic chambers were lentivirally transduced to express LifeAct-Ruby (red) and PSD95-YFP (green) vectors, respectively, to demonstrate isolated transductions in cell chambers. Scale bar = 2 mm. **C.** Boxed area in panel B at higher magnification. Scale bar = 500 µm. Zoomed area (C') is 3.4× magnified. **D.** A representative map of units identified through the spike-sorting algorithm (gray). One presynaptic unit and three postsynaptic units are color-coded for demonstration purposes. **E.** Spike waveform patterns corresponding to these four color-coded units. **F.** Cross-correlograms and the calculated *pre-post-drive* parameters for the three pre-post unit pairs that can be formed using these four units. **G.** Pre-post-drive histograms for representative microfluidic devices (one device per condition). Lines show the corresponding kernel distribution fits. **H.** Bubble chart showing *pre-post-drive* as a function of numbers of units detected in the pre- and postsynaptic chambers. The unit number ratios were normally distributed among all devices (see Supplementary figure 5), except for those with $|z\text{-score}|>1.5$ (dark gray). This threshold corresponds to a 4-fold difference in the unit number ratio (broken lines). Outlier data points according to median±3×MAD are included (light gray). **I-L.** *Pre-post-drive* (I), number of detected units (J), mean firing rate for these units (K) and mean amplitude for these units (L) (L) as a function of BIN1 isoform (or Mock vector) expression in the presynaptic chamber. In box plots, data points refer to individual devices. N = 6 independent cultures. Kruskal–Wallis ANOVA with Tukey-Kramer correction. * $p < 0.05$; ** $p < 0.005$. N/S: not significant.

Figure 1:

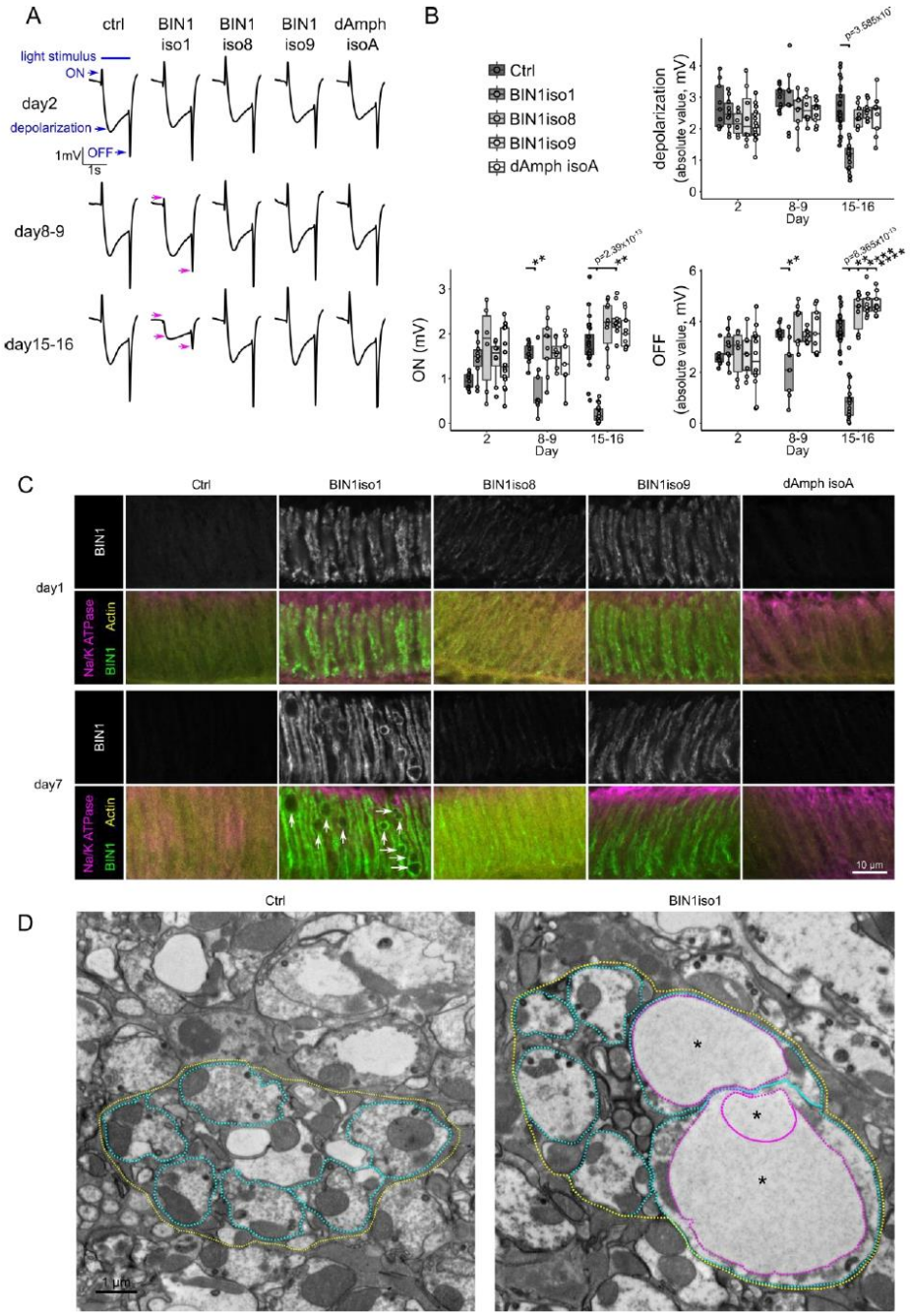

Figure 2:

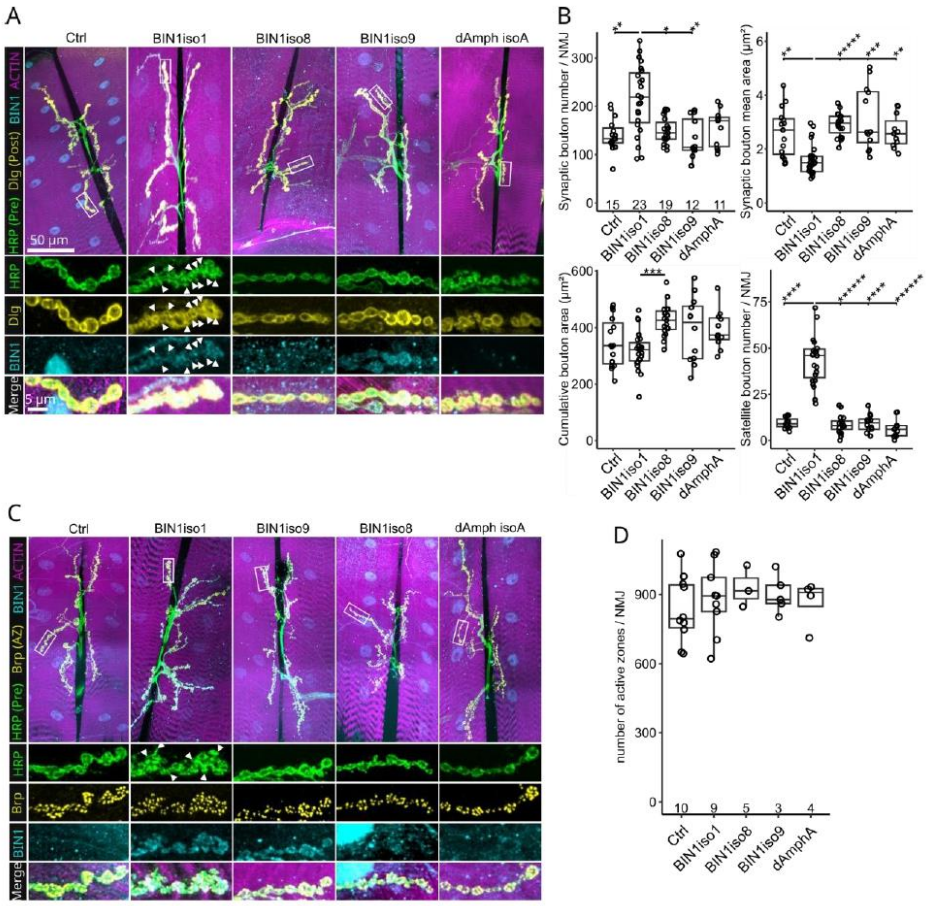

Figure 3:

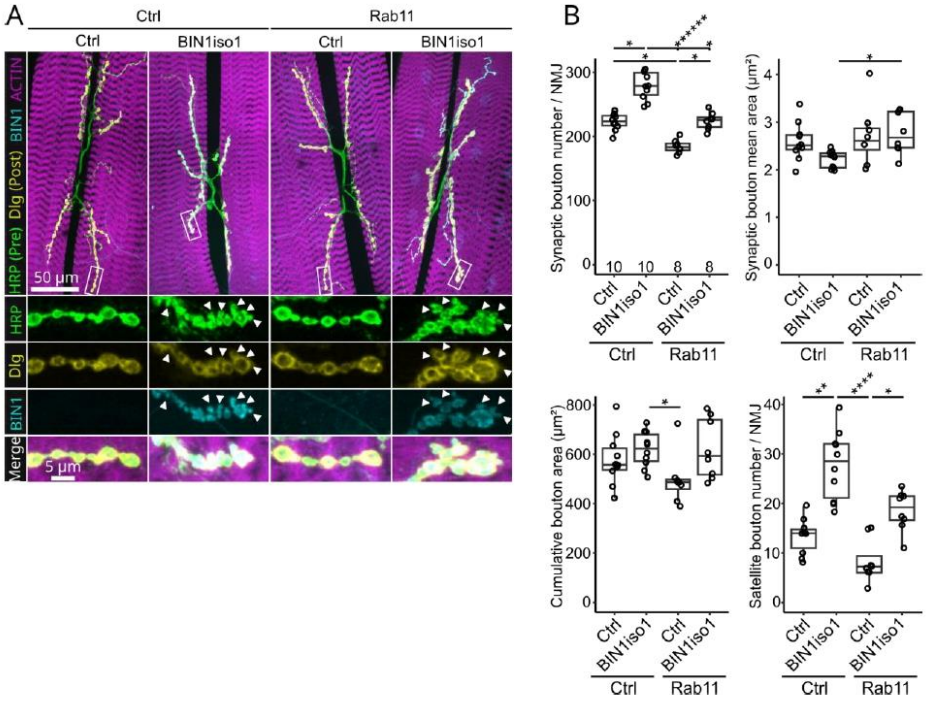

Figure 4:

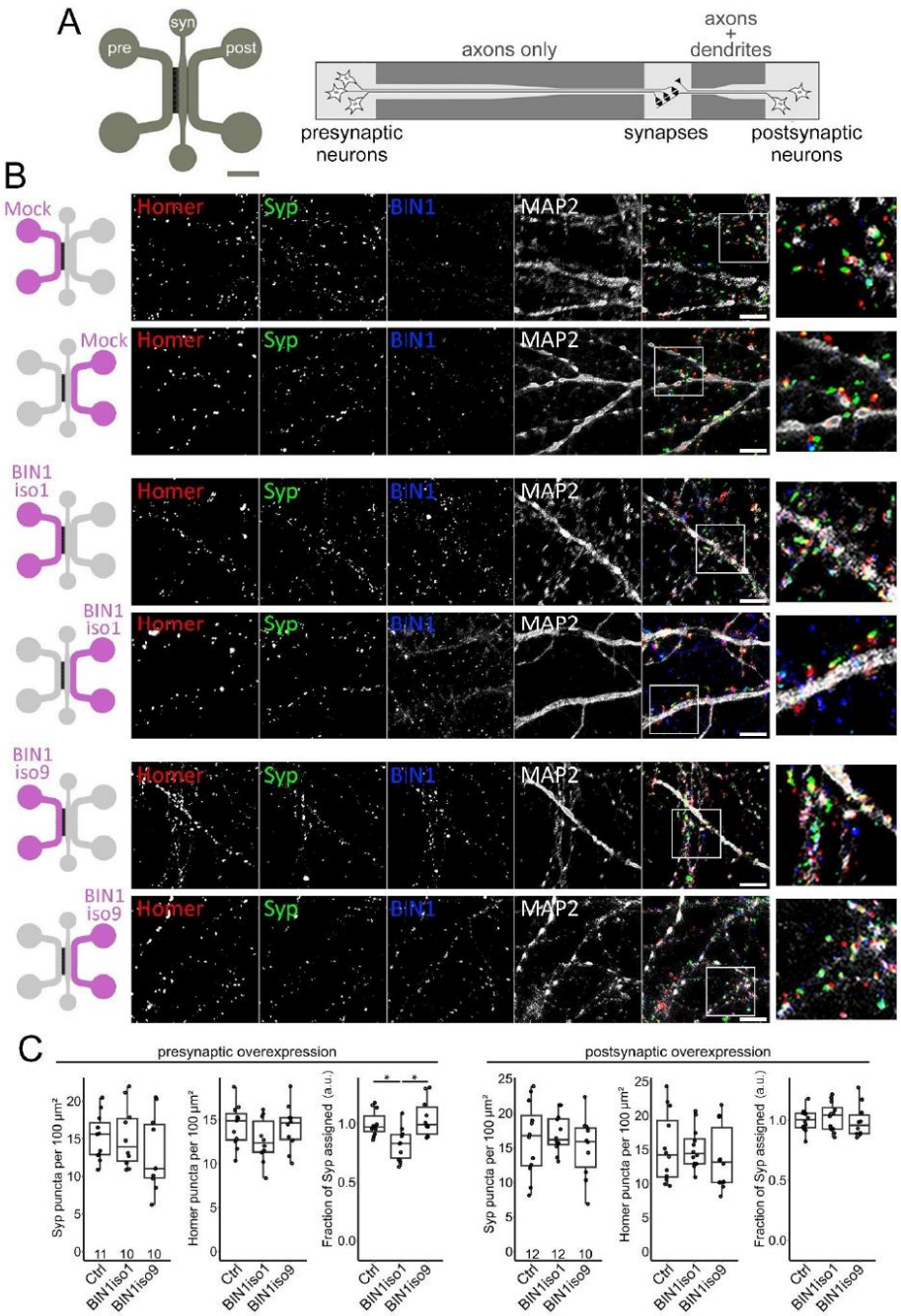

Figure 5:

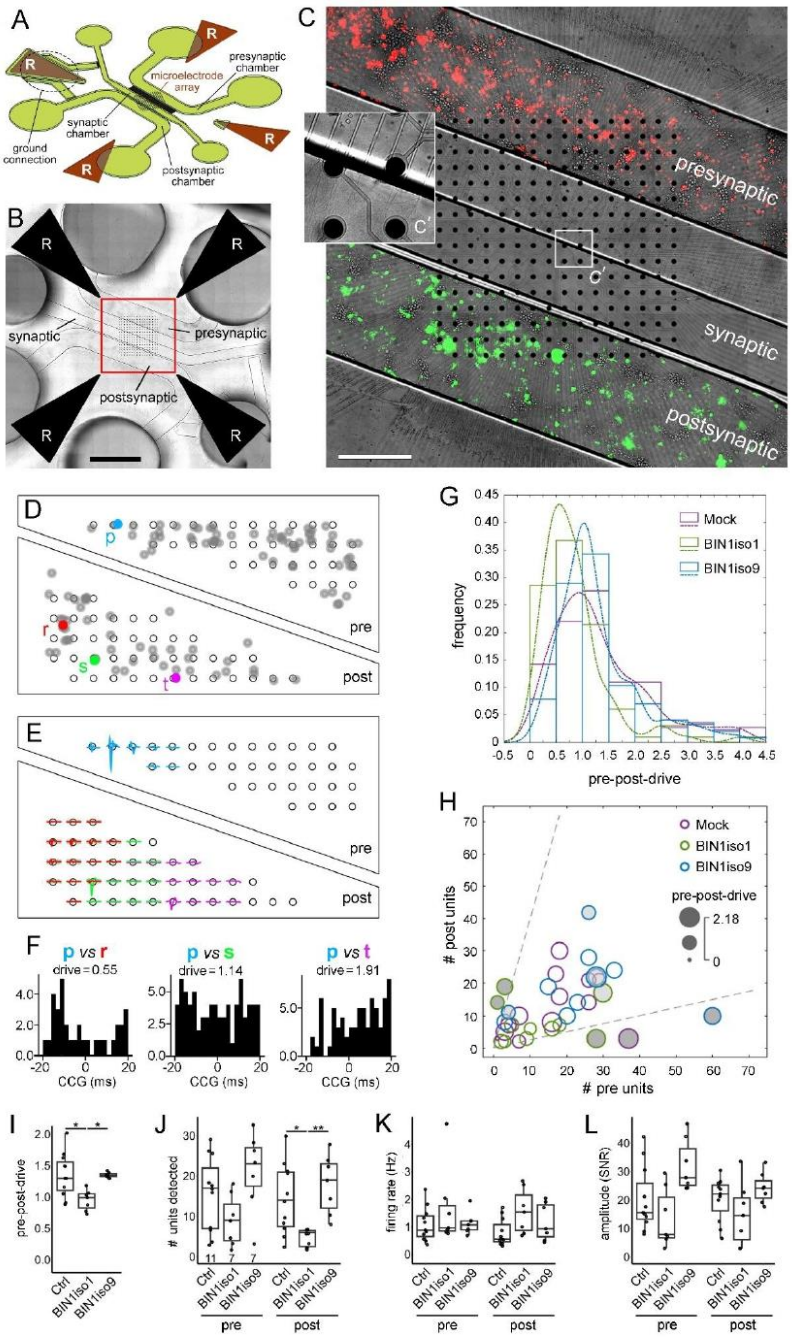

SUPPLEMENTARY MATERIALS

BIN1 expression in the presynaptic compartment leads to isoform-specific synaptotoxicity

Erwan Lambert[1†‡], Carla Gelle[1†], Valentin Leclerc[1†], Alejandra Freire-Regatillo[1†], Nicolas Barois[2,3], Tommy Malfoi[1], Xavier Hermant[1], Florie Demiautte[1], Frank Lafont[3], Philippe Amouyel[1], Karine Blary[4], Sabine Kuenen[5,6], Chloé Najdek[1], Patrik Versteken[5,6], Dolores Siedlecki-Wullich[1], Pierre Yger[7], Jean-Charles Lambert[1], Devrim Kilinc[1*], Pierre Dourlen[1*]

[1] Université de Lille, Inserm, CHU Lille, Institut Pasteur de Lille, U1167 – RID – AGE – Facteurs de risque et déterminants moléculaires liés au vieillissement, Lille, France
[2] Université de Lille, CNRS, Inserm, CHU Lille, Institut Pasteur de Lille, UAR CNRS 2014 - US Inserm 41 - PLBS, Lille, France.
[3] University of Lille, CNRS, Inserm, CHU Lille, Institut Pasteur Lille, U1019-UMR 9017-CIIL-Center for Infection and Immunity of Lille, Lille, France.
[4] Univ. Lille, CNRS, Centrale Lille, Univ. Polytechnique Hauts-de-France, UMR 8520 - IEMN - Institut d'Electronique de Microélectronique et de Nanotechnologie, F-59000 Lille, France
[5] VIB Center for Brain and Disease Research, KU Leuven, Leuven, Belgium
[6] Department of Neurosciences, Leuven Brain Institute, KU Leuven, Leuven, Belgium
[7] Lille Neurosciences & Cognition (lilNCog) – U1172 (INSERM, Lille), Univ Lille, CHU Lille 59045 Lille, France

[†] Equal contribution
[‡] Present address: Donders Center for Neuroscience, Department of Molecular Neurobiology, Radboud University, Nijmegen, the Netherlands
* Address for correspondence: devrim.kilinc@pasteur-lille.fr; pierre.dourlen@pasteur-lille.fr

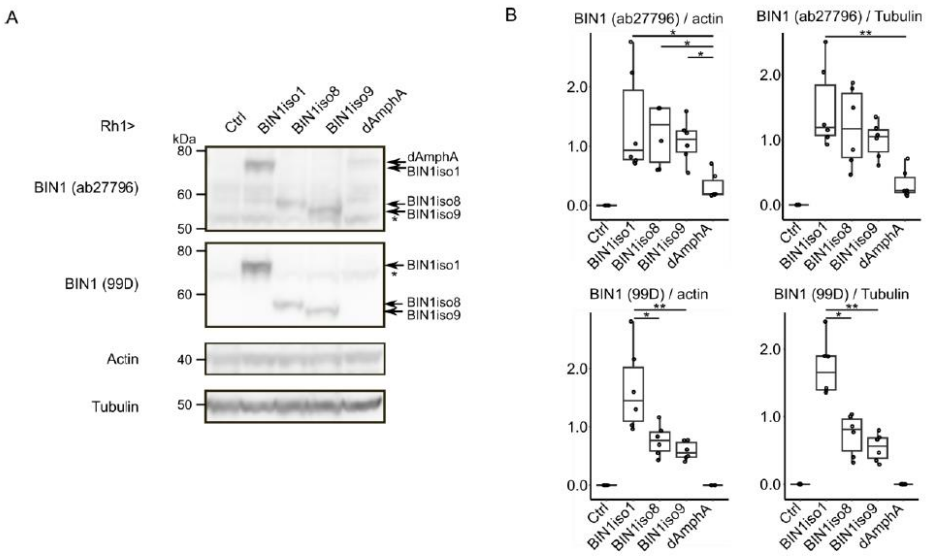

Supplementary Figure 1: Analysis of BIN1 levels in *Drosophila* expressing human BIN1 isoforms and *Drosophila* Amphiphysin isoformA under a Rh1 driver. **A.** Representative Western blots analyzing the transgenic expression of human BIN1 isoforms and *Drosophila* Amphiphysin in 1-2 day-old *Drosophila* heads. BIN1 was detected using two antibodies (ab27796 and 99D). Actin and Tubulin were used as loading controls. Non-specific bands were marked with stars. **B.** Quantification of data obtained from 6 independent experiments. Statistical analyses were performed with non-parametric Kruskal Wallis tests followed by Dunn's multiple comparisons (*p*-values adjusted using the Holm method, * $p<0.05$; ** $p<0.01$). The Ctrl group and the Ctrl and dAmphA groups were excluded from the statistical analysis for blots obtained using the BIN1 ab27796 and BIN1 99D antibodies, respectively.

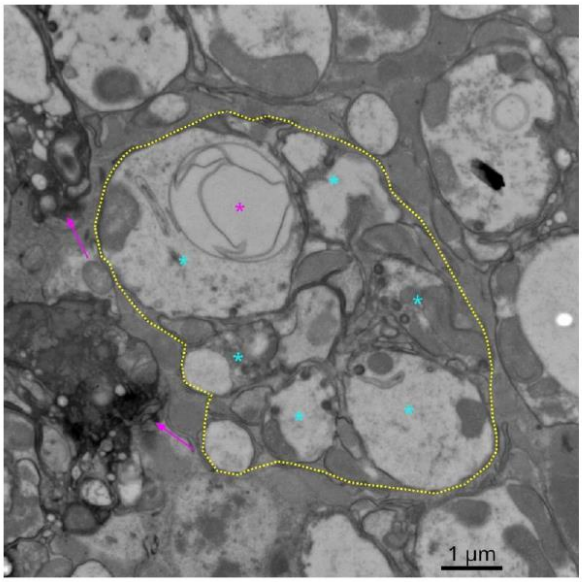

Supplementary Figure 2: Electron microscopy image showing the degeneration of synaptic terminals in *Drosophila* photoreceptor neurons expressing BIN1 iso1 at day 15. Six synaptic terminals (cyan stars) are gathered into a lamina cartridge (yellow dotted line). Expression of BIN1 iso1 resulted in the presence of giant vesicles (magenta star). Magenta arrows point to degenerating synaptic terminals in neighboring cartridges.

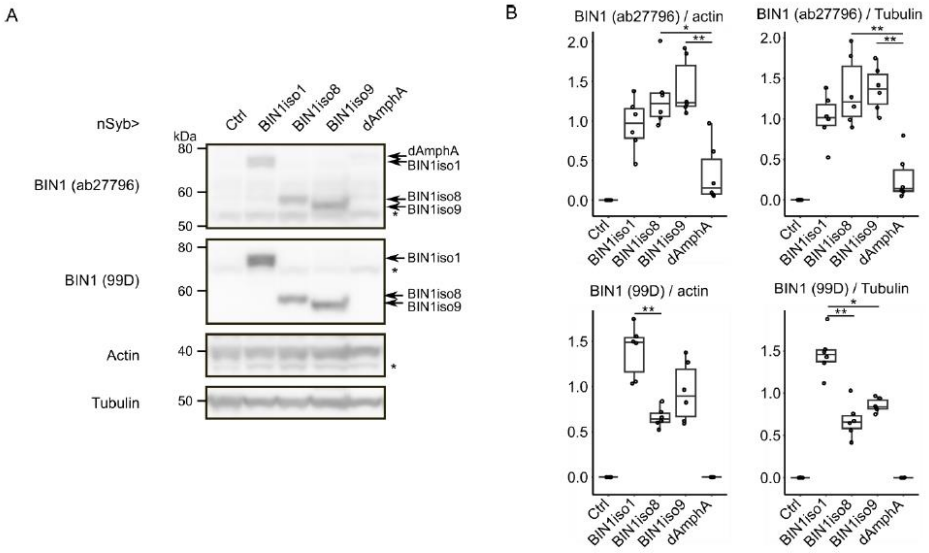

Supplementary Figure 3: Analysis of BIN1 levels in *Drosophila* expressing human BIN1 isoforms and *Drosophila* Amphiphysin under a nSyb driver. **A**. Representative Western blots analyzing the transgenic expression of human BIN1 isoforms and *Drosophila* Amphiphysin in 1-2 day-old *Drosophila* heads. BIN1 was detected using two antibodies (ab27796 and 99D). Actin and Tubulin were used as loading controls. Non-specific bands were marked with stars. **B.** Quantification of data obtained from 6 independent experiments. Statistical analyses were performed with non-parametric Kruskal Wallis tests followed by Dunn's multiple comparisons (*p*-values adjusted using the holm method, * p<0.05; ** p<0.01). The Ctrl group and the Ctrl and dAmphA groups were excluded from the statistical analysis for blots obtained using the BIN1 ab27796 and BIN1 99D antibodies, respectively.

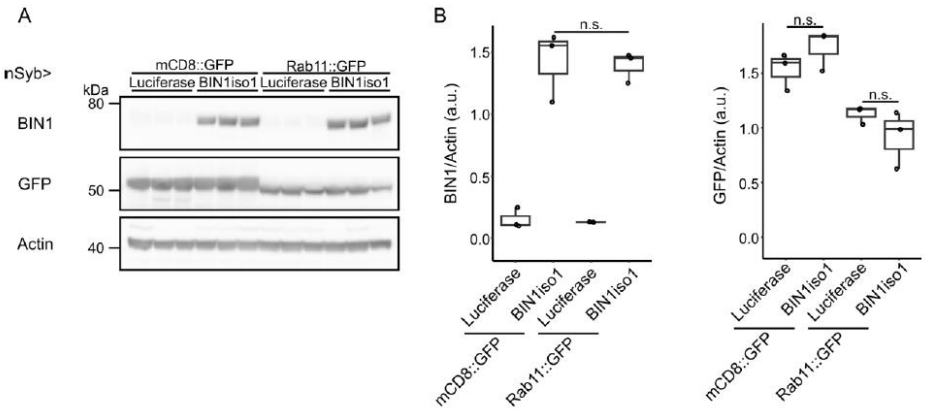

Supplementary Figure 4: Protein levels in *Drosophila* expressing BIN1iso1 and Rab11. **A.** Representative Western blots using *Drosophila* head protein extracts from animals expressing luciferase, mCD8::GFP (both used as controls), BIN1iso1 and Rab11::GFP, under a Nsyb driver, using anti-BIN1 (99D), anti-GFP and anti-actin antibodies. **B.** Quantification of BIN1 and GFP from 3 independent experiments. Statistical analyses were performed with non-parametric Kruskal Wallis tests followed by Dunn's multiple comparisons (*p*-values adjusted using the holm method, n.s. not significant).

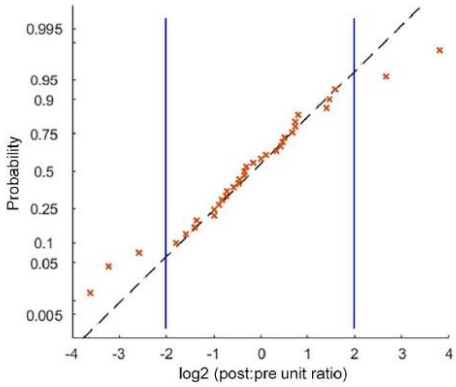

Supplementary Figure 5: Probability plot comparing the distribution of the fold differences between unit numbers detected in presynaptic and postsynaptic chambers to the normal distribution. Each point indicates one MEA-integrated microfluidic device, in which the spike sorting algorithm detected at least one unit in both chambers (n = 35 devices from 7 independent cultures). Dashed line passes through the lower and upper quartiles. Solid lines indicate the limits for 4-fold difference in unit numbers and correspond to the exclusion criteria used for this dataset (|*z*-score| = 1.5).

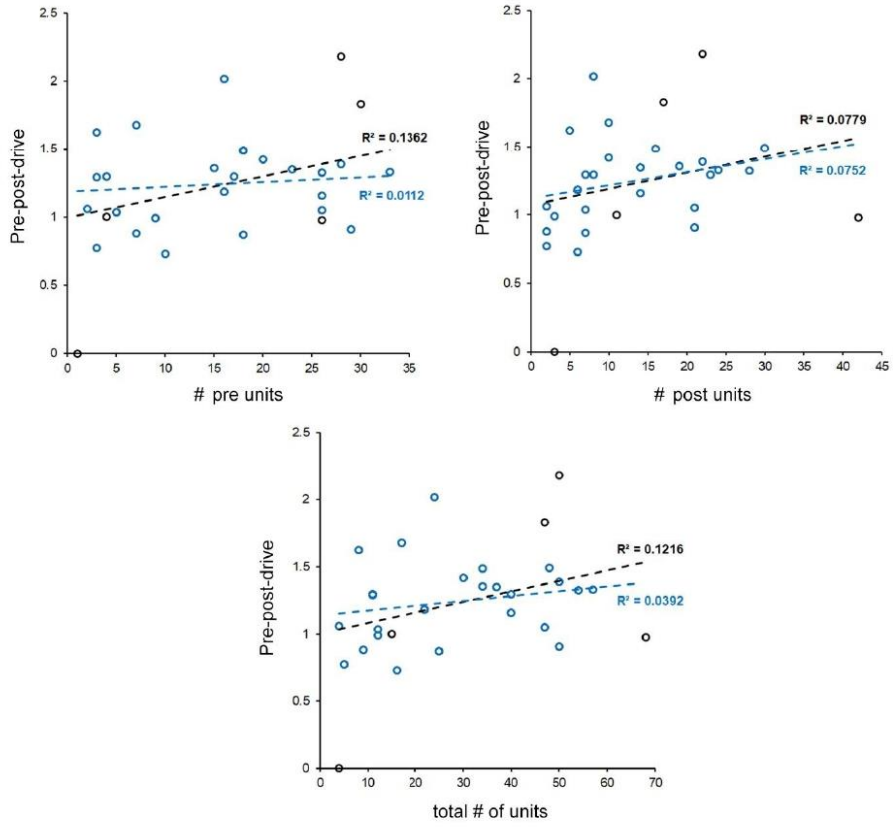

Supplementary Figure 6: Correlation between detected unit numbers and *pre-post-drive*. Each point indicates one MEA-integrated microfluidic device within the normal distribution of fold differences in unit numbers (n = 30 devices from 7 independent cultures). Outlier data points (black dots) were included for clarity. Dashed lines show the least-squares fits before (black) and after (blue) outlier exclusion.

ACS Biomaterials SCIENCE & ENGINEERING

pubs.acs.org/journal/abseba Article

Integration of Microfluidic Devices with Microelectrode Arrays to Functionally Assay Amyloid-β-Induced Synaptotoxicity

Camille Lefebvre, Anaïs-Camille Vreulx, Corentin Dumortier, Séverine Bégard, Carla Gelle, Dolores Siedlecki-Wullich, Morvane Colin, Devrim Kilinc,* and Sophie Halliez*

Cite This: https://doi.org/10.1021/acsbiomaterials.3c00997 Read Online

ACCESS | Metrics & More | Article Recommendations | Supporting Information

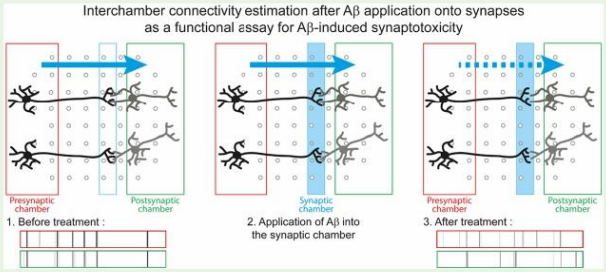

ABSTRACT: Alzheimer's disease (AD) is a neurodegenerative disease and the most frequent cause of dementia. It is characterized by the accumulation in the brain of two pathological protein aggregates: amyloid-β peptides (Aβ) and abnormally phosphorylated tau. The progressive cognitive decline observed in patients strongly correlates with the synaptic loss. Many lines of evidence suggest that soluble forms of Aβ accumulate into the brain where they cause synapse degeneration. Stopping their spreading and/or targeting the pathophysiological mechanisms leading to synaptic loss would logically be beneficial for the patients. However, we are still far from understanding these processes. Our objective was therefore to develop a versatile model to assay and study Aβ-induced synaptotoxicity. We integrated a microfluidic device that physically isolates synapses from presynaptic and postsynaptic neurons with a microelectrode array. We seeded mouse primary cortical cells in the presynaptic and postsynaptic chambers. After functional synapses have formed in the synaptic chamber, we exposed them to concentrated conditioned media from cell lines overexpressing the wild-type or mutated amyloid precursor protein and thus secreting different levels of Aβ. We recorded the neuronal activity before and after exposition to Aβ and quantified Aβ's effects on the connectivity between presynaptic and postsynaptic neurons. We observed that the application of Aβ on the synapses for 48 h strongly decreased the interchamber connectivity without significantly affecting the neuronal activity in the presynaptic or postsynaptic chambers. Thus, through this model, we are able to functionally assay the impact of Aβ peptides (or other molecules) on synaptic connectivity and to use the latter as a proxy to study Aβ-induced synaptotoxicity. Moreover, since the presynaptic, postsynaptic, and synaptic chambers can be individually targeted, our assay provides a powerful tool to evaluate the involvement of candidate genes in synaptic vulnerability and/or test therapeutic strategies for AD.

KEYWORDS: *synaptotoxicity, functional assay, connectivity, synaptic loss, amyloid-β, systems integration, microelectrode array, microfluidic device*

INTRODUCTION

Alzheimer's disease (AD) is the most common neurodegenerative disorder and therefore constitutes a major public health problem. It eventually leads to cognitive decline and dementia and still lacks effective treatments. Familial AD accounts for less than 1% of all AD cases, while most AD cases are sporadic with multiple etiological factors confirmed or suspected. Both familial and sporadic AD lead to the accumulation and aggregation of amyloid-β peptides (Aβ) and abnormally hyperphosphorylated microtubule-associated protein tau into, respectively, extracellular amyloid plaques and intracellular neurofibrillary tangles (NFTs) in the brain. Together, amyloid plaques, NFTs, and neuronal and synaptic

Received: July 21, 2023
Revised: February 9, 2024
Accepted: February 9, 2024

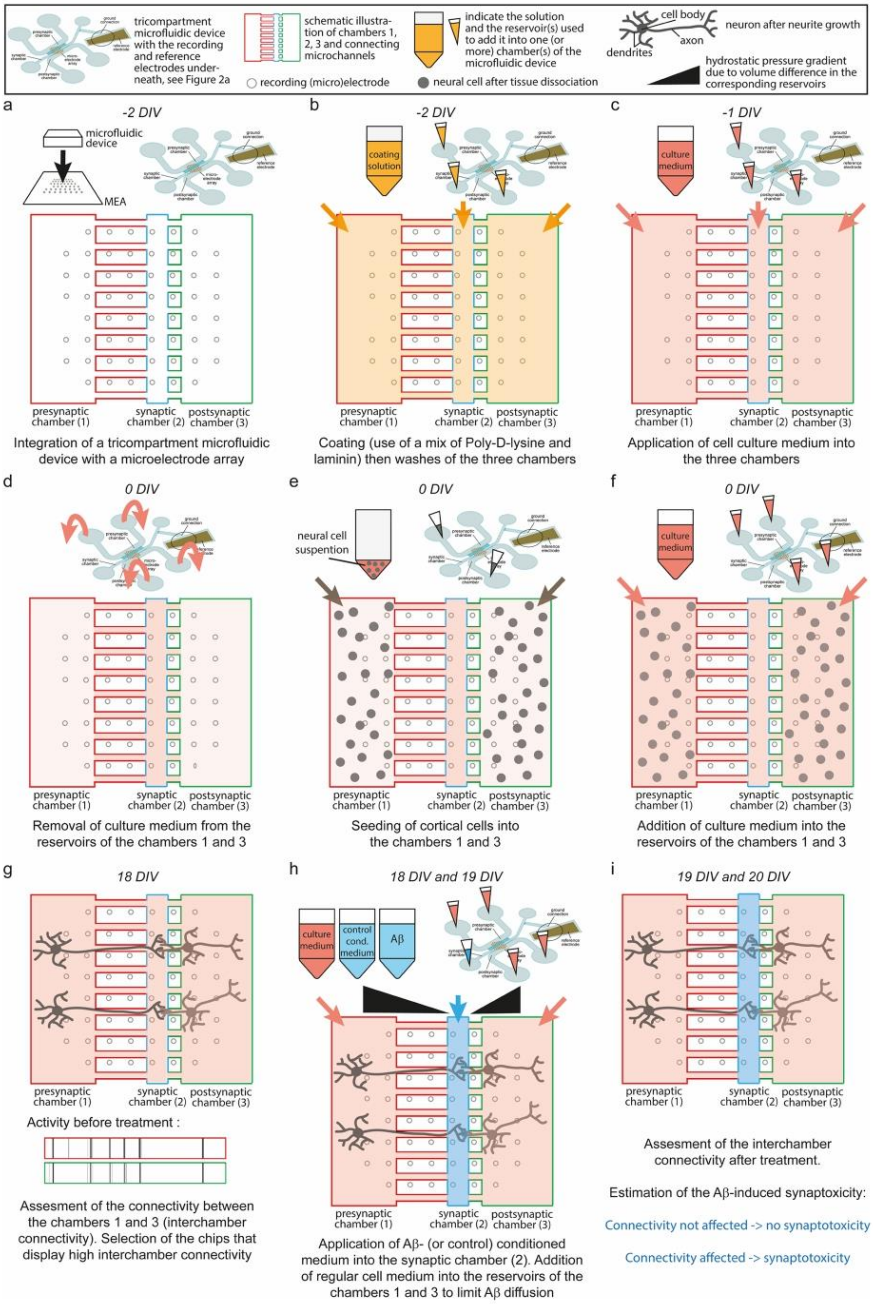

Figure 1. Key steps to functionally assay Aβ-induced synaptotoxicity. (a) Tricompartment microfluidic devices (presynaptic, synaptic and postsynaptic chambers connected by microchannels) were bonded to MEAs in order to have recording microelectrodes underneath the presynaptic and postsynaptic chambers. This step is further detailed in Figure 2 and below. Of note, each of the three chambers is served by two medium

https://doi.org/10.1021/acsbiomaterials.3c00997
ACS Biomater. Sci. Eng. XXXX, XXX, XXX−XXX

Figure 1. continued

reservoirs that will be used in the next steps to add solution into the different chambers. Reservoirs serving the chambers and the reservoir covering the reference electrode are highlighted in Figure 2b. (b) All surfaces were coated with a mixture of poly-D-lysine and laminin and then washed. (c) Cell culture medium was kept in the devices until cell seeding. (d) Once the cortical cells were ready to be seeded, the cell culture medium was removed from the reservoirs serving the presynaptic and postsynaptic chambers. (e) Cortical cells (1 μL of cell suspension) were seeded in the presynaptic and postsynaptic chambers of each microfluidic device, by disposing the suspension next to one of the entrances of the chambers. (f) A few minutes after cell seeding, cell culture medium were added into all reservoirs serving the presynaptic and postsynaptic chambers. (g) Then, the cells were allowed to develop and to form synapses for 18 days *in vitro* (DIV). Importantly, only axons were expected to cross the microchannels from the presynaptic chamber to the synaptic chamber, whereas both dendrites and axons were able to cross the microchannels from the postsynaptic chamber to the synaptic chamber. Neuronal activity was recorded for each device and the connectivity between the presynaptic and the postsynaptic chambers was estimated through a custom analysis workflow. Only the chips that displayed a high interchamber connectivity were considered for analysis. (h) Concentrated conditioned media from CHO cells secreting low and high amounts of Aβ were applied into the synaptic chamber twice, at 18 DIV (after the 18 DIV recording) and at 19 DIV (after the 19 DIV recording). At both times, a volume difference between the reservoirs of the synaptic chamber and the reservoirs of the presynaptic and postsynaptic chambers was imposed to counter the diffusion of Aβ molecules into the latter ones, thanks to the high fluidic resistance of the microchannels. (i) 24 h after each application of concentrated conditioned media into the synaptic chamber, the neuronal activity was recorded for each device and the connectivity between the presynaptic and the postsynaptic chambers was analyzed. Then, for each chip, the evolution of the interchamber connectivity before/after treatment was quantified. A drop in the interchamber connectivity would indicate a synaptotoxic effect induced by the treatment. All experimental and analytical procedures are detailed in subsequent sections.

loss are the characteristic histopathologic hallmarks of the AD brain. Historically, Aβ was viewed as the causative agent of AD as all the mutated genes involved in familial AD are known to affect the metabolism of amyloid precursor protein (APP), of which the Aβ peptide is a cleavage product. Moreover, soluble Aβ has been shown to promote neuronal hyperexcitability (or excitation/inhibition imbalance) and synaptic degeneration via direct and indirect effects at the synapse.[1−5] Together with other evidence, these have led to the amyloid cascade hypothesis where soluble Aβ is assumed to initiate a pathophysiological cascade leading to tau abnormal phosphorylation/misfolding and aggregation. Then, pathological soluble tau is assumed to spread throughout the brain, resulting in neuronal dysfunction, synaptic and neuronal loss, and cognitive impairment since the accumulation of NFTs, rather than amyloid plaques, correlates with the cognitive decline in AD patients. This view has been ultimately refined by the idea of synergistic effects and/or interactions between Aβ and tau rather than a linear model.[1,6,7] To add to this complexity, it is important to note that therapeutic strategies targeting Aβ had been so far unsuccessful even there are new promising approaches like the very recent clinical trial of Lecanemab performed on patients with early AD.[8] Thus, we are far from understanding what leads to synapse and neuronal loss in AD. In order to understand how Aβ and/or tau pathological species affect the integrity of the synapse, we need models allowing the functional study of Aβ- and tau-induced synaptotoxicity in combination or separately.

To develop such an assay, we used a tricompartment microfluidic device adapted from a previous design allowing to physically isolate synapses and providing exclusive access to the so-called presynaptic and postsynaptic chambers.[9] By employing sets of parallel microchannels, these microfluidic devices permit axons and dendrites pass from the side chambers to the central chamber, where they form functional synaptic connections. When the length of the microchannels between one side chamber and the central chamber is sufficiently long to minimize the passing of dendrites, the vast majority of dendrites observed in the central chamber are in fact arriving from the other side chamber. For convenience, we had termed the central chamber "synaptic", the side chamber that emits dendrites (as well as axons) to the central chamber "postsynaptic", and the side chamber that emits only axons to the central chamber "presynaptic".[9] We have recently developed a modified version of this model that contains an additional coculture chamber to specifically assay synapse loss due to chronic exposition to Aβ secreted by model cell lines overexpressing wild-type or mutated APP.[10] In this system, we quantified synapse loss by immunostaining and confocal imaging and subsequent distance-based assignment of postsynaptic puncta to presynaptic puncta as performed by others.[11] However, analyzing synaptic connectivity through immunolabeling presynaptic and postsynaptic markers or via live microscopy using, e.g., Ca^{2+} probes, is either limited in temporal resolution or does not allow one to collect information from the entire neuronal network. To overcome these limitations, recent work has focused on integrating microelectrode arrays (MEAs) with multichamber microfluidic neuron culture devices.[12] These studies aimed to record electrical activity from neurons in cell chambers or from isolated axons in microchannels. Some studies were based on commercial MEA chips where the electrode array covers an area of interest;[13−15] some others developed custom-design MEA chips to position the electrodes at specific stimulation and recording sites.[16−18] These studies were mostly proof-of-concept work, demonstrating various capabilities of compartmentalized neuron cultures, such as analyzing the directionality of electrophysiological activity between two neuron populations[13] or analyzing the connectivity between neuron populations harvested from different hippocampal regions.[15] As for local treatment of isolated synaptic connections, a recent study integrated a tricompartment microfluidic device with a custom MEA to demonstrate the coupling of presynaptic electrophysiological activity with postsynaptic calcium dynamics in cortical neurons.[17] However, to our knowledge, no previous study aimed at characterizing network-level connectivity in the context of synaptotoxicity or used interchamber connectivity (or its temporal evolution) as a read-out for synapse function.

In this study, we integrated our tricompartment microfluidic device with a commercial MEA to specifically assay the synaptic loss via the loss of functional connectivity. Through this system, we were able to estimate the connectivity between neurons cultured into presynaptic and postsynaptic chambers before and after we applied cell-secreted Aβ specifically onto mature synapses. Thus, we demonstrated that after 48 h, Aβ

https://doi.org/10.1021/acsbiomaterials.3c00997
ACS Biomater. Sci. Eng. XXXX, XXX, XXX−XXX

causes a loss of interchamber connectivity without significantly affecting the neuronal activity in the presynaptic or postsynaptic chambers, suggesting that Aβ induces the specific disruption of synapses.

MATERIALS AND METHODS

The key steps to perform the functional assay we developed are illustrated in the Figure 1.

Microfluidic Device Integration with Microelectrode Arrays (MEAs). Microfluidic devices were cast in polydimethylsiloxane (PDMS; Dow Corning, Midland, MI) via soft lithography and prepared for bonding according to established techniques.[10] The MEAs (60MEA200/30iR-Ti without glass rings) were purchased from Multi Channel Systems (MCS; Reutlingen, Germany). They encompass 59 recording electrodes and one reference electrode. The design of the microfluidic device was adapted from a previously described device[10] by adding a reservoir to maximize fluidic contact with the reference electrode (Figure 2a,b and Figure S1). We

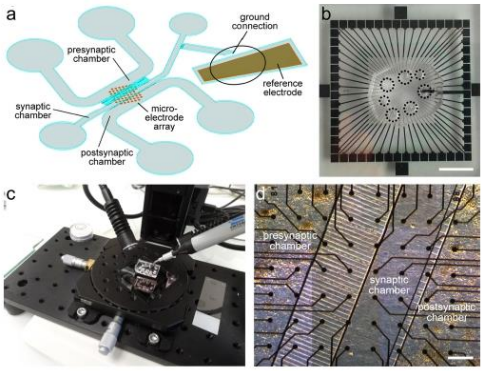

Figure 2. Integration of tricompartment microfluidic devices with microelectrode arrays. (a) Microfluidic device design with the recording and reference electrodes underneath. Ground connection is guaranteed by punching a medium reservoir at the location indicated by a circle. (b) Representative MEA-integrated microfluidic device with the different reservoirs highlighted. Scale bar = 1 cm. (c) Custom-made tool for align/bonding microfluidic devices onto MEAs consisting of a vacuum pen, a rotating stage, three linear stages, and a binocular. (d) Representative micrograph showing the relative positions of a subset of microelectrodes with respect to the microfluidic chambers. Mouse cortical neurons seeded in presynaptic and postsynaptic chambers extend neurites into the synaptic chamber and form functional synapses. Scale bar = 200 μm.

developed a mechanical tool to manually align the microfluidic layout with the MEA layout to consistently obtain desired numbers of electrodes in presynaptic and postsynaptic neuron chambers (10−14 electrodes per chamber) (Figure 2c). Of note, due to the MEA pattern, electrodes were also localized under microchannels and synaptic chambers (Figure 2d). The tool combines a vacuum pen (Virtual Industries Inc.; Colorado Springs, CO) that holds the microfluidic device above the MEA surface, with a rotation stage, a two-axis translation stage, and a one-axis linear stage (all from Newport; Irvine, CA), to manually align the patterns (Figure 2c). The microfluidic device and the MEA were washed with isopropanol, thoroughly dried, and exposed to O_2 plasma (Diener; Ebhausen, Germany). The nonexposed surface of the microfluidic device was then held by vacuum above the MEA surface. Using binoculars, the two layouts were aligned via manual micropositioners and the microfluidic device was lowered onto the MEA surface until contact was established. Vacuum was then released and the vacuum pen was elevated. To reinforce the bonding, the devices were baked in a convection oven (VWR; Radnor, PA) at 50 °C for 5 min, and microfluidic channels were wetted by adding Milli-Q water (mQ; Millipore; Burlington, MA). The MEA-integrated microfluidic devices were sterilized for 15 min in a UV chamber (254 nm; Vilber Lourmat; Collégien, France). Prior to cell culture, water was removed and surfaces were coated with a mixture of Poly-D-lysine (0.5 mg/mL; Sigma-Aldrich; St. Louis, MO) and laminin (10 μg/mL; Sigma-Aldrich) for 1 h followed by a new application of the coating solution overnight in a cell culture incubator. The devices were washed twice with Milli-Q water, then with cell culture medium. The devices were kept in the cell incubator with cell culture medium inside until the cells were seeded into them. A visual map has been generated for each MEA-integrated microfluidic device to list the electrodes corresponding to the presynaptic and postsynaptic chambers. After each primary culture, media were removed from the reservoirs and the MEA-integrated microfluidic devices were first washed in water and then in 1% Tergazyme (Alconox; White Plains, NY) for 1 h at 37 °C. The devices were then washed in water several times before being reused.

Primary Cortical Cell Culture. Media and supplements were purchased from Gibco (Thermo Fisher Scientific Inc., Waltham, MA) unless otherwise indicated. Primary cortical cells were prepared from 15 day-old C57BL/6JRj mouse embryos as previously described,[19] through mechanical dissociation of cerebral cortices, in a sterile class II biosafety cabinet (HERASAFE KS; Thermo Fisher Scientific). The experiments were carried out with the approval of an ethics committee (agreement APAFIS#2264−2015101320441671 from CEEA75, Lille, France) and followed the European guidelines for the use of animals in research. C57BL/6JRj gestating mice (Janvier Laboratories; Le Genest-Saint-Isle, France) were housed in a temperature-controlled (20−22 °C) room with a 12 h light, 12 h dark cycle. Food and water were provided *ad libitum*. The culture medium was made of Neurobasal (Gibco) supplemented with B27 (Gibco), Antibiotic-Antimycotic (Gibco) and L-glutamine (Gibco). The number of viable cells in the cell suspensions was determined through trypan blue exclusion test (Gibco). 40,000 viable cells (1 μL) were seeded in the presynaptic and postsynaptic chambers of each microfluidic device. Prior to cell seeding, regular MEAs (60MEA200/30iR-Ti with glass rings; MCS), were cleaned in ethanol, air-dried for 48 h, sterilized for 15 min in a UV chamber (254 nm; Vilber Lourmat), coated with a mixture of Poly-D-lysine (0.5 mg/mL; Sigma-Aldrich) and laminin (10 μg/mL; Sigma-Aldrich) for 30 min then washed using sterile water (Sigma-Aldrich) and air-dried. Regular MEAs were seeded with 80,000 viable cells onto the electrodes. After 5 min, cell culture medium was added and both the MEA-integrated microfluidic devices and the regular MEAs were covered with a removable, hydrophobic, semipermeable membrane cover (fluorinated ethylene-propylene, 12.5 μm thick; Sigma-Aldrich) mounted on a Teflon-ring (MCS). Cultures were kept in a cell incubator (Thermo Fisher Scientific) at 37 °C in a 5% CO_2 atmosphere.

Culture of CHO Cell Lines and Aβ Production. Chinese hamster ovary (CHO) cell lines stably overexpressing human APP, either wild-type (APP^{WT}) or with V717I (London) mutation (APP^{LDN}) secrete low and high amounts of Aβ, respectively.[20] CHO cell line stably transfected with an empty vector (pcDNA4), thus not expressing any exogenous APP, served as control. CHO cell lines were seeded in 75 cm^2 flasks and grown in DMEM/F-12 medium supplemented with 10% heat-inactivated fetal bovine serum FBS, 2% HT supplement, 0.2% Penicilin/Streptomycin, and 300 μM proline (Sigma-Aldrich). Medium was replaced every 3 days for maintenance. For Aβ production and media collection, cells were seeded in 10 cm Petri dishes (5 dishes per condition). To stimulate Aβ production, the medium was replaced with CHO-NBA medium: phenol red-/serum-free Neurobasal-A supplemented with 2% HT supplement, 0.2% Penicillin/Streptomycin, 300 μM proline (Sigma-Aldrich), 2% B27, and 1% Glutamax when 80% confluence was reached. After 48 h, the medium was collected from the dishes and centrifuged at 4000g at 4 °C for 10 min to remove debris. The supernatant was then loaded into a 3 kDa spin column (Ultracel-3K,

https://doi.org/10.1021/acsbiomaterials.3c00997
ACS Biomater. Sci. Eng. XXXX, XXX, XXX−XXX

#UFC9003; Merck; Rahway, NJ) pre-equilibrated with phenol/serum free Neurobasal (centrifuged at 4000*g* and 4 °C for 10 min) and concentrated at 4000g and 4 °C for 1 h. Concentrated media from APP^{WT}, APP^{LDN}, and control CHO cell lines were collected and the total protein concentration was adjusted to 200 $\mu g/\mu L$ using Pierce BCA Protein Assay Kit (Thermo Fisher Scientific). $A\beta_{1\text{-}x}$ concentration was quantified using the AlphaLISA detection kit (#AL288C; PerkinElmer; Waltham, MA) according to manufacturer's recommendations.

Application of Concentrated Conditioned Medium into the Synaptic Chamber. After the 18 DIV recording, we divided the chips displaying interchamber synchronized burst events into three groups. We collected the primary cell culture medium from the synaptic chambers and we applied the concentrated conditioned media from CHO cells at a 1:1 ratio with conditioned primary cell culture medium we have just collected. After the 19 DIV recording, we made a second application of concentrated conditioned media from CHO cells into the synaptic chambers still at a 1:1 ratio with fresh primary cell culture medium. At both times, when we applied the concentrated conditioned media from CHO cells into the synaptic chambers, we created a volume difference between the reservoirs serving the synaptic chamber and the reservoirs serving the presynaptic and postsynaptic chambers to limit the diffusion of the Aβ into the latter ones thanks to the high fluidic resistance of the microchannels.[21]

Extracellular Recordings of Neuronal Activity. Extracellular recordings were obtained using the MEA2100-System (MCS) as previously described.[22] Briefly, the system included a headstage for 2 × 60 channels (for signal amplification and digitization), an interface board (MCS-IFB), and a personal computer. A temperature controller (TC02, MCS) was used to maintain the culture temperature at 37 °C during the recording sessions. Real-time monitoring, signal filtering, and spike detection were carried out using the Multi Channel Experimenter software (MCS). For the MEA-integrated microfluidic devices, platinum wires (99.99%, 0.1 mm diameter, Advent Research Materials; Eynsham, UK) were added between one of the wells of the presynaptic or postsynaptic chambers and the well on top of the reference electrode for optimal grounding of the circuit. For the comparison between regular MEAs and MEA-integrated microfluidic devices, the spontaneous extracellular activity was recorded after 7, 11, 14, 18, 21, and 25 days *in vitro* (DIV) for 5 min after a rest period of 15 min on the headstage. For the synaptotoxicity assay, spontaneous extracellular activity was recorded at 18, 19, and 20 DIV for 5 min after a rest period of 10 min on the headstage. Spikes were detected by applying an amplitude threshold, which was set for each recording electrode. This value was calculated as the standard deviation of the baseline noise level, multiplied by −10. Recordings were exported in the NEX format using the Multi Channel DataManager software (MCS).

Analysis of the Firing and Bursting Activity Features. The analysis was carried out using the Burst Analysis function of the NeuroExplorer software (Nex Technologies; Colorado Springs, CO). For the cultures in MEA-integrated microfluidic devices, only electrodes into the presynaptic and postsynaptic chambers were analyzed. Electrodes that had at least 25 spikes during the 5 min recording period were defined as active electrodes. Percentage of active electrodes was calculated based on the number of electrodes in the chamber for MEA-integrated microfluidic devices or based on 59 for regular MEAs. Burst analysis was based on an interval algorithm that used the following parameters (thresholds): maximal interval to start burst: 0.01 s; minimal interval to end bursts: 0.01 s; minimum interval between bursts: 0.01 s; minimum burst duration: 0.02 s; and a minimum number of spikes in a burst: 4.[23] Alternatively, we used a second set of parameters: maximal interval to start burst: 0.17 s; minimal interval to end bursts: 0.3 s; minimum interval between bursts: 0.2 s; minimum burst duration: 0.01 s; and a minimum number of spikes in a burst: 3.[24] We also used a Poisson surprise algorithm[25] with the following parameters: minimum surprise: 2; minimum burst duration: 0.02 s; and a minimum number of spikes in a burst: 4. For each electrode that had at least one burst during the 5 min-long recording, mean number of spikes per burst, mean number of bursts per minute, and percentage of spikes within bursts were calculated. Separately for each method employed (*MaxInterval* algorithm, first set of parameters; *MaxInterval* algorithm, second set of parameters; *Surprise* algorithm), we calculated chip means for regular MEAs and (presynaptic or postsynaptic) chamber means for the MEA-integrated microfluidic devices, by averaging the values obtained from different electrodes. Percentage of electrodes recording bursts was calculated based on the number of electrodes in the relevant chamber for the MEA-integrated microfluidic devices or based on 59 electrodes for regular MEAs. Graphical representations of the extracellular neuronal activity (raster plots) were obtained using NeuroExplorer.

Analysis of the Evolution of the Interchamber Connectivity. The firing activity in the presynaptic and postsynaptic chambers was determined at 18 DIV using NeuroExplorer. Only the electrodes that recorded at least 50 spikes during the 5 min-long recording period were selected for the interchamber connectivity analysis. Note that the electrodes that totally shut down (0 spikes) at 19 or 20 DIV time points were excluded. The analysis was carried out first at 18 DIV for all the selected postsynaptic electrodes using the *Crosscorrelograms* function of NeuroExplorer by defining all selected presynaptic electrodes as references. The conditional probability of a spike in the postsynaptic chamber immediately after (within 50 ms) a spike occurring in the presynaptic chamber was calculated by using the following parameters: X_{min} = 0 s; X_{max} = 0.05 s; bin width = 0.05 s. In addition, we used for a subgroup of chips two alternative time intervals to calculate the conditional probability: X_{min} = 0 s; X_{max} = 0.02 s; bin width = 0.02 s and X_{min} = 0 s; X_{max} = 0.005 s; bin width = 0.005 s. For each chip, we averaged the conditional probabilities of the different pairs of electrodes (consisting of a selected postelectrode and a selected pre-electrode). Chips with an average conditional probability less than 0.15 were considered not sufficiently robust and were excluded.

We repeated the cross-correlogram analysis (with the same set of reference electrodes and using the same parameters) for recordings acquired at 18, 19, and 20 DIV, but considering only the electrodes that were selected at 18 DIV. This time, the Z-score method was used. As the purpose of the study was to estimate the impact of Aβ on functional synapses, we only selected the electrode pairs (consisting of a postelectrode and a pre-electrode) that obtained a Z-score of at least 2.58 (corresponding to a *p*-value <0.01) at 18 DIV. We set this specific threshold to ensure (with a probability higher than 99%) that the spikes did not randomly occur in the postsynaptic chamber immediately after a spike in the presynaptic chamber. These electrode pairs will be referred to as connected pairs. We then averaged the Z-scores of these connected pairs separately for recordings acquired at 18, 19, and 20 DIV. Finally, we calculated 19DIV/18DIV and 20DIV/18DIV ratios of average Z-scores as a read-out for the evolution of interchamber connectivity. Note that we did not take into account the connectivity ratios when the global firing activity in the presynaptic chamber decreased by more than 85% from 18 DIV to 19 DIV or to 20 DIV.

Analysis of the Evolution of the Intrachamber Connectivity. We used the electrodes in the presynaptic and postsynaptic chambers selected to estimate the evolution of the interchamber connectivity, i.e., electrodes forming the connected pairs, to assay the evolution of the intrachamber connectivity in, respectively, the presynaptic and postsynaptic chambers. The analysis was carried out separately for recordings acquired at 18, 19, and 20 DIV. To estimate the intrachamber connectivity in the presynaptic chamber, we used the *Crosscorrelograms* function of NeuroExplorer by selecting the presynaptic electrodes as references (by making sure that no electrode acts as a reference against itself). The conditional probability of a spike immediately before or after (within 50 ms before or after) a spike occurring in the presynaptic chamber was calculated by using the following parameters: X_{min} = −0.05 s; X_{max} = 0.05 s; bin width = 0.05 s. In addition, we used for a subgroup of chips two alternative time intervals to calculate the conditional probability: X_{min} = 0 s; X_{max} = 0.02 s; bin width = 0.02 s and X_{min} = 0 s; X_{max} = 0.005 s; bin width =

https://doi.org/10.1021/acsbiomaterials.3c00997
ACS Biomater. Sci. Eng. XXXX, XXX, XXX−XXX

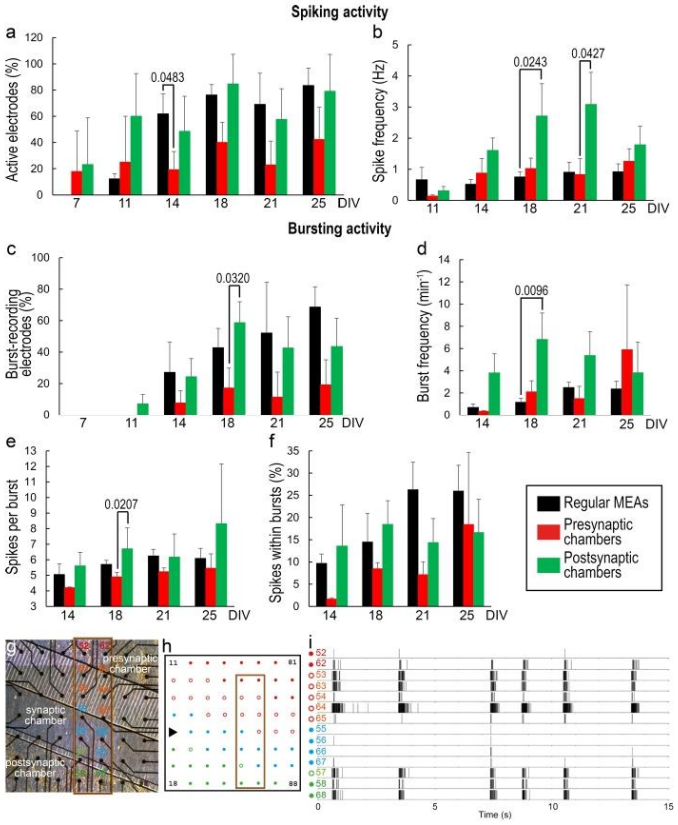

Figure 3. Characterization of the spontaneous firing and bursting activity of networks derived from primary cortical cells seeded in MEA-integrated microfluidic devices. Firing activity was measured using extracellular recordings of cortical cells grown on regular MEAs (black) or in the presynaptic (red) or postsynaptic (green) chambers of the MEA-integrated microfluidic devices. Mean percentages of active electrodes (a) and burst-recording electrodes (c) are shown for recordings acquired from the same devices at 7, 11, 14, 18, 21, and 25 DIV. Spike frequency (mean values) is shown for recordings at 11, 14, 18, 21, and 25 DIV (b). The following measures of burst activity (mean values) are shown for recordings at 14, 18, 21, and 25 DIV: number of bursts per minute (d), number of spikes per burst (e), and percentage of spikes within bursts (f). Error bars show standard error of the mean. $n = 4$ for each condition. Comparisons among all groups were performed using Dunn's test with Bonferroni correction. (g) A representative micrograph showing the relative positions of a subset of microelectrodes with respect to the microfluidic chambers. Boxed area shows 14 numbered (column-row) and color-coded recording electrodes. (h) Electrode map showing the alignment. Electrodes marked with solid red, solid blue, and solid green circles are positioned under presynaptic, synaptic, and postsynaptic chambers, respectively. Electrodes marked with hollow red and hollow green circles are positioned under the long and short microchannels, respectively. Boxed area shows the 14 electrodes marked in panel g. (i) Corresponding raster plots from selected microelectrodes (boxes in panels g and h) obtained at 21 DIV. Each vertical line represents a spike.

0.005 s. The Z-score method was used. We averaged the maximum Z-scores obtained for the different electrode pairs, separately for recordings acquired at 18, 19, and 20 DIV. Finally, we calculated 19DIV/18DIV and 20DIV/18DIV ratios of maximum Z-scores as a read-out for the evolution of intrachamber connectivity in the presynaptic chamber. We performed the same procedure for the postsynaptic electrodes to calculate the intrachamber connectivity in the postsynaptic chamber.

Analysis of the Evolution of the Intrachamber Firing Activity. For each chip, we determined the firing activity at 18, 19, and 20 DIV of the electrodes in the presynaptic and postsynaptic chambers ~~was~~ using NeuroExplorer. We considered those electrodes that had at least 50 spikes during the 5 min-long recording periods (acquired at 18, 19, or 20 DIV) for the analysis. This means that the electrodes that were active at one time point were included in the analysis, even if they were totally inactive (0 spikes) at other time points. We calculated the mean spike frequency of all selected electrodes and then averaged these values for each recording acquired at 18, 19, and 20 DIV. Finally, we calculated 19DIV/18DIV and 20DIV/18DIV ratios of mean spike frequencies as a read-out for the evolution of intrachamber firing activity.

Statistics. Statistical analyses were carried out using a non-parametric pairwise multiple-comparison test, Dunn's test with Bonferroni correction (multiple-comparison correction). For the comparison of the firing and bursting activity features between MEA-integrated microfluidic devices and regular MEAs (Figure 3, Figure S4

https://doi.org/10.1021/acsbiomaterials.3c00997
ACS Biomater. Sci. Eng. XXXX, XXX, XXX−XXX

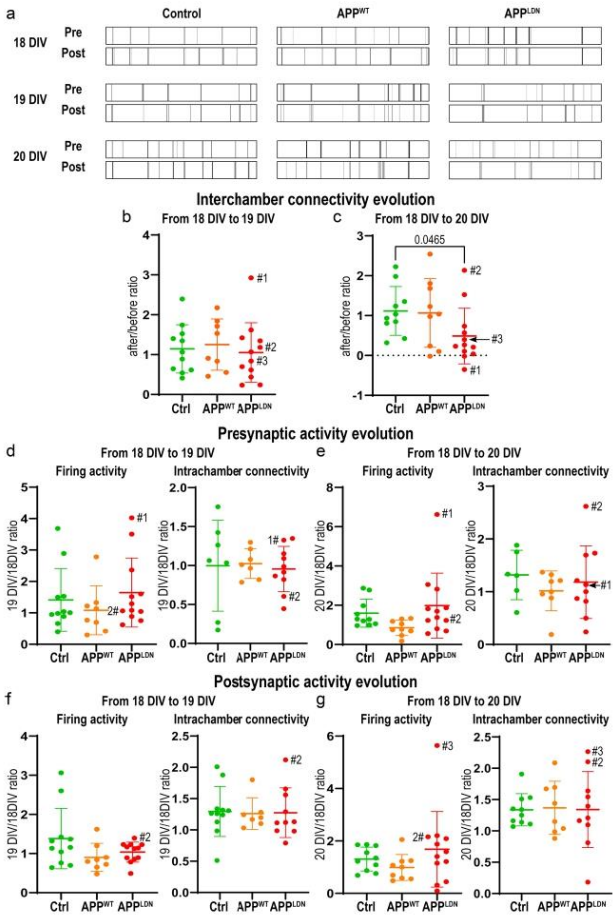

Figure 4. Functional assay of the Aβ-induced synaptotoxicity into 3-chamber microfluidic devices integrated with MEAs. (a) Representative raster plots of 20 s from microelectrodes located in the presynaptic and postsynaptic chambers at 18 DIV (before treatment), 19 DIV (after 24 h of treatment) and 20 DIV (after 48 h of treatment). Each vertical line represents a spike. The treatment entailed the application of concentrated conditioned media from control (left), APP^{WT} (middle) and APP^{LDN} (right) expressing CHO cells into the synaptic chamber. (b, c) Evolution of interchamber connectivity from 18 DIV to 19 DIV, i.e., 24 h of treatment (b) and from 18 DIV to 20 DIV, i.e., 48 h of treatment (c). Evolution of interchamber connectivity is defined as after/before ratios of the mean Z-scores. n = 11, 9, and 12 chips treated with concentrated conditioned media from, respectively, control (green), APP^{WT} (orange), and APP^{LDN} (red) CHO cells. Comparisons between control and other groups were performed using Dunn's test with Bonferroni correction. (d–g) Evolution of the neuronal activity given for neurons cultured in the presynaptic (d, e) or postsynaptic (f, g) chambers of the MEA-integrated microfluidic devices from 18 DIV to 19 DIV (d, f) and from 18 DIV to 20 DIV (e, g). The evolution of the neuronal activity is defined as after/before ratios of two distinct activity measures: the measured mean spike frequency (left) and the estimated intrachamber connectivity (mean cross-correlation Z-score, right). The results shown were based on analysis performed on the same devices than in panels b and c. Comparisons between control and other groups were performed using Dunn's test with Bonferroni correction. Note three outlier data are tagged (#1, #2 and #3) in panels b–g.

and S5), we performed comparisons among all three groups, so 3 comparisons (m = 3), and adjusted the p-value accordingly. For the synaptotoxicity assay (Figures 4 and 5, Figure S3), we only performed comparisons between the control group and each of the two other groups, so m = 2, and adjusted the p-value accordingly. For the comparison of the different time intervals to calculate the conditional probability of a spike in the postsynaptic chamber immediately after a spike occurring in the presynaptic chamber (Figure S6), we performed comparisons among all three groups, so 3 comparisons (m = 3), and adjusted the p-value accordingly. An adjusted p-value <0.05 was considered as significant.

RESULTS

Primary Cortical Neurons Mature into Functional Networks in MEA-Integrated Microfluidic Devices. We integrated tricompartment microfluidic devices encompassing

https://doi.org/10.1021/acsbiomaterials.3c00997
ACS Biomater. Sci. Eng. XXXX, XXX, XXX−XXX

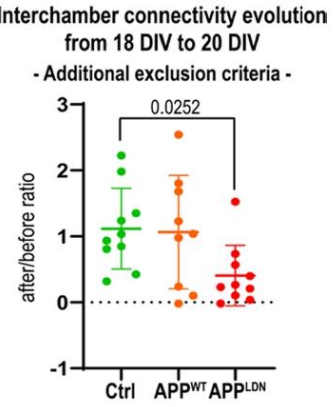

Figure 5. Refined functional assay of the Aβ-induced synaptotoxicity. Estimation of the interchamber connectivity evolution from 18 DIV to 20 DIV, i.e., 48 h of treatment. The interchamber connectivity evolution is defined as after/before ratios of the mean Z-scores. The results shown were based on the analysis presented in Figure 4 but with additional exclusion criteria applied on the evolution of the presynaptic activity (+400% as the upper threshold for the firing activity and +100% as the upper threshold for the intrachamber connectivity). n = 10, 9, and 10 chips treated with concentrated conditioned media from, respectively, control (green), APP^{WT} (orange) and APP^{LDN} (red) CHO cells. Comparisons between control and other groups were performed using Dunn's test with Bonferroni correction.

presynaptic, synaptic, and postsynaptic chambers with MEAs (Figures 1a and 2). In a first set of experiments, we examined the capacity of primary cortical neurons to mature into a functional network in these devices. We seeded primary cortical cells in the presynaptic and postsynaptic chambers and cultured them for 25 DIV. We recorded the spontaneous extracellular neuronal activity over time and compared it to the spontaneous activity recorded from primary cortical cells seeded onto regular MEAs, i.e., without any microfluidic device (Figure 3). After a period of maturation, cortical neurons cultured in both formats generated bursts, as we and others have previously reported.[26] However, we noted that the neurons cultured in the postsynaptic chambers tend to start generating bursts earlier (p = 0.062), suggesting that the neuronal maturation in the postsynaptic chamber is slightly accelerated (Figure 3c). We characterized the firing and bursting activities per chip for each condition using different measures: the percentage of active electrodes, the mean firing rate, the percentage of electrodes recording bursts, the mean number of bursts per minute, the mean number of spikes per burst, and the mean percentage of spikes occurring within bursts. We found a few differences between the three conditions, suggesting that cortical cells behave slightly differently not only when they develop in microfluidic devices compared to regular cultures, but also whether they are cultured in the presynaptic or the postsynaptic chambers. Grossly, the extracellular activity from cortical neurons cultured in presynaptic chambers tended to be slightly lower than when cultured in regular conditions with a lower percentage of active electrodes at 14 DIV (Figure 3a). On the contrary, the extracellular activity from cortical neurons in postsynaptic chambers was slightly higher than when cultured in regular conditions with a higher spike frequency (Figure 3b) and more bursts per minute (Figure 3d) at 18 DIV. Lastly, the extracellular activity from cortical neurons cultured in postsynaptic chambers was slightly higher than those cultured in presynaptic chambers with a higher spike frequency at 21 DIV (Figure 3b) and higher percentage of electrodes recording bursts (Figure 3c) and more spikes per burst (Figure 3e) at 18 DIV. Possible explanations for these differences are discussed below. However, regardless of the culture condition, the firing and bursting activity features were quite stable from 18 DIV onward.

Importantly, in microfluidic devices, we observed that cortical neurons had intra- but also interchamber synchronized burst events (example in Figure 3g–i), thus demonstrating that functional connections formed between the neurons in presynaptic and postsynaptic chambers. Importantly still, interchamber synchrony and/or bursting activity occurring in both the presynaptic and the postsynaptic chambers were not observed in all microfluidic devices. Robust interchamber connectivity was only present in 41.5% of the devices (see the definition of robust interchamber connectivity in the Materials and Methods, section "Analysis of the evolution of the interchamber connectivity"). Only these devices were considered for assaying Aβ-induced synaptotoxicity.

Aβ Treatment in the Synaptic Chamber Significantly Alters the Interchamber Connectivity. Next, we assayed the ability of Aβ to induce synaptotoxicity in a reproducible way in our microfluidic neuron cultures by specifically testing the ability of secreted Aβ to disrupt functional synapses. Instead of chronically exposing synapses to cell secreted Aβ as done previously using a coculture model,[10] we applied concentrated conditioned media containing cell-secreted Aβ into the synaptic chambers once the synapses were developed and a robust connectivity between presynaptic and postsynaptic chambers was achieved. We chose to start the treatment at 18 DIV as the neuronal activity in the presynaptic and postsynaptic chambers was quite stable from this point on (Figure 3) and synchronized burst events between the two chambers were evident (Figure 4a, top). We concentrated conditioned media from CHO cell lines overexpressing wild-type (APP^{WT}) or mutated APP (APP^{LDN}) that secrete low and high amounts of Aβ, respectively.[20] Conditioned media from CHO cells stably transfected with an empty vector were used as a control. The Aβ concentrations we obtained from each line are presented in Table 1 and, as expected, the conditioned medium from APP^{LDN} CHO cells contained a high amount of Aβ compared to control and APP^{WT} CHO cells. Our model represents an acute approach that intents to mimic a long chronic pathological process that is assumed to take a few

Table 1. Aβ concentrations obtained from CHO cell lines[a]

CHO cell line	Aβ concentration in concentrated conditioned medium	Aβ concentration applied into the synaptic chamber for the assay
control	5 ± 3 nM	2.5 nM
APP^{WT}	9 ± 2 nM	4.5 nM
APP^{LDN}	170 ± 5 nM	85 nM

[a]Concentrations of Aβ obtained by concentrating the conditioned media from the different CHO cell lines and the corresponding concentrations applied into the synaptic chamber to assay Aβ-induced synaptotoxicity.

https://doi.org/10.1021/acsbiomaterials.3c00997
ACS Biomater. Sci. Eng. XXXX, XXX, XXX−XXX

months in AD mouse models and a few years in AD patients. For this reason and relying on *in vitro* work done with synthetic and cell-secreted Aβ, we applied a higher concentration of Aβ than in the brain but still moderate compared to other in *vitro* approaches. These approaches commonly use concentration range varying between 50 nM to 10 μM for 24 to 96 h.[27,28] We therefore used an A$\beta_{1\text{-}X}$ concentration of 85 nM, a value that is 500 times higher than the A$\beta_{1\text{-}X}$ concentration measured in the hippocampal interstitial fluid of AD mice[29] and 600 times higher than the mean Aβ_{1-42} concentration in the human brain interstitial fluid.[30]

We recorded the spontaneous neuronal activity of the chips at 18 DIV, and then we applied the concentrated conditioned media from CHO cells into the synaptic chambers. The activity was recorded at 19 DIV, i.e., 24 h after the application of the conditioned medium containing cell-secreted Aβ. Burst events remained synchronized between the presynaptic and postsynaptic chambers regardless of the treatment (Figure 4a, middle). Aβ turnover has been shown to be rapid in the human central nervous system, with a half-life of approximately 9 h.[31,32] Moreover, it has also been demonstrated that the concentration of cell-secreted A$\beta_{1\text{-}X}$ and Aβ_{1-42} added to primary neuron cultures decreased by half in 24 h (Kilinc et al., 2020).[10] For this reason and to ensure more stable levels of Aβ, we applied a second dose of concentrated conditioned media into the synaptic chambers after 24 h. Activity was recorded at 20 DIV, i.e., 48 h after the first application of the conditioned medium. This time, the signal we recorded from the postsynaptic chamber was less synchronized with the signal from the presynaptic chamber, specifically for the chips that received concentrated conditioned media from APP^{LDN} CHO cells into their synaptic chambers (Figure 4a, bottom). This suggests that secreted Aβ altered synaptic connectivity between primary cortical neurons.

We investigated the potential diffusion of the cell-secreted Aβ applied into the synaptic chamber to the presynaptic and postsynaptic chambers during the Aβ-induced synaptotoxicity assay. We applied a fluorescent dye into the synaptic chamber under the same conditions we used during the assay and monitored its diffusion to the presynaptic and postsynaptic chambers over 24 h (Figure S2). The diffusion of the dye and, by extension, of Aβ to the presynaptic chamber was extremely limited, with an estimated maximum of 1 nM (lower than in concentrated conditioned medium from control CHO cells). The diffusion of the fluorescent dye and, by extension, of Aβ to the postsynaptic chamber was also extremely limited but a little higher from t = 16 h with an estimated maximum of 3.3 nM (similar to concentrated conditioned medium from control CHO cells). This difference could be explained by the less effective diffusion barrier between the synaptic chamber and the postsynaptic chamber compared to that between the synaptic chamber and the presynaptic chamber (due to the difference in the lengths of microchannels connecting the presynaptic or postsynaptic chamber with the synaptic chamber). We concluded that the diffusion of the Aβ applied into the synaptic chamber to the presynaptic and postsynaptic chambers during the assay was negligible.

To precisely characterize the synapse disruption, we measured the fold change in the interchamber connectivity between before and after treatment for different treatment conditions. As a proxy for the interchamber connectivity, we determined the conditional probability of a spike in the postsynaptic chamber immediately after (within 50 ms, the average burst duration) a spike occurring in the presynaptic chamber. We normalized it by the expected probability, i.e., as if presynaptic and postsynaptic neurons were not connected but randomly fired at the firing rates we measured. This was expressed in terms of a Z-score. Importantly, Z-scores and thus interchamber connectivity, together with neuronal activity features in the presynaptic and postsynaptic chambers, were comparable at 18 DIV between control and treatment groups (Figure S3). 19DIV/18DIV Z-score ratios (i.e., after 24 h of treatment) were comparable between control and treatment groups (Figure 4b). 20DIV/18DIV Z-score ratios (i.e., after 48 h of treatment) showed significant differences between chips that received concentrated conditioned media from control CHO cells versus APP^{LDN} CHO cells into their synaptic chambers (p = 0.0465) (Figure 4c). 20DIV/18DIV Z-score ratios were not significantly different between chips that received concentrated conditioned media from control CHO cells versus APP^{WT} CHO cells into their synaptic chambers. Thus, our results confirm that nanomolar concentrations of secreted Aβ, when applied onto fluidically isolated synapses, disrupts functional connectivity in a reproducible way.

We checked if the drop in interchamber connectivity was coupled to a decrease in the activity in presynaptic or postsynaptic chambers. It has to be mentioned at this point that we had intentionally excluded from the analysis the chips where an important drop (more than 85% reduction) in the presynaptic activity was observed. Indeed, we thought it was pointless to measure the connectivity if the presynaptic neurons shut down. We deduced that this was not related to the specific treatment the chips received, but to a more general stress caused by the manipulation as only two chips exhibited such behavior during the entire study, and they were not treated with concentrated conditioned media from APP^{LDN} CHO cells. One was treated with concentrated conditioned media from control CHO cells and shut down at 20 DIV, and the other one was treated with concentrated conditioned media from APP^{WT} CHO cells and shut down at 19 DIV. However, no exclusion criteria were defined regarding the evolution of the activity in the postsynaptic chamber. We observed no decrease in the firing activity associated with the loss of connectivity in the chips treated with concentrated conditioned media from APP^{LDN} CHO cells in neither the presynaptic (Figure 4d,e, left) nor the postsynaptic (Figure 4f,g, left) chambers, after 24 or 48 h of treatment. However, it has to be noted that we observed a nonsignificant decrease in the firing rate in the presynaptic chambers of the chips treated with concentrated conditioned media from APP^{WT} CHO cells (p = 0.058) that did not correlate with any changes in interchamber connectivity (Figure 4c,e). We also tested if the loss of interchamber connectivity in the chips treated with concentrated conditioned media from APP^{LDN} CHO cells was associated with a more general loss of connectivity in the whole network. To this end, we focused on the evolution of the correlation in the neuronal activity of neurons cultured in the same chamber, i.e., the intrachamber connectivity. We did not find an associated loss of intrachamber connectivity in the presynaptic (Figure 4d,e, right) or the postsynaptic (Figure 4f,g, right) chambers, after 24 or 48 h of treatment.

■ DISCUSSION

Integrating microfluidic devices with MEAs to recreate and functionally characterize neuronal networks is a powerful

https://doi.org/10.1021/acsbiomaterials.3c00997
ACS Biomater. Sci. Eng. XXXX, XXX, XXX−XXX

method to explore pathophysiological mechanisms underlying neurological and neurodegenerative disorders. The tricompartment microfluidic device[9] allows us to physically isolate synapses from their cell bodies and provides exclusive access to presynaptic and postsynaptic chambers. Major advantages of the fluidic isolation are (i) the capacity of culturing different populations of neurons in these different chambers, such as neurons harvested from different brain regions or from disease models, (ii) the capacity of manipulating the two neuron populations independently of each other via, e.g., gene expression modifications or drug treatments, (iii) the capacity of locally treating the neuronal network, and thereby the synaptic connections that spontaneously form thereon, independently of the neuronal cell bodies, and (iv) establishing a read-out for directional connectivity between the two chambers, such as the one we presented in this study. Here, we integrated an adapted version of the tricompartment device with an MEA and, as expected, the neurons cultured in the presynaptic and the postsynaptic chambers exhibited synchronized activity. Interestingly, the firing activity features observed in the two cell chambers were slightly different. To exclude that these small differences resulted only from the specific parameters/thresholds we used to detect bursts, we used an alternative set of thresholds and an alternative algorithm (Figures S4 and S5). The absolute measures of the bursting activity were modified accordingly. However, we still saw differences between the recordings of neurons cultured in the pre- or postsynaptic chambers and on regular MEAs without microfluidic devices, confirming these differences are not just the reflect of the burst detection parameters and/or the method we used. These differences could be due to the oriented nature of the circuit. Indeed, only the neurons in the postsynaptic chamber receive external input that could accelerate the network maturation. Moreover, the difference in the lengths of microchannels connecting the presynaptic or postsynaptic chamber with the synaptic chamber results in a less effective diffusion barrier between the synaptic chamber and the postsynaptic chamber compared to that between the synaptic chamber and the presynaptic chamber, as discussed previously. Thus, the synaptic chamber might act as a better source of fresh medium for neurons in the postsynaptic chamber than for those in the presynaptic chamber. These phenomena require further investigation.

To calculate the conditional probability of a spike in the postsynaptic chamber immediately after a spike occurring in the presynaptic chamber, we set an interval of 50 ms as it corresponds to the average burst duration we measured for primary cortical cell cultures. This was done in order to compensate for any possible missed spike (the amplitude threshold we use to detect spike is quite stringent). However, we checked whether setting a shorter interval could modify the outcome of the analysis. We reanalyzed the recordings performed on the control group with an interval set at 5 ms (close to the expected time to transmit a signal from the presynaptic chamber to the postsynaptic chamber) and 20 ms (intermediary). Under these conditions, only 3 and 9, respectively, out of the 11 control chips exhibited a conditional probability of at least 0.15 (Figure S6a, left). This could suggest a poor intrachamber connectivity; however, after normalization by the expected probability, all control chips exhibited Z-scores superior to 5, and therefore demonstrated strong interchamber connectivity, although the average values were clearly reduced when calculated with an interval set at 5 or 20 ms (Figure S6a, right). Importantly, the temporal evolution of the interchamber connectivity (Figure S6b with 19DIV/18DIV Z-score ratios) was similar regardless of the interval used. Similar results were obtained for the intrachamber connectivity (data not shown). Thus, this methodology, based on the evolution of the connectivity rather than a static analysis, is quite robust and works well with different parameters. However, appropriate thresholds have to be applied to preselect chips with good interchamber connectivity prior to toxicity application.

We took advantage of this model to propose a new method to assay Aβ-induced synaptotoxicity. We observed that after 48 h, but not 24 h, the functional connectivity decreased significantly due to the presence of 85 nM of cell-secreted Aβ. This is in full agreement with our previous experiments performed with synthetic Aβ where 16 h of treatment resulted in synapse disruption.[10] Whether the time difference is due to the cell model (primary rat hippocampal neurons), the treatment applied onto the synapse (100 nM of synthetic Aβ) and/or the read-out (the synaptic connectivity was quantified in fixed samples through distance-based assignment of postsynaptic puncta to presynaptic puncta) require further investigation. Importantly, we used cell-secreted Aβ and a concentration value that we estimate to be several hundred times higher than in the AD brain,[29,30] but still quite close from what is used chronically (10 nM applied on induced pluripotent stem cell-derived neurons for 30 days) to mimic AD *in vitro*.[33] We believe that the conditions we applied for our assay are a good compromise between the requirements of an acute approach (a few days of treatment to observe a functional impairment) and the need to mimic AD under physiologically relevant conditions.

We showed that the loss of connectivity was not associated with an obvious change in firing activity or in intrachamber connectivity in the presynaptic or postsynaptic chambers. This suggests that the firing activity of the neurons in the presynaptic and postsynaptic chambers was not massively affected by the application of Aβ into the synaptic chamber.

We also noted a few outlier data in the whole study. Most of these outliers were detected when analyzing specific features and they may reflect a deviation or potential delay in neural network behavior. The most aberrant data points we had were for three chips treated with concentrated conditioned media from APP^{LDN} CHO cells. One outlier showed a massive increase in interchamber connectivity at 19 DIV followed by a massive decrease at 20 DIV in interchamber connectivity and, in parallel, massive increases in firing activity at both time points in the presynaptic chamber (marked #1 in Figure 4). A second outlier showed a massive increase in interchamber connectivity at 20 DIV and, in parallel, a massive increase in intrachamber connectivity in the presynaptic chamber as well as in the postsynaptic chamber to a lesser extent (marked #2 in Figure 4). The third outlier showed massive increases in firing activity and intrachamber connectivity in the postsynaptic chamber only (marked #3 in Figure 4). One could apply exclusion criteria on the evolution of the presynaptic activity from 18 DIV to 20 DIV to eliminate chips that exhibited aberrant network behavior. For example, setting +400% as the upper threshold for the presynaptic chamber firing activity and +100% as the upper threshold for the intrachamber connectivity, our synaptotoxicity assay would still highlight statistically significant differences between control CHO cells and APP^{LDN} CHO groups after 48 h of treatment ($p = 0.0252$)

https://doi.org/10.1021/acsbiomaterials.3c00997
ACS Biomater. Sci. Eng. XXXX, XXX, XXX−XXX

(Figure 5). However, no exclusion criteria should be applied on the evolution of postsynaptic activity from 18 DIV to 20 DIV, as the loss of connections between the presynaptic and postsynaptic chambers could naturally affect the activity levels in the postsynaptic chamber.

■ CONCLUSIONS

Models to assay synaptotoxicity of biological agents are crucially needed not only to decipher the pathophysiological pathways involved in AD and other neurodegenerative disorders, but also to evaluate the involvement of genetic risk factors in synaptic vulnerability and to test therapeutic strategies. We believe that the functional assay we demonstrated in this study will be particularly helpful to answer such questions, since each synaptic compartment can be individually targeted and the functional impact can be easily evaluated. However, we would like to emphasize the importance of performing a preselection of microfluidic devices exhibiting a robust interchamber connectivity to ensure a good reproducibility. Defining specific inclusion/exclusion criteria that take into account the neuronal activity in the presynaptic chamber could also be considered for an improved experimental model.

■ ASSOCIATED CONTENT

Supporting Information

The Supporting Information is available free of charge at https://pubs.acs.org/doi/10.1021/acsbiomaterials.3c00997.

Additional materials and methods, and six supplementary Figures: Figure S1: design of the microfluidic device we adapted to the commercial MEA; Figure S2: limited diffusion to the presynaptic and postsynaptic chambers of a fluorescent dye, and by extension, Aβ when applied into the synaptic chamber under the conditions we used during the Aβ-induced synaptotoxicity assay; Figure S3: neuronal activity features in the presynaptic and the postsynaptic chambers before treatment; Figure S4 and S5: results of the bursting analyses displayed in Figure 3 if an alternative set of parameters are used for the burst detection via the *MaxInterval* algorithm or if the *Surprise* algorithm is used; Figure S6: results of the interchamber connectivity measures for the control chips at 18 DIV and its evolution if an interval of 5 or 20 ms is used to calculate the conditional probability of a spike in the postsynaptic chamber immediately after a spike occurring in the presynaptic chamber (PDF)

■ AUTHOR INFORMATION

Corresponding Authors

Devrim Kilinc − *Université de Lille, Institut Pasteur de Lille, CHU Lille, INSERM U1167, LabEx DISTALZ, 59019 Lille, France*; orcid.org/0000-0003-3321-5203; Email: devrim.kilinc@pasteur-lille.fr

Sophie Halliez − *Université de Lille, Inserm, CHU Lille, U1172 - LilNCog - Lille Neuroscience & Cognition, F-59000 Lille, France*; orcid.org/0000-0002-6173-9752; Email: sophie.halliez@univ-lille.fr

Authors

Camille Lefebvre − *Université de Lille, Inserm, CHU Lille, U1172 - LilNCog - Lille Neuroscience & Cognition, F-59000 Lille, France*

Anaïs-Camille Vreulx − *Université de Lille, Institut Pasteur de Lille, CHU Lille, INSERM U1167, LabEx DISTALZ, 59019 Lille, France*

Corentin Dumortier − *Université de Lille, Inserm, CHU Lille, U1172 - LilNCog - Lille Neuroscience & Cognition, F-59000 Lille, France*

Séverine Bégard − *Université de Lille, Inserm, CHU Lille, U1172 - LilNCog - Lille Neuroscience & Cognition, F-59000 Lille, France*

Carla Gelle − *Université de Lille, Institut Pasteur de Lille, CHU Lille, INSERM U1167, LabEx DISTALZ, 59019 Lille, France*

Dolores Siedlecki-Wullich − *Université de Lille, Institut Pasteur de Lille, CHU Lille, INSERM U1167, LabEx DISTALZ, 59019 Lille, France*; orcid.org/0000-0002-9099-9406

Morvane Colin − *Université de Lille, Inserm, CHU Lille, U1172 - LilNCog - Lille Neuroscience & Cognition, F-59000 Lille, France*

Complete contact information is available at: https://pubs.acs.org/10.1021/acsbiomaterials.3c00997

Funding

This work was supported by the European Union under the European Regional Development Fund (ERDF) and by the Hauts de France Regional Council (contract 20000007), the MEL (contract_2020_ESR_02), the French State (contract n°2019-R3-CTRL_IPL_Phase3), Fondation Vaincre Alzheimer (FR-17006p), the ERC IONOS, the French government's LABEX DISTALZ program (Development of innovative strategies for a transdisciplinary approach to Alzheimer's disease), and the Joint Inserm-University Chairs program. This work was also supported by the French RENATECH network (P-18−02737).

Notes

The authors declare no competing financial interest.

■ ACKNOWLEDGMENTS

CHO cell lines were a kind gift from Dr. Frédéric Checler at the IPMC Sophia Antipolis. The authors thank Dr. Karine Blary at the IEMN Lille for the microfabrication work. The authors also thank the animal care staff of the EOPS facility (UMS-2014 US41 PLBS).

■ ABBREVIATIONS

AD, Alzheimer's disease; Aβ, amyloid-β peptides; NFTs, neurofibrillary tangles; APP, amyloid precursor protein; APP^{WT}, wild-type APP; APP^{LDN}, APP with V717I "London" mutation; MEA, microelectrode array; CHO, Chinese hamster ovary; DIV, days *in vitro*

■ REFERENCES

(1) Ittner, L. M.; Ke, Y. D.; Delerue, F.; Bi, M.; Gladbach, A.; van Eersel, J.; Wölfing, H.; Chieng, B. C.; Christie, M. J.; Napier, I. A.; Eckert, A.; Staufenbiel, M.; Hardeman, E.; Götz, J. Dendritic Function of Tau Mediates Amyloid-Beta Toxicity in Alzheimer's Disease Mouse Models. *Cell* **2010**, *142* (3), 387−397.

(2) Lee, A.; Kondapalli, C.; Virga, D. M.; Lewis, T. L.; Koo, S. Y.; Ashok, A.; Mairet-Coello, G.; Herzig, S.; Foretz, M.; Viollet, B.; Shaw, R.; Sproul, A.; Polleux, F. Aβ42 Oligomers Trigger Synaptic Loss through CAMKK2-AMPK-Dependent Effectors Coordinating Mitochondrial Fission and Mitophagy. *Nat. Commun.* **2022**, *13* (1), 4444.

(3) Sciaccaluga, M.; Megaro, A.; Bellomo, G.; Ruffolo, G.; Romoli, M.; Palma, E.; Costa, C. An Unbalanced Synaptic Transmission: Cause or Consequence of the Amyloid Oligomers Neurotoxicity? *Int. J. Mol. Sci.* **2021**, *22* (11), 5991.
(4) Zempel, H.; Luedtke, J.; Kumar, Y.; Biernat, J.; Dawson, H.; Mandelkow, E.; Mandelkow, E.-M. Amyloid-β Oligomers Induce Synaptic Damage via Tau-Dependent Microtubule Severing by TTLL6 and Spastin. *EMBO J.* **2013**, *32* (22), 2920−2937.
(5) Zott, B.; Simon, M. M.; Hong, W.; Unger, F.; Chen-Engerer, H.-J.; Frosch, M. P.; Sakmann, B.; Walsh, D. M.; Konnerth, A. A Vicious Cycle of β Amyloid-Dependent Neuronal Hyperactivation. *Science* **2019**, *365* (6453), 559−565.
(6) Busche, M. A.; Hyman, B. T. Synergy between Amyloid-β and Tau in Alzheimer's Disease. *Nat. Neurosci.* **2020**, *23* (10), 1183−1193.
(7) Roberson, E. D.; Halabisky, B.; Yoo, J. W.; Yao, J.; Chin, J.; Yan, F.; Wu, T.; Hamto, P.; Devidze, N.; Yu, G.-Q.; Palop, J. J.; Noebels, J. L.; Mucke, L. Amyloid-β/Fyn-Induced Synaptic, Network, and Cognitive Impairments Depend on Tau Levels in Multiple Mouse Models of Alzheimer's Disease. *J. Neurosci. Off. J. Soc. Neurosci.* **2011**, *31* (2), 700−711.
(8) van Dyck, C. H.; Swanson, C. J.; Aisen, P.; Bateman, R. J.; Chen, C.; Gee, M.; Kanekiyo, M.; Li, D.; Reyderman, L.; Cohen, S.; Froelich, L.; Katayama, S.; Sabbagh, M.; Vellas, B.; Watson, D.; Dhadda, S.; Irizarry, M.; Kramer, L. D.; Iwatsubo, T. Lecanemab in Early Alzheimer's Disease. *N. Engl. J. Med.* **2023**, *388* (1), 9−21.
(9) Taylor, A. M.; Dieterich, D. C.; Ito, H. T.; Kim, S. A.; Schuman, E. M. Microfluidic Local Perfusion Chambers for the Visualization and Manipulation of Synapses. *Neuron* **2010**, *66* (1), 57−68.
(10) Kilinc, D.; Vreulx, A. C.; Mendes, T.; Flaig, A.; Marques-Coelho, D.; Verschoore, M.; Demiautte, F.; Amouyel, P.; Eysert, F.; Dourlen, P.; Chapuis, J.; Costa, M. R.; Malmanche, N.; Checler, F.; Lambert, J. C. Pyk2 Overexpression in Postsynaptic Neurons Blocks Amyloid B1−42-Induced Synaptotoxicity in Microfluidic Co-Cultures. *Brain Commun.* **2020**, *2* (2), fcaa139.
(11) Hong, S.; Beja-Glasser, V. F.; Nfonoyim, B. M.; Frouin, A.; Li, S.; Ramakrishnan, S.; Merry, K. M.; Shi, Q.; Rosenthal, A.; Barres, B. A.; Lemere, C. A.; Selkoe, D. J.; Stevens, B. Complement and Microglia Mediate Early Synapse Loss in Alzheimer Mouse Models. *Science* **2016**, *352* (6286), 712−716.
(12) Blasiak, A.; Kilinc, D.; Peyrin, J.-M. Subcellular Compartmentalization for Neurobiology: Focusing on the Axon. In *Handbook of Neuroengineering*; Thakor, N. V., Ed.; Springer: Singapore, 2020; pp 1−35. DOI: 10.1007/978-981-15-2848-4_1-1.
(13) Gladkov, A.; Pigareva, Y.; Kutyina, D.; Kolpakov, V.; Bukatin, A.; Mukhina, I.; Kazantsev, V.; Pimashkin, A. Design of Cultured Neuron Networks in Vitro with Predefined Connectivity Using Asymmetric Microfluidic Channels. *Sci. Rep.* **2017**, *7* (1), 15625.
(14) Kanagasabapathi, T. T.; Franco, M.; Barone, R. A.; Martinoia, S.; Wadman, W. J.; Decré, M. M. J. Selective Pharmacological Manipulation of Cortical-Thalamic Co-Cultures in a Dual-Compartment Device. *J. Neurosci. Methods* **2013**, *214* (1), 1−8.
(15) Poli, D.; Wheeler, B. C.; DeMarse, T. B.; Brewer, G. J. Pattern Separation and Completion of Distinct Axonal Inputs Transmitted via Micro-Tunnels between Co-Cultured Hippocampal Dentate, CA3, CA1 and Entorhinal Cortex Networks. *J. Neural Eng.* **2018**, *15* (4), No. 046009.
(16) Hong, N.; Joo, S.; Nam, Y. Characterization of Axonal Spikes in Cultured Neuronal Networks Using Microelectrode Arrays and Microchannel Devices. *IEEE Trans. Biomed. Eng.* **2017**, *64* (2), 492−498.
(17) Moutaux, E.; Charlot, B.; Genoux, A.; Saudou, F.; Cazorla, M. An Integrated Microfluidic/Microelectrode Array for the Study of Activity-Dependent Intracellular Dynamics in Neuronal Networks. *Lab. Chip* **2018**, *18* (22), 3425−3435.
(18) Wang, L.; Riss, M.; Buitrago, J. O.; Claverol-Tinturé, E. Biophysics of Microchannel-Enabled Neuron-Electrode Interfaces. *J. Neural Eng.* **2012**, *9* (2), No. 026010.
(19) Galas, M.-C.; Dourlen, P.; Bégard, S.; Ando, K.; Blum, D.; Hamdane, M.; Buée, L. The Peptidylprolyl Cis/Trans-Isomerase Pin1Modulates Stress-Induced Dephosphorylation of Tau in Neurons: IMPLICATION IN A PATHOLOGICAL MECHANISM RELATED TO ALZHEIMER DISEASE *. *J. Biol. Chem.* **2006**, *281* (28), 19296−19304.
(20) Guillot-Sestier, M.-V.; Sunyach, C.; Ferreira, S. T.; Marzolo, M.-P.; Bauer, C.; Thevenet, A.; Checler, F. α-Secretase-Derived Fragment of Cellular Prion, N1, Protects against Monomeric and Oligomeric Amyloid β (Aβ)-Associated Cell Death. *J. Biol. Chem.* **2012**, *287* (7), 5021−5032.
(21) Taylor, A. M.; Blurton-Jones, M.; Rhee, S. W.; Cribbs, D. H.; Cotman, C. W.; Jeon, N. L. A Microfluidic Culture Platform for CNS Axonal Injury, Regeneration and Transport. *Nat. Methods* **2005**, *2* (8), 599−605.
(22) Bouillet, T.; Ciba, M.; Alves, C. L.; Rodrigues, F. A.; Thielemann, C.; Colin, M.; Buée, L.; Halliez, S. Revisiting the Involvement of Tau in Complex Neural Network Remodeling: Analysis of the Extracellular Neuronal Activity in Organotypic Brain Slice Co-Cultures. *J. Neural Eng.* **2022**, *19* (6). 066026.
(23) Habibey, R.; Golabchi, A.; Blau, A. Microchannel Scaffolds for Neural Signal Acquisition and Analysis. In *Neurotechnology, Electronics, and Informatics: Revised selected papers from Neurotechnix 2013*; Londral, A. R.; Encarnacao, P.; Rovira, J. L. P., Eds.; Springer Series in Computational Neuroscience; Springer: New York, 2015; Vol. *13*, pp 47−64. DOI: 10.1007/978-3-319-15997-3_4.
(24) Cotterill, E.; Eglen, S. J. Burst Detection Methods. In *In Vitro Neuronal Networks: From Culturing Methods to Neuro-Technological Applications*; Chiappalone, M.; Pasquale, V.; Frega, M., Eds.; Advances in Neurobiology; Springer International Publishing: Cham, 2019; pp 185−206. DOI: 10.1007/978-3-030-11135-9_8.
(25) Legéndy, C. R.; Salcman, M. Bursts and Recurrences of Bursts in the Spike Trains of Spontaneously Active Striate Cortex Neurons. *J. Neurophysiol.* **1985**, *53* (4), 926−939.
(26) Susloparova, A.; Halliez, S.; Begard, S.; Colin, M.; Buee, L.; Pecqueur, S.; Alibart, F.; Thomy, V.; Arscott, S.; Pallecchi, E.; Coffinier, Y. Low Impedance and Highly Transparent Microelectrode Arrays (MEA) for in Vitro Neuron Electrical Activity Probing. *Sens. Actuators B-Chem.* **2021**, *327*, No. 128895.
(27) Corbett, G. T.; Wang, Z.; Hong, W.; Colom-Cadena, M.; Rose, J.; Liao, M.; Asfaw, A.; Hall, T. C.; Ding, L.; DeSousa, A.; Frosch, M. P.; Collinge, J.; Harris, D. A.; Perkinton, M. S.; Spires-Jones, T. L.; Young-Pearse, T. L.; Billinton, A.; Walsh, D. M. PrP Is a Central Player in Toxicity Mediated by Soluble Aggregates of Neurodegeneration-Causing Proteins. *Acta Neuropathol. (Berl.)* **2020**, *139* (3), 503−526.
(28) Evans, N. A.; Facci, L.; Owen, D. E.; Soden, P. E.; Burbidge, S. A.; Prinjha, R. K.; Richardson, J. C.; Skaper, S. D. Aβ1−42 Reduces Synapse Number and Inhibits Neurite Outgrowth in Primary Cortical and Hippocampal Neurons: A Quantitative Analysis. *J. Neurosci. Methods* **2008**, *175* (1), 96−103.
(29) Cirrito, J. R.; May, P. C.; O'Dell, M. A.; Taylor, J. W.; Parsadanian, M.; Cramer, J. W.; Audia, J. E.; Nissen, J. S.; Bales, K. R.; Paul, S. M.; DeMattos, R. B.; Holtzman, D. M. In Vivo Assessment of Brain Interstitial Fluid with Microdialysis Reveals Plaque-Associated Changes in Amyloid-β Metabolism and Half-Life. *J. Neurosci.* **2003**, *23* (26), 8844−8853.
(30) Herukka, S. K.; Rummukainen, J.; Ihalainen, J.; von und zu Fraunberg, M.; Koivisto, A. M.; Nerg, O.; Puli, L. K.; Seppälä, T. T.; Zetterberg, H.; Pyykkö, O. T.; Helisalmi, S.; Tanila, H.; Alafuzoff, I.; Hiltunen, M.; Rinne, J.; Soininen, H.; Jääskeläinen, J. E.; Leinonen, V. Amyloid-β and Tau Dynamics in Human Brain Interstitial Fluid in Patients with Suspected Normal Pressure Hydrocephalus. *J. Alzheimers Dis.* **2015**, *46* (1), 261−269.
(31) Bateman, R. J.; Munsell, L. Y.; Morris, J. C.; Swarm, R.; Yarasheski, K. E.; Holtzman, D. M. Human Amyloid-Beta Synthesis and Clearance Rates as Measured in Cerebrospinal Fluid in Vivo. *Nat. Med.* **2006**, *12* (7), 856−861.
(32) Patterson, B. W.; Elbert, D. L.; Mawuenyega, K. G.; Kasten, T.; Ovod, V.; Ma, S.; Xiong, C.; Chott, R.; Yarasheski, K.; Sigurdson, W.; Zhang, L.; Goate, A.; Benzinger, T.; Morris, J. C.; Holtzman, D.;

Bateman, R. J. Age and Amyloid Effects on Human CNS Amyloid-Beta Kinetics. *Ann. Neurol.* **2015**, *78* (3), 439–453.
(33) Berry, B. J.; Smith, A. S. T.; Long, C. J.; Martin, C. C.; Hickman, J. J. Physiological Aβ Concentrations Produce a More Biomimetic Representation of the Alzheimer's Disease Phenotype in IPSC Derived Human Neurons. *ACS Chem. Neurosci.* **2018**, *9* (7), 1693–1701.

https://doi.org/10.1021/acsbiomaterials.3c00997
ACS Biomater. Sci. Eng. XXXX, XXX, XXX–XXX

Title: Integration of Microfluidic Devices with Microelectrode Arrays to Functionally Assay Amyloid-β-Induced Synaptotoxicity

Authors: Camille Lefebvre,[1] Anaïs-Camille Vreulx,[2] Corentin Dumortier,[1] Séverine Bégard,[1] Carla Gelle,[2] Dolores Siedlecki-Wullich,[2] Morvane Colin,[1] Devrim Kilinc*[,2] and Sophie Halliez*[,1]

[1]Université de Lille, Inserm, CHU Lille, U1172 - LilNCog - Lille Neuroscience & Cognition, F-59000 Lille, France

[2]Université de Lille, Institut Pasteur de Lille, CHU Lille, INSERM U1167, LabEx DISTALZ, Lille 59019, France

***Email:** devrim.kilinc@pasteur-lille.fr

***Email:** sophie.halliez@univ-lille.fr

8 pages, 6 figures

Estimation of the Aβ diffusion from the synaptic chamber to the presynaptic and postsynaptic chambers during the Aβ-induced synaptotoxicity assay

The test was performed on chips bonded onto FluoroDishes (FD5040-100; WPI; Sarasota, FL) seeded beforehand with cortical cells into the presynaptic and postsynaptic chambers. We applied dextran(4 kDa)-FITC (FluoProbes) at 5 mg/mL into the synaptic chamber and we created a volume difference between the reservoirs serving the synaptic chamber and the reservoirs serving the presynaptic and postsynaptic chambers just as we did during the Aβ-induced synaptotoxicity assay. The presynaptic and postsynaptic chambers were imaged at t = 0, 3, 6, 9, 16 and 24 h using an inverted microscope (Leica DM IL LED Fluo) equipped with a camera (Leica MC120 HD) and with a 20x lens. The *Measure*

tool of the ImageJ software was used to quantify the fluorescence intensity in each chamber. The mean pixel value in the synaptic chamber (minus background) at t = 0 was assigned to 100 %, corresponding to the 85 nM of Aβ applied into the synaptic chamber during the Aβ-induced synaptotoxicity assay. The fluorescence intensity in the presynaptic and postsynaptic chambers overtime was normalized by the 100% value, and then we used it to estimate the Aβ diffusion from the synaptic chamber to the presynaptic and postsynaptic chambers during the Aβ-induced synaptotoxicity assay.

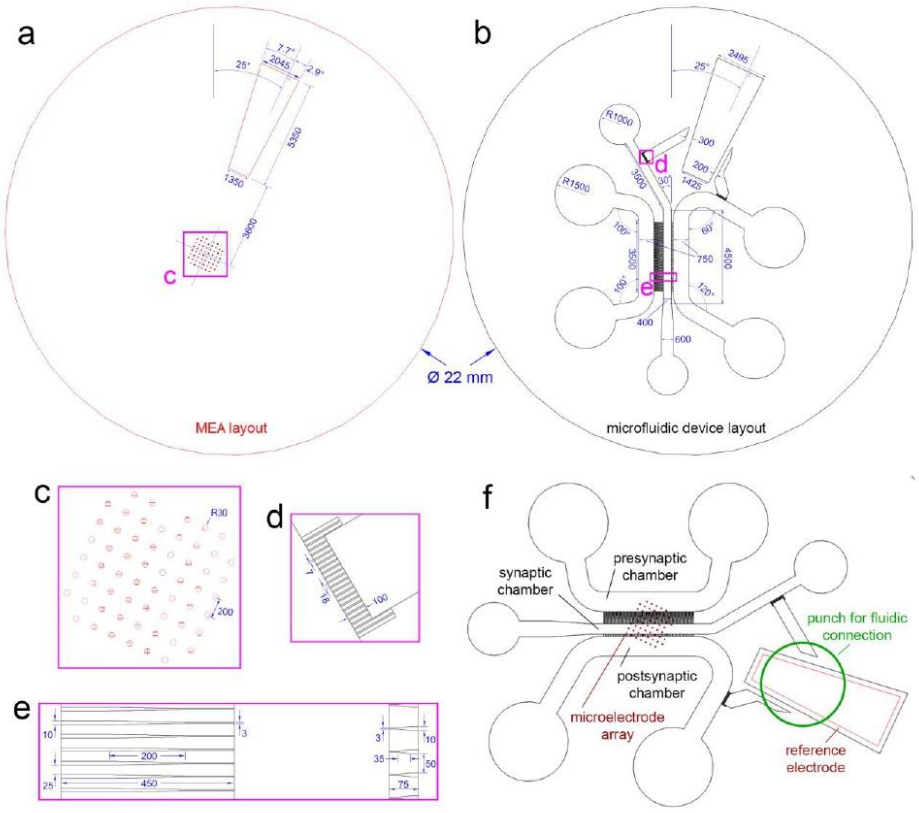

Figure S1: Design of the microfluidic device adapted to the commercial MEA

(a, b) Technical drawings of the commercial MEA (a) and the adapted microfluidic device (b). All dimensions are given in micrometers. (c) Detail of panel a. (d, e) Details of panel b. (f) Microfluidic

device design with the recording microelectrodes and the reference electrode underneath. Ground connection is guaranteed by punching a medium reservoir at the location indicated by the green circle.

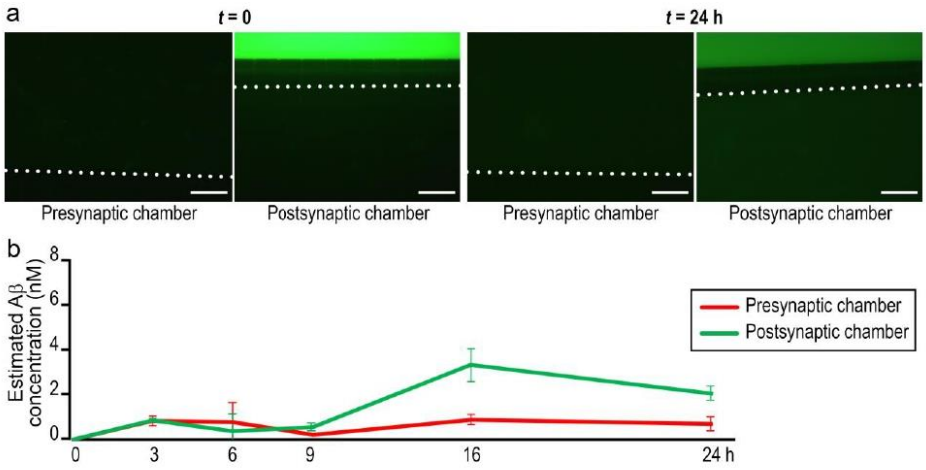

Figure S2: Estimation of the Aβ diffusion from the synaptic chamber to the presynaptic and postsynaptic chambers during the Aβ-induced synaptotoxicity assay

Dextran-FITC was applied into the synaptic chamber under the same conditions we used during the Aβ-induced synaptotoxicity assay and its diffusion to the presynaptic and postsynaptic chambers was monitored over 24 h. In (a) are shown the presynaptic and postsynaptic chambers, delimited by dotted lines, at, respectively, t = 0 and t = 24 h. The fluorescence intensity measured in the presynaptic and postsynaptic chambers overtime were used to estimate the diffusion of the Aβ applied into the synaptic chamber to the presynaptic and postsynaptic chambers during the Aβ-induced synaptotoxicity assay (b). Scale bar: 100 μm.

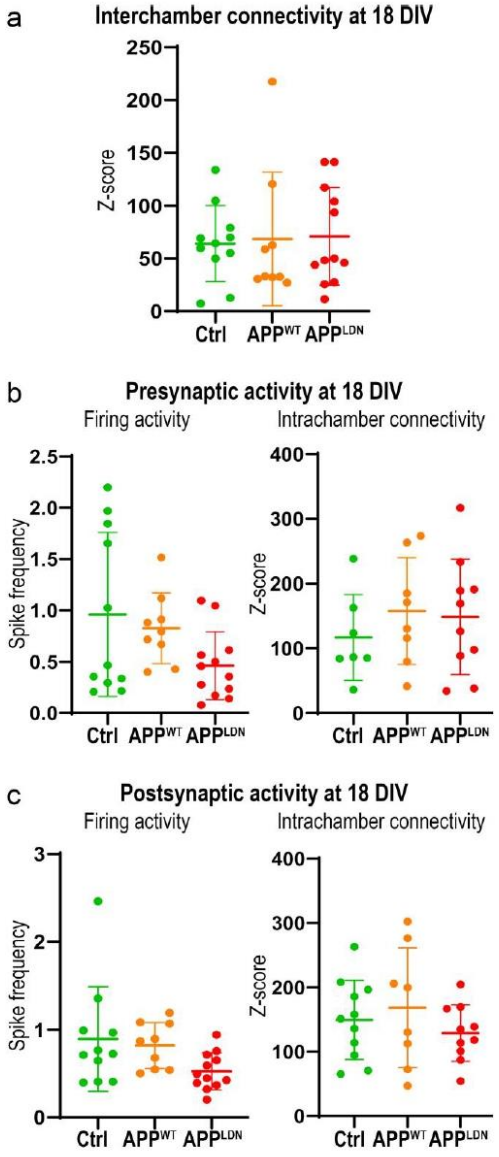

Figure S3: Neuronal activity features before treatment

(a) Estimation of the interchamber connectivity at 18 DIV, *i.e.*, before treatment. The interchamber connectivity is estimated through the calculation of a Z-score. n = 11, 9 and 12 chips before treatment with concentrated conditioned media from, respectively, control (green), APP^{WT} (orange) and APP^{LDN}

(red) CHO cells. Comparisons between control and other groups were performed using Dunn's test with Bonferroni correction. (b, c) Neuronal activity given for neurons in the presynaptic (b) and postsynaptic (c) chambers at 18 DIV. Two neuronal activity measures are displayed: the mean spike frequency (left) and an estimation of the intrachamber connectivity (mean cross-correlation Z-score, right). The analysis was performed on the same devices as in (a). Comparisons between control and other groups were performed using Dunn's test with Bonferroni correction.

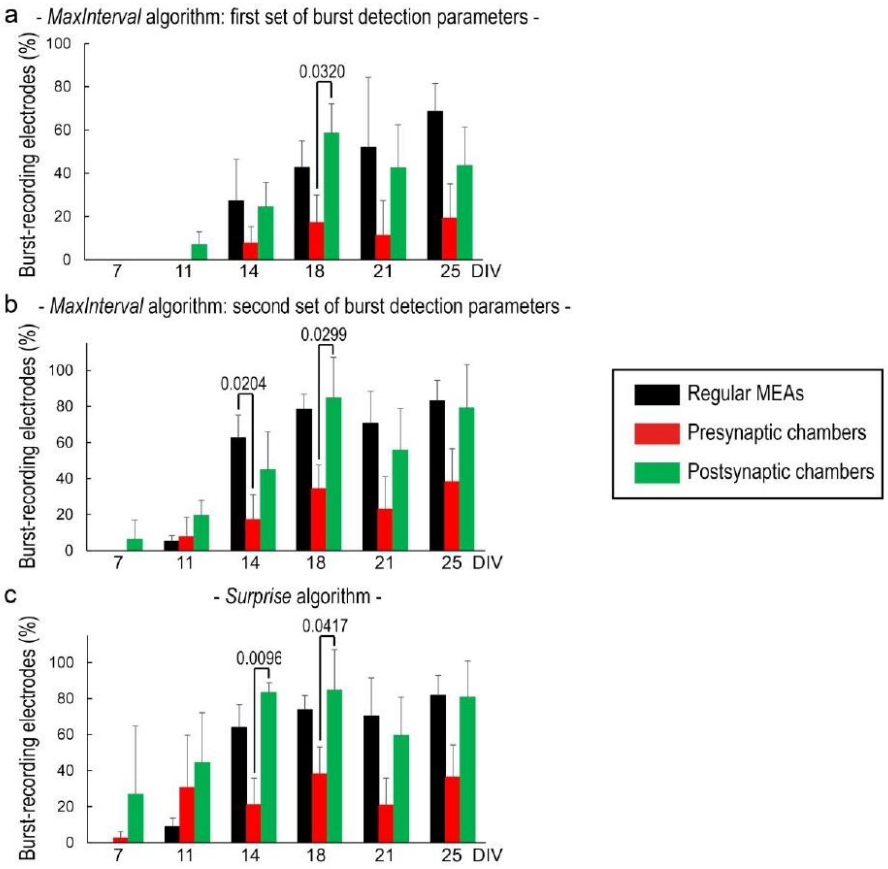

Figure S4: Percentage of burst-recording electrodes for networks derived from primary cortical cells seeded in regular MEAs or MEA-integrated microfluidic devices using the *MaxInterval* algorithm with two different sets of burst detection parameters and the *Surprise* algorithm

Spontaneous firing activity was measured using extracellular recordings of cortical cells grown on regular MEAs (black) or in the presynaptic (red) or postsynaptic (green) chambers of the MEA-integrated microfluidic devices, and measures of the bursting activity were extracted. Two different algorithms were used : the *MaxInterval* algorithm (a, b) and the *Surprise* algorithm (c) and two different sets of parameters were used for burst detection *via* the *MaxInterval* algorithm. Mean percentages of burst-recording electrodes are shown for recordings acquired from the same devices at 7, 11, 14, 18, 21 and 25 DIV. Error bars show standard error of the mean. n = 4 for each condition. Comparisons among all groups were performed using Dunn's test with Bonferroni correction.

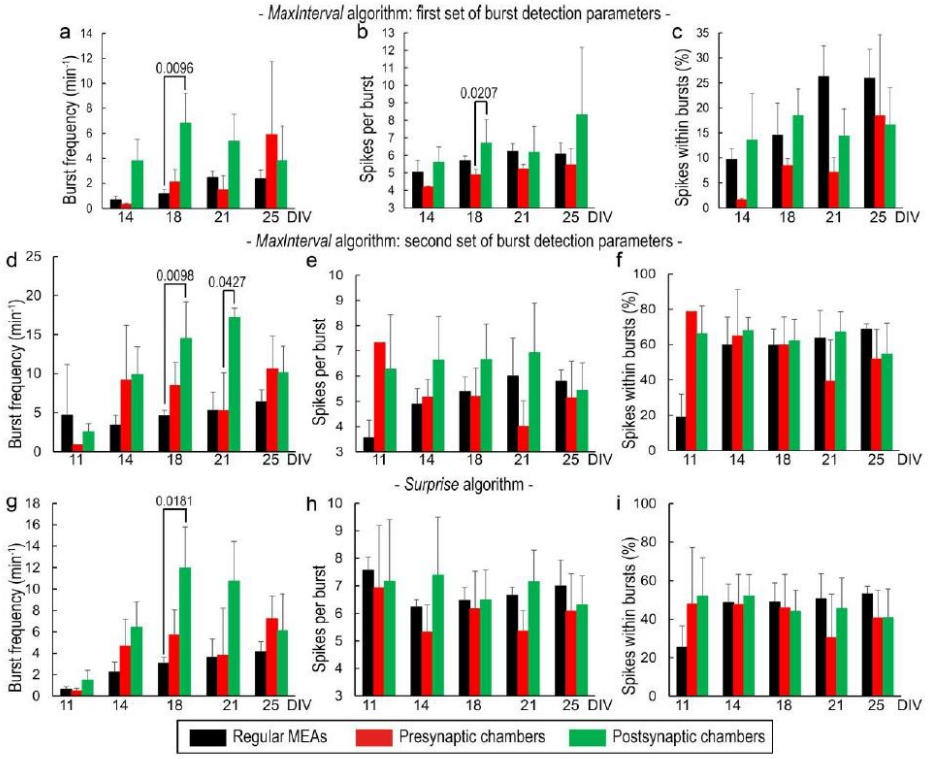

Figure S5: Measures of the spontaneous bursting activity of networks derived from primary cortical cells seeded in regular MEAs or MEA-integrated microfluidic devices using the *MaxInterval* algorithm with two different sets of burst detection parameters and the *Surprise* algorithm

Firing activity was measured using extracellular recordings of cortical cells grown on regular MEAs (black) or in the presynaptic (red) or postsynaptic (green) chambers of the MEA-integrated microfluidic devices, and measures of the bursting activity were extracted. Two different algorithms were used : the *MaxInterval* algorithm (a-f) and the *Surprise* algorithm (g-i) and two different sets of parameters were used for burst detection *via* the *MaxInterval* algorithm. The following measures of burst activity (mean values) are shown for recordings at 11, 14, 18, 21 and 25 DIV: number of bursts per minute (a, d, g), number of spikes per burst (b, e, h), and percentage of spikes within bursts (c, f, i). Error bars show standard error of the mean. n = 4 for each condition. Comparisons among all groups were performed using Dunn's test with Bonferroni correction.

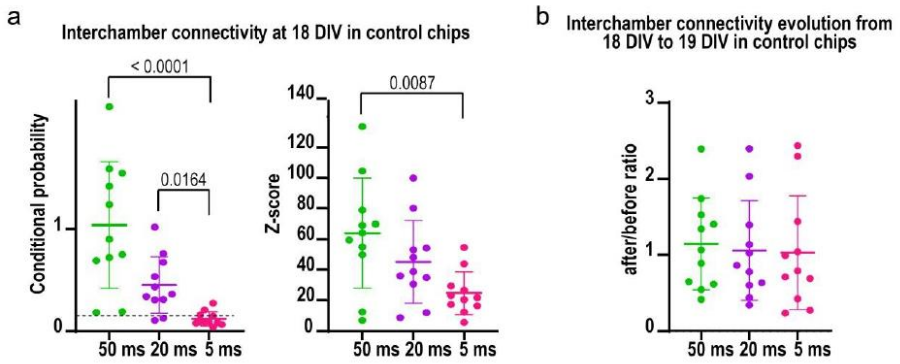

Figure S6: Interchamber connectivity measures and evolution for control chips for varying time intervals (thresholds)

(a) Estimation of the interchamber connectivity for the control chips at 18 DIV through the calculation of the conditional probability of a spike in the postsynaptic chamber immediately after a spike occurring in the presynaptic chamber. Three time intervals were used for the calculation: 50 milliseconds (the value we used in the present study), 20 milliseconds and 5 milliseconds. The data are shown raw (left) and normalized by the expected probability, i.e., as if presynaptic and postsynaptic neurons were not connected but randomly fired at the firing rates we measured (right). n = 11, (b) Evolution of interchamber connectivity from 18 DIV to 19 DIV in the control chips. Evolution of interchamber connectivity is defined as after/before ratios of the mean Z-scores. n = 11. Comparisons between all the groups were performed using Dunn's test with Bonferroni correction.

Neuronal downregulation of *PLCG2* impairs synaptic function and elicits Alzheimer disease hallmarks

Audrey Coulon[1]†, Florian Rabiller[1]†, Mari Takalo[2]†, Avishek Roy[3]†, Henna Martiskainen[2]†, Dolores Siedlecki-Wullich[1], Tiago Mendes[1], Celia Lemeu[1], Lukas-Iohan Carvalho[1], Anaël Ehrardt[3], Ana Raquel Melo de Farias[1], Marc Hulsman[4-7], Chloé Najdek[1], Nina Lannette-Weimann[1], Alejandra Freire-Regatillo[1], Philippe Amouyel[1], Camille Charbonnier[8], Orio Dols-Icardo[9,10], Heli Jeskanen[2], Roosa-Maria Willman[2], Teemu Kuulasmaa[2], Mitja Kurki[11], John Hardy[12], Richard Wagner, Sami Heikkinen[2], Henne Holstege[4-7], Petra Mäkinen[2], Gaël Nicolas[13], Simon Mead[14], Michael Wagner[15,16], Alfredo Ramirez[15-19], Tuomas Rauramaa[20], Aarno Palotie[11], Rebecca Sims[21], Hilkka Soininen[22], John van Swieten[23], Julie Williams[21], Céline Bellenguez[1], Benjamin Grenier-Boley[1], Carla Gelle[1], Erwan Lambert[1], Anne-Marie Ayral[1], Florie Demiautte[1], Marcos R. Costa[1,24], Séverine Deforges[3], Devrim Kilinc[1], Christophe Mulle[3]‡ Julien Chapuis[1]‡, Mikko Hiltunen[2]‡, Julie Dumont[1]‡#, Jean-Charles Lambert[1]‡#

[1] Univ. Lille, Inserm, CHU Lille, Institut Pasteur de Lille, U1167 - RID-AGE - Facteurs de risque et déterminants moléculaires des maladies liées au vieillissement, Lille, France

[2] Institute of Biomedicine, University of Eastern Finland, Kuopio, Finland

[3] Interdisciplinary Institute for Neuroscience, CNRS UMR 5297, University of Bordeaux, Bordeaux, France

[4] Genomics of Neurodegenerative Diseases and Aging, Human Genetics, Vrije Universiteit Amsterdam, Amsterdam UMC location VUmc, Amsterdam, the Netherlands

[5] Alzheimer Center Amsterdam, Neurology, Vrije Universiteit Amsterdam, Amsterdam UMC location VUmc, Amsterdam, the Netherlands

[6] Amsterdam Neuroscience, Neurodegeneration, Amsterdam, the Netherlands

[7] Delft Bioinformatics Lab, Delft University of Technology, Delft, the Netherlands

[8] Univ Rouen Normandie, Inserm U1245 and CHU Rouen, Department of Biostatistics and CNRMAJ, F-76000 Rouen, France

[9] Department of Neurology, II B Sant Pau, Hospital de la Santa Creu i Sant Pau, Universitat Autonota de Barcelona, Barcelona, Spain

[10] Biomedical Research Networking Center on Neurodegenerative Diseases, National Institute of Health Carlos III, Madrid, Spain

[11] Institute for Molecular Medicine Finland, University of Helsinki, Helsinki, Finland.

[12] Reta Lila Weston Research Laboratories, Department of Molecular Neuroscience, University College London Institute of Neurology, London, UK

[13] Univ Rouen Normandie, Inserm U1245 and CHU Rouen, Department of Genetics and CNRMAJ, F-76000 Rouen, France

[14] Medical Research Council Prion Unit at University College London, University College London Institute of Prion Diseases, London, UK

[15] Department of Cognitive Disorders and Old Age Psychiatry, University Hospital Bonn, Medical Faculty, Bonn, Germany

[16] German Center for Neurodegenerative Diseases, Bonn, Germany

[17] Division of Neurogenetics and Molecular Psychiatry, Department of Psychiatry and Psychotherapy, Faculty of Medicine and University Hospital Cologne, University of Cologne, Cologne, Germany

[18] Department of Psychiatry and Glenn Biggs Institute for Alzheimer's and Neurodegenerative Diseases, San Antonio, TX, USA

[19] Cologne Excellence Cluster on Cellular Stress Responses in Aging-Associated Disease (CECAD), University of Cologne, Cologne, Germany

[20] Department of Pathology, Kuopio University Hospital, Kuopio, Finland and Unit of Pathology, Institute of Clinical Medicine, University of Eastern Finland, Kuopio, Finland

[21] Medical Research Council Centre for Neuropsychiatric Genetics and Genomics, Division of Psychological Medicine and Clinical Neuroscience, School of Medicine, Cardiff University, Cardiff, UK

[22] Department of Neurology, University of Eastern Finland, Kuopio, Finland

[23] Department of Neurology, Erasmus Medical Centre, Rotterdam, the Netherlands

[24] Brain Institute, Federal University of Rio Grande do Norte, Natal, Brazil

† Contributed equally as co-first author

‡ Contributed equally as co-last author

[#] Address correspondence to: julie.dumont@univ-lille.fr, jean-charles.lambert@pasteur-lille.fr

ABSTRACT

We developed a high content screening to investigate how Alzheimer disease (AD) genetic risk factors may impair synaptic mechanisms in rat primary neuronal cultures. Out of the gene targets identified, we found that shRNA-mediated downregulation of *Plcg2* in mouse dentate gyrus neurons consistently impaired dendritic morphology and synaptic function. In human neuronal cultures (hNCs), *PLCG2* downregulation also impaired synaptic function and was associated with increased levels of Aβ and Tau phosphorylation, potentially *via* the AKT/GSK3β axis. Very rare *PLCG2* loss-of-function (LoF) variants were associated with a 10-fold increased AD risk. *PLCG2* LoF carriers exhibit low mRNA/protein *PLCG2/*PLCγ2 levels, consistent with nonsense-mediated mRNA decay mechanisms. Restoring PLCγ2 levels in shPLCG2-hNCs fully reversed the disease-related phenotypes. Our findings indicate that the downregulation of PLCγ2 increases the risk of AD by impairing synaptic function and increasing the levels of Aβ and Tau phosphorylation in neurons.

Key words: Alzheimer's disease, *PLCG2*, synapse, high-content screening, patch-clamp, iPSCs, GSK3β, Tau, microelectrode arrays

INTRODUCTION

Alzheimer's disease (AD) is characterized by intracellular aggregation of abnormally hyperphosphorylated Tau protein and extracellular accumulation of amyloid-beta (Aβ) in plaques. According to the "amyloid cascade hypothesis", Aβ aggregation is an early toxic condition that can induce Tau aggregation and neuronal death. However, while recent clinical studies using anti-Aβ therapies in principle support this hypothesis (*1*), it has been regularly modified to reflect the advancements in our understanding of AD (*2, 3, 4*). It is now well accepted that the amyloid cascade hypothesis appears to be over-simplistic and fails to account for the intricacy and heterogeneity of the pathophysiological processes involved in the common forms of the disease.

Since the proportion of risk attributable to genetic susceptibility factors for AD has been estimated to be between 60% and 80% in twin studies (*5*), defining the AD genetic component has been considered as a means of gaining a better understanding of the pathophysiological processes and generating complementary or alternative hypotheses. The development of genome-wide association studies (GWASs) and high-throughput sequencing has considerably advanced the AD genetic landscape over the last fifteen years, leading to the characterization of 76 loci associated with the AD risk (*6–8*). Based on this new genetic landscape of AD, we and others developed parallel approaches employing systematic post-GWAS studies. Beyond inflammation processes, we also proposed synaptic fragility/sensitivity as a pathological trigger, depending on genetic risk factors, some of which have already been linked to synaptic mechanisms, such as BIN1, FERMT2, PTK2B or CD2AP. (*9–12*). This notion fits with key clinical observations suggesting that synapse dysfunction/loss is (i) one of the earliest pathological hallmarks in the brain before hippocampal neuronal death and (ii) the strongest marker of cognitive decline (for a review, see (*13–15*)). Within this background, we systematically addressed the potential implication of the genes located in the loci associated with AD risk (as reported in (*6*)) in synaptic mechanisms. For this purpose, we developed a high-content screening (HCS) approach to systematically analyze the impact of the downregulation of a large number of AD risk genes on synaptic density and to reveal the potential implication of these genes in synaptic function.

RESULTS

HCS identifies GWAS-defined genes as potential modulators of synapse density

We developed a HCS approach to systematically characterize the effect on synaptic density of 198 genes located in the 76 loci associated with AD risk and selected as being expressed in brain cells (according to publicly available RNAseq datasets, see Material and Methods). A lentiviral shRNA library targeting these 198 genes was developed. The screen was performed in 384-well plates using rat hippocampal primary neuronal cultures (PNCs) transduced at day 1 in vitro (DIV1) using two multiplicities of infection (MOI 2 and 4, **Fig. 1a, b**). Immunocytochemistry was conducted at DIV21 against Synaptophysin 1 (Syp), Homer1 and Map2, pre-synaptic, post-synaptic and somatodendritic markers, respectively (**Fig. 1d, e**) (*16*). Synaptic density was then assessed via a high-content analysis workflow by assigning each post-synaptic structure to the nearest pre-synaptic structure, as previously described (*17*). Non-targeting shRNA (shNT) and shRNA against Syp (shSyp) were used as controls. The complete HCS results are presented in **Table S1**. We selected AD risk genes with the strongest effect on synaptic density (top and bottom 2.5%) in three independent experiments, resulting in five genes (*Usp6nl*, *Psmc3*, *Plcg2*, *Csnk1g1*, *Cyb561*) associated with lower synaptic density and four genes (*Snx1*, *Ica1l*, *Oplah* and *Nck2*) associated with higher synaptic density when downregulated (**Fig. 1c**). For these

nine genes, we confirmed the impact of shRNA-mediated downregulation on protein levels in PNCs (**Fig. 1f, g**). In conclusion, HCS allowed us to identify several genes located within the loci associated with AD risk that strongly modulate synaptic density in rat PNCs.

GWAS-defined genes, including *Plcg2*, impact electrophysiological properties of PNCs

We first determined whether proteins encoded by the nine selected genes could be detected in synaptosomes purified from PNCs (**Fig. S1**). Except for Cyb561 (data not shown), we detected their presence in the PSD95 and/or non-PSD95 fractions. We then analyzed the impact of their downregulation on the electrophysiological properties of mature PNCs (at DIV21) using multielectrode arrays (MEAs). As a positive control, the downregulation of *Syp* showed significant decreases in the mean spike and burst frequencies, two read-outs for neuronal activity (**fig. 1h** and **1i,** respectively). Similarly, the downregulation of *Usp6nl* and *Plcg2* significantly decreased the mean spike and burst frequencies. These results are of particular interest since *Plcg2* was believed to be almost only expressed in microglia and, as a consequence, this AD risk gene was almost exclusively investigated in this cell type (*18*–*21*). Thus, we focused on *Plcg2*, which is also expressed in glutamatergic neurons as evidenced by publicly available single nuclei RNA sequencing (snRNA) datasets from mouse hippocampus (*22*), human brain (*23*) and snRNAseq datasets generated in-house using human brain organoids (*24*)(**Fig. S2**).

***Plcg2* downregulation in the mouse dentate gyrus reduces dendritic arborization complexity and spine density of granule cells**

Plcg2/PLCG2 is highly expressed in the mouse and human dentate gyrus (DG) (*25*), which is the main gateway from the entorhinal cortex inputs to the hippocampus. Synaptic plasticity in the DG is strongly affected in mouse models of AD (*26*, *27*). Lentiviral vectors encoding either an shRNA against *Plcg2* (LV-shPLCG2) or a non-targeting control shRNA (LV-shNT), combined with GFP were injected in the dorsal hippocampus of adult mice of both sexes in the ipsi- (LV-shPLCG2) and contra-lateral (LV-shNT) hemispheres, respectively (**Fig. 2a and Fig. S3**). An analysis on GFP fluorescence images of DG neurons from shNT (n=35 neurons) and shPLCG2 (n=42 neurons) injected mice (**Fig. 2b)** revealed that *Plcg2* downregulation resulted in a reduction in dendritic length (shNT = 148±12 µm *vs* shPLCG2 = 77±9 µm; p<0.001), dendritic volume (shNT = 270±32 µm^3 *vs* shPLCG2 = 87±5 µm^3; p<0.001, **Fig.2c, d**) and in the number of intersections in a Sholl analysis ((p<0.0001; intersection vs. distance from soma $F_{(24, 1560)}$=23.23) **(Fig. 2g, h),** but not in the complexity index (p=0.24) or total branch number (p=0.52) **(Fig. 2e, f)**. We observed a decrease in the density and morphology of dendritic spines in shPLCG2-transduced DG granule cells (number of spines per µm: shNT = 0.70±0.04, n=73 neurites *vs* shPLCG2 = 0.27±0.01, n=75 neurites; p<0.0001), and an alteration of their morphology with decreased head diameter (shNT = 0.48±0.02 µm, n=100 *vs* shPLCG2 = 0.29±0.01 µm, n=103; p<0.0001), and spine length (shNT = 0.73±0.06 µm, n=89 *vs* shPLCG2 = 0.53±0.05 µm, n=101; p<0.0001; **Fig. 2j, l**). In conclusion, consistently with our results *in vitro*, *Plcg2* downregulation markedly impairs neuronal dendritic morphology and spine density in DG granule cells *in situ*.

***Plcg2* downregulation in the mouse dentate gyrus impairs electrophysiological properties of granule cells**

We then prepared slices for the electrophysiological recording of DG granule cells transduced with shPLCG2 or shNT as visualized and targeted by their GFP fluorescence (**Fig. 3a**). We assessed the intrinsic electrophysiological properties (shNT, n=15 cells; shPLCG2, n=13 cells; **Fig. 3b, f; Fig. S4b**).

Plcg2 downregulation led to a reduction of the input resistance (shNT = 570±79 MOhm *vs* shPLCG2 = 312±35 MOhm; p=0.0061; **Fig. 3d**) and of the firing threshold (shNT = –64.4±3.2 mV *vs* shPLCG2 = –71.4±0.8 mV; p=0.009) which was accompanied with an increase in the half-width of action potentials (shNT = 1.17 ms *vs* shPLCG2 = 1.25 ms; p=0.027, Mann-Whitney test; **Fig. S4c, d**). We found that the amount of current required for the cell to fire an action potential (the rheobase) was significantly higher following *Plcg2* downregulation (shNT = –57±11 pA *vs* shPLCG2 = –86±10 pA; p=0.022) (**Fig. 3c**). The number of spikes triggered by depolarizing pulses as a function of the amplitude of current injected also showed that shPLCG2-transduced DG neurons were less excitable ($F_{(1, 588)}$ = 10.87; df=1; p=0.001, ordinary 2-way ANOVA) (**Fig. 3g**). Overall, *Plcg2* downregulation leads to a substantial decrease in input resistance and in neuronal excitability. It can be suggested that Plcg2 contributes to the regulation of voltage-dependent ion channels around resting membrane potential of DG granule cells. We then performed voltage-clamp recordings in the presence of tetrodotoxin (TTX; 500 nM) to assess the impact of *Plcg2* downregulation on spontaneous miniature excitatory post-synaptic currents (mEPSCs) (mEPSCs) (**Fig. 3h**). We found significant differences in the average frequency of mEPSCs between shNT (n=27) and shPLCG2 (n=15) transduced neurons (shNT = 0.47±0.07 Hz *vs* shPLCG2 = 0.27±0.08 Hz; p=0.026; **Fig. 3i**). This result is consistent with the observed reduction of spine density. In addition, *Plcg2* downregulation resulted in a decrease of the amplitude of mEPSCs (shNT = 13.6±0.7 pA *vs* shPLCG2 = 10.8±0.5 pA; p=0.034; cumulative distribution of mEPSC amplitudes, p=0.0008, Kolmogorov-Smirnov test**; Fig. 3j, k)**. In conclusion, in accordance with our results *in vitro*, *Plcg2* downregulation markedly impairs electrophysiological properties of DG granule cells.

Downregulation of PLCγ2 in human neuronal cultures negatively impacts synaptic density and function

We then sought to extend our findings in rodents to *in vitro* model of human neurons, derived from human induced pluripotent stem cells (iPSCs). After 4 weeks of spontaneous differentiation from neural progenitor cells, transduced with either a non-targeting control shRNA (shNT) or a shRNA targeting *PLCG2* (shPLCG2), we obtained a mixed culture of mature human induced neurons and astrocytes, which we will refer to as human neuronal cultures (shNT-hNCs or shPLCG2-hNCs; **Fig. 4a**). We validated via immunoblotting that PLCγ2 downregulation in this mixed culture was specific as it did not impact PLCγ1 expression (**Fig. 4b**). To characterize the impact of *PLCG2* downregulation on synaptic density in hNCs, we used custom microfluidic devices in which mature neuronal synapses can be fluidically isolated in a distinct (synaptic) chamber and easily quantified. As in the case of HCS, we performed immunocytochemistry against synaptic markers and assessed synaptic density using a previously described algorithm (*17*) (**Fig. 4c**). We fully replicated in hNCs the results obtained in the HCS experiments using rat NPCs, *i.e.*, *PLCG2* downregulation decreased synaptic density (**Fig. 4c-d**). Similar results were obtained when using rat PNCs cultured in microfluidic devices (**Fig. S5**). Lastly, we analyzed the impact of *PLCG2* downregulation on the electrophysiological properties of hNCs using MEAs. Again, we replicated in hNCs the results we obtained in rat PNCs, *i.e.*, *PLCG2* downregulation induced a significant decrease in spike and burst frequencies (**Fig. 4e**). In conclusion and in accordance with our results observed in the rodent brain, *PLCG2* downregulation impacts synaptic density and function *in vitro* in hNCs.

Downregulation of PLCγ2 in human neuronal cultures increases both TAU phosphorylation and the levels of Aβ

We next tested the potential impact of *PLCG2* downregulation in hNCs on the different hallmarks of

AD, *i.e.*, amyloid precursor protein (APP) metabolism and quantity/phosphorylation state of Tau. In shPLCG2-hNCs, a significant increase in both APP (**Fig. 4f, g**) and Aβ levels (**Fig. 4h**) was detected. *PLCG2* downregulation was also associated with a strong increase in Tau phosphorylation at multiple epitopes (**Fig. 4f, i**). To note, an increase in total Tau protein levels was also detected (**Fig. 4f, g**). We finally investigated whether the impact of *PLCG2* downregulation on Tau hyperphosphorylation could be mediated through the regulation of ERK1/2, GSK3β, p38/MAPK and AKT kinases, known regulators of Tau phosphorylation (**Fig. 4k, l**). No difference in the total protein levels or phosphorylation status of ERK1/2 or p38/MAPK was observed when *PLCG2* was downregulated. However, *PLCG2* downregulation increased the level of phosphorylated GSK3β at Y216 and decreased the level of phosphorylated AKT at S473 (**Fig. 4l**). Both epitope sites are indicative of the active forms of the kinases. Altogether, these data indicate that *PLCG2* downregulation is associated with increased Aβ level, and Tau phosphorylation, potentially *via* the AKT/GSK3β axis.

Rare *PLCG2* loss-of-function variants are associated with an increase in AD risk

Importantly, our above-mentioned data suggest that the *PLCG2* downregulation may be deleterious and favor the development of AD through synaptic impairment and increased Aβ levels and Tau hyperphosphorylation. Therefore, we postulated that loss-of-function (LoF) variants responsible for a univocal reduction in *PLCG2*/PLCγ2 expression/activity might be associated with an increased risk of AD. To address this possibility, we first used two independent whole exome sequencing (WES) datasets. In a Finnish sample of 527 AD cases (ADGEN) and 8,707 controls (see Material and Methods), the comparison of allele number between AD patients (2 carriers) and controls (3 carriers) indicated overrepresentation of LoF variants in AD cases (OR = 11.0, 95% CI = 1.8-66.3; Pearson's χ^2 test, p = 0.0009; Fisher's exact test, p=0.03). In the ADES dataset (including 8,732 AD cases and 8,955 controls from Germany, France, Spain, the Netherlands and the United Kingdom (*7*)), the comparison of LoF allele number between AD patient (9 carriers) and control (one carrier) groups also indicated an overrepresentation in AD cases (OR = 9.2, 95% CI = 1.2-72.9; Pearson's χ^2 test, p = 0.01; Fisher's exact test p=0.01). Finally, a meta-analysis was performed, which, in turn, indicated that the *PLCG2* LoF variants increase the risk of AD (OR = 9.7, 95% CI = 2.0-47.7; p=0.005; **Fig. 5a** and **Table S2** for a full description of the LoF variants).

Effects of *PLCG2* LoF variants on AD pathological markers of AD and on *PLCG2* expression

We next analyzed the post-mortem sample obtained from the temporal cortex of an AD patient carrying the *PLCG2* LoF p.R953X variant to see whether partial loss-of-function of PLCγ2 influences AD-related neuropathology. This female was previously diagnosed as clinical AD and was classified as a Braak stage VI case according to neurofibrillary pathology in the neuropathological examination. Quantification of AD-related pathological hallmarks in the brain and CSF of this patient did not show any major alterations with respect to the Braak stage-matched AD patient samples (**Table S3** and **Fig. S6)**. The protein levels of PLCγ2 in brain lysates from the p.R953X carrier and four matched post-mortem AD samples were compared. As expected, protein levels of PLCγ2 were low in the cortical lysates based on Western blot analysis and a large variation was observed between individuals. However, protein levels of PLCγ2 were on average 70% lower in the *PLCG2* p.R953X variant carrier as compared to other AD cases (**Fig. 5b, c**). We did not detect additional specific bands for the p.R953X variant below the full-length PLCγ2. In addition, we had access to RNA extracted from the frozen blood sample of an ADGEN AD patient carrying the PLCG2 p.Q816X variant. We randomly selected four age-matched AD patients without *PLCG2* LoF variants from the ADGEN cohort. RNA analysis of these

samples revealed on average 40% reduction in the mRNA levels of *PLCG2* in the p.Q816X variant sample as compared to the other AD samples (**Fig. 5d**). However, the detailed examination of the RNA reads showed that the T allele (*i.e.*, allele encoding the stop codon)-containing reads were not completely excluded by nonsense-mediated mRNA decay (NMD) machinery as 20% of the total *PLCG2* reads still contained this allele. In conclusion, our data suggest that both LoF variants, *PLCG2* p.Q816X and *PLCG2* p.R953X, likely lead to NMD and therefore, reduce mRNA and protein levels of *PLCG2*/PLCγ2. However, we cannot rule out the possibility that low levels of truncated PLCγ2 are also produced.

Rescuing expression of *PLCG2* abolishes disease-related hallmarks in shPLCG2-hNCs

As NMD results in a decrease in the levels of PLCγ2, our shPLCG2-hNC model is relevant to assess the potential impact of the LoF variants on *PLCG2* expression and the subsequent phenotypes of interest. To confirm that the effect of *PLCG2* downregulation on AD hallmarks was specific, we performed rescue experiments by overexpressing *PLCG2* in shPLCG2-hNCs. Remarkably, restoring PLCγ2 levels also restored the full-length APP levels (**Fig. 5e, f**), Aβ levels (**Fig. 5g**), as well as total Tau levels (**Fig. 5e, f**) and Tau phosphorylation (**Fig. 5e, h**) close to shNT-hNCs levels. In addition, whereas downregulation of *PLCG2* was associated with a missorting of phosphorylated Tau into the soma, this pattern was largely abolished after *PLCG2* overexpression in shPLCG2-hNCs (**fig. 5i, j**). Finally, the observed changes in GSK3β and AKT phosphorylation levels were also restored after overexpressing *PLCG2* in shPLCG2-hNCs (**Fig. 5e, k**). In conclusion, restoring *PLCG2* expression in a human cellular model that mimics the consequences of *PLCG2* LoF on PLCγ2 levels can reverse the AD hallmark changes.

DISCUSSION

To determine if and how AD genetic risk factors contribute to synaptic failure, we developed an HCS to systematically characterize the impact of the downregulation of GWAS-defined genes on synaptic density. Surprisingly, among the genes with the strongest impact on synaptic density, *PLCG2* was one of the best hits (despite the absence of microglia in our HCS). This result was unexpected since in AD, *PLCG2* has been mostly studied in microglia and shown to be implicated in multiple microglia-related signaling pathways (*18*–*21*). However, strong evidence supports a role for PLCγ2 in synaptic function: (i) we and others found that *PLCG2* is also expressed in neurons (*23*, *25*); (ii) we observed that Plcγ2 is localized to both the pre- and post-synaptic compartments; (iii) we demonstrated that PLCγ2 downregulation impacts synaptic density and neuronal electrophysiological properties using three distinct experimental models (and different shRNAs). It is worth noting that downregulation of Plcγ2 *in vivo*, which leads to profound changes in DG granule cell morphology and physiology, was performed in adult (>3 months old) mice, thus precluding a potential developmental effect that could be argued to explain part of the synaptic phenotype observed in rat PNCs and hNCs.

Remarkably, we also observed that *PLCG2* downregulation in hNCs increases Tau phosphorylation as well as Aβ levels, suggesting that PLCγ2 participates in the development of the two main hallmarks of AD. Interestingly, our results highlight the AKT/GSK3β pathway, among others, to be involved in the neuronal response downstream of PLCγ2 downregulation. Indeed, a decrease in AKT activity and the subsequent increase in GSK3β activity has been previously described (*28*). GSK3β has already been shown to be involved in the regulation of the APP metabolism, Tau phosphorylation and synaptic functions (*29*–*31*), making it a credible intermediary between PLCγ2 and the different phenotypes associated with its downregulation. Of note, activation of the AKT/GSK3β pathway and increases in Aβ

levels/Tau phosphorylation were fully abolished when PLCγ2 level was restored, indicating a specific impact of PLCγ2 on these phenotypes. Interestingly, neurons derived from iPSCs obtained from sporadic AD cases also exhibit elevated Tau hyperphosphorylation, increased Aβ levels, and GSK3β activation (*32*).

To further support the importance of PLCγ2 and its downregulation in AD pathophysiology, we determined that rare LoF variants in *PLCG2* are associated with an increased risk of AD in two independent WES datasets. Two of these LoF variants, p.Q816X and p.R953X likely lead to NMD mechanisms resulting in decreased *PLCG2*/PLCγ2 expression. Our shPLCG2-hNC model is thus able to mimic the potential impact of these two LoF variants on *PLCG2* expression and consequently on AD phenotypes. In addition, at the genetic level, the association of LoF variants of *PLCG2* with increased AD risk is consistent with the fact that the functionally hypermorphic *PLCG2* p.P522R variant is protective against AD (*25*). In other words, an increase in the expression/activity of *PLCG2*/PLCγ2 is protective and a decrease is harmful. More specifically, the amino acid substitution P522R increases the activity of PLCγ2, which in turn enhances the conversion of phosphatidylinositol 4,5-bisphosphate (PIP2) to generate cytosolic inositol 3,4,5-trisphosphate (IP3) and diacylglycerol (DAG) (*18*, *20*, *33*). Thus, the enhanced activity of PLCγ2 may affect the generation of phosphatidylinositol 3,4,5-trisphosphate (PIP3) from PIP2 due to reduced substrate availability for phosphoinositide 3-kinase. This is important since PIP3 serves as a second messenger to recruit AKT and protein kinase C (PKC) to the plasma membrane, while the DAG-mediated activation of PKC can enhance AKT signaling through various mechanisms. This suggests that the observed alterations in the activity of AKT/GSK3β pathway in hNCs could be linked to the reduced total activity of PLCγ2. In this context, however, it should be noted that activity-related phosphorylation of Akt1/2 was significantly reduced in the brain tissue of Plcγ2-P522R knock-in (KI) mice (*18*), which is similar to what we observed in hNCs upon downregulation of PLCγ2. Finally, a previous study using human iPSC-derived microglia knockout for *PLCG2* and *TREM2* revealed a shared expressional dysregulation in these cells, emphasizing the importance of having sufficient levels and activity of PLCγ2 to avoid adverse cellular effects linked to AD (*34*). Although the focus in these previous studies has been set on microglia and myeloid-derived cells, a recent study using the cross-bred 5xFAD x Plcγ2-P522R KI mice revealed that the hypermorphic P522R variant improves impaired synaptic function as well as behavioral deficits observed in 5xFAD mice (*21*). This is particularly important in the context of the present study as the synaptic density and function were impaired in hNCs upon downregulation of PLCγ2. Collectively, these findings suggest a mechanism where the sustained activity of PLCγ2 becomes instrumental when the risk of AD (protective *vs* deleterious) is considered not only in microglia, but also in neurons.

In conclusion, our results report a new role for the AD genetic risk factor *PLCG2*. Downregulation of *PLCG2* specifically in neurons results in a signaling cascade leading to activation of GSK3β. This likely promotes increases in Aβ secretion, Tau hyperphosphorylation and synaptic dysfunction. This is in line with the observation that PLCγ2 may modulate Tau pathology and disease progression in patients with mild cognitive impairment (*35*). Emerging as a major genetic risk factor for AD (but also for other neurodegenerative diseases (*36*), *PLCG2* appears as a target of interest for drug development. In this context, determining which signaling pathways are related to *PLCG2,* not only in microglia, but also in neurons, will be important for identifying relevant druggable targets.

REFERENCES

1. C. Van Dyck, Lecanemab in Early Alzheimer's disease. *N Engl J Med.* **388**, 9-21 (2023).
2. K. Herrup, The case for rejecting the amyloid cascade hypothesis. *Nat. Neurosci.* **18**, 794–799 (2015).
3. D. J. Selkoe, J. Hardy, The amyloid hypothesis of Alzheimer's disease at 25 years. *EMBO Mol. Med.* **8**, 595–608 (2016).
4. G. B. Frisoni, D. Altomare, D. R. Thal, F. Ribaldi, R. van der Kant, R. Ossenkoppele, K. Blennow, J. Cummings, C. van Duijn, P. M. Nilsson, P. Y. Dietrich, P. Scheltens, B. Dubois, The probabilistic model of Alzheimer disease: the amyloid hypothesis revised. *Nat. Rev. Neurosci.* **23**, 53–66 (2022).
5. M. Gatz, C. A. Reynolds, L. Fratiglioni, B. Johansson, J. A. Mortimer, S. Berg, A. Fiske, N. L. Pedersen, Role of genes and environments for explaining Alzheimer disease. *Arch. Gen. Psychiatry* **63**, 168–174 (2006).
6. C. Bellenguez, F. Küçükali, I. E. Jansen, L. Kleineidam, S. Moreno-Grau, N. Amin, A. C. Naj, R. Campos-Martin, B. Grenier-Boley, V. Andrade, P. A. Holmans, A. Boland, V. Damotte, S. J. van der Lee, M. R. Costa, T. Kuulasmaa, Q. Yang, I. de Rojas, J. C. Bis, A. Yaqub, I. Prokic, J. Chapuis, S. Ahmad, V. Giedraitis, D. Aarsland, P. Garcia-Gonzalez, C. Abdelnour, E. Alarcón-Martín, D. Alcolea, M. Alegret, I. Alvarez, V. Álvarez, N. J. Armstrong, A. Tsolaki, C. Antúnez, I. Appollonio, M. Arcaro, S. Archetti, A. A. Pastor, B. Arosio, L. Athanasiu, H. Bailly, N. Banaj, M. Baquero, S. Barral, A. Beiser, A. B. Pastor, J. E. Below, P. Benchek, L. Benussi, C. Berr, C. Besse, V. Bessi, G. Binetti, A. Bizarro, R. Blesa, M. Boada, E. Boerwinkle, B. Borroni, S. Boschi, P. Bossù, G. Bråthen, J. Bressler, C. Bresner, H. Brodaty, K. J. Brookes, L. I. Brusco, D. Buiza-Rueda, K. Bûrger, V. Burholt, W. S. Bush, M. Calero, L. B. Cantwell, G. Chene, J. Chung, M. L. Cuccaro, Á. Carracedo, R. Cecchetti, L. Cervera-Carles, C. Charbonnier, H. H. Chen, C. Chillotti, S. Ciccone, J. A. H. R. Claassen, C. Clark, E. Conti, A. Corma-Gómez, E. Costantini, C. Custodero, D. Daian, M. C. Dalmasso, A. Daniele, E. Dardiotis, J. F. Dartigues, P. P. de Deyn, K. de Paiva Lopes, L. D. de Witte, S. Debette, J. Deckert, T. del Ser, N. Denning, A. DeStefano, M. Dichgans, J. Diehl-Schmid, M. Diez-Fairen, P. D. Rossi, S. Djurovic, E. Duron, E. Düzel, C. Dufouil, G. Eiriksdottir, S. Engelborghs, V. Escott-Price, A. Espinosa, M. Ewers, K. M. Faber, T. Fabrizio, S. F. Nielsen, D. W. Fardo, L. Farotti, C. Fenoglio, M. Fernández-Fuertes, R. Ferrari, C. B. Ferreira, E. Ferri, B. Fin, P. Fischer, T. Fladby, K. Fließbach, B. Fongang, M. Fornage, J. Fortea, T. M. Foroud, S. Fostinelli, N. C. Fox, E. Franco-Macías, M. J. Bullido, A. Frank-García, L. Froelich, B. Fulton-Howard, D. Galimberti, J. M. García-Alberca, P. García-González, S. Garcia-Madrona, G. Garcia-Ribas, R. Ghidoni, I. Giegling, G. Giorgio, A. M. Goate, O. Goldhardt, D. Gomez-Fonseca, A. González-Pérez, C. Graff, G. Grande, E. Green, T. Grimmer, E. Grünblatt, M. Grunin, V. Gudnason, T. Guetta-Baranes, A. Haapasalo, G. Hadjigeorgiou, J. L. Haines, K. L. Hamilton-Nelson, H. Hampel, O. Hanon, J. Hardy, A. M. Hartmann, L. Hausner, J. Harwood, S. Heilmann-Heimbach, S. Helisalmi, M. T. Heneka, I. Hernández, M. J. Herrmann, P. Hoffmann, C. Holmes, H. Holstege, R. H. Vilas, M. Hulsman, J. Humphrey, G. J. Biessels, X. Jian, C. Johansson, G. R. Jun, Y. Kastumata, J. Kauwe, P. G. Kehoe, L. Kilander, A. K. Ståhlbom, M. Kivipelto, A. Koivisto, J. Kornhuber, M. H. Kosmidis, W. A. Kukull, P. P. Kuksa, B. W. Kunkle, A. B. Kuzma, C. Lage, E. J. Laukka, L. Launer, A. Lauria, C. Y. Lee, J. Lehtisalo, O. Lerch, A. Lleó, W. Longstreth, O. Lopez, A. L. de Munain, S. Love, M. Löwemark, L. Luckcuck, K. L. Lunetta, Y. Ma, J. Macías, C. A. MacLeod, W. Maier, F. Mangialasche, M. Spallazzi, M. Marquié, R. Marshall, E. R. Martin, A. M. Montes, C. M. Rodríguez, C. Masullo, R. Mayeux, S. Mead, P. Mecocci, M. Medina, A. Meggy, S. Mehrabian, S. Mendoza, M. Menéndez-González, P. Mir, S. Moebus, M. Mol, L. Molina-Porcel, L. Montrreal, L. Morelli, F. Moreno, K. Morgan, T. Mosley, M. M. Nöthen, C. Muchnik, S. Mukherjee, B. Nacmias, T. Ngandu, G. Nicolas, B. G. Nordestgaard, R. Olaso, A. Orellana, M. Orsini, G. Ortega, A. Padovani, C. Paolo, G. Papenberg, L. Parnetti, F. Pasquier, P. Pastor, G. Peloso, A. Pérez-Cordón, J. Pérez-Tur, P. Pericard, O. Peters, Y. A. L. Pijnenburg, J. A. Pineda, G. Piñol-Ripoll, C. Pisanu, T. Polak, J. Popp, D. Posthuma, J.

Priller, R. Puerta, O. Quenez, I. Quintela, J. Q. Thomassen, A. Rábano, I. Rainero, F. Rajabli, I. Ramakers, L. M. Real, M. J. T. Reinders, C. Reitz, D. Reyes-Dumeyer, P. Ridge, S. Riedel-Heller, P. Riederer, N. Roberto, E. Rodriguez-Rodriguez, A. Rongve, I. R. Allende, M. Rosende-Roca, J. L. Royo, E. Rubino, D. Rujescu, M. E. Sáez, P. Sakka, I. Saltvedt, Á. Sanabria, M. B. Sánchez-Arjona, F. Sanchez-Garcia, P. S. Juan, R. Sánchez-Valle, S. B. Sando, C. Sarnowski, C. L. Satizabal, M. Scamosci, N. Scarmeas, E. Scarpini, P. Scheltens, N. Scherbaum, M. Scherer, M. Schmid, A. Schneider, J. M. Schott, G. Selbæk, D. Seripa, M. Serrano, J. Sha, A. A. Shadrin, O. Skrobot, S. Slifer, G. J. L. Snijders, H. Soininen, V. Solfrizzi, A. Solomon, Y. Song, S. Sorbi, O. Sotolongo-Grau, G. Spalletta, A. Spottke, A. Squassina, E. Stordal, J. P. Tartan, L. Tárraga, N. Tesí, A. Thalamuthu, T. Thomas, G. Tosto, L. Traykov, L. Tremolizzo, A. Tybjærg-Hansen, A. Uitterlinden, A. Ullgren, I. Ulstein, S. Valero, O. Valladares, C. Van Broeckhoven, J. Vance, B. N. Vardarajan, A. van der Lugt, J. Van Dongen, J. van Rooij, J. van Swieten, R. Vandenberghe, F. Verhey, J. S. Vidal, J. Vogelgsang, M. Vyhnalek, M. Wagner, D. Wallon, L. S. Wang, R. Wang, L. Weinhold, J. Wiltfang, G. Windle, B. Woods, M. Yannakoulia, H. Zare, Y. Zhao, X. Zhang, C. Zhu, M. Zulaica, J. Laczo, V. Matoska, M. Serpente, F. Assogna, F. Piras, F. Piras, V. Ciullo, J. Shofany, C. Ferrarese, S. Andreoni, G. Sala, C. P. Zoia, M. Del Zompo, A. Benussi, P. Bastiani, M. Takalo, T. Natunen, T. Laatikainen, J. Tuomilehto, R. Antikainen, T. Strandberg, J. Lindström, M. Peltonen, R. Abraham, A. Al-Chalabi, N. J. Bass, C. Brayne, K. S. Brown, J. Collinge, D. Craig, P. Deloukas, N. Fox, A. Gerrish, M. Gill, R. Gwilliam, D. Harold, P. Hollingworth, J. A. Johnston, L. Jones, B. Lawlor, G. Livingston, S. Lovestone, M. Lupton, A. Lynch, D. Mann, B. McGuinness, A. McQuillin, M. C. O'Donovan, M. J. Owen, P. Passmore, J. F. Powell, P. Proitsi, M. Rossor, C. E. Shaw, A. D. Smith, H. Gurling, S. Todd, C. Mummery, N. Ryan, G. Lacidogna, A. Adarmes-Gómez, A. Mauleón, A. Pancho, A. Gailhajenet, A. Lafuente, D. Macias-García, E. Martín, E. Pelejà, F. Carrillo, I. S. Merlín, L. Garrote-Espina, L. Vargas, M. Carrion-Claro, M. Marín, M. Labrador, M. Buendia, M. D. Alonso, M. Guitart, M. Moreno, M. Ibarria, M. Periñán, N. Aguilera, P. Gómez-Garre, P. Cañabate, R. Escuela, R. Pineda-Sánchez, R. Vigo-Ortega, S. Jesús, S. Preckler, S. Rodrigo-Herrero, S. Diego, A. Vacca, F. Roveta, N. Salvadori, E. Chipi, H. Boecker, C. Laske, R. Perneczky, C. Anastasiou, D. Janowitz, R. Malik, A. Anastasiou, K. Parveen, C. Lage, S. López-García, A. Antonell, K. Y. Mihova, D. Belezhanska, H. Weber, S. Kochen, P. Solis, N. Medel, J. Lisso, Z. Sevillano, D. G. Politis, V. Cores, C. Cuesta, C. Ortiz, J. I. Bacha, M. Rios, A. Saenz, M. S. Abalos, E. Kohler, D. L. Palacio, I. Etchepareborda, M. Kohler, G. Novack, F. A. Prestia, P. Galeano, E. M. Castaño, S. Germani, C. R. Toso, M. Rojo, C. Ingino, C. Mangone, D. C. Rubinsztein, S. Teipel, N. Fievet, V. Deramerourt, C. Forsell, H. Thonberg, M. Bjerke, E. De Roeck, M. T. Martínez-Larrad, N. Olivar, N. Aguilera, A. Cano, P. Cañabate, J. Macias, O. Maroñas, R. Nuñez-Llaves, C. Olivé, E. Pelejá, A. D. Adarmes-Gómez, M. D. Alonso, G. Amer-Ferrer, M. Antequera, J. A. Burguera, F. Carrillo, M. Carrión-Claro, M. J. Casajeros, M. Martinez de Pancorbo, R. Escuela, L. Garrote-Espina, P. Gómez-Garre, S. Hevilla, S. Jesús, M. A. L. Espinosa, A. Legaz, S. López-García, D. Macias-García, S. Manzanares, M. Marín, J. Marín-Muñoz, T. Marín, B. Martínez, V. Martínez, P. Martínez-Lage Álvarez, M. M. Iriarte, M. T. Periñán-Tocino, R. Pineda-Sánchez, D. Real de Asúa, S. Rodrigo, I. Sastre, M. P. Vicente, R. Vigo-Ortega, L. Vivancos, J. Epelbaum, D. Hannequin, D. campion, V. Deramecourt, C. Tzourio, A. Brice, B. Dubois, A. Williams, C. Thomas, C. Davies, W. Nash, K. Dowzell, A. C. Morales, M. Bernardo-Harrington, J. Turton, J. Lord, K. Brown, E. Vardy, E. Fisher, J. D. Warren, M. Rossor, N. S. Ryan, R. Guerreiro, J. Uphill, N. Bass, R. Heun, H. Kölsch, B. Schürmann, A. Lacour, C. Herold, J. A. Johnston, P. Passmore, J. Powell, Y. Patel, A. Hodges, T. Becker, D. Warden, G. Wilcock, R. Clarke, P. Deloukas, Y. Ben-Shlomo, N. M. Hooper, S. Pickering-Brown, R. Sussams, N. Warner, A. Bayer, I. Heuser, D. Drichel, N. Klopp, M. Mayhaus, M. Riemenschneider, S. Pinchler, T. Feulner, W. Gu, H. van den Bussche, M. Hüll, L. Frölich, H. E. Wichmann, K. H. Jöckel, M. O'Donovan, M. Owen, S. Bahrami, I. Bosnes, P. Selnes, S. Bergh, A. Palotie, M. Daly, H. Jacob, A. Matakidou, H. Runz, S. John, R. Plenge, M. McCarthy, J. Hunkapiller, M. Ehm, D. Waterworth, C. Fox, A. Malarstig, K. Klinger, K. Call, T. Behrens, P. Loerch, T. Mäkelä, J. Kaprio, P. Virolainen, K. Pulkki, T. Kilpi, M. Perola, J. Partanen, A. Pitkäranta, R. Kaarteenaho, S. Vainio, M. Turpeinen, R. Serpi, T. Laitinen, J. Mäkelä, V. M. Kosma, U. Kujala,

O. Tuovila, M. Hendolin, R. Pakkanen, J. Waring, B. Riley-Gillis, J. Liu, S. Biswas, D. Diogo, C. Marshall, X. Hu, M. Gossel, R. Graham, B. Cummings, S. Ripatti, J. Schleutker, M. Arvas, O. Carpén, R. Hinttala, J. Kettunen, A. Mannermaa, J. Laukkanen, V. Julkunen, A. Remes, R. Kälviäinen, J. Peltola, P. Tienari, J. Rinne, A. Ziemann, J. Waring, S. Esmaeeli, N. Smaoui, A. Lehtonen, S. Eaton, S. Lahdenperä, J. van Adelsberg, J. Michon, G. Kerchner, N. Bowers, E. Teng, J. Eicher, V. Mehta, P. Gormley, K. Linden, C. Whelan, F. Xu, D. Pulford, M. Färkkilä, S. Pikkarainen, A. Jussila, T. Blomster, M. Kiviniemi, M. Voutilainen, B. Georgantas, G. Heap, F. Rahimov, K. Usiskin, T. Lu, D. Oh, K. Kalpala, M. Miller, L. McCarthy, K. Eklund, A. Palomäki, P. Isomäki, L. Pirilä, O. Kaipiainen-Seppänen, J. Huhtakangas, A. Lertratanakul, M. Hochfeld, N. Bing, J. E. Gordillo, N. Mars, M. Pelkonen, P. Kauppi, H. Kankaanranta, T. Harju, D. Close, S. Greenberg, H. Chen, J. Betts, S. Ghosh, V. Salomaa, T. Niiranen, M. Juonala, K. Metsärinne, M. Kähönen, J. Junttila, M. Laakso, J. Pihlajamäki, J. Sinisalo, M. R. Taskinen, T. Tuomi, B. Challis, A. Peterson, A. Chu, J. Parkkinen, A. Muslin, H. Joensuu, T. Meretoja, L. Aaltonen, J. Mattson, A. Auranen, P. Karihtala, S. Kauppila, P. Auvinen, K. Elenius, R. Popovic, J. Schutzman, A. Loboda, A. Chhibber, H. Lehtonen, S. McDonough, M. Crohns, D. Kulkarni, K. Kaarniranta, J. A. Turunen, T. Ollila, S. Seitsonen, H. Uusitalo, V. Aaltonen, H. Uusitalo-Järvinen, M. Luodonpää, N. Hautala, S. Loomis, E. Strauss, H. Chen, A. Podgornaia, J. Hoffman, K. Tasanen, L. Huilaja, K. Hannula-Jouppi, T. Salmi, S. Peltonen, L. Koulu, I. Harvima, Y. Wu, D. Choy, P. Pussinen, A. Salminen, T. Salo, D. Rice, P. Nieminen, U. Palotie, M. Siponen, L. Suominen, P. Mäntylä, U. Gursoy, V. Anttonen, K. Sipilä, J. W. Davis, D. Quarless, S. Petrovski, E. Wigmore, C. Y. Chen, P. Bronson, E. Tsai, Y. Huang, J. Maranville, E. Shaikho, E. Mohammed, S. Wadhawan, E. Kvikstad, M. Caliskan, D. Chang, T. Bhangale, S. Pendergrass, E. Holzinger, X. Chen, Å. Hedman, K. S. King, C. Wang, E. Xu, F. Auge, C. Chatelain, D. Rajpal, D. Liu, K. Call, T. he Xia, M. Brauer, M. Kurki, J. Karjalainen, A. Havulinna, A. Jalanko, P. Palta, P. della Briotta Parolo, W. Zhou, S. Lemmelä, M. Rivas, J. Harju, A. Lehisto, A. Ganna, V. Llorens, H. Laivuori, S. Rüeger, M. E. Niemi, T. Tukiainen, M. P. Reeve, H. Heyne, K. Palin, J. Garcia-Tabuenca, H. Siirtola, T. Kiiskinen, J. Lee, K. Tsuo, A. Elliott, K. Kristiansson, K. Hyvärinen, J. Ritari, M. Koskinen, K. Pylkäs, M. Kalaoja, M. Karjalainen, T. Mantere, E. Kangasniemi, S. Heikkinen, E. Laakkonen, C. Sipeky, S. Heron, A. Karlsson, D. Jambulingam, V. S. Rathinakannan, R. Kajanne, M. Aavikko, M. G. Jiménez, P. della Briotta Parola, A. Lehistö, M. Kanai, M. Kaunisto, E. Kilpeläinen, T. P. Sipilä, G. Brein, G. Awaisa, A. Shcherban, K. Donner, A. Loukola, P. Laiho, T. Sistonen, E. Kaiharju, M. Laukkanen, E. Järvensivu, S. Lähteenmäki, L. Männikkö, R. Wong, H. Mattsson, T. Hiekkalinna, T. Paajanen, K. Pärn, J. Gracia-Tabuenca, E. Abner, P. M. Adams, A. Aguirre, M. S. Albert, R. L. Albin, M. Allen, L. Alvarez, L. G. Apostolova, S. E. Arnold, S. Asthana, C. S. Atwood, G. Ayres, C. T. Baldwin, R. C. Barber, L. L. Barnes, S. Barral, T. G. Beach, J. T. Becker, G. W. Beecham, D. Beekly, J. E. Below, P. Benchek, B. A. Benitez, D. Bennett, J. Bertelson, F. E. Margaret, T. D. Bird, D. Blacker, B. F. Boeve, J. D. Bowen, A. Boxer, J. Brewer, J. R. Burke, J. M. Burns, W. S. Bush, J. D. Buxbaum, N. J. Cairns, C. Cao, C. S. Carlson, C. M. Carlsson, R. M. Carney, M. M. Carrasquillo, S. Chasse, M. F. Chesselet, A. Chesi, N. A. Chin, H. C. Chui, J. Chung, S. Craft, P. K. Crane, D. H. Cribbs, E. A. Crocco, C. Cruchaga, M. Cullum, E. Darby, B. Davis, P. L. De Jager, C. DeCarli, J. DeToledo, M. Dick, D. W. Dickson, B. A. Dombroski, R. S. Doody, R. Duara, N. Ertekin-Taner, D. A. Evans, T. J. Fairchild, K. B. Fallon, M. R. Farlow, J. J. Farrell, V. Fernandez-Hernandez, S. Ferris, M. P. Frosch, B. Fulton-Howard, D. R. Galasko, A. Gamboa, M. Gearing, D. H. Geschwind, B. Ghetti, J. R. Gilbert, T. J. Grabowski, N. R. Graff-Radford, S. F. A. Grant, R. C. Green, J. H. Growdon, J. L. Haines, H. Hakonarson, J. Hall, R. L. Hamilton, O. Harari, L. E. Harrell, J. Haut, E. Head, V. W. Henderson, M. Hernandez, T. Hohman, L. S. Honig, R. M. Huebinger, M. J. Huentelman, C. M. Hulette, B. T. Hyman, L. S. Hynan, L. Ibanez, G. P. Jarvik, S. Jayadev, L. W. Jin, K. Johnson, L. Johnson, M. I. Kamboh, A. M. Karydas, M. J. Katz, J. A. Kaye, C. D. Keene, A. Khaleeq, R. Kim, J. Knebl, N. W. Kowall, J. H. Kramer, P. P. Kuksa, F. M. LaFerla, J. J. Lah, E. B. Larson, C. Y. Lee, E. B. Lee, A. Lerner, Y. Y. Leung, J. B. Leverenz, A. I. Levey, M. Li, A. P. Lieberman, R. B. Lipton, M. Logue, C. G. Lyketsos, J. Malamon, D. Mains, D. C. Marson, F. Martiniuk, D. C. Mash, E. Masliah, P. Massman, A. Masurkar, W. C. McCormick, S. M. McCurry, A. N. McDavid, S. McDonough, A. C. McKee, M.

Mesulam, J. Mez, B. L. Miller, C. A. Miller, J. W. Miller, T. J. Montine, E. S. Monuki, J. C. Morris, A. J. Myers, T. Nguyen, S. O'Bryant, J. M. Olichney, M. Ory, R. Palmer, J. E. Parisi, H. L. Paulson, V. Pavlik, D. Paydarfar, V. Perez, E. Peskind, R. C. Petersen, J. E. Phillips-Cremins, A. Pierce, M. Polk, W. W. Poon, H. Potter, L. Qu, M. Quiceno, J. F. Quinn, A. Raj, M. Raskind, E. M. Reiman, B. Reisberg, J. S. Reisch, J. M. Ringman, E. D. Roberson, M. Rodriguear, E. Rogaeva, H. J. Rosen, R. N. Rosenberg, D. R. Royall, M. A. Sager, M. Sano, A. J. Saykin, J. A. Schneider, L. S. Schneider, W. W. Seeley, S. H. Slifer, S. Small, A. G. Smith, J. P. Smith, Y. E. Song, J. A. Sonnen, S. Spina, P. S. George-Hyslop, R. A. Stern, A. B. Stevens, S. M. Strittmatter, D. Sultzer, R. H. Swerdlow, R. E. Tanzi, J. L. Tilson, J. Q. Trojanowski, J. C. Troncoso, D. W. Tsuang, O. Valladares, V. M. Van Deerlin, L. J. van Eldik, R. Vassar, H. V. Vinters, J. P. Vonsattel, S. Weintraub, K. A. Welsh-Bohmer, P. L. Whitehead, E. M. Wijsman, K. C. Wilhelmsen, B. Williams, J. Williamson, H. Wilms, T. S. Wingo, T. Wisniewski, R. L. Woltjer, M. Woon, C. B. Wright, C. K. Wu, S. G. Younkin, C. E. Yu, L. Yu, Y. Zhang, Y. Zhao, X. Zhu, H. Adams, R. O. Akinyemi, M. Ali, H. J. Aparicio, M. Bahadori, J. T. Becker, M. Breteler, D. Chasman, G. Chauhan, H. Comic, S. Cox, A. L. Cupples, G. Davies, C. S. DeCarli, M. G. Duperron, J. Dupuis, T. Evans, F. Fan, A. Fitzpatrick, A. E. Fohner, M. Ganguli, M. Geerlings, S. J. Glatt, H. M. Gonzalez, M. Goss, H. Grabe, M. Habes, S. R. Heckbert, E. Hofer, E. Hong, T. Hughes, T. F. Kautz, M. Knol, W. Kremen, P. Lacaze, J. Lahti, Q. Le Grand, E. Litkowski, S. Li, D. Liu, X. Liu, M. Loitfelder, A. Manning, P. Maillard, R. Marioni, B. Mazoyer, D. M. van Lent, H. Mei, A. Mishra, P. Nyquist, J. O'Connell, Y. Patel, T. Paus, Z. Pausova, K. Raikkonen-Talvitie, M. Riaz, S. Rich, J. Rotter, J. Romero, G. Roshchupkin, Y. Saba, M. Sargurupremraj, H. Schmidt, R. Schmidt, J. M. Shulman, J. Smith, H. Sekhar, R. Rajula, J. Shin, J. Simino, E. Sliz, A. Teumer, A. Thomas, A. Tin, E. Tucker-Drob, D. Vojinovic, Y. Wang, G. Weinstein, D. Williams, K. Wittfeld, L. Yanek, Y. Yang, L. A. Farrer, B. M. Psaty, M. Ghanbari, T. Raj, P. Sachdev, K. Mather, F. Jessen, M. A. Ikram, A. de Mendonça, J. Hort, M. Tsolaki, M. A. Pericak-Vance, P. Amouyel, J. Williams, R. Frikke-Schmidt, J. Clarimon, J. F. Deleuze, G. Rossi, S. Seshadri, O. A. Andreassen, M. Ingelsson, M. Hiltunen, K. Sleegers, G. D. Schellenberg, C. M. van Duijn, R. Sims, W. M. van der Flier, A. Ruiz, A. Ramirez, J. C. Lambert, New insights into the genetic etiology of Alzheimer's disease and related dementias. *Nat. Genet.* **54**, 412–436 (2022).

7. H. Holstege, M. Hulsman, C. Charbonnier, B. Grenier-Boley, O. Quenez, D. Grozeva, J. G. J. van Rooij, R. Sims, S. Ahmad, N. Amin, P. J. Norsworthy, O. Dols-Icardo, H. Hummerich, A. Kawalia, P. Amouyel, G. W. Beecham, C. Berr, J. C. Bis, A. Boland, P. Bossù, F. Bouwman, J. Bras, D. Campion, J. N. Cochran, A. Daniele, J. F. Dartigues, S. Debette, J. F. Deleuze, N. Denning, A. L. DeStefano, L. A. Farrer, M. V. Fernández, N. C. Fox, D. Galimberti, E. Genin, J. J. P. Gille, Y. Le Guen, R. Guerreiro, J. L. Haines, C. Holmes, M. A. Ikram, M. K. Ikram, I. E. Jansen, R. Kraaij, M. Lathrop, A. W. Lemstra, A. Lleó, L. Luckcuck, M. M. A. M. Mannens, R. Marshall, E. R. Martin, C. Masullo, R. Mayeux, P. Mecocci, A. Meggy, M. O. Mol, K. Morgan, R. M. Myers, B. Nacmias, A. C. Naj, V. Napolioni, F. Pasquier, P. Pastor, M. A. Pericak-Vance, R. Raybould, R. Redon, M. J. T. Reinders, A. C. Richard, S. G. Riedel-Heller, F. Rivadeneira, S. Rousseau, N. S. Ryan, S. Saad, P. Sanchez-Juan, G. D. Schellenberg, P. Scheltens, J. M. Schott, D. Seripa, S. Seshadri, D. Sie, E. A. Sistermans, S. Sorbi, R. van Spaendonk, G. Spalletta, N. Tesi, B. Tijms, A. G. Uitterlinden, S. J. van der Lee, P. J. Visser, M. Wagner, D. Wallon, L. S. Wang, A. Zarea, J. Clarimon, J. C. van Swieten, M. D. Greicius, J. S. Yokoyama, C. Cruchaga, J. Hardy, A. Ramirez, S. Mead, W. M. van der Flier, C. M. van Duijn, J. Williams, G. Nicolas, C. Bellenguez, J. C. Lambert, Exome sequencing identifies rare damaging variants in ATP8B4 and ABCA1 as risk factors for Alzheimer's disease. *Nat. Genet.* **54**, 1786–1794 (2022).

8. J. C. Lambert, A. Ramirez, B. Grenier-Boley, C. Bellenguez, Step by step: towards a better understanding of the genetic architecture of Alzheimer's disease. *Mol. Psychiatry.* **28**, 2716-2727 (2023).

9. B. Schürmann, D. P. Bermingham, K. J. Kopeikina, K. Myczek, S. Yoon, K. E. Horan, C. J. Kelly, M. D. Martin-de-Saavedra, M. P. Forrest, J. M. Fawcett-Patel, K. R. Smith, R. Gao, A. Bach, A. C. Burette, J. Z. Rappoport, R. J. Weinberg, M. Martina, P. Penzes, A novel role for the late-onset Alzheimer's disease (LOAD)-associated protein Bin1 in regulating postsynaptic trafficking and

glutamatergic signaling. *Mol. Psychiatry* **25**, 2000–2016 (2020).

10. F. Eysert, A. Coulon, E. Boscher, A. C. Vreulx, A. Flaig, T. Mendes, S. Hughes, B. Grenier-Boley, X. Hanoulle, F. Demiautte, C. Bauer, M. Marttinen, M. Takalo, P. Amouyel, S. Desai, I. Pike, M. Hiltunen, F. Chécler, M. Farinelli, C. Delay, N. Malmanche, S. S. Hébert, J. Dumont, D. Kilinc, J. C. Lambert, J. Chapuis, Alzheimer's genetic risk factor FERMT2 (Kindlin-2) controls axonal growth and synaptic plasticity in an APP-dependent manner. *Mol. Psychiatry* **26**, 5592–5607 (2021).
11. A. Giralt, V. Brito, Q. Chevy, C. Simonnet, Y. Otsu, C. Cifuentes-DÍaz, B. De Pins, R. Coura, J. Alberch, S. Ginés, J. C. Poncer, J. A. Girault, Pyk2 modulates hippocampal excitatory synapses and contributes to cognitive deficits in a Huntington's disease model. *Nat. Commun. 2017 81* **8**, 1–16 (2017).
12. S. A. Ojelade, T. V. Lee, N. Giagtzoglou, L. Yu, B. Ugur, Y. Li, L. Duraine, Z. Zuo, V. Petyuk, P. L. De Jager, D. A. Bennett, B. R. Arenkiel, H. J. Bellen, J. M. Shulman, cindr, the Drosophila Homolog of the CD2AP Alzheimer's Disease Risk Gene, Is Required for Synaptic Transmission and Proteostasis. *Cell Rep.* **28**, 1799-1813.e5 (2019).
13. E. Masliah, Mechanisms of synaptic dysfunction in Alzheimer's disease. *Histol. Histopathol.* **10**, 509-19 (1995).
14. G. Barthet, C. Mulle, Presynaptic failure in Alzheimer's disease. *Prog. Neurobiol.* **194**, 101801. (2020).
15. S. Ribarič, Detecting Early Cognitive Decline in Alzheimer's Disease with Brain Synaptic Structural and Functional Evaluation. *Biomedicines* **11**, 355 (2023).
16. A. Coulon, D. Siedlecki-Wullich, C. Najdek, C. Gelle, A. M. Ayral, F. Demiautte, E. Lambert, A. Vandeputte, P. Brodin, T. Mendes, J. C. Lambert, D. Kilinc, J. Dumont, J. Chapuis, High-Content Screening of Synaptic Density Modulators in Primary Neuronal Cultures. *Curr. Protoc.* **3** (2023).
17. D. Kilinc, A.-C. Vreulx, T. Mendes, A. Flaig, D. Marques-Coelho, M. Verschoore, F. Demiautte, P. Amouyel, F. Eysert, P. Dourlen, J. Chapuis, M. R. Costa, N. Malmanche, F. Checler, J.-C. Lambert, Pyk2 overexpression in postsynaptic neurons blocks amyloid β1-42-induced synaptotoxicity in microfluidic co-cultures. *Brain Commun.* **2,** fcaa139 (2020).
18. M. Takalo, R. Wittrahm, B. Wefers, S. Parhizkar, K. Jokivarsi, T. Kuulasmaa, P. Mäkinen, H. Martiskainen, W. Wurst, X. Xiang, M. Marttinen, P. Poutiainen, A. Haapasalo, M. Hiltunen, C. Haass, The Alzheimer's disease-associated protective Plcγ2-P522R variant promotes immune functions. *Mol. Neurodegener.* **15**, 1–14 (2020).
19. C. Claes, W. E. England, E. P. Danhash, S. Kiani Shabestari, A. Jairaman, J. P. Chadarevian, J. Hasselmann, A. P. Tsai, M. A. Coburn, J. Sanchez, T. E. Lim, J. L. S. Hidalgo, C. Tu, M. D. Cahalan, B. T. Lamb, G. E. Landreth, R. C. Spitale, M. Blurton-Jones, H. Davtyan, The P522R protective variant of PLCG2 promotes the expression of antigen presentation genes by human microglia in an Alzheimer's disease mouse model. *Alzheimers. Dement.* **18**, 1765-1778 (2022).
20. A. P. Tsai, C. Dong, P. B. C. Lin, E. J. Messenger, B. T. Casali, M. Moutinho, Y. Liu, A. L. Oblak, B. T. Lamb, G. E. Landreth, S. J. Bissel, K. Nho, PLCG2 is associated with the inflammatory response and is induced by amyloid plaques in Alzheimer's disease. *Genome Med.* **14**, 17 (2022).
21. A. P. Tsai, C. Dong, P. B. C. Lin, A. L. Oblak, G. Viana Di Prisco, N. Wang, N. Hajicek, A. J. Carr, E. K. Lendy, O. Hahn, M. Atkins, A. G. Foltz, J. Patel, G. Xu, M. Moutinho, J. Sondek, Q. Zhang, A. D. Mesecar, Y. Liu, B. K. Atwood, T. Wyss-Coray, K. Nho, S. J. Bissel, B. T. Lamb, G. E. Landreth, Genetic variants of phospholipase C-γ2 alter the phenotype and function of microglia and confer differential risk for Alzheimer's disease. *Immunity* **56**, 2121-2136.e6 (2023).
22. Z. Yao, C. T. J. van Velthoven, T. N. Nguyen, J. Goldy, A. E. Sedeno-Cortes, F. Baftizadeh, D. Bertagnolli, T. Casper, M. Chiang, K. Crichton, S. L. Ding, O. Fong, E. Garren, A. Glandon, N. W. Gouwens, J. Gray, L. T. Graybuck, M. J. Hawrylycz, D. Hirschstein, M. Kroll, K. Lathia, C. Lee, B. Levi, D. McMillen, S. Mok, T. Pham, Q. Ren, C. Rimorin, N. Shapovalova, J. Sulc, S. M. Sunkin, M. Tieu, A. Torkelson, H. Tung, K. Ward, N. Dee, K. A. Smith, B. Tasic, H. Zeng, A taxonomy of transcriptomic cell types across the isocortex and hippocampal formation. *Cell* **184**, 3222-3241.e26 (2021).

23. K. Leng, E. Li, R. Eser, A. Piergies, R. Sit, M. Tan, N. Neff, S. H. Li, R. D. Rodriguez, C. K. Suemoto, R. E. P. Leite, A. J. Ehrenberg, C. A. Pasqualucci, W. W. Seeley, S. Spina, H. Heinsen, L. T. Grinberg, M. Kampmann, Molecular characterization of selectively vulnerable neurons in Alzheimer's disease. *Nat. Neurosci.* **24**, 276–287 (2021).
24. O. Saha, A. R. Melo de Farias, A. Pelletier, D. Siedlecki-Wullich, B. S. Landeira, J. Gadaut, A. Carrier, A. C. Vreulx, K. Guyot, Y. Shen, A. Bonnefond, P. Amouyel, J. TCW, D. Kilinc, C. M. Queiroz, F. Delahaye, J. C. Lambert, M. R. Costa, The Alzheimer's disease risk gene BIN1 regulates activity-dependent gene expression in human-induced glutamatergic neurons. *Mol. Psychiatry*, doi: 10.1038/S41380-024-02502-Y (2024).
25. L. Magno, C. B. Lessard, M. Martins, V. Lang, P. Cruz, Y. Asi, M. Katan, J. Bilsland, T. Lashley, P. Chakrabarty, T. E. Golde, P. J. Whiting, Alzheimer's disease phospholipase C-gamma-2 (PLCG2) protective variant is a functional hypermorph. *Alzheimers. Res. Ther.* **11**, 16 (2019).
26. N. Jiang, D. Cupolillo, N. Grosjean, E. Muller, S. Deforges, C. Mulle, T. Amédée, Impaired plasticity of intrinsic excitability in the dentate gyrus alters spike transfer in a mouse model of Alzheimer's disease. *Neurobiol. Dis.* **154**, 105345 (2021)..
27. S. Viana Da Silva, P. Zhang, M. G. Haberl, V. Labrousse, N. Grosjean, C. Blanchet, A. Frick, C. Mulle, Hippocampal Mossy Fibers Synapses in CA3 Pyramidal Cells Are Altered at an Early Stage in a Mouse Model of Alzheimer's Disease. *J. Neurosci.* **39**, 4193–4205 (2019).
28. B. W. Doble, J. R. Woodgett, GSK-3: tricks of the trade for a multi-tasking kinase. *J. Cell Sci.* **116**, 1175–1186 (2003).
29. P. H. Reddy, Amyloid beta-induced glycogen synthase kinase 3β phosphorylated VDAC1 in Alzheimer's disease: implications for synaptic dysfunction and neuronal damage. *Biochim. Biophys. Acta* **1832**, 1913–1921 (2013).
30. F. Hernandez, J. J. Lucas, J. Avila, GSK3 and tau: two convergence points in Alzheimer's disease. *J. Alzheimers. Dis.* **33 Suppl 1** (2013).
31. P. T. T. Ly, Y. Wu, H. Zou, R. Wang, W. Zhou, A. Kinoshita, M. Zhang, Y. Yang, F. Cai, J. Woodgett, W. Song, Inhibition of GSK3β-mediated BACE1 expression reduces Alzheimer-associated phenotypes. *J. Clin. Invest.* **123**, 224–235 (2013).
32. A. Ochalek, B. Mihalik, H. X. Avci, A. Chandrasekaran, A. Téglási, I. Bock, M. Lo Giudice, Z. Táncos, K. Molnár, L. László, J. E. Nielsen, B. Holst, K. Freude, P. Hyttel, J. Kobolák, A. Dinnyés, Neurons derived from sporadic Alzheimer's disease iPSCs reveal elevated TAU hyperphosphorylation, increased amyloid levels, and GSK3B activation. *Alzheimers. Res. Ther.* **9**, 90 (2017).
33. S. Solomon, N. K. Sampathkumar, I. Carre, M. Mondal, G. Chennell, A. C. Vernon, M. D. Ruepp, J. C. Mitchell, Heterozygous expression of the Alzheimer's disease-protective PLCγ2 P522R variant enhances Aβ clearance while preserving synapses. *Cell. Mol. Life Sci.* **79**, 453 (2022).
34. B. J. Andreone, L. Przybyla, C. Llapashtica, A. Rana, S. S. Davis, B. van Lengerich, K. Lin, J. Shi, Y. Mei, G. Astarita, G. Di Paolo, T. Sandmann, K. M. Monroe, J. W. Lewcock, Alzheimer's-associated PLCγ2 is a signaling node required for both TREM2 function and the inflammatory response in human microglia. *Nat. Neurosci.* **23**, 927–938 (2020).
35. L. Kleineidam, V. Chouraki, T. Próchnicki, S. J. van der Lee, L. Madrid-Márquez, H. Wagner-Thelen, I. Karaca, L. Weinhold, S. Wolfsgruber, A. Boland, P. V. Martino Adami, P. Lewczuk, J. Popp, F. Brosseron, I. E. Jansen, M. Hulsman, J. Kornhuber, O. Peters, C. Berr, R. Heun, L. Frölich, C. Tzourio, J. F. Dartigues, M. Hüll, A. Espinosa, I. Hernández, I. de Rojas, A. Orellana, S. Valero, N. Stringa, N. M. van Schoor, M. Huisman, P. Scheltens, P. Amouyel, A. Ramirez, E. Rüther, J. F. Deleuze, J. Wiltfang, L. Tarraga, M. Schmid, M. Scherer, S. Riedel-Heller, M. T. Heneka, P. Amouyel, F. Jessen, M. Boada, W. Maier, A. Schneider, A. González-Pérez, W. M. van der Flier, M. Wagner, J. C. Lambert, H. Holstege, M. ªE Sáez, E. Latz, A. Ruiz, PLCG2 protective variant p.P522R modulates tau pathology and disease progression in patients with mild cognitive impairment. *Acta Neuropathol.* **139**, 1025–1044 (2020).
36. S. J. van der Lee, O. J. Conway, I. Jansen, M. M. Carrasquillo, L. Kleineidam, E. van den Akker, I. Hernández, K. R. van Eijk, N. Stringa, J. A. Chen, A. Zettergren, T. F. M. Andlauer, M. Diez-Fairen, J. Simon-Sanchez, A. Lleó, H. Zetterberg, M. Nygaard, C. Blauwendraat, J. E. Savage, J. Mengel-

From, S. Moreno-Grau, M. Wagner, J. Fortea, M. J. Keogh, K. Blennow, I. Skoog, M. A. Friese, O. Pletnikova, M. Zulaica, C. Lage, I. de Rojas, S. Riedel-Heller, I. Illán-Gala, W. Wei, B. Jeune, A. Orellana, F. Then Bergh, X. Wang, M. Hulsman, N. Beker, N. Tesi, C. M. Morris, B. Indakoetxea, L. E. Collij, M. Scherer, E. Morenas-Rodríguez, J. W. Ironside, B. N. M. van Berckel, D. Alcolea, H. Wiendl, S. L. Strickland, P. Pastor, E. Rodríguez Rodríguez, B. F. Boeve, R. C. Petersen, T. J. Ferman, J. A. van Gerpen, M. J. T. Reinders, R. J. Uitti, L. Tárraga, W. Maier, O. Dols-Icardo, A. Kawalia, M. C. Dalmasso, M. Boada, U. K. Zettl, N. M. van Schoor, M. Beekman, M. Allen, E. Masliah, A. L. de Munain, A. Pantelyat, Z. K. Wszolek, O. A. Ross, D. W. Dickson, N. R. Graff-Radford, D. Knopman, R. Rademakers, A. W. Lemstra, Y. A. L. Pijnenburg, P. Scheltens, T. Gasser, P. F. Chinnery, B. Hemmer, M. A. Huisman, J. Troncoso, F. Moreno, E. A. Nohr, T. I. A. Sørensen, P. Heutink, P. Sánchez-Juan, D. Posthuma, G. Coppola, A. M. Karydas, A. Varpetian, T. M. Foroud, A. I. Levey, W. A. Kukull, M. F. Mendez, J. Ringman, H. Chui, C. Cotman, C. DeCarli, B. L. Miller, D. H. Geschwind, J. Clarimón, K. Christensen, N. Ertekin-Taner, S. W. Scholz, A. Ramirez, A. Ruiz, E. Slagboom, W. M. van der Flier, H. Holstege, A nonsynonymous mutation in PLCG2 reduces the risk of Alzheimer's disease, dementia with Lewy bodies and frontotemporal dementia, and increases the likelihood of longevity. *Acta Neuropathol.* **138**, 237–250 (2019).

37. S. Kaech, G. Banker, Culturing hippocampal neurons. *Nat. Protoc.* **1**, 2406–2415 (2006).

38. B. W. Kunkle, B. Grenier-Boley, R. Sims, J. C. Bis, V. Damotte, A. C. Naj, A. Boland, M. Vronskaya, S. J. van der Lee, A. Amlie-Wolf, C. Bellenguez, A. Frizatti, V. Chouraki, E. R. Martin, K. Sleegers, N. Badarinarayan, J. Jakobsdottir, K. L. Hamilton-Nelson, S. Moreno-Grau, R. Olaso, R. Raybould, Y. Chen, A. B. Kuzma, M. Hiltunen, T. Morgan, S. Ahmad, B. N. Vardarajan, J. Epelbaum, P. Hoffmann, M. Boada, G. W. Beecham, J.-G. Garnier, D. Harold, A. L. Fitzpatrick, O. Valladares, M.-L. Moutet, A. Gerrish, A. V. Smith, L. Qu, D. Bacq, N. Denning, X. Jian, Y. Zhao, M. Del Zompo, N. C. Fox, S.-H. Choi, I. Mateo, J. T. Hughes, H. H. Adams, J. Malamon, F. Sanchez-Garcia, Y. Patel, J. a. Brody, B. a. Dombroski, M. C. D. Naranjo, M. Daniilidou, G. Eiriksdottir, S. Mukherjee, D. Wallon, J. Uphill, T. Aspelund, L. B. Cantwell, F. Garzia, D. Galimberti, E. Hofer, M. Butkiewicz, B. Fin, E. Scarpini, C. Sarnowski, W. S. Bush, S. Meslage, J. Kornhuber, C. C. White, Y. Song, R. C. Barber, S. Engelborghs, S. Sordon, D. Voijnovic, P. M. Adams, R. Vandenberghe, M. Mayhaus, L. A. Cupples, M. S. Albert, P. P. De Deyn, W. Gu, J. J. Himali, D. Beekly, A. Squassina, A. M. Hartmann, A. Orellana, D. Blacker, E. Rodriguez-Rodriguez, S. Lovestone, M. E. Garcia, R. S. Doody, C. Munoz-Fernadez, R. Sussams, H. Lin, T. J. Fairchild, Y. a. Benito, C. Holmes, H. Karamujić-Čomić, M. P. Frosch, H. Thonberg, W. Maier, G. Roschupkin, B. Ghetti, V. Giedraitis, A. Kawalia, S. Li, R. M. Huebinger, L. Kilander, S. Moebus, I. Hernández, M. I. Kamboh, R. Brundin, J. Turton, Q. Yang, M. J. Katz, L. Concari, J. Lord, A. S. Beiser, C. D. Keene, S. Helisalmi, I. Kloszewska, W. a. Kukull, A. M. Koivisto, A. Lynch, L. Tarraga, E. B. Larson, A. Haapasalo, B. Lawlor, T. H. Mosley, R. B. Lipton, V. Solfrizzi, M. Gill, W. T. Longstreth, T. J. Montine, V. Frisardi, M. Diez-Fairen, F. Rivadeneira, R. C. Petersen, V. Deramecourt, I. Alvarez, F. Salani, A. Ciaramella, E. Boerwinkle, E. M. Reiman, N. Fievet, J. I. Rotter, J. S. Reisch, O. Hanon, C. Cupidi, a. G. Andre Uitterlinden, D. R. Royall, C. Dufouil, R. G. Maletta, I. de Rojas, M. Sano, A. Brice, R. Cecchetti, P. S. George-Hyslop, K. Ritchie, M. Tsolaki, D. W. Tsuang, B. Dubois, D. Craig, C.-K. Wu, H. Soininen, D. Avramidou, R. L. Albin, L. Fratiglioni, A. Germanou, L. G. Apostolova, L. Keller, M. Koutroumani, S. E. Arnold, F. Panza, O. Gkatzima, S. Asthana, D. Hannequin, P. Whitehead, C. S. Atwood, P. Caffarra, H. Hampel, I. Quintela, Á. Carracedo, L. Lannfelt, D. C. Rubinsztein, L. L. Barnes, F. Pasquier, L. Frölich, S. Barral, B. McGuinness, T. G. Beach, J. a. Johnston, J. T. Becker, P. Passmore, E. H. Bigio, J. M. Schott, T. D. Bird, J. D. Warren, B. F. Boeve, M. K. Lupton, J. D. Bowen, P. Proitsi, A. Boxer, J. F. Powell, J. R. Burke, J. S. K. Kauwe, J. M. Burns, M. Mancuso, J. D. Buxbaum, U. Bonuccelli, N. J. Cairns, A. McQuillin, C. Cao, G. Livingston, C. S. Carlson, N. J. Bass, C. M. Carlsson, J. Hardy, R. M. Carney, J. Bras, M. M. Carrasquillo, R. Guerreiro, M. Allen, H. C. Chui, E. Fisher, C. Masullo, E. a. Crocco, C. DeCarli, G. Bisceglio, M. Dick, L. Ma, R. Duara, N. R. Graff-Radford, D. a. Evans, A. Hodges, K. M. Faber, M. Scherer, K. B. Fallon, M. Riemenschneider, D. W. Fardo, R. Heun, M. R. Farlow, H. Kölsch, S. Ferris, M. Leber, T. M. Foroud, I. Heuser, D. R. Galasko, I. Giegling, M. Gearing, M. Hüll, D. H. Geschwind, J. R.

Gilbert, J. Morris, R. C. Green, K. Mayo, J. H. Growdon, T. Feulner, R. L. Hamilton, L. E. Harrell, D. Drichel, L. S. Honig, T. D. Cushion, M. J. Huentelman, P. Hollingworth, C. M. Hulette, B. T. Hyman, R. Marshall, G. P. Jarvik, A. Meggy, E. Abner, G. E. Menzies, L.-W. Jin, G. Leonenko, L. M. Real, G. R. Jun, C. T. Baldwin, D. Grozeva, A. Karydas, G. Russo, J. a. Kaye, R. Kim, F. Jessen, N. W. Kowall, B. Vellas, J. H. Kramer, E. Vardy, F. M. LaFerla, K.-H. Jöckel, J. J. Lah, M. Dichgans, J. B. Leverenz, D. Mann, A. I. Levey, S. Pickering-Brown, A. P. Lieberman, N. Klopp, K. L. Lunetta, H.-E. Wichmann, C. G. Lyketsos, K. Morgan, D. C. Marson, K. Brown, F. Martiniuk, C. Medway, D. C. Mash, M. M. Nöthen, E. Masliah, N. M. Hooper, W. C. McCormick, A. Daniele, S. M. McCurry, A. Bayer, A. N. McDavid, J. Gallacher, A. C. McKee, H. van den Bussche, M. Mesulam, C. Brayne, B. L. Miller, S. Riedel-Heller, C. a. Miller, J. W. Miller, A. Al-Chalabi, J. C. Morris, C. E. Shaw, A. J. Myers, J. Wiltfang, S. O'Bryant, J. M. Olichney, V. Alvarez, J. E. Parisi, A. B. Singleton, H. L. Paulson, J. Collinge, W. R. Perry, S. Mead, E. Peskind, D. H. Cribbs, M. Rossor, A. Pierce, N. S. Ryan, W. W. Poon, B. Nacmias, H. Potter, S. Sorbi, J. F. Quinn, E. Sacchinelli, A. Raj, G. Spalletta, M. Raskind, C. Caltagirone, P. Bossù, M. D. Orfei, B. Reisberg, R. Clarke, C. Reitz, a D. Smith, J. M. Ringman, D. Warden, E. D. Roberson, G. Wilcock, E. Rogaeva, A. C. Bruni, H. J. Rosen, M. Gallo, R. N. Rosenberg, Y. Ben-Shlomo, M. a. Sager, P. Mecocci, A. J. Saykin, P. Pastor, M. L. Cuccaro, J. M. Vance, J. a. Schneider, L. S. Schneider, S. Slifer, W. W. Seeley, A. G. Smith, J. a. Sonnen, S. Spina, R. a. Stern, R. H. Swerdlow, M. Tang, R. E. Tanzi, J. Q. Trojanowski, J. C. Troncoso, V. M. Van Deerlin, L. J. Van Eldik, H. V. Vinters, J. P. Vonsattel, S. Weintraub, K. a. Welsh-Bohmer, K. C. Wilhelmsen, J. Williamson, T. S. Wingo, R. L. Woltjer, C. B. Wright, C.-E. Yu, L. Yu, Y. Saba, A. Pilotto, M. J. Bullido, O. Peters, P. K. Crane, D. Bennett, P. Bosco, E. Coto, V. Boccardi, P. L. De Jager, A. Lleo, N. Warner, O. L. Lopez, M. Ingelsson, P. Deloukas, C. Cruchaga, C. Graff, R. Gwilliam, M. Fornage, A. M. Goate, P. Sanchez-Juan, P. G. Kehoe, N. Amin, N. Ertekin-Taner, C. Berr, S. Debette, S. Love, L. J. Launer, S. G. Younkin, J.-F. Dartigues, C. Corcoran, M. A. Ikram, D. W. Dickson, G. Nicolas, D. Campion, J. Tschanz, H. Schmidt, H. Hakonarson, J. Clarimon, R. Munger, R. Schmidt, L. a. Farrer, C. Van Broeckhoven, M. C. O'Donovan, A. L. DeStefano, L. Jones, J. L. Haines, J.-F. Deleuze, M. J. Owen, V. Gudnason, R. Mayeux, V. Escott-Price, B. M. Psaty, A. Ramirez, L.-S. Wang, A. Ruiz, C. M. van Duijn, P. a. Holmans, S. Seshadri, J. Williams, P. Amouyel, G. D. Schellenberg, J.-C. Lambert, M. a. Pericak-Vance, Genetic meta-analysis of diagnosed Alzheimer's disease identifies new risk loci and implicates Aβ, tau, immunity and lipid processing. *Nat. Genet.* **51**, 414–430 (2019).

39. A. Blasiak, G. U. Lee, D. Kilinc, Neuron Subpopulations with Different Elongation Rates and DCC Dynamics Exhibit Distinct Responses to Isolated Netrin-1 Treatment. *ACS Chem. Neurosci.* **6**, 1578–1590 (2015).
40. A. Rodriguez, D. B. Ehlenberger, P. R. Hof, S. L. Wearne, Rayburst sampling, an algorithm for automated three-dimensional shape analysis from laser scanning microscopy images. *Nat. Protoc.* **1**, 2152–61 (2006).
41. J. Schindelin, I. Arganda-Carreras, E. Frise, V. Kaynig, M. Longair, T. Pietzsch, S. Preibisch, C. Rueden, S. Saalfeld, B. Schmid, J.-Y. Tinevez, D. J. White, V. Hartenstein, K. Eliceiri, P. Tomancak, A. Cardona, Fiji: an open-source platform for biological-image analysis. *Nat. Methods* **9**, 676–82 (2012).
42. G. McKhann, D. Drachman, M. Folstein, R. Katzman, D. Price, E. M. Stadlan, Clinical diagnosis of Alzheimer's disease: report of the NINCDS-ADRDA Work Group under the auspices of Department of Health and Human Services Task Force on Alzheimer's Disease. *Neurology* **34**, 939–944 (1984).
43. J. C. Bis, X. Jian, B. W. Kunkle, Y. Chen, K. L. Hamilton-Nelson, W. S. Bush, W. J. Salerno, D. Lancour, Y. Ma, A. E. Renton, E. Marcora, J. J. Farrell, Y. Zhao, L. Qu, S. Ahmad, N. Amin, P. Amouyel, G. W. Beecham, J. E. Below, D. Campion, L. Cantwell, C. Charbonnier, J. Chung, P. K. Crane, C. Cruchaga, L. A. Cupples, J. F. Dartigues, S. Debette, J. F. Deleuze, L. Fulton, S. B. Gabriel, E. Genin, R. A. Gibbs, A. Goate, B. Grenier-Boley, N. Gupta, J. L. Haines, A. S. Havulinna, S. Helisalmi, M. Hiltunen, D. P. Howrigan, M. A. Ikram, J. Kaprio, J. Konrad, A. Kuzma, E. S. Lander, M. Lathrop, T. Lehtimäki, H. Lin, K. Mattila, R. Mayeux, D. M. Muzny, W. Nasser, B. Neale, K.

Nho, G. Nicolas, D. Patel, M. A. Pericak-Vance, M. Perola, B. M. Psaty, O. Quenez, F. Rajabli, R. Redon, C. Reitz, A. M. Remes, V. Salomaa, C. Sarnowski, H. Schmidt, M. Schmidt, R. Schmidt, H. Soininen, T. A. Thornton, G. Tosto, C. Tzourio, S. J. van der Lee, C. M. van Duijn, O. Valladares, B. Vardarajan, L. S. Wang, W. Wang, E. Wijsman, R. K. Wilson, D. Witten, K. C. Worley, X. Zhang, C. Bellenguez, J. C. Lambert, M. I. Kurki, A. Palotie, M. Daly, E. Boerwinkle, K. L. Lunetta, A. L. Destefano, J. Dupuis, E. R. Martin, G. D. Schellenberg, S. Seshadri, A. C. Naj, M. Fornage, L. A. Farrer, Whole exome sequencing study identifies novel rare and common Alzheimer's-Associated variants involved in immune response and transcriptional regulation. *Mol. Psychiatry* **25**, 1859–1875 (2020).

44. A. Korpioja, J. Krüger, S. Koivuluoma, K. Pylkäs, V. Moilanen, S. Helisalmi, M. Hiltunen, A. M. Remes, L. Q. Zhu, Novel Rare SORL1 Variants in Early-Onset Dementia. *J. Alzheimers. Dis.* **82**, 761–770 (2021).
45. S. Balduzzi, G. Rücker, G. Schwarzer, How to perform a meta-analysis with R: a practical tutorial. *Evid. Based. Ment. Health* **22**, 153–160 (2019).
46. A. M. Bolger, M. Lohse, B. Usadel, Trimmomatic: a flexible trimmer for Illumina sequence data. *Bioinformatics* **30**, 2114–2120 (2014).
47. A. Dobin, C. A. Davis, F. Schlesinger, J. Drenkow, C. Zaleski, S. Jha, P. Batut, M. Chaisson, T. R. Gingeras, STAR: ultrafast universal RNA-seq aligner. *Bioinformatics* **29**, 15–21 (2013).
48. Y. Liao, G. K. Smyth, W. Shi, The R package Rsubread is easier, faster, cheaper and better for alignment and quantification of RNA sequencing reads. *Nucleic Acids Res.* **47**, e47 (2019).
49. M. I. Love, W. Huber, S. Anders, Moderated estimation of fold change and dispersion for RNA-seq data with DESeq2. *Genome Biol.* **15**, 550 (2014).
50. H. Braak, I. Alafuzoff, T. Arzberger, H. Kretzschmar, K. Tredici, Staging of Alzheimer disease-associated neurofibrillary pathology using paraffin sections and immunocytochemistry. *Acta Neuropathol.* **112**, 389–404 (2006).
51. M. Marttinen, J. Paananen, A. Neme, V. Mitra, M. Takalo, T. Natunen, K. M. A. Paldanius, P. Mäkinen, M. Bremang, M. I. Kurki, T. Rauramaa, V. Leinonen, H. Soininen, A. Haapasalo, I. Pike, M. Hiltunen, A multiomic approach to characterize the temporal sequence in Alzheimer's disease-related pathology. *Neurobiol. Dis.* **124**, 454–468 (2019).
52. H. Martiskainen, J. Viswanathan, N. P. Nykänen, M. Kurki, S. Helisalmi, T. Natunen, T. Sarajärvi, K. M. A. Kurkinen, J. P. Pursiheimo, T. Rauramaa, I. Alafuzoff, J. E. Jääskeläinen, V. Leinonen, H. Soininen, A. Haapasalo, H. J. Huttunen, M. Hiltunen, Transcriptomics and mechanistic elucidation of Alzheimer's disease risk genes in the brain and in vitro models. *Neurobiol. Aging* **36**, 1221.e15-1221.e28 (2015).
53. T. Natunen, H. Martiskainen, T. Sarajaŕvi, S. Helisalmi, J. P. Pursiheimo, J. Viswanathan, M. Laitinen, P. Maḱinen, T. Kauppinen, T. Rauramaa, V. Leinonen, I. Alafuzoff, A. Haapasalo, H. Soininen, M. Hiltunen, Effects of NR1H3 genetic variation on the expression of liver X receptor α and the progression of Alzheimer's disease. *PLoS One* **8,** e80700 (2013).
54. T. Natunen, H. Martiskainen, M. Marttinen, S. Gabbouj, H. Koivisto, S. Kemppainen, S. Kaipainen, M. Takalo, H. Svobodová, L. Leppänen, B. Kemiläinen, S. Ryhänen, T. Kuulasmaa, E. Rahunen, S. Juutinen, P. Mäkinen, P. Miettinen, T. Rauramaa, J. Pihlajamäki, A. Haapasalo, V. Leinonen, H. Tanila, M. Hiltunen, Diabetic phenotype in mouse and humans reduces the number of microglia around β-amyloid plaques. *Mol. Neurodegener.* **15**, 66 (2020).
55. S. Kemppainen, N. Huber, R. M. Willman, A. Zamora, P. Mäkinen, H. Martiskainen, M. Takalo, A. Haapasalo, T. Sobrino, M. A. González Gómez, Y. Piñeiro, J. Rivas, U. Himmelreich, M. Hiltunen, Organotypic Hippocampal Slice Cultures from Adult Tauopathy Mice and Theragnostic Evaluation of Nanomaterial Phospho-TAU Antibody-Conjugates. *Cells* **12**, 1422 (2023).
56. S. Gabbouj, T. Natunen, H. Koivisto, K. Jokivarsi, M. Takalo, M. Marttinen, R. Wittrahm, S. Kemppainen, R. Naderi, A. Posado-Fernández, S. Ryhänen, P. Mäkinen, K. M. A. Paldanius, G. Doria, P. Poutiainen, O. Flores, A. Haapasalo, H. Tanila, M. Hiltunen, Intranasal insulin activates Akt2 signaling pathway in the hippocampus of wild-type but not in APP/PS1 Alzheimer model mice. *Neurobiol. Aging* **75**, 98–108 (2019).

57. H. Martiskainen, S. Helisalmi, J. Viswanathan, M. Kurki, A. Hall, S. K. Herukka, T. Sarajärvi, T. Natunen, K. M. A. Kurkinen, J. Huovinen, P. Mäkinen, M. Laitinen, A. M. Koivisto, K. M. Mattila, T. Lehtimäki, A. M. Remes, V. Leinonen, A. Haapasalo, H. Soininen, M. Hiltunen, Effects of Alzheimer's disease-associated risk loci on cerebrospinal fluid biomarkers and disease progression: a polygenic risk score approach. *J. Alzheimers. Dis.* **43**, 565–573 (2015).

Acknowledgement

The authors thank the BICeL platform of the Institut Biologie de Lille and the Vect'viral platform (INSERM US 005 – CNRS 3427 – TBMCore, Université de Bordeaux, France). The authors thank Karine Blary at the IEMN Lille for the microfabrication work.

The authors also thank Sisko Juutinen, Eija Rahunen, and Minna Turunen for excellent technical support with immunohistochemistry. Fluorescent microscopy of human brain samples was carried out with the support of UEF Cell and Tissue Imaging Unit, University of Eastern Finland, Finland.

Funding

JPND (JPND2019-466-128, project PGM-AD)

ANR (GENSYNALZ; ANR-21-CE16-0010)

Fondation Alzheimer (grant number 903716)

Fondation Claude Pompidou

Fondation pour la Recherche Médicale (ALZ201912009628)

Fondation Recherche Alzheimer

the French RENATECH network (P-18-02737)

Lille Métropole Communauté Urbaine and the French government's LABEX DISTALZ program (Development of innovative strategies for a transdisciplinary approach to Alzheimer's disease).

European Union under the European Regional Development Fund (ERDF)

Hauts de France Regional Council (contract469 no.18006176)

MEL (contract_18006176), and the French State (contract no. 2018-3-470 CTRL_IPL_Phase2).

Research Council of Finland (grant number 330178, 338182, 355604, 334802)

the Sigrid Jusélius Foundation

the Strategic Neuroscience Funding of the University of Eastern Finland, Faculty of Health Sciences of University of Eastern Finland

Alzheimer's Association (ADSF-24-1284326-C and AARG-22-926152).

Author's Contribution

Conceptualization: J.C., J.D.; J-C.L.

High content screening: A.C., T.M., D.K., J.C., J-C.L.;

Cell culture experiments: A.C., F.R., D.S-W., A.R.M.F., C.N., N.L-W., A. F-R., C.G., E.L., A-M.A, F.D., M.R.C., D.K., J.D.

Electrophysiological analyses: A.R., A.E., S.D., C.M.;

Immunohistochemistry and RNAseq analyses: L-I.C., M.T., H.M., R.M.W., H.J., P.M., S.H., M.Hil.;

WES sequencing data: M.Hul., P.A., C.C., O.D-I., H.J., T.K., M.K., J.H., S.H., H.H., P.M., G.N., S.M., M.W., A.R., T.R., A.P., R.S., H.S., J.V.S., J.W., R.M.W., J-C.L.;

Genetic Analysis: M.Hul., T.R., B.G-B., M.Hil., J-C.L.

Writing: A.C., F.R., M.T., A.R., H.M., D.K., C.M., J.C., M.Hil., J.D., J-C.L.

Conflicts of interest:

None

Availability of data and material

Cellular models used and/or analyzed in the current study are available from the corresponding authors upon request.

Figure 1. High-content screening identified nine AD-associated genes that significantly impact synaptic density and function in rat primary neurons. **(a-b)** Impact of shRNA-mediated downregulation of 198 AD-associated genes on synaptic density in rat hippocampal primary neuronal cultures (PNCs), virally transduced at MOI 2 **(a)** and MOI 4 **(b)**. Data given as mean±SEM, n=3, top and bottom 2.5% genes are shown in red. **(c)** Quantification of synapse density following the assignment of Homer1 to Syp spots on Map2-positive dendrites. Data given as mean±SEM, n=3. **(d-e)** Representative images of Map2, Syp and Homer1 immunostainings following shRNA-mediated downregulation of *Syp, Psmc3, Plcg2, Cyb561, Snx1, Ical1,* and *Nck2* at MOI 2 **(c)** and of *Syp, Csnk1g1, Usp6nl, Oplah* and *Nck2* at MOI 4 **(d)**; Scale bars = 20 µm. **(f)** Western blots showing the validation of gene downregulation for Usp6nl, Psmc3, Plcγ2, Csnk1g1, Cybk1g1, Cyb561, Snx1, Ica1l, Oplah, and Nck2 transduced at MOI 2 in PNCs. **(g)** Quantification of protein levels in PNCs transduced with these nine shRNAs, normalized by the non-targeting control (shNT) levels. Data given as mean±SD, n=3. **(h-i)** Impact of these nine shRNAs on the mean spike **(h)** and burst frequencies **(i)** in PNCs at DIV21, measured by MEA. Violin plots show median and quartile lines, n=3.
All statistical analyses were performed using Mann-Whitney test. *p<0.05, ** p<0.01, *** p<0.001.

Figure 2: *Plcg2* downregulation alters the morphology of DG granule cells. **(a)** Schematic representation of the experimental approach to downregulate *Plcg2* in the DG. The lentiviral constructs were injected by sterotaxy in either the ipsi- (LV-shPLCG2 for knock-down of *Plcg2*) or contralateral (LV-shNT, control) hemispheres. **(b)** High magnification immunofluorescence images of transduced DG cells as indicated by GFP expression, as well as a portion of dendritic branch with spines (control shNT left; shPLCG2 right); scale bars = 20 µm for left panels and 7 µm for right panels. **(c-f)** Measurements of dendritic length **(c)**, dendritic volume **(d)**, complexity index **(e)**, and branch number **(f)** in transduced DG granule cells. **(g)** Schematic diagram of the Sholl analysis illustrating the morphological change in the dendritic tree of representative control (grey) vs shPLCG2 (red) transduced DG granule cells. Scale bar = 20 µm. **(h)** Distribution of intersections based on the Sholl analysis. **(i-k)** Graphs comparing average spine density **(i)**, spine length **(j)** and spine head diameter **(k)**, indicating a marked alteration in synaptic contacts onto DG granule cells. Data expressed as mean±SEM for bar graphs with individual data points.
All statistical analyses were performed using Mann-Whitney test (for Sholl analysis n ≥90 per condition. * p<0.05, **** p<0.0001

Figure 3: *PLCG2* downregulation in DG granule cells leads to decreased excitability and reduced mEPSC frequency and amplitude. (a) Representative image of maximum intensity projection of section labeled with iba-1 (in magenta) and GFP (in green) showing the selective expression of viral vector in DG granule cells. MolDG= molecular layer of DG, GrDG= granular DG, PoDG= polymorph layer of DG. Patch-clamp recordings were performed from GFP expressing granule cells identified under the electrophysiology microscope. Scale bar = 10 µm. **(b)** Representative traces from shNT (in grey) and shPLCG2 (in red) transduced DG granule cells recorded in the current-clamp mode, with injection of current steps from –80 pA to 0 pA with 10 pA increments. **(c)** Representative traces of current-clamp recordings showing spike discharges triggered by a depolarization pulse of current (120 pA) from shNT (in grey) and shPLCG2 (in red) transduced DG cells. **(d-f)** Current-clamp recordings were used to assess input resistance **(d)**, resting membrane potential (RMP) **(e)** and rheobase **(f)**. **(g)** Number of spikes plotted against current injected. **(h)** Representative traces of miniature excitatory post-synaptic currents (mEPSCs) recorded in the voltage-clamp mode from shNT (in grey) and shRNA (in red) DG cells in presence of 500 nM TTX. **(i-k)** Measurements of average frequency of mEPSCs **(i),** average amplitude of mEPSCs **(j)** and cumulative distribution of mEPSC amplitudes **(k)**. Data are represented as mean±SEM with bar and individual data points for average values, where individual data points indicate each cell recorded; shNT n=27 and shRNA n=15 with scale bar for mEPSCs= 10pA/1s; for RMP and input resistance shNT n=15 and shRNA n=14 with scale 40mV/20mV.
All statistical analyses were performed using Mann-Whitney test at the exception of the cumulative distribution were a Kolmogorov-Smirnov (KS) test was applied. * p<0.05, ** p<0.01, ***p<0.001.

Figure 4. Downregulation of PLCγ2 in hNCs negatively impacts synapses and AD hallmarks
(a) Representative images of hNCs after 4 weeks of spontaneous differentiation from progenitors stably expressing either a non-targeting shRNA (shNT) or a shRNA targeting *PLCG2* (shPLCG2); scale bar = 20 µm. **(b)** Western blots showing the specificity of PLCγ2 downregulation via shPLCG2 in hNCs. **(c)** Immunofluorescence images of MAP2, SYP and HOMER1 synaptic markers in shNT- and shPLCG2-transduced hNCs at 4 weeks. Scale bar = 20 µm. **(d)** Synaptic marker densities for the two conditions. Data given as mean±SEM, n=3; **(e)** Impact of shPLCG2 on spike and burst frequencies in hNCs, measured via MEA. Violin plots show median and quartile lines, n=3; **(f)** Representative Western blots of APP, total Tau and Tau phosphorylated at T181, S202-T205, T217, T231 and S396-S404 in shNT- and shPLCG2-transduced hNCs; **(g)** Quantification of APP and TAU levels for the two conditions. Data given as mean ± SD, n=3; **(h)** Aβ peptides levels in shNT- or shPLCG2- transduced hNCs, measured by Alpha-LISA. Data given as means ± SEM, n=3; **(i)** Tau phosphorylation levels in hNCs expressing (or not) shPLCG2. Data given as mean ± SD, n=3; **(j)** Representative Western blots of total and phosphorylated forms of ERK1/2, GSK3β, P38-MAPK and AKT in shNT- and shPLCG2-transduced hNCs. **(k)** Quantification of total and phosphorylated protein levels for these targets in shNT- and shPLCG2-transduced hNCs. Data given as mean ± SD, n=3.
All statistical analyses were performed using Mann-Whitney test. *p<0.05, ***p<0.001, ****p<0.0001

Figure 5. The *PLCG2* p.Q816X and p.R953X non-sense variants increase AD risk and reduce *PLCG2* expression and PLCγ2 protein levels, consistently with a protective effect of PLCG2 re-expression in shPLCG2-hNCs. (a) Meta-analysis of the ADGEN and ADES Whole Exome Sequencing data **(b)** Western blot of the post-mortem brain tissue of an AD patient carrying the p.R953X variant in comparison with four other AD cases. **(c)** Quantification of PLCγ2 protein levels in these samples. **(d)** RNAseq showing a 40% decrease in the blood *PLCG2* mRNA expression in the p.Q816X carrier as compared to the average of matched control group (n=4). **(e)** Representative Western blots of APP, total and T231-phospho-Tau total and phospho-GSK3β, and total and phospho-AKT protein levels in shNT-hNCs, shPLCG2-hNCs, and shPLCG2-hNCs overexpressing PLCG2. Quantification of APP and Tau protein levels **(f),** Aβ peptides levels in the culture medium measured by Alpha-LISA and normalized to total protein levels **(g)** and Tau phosphorylated levels at T231 (normalized by total Tau) **(h)** in shNT-hNCs, shPLCG2-hNCs, and shPLCG2-hNCs overexpressing PLCG2. For these groups. Data given as mean ± SD, n=3. **(i)** Representative images of T231-phospho-Tau, total Tau, and MAP2 immunostainings in shNT-hNCs, shPLCG2-hNCs, and shPLCG2-hNCs overexpressing PLCG2. Scale bar = 20 µm. **(j)** Quantification of T231-pTAU in the neuronal somata for these groups. Data given as mean ± SEM, n=3. **(k)** Changes in total and phospho-protein levels for GSK3β and AKT in shNT-hNCs, shPLCG2-hNCs, and shPLCG2-hNCs overexpressing PLCγ2. Data given as mean ± SD, n=3.
All statistical analyses were performed using Mann-Whitney test. *p<0.05.

Figure 1.

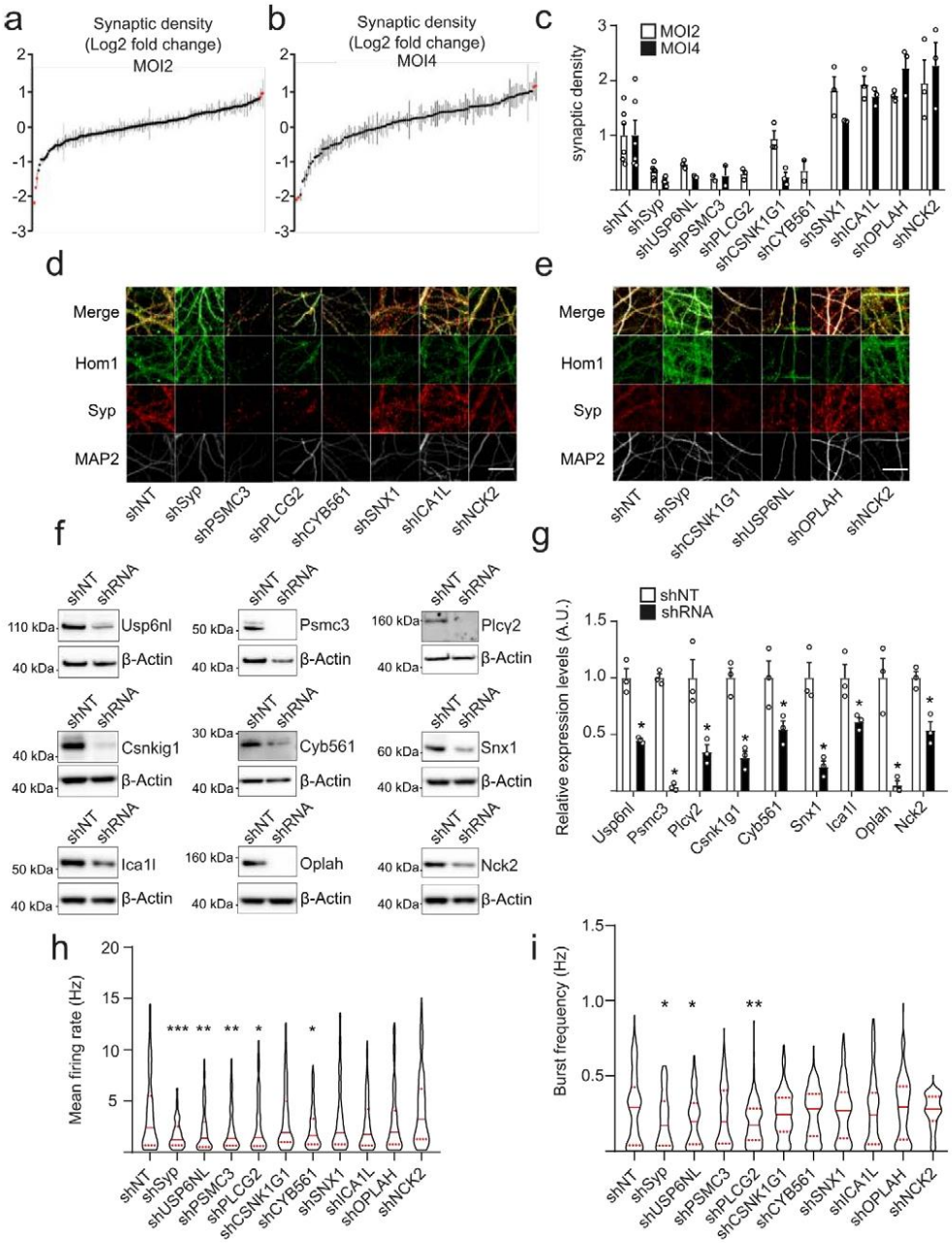

Figure 2.

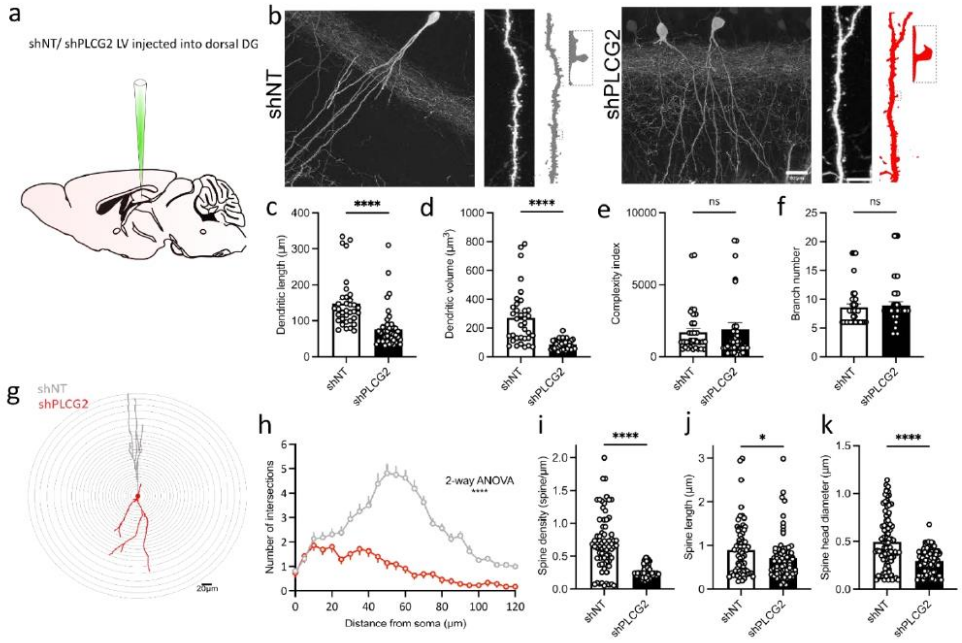

Figure 3.

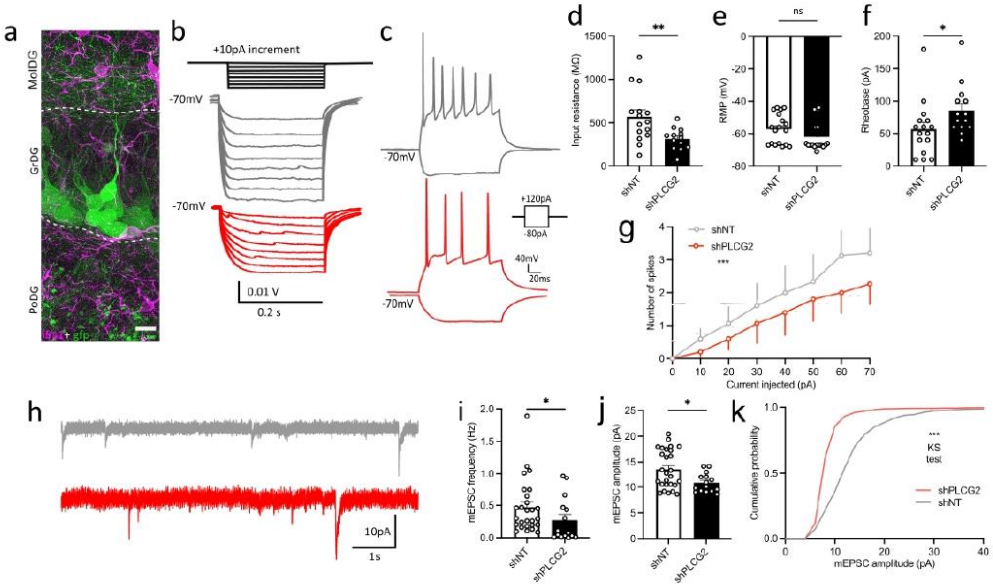

Figure 4.

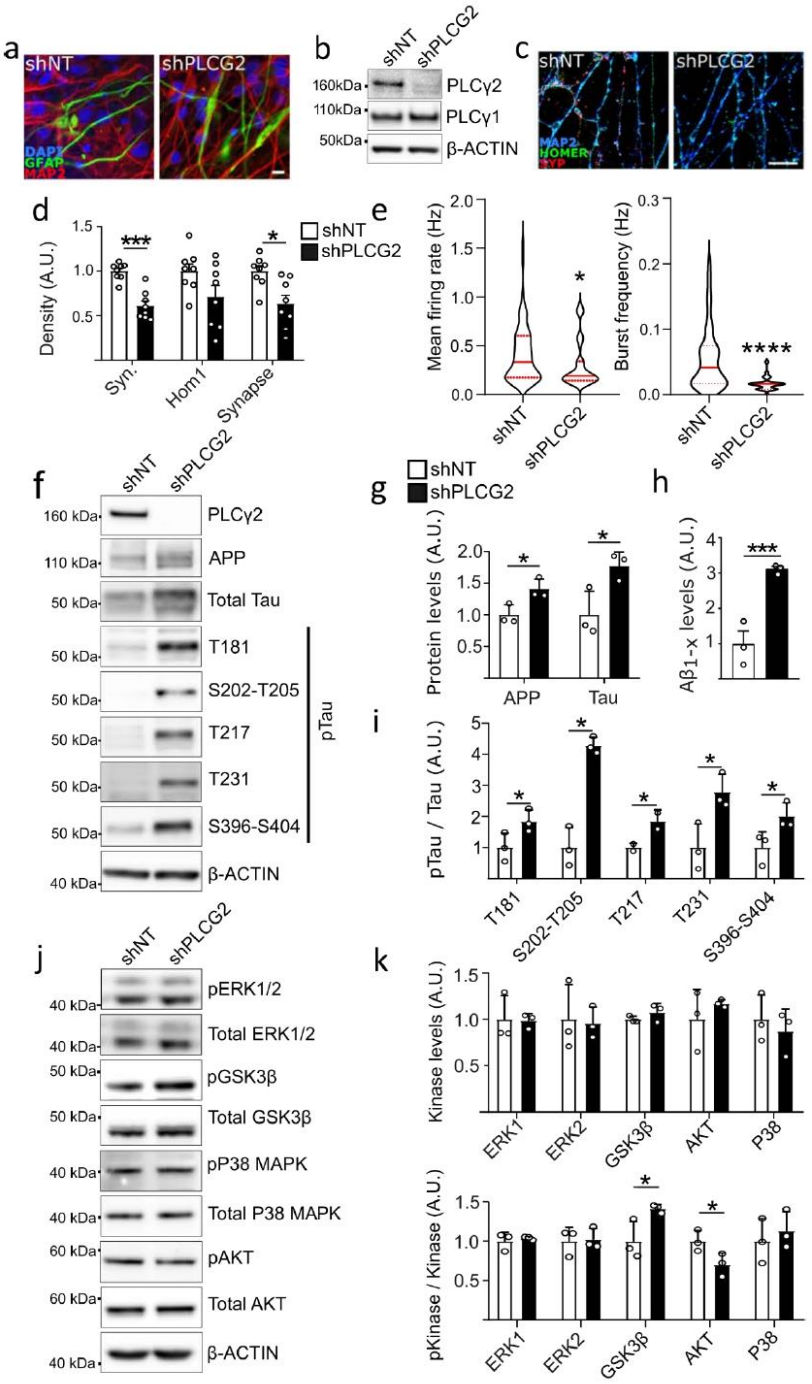

Figure 5.

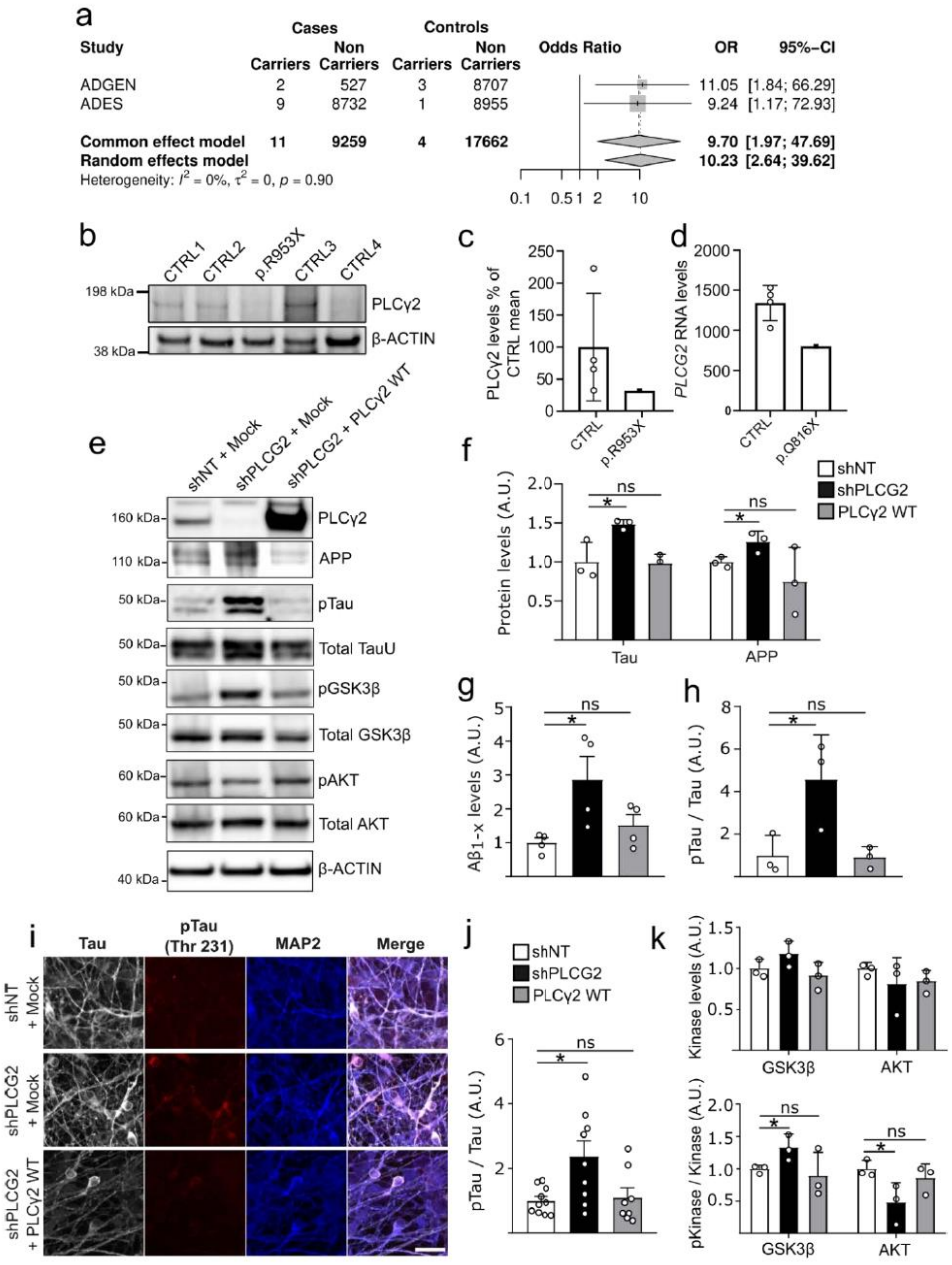

Neurobiology of Aging 151 (2025) 117–125

Contents lists available at ScienceDirect

Neurobiology of Aging

journal homepage: www.elsevier.com/locate/neuaging.org

Calpain and caspase regulate Aβ peptide production via cleavage of KINDLIN2 encoded by the AD-associated gene *FERMT2*

Chloé Najdek [1], Pauline Walle [1], Amandine Flaig, Anne-Marie Ayral, Florie Demiautte, Audrey Coulon, Valérie Buiche, Neuro-CEB Brain Bank, Erwan Lambert [2], Philippe Amouyel, Carla Gelle, Dolores Siedlecki-Wullich, Julie Dumont, Devrim Kilinc, Fanny Eysert [3], Jean-Charles Lambert, Julien Chapuis *

Univ. Lille, Inserm, CHU Lille, Institut Pasteur de Lille, U1167 - RID-AGE - Facteurs de risque et déterminants moléculaires des maladies liées au vieillissement, Lille 59019, France

ARTICLE INFO

Keywords:
KINDLIN2 ALZHEIMER APP

ABSTRACT

The adapter protein KINDLIN2, encoded by the Alzheimer's disease (AD) genetic risk factor *FERMT2*, was identified as a modulator of APP processing. KINDLIN2 directly interacts with APP to modulate its metabolism, and KINDLIN2 underexpression impairs long-term potentiation in an APP-dependent manner. Altogether, these data suggest that loss of KINDLIN2 could have a detrimental effect on synaptic function and promote AD pathophysiological process. In this study, we identified KINDLIN2 as a novel substrate of caspases and calpain I, two well-characterized cysteine proteases involved in the regulation of synaptic plasticity. These cleavages resulted in the dissociation of the F0 and F1 domains of KINDLIN2 that are necessary for it to function as an adapter protein. Furthermore, we demonstrate that these cleavages lead to a decrease in KINDLIN2's ability to control APP processing. Overall, these KINDLIN2 cleavages appear as potential new mechanisms in the regulation of KINDLIN2 functions at the synapse and could be of interest for the pathophysiology of AD.

1. Introduction

The main pathological features of Alzheimer's disease (AD) are neurofibrillary tangles and senile plaque formation. The latter is caused by the progressive deposition of amyloid β (Aβ) peptides in the brain, and multiple lines of evidence suggest that these Aβ peptides are one of the primary causes of AD (Aleksis et al., 2017; Hardy and Higgins, 1992). Aβ peptides are generated through sequential cleavages of β-amyloid precursor protein (APP) first by β-secretase and then by the γ-secretase complex (Haass, 2004). APP metabolism is a highly regulated cellular process that depends on biosynthetic-secretory and endocytic pathways and involves molecular mechanisms that are not fully characterized (Lin et al., 2021).

Since the mutations responsible for the monogenic forms of AD have a strong impact on APP metabolism, and given the importance of the genetic component of AD even in the common forms of the disease (estimated to account for between 60 % and 80 % of the attributable risk in twin studies (Gatz et al., 2006), it has been suggested that dissecting the AD genetic component could provide a better understanding of the APP metabolism, especially in a pathophysiological context. This approach was clearly supported by genome-wide association studies, where pathway enrichment analyses confirmed the involvement of APP metabolism. In this context, we previously developed a genome-wide, high-content siRNA screening approach to identify AD risk genes that affect APP metabolism. This allowed us to identify the genetic risk factor *FERMT2* (FERM Domain Containing Kindlin 2, coding for KINDLIN2) as a strong modulator of APP metabolism (Chapuis et al., 2017).

KINDLIN2 is known to be an adapter protein that is required for integrin activation and focal adhesion (FA) complex formation (Li et al., 2017; Montanez et al., 2008). In neurons, there are also adhesion

* Correspondence to: Inserm UMR1167, Institut Pasteur de Lille, 1 rue du Pr. Calmette, Lille 59019, France.
E-mail address: julien.chapuis@pasteur-lille.fr (J. Chapuis).
[1] These authors contributed equally.
[2] Current affiliation: Donders Center for Neuroscience, Department of Molecular Neurobiology, Radboud University, Nijmegen, the Netherlands.
[3] Current affiliation: Institute of molecular and cellular pharmacology, INSERM U1323, CNRS UMR7275, Université Côte d'Azur, Laboratory of excellence DistALZ, 06560, Sophia-Antipolis, Valbonne, France.

https://doi.org/10.1016/j.neurobiolaging.2025.04.009
Received 4 July 2024; Received in revised form 14 April 2025; Accepted 19 April 2025
Available online 21 April 2025

complexes, known as point contacts, involved in the modulation of synaptic density and activity through regulating dendritic spine shape, stability, and the signaling machinery therein (Hotulainen and Hoogenraad, 2010). Interestingly, numerous studies have highlighted the role of APP as a neuronal cell adhesion molecule, with roles in neurite migration and growth (Perez et al., 1997; Sabo et al., 2003; Small et al., 1999), adhesion of the growth cone (Sosa et al., 2013), as well as synaptic adhesion and stabilization of pre- and postsynaptic compartments (Müller et al., 2017; Wang et al., 2009). The cytoplasmic tail of APP presents the YENPTY amino acid motif that is a highly conserved motif present in all APP family members as well as in other adhesion molecules, such as integrin β1. This domain is involved in the interaction with adaptor proteins that contain a phosphotyrosine-binding domain (PTB) and are related to cell adhesion and migration, notably, KINDLIN2 (Eysert et al., 2021). Indeed, our recent work demonstrated that KINDLIN2's F3 domain can interact with the YENPTY motif within APP's intracellular domain and that this interaction is necessary for KINDLIN2 to control the presence of APP on the cell surface (Eysert et al., 2021). We also demonstrated that KINDLIN2 controls axonal growth and synaptic plasticity in an APP-dependent manner (Eysert et al., 2021). Altogether, these data suggest that KINDLIN2 and APP may be playing an important role as a molecular complex, just like KINDLIN2 and Integrin do, to regulate cellular adhesion processes in the nervous system.

Spatial and temporal control of FA turnover is mediated by multiple mechanisms, one of which is the proteolytic cleavage of multiple FA-related proteins. Multiple studies show that members of the calpain and caspase protease families are involved in the proteolytic cleavage of several FA components, such as TALIN, PAXILLIN and FAK, leading to the disassembly of the complexes they form (Chan et al., 2010; Cortesio et al., 2011; Franco et al., 2004; Levkau et al., 1998; Wen et al., 1997). Through the proteolysis of these substrates, these two protease families are involved in the regulation of of the growth cone motility, neuronal morphology and plasticity (Aylsworth et al., 2009; Baudry et al., 2021; Wang et al., 2016; Westphal et al., 2010; Williams et al., 2006), corresponding to functions previously described to be regulated by the FERMT2-APP complex (Eysert et al., 2021). In this study, we report novel mechanisms that are involved in the regulation of KINDLIN2 function. We characterize KINDLIN2 as a new substrate of calpains and caspases. We also provide evidence suggesting that these KINDLIN2 cleavages result in a decrease in the previously reported ability of KINDLIN2 to regulate APP metabolism.

2. Methods

2.1. Human post-mortem samples

Brain samples were collected through a brain donation program dedicated to neurodegenerative dementias coordinated by the Neuro-CEB Brain Bank Network, as previously described (Kilinc et al., 2020). Briefly, the informed consent for post-mortem examination and research studies was signed by the legal representative of each patient in patient's name, as allowed by the French law and approved by the local ethics committee. The brain bank has been officially authorized to provide samples to scientists (agreement AC-2013–1887). All procedures performed in this study involving human participants were in accordance with the ethical standards of the institutional research committees and with the 1964 Declaration of Helsinki. The brain bank fulfils the criteria of the French Law on biological resources including informed consent, ethics review committee and data protection (article L1243–4 du Code de la Santé publique, August 2007). The Neuro-CEB Brain Bank (BioResource Research Impact Factor number BB-0033–00011) has been declared to the Ministry of Research and Higher Education, as required by French law. The assessment of Alzheimer's disease-related neurofibrillary pathology (Braak stage) in post-mortem brain tissue samples from 28 individuals (Supplementary Table 1) has been described previously (Kilinc et al., 2020).

2.2. Cell culture

Human embryonic kidney (HEK) 293 cells were cultured in 1:1 mixture of Dulbecco's Modified Eagle Medium and Ham's F12 nutrient mixture (DMEM-F12, 21331020, Thermo Fisher Scientific) supplemented with 10 % heat-inactivated fetal bovine serum (FBS; 10270106, Gibco), 2 mM L-glutamine (25030149, Thermo Fisher) and 50 UI/ml penicillin/streptomycin (15140122, Thermo Fisher) at 37°C in a humidified atmosphere with 5 % CO_2. Prior to transfection, cells were plated at a density of ~70 %. Transient transfection of FERMT2 cDNA (cloned into a pcDNA4 vector; GeneArt) was performed using Fugene HD (E2312, Promega) according to the manufacturer's instructions. The cell line was tested negative for mycoplasma contamination using PCR test (Venor GeM OneStep, Minerva Biolabs).

2.3. *Kindlin-2*$^{fl/fl}$ mice and primary neuron culture

Kindlin-2 floxed mice (*Kindlin-2*$^{fl/fl}$) (EUCOMM)Wtsi (GSF-EPD0087_1_G04–1), which carries loxP sites flanking exon 5 and 6, were purchased from the International Mouse Phenotyping Consortium (IMPC). The mouse was mated with Flp-deleter mouse to remove LacZ and neo cassettes. *Kindlin-2*$^{fl/+}$ mice were intercrossed to obtain *Kindlin-2*$^{fl/fl}$ mice. Animal housing and experimentation were performed according to procedures approved by the local Animal Ethical Committee following European standards for the care and use of laboratory animal (agreement APAFIS #32824–202112051852l661, Lille, France). Culture media and supplements were from Thermo Fisher, unless mentioned otherwise. Cortical neurons were dissected from E14-E15 Kindlin-2$^{fl/fl}$ mice, according to previously described procedures (Fath et al., 2009; Jan et al., 2010). Briefly, cortices were isolated from E14-E15 mice in ice-cold dissection medium (Hank's balanced salt solution supplemented with 10 mM HEPES, 1 mM sodium pyruvate, 10 mM glucose, and penicillin/streptomycin) and trypsinized at 37°C for 30 min (Trypsin solution, T4549, Sigma). DNase I was added to the trypsin-incubated tissue suspension to break down DNA and to avoid clumping of tissue during the subsequent trituration (DN25, Sigma). Trypsin was inactivated by the addition of isolation medium (Neurobasal™ medium supplemented with 10 % of heat-inactivated fetal bovine serum, 1 % GlutaMAX, 20 mM Hepes and Gentamycine). The cell suspension was passed through a 100 µm then 70 µm cell strainer, followed by two centrifugations (300 ×*g* for 10 min). Cells were resuspended in culture medium composed of MACS Neuro Medium (130−093−570) supplemented with 0.25 % GlutaMAX, 2 % MACS NeuroBrew-21 (130−093−566) and Gentamycine, and counted. For immunoblots, cells were plated at a density of 100,000 cells/cm^2 in 24-well plates, pre-coated with 0.1 mg/ml poly-D-lysine in 0.1 M borate buffer (0.31 % boric acid, 0.475 % sodium tetraborate, pH 8.5; Sigma) overnight at 37°C and rinsed thoroughly with water. To delete Kindlin-2 expression specifically in neurons, transductions of lentiviral vectors that drive Cre expression under the synapsin promoter were carried out at 1 day in vitro (DIV1) at multiplicities of infection (MOI) 4 and 6. Briefly, lentiviruses were diluted in culture medium containing 4 µg/ml polybrene (hexadimethrine bromide, Sigma) and were added to the cells. After 4 h of transduction, lentivirus suspension was replaced with fresh medium.

2.4. Synapse fractionation

Subcellular fractionations were performed as previously described (Frandemiche et al., 2014). Briefly, cortical neurons were resuspended in a cold buffer containing 0.32 M sucrose and 10 mM HEPES, pH = 7.4, and were centrifuged at 1000×*g* for 10 min to remove nuclei and debris. To remove the cytosolic fraction, the supernatant was concentrated at 12,000×*g* for 20 min. The resulting pellet was resuspended in a second

solution solution (4 mM HEPES, 1 mM EDTA, pH = 7.4) and was centrifuged 2 times at 12,000 ×*g* for 20 min. The pellet was incubated in a third solution (20 mM HEPES, 100 mM NaCl, and 0.5 % Triton X-100, pH = 7.2) for 1 h at 4°C and centrifuged at 12,000 ×*g* for 20 min to pellet the synaptosomal membrane fraction. The supernatant was collected as the non-PSD membrane fraction (Triton-soluble). The remaining pellet was then solubilized (20 mM HEPES, 0.15 mM NaCl, 1 % Triton X-100, 1 % deoxycholic acid and 1 % SDS, pH 7.5) for 1 h at 4°C and was centrifuged at 10,000 ×*g* for 15 min. The supernatant contained the PSD membrane fraction (Triton-insoluble). The cytosolic, non-PSD and PSD fractions were then analyzed by immunoblotting.

2.5. Western blot

Solutions and buffers were from Thermo Fisher, unless mentioned otherwise. Lysis buffer, containing trizma-base 20 mM, NaCl 150 mM, Complete Protease Inhibitor Cocktail 1x (11697498001, Roche Applied Science) and 1 % Triton X-100, was added to single pieces of whole brain tissue (~100 mg). Brain samples were homogenized by beads beating using a Precellys soft tissue CK14 2 ml (3 times for 30 s at 4500g. The lysate was then centrifuged at 2000g for 15 min at 4°C. The supernatant was used for analysis. Protein lysates from HEK293 or PNCs were harvested in minimum volume of 100 µl/well in 24-well plates, in ice-cold lysis buffer as described previously (Chapuis et al., 2017). Protein quantification was performed by using Pierce™ BCA Protein Assay Kit (23225). Lysates were mixed with 1X lithium dodecyl sulfate (LDS) sample buffer (NP0008) and 1X reducing agent (NP0009), sonicated and boiled at 95°C for 5 min. Total proteins (6 µg/lane for HEK293 and NPCs sample, 40 µg/lane for brain samples) were separated onto precast 4–12 % Bis-Tris Protein Gels, and electrophoresis was achieved by applying a tension of 150 V for 90 min using an Invitrogen™ XCell SureLock™ Electrophoresis system with the NuPAGE® MOPS SDS running buffer (1X; NP000102). Proteins were transferred to a nitrocellulose membrane of 0.2 µM pore size (Bio-Rad) using the Trans-Blot Turbo Transfer System (Bio-Rad). Membranes were rinsed 3 times for 5 min in TNT (0.01 M Tris.HCl (pH = 8.0), 0.15 M NaCl, 0.05 % Tween-20) before incubation with primary antibodies overnight at 4°C. Membranes were rinsed 3 times for 5 min with TNT and then incubated with the secondary antibodies diluted in 5 % milk for 2 h at RT. Blots were developed using Amersham ECL Western Blotting Detection Kit (WBLUC0500; Millipore). Glyceraldehyde 3-phosphate dehydrogenase (GAPDH) and β-Actin were used as loading controls.

2.6. Quantification of secreted APP byproducts

Culture media were collected for assaying secretion of APP byproducts using Alpha-LISA assays according to the manufacturer's instructions. For Aβ, we used Alpha-LISA Amyloid β1-X Kit (AL288C, http://www.revvity.com). sAPPα and sAPPβ were quantified using sAPPα (AL254C/F) and sAPPβ (AL255C/F) kits from PerkinElmer, respectively.

2.7. Chemicals and antibodies

KINDLIN2 was detected with a mouse Kindlin2 C-ter (9E4) antibody obtained from GeneTex, (1/1000; GTX84507). The KINDLIN2 N-ter fragments were detected with the Kindlin2 PA5–31168 Rabbit antibody (1/1000) from Thermo Scientific Pierce. Anti-Synaptophysin (1/5000; 101006) and anti-PSD95 (1/1000; 124014) were obtained from Synaptic Systems. Anti-β-Actin (1/10000; A1978) and anti-Amyloid precursor protein C-Terminal (1/5000; A8717) and were purchased from Sigma-Aldrich. Anti-GAPDH (1/10000; AB2302) was obtained from Merck Millipore. All secondary antibodies coupled with horseradish peroxidase were purchased from Jackson ImmunoResearch. Glutamate, Ionomycin, ALLN and ALLM were purchased from Calbiochem, Z-VAD-FMK was purchased from Promega, and Caspase-3/7 Inhibitor I (sc-293986) was purchased from Santa Cruz.

2.8. Co-immunoprecipitation

Cell lysates were collected in co-immunoprecipitation buffer (10 mM HEPES, 140 mM NaCl, and 0.5 % NP-40, pH = 7.4) containing phosphatase and protease inhibitors (11697498001; 4906845001, Roche Applied Science). Samples were incubated for 20 min on ice and centrifuged (12,000 ×*g* for 15 min at 4°C). For immunoprecipitation experiments, equal amounts of total lysates were incubated with the primary anti-β-Amyloid, 17–24 Antibody clone 4G8 (RRID:_AB_662812) overnight at 4°C, with gentle rocking. Immunoprecipitation was carried out using Pierce Protein A/G magnetic beads kit (Thermo Scientific, 88802) according to the manufacturer's instructions. Samples with proteins and antibody complexes were incubated with 40 µL (0.4 mg) of A/G magnetic beads previously washed with co-immunoprecipitation buffer. After 2 h of incubation at 4°C, the magnetic beads were washed 3 times and resuspended with a loading buffer (LDS, DTT and reducing agent) for 20 min at RT. Subsequently, samples were processed for immunoblotting.

2.9. Protein identification by mass spectrometry

Proteins were separated under reducing conditions in a 10 % polyacrylamide NuPage gel. The gel was stained for 3 days in a solution of colloidal Coomassie blue. Stained bands were excised from the gel, reduced, alkylated with iodoacetamide (10 mg/ml in 20 mM NH_4HCO_3) and digested overnight with 50 ng trypsin (Promega) in 20 mM NH_4HCO_3. The resulting peptides mixtures were eluted from the gel, desalted, and spotted on a MALDI plate with freshly dissolved α-cyano-4-hydroxycinnaminic acid (10 mg/ml in 50 % CH3CN, TFA 1/1000). Mass spectrometry was performed with a MALDI-TOF-TOF Autoflex Speed (Bruker Daltonics). MS and MS/MS data were analyzed using BioTools software. Identification of peptides was performed using Mascot, http://www.matrixscience.com.

2.10. Statistical analysis

A normality test (Lilliefors test) was performed on all data. Data were analyzed using the non-parametric Mann–Whitney test. All data are reported as mean±standard error of the mean (SEM) of at least n = 3 experiments. Statistical significance was accepted at the level of $p < 0.05$.

3. Results

3.1. KINDLIN2 cleavage products were observed in human brains and in synapses of primary neurons

We observed several uncharacterized bands in the KINDLIN2 electrophoretic mobility pattern when using hippocampal protein extracts obtained from different human brain samples, both in control individuals and in AD patients at different Braak stages (Fig. 1a and supplementary Figure 1). In addition to the 75-kDa band corresponding to the expected full-length KINDLIN2 (FL), two other bands, a 57-kDa band and a 39-kDa band, were labeled by an anti-C-terminal (C-ter) KINDLIN2 antibody, although the small number of samples available did not allow us to detect any significant difference between patients and controls (n = 20 and 8, respectively). Interestingly, a similar electrophoretic profile was observed using protein extracts from mouse primary cortical neuron cultures (PNCs) (Fig. 1b). However, the 39-kDa band appeared to be the more abundant in mouse PNCs, compared to what was observed in the human brain samples.

To rule out the possibility of non-specific binding, we first checked if the presence of these bands was dependent on KINDLIN2 expression level. For this purpose, we analyzed the KINDLIN2 electrophoretic mobility profile using protein extracts of PNC from KINDLIN2 Cre-dependent conditional knockout mice. As expected, transduction of a

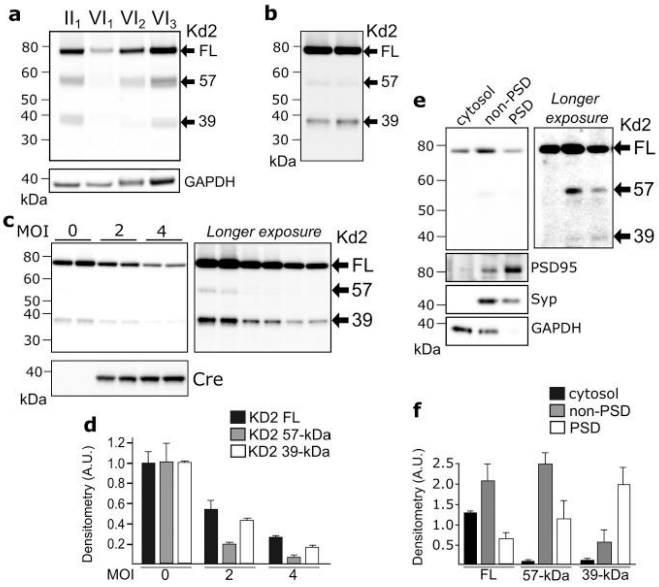

Fig. 1. a, Representative western blot (WB) showing the electrophoretic mobility of KINDLIN2 (KD2) using protein extracts from human hippocampi harboring different Braak stages (II or VI). **b,** Representative WB using protein extracts from mouse PNCs at 21 days in vitro. A replicate is shown. **c,d**, Representative WB showing the impact of Cre expression on the electrophoretic mobility of KINDLIN2 using mouse PNCs. Black arrows indicate full-length (FL) KINDLIN2 and 57-kDa (57) and 39-kDa (39) bands. **e,f** Synaptic fractionation experiment revealed the presence of KINDLIN2 by-products in both pre- and post-synaptic compartments from PNCs synaptosomal purification. Syn (Synapsin) and PSD95 were used as pre- and post-synaptic markers, respectively.

lentivirus overexpressing Cre resulted in a dose-dependent decrease in KINDLIN2 FL expression. 57-kDa and 39-kDa bands were also dependent on the level of lentivirus transduction, suggesting that the bands were specific and their identification as potential by-products of KINDLIN2 metabolism was valid (Fig. 1c-d). Since we previously identified KINDLIN2 as a synaptic protein (Eysert et al., 2021), we investigated the potential presence of KINDLIN2 by-products in synaptosomal purifications. Both 57-kDa and 39-kDa bands were observed in the synaptosomal fractions from PNCs (Fig. 1e-f). Altogether, our data suggest that KINDLIN2 undergoes at least two cleavages, and these cleavages could be taking place in neurons, suggesting a potential role of the KINDLIN2 metabolism in the regulation of its neuronal functions.

3.2. The 57-kDa fragment of KINDLIN2 is generated through calpain I cleavage

Having observed the KINDLIN2 cleavage products in synaptic purifications, we investigated the potential role of calpain, a well-characterized cysteine protease involved in synaptic plasticity in a calcium-dependent manner, in KINDLIN2 cleavage. To address the possibility that KINDLIN2 may be a calpain substrate, we first used an *in silico* prediction tool (CALPCLEAV) to identify potential calpain cleavage sites. The highest prediction score for a potential calpain cleavage site was obtained to be between amino acids 185 and 186, which would release a 57.4-kDa protein fragment (Fig. 2a), consistent with the 57-kDa band observed in the electrophoretic mobility profile we obtained. The involvement of calpain I in the production of this fragment was confirmed by the strong accumulation of the 57-kDa band after ionomycin-induced calpain activation, which was fully abolished when the PNCs were pre-treated with specific calpain inhibitors ALLN or ALLM (Fig. 2b). Excessive glutamate can produce an influx of calcium resulting in an overactivation of calcium-dependent proteases such as calpain, leading to neuronal excitotoxicity. In this context, we validated the involvement of calpain in KINDLIN2 cleavage by stimulating the neurons with glutamate with or without pre-treatment with ALLN or ALLM (Fig. 2c). Together, our results identified KINDLIN2 as a calpain substrate, where the calpain-mediated cleavage of KINDLIN2 leads to the release of a 57-kDa byproduct. However, no impact of calpain activity on the generation of the 39-kDa fragment was observed (Fig. 2d), suggesting the potential involvement of other proteases to fully explain the KINDLIN2 electrophoretic profile.

3.3. The 39-kDa fragment of KINDLIN2 is generated through caspase cleavage

To characterize the potential involvement of other proteases in the KINDLIN2 metabolism, we took advantage of the HEK293 cell line, which we previously used to characterize the impact of KINDLIN2 on APP metabolism (Chapuis et al., 2017). Here, we aimed to compare the mass spectroscopy spectra of the full-length protein with those of the cleavage products, to identify potential cleavage sites. First, we observed that overexpression of KINDLIN2 in HEK293 cells resulted in an electrophoretic mobility pattern comparable to the one observed for endogenous KINDLIN2 in mouse PNCs, indicating that the HEK293 cells have the cellular machinery needed for KINDLIN2 metabolism (Fig. 3a).

Next, we performed immunoprecipitation to concentrate KINDLIN2 and its by-products (Fig. 3b), followed by electrophoresis in Coomassie gel to visualize and isolate them for mass spectrometry analysis (Fig. 3c). Unfortunately, the KINDLIN2 57-kDa fragment was too close to IgG, precluding its isolation. However, we succeeded to purify the 39-kDa fragment and analyzed it using mass spectrometry in parallel with the full-length protein (Fig. 3d). As expected, this analysis identified the 39-

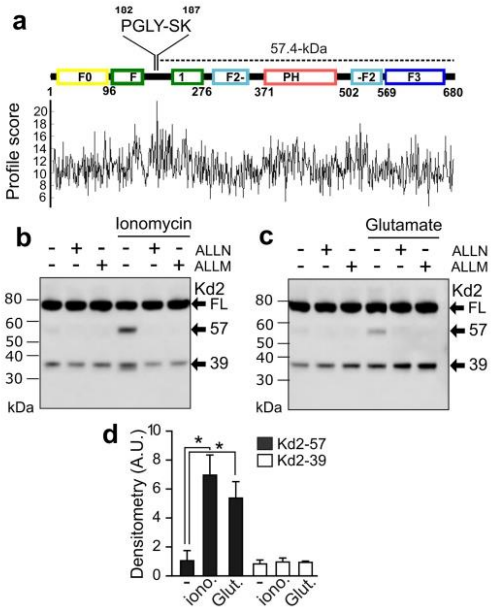

Fig. 2. a, Schematic showing KINDLIN2 structure and the profile score of predicted calpain cleavages using CALPCLEAV tool (http://calpcleav.szialab.org/). Calpain consensus site (PGLY-SK) harbors the highest profile score. **b-c**, Representative WBs showing the impact of pre-treatment of calpain I inhibitors (ALLN or ALLM) (20 μM; 30 min) on the electrophoretic mobility of KINDLIN2, as a function of ionomycin (10 μM; 2 h) or (c) glutamate (100 μM; 6 h) treatments of primary neurons. **d**, Bar charts indicate sample mean + SD. a. u., arbitrary units. * $p < 0.05$.

kDa fragment as the C-ter part of KINDLIN2, and the comparison of the two spectra allowed us to map the potential cleavage site between the amino acids 286 and 361. We then used the PeptideCutter prediction tool to identify the proteases susceptible to cleave KINDLIN2 within the identified sequence. A very well-conserved consensus site (DEVD-AA) was predicted between amino acids 344 and 349, which would be recognized by Caspases and susceptible to generate a 38.8-kDa fragment, comparable with the electrophoretic mobility pattern observed (Fig. 3e).

To validate the predicted cleavage site, we generated an aspartate-to-asparagine mutation (KINDLIN2^{D347A}) and transfected the 293HEK cells to overexpress this construct. Compared to wild-type (WT) KINDLIN2, the D347A mutation abolished the generation of the 39-kDa fragment with no impact on the production of the 57-kDa fragment (Fig. 3f). Next, to validate caspase-dependent cleavage of KINDLIN2, we overexpressed KINDLIN2 FL in HEK293 cells and treated the cells with a pan-caspase inhibitor (Z-VAD-FMK). Inhibition of the caspase activity was associated with a significant decrease in the 39-kDa fragment, with –once again– no impact on the generation of the 57-kDa fragment (Fig. 3g). Lastly, the same result was observed after treating the PNCs with the pan-caspase inhibitor (Fig. 3h). Together, these results demonstrate that KINDLIN2 is also a substrate of caspases, suggesting that KINDLIN2 can function as an adaptor protein controlled by two independent mechanisms, i.e., via caspases- or calpain I-mediated cleavages.

3.4. Impact of KINDLIN2 cleavage on the APP metabolism

A large number of binding partners have already been described for KINDLIN2 (Huet-Calderwood et al., 2014; Qu et al., 2014; Tu et al., 2003; Wei et al., 2017; Yu et al., 2012). We have recently demonstrated a direct interaction between the C-terminal F3 domain of KINDLIN2 and the YENPTY motif of the cytosolic tail of APP (Eysert et al., 2021). Considering that both cleavage products of KINDLIN2 possess the F3 domain, we hypothesized that they could also directly interact with APP. To test this hypothesis, we performed immunoprecipitation experiments using protein extracts from HEK293 cells stably expressing APP (293HEK-APP^{695WT}) and transiently overexpressing (or not) WT KINDLIN2. As expected, KINDLIN2 FL co-immunoprecipitated with APP (Fig. 4a). Such co-immunoprecipitation was also observed with both 57-kDa and 39-kDa fragments, suggesting that KINDLIN2 cleavage products can also interact with APP.

Since we previously observed that KINDLIN2 FL was able to regulate APP degradation by controlling level of mature APP at the cell surface and by facilitating its recycling, we assessed the impact of KINDLIN2cleavages on its capacity to regulate APP degradation. To this end, we generated constructs to express the 57-kDa (57C-ter) and 39-kDa (39C-ter) KINDLIN2 fragments, mimicking those resulting from calpain I or caspases cleavages, respectively. To note, the overexpression of 57C-ter also led to the production of the 39-kDa fragment, suggesting that the fragment resulting from calpain I cleavage can be recognized and cleaved by caspases. In contrast with the impact of KINDLIN2 FL overexpression previously reported (Chapuis et al., 2017), overexpression of 57C-ter or 39C-ter did not show any impact on the APP metabolism, neither on mature nor immature APP, or APP C-terminal α and β fragments (APP-CTF) levels (Fig. 4b and d). However, overexpression of 57C-ter and 39C-ter were associated with an increase of Aβ and soluble APP β (sAPPβ) levels in the culture medium (Fig. 4e and f), suggesting a potential dominant-negative effect, i.e., similar to the impact of *FERMT2* underexpression, as previously reported (Chapuis et al., 2017). However, no impact on the amount of secreted sAPPα was observed (Fig. 4g), which could support a potential specific impact of KINDLIN2 cleavage on the amyloid pathway.

To go further, we sought to investigate the impact of the N-ter fragments of KINDLIN2, KINDLIN2$^{1-347}$ and KINDLIN2$^{1-185}$, generated by caspases and calpain I cleavages, respectively, that are complementary to 39C-ter and 57C-ter (Fig. 4c). As observed for the C-ter fragments, overexpression of KINDLIN2$^{1-347}$ and KINDLIN2$^{1-185}$ did not induce an impact on APP metabolism observed after KINDLIN2 FL overexpression (Fig. 4d-f). However, compared to C-ter fragments, KINDLIN2$^{1-347}$ and KINDLIN2$^{1-185}$ were not associated with increased Aβ and sAPPβ levels (Fig. 4e and f), suggesting that only C-ter fragments may induce a blockade of the KINDLIN2-dependent regulatory mechanism of APP metabolism. Their ability to interact with APP, despite not recruiting other key partners *via* their F0 and F1 domains, appears to be sufficient to interfere with APP metabolism. Together, these data show that KINDLIN2 cleavage products can interact with APP to modulate its metabolism.

4. Discussion

In this work, we identify KINDLIN2 as a new substrate for two cysteine proteases already known for their roles in regulating synaptic functions, calpain I and caspases. In physiological conditions, the activities of these proteases are restricted in space and time. Calpain I activation is required for the induction of long-term potentiation (LTP) (Baudry, 2019), whereas the non-apoptotic activity of caspase 3 is mainly involved in long-term depression (LTD) (Hollville and Deshmukh, 2018). These functions are exerted through cleavage of various substrates, such as cytoskeletal proteins, membrane-associated proteins, receptors/channels, scaffolding/anchoring proteins, protein kinases and phosphatases. As we previously reported that KINDLIN2 inactivation impairs LTP (Eysert et al., 2021), we could hypothesize that KINDLIN2 cleavage could be a mechanism involved in synaptic plasticity in the physiological context and play a role in pathophysiological processes.

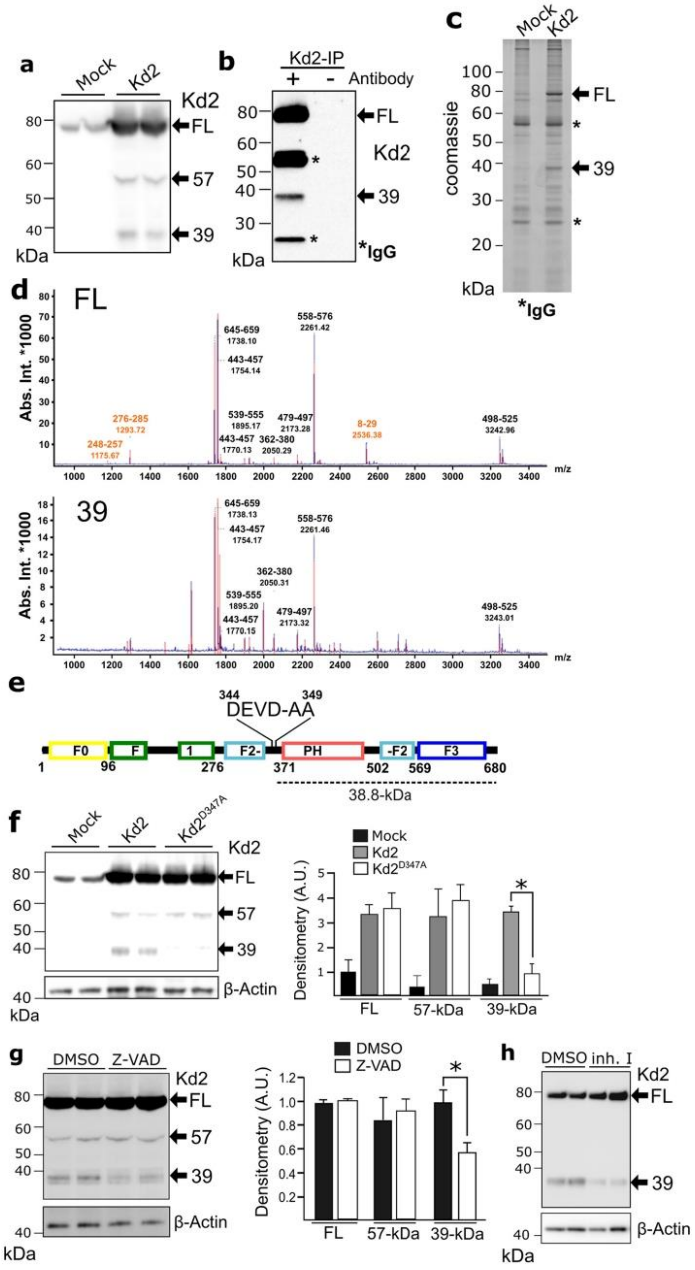

(caption on next page)

Fig. 3. **a,** Representative WB using protein extracts from HEK293 cells transfected with KINDLIN2 cDNA (KD2) or empty vector (Mock). **b,** Immunoprecipitation (IP) from protein extract of cells overexpressing KINDLIN2 as in panel a, using an anti-KINDLIN2 antibody or not. **c,** Coomassie gel using IP extract as in panel b, before the isolation of KINDLIN2 FL and 39-kDa bands for mass spectrometry analysis. **d,** Mass spectrometry spectra of isolated KINDLIN2 FL or 39-kDa fragments. Peptides identified only for KINDLIN2 FL are shown in orange. **e,** Schematic showing KINDLIN2 structure including the DEVD-AA consensus site predicted to be recognized by caspases. **f,** Representative WB using lysates of HEK293 cells transfected either with KINDLIN2 cDNA (KD2), KINDLIN2 with D347A mutation ($KD2^{D347A}$) or empty vector (Mock). **g,** Representative WB using lysates from HEK293 cells treated with caspase inhibitor (Z-VAD-FMK; 10 μM, for 6 h) or DMSO. Densitometric analysis and quantification of FL, 57-kDa fragment and 39-kDa fragment levels in 3 independent experiments. Bar charts indicate sample mean + SD. a.u., arbitrary units. * $p < 0.05$. **h,** Representative WB using PNCs lysates treated with caspase inhibitor (Inhibitor I; 5 μM, for 6 h).

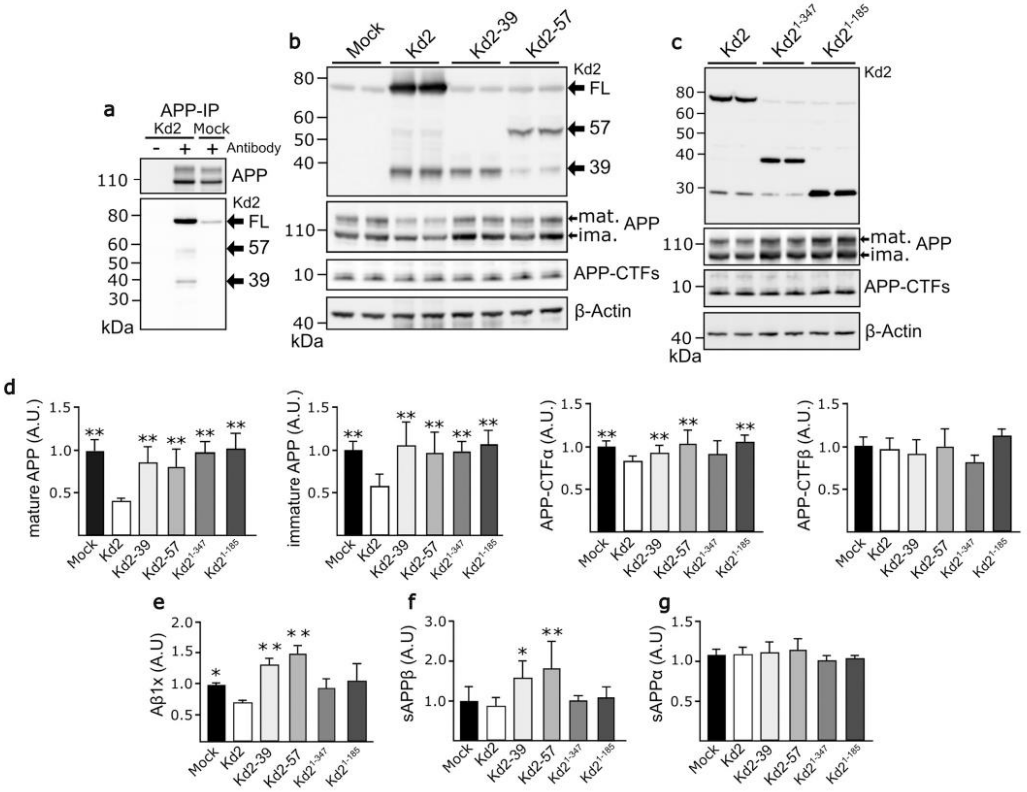

Fig. 4. **a,** Immunoprecipitation using an anti-APP antibody and protein extracts of HEK293-APP cells transfected with KINDLIN2 cDNA (KD2) or empty vector (Mock). **b,** Representative WBs reporting KINDLIN2 (KD) and APP levels using lysates from HEK293-APP cells transfected with cDNAs allowing the expression of KINDLIN2 FL (KD2-FL), $KINDLIN2^{197–600}$ (KD2–57) or $KINDLIN2^{340–600}$ (KD2–39) or an empty vector. **c,** Representative WBs reporting KINDLIN2 (kd2) and APP levels using lysates from HEK293-APP cells transfected with cDNAs allowing the expression of KINDLIN2 FL (KD2-FL), $KINDLIN2^{1–347}$ or $KINDLIN2^{1–185}$. **d,** Densitometric analysis and quantification of mature (mat.) and immature (imm.) APP and APP-CTFα and CTFβ for the same groups. **e,** $Aβ_{1-x}$ levels in the culture medium for the same groups. **f-g,** sAPPβ and sAPPα levels in the culture medium for the same groups. N = 3 independent experiments. Bar charts indicate sample mean + SEM. a.u., arbitrary units. * $p < 0.05$; ** $p < 0.01$. Each condition was compared to Kd2.

Indeed, overactivation of calpains has been observed in AD brains (Higuchi et al., 2012; Saito et al., 1993) and calpain activity dysregulation has been described to be involved in the generation of toxic aggregates (Nguyen et al., 2012; Shams et al., 2019) and in synaptic dysfunction (Metwally et al., 2023). Caspases also appeared to be abnormally activated in AD brains (Gervais et al., 1999; Rohn et al., 2001) and were shown to have an impact on neuronal structure and activity (D'Amelio et al., 2011; Dhage et al., 2023). Although we did not observe any significant differences in the amount of KINDLIN2 fragments between patients and controls (despite a trend ($p = 0.09$) towards a greater presence of the 57-kDa C-ter fragment in the hippocampus of patients compared with controls, supplementary Figure 2), an upregulation of KINDLIN2 was observed in the post-mortem human temporal cortex of AD patients compared to healthy controls (Eysert et al., 2021; Sullivan et al., 2019). However, the approaches used do not allow for the quantification of KINDLIN2 by-products and additional studies will be necessary to investigate the potential association between KINDLIN2 cleavage and AD process.

The calpain- and caspase-mediated cleavages of KINDLIN2 result in the separation of the F0 and F1 domains, which participate in the

recruitment of several KINDLIN2 partners such as SRC, SMURF1 or SMAD3 (Qu et al., 2014; Wei et al., 2017, 2013). The rest of the protein encompasses the PH domain, which is required for the association of KINDLIN2 with the plasma membrane, and the F3 domain, which allows KINDLIN2 to bind to the NxxY motif such that it can interact with integrin or APP. The separation of the F0 and F1 domains could inhibit the adapter function of KINDLIN2, i.e., bringing together different partners to form protein complexes (Theodosiou et al., 2016). We had previously shown that the KINDLIN2/APP interaction is a key driver of synaptic plasticity (Eysert et al., 2021). Our current findings suggest that KINDLIN2 cleavage could be a mechanism regulating synaptic functions through modulating the capacity of KINDLIN2 to interact with APP and/or with other partners. Recent crystallography experiments have demonstrated that KINDLIN2 can form homo-dimers through its F2 domain in a domain-swapped manner (Jahed et al., 2019), allowing for its proper localization and for activating integrin. In this context, it could be interesting to determine the consequences of KINDLIN2 cleavages on its capacity to dimerize and execute its different functions such as regulating the APP metabolism.

We had previously shown that the underexpression of KINDLIN2 increases Aβ peptide production by raising levels of mature APP at the cell surface (Chapuis et al., 2017). Our current results suggest that these cleavages lead to the abolishment of the capacity of KINDLIN2 to regulate APP metabolism, even when the F3 domain allowing the KINDLIN2-APP interaction is present. Remarkably, overexpression of the C-ter fragments (57- and 39-kDa), lacking the F0 and F1 domains, exerts a dominant-negative effect on the Aβ peptide level, consistent with the impact of KINDLIN2 inactivation previously reported (Chapuis et al., 2017). This dominant-negative effect is not observed after expression of N-ter fragments, lacking the F3 domain, suggest that the C-ter fragments could retain their ability to interact with APP, but induce a blockage of the mechanism by which KINDLIN2 regulates APP metabolism, through currently unknown mechanisms.

These data also highlight the importance of the F0 and F1 domains of KINDLIN2 in decreasing Aβ peptide levels. Interestingly, the F1 domain of KINDLIN2 recruits the E3 ubiquitin-protein ligase SMURF1, allowing for the ubiquitination of the transmembrane receptor LRP1 and thus controlling its degradation (Wei et al., 2017; Wujak et al., 2018). Since we reported that KINDLIN2 controls APP degradation (Eysert et al., 2021), we could speculate that the KINDLIN2 F1 domain is also required for KINDLIN2 to impact APP degradation and processing. In this context, further research is needed to determine whether these mechanisms depend on the endosome-lysosome system or the ubiquitin-proteasome pathway.

Notably, KINDLIN2 has been implicated in the progression of cancers of different origins: colorectal (Ren et al., 2015), prostate (Gao et al., 2013; Yang et al., 2016), pancreatic (Mia et al., 2021) and breast cancer (Ma et al., 2022), among others. Although not yet reported, KINDLIN2 cleavage by calpain and caspases could be an interesting new mechanism to investigate in the context of these pathologies.

CRediT authorship contribution statement

Amouyel Philippe: Supervision. **Lambert Erwan:** Investigation. **Ayral Anne-Marie:** Methodology, Investigation. **Lambert Jean-Charles:** Writing – review & editing, Supervision, Funding acquisition. **Kilinc Devrim:** Writing – review & editing, Conceptualization. **Coulon Audrey:** Investigation. **Demiautte Florie:** Methodology, Investigation. **Siedlecki-Wullich Dolores:** Writing – review & editing, Investigation. **Najdek Chloé:** Writing – original draft, Methodology, Investigation, Conceptualization. **Gelle Carla:** Investigation. **Chapuis Julien:** Writing – original draft, Supervision, Funding acquisition, Conceptualization. **Dumont Julie:** Formal analysis. **Flaig Amandine:** Investigation. **Eysert Fanny:** Investigation. **Walle Pauline:** Investigation. **Buiche Valérie:** Investigation.

Acknowledgements

The authors thank Charles Duyckaerts and the 'NeuroCEB' Brain Bank (GIE Neuro-CEB BB-0033-00011) for providing the brain tissue samples. We also thank Valérie Vingtdeux for providing the samples treated with calpain inhibitors and Olivia Beseme and Herve Drobecq for mass spectrometry analysis. C.N. was supported by France Alzheimer Program Grant (Genetic of Synaptic Dysfunction, 6362, 2023). INSERM UMR1167 is also funded by the INSERM, Institut Pasteur de Lille, Lille Métropole Communauté Urbaine and French government's LABEX DISTALZ program (development of innovative strategies for a trans-disciplinary approach to AD).

Appendix A. Supporting information

Supplementary data associated with this article can be found in the online version at doi:10.1016/j.neurobiolaging.2025.04.009.

References

Aleksis, R., Oleskovs, F., Jaudzems, K., Pahnke, J., Biverstål, H., 2017. Structural studies of amyloid-β peptides: unlocking the mechanism of aggregation and the associated toxicity. Biochimie 140, 176–192. https://doi.org/10.1016/j.biochi.2017.07.011.

Aylsworth, A., Jiang, S.X., Desbois, A., Hou, S.T., 2009. Characterization of the role of full-length CRMP3 and its calpain-cleaved product in inhibiting microtubule polymerization and neurite outgrowth. Exp. Cell Res. 315, 2856–2868. https://doi.org/10.1016/j.yexcr.2009.06.014.

Baudry, M., 2019. Calpain-1 and calpain-2 in the brain: Dr. Jekill and Mr Hyde? Curr. Neuropharmacol. 17, 823–829. https://doi.org/10.2174/1570159X17666190228112451.

Baudry, M., Su, W., Seinfeld, J., Sun, J., Bi, X., 2021. Role of calpain-1 in neurogenesis. Front. Mol. Biosci. 8. https://doi.org/10.3389/fmolb.2021.685938.

Chan, K.T., Bennin, D.A., Huttenlocher, A., 2010. Regulation of adhesion dynamics by calpain-mediated proteolysis of focal adhesion kinase (FAK). J. Biol. Chem. 285, 11418–11426. https://doi.org/10.1074/jbc.M109.090746.

Chapuis, J., Flaig, A., Grenier-Boley, B., Eysert, F., Pottiez, V., Deloison, G., Vandeputte, A., Ayral, A.-M., Mendes, T., Desai, S., Goate, A.M., Kauwe, J.S.K., Leroux, F., Herledan, A., Demiautte, F., Bauer, C., Checler, F., Petersen, R.C., Blennow, K., Zetterberg, H., Minthon, L., Van Deerlin, V.M., Lee, V.M.-Y., Shaw, L. M., Trojanowski, J.Q., Albert, M., Moghekar, A., O'Brien, R., Peskind, E.R., Malmanche, N., Schellenberg, G.D., Dourlen, P., Song, O.-R., Cruchaga, C., Amouyel, P., Deprez, B., Brodin, P., Lambert, J.-C., 2017. Genome-wide, high-content siRNA screening identifies the Alzheimer's genetic risk factor FERMT2 as a major modulator of APP metabolism. Acta Neuropathol. (Berl.) 133, 955–966. https://doi.org/10.1007/s00401-016-1652-z.

Cortesio, C.L., Boateng, L.R., Piazza, T.M., Bennin, D.A., Huttenlocher, A., 2011. Calpain-mediated proteolysis of paxillin negatively regulates focal adhesion dynamics and cell migration. J. Biol. Chem. 286, 9998–10006. https://doi.org/10.1074/jbc.M110.187294.

D'Amelio, M., Cavallucci, V., Middei, S., Marchetti, C., Pacioni, S., Ferri, A., Diamantini, A., De Zio, D., Carrara, P., Battistini, L., Moreno, S., Bacci, A., Ammassari-Teule, M., Marie, H., Cecconi, F., 2011. Caspase-3 triggers early synaptic dysfunction in a mouse model of Alzheimer's disease. Nat. Neurosci. 14, 69–76. https://doi.org/10.1038/nn.2709.

Dhage, P.A., Sharbidre, A.A., Magdum, S.M., 2023. Interlacing the relevance of caspase activation in the onset and progression of Alzheimer's disease. Brain Res. Bull. 192, 83–92. https://doi.org/10.1016/j.brainresbull.2022.11.008.

Eysert, F., Coulon, A., Boscher, E., Vreulx, A.-C., Flaig, A., Mendes, T., Hughes, S., Grenier-Boley, B., Hanoulle, X., Demiautte, F., Bauer, C., Marttinen, M., Takalo, M., Amouyel, P., Desai, S., Pike, I., Hiltunen, M., Chécler, F., Farinelli, M., Delay, C., Malmanche, N., Hébert, S.S., Dumont, J., Kilinc, D., Lambert, J.-C., Chapuis, J., 2021. Alzheimer's genetic risk factor FERMT2 (Kindlin-2) controls axonal growth and synaptic plasticity in an APP-dependent manner. Mol. Psychiatry 26, 5592–5607. https://doi.org/10.1038/s41380-020-00926-w.

Fath, T., Ke, Y.D., Gunning, P., Götz, J., Ittner, L.M., 2009. Primary support cultures of hippocampal and substantia nigra neurons. Nat. Protoc. 4, 78–85. https://doi.org/10.1038/nprot.2008.199.

Franco, S.J., Rodgers, M.A., Perrin, B.J., Han, J., Bennin, D.A., Critchley, D.R., Huttenlocher, A., 2004. Calpain-mediated proteolysis of talin regulates adhesion dynamics. Nat. Cell Biol. 6, 977–983. https://doi.org/10.1038/ncb1175.

Frandemiche, M.L., De Seranno, S., Rush, T., Borel, E., Elie, A., Arnal, I., Lanté, F., Buisson, A., 2014. Activity-dependent tau protein translocation to excitatory synapse is disrupted by exposure to amyloid-beta oligomers. J. Neurosci. 34, 6084–6097. https://doi.org/10.1523/JNEUROSCI.4261-13.2014.

Gao, J., Khan, A.A., Shimokawa, T., Zhan, J., Strömblad, S., Fang, W., Zhang, H., 2013. A feedback regulation between Kindlin-2 and GLI1 in prostate cancer cells. FEBS Lett. 587, 631–638. https://doi.org/10.1016/j.febslet.2012.12.028.

Gatz, M., Reynolds, C.A., Fratiglioni, L., Johansson, B., Mortimer, J.A., Berg, S., Fiske, A., Pedersen, N.L., 2006. Role of genes and environments for explaining Alzheimer

disease. Arch. Gen. Psychiatry 63 (2), 168. https://doi.org/10.1001/archpsyc.63.2.168.
Gervais, F.G., Xu, D., Robertson, G.S., Vaillancourt, J.P., Zhu, Y., Huang, J., LeBlanc, A., Smith, D., Rigby, M., Shearman, M.S., Clarke, E.E., Zheng, H., Van Der Ploeg, L.H.T., Ruffolo, S.C., Thornberry, N.A., Xanthoudakis, S., Zamboni, R.J., Roy, S., Nicholson, D.W., 1999. Involvement of caspases in proteolytic cleavage of Alzheimer's amyloid-β precursor protein and amyloidogenic Aβ peptide formation. Cell 97, 395–406. https://doi.org/10.1016/S0092-8674(00)80748-5.
Haass, C., 2004. Take five—BACE and the γ-secretase quartet conduct Alzheimer's amyloid β-peptide generation. EMBO J. 23, 483–488. https://doi.org/10.1038/sj.emboj.7600061.
Hardy, J.A., Higgins, G.A., 1992. Alzheimer's disease: the amyloid cascade hypothesis. Science 256, 184–185. https://doi.org/10.1126/science.1566067.
Higuchi, M., Iwata, N., Matsuba, Y., Takano, J., Suemoto, T., Maeda, J., Ji, B., Ono, M., Staufenbiel, M., Suhara, T., Saido, T.C., 2012. Mechanistic involvement of the calpain-calpastatin system in Alzheimer neuropathology. FASEB J. 26, 1204–1217. https://doi.org/10.1096/fj.11-187740.
Hollville, E., Deshmukh, M., 2018. Physiological functions of non-apoptotic caspase activity in the nervous system. Semin. Cell Dev. Biol. 82, 127–136. https://doi.org/10.1016/j.semcdb.2017.11.037.
Hotulainen, P., Hoogenraad, C.C., 2010. Actin in dendritic spines: connecting dynamics to function. J. Cell Biol. 189, 619–629. https://doi.org/10.1083/jcb.201003008.
Huet-Calderwood, C., Brahme, N.N., Kumar, N., Stiegler, A.L., Raghavan, S., Boggon, T. J., Calderwood, D.A., 2014. Differences in binding to the ILK complex determines kindlin isoform adhesion localization and integrin activation. J. Cell Sci. 127, 4308–4321. https://doi.org/10.1242/jcs.155879.
Jahed, Z., Haydari, Z., Rathish, A., Mofrad, M.R.K., 2019. Kindlin is mechanosensitive: force-induced conformational switch mediates cross-talk among integrins. Biophys. J. 116, 1011–1024. https://doi.org/10.1016/j.bpj.2019.01.038.
Jan, A., Hartley, D.M., Lashuel, H.A., 2010. Preparation and characterization of toxic Aβ aggregates for structural and functional studies in Alzheimer's disease research. Nat. Protoc. 5, 1186–1209. https://doi.org/10.1038/nprot.2010.72.
Kilinc, D., Vreulx, A.-C., Mendes, T., Flaig, A., Marques-Coelho, D., Verschoore, M., Demiautte, F., Amouyel, P., Neuro-CEB Brain Bank, Eysert, F., Dourlen, P., Chapuis, J., Costa, M.R., Malmanche, N., Checler, F., Lambert, J.-C., 2020. Pyk2 overexpression in postsynaptic neurons blocks amyloid β1–42-induced synaptotoxicity in microfluidic co-cultures. Brain Commun. 2. https://doi.org/10.1093/braincomms/fcaa139.
Levkau, B., Herren, B., Koyama, H., Ross, R., Raines, E.W., 1998. Caspase-mediated cleavage of focal adhesion kinase pp125FAK and disassembly of focal adhesions in human endothelial cell apoptosis. J. Exp. Med. 187, 579–586. https://doi.org/10.1084/jem.187.4.579.
Li, H., Deng, Y., Sun, K., Yang, H., Liu, J., Wang, M., Zhang, Z., Lin, J., Wu, C., Wei, Z., Yu, C., 2017. Structural basis of kindlin-mediated integrin recognition and activation. Proc. Natl. Acad. Sci. 114, 9349–9354.
Lin, T., Tjernberg, L.O., Schedin-Weiss, S., 2021. Neuronal trafficking of the amyloid precursor protein—what do we really know? Biomedicines 9, 801. https://doi.org/10.3390/biomedicines9070801.
Ma, Luyao, Tian, Y., Qian, T., Li, W., Liu, C., Chu, B., Kong, Q., Cai, R., Bai, P., Ma, Lisha, Deng, Y., Tian, R., Wu, C., Sun, Y., 2022. Kindlin-2 promotes Src-mediated tyrosine phosphorylation of androgen receptor and contributes to breast cancer progression. Cell Death Dis. 13, 482. https://doi.org/10.1038/s41419-022-04945-z.
Metwally, E., Al-Abbadi, H.A., Hussain, T., Murtaza, G., Abdellatif, A.M., Ahmed, M.F., 2023. Calpain signaling: from biology to therapeutic opportunities in neurodegenerative disorders. Front. Vet. Sci. 10, 1235163. https://doi.org/10.3389/fvets.2023.1235163.
Mia, M.S., Jarajapu, Y., Rao, R., Mathew, S., 2021. Integrin β1 promotes pancreatic tumor growth by upregulating Kindlin-2 and TGF-β receptor-2. Int. J. Mol. Sci. 22, 10599. https://doi.org/10.3390/ijms221910599.
Montanez, E., Ussar, S., Schifferer, M., Bösl, M., Zent, R., Moser, M., Fässler, R., 2008. Kindlin-2 controls bidirectional signaling of integrins. Genes Dev. 22, 1325–1330. https://doi.org/10.1101/gad.469408.
Müller, U.C., Deller, T., Korte, M., 2017. Not just amyloid: physiological functions of the amyloid precursor protein family. Nat. Rev. Neurosci. 18, 281–298. https://doi.org/10.1038/nrn.2017.29.
Nguyen, H.T., Sawmiller, D.R., Wu, Q., Maleski, J.J., Chen, M., 2012. Evidence supporting the role of calpain in the α-processing of amyloid-β precursor protein. Biochem. Biophys. Res. Commun. 420, 530–535. https://doi.org/10.1016/j.bbrc.2012.03.026.
Perez, R.G., Zheng, H., Van der Ploeg, L.H.T., Koo, E.H., 1997. The β-amyloid precursor protein of Alzheimer's disease enhances neuron viability and modulates neuronal polarity. J. Neurosci. 17, 9407–9414. https://doi.org/10.1523/JNEUROSCI.17-24-09407.1997.
Qu, H., Tu, Y., Guan, J.-L., Xiao, G., Wu, C., 2014. Kindlin-2 tyrosine phosphorylation and interaction with Src serve as a regulatable switch in the integrin outside-in signaling circuit. J. Biol. Chem. 289, 31001–31013. https://doi.org/10.1074/jbc.M114.580811.
Ren, Y., Jin, H., Xue, Z., Xu, Q., Wang, S., Zhao, G., Huang, J., Huang, H., 2015. Kindlin-2 inhibited the growth and migration of colorectal cancer cells. Tumour Biol. J. Int. Soc. Oncodev. Biol. Med. 36, 4107–4114. https://doi.org/10.1007/s13277-015-3044-8.
Rohn, T.T., Head, E., Nesse, W.H., Cotman, C.W., Cribbs, D.H., 2001. Activation of caspase-8 in the Alzheimer's disease brain. Neurobiol. Dis. 8, 1006–1016. https://doi.org/10.1006/nbdi.2001.0449.
Sabo, S.L., Ikin, A.F., Buxbaum, J.D., Greengard, P., 2003. The amyloid precursor protein and its regulatory protein, FE65, in growth cones and synapses in vitro and in vivo. J. Neurosci. 23, 5407–5415. https://doi.org/10.1523/JNEUROSCI.23-13-05407.2003.
Saito, K., Elce, J.S., Hamos, J.E., Nixon, R.A., 1993. Widespread activation of calcium-activated neutral proteinase (calpain) in the brain in Alzheimer disease: a potential molecular basis for neuronal degeneration. Proc. Natl. Acad. Sci. 90, 2628–2632. https://doi.org/10.1073/pnas.90.7.2628.
Shams, R., Banik, N.L., Haque, A., 2019. Chapter Four - Calpain in the cleavage of alpha-synuclein and the pathogenesis of Parkinson's disease. In: Rahman, S. (Ed.), Progress in Molecular Biology and Translational Science, Molecular Basis of Neuropsychiatric Disorders: From Bench to Bedside. Academic Press, pp. 107–124. https://doi.org/10.1016/bs.pmbts.2019.06.007.
Small, D.H., Clarris, H.L., Williamson, T.G., Reed, G., Key, B., Mok, S.S., Beyreuther, K., Masters, C.L., Nurcombe, V., 1999. Neurite-outgrowth regulating functions of the amyloid protein precursor of Alzheimer's disease. J. Alzheimers Dis. JAD 1, 275–285. https://doi.org/10.3233/jad-1999-14-508.
Sosa, L.J., Bergman, J., Estrada-Bernal, A., Glorioso, T.J., Kittelson, J.M., Pfenninger, K. H., 2013. Amyloid precursor protein is an autonomous growth cone adhesion molecule engaged in contact guidance. PLoS ONE 8, e64521. https://doi.org/10.1371/journal.pone.0064521.
Sullivan, S.E., Liao, M., Smith, R.V., White, C., Lagomarsino, V.N., Xu, J., Taga, M., Bennett, D.A., De Jager, P.L., Young-Pearse, T.L., 2019. Candidate-based screening via gene modulation in human neurons and astrocytes implicates FERMT2 in Aβ and TAU proteostasis. Hum. Mol. Genet 28, 718–735. https://doi.org/10.1093/hmg/ddy376.
Theodosiou, M., Widmaier, M., Böttcher, R.T., Rognoni, E., Veelders, M., Bharadwaj, M., Lambacher, A., Austen, K., Müller, D.J., Zent, R., Fässler, R., 2016. Kindlin-2 cooperates with talin to activate integrins and induces cell spreading by directly binding paxillin. eLife 5, e10130. https://doi.org/10.7554/eLife.10130.
Tu, Y., Wu, S., Shi, X., Chen, K., Wu, C., 2003. Migfilin and Mig-2 link focal adhesions to filamin and the actin cytoskeleton and function in cell shape modulation. Cell 113, 37–47. https://doi.org/10.1016/S0092-8674(03)00163-6.
Wang, Y., Hersheson, J., Lopez, D., Hamad, M.B., Liu, Y., Lee, K.-H., Pinto, V., Seinfeld, J., Wiethoff, S., Sun, J., Amouri, R., Hentati, F., Baudry, N., Tran, J., Singleton, A.B., Coutelier, M., Brice, A., Stevanin, G., Durr, A., Bi, X., Houlden, H., Baudry, M., 2016. Defects in the CAPN1 gene result in alterations in cerebellar development and in cerebellar ataxia in mice and humans. Cell Rep. 16, 79–91. https://doi.org/10.1016/j.celrep.2016.05.044.
Wang, Z., Wang, B., Yang, L., Guo, Q., Aithmitti, N., Songyang, Z., Zheng, H., 2009. Presynaptic and postsynaptic interaction of the amyloid precursor protein promotes peripheral and central synaptogenesis. J. Neurosci. 29, 10788–10801.
Wei, X., Xia, Y., Li, F., Tang, Y., Nie, J., Liu, Y., Zhou, Z., Zhang, H., Hou, F.F., 2013. Kindlin-2 mediates activation of TGF-β/Smad signaling and renal fibrosis. J. Am. Soc. Nephrol. JASN 24, 1387–1398. https://doi.org/10.1681/ASN.2012101041.
Wei, X., Wang, X., Zhan, J., Chen, Y., Fang, W., Zhang, L., Zhang, H., 2017. Smurf1 inhibits integrin activation by controlling Kindlin-2 ubiquitination and degradation. J. Cell Biol. 216, 1455–1471. https://doi.org/10.1083/jcb.201609073.
Wen, L.-P., Fahrni, J.A., Troie, S., Guan, J.-L., Orth, K., Rosen, G.D., 1997. Cleavage of focal adhesion kinase by caspases during apoptosis. J. Biol. Chem. 272, 26056–26061. https://doi.org/10.1074/jbc.272.41.26056.
Westphal, D., Sytnyk, V., Schachner, M., Leshchyns'ka, I., 2010. Clustering of the neural cell adhesion molecule (NCAM) at the neuronal cell surface induces caspase-8- and -3-dependent changes of the spectrin meshwork required for NCAM-mediated neurite outgrowth. J. Biol. Chem. 285, 42046–42057. https://doi.org/10.1074/jbc.M110.177147.
Williams, D.W., Kondo, S., Krzyzanowska, A., Hiromi, Y., Truman, J.W., 2006. Local caspase activity directs engulfment of dendrites during pruning. Nat. Neurosci. 9, 1234–1236. https://doi.org/10.1038/nn1774.
Wujak, L., Böttcher, R.T., Pak, O., Frey, H., El Agha, E., Chen, Y., Schmitt, S., Bellusci, S., Schaefer, L., Weissmann, N., Fässler, R., Wygrecka, M., 2018. Low density lipoprotein receptor-related protein 1 couples β1 integrin activation to degradation. Cell. Mol. Life Sci. CMLS 75, 1671–1685. https://doi.org/10.1007/s00018-017-2707-6.
Yang, J., Pan, T., Yang, H., Wang, T., Liu, W., Liu, B., Qian, W., 2016. Kindlin-2 promotes invasiveness of prostate cancer cells via NF-κB-dependent upregulation of matrix metalloproteinases. Gene 576, 571–576. https://doi.org/10.1016/j.gene.2015.11.005.
Yu, Y., Wu, J., Wang, Y., Zhao, T., Ma, B., Liu, Y., Fang, W., Zhu, W.-G., Zhang, H., 2012. Kindlin 2 forms a transcriptional complex with β-catenin and TCF4 to enhance Wnt signalling. EMBO Rep. 13, 750–758. https://doi.org/10.1038/embor.2012.88.

High-Content Screening of Synaptic Density Modulators in Primary Neuronal Cultures

Audrey Coulon,[1] Dolores Siedlecki-Wullich,[1] Chloé Najdek,[1] Carla Gelle,[1] Anne-Marie Ayral,[1] Florie Demiautte,[1] Erwan Lambert,[1] Alexandre Vandeputte,[2] Priscille Brodin,[2] Tiago Mendes,[1] Jean-Charles Lambert,[1] Devrim Kilinc,[1] Julie Dumont,[1] and Julien Chapuis[1,3]

[1]Université de Lille, Inserm, CHU Lille, Institut Pasteur de Lille, U1167 - RID-AGE - Facteurs de risque et déterminants moléculaires des maladies liées au vieillissement, Lille, France
[2]Université de Lille, CNRS, Inserm, CHU Lille, Institut Pasteur de Lille, Center for Infection and Immunity of Lille (CIIL), Lille, France
[3]Corresponding author: *julien.chapuis@pasteur-lille.fr*

Published in the Neuroscience section

The synapse, which represents the structural and functional basis of neuronal communication, is one of the first elements affected in several neurodegenerative diseases. To better understand the potential role of gene expression in synapse loss, we developed an original high-content screening (HCS) model capable of quantitatively assessing the impact of gene silencing on synaptic density. Our approach is based on a model of primary neuronal cultures (PNCs) from the neonatal rat hippocampus, whose mature synapses are visualized by the relative localization of the presynaptic protein Synaptophysin with the postsynaptic protein Homer1. The heterogeneity of PNCs and the small sizes of the synaptic structures pose technical challenges associated with the level of automation necessary for HCS studies. We overcame these technical challenges, automated the processes of image analysis and data analysis, and carried out tests under real-world conditions to demonstrate the robustness of the model developed. In this article, we describe the screening of a custom library of 198 shRNAs in PNCs in the 384-well plate format. © 2023 The Authors. Current Protocols published by Wiley Periodicals LLC.

Basic Protocol 1: Culture of primary hippocampal rat neurons in 384-well plates
Basic Protocol 2: Lentiviral shRNA transduction of primary neuronal culture in 384-well plates
Basic Protocol 3: Immunostaining of the neuronal network and synaptic markers in 384-well plates
Basic Protocol 4: Image acquisition using a high-throughput reader
Basic Protocol 5: Image segmentation and analysis
Basic Protocol 6: Synaptic density analysis

Keywords: automated microscopy • high-content screening • neurons • shRNA • synapses

CURRENT PROTOCOLS
A Wiley Brand

Current Protocols e904, Volume 3
Published in Wiley Online Library (wileyonlinelibrary.com).
doi: 10.1002/cpz1.904

How to cite this article:
Coulon, A., Siedlecki-Wullich, D., Najdek, C., Gelle, C., Ayral, A.-M., Demiautte, F., Lambert, E., Vandeputte, A., Brodin, P., Mendes, T., Lambert, J.-C., Kilinc, D., Dumont, J., & Chapuis, J. (2023). High-content screening of synaptic density modulators in primary neuronal cultures. *Current Protocols*, *3,* e904.
doi: 10.1002/cpz1.904

INTRODUCTION

Failure to correctly regulate the number and distribution of synapses is a neuropathological feature shared by a variety of neurological and psychiatric disorders, such as autism (Monteiro & Feng, 2017), epilepsy (Wong & Guo, 2013), schizophrenia (Gigg et al., 2020), amyotrophic lateral sclerosis (Fogarty, 2019), Parkinson's disease (Bellucci et al., 2016), and Alzheimer's disease (AD) (DeKosky & Scheff, 1990). Identifying chemical or biological modulators of synaptic density may contribute to the understanding of pathophysiological mechanisms and to the identification of new therapeutic targets. Thus, our objective was to develop a medium-throughput assay to assess the impact of each currently known AD genetic risk factor (Bellenguez et al., 2022) on the synaptic density of primary neuronal cultures (PNCs).

In this context, high-content screening (HCS) of a library of short-hairpin RNAs (shRNAs) that individually target each of these genetic risk factors provides a powerful approach to systematically analyze their impact on synaptic density. Compared to high-throughput screening (HTS), which evaluates the activity of thousands of compounds in parallel in miniaturized biochemical or conventional cellular assays, HCS provides more biologically complex information through the use of fluorescence microscopy, multiplexing, and sophisticated image analysis at the cellular or sub-cellular scale. HCS can therefore be useful for studying diseases where the disease-associated cellular phenotypes are known but the underlying molecular mechanisms are not fully characterized, such as AD. To understand the implications of a quantitative analysis of synaptic density using HCS, several critical points should be considered. First, although the resolution of HCS/HTS microscopes has been strongly improved over the last decade, visualization of small structures such as synapses (<100 nm) requires one to work with the highest magnification available. Another important consideration is that the detection of mature synapses has been strongly improved by analyzing the colocalization of a presynaptic marker and a postsynaptic marker (Nieland et al., 2014; Verschuuren et al., 2019), even though this makes the image acquisition and analysis cumbersome. Second, these automated approaches require a robust and reproducible assay to overcome additional limitations, such as the complexity of the neuronal network and the heterogeneity in synaptic density in primary cultures. Third, the choice of synaptic markers used is also a critical point because antibodies may show non-uniform labeling (Verstraelen et al., 2020). Last, the majority of HCS methodologies aiming to visualize synapses are usually developed in the 96-well plate format, which limits screening capacity and/or increases the associated costs.

We recently developed an image analysis workflow that permits us to identify synapses by the proximity-based assignment of postsynaptic puncta to presynaptic puncta (Kilinc et al., 2020). The workflow is based on the detection of fluorescent puncta following immunolabeling of the endogenous synaptic proteins Synaptophysin and Homer1, and the automated analysis of their relative localization. Here, we adapted this workflow to

the 384-well plate format and used it in the HCS of a lentiviral shRNA library targeting 198 AD-associated genes (Bellenguez et al., 2022). The screen was organized in two parts: (i) the 105 genes we reported in 2019 (Kunkle et al., 2019) and (ii) the 93 genes we reported in 2022 (Bellenguez et al., 2022). The assay is reproducible and robust and therefore constitutes a promising medium-throughput screening tool to identify new compounds of potential therapeutic interest in neurodevelopmental and neurodegenerative diseases.

In this article, we describe (i) the culture of primary hippocampal neurons in 384-well plates (Basic Protocol 1), (ii) their transduction with lentiviral shRNAs (Basic Protocol 2), (iii) the immunolabeling of synaptic and structural markers (Basic Protocol 3), (iv) image acquisition using a high-throughput reader (Basic Protocol 4), (v) the automated image analysis process (Basic Protocol 5), and (vi) synapse density quantification (Basic Protocol 6).

CULTURE OF PRIMARY HIPPOCAMPAL RAT NEURONS IN 384-WELL PLATES

BASIC PROTOCOL 1

This protocol is adapted from a classical protocol of primary hippocampal neuron culture (Kaech & Banker, 2006; see Current Protocols article: Mendes et al., 2020). The aim of HCS is to study the effect of a large number of compounds or genes in a limited time. To increase experimental efficiency, the cell culture needs to be miniaturized. Cells are grown in 384-well plates with a surface area of 8 mm^2 per well. To enable individual cells to be imaged and analyzed, cell density must be relatively low, cell culture must be homogeneous throughout the well, and cells must not form aggregates. A frequent problem with HCS is the edge effect, i.e., a phenotypic difference between cells seeded in the center of the plate and those seeded at the edge, which can lead to high inter-well variability. To avoid this problem, we chose not to seed cells in the wells at the edge of the plate, but to fill these wells with Dulbecco's phosphate-buffered saline (DPBS). These cultures are maintained for up to 21 days *in vitro* to ensure sufficient maturation for the formation of a dense neuronal network and functional synapses. The screening of up to 107 lentiviral shRNAs, at two different multiplicity of infection (MOI) values, with each shRNA present in technical quadruplicate, requires the preparation of four 384-well plates with primary hippocampal neurons plated in 308 wells (Fig. 1).

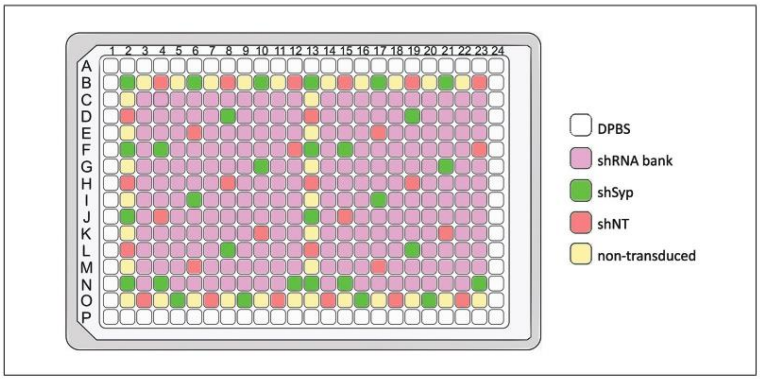

Figure 1 High-content screening (HCS) plate map. Non-transduced wells (NT), non-targeting shRNA (shNT), and shRNA targeting Synaptophysin (shSyp) are used as technical controls for transduction. The plate map is designed to semi-randomly distribute the control wells in the 384-well plate.

Materials

10 µg/ml poly-D-lysine (PDL; Sigma, cat. no. P6407) dissolved in 0.1 M borate buffer (see recipe)
1× DPBS
P0 Wistar rat pups
Dissection buffer (see recipe), 4°C
2.5% (w/v) trypsin (Gibco, cat. no. 15090-046), 37°C
5 mg/ml DNase I (Sigma, cat. no. DN25; diluted in water)
Dissociation medium (see recipe), 37°C
Culture medium (see recipe), 37°C
Trypan blue

384-well cell culture microplates (Greiner Bio-One, cat. no. 781091)
16-channel pipet (Finnpipette F1, Thermo Scientific, cat. no. 4661090N)
Surgical scissors (Fine Science Tools, cat. no. 14007-14)
15- and 50-ml tubes
Petri dishes
Forceps (Dumont #5; Fine Science Tools, cat. no. 11254-20)
Inverted binocular microscope
Agitator (Fisher Scientific, cat. no. 13490577) or similar
Standard tabletop centrifuge
Counting chamber
50-ml sterile reservoirs (Clearline, cat. no. 097803)

NOTE: All protocols involving animals must be reviewed and approved by the appropriate Animal Care and Use Committee and must follow regulations for the care and use of laboratory animals.

NOTE: All solutions and equipment coming into contact with cells must be sterile, and proper sterile technique should be used accordingly.

NOTE: All culture incubations are performed in a 37°C, 5% CO_2 tissue culture incubator unless otherwise specified.

Coat 384-well plates

1. One day before primary culture, coat 384-well cell culture microplates (excluding edge wells: rows A and P, columns 1 and 24) with 15 µl PDL per well and incubate overnight at 37°C and 5% CO_2. Fill edge wells with 100 µl of 1× DPBS.

   Coated plates can be stored ≤1 week at 37°C.

2. On the day of primary culture, wash the plates twice with 40 µl of 1× DPBS per well using a 16-channel pipet and then keep them with 1× DPBS in the incubator.

Dissect hippocampi

3. Put the P0 Wistar rat pups on ice. Decapitate the pups with surgical scissors and keep the heads in a 50-ml tube containing ice-cold dissection buffer.

   On average, one pup yields 1 million hippocampal cells. For four PNC plates, 6 to 8 brains are needed.

   All the dissection steps should be performed on ice.

4. Transfer a head into a Petri dish filled with ice-cold dissection buffer. With a pair of forceps, pinch the skin at the front of the head and pull it to the back of the head. Open the skull from the back to the front of the head with a pair of forceps and

carefully lift the brain with another pair of forceps to transfer it into a second Petri dish filled with ice-cold dissection buffer.

5. Repeat with each of the heads, dispatching the brains into different dishes.
6. Put one of the dishes under an inverted binocular microscope at 10× magnification and separate the two hemispheres of the brain. Lay each hemisphere with its ventral side up and pinch the olfactory bulb backward to pull out the meninges. Flip the hemisphere with its ventral side down and carefully peel the meninges off.
7. Dissect the hippocampus from each cortex and transfer to a 15-ml tube fully filled with ice-cold dissection buffer.
8. Repeat steps 6 and 7 for each brain before proceeding to the next step.

   For optimal neuronal culture, dissection should be done in <30 min. We recommend dissecting no more than 15 brains in one preparation.

Dissociate and plate neurons

9. Wash the hippocampi three times with 10 ml ice-cold dissection buffer.
10. Remove all the dissection buffer and add 0.25 ml pre-warmed 2.5% trypsin per brain. Incubate for 10 min on an agitator or similar placed in the tissue culture incubator.
11. During the incubation, add 12.5 µl of 5 mg/ml DNase I in 10 ml pre-warmed dissociation medium per brain.
12. Remove as much trypsin as possible using a 1000-µl pipet tip and then add the 10 ml of dissociation medium with DNase. Invert each tube three times, letting the hippocampi sediment between inversions.
13. Wash the hippocampi three times with 10 ml pre-warmed dissociation medium.
14. Remove all the dissociation medium and add 2 ml pre-warmed culture medium. Mechanically dissociate the tissue using a 1000-µl pipet tip by gently pipetting up and down 30 times.

    All pieces of tissue should be dissociated, and the suspension should be turbid but homogeneous. Try to avoid generating bubbles and do not dissociate the tissue more than 40 times to avoid damaging the cells.

15. Centrifuge 8 min at 200 × *g* at room temperature.
16. Remove the supernatant and resuspend the cells in 2 ml pre-warmed culture medium.
17. Dilute 10 µl cell suspension in 40 µl pre-warmed culture medium and 50 µl trypan blue.
18. Count the cells using a counting chamber.

    Each brain is expected to provide 1 × 10^6 cells. Cell death should not exceed 10%.

19. Dilute the cell suspension in pre-warmed culture medium to 100,000 cells/ml.

    For four PNC plates, dilute 5.6 × 10^6 cells in 56 ml culture medium.

20. Pour the cell suspension into a 50-ml sterile reservoir and add 40 µl to each well within rows B to O and columns 2 to 23 using a 16-channel pipet.

    Resuspend the cell suspension in the reservoir by pipetting up and down every 5 to 8 columns using the 16-channel pipet.

21. Incubate the screening plates overnight in the tissue culture incubator and proceed directly to Basic Protocol 2.

BASIC PROTOCOL 2

LENTIVIRAL shRNA OF PRIMARY NEURONAL CULTURE IN 384-WELL PLATES

The choice of experimental controls is crucial in HCS, as controls help to ensure data quality and reliability. Controls should be chosen to produce an easily detectable and reproducible response. As a positive control, we choose to use an shRNA targeting Synaptophysin (shSyp), resulting in a decrease in the expression of the corresponding protein. The negative control used is a non-targeting shRNA (shNT). The transduction is performed at 1 day *in vitro* (DIV1) according to the plate map (Fig. 1). Each shRNA is present in technical duplicates in each plate, and two plates are transduced for each MOI, namely MOI2 and MOI4. These numbers are arbitrary and can be adapted to other HCS applications. Our plate map allows for testing the impact of the under-expression of a maximum of 107 genes of interest in technical quadruplicates at two different MOIs.

Materials

1000× polybrene (Hexadimethrine bromide 4 mg/ml; Sigma, cat. no. 107689-10G)
Culture medium (see recipe)
Four screening plates, containing rat postnatal hippocampal cultures at DIV1 (see Basic Protocol 1)
Lentiviral shRNA bank source plate, containing lentiviral shRNAs targeting genes of interest and lentiviral control shRNAs shNT (Merck, MISSION® shC002V) and shSyp (Merck, MISSION® NM_009305 TRCN0000379864)
384-well plates (for intermediate dilutions; Brand, cat. no. 701355)
16-channel pipet (Finnpipette F1; Thermo Scientific, cat. no. 4661090N)

NOTE: Use sterile pipet tips with filters (Finntip 50; Thermo Scientific, cat. no. 94052060).

NOTE: All culture incubations are performed in a 37°C, 5% CO_2 tissue culture incubator unless otherwise specified.

Change medium in the screening plates

1. Dilute 6.7 µl of 1000× polybrene in 10 ml culture medium (0.67× polybrene) and warm it to 37°C.
2. Warm culture medium to 37°C.
3. Allocate two screening plates each for transduction at MOI2 and MOI4 (four plates total).
4. For each MOI4 screening plate, remove 40 µl medium from each well and add 10 µl fresh pre-warmed culture medium from step 2.

   Execute this step column by column to avoid drying of the cells.
5. For each MOI2 screening plate, remove 40 µl medium from each well and add 15 µl fresh pre-warmed culture medium containing 0.67× polybrene from step 1.

   Execute this step column by column to avoid drying of the cells.
6. Store the screening plates in the incubator until the intermediate plates are ready (see steps 7 to 11).

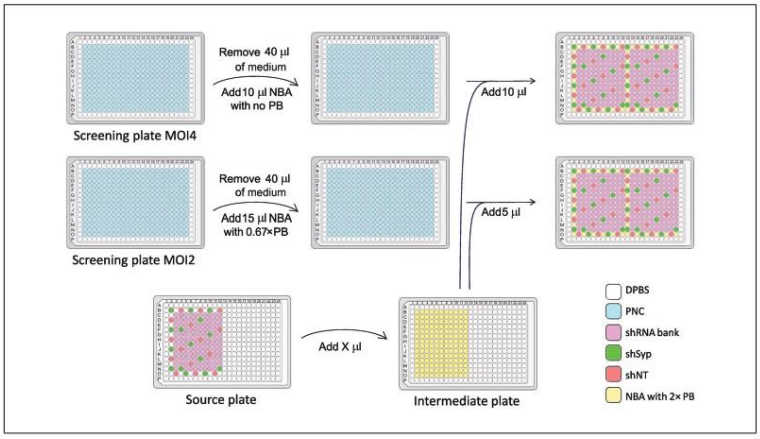

Figure 2 Workflow for lentiviral transduction of primary neuronal cells with the shRNA bank in the screening plates. Lentiviral shRNAs from the source plate are diluted in the intermediate plate to reach a transduction unit of 1.6. 10^6 VP/ml and used for transducing cells cultured in two screening plates at MOI4 and two screening plates at MOI2. All these steps are performed using a 16-channel pipet. shNT: non-targeting shRNA; shSyp: shRNA targeting Synaptophysin; PNC: primary neuronal culture; PB: polybrene; NBA: Neurobasal-A Medium; DPBS: Dulbecco's phosphate-buffered saline.

Prepare intermediate plates

7. To dilute the lentiviruses from the source plate into the intermediate plate to reach a transduction unit of 1.6×10^6 viral particles per milliliter (VP/ml), calculate the volume of the medium required separately for each shRNA in the bank (Fig. 2).

   The volume in the intermediate plate should be between 70 µl and 280 µl per well.

   There is inherent variation in the virus titer received from the producer. For screening, the virus titer needs to be uniform throughout the plate (for a given MOI). The intermediate plate is where the lentiviruses are diluted to a common transduction unit before they are added to the screening plates. A minimum 70 µl lentivirus suspension is needed to screen an shRNA in quadruplicate (two plates per MOI and two wells per plate) at MOI2 and MOI4. Here, a total of 10 µl × 4 = 40 µl is needed for MOI4 plates and a total of 5 µl × 4 = 20 µl is needed for MOI2 plates, plus 10 µl dead volume, resulting in 70 µl. One well of a 384-well plate can safely receive a maximum of 280 µl, considering the tip volume.

   For example, for a lentivirus bank where the titer varies between 1.3×10^7 VP/ml and 4.3×10^7 VP/ml, one can dilute 9 µl shRNA into a total volume varying from [9 µl × ($1.3 \times 10^7/1.6 \times 10^6$) =] 73 µl to [9 µl × ($4.3 \times 10^7/1.6 \times 10^6$ =] 242 µl. Similarly, one can dilute 10 µl shRNA into a total volume varying from [10 µl × ($1.3 \times 10^7/1.6 \times 10^6$) =] 81 µl to [10 µl × ($4.3 \times 10^7/1.6 \times 10^6$) =] 268 µl. Diluting 8 µl of the shRNA with the lowest titer would result in a final volume of [8 µl × ($1.3 \times 10^7/1.6 \times 10^6$) =] 65 µl, which is not desirable because it is <70 µl. On the other hand, diluting 11 µl of the shRNA with the highest titer would result in a final volume of [11 µl × ($4.3 \times 10^7/1.6 \times 10^6$) =] 295 µl, which is beyond the 280-µl safe well capacity.

   These calculations will have to be repeated for each lentivirus bank and for the number of technical replications and MOI(s) chosen by the user.

8. For each shRNA, round the volume of medium required to dilute the lentivirus suspension (equal to the final volume calculated in step 7 minus the volume of the lentiviral suspension) to the nearest 10 µl.

Following one of the examples in step 7, if one decided to dilute 10 µl shRNA at a titer of 1.3×10^7 VP/ml, the rounded volume for this shRNA would be 81 µl – 10 µl = 71 µl ≈ 70 µl.

9. Thaw the lentiviral shRNA bank source plate.

   The source plate is ideally packaged in the 384-well plate format with a minimum volume of 15 µl and a minimum transduction unit of 10^7 VP/ml.

10. Dilute 40 µl of 1000× polybrene in 20 ml pre-warmed culture medium to obtain 2× polybrene. Using a single-channel pipet, fill the wells of a 384-well plate (the intermediate plate) with the different volumes of medium calculated in step 7 for each shRNA. Fill the non-transduced wells with 100 µl pre-warmed culture medium.

11. Using a 16-channel pipet, transfer the volume of shRNAs from the source plate to the corresponding wells of the intermediate plate.

    It is important for the quality of the shRNA bank that a multichannel pipet is used to minimize the time required for dilution after thawing. This can only be assured by fixing a set volume of lentivirus suspension, regardless of the titer. This, however, requires that the medium volume for each shRNA should be calculated and added to the wells in advance (see step 10).

Transduce cells with lentiviruses

12. Transfer 10 µl lentivirus suspension at 1.6×10^6 VP/ml from each well of the intermediate plate to the corresponding well and its duplicate in the two MOI4 screening plates (see step 6).

13. Transfer 5 µl lentivirus suspension at 1.6×10^6 VP/ml from each well of the intermediate plate to the corresponding well and its duplicate in the two MOI2 screening plates (see step 6).

14. Incubate screening plates for 6 hr in the tissue culture incubator.

15. Add 20 µl fresh pre-warmed NBA medium to each transduction well (40 ml in total).

16. Incubate the screening plates in the tissue culture incubator until DIV21 and then proceed directly to Basic Protocol 3.

BASIC PROTOCOL 3

IMMUNOSTAINING OF THE NEURONAL NETWORK AND SYNAPTIC MARKERS IN 384-WELL PLATES

This HCS approach is based on the immunolabeling of a presynaptic protein (Synaptophysin) and a postsynaptic protein (Homer1) and the quantitative analysis of their relative positions. This strategy has recently been shown to have sufficient sensitivity to detect the changes in synaptic connectivity induced by exposing neurons to cell-secreted Aβ oligomers at physiologically relevant concentrations (Kilinc et al., 2020). To ensure an efficient and reproducible immunolabeling process in 384-well plates, washing steps are automated using a robotic platform. To reduce the damage to fixed cells, the position of the distribution/aspiration heads is optimized and the flow rate is reduced. Automated steps of the protocol need to be adapted to the material available to the user. Addition of primary and secondary antibody mixes, however, is done manually to avoid waste due to the relatively large dead volume.

Materials

Four screening plates, containing transduced rat hippocampal cultures at DIV21 (see Basic Protocol 2)
4% (v/v) formaldehyde in DPBS
0.3% (v/v) Triton X-100 in DPBS

2.5% (w/v) bovine serum albumin (BSA) in DPBS with 0.1% (v/v) Triton X-100
Primary antibodies:
Chicken anti-Homer1 (Synaptic Systems, cat. no. 160006)
Guinea pig anti-Synaptophysin (Synaptic Systems, cat. no. 101004)
Mouse anti-MAP2 (Synaptic Systems, cat. no. 188011)
1× DPBS
Secondary antibodies:
Donkey anti-chicken Alexa 488 (Jackson ImmunoResearch, cat. no. 703-545-155)
Goat anti-guinea pig Alexa 555 (Life Technologies, cat. no. A21435)
Donkey anti-mouse Alexa 647 (Jackson ImmunoResearch, cat. no. 715-605-151)

16-channel pipet (Finnpipette F1; Thermo Scientific, cat. no. 4661090N)
Aluminum sealing tape (Dutscher, cat. no. 106570, or similar)
PlateHUB rotating plate-storage carousel (Agilent, model G5500-23447)
Plate washer associated with liquid handler (BioTek, model EL406)
Wash_Primary.pro and Wash_Secondary.pro programs (see Supporting Information)
VWorks automation control software (Agilent)
Aspirate.LHC and Aspirate-Dispense.LHC subroutines (see Supporting Information)
Direct Drive Robot (Agilent)

NOTE: Use sterile pipet tips with filters (Finntip 50; Thermo Scientific, cat. no. 94052060).

Fix, permeabilize, and saturate the cells

1. Using a 16-channel pipet, carefully remove the culture medium from each of the four screening plates and add 20 µl of 4% formaldehyde in DPBS per well. Incubate for 15 to 20 min at room temperature.

   Execute this step column by column to avoid drying and harming the neurons.

   Use the 16-channel pipet in steps 1 to 7.

2. Remove formaldehyde and wash for 10 min with 40 µl DPBS per well.
3. Remove DPBS and permeabilize the cells using 20 µl of 0.3% Triton X-100 in DPBS per well for 5 min.
4. Remove Triton X-100 and saturate the cells using 20 µl of 2.5% BSA in DPBS with 0.1% Triton X-100 per well.
5. Incubate 2 hr at room temperature.

Incubate screening plates with primary antibodies

6. Prepare the primary antibody mix by diluting primary antibodies 1:500 in 1× DPBS.
7. Remove buffer from step 4 and add 15 µl primary antibody mix to each per well.
8. Seal all plates with aluminum sealing tape and incubate overnight at 4°C.
9. Bring assay plates from 4°C to room temperature, remove their seals, and place them on PlateHUB cassette 1 of the PlateHUB rotating plate-storage carousel.
10. Plug a bottle of 1× DPBS bottle to the plate washer associated with the liquid handler and install the distribution heads.

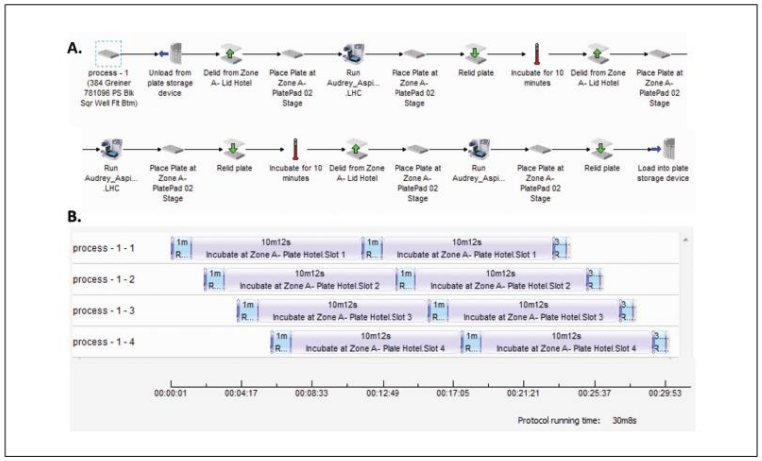

Figure 3 Automation of the washing steps for immunostained screening plates. **(A)** VWorks workflow for primary or secondary washes. **(B)** Gantt chart adjusted for the washing of four plates twice.

To minimize damage to the sample, we set the positions of the heads as follows: X-offset: 0.46 mm left of center; Y-offset: 0.74 mm back of center; Z-offset for aspiration: 3.18 mm above carrier; Z-offset for dispensing: 15.22 mm above carrier. Dispensing is preceded by two pre-dispensing steps of 10 µl/tube.

11. Run the program Wash_Primary.pro on the VWorks automation control software by defining the number of plates (four in our case), which allows automated plate transfers by the Direct Drive Robot:

    a. Pick a plate, remove its lid, and place it on plate washer.
    b. Aspirate the buffer from each well and add 40 µl DPBS per well.
    c. Remove the plate from plate washer, replace its lid, and move it to plate pad. Incubate for 10 min.
    d. Repeat steps 11a to 11c. During incubation, prepare the secondary antibody mix by diluting secondary antibodies 1:500 in 1× DPBS.
    e. Pick a plate, remove its lid, and place it on plate washer.
    f. Aspirate the buffer from each well.
    g. Remove the plate from plate washer, replace its lid, and move it to PlateHUB cassette 7.

    When step 11g is finished for the last screening plate, this completes program Wash_Primary.pro. This program runs steps 11a to 11g in an automated fashion for each plate (Fig. 3). This program automatically calls the Aspirate.LHC and Aspirate-Dispense.LHC subroutines for the BioTek plate washer to perform the buffer aspiration and the PBS-dispensing steps, respectively.

Incubate screening plates with secondary antibodies

12. Each time a plate is placed on PlateHUB cassette 7, move it to the bench and add 15 µl secondary antibody mix per well using a 16-channel pipet.

    Proceed as quickly as possible to avoid drying and damaging the sample.

13. Seal all plates with aluminum sealing tape and incubate 2 hr at room temperature.

14. Run program Wash_Secondary.pro on VWorks by defining the number of plates (four in our case):

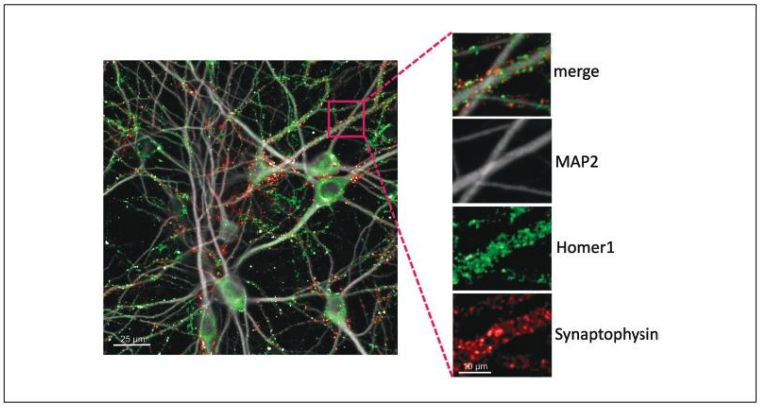

Figure 4 Representative images of MAP2, Homer1, and Synaptophysin staining acquired with IN Cell Analyzer 6000.

a. Repeat steps 11a to 11c twice.
b. Pick a plate, remove its lid, and place it on plate washer.
c. Aspirate the buffer from each well and add 40 µl DPBS per well.
d. Remove the plate from plate washer, replace its lid, and move it to PlateHUB cassette 7.

When step 14d is finished the last assay plate, this completes program Wash_Secondary.pro. This program runs steps 14a to 14d in an automated fashion for each plate (Fig. 3). This program automatically calls Aspirate.LHC and _Aspirate-Dispense.LHC subroutines for the BioTek plate washer to perform respectively the buffer aspiration and the PBS dispensing steps. All automated plate transfers are done by the Direct Drive Robot.

15. Remove DPBS bottle from the plate washer and wash tubes, pumps, and distribution heads.

16. Proceed immediately to image acquisition (see Basic Protocol 4) for the first plate and store other plates at 4°C.

IMAGE ACQUISITION USING A HIGH-THROUGHPUT READER

BASIC PROTOCOL 4

Imaging three wavelengths at sufficiently high spatial resolution (0.1083 µm/px in our case) should produce satisfactory presynaptic and postsynaptic signals, as well as imaging of the somatodendritic network (Fig. 4).

Materials

Immunostained screening plates (see Basic Protocol 3)
IN Cell Analyzer 6000 (GE Healthcare; or similar automated confocal microscope)

1. Once immunostaining is completed (see Basic Protocol 3), pick an immunostained screening plate and proceed to setting up the image acquisition parameters (steps 2 to 8).

   Keep the other plates at 4°C.

2. When using the IN Cell Analyzer 6000 (GE Healthcare) for the first time, select (or define) the plate used (in our case, Greiner µclear 384-well plate 781091). Select the lowest-magnification objective available and verify that the autofocus range in

different wells of the plate is sufficiently large. Adjust the plate thickness parameter if necessary.

Plate thickness varies between different production batches and affects the microscope autofocus function.

A similar automated confocal microscope may be used.

3. In the Dashboard tab, select the highest-magnification objective (in our case, Nikon 60 × /0.95, Plan Apo, Corr Collar 0.11-0.23, CFI/60 Lambda), set binning as 1 × 1, and set laser autofocus power level at 50%. Additionally, select the following acquisition wavelengths: Cy5 (642/706 nm) for MAP2, dsRed (561/605 nm) for Synaptophysin, and FITC (488/525 nm) for Homer1.
4. For all channels, set image mode as "maximum intensity projection" and set Z-slice number as 3. Deselect open aperture and set laser power to 100% and aperture to 1.05.
5. For each channel, define laser intensity as 100% and set up the autofocus offset and exposure time.

   In our setup, i.e., with the antibody concentrations and incubation periods described, the exposure times were 200 ms for Cy5, 200 ms for FITC, and 150 ms for dsRed. The autofocus offsets varied between 0.5 and 1.5 µm. Exposure times and autofocus offsets need to be verified for each acquisition batch.
6. Define the wells to be imaged: 308 wells from B2 (top left corner) to O23 (bottom right corner).
7. In the Field tab, define number of fields per well as 16, acquisition sequence as "horizontal serpentine", and spacing between fields as X: 100 µm and Y: 100 µm. Position the fields in the center-right portion of the well.
8. In the Z-Stack setup tab, define the Z Step as 0.5 µm. Position the 3D focus at the center slice.
9. Save image acquisition parameters in a .xaqp file.
10. Insert the first plate in the IN Cell microscope and start automated imaging.

    The imaging time per plate (308 wells; 16 fields per well; 3 wavelengths; 3 Z slices) is <7 hr.
11. Repeat step 10 for the remaining plates. Store imaged plates at 4°C.
12. When the last plate imaged, proceed to Basic Protocol 5 to transfer the images to the Columbus server for image segmentation and analysis.

BASIC PROTOCOL 5

IMAGE SEGMENTATION AND ANALYSIS

Image segmentation is an essential step for defining the synaptic puncta. Considering the large number of images acquired, this process needs to be done automatically (or semi-automatically) with specialized software. In this protocol, we will describe the image analysis conducted in Columbus software, but the commands can be adapted to any software with similar capabilities (Fig. 5).

Materials

Columbus Image Data Storage and Analysis System, version 2.7 or above (Perkin Elmer; or similar software)
Data from Basic Protocol 4

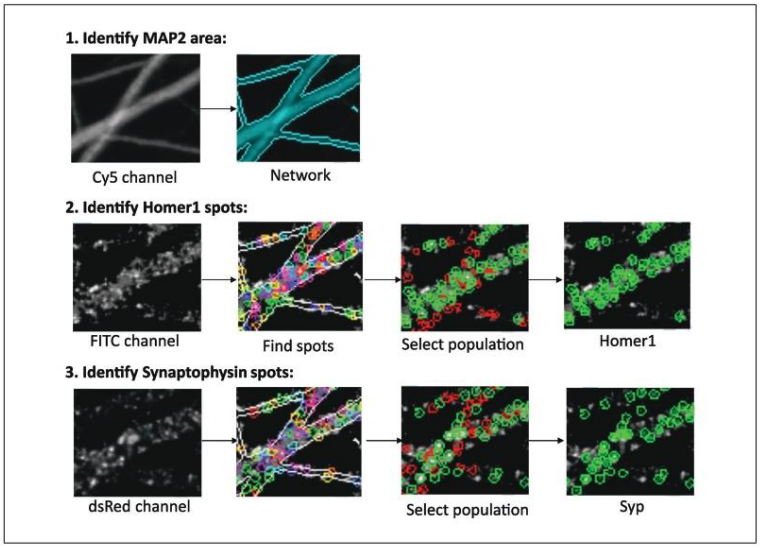

Figure 5 Image segmentation and analysis using Columbus software. MAP2 staining was used to define the somatodendritic network area, and Homer1 and Synaptophysin spots were detected within the network area. At the "select population" step, spots that did not satisfy the defined criteria (red spots) were excluded from final results (green spots).

Identify and measure MAP2 areas

1. Open "Import" under the Workflow menu in the Columbus Image Data Storage and Analysis System, select Import Type as "InCell XDCE/TIF", select source folder (where images and .XDCE files are stored), define the name of the screen/imaging, and start importing data from Basic Protocol 4.

   Giving the same screening name to each of the imported plates will save them into the same folder.

2. Select "Image Analysis", select an "Assay Plate" under the "Data Tree", and select an shNT control well from the "Image Selection" menu.

   Columbus uses an "Image Analysis" interface with building blocks that are used for image segmentation. This interface contains two default building blocks: Input Image and Define Results. All other building blocks need to be added between these two building blocks and validated. The next steps describe how to set up the image analysis in Columbus software. Alternatively, you can import the HCS_Synapse.aas program (see Supporting Information) and only proceed to the training for spot identification (steps 9 and 13) before analyzing images of full plates (steps 24 and 25).

3. In the **Input Image** building block, select "Maximum Projection" for Stack Processing and "None" for Flatfield Correction.

4. Add a **Find Image Region** building block with "Channel" = "Cy5"; "ROI" = "None"; "Method" = "Common Threshold". As second-tier inputs, define "Threshold" as 0.40 and "Area cut-offs" as 0 and deselect "Split into Objects" and "Fill Holes" options. Name "Output Population" and "Output Region" as "Network".

   Depending on your images, "Threshold" can be adjusted in order to better delineate MAP2 areas.

5. Add a **Calculate Morphology Properties** building block with "Population" = "Network"; "Region" = "Network"; "Method" = "Standard". As second-tier inputs, select "Area (in μm^2)". Name "Output Properties" as "Network".

6. Add a **Calculate Intensity Properties** building block with "Channel" = "Cy5"; "Population" = "Network"; "Region" = "Network"; "Method" = "Standard". As second-tier inputs, select "mean" and "sum". Name "Output Properties" as "Intensity Network".

Identify and quantify Homer1 spots

7. Add a **Find Spots** building block with "Channel" = "FITC"; "ROI" = "Network"; "Population" = "Network"; Region = "Network"; "Method" = "C". As second-tier inputs, set "Radius" to "< 0.1", "Contrast" to "> 0", "Uncorrected Spot to Region Intensity" to "> 0", "Distance" to "≥ 0.75 μm", and "Spot Peak Radius" to "0.21 μm". Select "Calculate Spot Properties". Name "Output Population" as "Homer Spot".

8. Add a **Calculate Intensity Properties** building block with "Channel" = "FITC"; "Population" = "Homer Spot"; "Region" = "Homer Spot"; "Method" = "Standard". As second-tier inputs, select "mean", "sum", "max", "90% quantile fraction", and "contrast". Name "Output Properties" as "Intensity Spot FITC".

9. Add a **Select Population** building block with "Population" = "Homer Spot"; "Method" = "Linear Classifier". As second-tier inputs, select "2" as "number of classes" and select the following fields: "Relative Spot Intensity"; "Corrected Spot Intensity"; "Uncorrected Spot Peak Intensity"; "Spot Contrast"; "Spot Background Intensity"; "Spot Area [px2]"; "Region Intensity"; "Spot to Region Intensity"; "Intensity Spot FITC Mean"; "Intensity Spot FITC Maximum"; "Intensity Spot FITC Sum"; "Intensity Spot FITC Quantile 90%"; "Intensity Spot FITC Contrast". Name "Output Population A" as "Homerselect" and "Output Population B" as "fake". Choose an shNT control well and click on "Train…". Select "Class A: green" and click on spots that one could consider as true Homer1 spots. Select "Class B: red" and click on spots that one could consider as falsely identified Homer1 spots. Train the computer by selecting at least 10 spots for each class in at least 10 images from different shNT control wells. Once satisfied with the selection, accept and exit the training.

10. Add another **Select Population** building block with "Population" = "Homerselect"; "Method" = "Filter By Property". As second-tier inputs, set "Intensity Spot FITC mean" as ">1500". Name "Output Population" as "Homer1".

    Depending on your images, adjust the threshold (set as 1500) to optimize the identification of Homer1 spots.

Identify and quantify Synaptophysin spots

11. Add a **Find Spots** building block with "Channel" = "dsRed"; "ROI" = "Network"; "Population" = "Network"; Region = "Network"; "Method" = "C". "Radius" to "< 0.1", "Contrast" to "> 0", "Uncorrected Spot to Region Intensity" to "> 0", "Distance" to "≥ 0.75 μm", and "Spot Peak Radius" to "0.21 μm". Select "Calculate Spot Properties". Name "Output Population" as "Syn Spot".

12. Add a **Calculate Intensity Properties** building with "Channel" = "dsRed"; "Population" = "Syn Spot"; "Region" = "Syn Spot"; "Method" = "Standard". As second-tier inputs, select "mean", "sum", "max", "90% quantile fraction", and "contrast". Name "Output Properties" as "Intensity Spot dsRed".

13. Add a **Select Population** building block with "Population" = "Syn Spot"; "Method" = "Linear Classifier". As second-tier inputs, select "2" as "number of classes" and select the following fields: "Relative Spot Intensity"; "Corrected Spot Intensity"; "Uncorrected Spot Peak Intensity"; "Spot Contrast"; "Spot Background Intensity"; "Spot Area [px2]"; "Region Intensity"; "Spot to Region Intensity"; "Intensity Spot dsRed Mean"; "Intensity Spot dsRed Maximum"; "Intensity Spot dsRed Sum"; "Intensity Spot dsRed Quantile 90%"; "Intensity Spot dsRed Contrast". Name "Output Population A" as "Synselect" and "Output Population B" as "fake(2)". Choose an shNT control well and click on "Train…". Select "Class A: green" and click on spots that one could consider as true Synaptophysin spots. Select "Class B: red" and click on spots that one could consider as falsely identified Synaptophysin spots. Train the computer by selecting at least 10 spots for each class in at least 10 images from different shNT control wells. Once satisfied with the selection, accept and exit the training.

14. Add another **Select Population** building block with "Population" = "Synselect"; "Method" = "Filter By Property". As second-tier inputs, set "Intensity Spot dsRed mean" as "> 1100". Name "Output Population" as "Syn1".

    Depending on your images, adjust the threshold (set as 1100) to optimize the identification of Synaptophysin spots.

Define Results

15. In the **Define Results** building block, select "List of Outputs" as "Method". Open "fake", "fake(2)", "Homerselect", and "Synselect" input fields to confirm that nothing is selected. In "Population: Homer Spots" and "Population: Syn Spots" input fields, select only "Number of Objects". In "Population: Homer1" and "Population: Syn1" input fields, select "Number of Objects", set "Apply to all" as "Individual Selection", and select "ALL" for "Intensity Spot Mean", "Intensity Spot Maximum", and "Intensity Spot Sum". In "Population: Network" input field, deselect "Number of Objects", set "Apply to all" as "Individual Selection", and select "ALL" for "Network Area" and "Intensity Network Sum".

16. For steps 17 to 21, remain in the same **Define Results** building block, add "Formula" as "Method" and confirm that "a/b" is set as "Formula".

17. Select "Syn1 - Number of Objects" as "Variable A" and "Network - Network Area [μm2] Mean" as "Variable B". Name "Output Population" as "Syn1 density".

18. Select "Homer1 - Number of Objects" as "Variable A" and "Network - Network Area [μm2] Mean" as "Variable B". Name "Output Population" as "Hom1 density".

19. Select "Homer1 - Number of Objects" as "Variable A" and "Syn1 - Number of Objects" as "Variable B". Name "Output Population" as "Hom1/Syn1".

20. Select "Syn1 - Number of Objects" as "Variable A" and "Syn Spots - Number of Objects" as "Variable B". Name "Output Population" as "Syn1/Syn".

21. Select "Hom1 - Number of Objects" as "Variable A" and "Homer Spots - Number of Objects" as "Variable B". Name "Output Population" as "Hom1/Hom".

22. In the **Object Results** building block, select "ALL" for "Homer1", "Syn1", and "Network" populations. Select "None" for the other population.

23. Save Columbus script via "Save Analysis to Disk".

Analyze images of full plates

24. Open "Batch Analysis" under the Workflow menu, select the measurement to analyze (i.e., "Assay Plate" subfolder) and the analysis script in "Data Tree", and start analysis.

    Repeat this step for all assay plates. Analysis of each plate takes 4 hr.

25. Open "Export" under the Workflow menu and select the measurement folder (automatically generated by Columbus) in "Data Tree". In the "Select Export Options" tab, select "Export to Disk" as "Method", designate an "Export Folder", select "Excel (txt)" as "Results", and choose "Generate Subfolders" and "Include Header".

    Repeat this step for all assay plates. Export of each plate takes 30 min.

BASIC PROTOCOL 6

SYNAPTIC DENSITY ANALYSIS

Columbus generates tabulated data that contains information for each detected synaptic spot, for each field in each well in each plate. To analyze this massive amount of tabulated data, we have generated a custom Matlab algorithm that extracts data from .txt files in stored specific folders into matrices that contain network area and network staining intensity per field, as well as *xy*-position and staining intensity for all Synaptophysin and Homer1 spots. The algorithm first excludes fields with no presynaptic or postsynaptic spots detected. It then identifies outlier fields within a well in terms of network area or network staining intensity. After excluding the outlier fields, the algorithm runs a subroutine to calculate, for each Homer1 spot, its Euclidian distance to all Synaptophysin spots in the same field. Each Homer1 spot is then assigned to the nearest Synaptophysin spot with a pre-determined cut-off distance. In control cultures, the fraction of Synaptophysin spots with at least one Homer1 spot assigned linearly increases with increasing cut-off distance, until it starts to reach a plateau. We thus select a cut-off distance in the linear portion of the curve and apply it to all images in the screen. The ultimate read-out of the screen, synapse density, is then defined as the area density of Synaptophysin spots with at least one Homer1 spot assigned.

Materials

Columbus results (see Basic Protocol 5)
Matlab, version R2017b or above (Mathworks; or similar numerical analysis software)
Matlab code HCS_CPCB_annotated.m (see Supporting Information)
Microsoft Excel (or similar spreadsheet software)

Copy Columbus results to a local folder and run Matlab code

1. For each plate, copy Columbus results (.txt files) into the "data" folder of the Matlab environment (or similar numerical analysis software) and run Matlab code HCS_CPCB_annotated.m.

   Columbus results will be stored in three text files per well: one each for MAP2 network, Synaptophysin spots, and Homer1 spots.

2. Set the initial parameters in the *Matlab* code: "cutoffs" stands for the different cut-off distances in micrometers; "fieldnum" stands for the number of fields acquired per well; and "resolution" stands for the pixel resolution of images in µm/px.

   The length of the cut-off distances vector is arbitrary and can be 1. The code acquires well names from .txt file names using the following command:

```
wellnames(k) = strrep(strrep(eraseBetween(eraseBetween(My
FolderInfo(k*3+2).name,'Syn','.'), '[','txt'), 'Syn.
result.', ''), '[txt', '');
```

Table 1 Matlab Output Parameters

Output parameter	Definition
1	Number of Syn spots (× 1000)
2	Number of Homer1 spots (× 1000)
3	% of Synaptophysin spots assigned by any Homer1 spot
4	Mean distance of assignments
5	Mean number of assignments per Synaptophysin spot
6	Mean distance of assignments (μm)
7	% of Homer1 spots assigned to any Synaptophysin spot
8	Network area (μm^2)
9	Network intensity
10	Number of fields remaining after removing outliers
11	Synaptophysin1 – Intensity Spot dsRed Sum
12	Homer1 – Intensity Spot FITC Sum

Table 2 Column Headers of the display.mat File

Row	Column	Well names	Number of fields (10)	Output parameter mean	Output parameter mean			Output parameter SD	Output parameter SD		
					Cutoff 1	Cutoff 2	Cutoff…		Cutoff 1	Cutoff 2	Cutoff…
				1 2 8 9 11 12	3 5 6 7	3 5 6 7	… … … …	1 2 8 9 11 12	3 5 6 7	3 5 6 7	… … … …

If the output file name format of Columbus changes, adapt the Matlab command to the new name needed.

The code will exclude fields with no Homer1 spots or Synaptophysin spots by looking at the corresponding network file.

For each well, the code will exclude fields with network area outside median ± 2 median absolute differences (MADs), as wells as fields with mean network intensity outside median ± 2 MADs.

3. Back up the three output files generated by the Matlab code (batchres.mat, display.mat, and wellnames.mat) by associating them with the screen name.

The results are first written in BATCHRES, a 4D matrix with the following dimensions: wellnum × fieldnum × cutoffnum × 12, corresponding to the number of wells to be analyzed, number of fields per well, length of the cut-off distances vector, and number of output parameters (Table 1).

The well-averaged summary data are then stored in DISPLAY, a 2D matrix with the following dimensions: wellnum × n, where n = 13 + 8 × length of the cut-off distances matrix. The DISPLAY matrix stores, for each well, the number of fields that are remaining after removing outlier fields and the mean and standard deviation (per well) of six output parameters that are independent of the assignment cut-off distance (1, 2, 8, 9, 11, 12) and four output parameters that vary with the assignment cut-off distance (3, 5, 6, 7).

Extract Matlab results to Excel and conduct post-analysis

4. Open wellnames.mat in Matlab and copy the only column to column C of a new Microsoft Excel file.
5. Open display.mat in Matlab and copy table into columns D to CJ of the Excel file.
6. Insert three lines at the top of the sheet and label the columns as in Table 2.

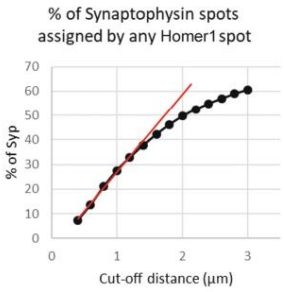

Figure 6 Plot of the percentage of Synaptophysin spots assigned by at least one Homer1 spot as a function of cut-off distance. The red line indicates the linear part of the curve. For this set of experiments, 1 µm is chosen as the cut-off distance.

7. Complete columns A and B with the column number and the row number corresponding to each well and use these columns to sort the wells from B2 to O23.
8. Use column CK to associate each well with its respective shRNA (e.g., shNT, shSyp, shGeneX).
9. Calculate the β-score of the plate: $\beta = \frac{\mu_{shNT} - \mu_{shSyp}}{\sigma^2_{shNT} + \sigma^2_{shSyp}}$, where µ and σ are the mean and standard deviation of Syp density for control wells treated with shNT and shSyp. Analyze only the plates with a β-score > 1.
10. Use the data from non-transduced wells to calculate the mean of "% of Synaptophysin with no Homer assigned" for each cut-off. Plot % of Synaptophysin spots assigned by at least one Homer1 spot as a function of cut-off distance (Fig. 6).

    The curve should reach a plateau. For the rest of the analysis, use a single cut-off value, located before the upper end of the linear part of the curve (typically 1 µm).

11. Add a column to calculate "Synapse density" for each well.

    Synapse density = % Synaptophysin assigned × Syn1 density.

12. Copy the results of all shNT control wells into a new Excel tab and calculate the means for each parameter.
13. Copy the results of all wells to a new Excel tab and normalize them using the means calculated in step 12.
14. Repeat steps 4 to 13 for each plate.
15. Copy the normalized results from each plate into a new Excel file.
16. Exclude the wells with shRNA-induced toxicity, as defined by normalized Network Area < 0.4 (<40% of control average).
17. Pool the data for the entire screen and discard shRNAs for which there are fewer than two values.
18. Identify shRNAs that have the strongest effect on synapse density.

REAGENTS AND SOLUTIONS

Borate buffer (pH 8.5), 0.1 M

1.55 g boric acid (Sigma-Aldrich, cat. no. B9645-500G)

2.375 g sodium tetraborate
400 ml ultrapure H_2O
Stir for 4 hr at room temperature to dissolve sodium tetraborate
After reagents dissolve, pH should be stable at 8.5
Bring to 500 ml with ultrapure H_2O
Filter-sterilize
Store ≤4-6 weeks at 4°C

Culture medium

2 ml 50× B27 supplement (Gibco, cat. no. 17504001)
250 µl 100× GlutaMAX (Gibco, cat. no. 35050038)
Bring to 100 ml with Neurobasal-A Medium (Gibco, cat. no. 10888022)
Filter-sterilize
Store ≤4 days at 4°C

Dissection buffer

2.5 ml 20× penicillin/streptomycin (Gibco, cat. no. 1507063)
5 ml 1 M HEPES (Gibco, cat. no. 15630056)
5 ml 100 mM sodium pyruvate (Gibco, cat. no. 11360039)
50 ml 10× Hank's Balanced Salt Solution (HBSS; Gibco, cat. no. 14185045)
Bring to 500 ml with ultrapure H_2O
Filter-sterilize
Store ≤6 weeks at 4°C

Dissociation medium

0.25 ml 20× penicillin/streptomycin (Gibco, cat. no. 15070063)
0.4 ml 1× MEM vitamins (Gibco, cat. no. 11120037)
0.5 ml 100× GlutaMAX (Gibco, cat. no. 35050038)
1.5 ml 20% (w/v) D-glucose (Sigma, cat. no. G8270)
5 ml fetal bovine serum (FBS; Gibco, cat. no. 10270106)
Bring to 50 ml with minimum essential medium (MEM) without glutamine (Gibco, cat. no. 21090022)
Filter-sterilize
Store ≤4 days at 4°C

COMMENTARY

Background Information

Quantification of synaptic density can help decipher the mechanisms of synaptogenesis, synaptic plasticity, and synaptic loss observed in neurodevelopmental and neurodegenerative disorders. Here, we describe an HCS method that we applied to assess the impact of an shRNA library targeting 198 AD-associated genes on synaptic density to test the hypothesis if synapse loss driven by genetic risk factors plays a role in AD pathophysiology.

HCS combines automated imaging and quantitative data analysis in a high-throughput format suitable for large-scale applications. However, accurate assessment of synaptic density in an HCS pipeline requires mature neuronal cell cultures, adequate methods for imaging synapses, and a reliable approach to quantify synaptic density. Several HCS approaches have been developed, but most of them encountered (i) limited scalability due to the use of low-density (96-well) assay plates (Berryer et al., 2023; Jiang et al., 2020; Nieland et al., 2014), (ii) difficulties in maintaining native synaptic properties *in vitro* using transfection-based overexpressed synaptic proteins (Green et al., 2019), and (iii) challenges in identifying and quantifying functional/mature synapses due to the use of a single presynaptic or postsynaptic marker (Berryer et al., 2023; Spicer et al., 2017). Although several open-source methods for synaptic quantification have been developed, such as SynQuant (Wang et al., 2020), SynapseJ (Moreno Manrique et al., 2021), SynPAnal (Danielson & Lee, 2014), and ALPAQAS (Berryer et al., 2023), the HCS method we describe here is one of the

few that use automated imaging of fluorescently labeled endogenous presynaptic and postsynaptic markers in mature primary neurons cultured in 384-well microplates, as well as a semi-automated image analysis workflow to quantify synapses by the proximity-based assignment of postsynaptic puncta to presynaptic puncta. Process automation ensures the throughput, accuracy, and reproducibility of our HCS, and as proof of concept, we generated data showing that our method robustly identifies modulators of synaptic density through unbiased screening of 198 shRNAs targeting AD-associated genes.

The present approach permits us not only to identify modulators of synaptic density but also to screen potential therapeutic molecules for neurodevelopmental or neurodegenerative diseases. Our future directions include the use of human induced pluripotent stem cell–derived neurons to analyze the convergent or divergent mechanisms of synaptic development and alteration between humans and rodents, as well as the use of patient-derived pluripotent stem cells for *in vitro* modeling of neurological diseases.

Critical Parameters

Before transducing the shRNA lentiviral library (Basic Protocol 2), it is recommended to check the quality of the PNC (Basic Protocol 1). If the cells have not adhered well to the substrate or if the neuronal network appears fragmented and/or vacuolated, it is preferable not to proceed with transduction because it is highly likely that the neurons will not survive. During the 21 days of neuronal maturation, no change of medium is needed, but it is recommended to check the level of culture medium and to add medium in the event of excessive evaporation. In our screening model, we chose to use a large number of positive and negative controls per screening plate. After optimization, the number and the semi-random distribution of control wells proved necessary to ensure the quality of our approach. As the cellular model we used is a neonatal rat neuronal culture model, it is necessary to verify that the lentiviral shRNA library used targets the rat genome. This article presents the optimal conditions for immunolabeling (Basic Protocol 3), but it is possible to adapt the protocol according to the needs of the user. Formalin use for fixation and natural donkey serum as a blocking agent are perfectly acceptable alternatives. Before starting image acquisition on a full plate (Basic Protocol 4), it is always advisable to check the quality of immunolabeling in several randomly selected wells located in different parts of the plate. Immunolabeling is highly sensitive to the ambient temperature, and image acquisition takes place at room temperature. For this reason, the reading of a plate should never exceed 8 hr of acquisition, and plates should always be stored at 4°C. Monitoring the temperature of the microscope is recommended to ensure that it does not overheat during plate reading, which would decrease the signal quality in parts of the plate. Once the image analysis has been completed, it is recommended to quickly check the quality of the acquisition using the Columbus software. To do so, one can obtain heat maps for the following parameters: Syn1 density, Hom1 density, and Network Area - Mean per Well. For Hom1 density and Network Area, values must be homogeneous within the plate (no edge or gradient effects). Syn1 density values should follow the same plate layout as the positive controls. After complete data analysis (Basic Protocols 5 and 6), any plate with a β-score below 1 should be excluded from the final results.

Troubleshooting

See Table 3 for a list of potential problems, possible causes, and suggested solutions.

Understanding Results

To reduce the risk of false negatives and false positives, we performed our screen three times using three independent neuronal cultures. Transduction of shSyp at MOI2 and MOI4 decreased the average Synaptophysin density by 69 ± 12% and 85 ± 7%, respectively. Strictly standardized mean difference (SSMD) was assessed through the β-score using positive and negative controls from each plate. Due to the inherent heterogeneity of our phenotype, a plate should be considered suitable for analysis when its β-score is >1 (Zhang et al., 2007). Among the 11 plates in our HCS study, we obtained a range of β-scores from 1.31 to 2.88 (Table 4), indicating a good level of reproducibility of our model. The synaptic density observed for each shRNA from the bank needs to be normalized by the mean synaptic density of the shNT controls from the same plate to overcome any potential inter-plate variability in terms of cell culture, immunocytochemistry, and image acquisition.

Time Considerations

To simplify the experimentation, we recommend preparing culture medium, coating solutions, and the intermediate dilution plate on the days prior to neuronal culture. Medium

Table 3 Troubleshooting Guide for High-Content Screening of Synaptic Density Modulators in Primary Neuronal Cultures

Problem	Possible cause	Solution
Cell death after seeding	Dissection and/or dissociation took too long	Dissection should be performed in <30 min. We recommend not to dissect more than 15 brains in one preparation.
	Cell density is too low	Increase the cell density (≥100,000 cells/ml). Homogenize well before seeding to avoid inter-well variability.
Cell death after lentiviral shRNA transduction	MOI is too high	Decrease the MOI
Staining shows a fragmented network	Cells dried	Never let the cells go without 1× DPBS or medium. When changing medium, always proceed column-by-column to avoid drying of the cells.
	Over-fixed or over-permeabilized cells	Decrease the time of fixation and/or permeabilization
	Washing steps are too rough	Decrease the flow rate of the washer for automated aspiration/dispensation steps
Weak staining intensity	Over-fixed cells	Decrease the time for fixation
	Non-permeabilized cells	Increase the time for permeabilization
	Antibody concentration is too low	Use a higher concentration of antibodies or increase the time for incubation
High background signal	Insufficient blocking	Increase the saturation time or consider changing the blocking agent to 5% natural donkey serum
	Insufficient washing steps	Add one more washing step or increase the time for washes
	Antibody concentration is too high	Use a lower concentration of antibody
Edge effect	Medium evaporates faster in the border wells than in the center wells	Check the medium level once or twice a week and add some medium if necessary. Do not seed cells in the border wells; instead, fill them with 1× DPBS.
Decrease in fluorescence intensity over time during acquisition	Increase in ambient temperature	The acquisition temperature must be recorded and controlled all along. Plates should always be kept at 4°C and imaged one after the other to avoid inter-plate variability.
	Plates were left at room temperature	Always keep the plates at 4°C. Imaging should be done within <3 days. Plates should be imaged within <8 hr.
β-score is <1	Positive control is not efficient	Avoid freeze-thawing of the lentiviral shRNAs to avoid a decrease in the lentivirus titer
	Inter-well variability is too high	Check for pipetting errors. In Basic Protocol 3, using an automatic pipet with a stepper mode (Thermo Scientific, cat. no. 46300200) can decrease the inter-well variability.
	Image analysis is not optimal	In the Columbus "Select Population" building block, train the computer on additional images from different wells

and coating solutions can be stored ≤1 week at 4°C. The first day is devoted to PNC (~3 hr; Basic Protocol 1). Dissection should be carried out as quickly as possible (<30 min) to ensure optimum quality. The second day is devoted to transducing the lentiviral shRNA library (Basic Protocol 2). Transduction itself takes ~2 hr, followed by a 6-hr-long incubation period before the addition of the culture medium. It then takes 21 days for the

Table 4 β-scores of Different Plates After Transduction at MOI2 or MOI4

	β-score	
	MOI2	MOI4
Plate 1	2.26	3.9
Plate 2	1.66	1.67
Plate 3	1.38	1.61
Plate 4	2.14	2.67
Plate 5	2.05	1.33
Plate 6	2.82	2.33
Plate 7	1.94	2.35
Plate 8	1.86	2.67
Plate 9	1.31	2.46
Plate 10	1.33	1.6
Plate 11	1.56	2.02
Mean ± SD	**1.85 ± 0.46**	**2.24 ± 0.72**

development of the neural network and the maturation of synapses. During these 21 days, the level of medium must be regularly monitored (1 to 2 times a week). Day 21 is devoted to cell fixation, saturation, and incubation with primary antibodies (Basic Protocol 3). These steps take 3 hr, including 2 hr of incubation. Day 22 is devoted to washing and incubation with secondary antibodies, followed by image acquisition. This immunostaining also takes 3 hr, including 2 hr of incubation. Image acquisition (Basic Protocol 4) must be carried out immediately after immunolabeling and usually takes 8 hr per plate. Each plate must be read immediately, one after the other. Data analysis in Columbus (Basic Protocol 5) takes a variable amount of time, depending on the training time required for successful spot detection. Approximately 10 hr is required for one screening (four plates). Data analysis in Matlab (Basic Protocol 6) takes ~6 hr per screening plate.

Acknowledgments

The authors thank Equipex for the Equipex ImagInEx HCS platform for the robotic control and automated microscopy. This work was supported by Fondation Alzheimer (903716), Agence national de la recherché (ANR-21-CE16-0010), Sanofi iAwards Europe 2019 (196026), and Fondation pour la recherche médicale (ALZ201912009628). This work was also funded by the Lille Métropole Communauté Urbaine and the French government's LABEX DISTALZ program (Development of innovative strategies for a transdisciplinary approach to Alzheimer's disease). In addition, this work was funded by the Network of Centres of Excellence in Neurodegeneration (CoEN, pathfinder 5010).

Author Contributions

AC conducted the experiments and wrote the original draft; AC, DSW, CN, CG, AMA, FD, and EL conducted primary rat hippocampal cultures; AC, TM, and DK developed methodology and analyzed the data; AV and PB provided access to and technical help for the ImagInEx platform; JCL, DK, JD, and JC conceived the idea and managed the project. All authors reviewed and edited the manuscript.

Conflict of Interest

The authors declare no conflict of interest.

Data Availability Statement

Screening data are available from the corresponding author upon request.

Supporting Information

Aspirate.LHC

Program for BioTek plate washer used in Basic Protocol 3.

Aspirate-Dispense.LHC

Program for BioTek plate washer used in Basic Protocol 3.

HCS_CPCB_annotated.m

Program for Matlab used in Basic Protocol 6. Please note that we annotated the .m file such that readers can rewrite the code in the computational platform of their choice.

HCS_Synapse.aas

Program for Columbus software used in Basic Protocol 5.

Wash_primary.pro

Program for VWorks software used in Basic Protocol 3.

Wash_secondary.pro

Program for VWorks software used in Basic Protocol 3.

Literature Cited

Bellenguez, C., Küçükali, F., Jansen, I. E., Kleineidam, L., Moreno-Grau, S., Amin, N., Naj, A. C., Campos-Martin, R., Grenier-Boley, B., Andrade, V., Holmans, P. A., Boland, A., Damotte, V., van der Lee, S. J., Costa, M. R., Kuulasmaa, T., Yang, Q., de Rojas, I., Bis, J. C., … Lambert, J.-C. (2022). New insights into the genetic etiology of Alzheimer's disease and

related dementias. *Nature Genetics*, *54*, 412–436. https://doi.org/10.1038/s41588-022-01024-z

Bellucci, A., Mercuri, N. B., Venneri, A., Faustini, G., Longhena, F., Pizzi, M., Missale, C., & Spano, P. (2016). Review: Parkinson's disease: From synaptic loss to connectome dysfunction. *Neuropathology and Applied Neurobiology*, *42*, 77–94. https://doi.org/10.1111/nan.12297

Berryer, M. H., Rizki, G., Nathanson, A., Klein, J. A., Trendafilova, D., Susco, S. G., Lam, D., Messana, A., Holton, K. M., Karhohs, K. W., Cimini, B. A., Pfaff, K., Carpenter, A. E., Rubin, L. L., & Barrett, L. E. (2023). High-content synaptic phenotyping in human cellular models reveals a role for BET proteins in synapse assembly. *eLife*, *12*, e80168. https://doi.org/10.7554/eLife.80168

Danielson, E., & Lee, S. H. (2014). SynPAnal: Software for rapid quantification of the density and intensity of protein puncta from fluorescence microscopy images of neurons. *PLOS ONE*, *9*, e115298. https://doi.org/10.1371/journal.pone.0115298

DeKosky, S. T., & Scheff, S. W. (1990). Synapse loss in frontal cortex biopsies in Alzheimer's disease: Correlation with cognitive severity. *Annals of Neurology*, *27*, 457–464. https://doi.org/10.1002/ana.410270502

Fogarty, M. J. (2019). Amyotrophic lateral sclerosis as a synaptopathy. *Neural Regeneration Research*, *14*, 189–192. https://doi.org/10.4103/1673-5374.244782

Gigg, J., McEwan, F., Smausz, R., Neill, J., & Harte, M. K. (2020). Synaptic biomarker reduction and impaired cognition in the sub-chronic PCP mouse model for schizophrenia. *Journal of Psychopharmacology*, *34*, 115–124. https://doi.org/10.1177/0269881119874446

Green, M. V., Pengo, T., Raybuck, J. D., Naqvi, T., McMullan, H. M., Hawkinson, J. E., Marron Fernandez de Velasco, E., Muntean, B. S., Martemyanov, K. A., Satterfield, R., Young Jr, S. M., & Thayer, S. A. (2019). Automated live-cell imaging of synapses in rat and human neuronal cultures. *Frontiers in Cellular Neuroscience*, *13*, 467. https://doi.org/10.3389/fncel.2019.00467

Jiang, H., Esparza, T. J., Kummer, T. T., Zhong, H., Rettig, J., & Brody, D. L. (2020). Live neuron high-content screening reveals synaptotoxic activity in alzheimer mouse model homogenates. *Scientific Reports*, *10*, 3412. https://doi.org/10.1038/s41598-020-60118-y

Kaech, S., & Banker, G. (2006). Culturing hippocampal neurons. *Nature Protocols*, *1*, 2406–2415. https://doi.org/10.1038/nprot.2006.356

Kilinc, D., Vreulx, A.-C., Mendes, T., Flaig, A., Marques-Coelho, D., Verschoore, M., Demiautte, F., Amouyel, P., Neuro-CEB Brain Bank, Eysert, F., Dourlen, P., Chapuis, J., Costa, M. R., Malmanche, N., Checler, F., & Lambert, J.-C. (2020). Pyk2 overexpression in postsynaptic neurons blocks amyloid β1-42-induced synaptotoxicity in microfluidic co-cultures. *Brain Communications*, *2*, fcaa139. https://doi.org/10.1093/braincomms/fcaa139

Kunkle, B. W., Grenier-Boley, B., Sims, R., Bis, J. C., Damotte, V., Naj, A. C., Boland, A., Vronskaya, M., van der Lee, S. J., Amlie-Wolf, A., Bellenguez, C., Frizatti, A., Chouraki, V., Martin, E. R., Sleegers, K., Badarinarayan, N., Jakobsdottir, J., Hamilton-Nelson, K. L., Moreno-Grau, S., Polygenic and Environmental Risk for Alzheimer's Disease Consortium (GERAD/PERADES). (2019). Genetic meta-analysis of diagnosed Alzheimer's disease identifies new risk loci and implicates Aβ, tau, immunity and lipid processing. *Nature Genetics*, *51*, 414–430. https://doi.org/10.1038/s41588-019-0358-2

Mendes, T., Herledan, A., Leroux, F., Deprez, B., Lambert, J.-C., & Kilinc, D. (2020). High-content screening for protein-protein interaction modulators using proximity ligation assay in primary neurons. *Current Protocols in Cell Biology*, *86*, e100. https://doi.org/10.1002/cpcb.100

Monteiro, P., & Feng, G. (2017). SHANK proteins: Roles at the synapse and in autism spectrum disorder. *Nature Reviews. Neuroscience*, *18*, 147–157. https://doi.org/10.1038/nrn.2016.183

Moreno Manrique, J. F., Voit, P. R., Windsor, K. E., Karla, A. R., Rodriguez, S. R., & Beaudoin, G. M. J. (2021). SynapseJ: An automated, synapse identification macro for ImageJ. *Frontiers in Neural Circuits*, *15*, 731333. https://doi.org/10.3389/fncir.2021.731333

Nieland, T. J. F., Logan, D. J., Saulnier, J., Lam, D., Johnson, C., Root, D. E., Carpenter, A. E., & Sabatini, B. L. (2014). High content image analysis identifies novel regulators of synaptogenesis in a high-throughput RNAi screen of primary neurons. *PLOS ONE*, *9*, e91744. https://doi.org/10.1371/journal.pone.0091744

Spicer, T. P., Hubbs, C., Vaissiere, T., Collia, D., Rojas, C., Kilinc, M., Vick, K., Madoux, F., Baillargeon, P., Shumate, J., Martemyanov, K. A., Page, D. T., Puthanveettil, S., Hodder, P., Davis, R., Miller, C. A., Scampavia, L., & Rumbaugh, G. (2017). Improved scalability of neuron-based phenotypic screening assays for therapeutic discovery in neuropsychiatric disorders. *Molecular Neuropsychiatry*, *3*, 141–150. https://doi.org/10.1159/000481731

Verschuuren, M., Verstraelen, P., García-Díaz Barriga, G., Cilissen, I., Coninx, E., Verslegers, M., Larsen, P. H., Nuydens, R., & de vos, W. H. (2019). High-throughput microscopy exposes a pharmacological window in which dual leucine zipper kinase inhibition preserves neuronal network connectivity. *Acta Neuropathologica Communications*, *7*, 93. https://doi.org/10.1186/s40478-019-0741-3

Verstraelen, P., Garcia-Diaz Barriga, G., Verschuuren, M., Asselbergh, B., Nuydens, R., Larsen, P. H., Timmermans, J.-P., & de Vos, W. H. (2020). Systematic quantification of synapses in primary neuronal culture. *iScience*,

23, 101542. https://doi.org/10.1016/j.isci.2020.101542

Wang, Y., Wang, C., Ranefall, P., Broussard, G. J., Wang, Y., Shi, G., Lyu, B., Wu, C.-T., Wang, Y., Tian, L., & Yu, G. (2020). SynQuant: An automatic tool to quantify synapses from microscopy images. *Bioinformatics*, *36*, 1599–1606. https://doi.org/10.1093/bioinformatics/btz760

Wong, M., & Guo, D. (2013). Dendritic spine pathology in epilepsy: Cause or consequence? *Neuroscience*, *251*, 141–150. https://doi.org/10.1016/j.neuroscience.2012.03.048

Zhang, X. D., Ferrer, M., Espeseth, A. S., Marine, S. D., Stec, E. M., Crackower, M. A., Holder, D. J., Heyse, J. F., & Strulovici, B. (2007). The use of strictly standardized mean difference for hit selection in primary RNA interference high-throughput screening experiments. *Journal of Biomolecular Screening*, *12*, 497–509. https://doi.org/10.1177/1087057107300646

References

1. Terry, R. D. Chapter 3 Interrelations among the lesions of normal and abnormal aging of the brain. *Progress in Brain Research* **70**, 41–48 (1986).
2. Alzheimer, A. Ueber eine eigenartige erkrankung der hirnrinde. *Z Gesamte Neurologie und Psychiatrie* **18**, (1907).
3. Pini, L. *et al*. Brain atrophy in Alzheimer's Disease and aging. *Ageing Research Reviews* **30**, 25–48 (2016).
4. Perl, D. P. Neuropathology of Alzheimer's disease. *Mount Sinai Journal of Medicine* **77**, 32–42 (2010).
5. CESE, H.-F. *Eclairer l'avenir RAPPORT-AVIS*. (2017).
6. Alzheimer Europe. *Dementia in Europe Yearbook 2019: Estimating the Prevalence of Dementia in Europe*. https://www.alzheimer-europe.org/sites/default/files/alzheimer_europe_dementia_in_europe_yearbook_2019.pdf (2019).
7. 2024 Alzheimer's disease facts and figures. *Alzheimer's & Dementia* **20**, 3708 (2024).
8. Alzheimer's Association. *American Perspectives on Early Detection of Alzheimer's Disease in the Era of Treatment*.
9. Belger, M. *et al*. Determinants of time to institutionalisation and related healthcare and societal costs in a community-based cohort of patients with Alzheimer's disease dementia. *European Journal of Health Economics* **20**, 343–355 (2019).
10. Moloney, C. M., Lowe, V. J. & Murray, M. E. Visualization of neurofibrillary tangle maturity in Alzheimer's disease: A clinicopathologic perspective for biomarker research. *Alzheimer's and Dementia* **17**, 1554–1574 (2021).
11. Querol-Vilaseca, M. *et al*. Nanoscale structure of amyloid-β plaques in Alzheimer's disease. *Scientific Reports* **9**, (2019).
12. Morales, I., Farías, G. & MacCioni, R. B. Neuroimmunomodulation in the pathogenesis of Alzheimer's disease. *NeuroImmunoModulation* **17**, 202–204 (2010).
13. Jack, C. R. *et al*. Brain beta-amyloid measures and magnetic resonance imaging atrophy both predict time-to-progression from mild cognitive impairment to Alzheimer's disease. *Brain* **133**, 3336–3348 (2010).
14. Sperling, R. A. *et al*. Toward defining the preclinical stages of Alzheimer's disease: Recommendations from the National Institute on Aging-Alzheimer's Association workgroups on diagnostic guidelines for Alzheimer's disease. *Alzheimer's and Dementia* **7**, 280–292 (2011).
15. Dubois, B. *et al*. Preclinical Alzheimer's disease: Definition, natural history, and diagnostic criteria. *Alzheimer's and Dementia* **12**, 292–323 (2016).
16. Thal, D. R., Rüb, U., Orantes, M. & Braak, H. Phases of Aβ-deposition in the human brain and its relevance for the development of AD. *Neurology* **58**, 1791–1800 (2002).
17. Braak, H. & Braak, E. Staging of Alzheimer's disease-related neurofibrillary changes. *Neurobiology of Aging* **16**, 271–278 (1995).

18. Jack, C. R. *et al*. Tracking pathophysiological processes in Alzheimer's disease: An updated hypothetical model of dynamic biomarkers. *The Lancet Neurology* **12**, 207–216 (2013).
19. Marshall, G. A. *et al*. Executive function and instrumental activities of daily living in MCI and AD. *Alzheimer's & Dementia* **7**, 300 (2011).
20. Chen, Y., Dang, M. & Zhang, Z. Brain mechanisms underlying neuropsychiatric symptoms in Alzheimer's disease: a systematic review of symptom-general and –specific lesion patterns. *Molecular Neurodegeneration* **16**, 38 (2021).
21. Jack, C. R. *et al*. A/T/N: An unbiased descriptive classification scheme for Alzheimer disease biomarkers. *Neurology* **87**, 539 (2016).
22. Goedert, M. Alzheimer's and Parkinson's diseases: The prion concept in relation to assembled Aβ, tau, and α-synuclein. *Science* **349**, (2015).
23. Aretouli, E. & Brandt, J. Everyday functioning in mild cognitive impairment and its relationship with executive cognition. *International Journal of Geriatric Psychiatry* **25**, 224 (2010).
24. Jack, C. R. *et al*. NIA-AA Research Framework: Toward a biological definition of Alzheimer's disease. *Alzheimer's and Dementia* **14**, 535–562 (2018).
25. Jack, C. R. *et al*. Revised criteria for diagnosis and staging of Alzheimer's disease: Alzheimer's Association Workgroup. *Alzheimer's and Dementia* **20**, 5143–5169 (2024).
26. Mitchell, S. L. *et al*. The Clinical Course of Advanced Dementia. *New England Journal of Medicine* **361**, 1529–1538 (2009).
27. Kim, H. & Chung, J. Y. Pathobiolgy and Management of Alzheimer's Disease. *Chonnam Medical Journal* **57**, 108 (2021).
28. Arriagada, P. V., Growdon, J. H., Hedley-Whyte, E. T. & Hyman, B. T. Neurofibrillary tangles but not senile plaques parallel duration and severity of Alzheimer's disease. *Neurology* **42**, 631–639 (1992).
29. Scheff, S. W., Price, D. A., Schmitt, F. A., Dekosky, S. T. & Mufson, E. J. Synaptic alterations in CA1 in mild Alzheimer disease and mild cognitive impairment. *Neurology* **68**, 1501–1508 (2007).
30. Scheff, S. W. & Price, D. A. Alzheimer's disease-related alterations in synaptic density: Neocortex and hippocampus. *Journal of Alzheimer's Disease* **9**, 101–115 (2006).
31. DeKosky, S. T., Scheff, S. W. & Styren, S. D. Structural Correlates of Cognition in Dementia: Quantification and Assessment of Synapse Change. *Neurodegeneration* **5**, 417–421 (1996).
32. Terry, R. D. *et al*. Physical basis of cognitive alterations in Alzheimer's disease: Synapse loss is the major correlate of cognitive impairment. *Annals of Neurology* **30**, 572–580 (1991).
33. Furukawa, K. *et al*. Increased activity-regulating and neuroprotective efficacy of α-secretase-derived secreted amyloid precursor protein conferred by a C- terminal heparin-binding domain. *Journal of Neurochemistry* **67**, 1882–1896 (1996).
34. Mattson, M. P. Cellular actions of β-amyloid precursor protein and its soluble and fibrillogenic derivatives. *Physiological Reviews* **77**, 1081–1132 (1997).
35. Gakhar-Koppole, N. *et al*. Activity requires soluble amyloid precursor protein α to promote neurite outgrowth in neural stem cell-derived neurons via activation of the MAPK pathway. *European Journal of Neuroscience* **28**, 871–882 (2008).

36. Kuhn, A. J. & Raskatov, J. Is the p3 peptide (Aβ17-40, Aβ17-42) relevant to the pathology of Alzheimer's disease? *Journal of Alzheimer's Disease* **74**, 43–53 (2020).
37. Müller, T., Meyer, H. E., Egensperger, R. & Marcus, K. The amyloid precursor protein intracellular domain (AICD) as modulator of gene expression, apoptosis, and cytoskeletal dynamics—Relevance for Alzheimer's disease. *Progress in Neurobiology* **85**, 393–406 (2008).
38. Penke, B., Bogár, F. & Fülöp, L. β-Amyloid and the Pathomechanisms of Alzheimer's Disease: A Comprehensive View. *Molecules : A Journal of Synthetic Chemistry and Natural Product Chemistry* **22**, 1692 (2017).
39. Tomita, S., Kirino, Y. & Suzuki, T. Cleavage of Alzheimer's amyloid precursor protein (APP) by secretases occurs after O-glycosylation of APP in the protein secretory pathway. Identification of intracellular compartments in which APP cleavage occurs without using toxic agents that interfere with protein metabolism. *The Journal of Biological Chemistry* **273**, 6277–6284 (1998).
40. Furukawa, K., Barger, S. W., Blalock, E. M. & Mattson, M. P. Activation of K+ channels and suppression of neuronal activity by secreted β-amyloid-precursor protein. *Nature* **379**, 74–78 (1996).
41. Mawuenyega, K. G. *et al*. Decreased clearance of CNS beta-amyloid in Alzheimer's disease. *Science* **330**, 1774 (2010).
42. Hampel, H. *et al*. The β-Secretase BACE1 in Alzheimer's Disease. *Biological Psychiatry* **89**, 745–756 (2021).
43. Wildburger, N. C. *et al*. Diversity of Amyloid-beta Proteoforms in the Alzheimer's Disease Brain. *Scientific Reports* **7**, (2017).
44. Chen, G. F. *et al*. Amyloid beta: structure, biology and structure-based therapeutic development. *Acta Pharmacologica Sinica* **38**, 1205–1235 (2017).
45. Jarrett, J. T., Berger, E. P. & Lansbury, P. T. The C-Terminus of the β Protein is Critical in Amyloidogenesis. *Annals of the New York Academy of Sciences* **695**, 144–148 (1993).
46. Selkoe, D. J. Alzheimer's disease: genes, proteins, and therapy. *Physiological Reviews* **81**, 741–766 (2001).
47. Lesné, S. E. *et al*. Brain amyloid-β oligomers in ageing and Alzheimer's disease. *Brain* **136**, 1383–1398 (2013).
48. Price, K. A. *et al*. Altered synaptic structure in the hippocampus in a mouse model of Alzheimer's disease with soluble amyloid-β oligomers and no plaque pathology. *Molecular Neurodegeneration* **9**, 41 (2014).
49. Shankar, G. M. *et al*. Amyloid-β protein dimers isolated directly from Alzheimer's brains impair synaptic plasticity and memory. *Nature Medicine* **14**, 837–842 (2008).
50. Walsh, D. M. *et al*. Naturally secreted oligomers of amyloid β protein potently inhibit hippocampal long-term potentiation in vivo. *Nature* **416**, 535–539 (2002).
51. Ahmed, M. *et al*. Structural conversion of neurotoxic amyloid-β(1–42) oligomers to fibrils. *Nature Structural & Molecular Biology* **17**, 561 (2010).
52. Koffie, R. M. *et al*. Oligomeric amyloid beta associates with postsynaptic densities and correlates with excitatory synapse loss near senile plaques. *Proceedings of the National Academy of Sciences of the United States of America* **106**, 4012–4017 (2009).
53. Ebrahimi, R. *et al*. Microglial activation as a hallmark of neuroinflammation in Alzheimer's disease. *Metabolic Brain Disease* **40**, (2025).

54. Baligács, N. *et al*. Homeostatic microglia initially seed and activated microglia later reshape amyloid plaques in Alzheimer's Disease. *Nature Communications 2024 15:1* **15**, 1–14 (2024).
55. Stalder, M. *et al*. Association of Microglia with Amyloid Plaques in Brains of APP23 Transgenic Mice. *The American Journal of Pathology* **154**, 1673 (1999).
56. Dresser, L. *et al*. Amyloid-β oligomerization monitored by single-molecule stepwise photobleaching. *Methods* **193**, 80 (2021).
57. Cajal, S. R. Y., Azoulay, D. L., swanson, N. & Swanson, larry W. *Histology Of The Nervous System: Of Man And Vertebrates*. (Oxford University Press, 1995).
58. Eccles, J. C. *The Physiology of Synapses*. (Springer Berlin Heidelberg, 1964).
59. Sherrington, C. S. *The Integrative Action of the Nervous System*. (Routledge, 1906).
60. Bezaire, M. J. & Soltesz, I. Quantitative assessment of CA1 local circuits: knowledge base for interneuron-pyramidal cell connectivity. *Hippocampus* **23**, 751–785 (2013).
61. Buhl, E. H., Halasy, K. & Somogyi, P. Diverse sources of hippocampal unitary inhibitory postsynaptic potentials and the number of synaptic release sites. *Nature* **368**, 823–828 (1994).
62. Gulyás, A. I., Megías, M., Emri, Z. & Freund, T. F. Total Number and Ratio of Excitatory and Inhibitory Synapses Converging onto Single Interneurons of Different Types in the CA1 Area of the Rat Hippocampus. *Journal of Neuroscience* **19**, 10082–10097 (1999).
63. Megías, M., Emri, Z., Freund, T. F. & Gulyás, A. I. Total number and distribution of inhibitory and excitatory synapses on hippocampal CA1 pyramidal cells. *Neuroscience* **102**, 527–540 (2001).
64. Klausberger, T. & Somogyi, P. Neuronal diversity and temporal dynamics: The unity of hippocampal circuit operations. *Science* **321**, 53–57 (2008).
65. Blakely, R. D. & Edwards, R. H. Vesicular and Plasma Membrane Transporters for Neurotransmitters. *Cold Spring Harbor Perspectives in Biology* **4**, a005595 (2012).
66. Südhof, T. C. & Rizo, J. Synaptic Vesicle Exocytosis. *Cold Spring Harbor Perspectives in Biology* **3**, a005637 (2011).
67. Stuart, G., Spruston, N., Sakmann, B. & Häusser, M. Action potential initiation and backpropagation in neurons of the mammalian CNS. *Trends in Neurosciences* **20**, 125–131 (1997).
68. Schmidt-hieber, C., Jonas, P. & Bischofberger, J. Action potential initiation and propagation in hippocampal mossy fibre axons. *Journal of Physiology* **586**, 1849–1857 (2008).
69. Katz, B. & Miledi, R. Ionic requirements of synaptic transmitter release. *Nature* **215**, 651 (1967).
70. Borst, J. G. G. & Sakmann, B. Calcium influx and transmitter release in a fast CNS synapse. *Nature* **383**, 431–434 (1996).
71. Holroyd, C., Kistner, U., Annaert, W. & Jahn, R. Fusion of Endosomes Involved in Synaptic Vesicle Recycling. *Molecular Biology of the Cell* **10**, 3035 (1999).
72. Baude, A. *et al*. The metabotropic glutamate receptor (mGluR1 alpha) is concentrated at perisynaptic membrane of neuronal subpopulations as detected by immunogold reaction. *Neuron* **11**, 771–787 (1993).
73. Takumi, Y., Ramírez-León, V., Laake, P., Rinvik, E. & Ottersen, O. P. Different modes of expression of AMPA and NMDA receptors in hippocampal synapses. *Nature Neuroscience* **2**, 618–624 (1999).

74. Hwa, G. G. C. & Avoli, M. Excitatory postsynaptic potentials recorded from regular-spiking cells in layers II/III of rat sensorimotor cortex. *Journal of Neurophysiology* **67**, 728–737 (1992).
75. Pare, D., Dossi, R. C. & Steriade, M. Three types of inhibitory postsynaptic potentials generated by interneurons in the anterior thalamic complex of cat. *Journal of Neurophysiology* **66**, 1190–1204 (1991).
76. Bekkers, J. M., Richerson, G. B. & Stevens, C. F. Origin of variability in quantal size in cultured hippocampal neurons and hippocampal slices. *Proceedings of the National Academy of Sciences* **87**, 5359–5362 (1990).
77. Harris, K. M. & Sultan, P. Variation in the number, location and size of synaptic vesicles provides an anatomical basis for the nonuniform probability of release at hippocampal CA1 synapses. *Neuropharmacology* **34**, 1387–1395 (1995).
78. Liu, G. Presynaptic control of quantal size: kinetic mechanisms and implications for synaptic transmission and plasticity. *Current Opinion in Neurobiology* **13**, 324–331 (2003).
79. Midgett, C. R. & Madden, D. R. The Quaternary Structure of a Calcium-Permeable AMPA Receptor: Conservation of Shape and Symmetry across Functionally Distinct Subunit Assemblies. *Journal of Molecular Biology* **382**, 578–584 (2008).
80. Park, H., Li, Y. & Tsien, R. W. Influence of synaptic vesicle position on release probability and exocytotic fusion mode. *Science* **335**, 1362–1366 (2012).
81. Sanz-Clemente, A., Nicoll, R. A. & Roche, K. W. Diversity in NMDA Receptor Composition. *The Neuroscientist* **19**, 62–75 (2013).
82. Takumi, Y., Matsubara, A., Rinvik, E. & Ottersen, O. P. The arrangement of glutamate receptors in excitatory synapses. *Annals of the New York Academy of Sciences* **868**, 474–482 (1999).
83. Margulis, M. & Tang, C. M. Temporal integration can readily switch between sublinear and supralinear summation. *Journal of Neurophysiology* **79**, 2809–2813 (1998).
84. Nettleton, J. S. & Spain, W. J. Linear to supralinear summation of AMPA-mediated EPSPs in neocortical pyramidal neurons. *Journal of Neurophysiology* **83**, 3310–3322 (2000).
85. Danbolt, N. C. Glutamate uptake. *Progress in Neurobiology* **65**, 1–105 (2001).
86. Verkhratsky, A. & Parpura, V. Astrogliopathology in neurological, neurodevelopmental and psychiatric disorders. *Neurobiology of Disease* **85**, 254–261 (2016).
87. Lau, A. & Tymianski, M. Glutamate receptors, neurotoxicity and neurodegeneration. *Pflugers Archiv European Journal of Physiology* **460**, 525–542 (2010).
88. Fusi, S., Drew, P. J. & Abbott, L. F. Cascade models of synaptically stored memories. *Neuron* **45**, 599–611 (2005).
89. Kandel, E. R. The molecular biology of memory storage: A dialogue between genes and synapses. *Science* **294**, 1030–1038 (2001).
90. Kullmann, D. M. & Lamsa, K. P. Long-term synaptic plasticity in hippocampal interneurons. *Nature reviews. Neuroscience* **8**, 687–699 (2007).
91. Bliss, T. V. P. & Collingridge, G. L. A synaptic model of memory: long-term potentiation in the hippocampus. *Nature 1993 361:6407* **361**, 31–39 (1993).
92. Bliss, T. V. P. & Lømo, T. Long-lasting potentiation of synaptic transmission in the dentate area of the anaesthetized rabbit following stimulation of the perforant path. *The Journal of Physiology* **232**, 331–356 (1973).

93. Engert, F. & Bonhoeffer, T. Dendritic spine changes associated with hippocampal long-term synaptic plasticity. *Nature* **399**, 66–70 (1999).
94. Derkach, V., Barria, A. & Soderling, T. R. Ca2+/calmodulin-kinase II enhances channel conductance of α-amino-3-hydroxy-5-methyl-4-isoxazolepropionate type glutamate receptors. *Proceedings of the National Academy of Sciences of the United States of America* **96**, 3269 (1999).
95. Barria, A., Muller, D., Derkach, V., Griffith, L. C. & Soderling, T. R. Regulatory phosphorylation of AMPA-type glutamate receptors by CaM-KII during long-term potentiation. *Science* **276**, 2042–2045 (1997).
96. Ren, S. Q. *et al*. PKCλ is critical in AMPA receptor phosphorylation and synaptic incorporation during LTP. *The EMBO Journal* **32**, 1365 (2013).
97. Esteban, J. A. *et al*. PKA phosphorylation of AMPA receptor subunits controls synaptic trafficking underlying plasticity. *Nature Neuroscience* **6**, 136–143 (2003).
98. Abel, T. *et al*. Genetic Demonstration of a Role for PKA in the Late Phase of LTP and in Hippocampus-Based Long-Term Memory. *Cell* **88**, 615–626 (1997).
99. Banke, T. G. *et al*. Control of GluR1 AMPA Receptor Function by cAMP-Dependent Protein Kinase. *The Journal of Neuroscience* **20**, 89 (2000).
100. Benke, T. A., Luthl, A., Isaac, J. T. R. & Collingridge, G. L. Modulation of AMPA receptor unitary conductance by synaptic activity. *Nature* **393**, 793–797 (1998).
101. Davies, S. N., Lester, R. A. J., Reymann, K. G. & Collingridge, G. L. Temporally distinct pre- and post-synaptic mechanisms maintain long-term potentiation. *Nature* **338**, 500–503 (1989).
102. Romero, A. M., Yovanno, R. A., Lau, A. Y. & Twomey, E. C. Mechanisms of Ion Permeation in the AMPA Receptor Ion Channel. *bioRxiv* (2025).
103. Lisman, J., Yasuda, R. & Raghavachari, S. Mechanisms of CaMKII action in long-term potentiation. *Nature reviews. Neuroscience* **13**, 169 (2012).
104. Young, J. Z., Isiegas, C., Abel, T. & Nguyen, P. V. Metaplasticity of the late-phase of long-term potentiation: a critical role for protein kinase A in synaptic tagging. *The European Journal of Neuroscience* **23**, 1784 (2006).
105. Herdegen, T. & Leah, J. D. Inducible and constitutive transcription factors in the mammalian nervous system: Control of gene expression by Jun, Fos and Krox, and CREB/ATF proteins. *Brain Research Reviews* **28**, 370–490 (1998).
106. Yukimasa, N., Isobe, K., Nagai, H., Takuwa, Y. & Nakai, T. Successive occupancy by immediate early transcriptional factors of the tyrosine hydroxylase gene TRE and CRE sites in PACAP-stimulated PC12 pheochromocytoma cells. *Neuropeptides* **33**, 475–482 (1999).
107. Morgan, J. I. & Curran, T. Calcium as a modulator of the immediate-early gene cascade in neurons. *Cell Calcium* **9**, 303–311 (1988).
108. Milbrandt, J. A nerve growth factor-induced gene encodes a possible transcriptional regulatory factor. *Science* **238**, 797–799 (1987).
109. Sukhatme, V. P. *et al*. A zinc finger-encoding gene coregulated with c-fos during growth and differentiation, and after cellular depolarization. *Cell* **53**, 37–43 (1988).
110. Williams, J. M. *et al*. Sequential increase in Egr-1 and AP-1 DNA binding activity in the dentate gyrus following the induction of long-term potentiation. *Molecular Brain Research* **77**, 258–266 (2000).

111. Chowdhury, S. *et al*. Arc Interacts with the Endocytic Machinery to Regulate AMPA Receptor Trafficking. *Neuron* **52**, 445 (2006).
112. Sagar, S. M., Sharp, F. R. & Curran, T. Expression of c-fos protein in brain: Metabolic mapping at the cellular level. *Science* **240**, 1328–1331 (1988).
113. Leal, G., Comprido, D. & Duarte, C. B. BDNF-induced local protein synthesis and synaptic plasticity. *Neuropharmacology* **76**, 639–656 (2014).
114. Hayashi, Y. *et al*. Driving AMPA receptors into synapses by LTP and CaMKII: requirement for GluR1 and PDZ domain interaction. *Science* **287**, 2262–2267 (2000).
115. Kopec, C. D., Li, B., Wei, W., Boehm, J. & Malinow, R. Glutamate Receptor Exocytosis and Spine Enlargement during Chemically Induced Long-Term Potentiation. *The Journal of Neuroscience* **26**, 2000 (2006).
116. Lu, W. Y. *et al*. Activation of Synaptic NMDA Receptors Induces Membrane Insertion of New AMPA Receptors and LTP in Cultured Hippocampal Neurons. *Neuron* **29**, 243–254 (2001).
117. Harris, K. M., Jensen, F. E. & Tsao, B. Three-dimensional structure of dendritic spines and synapses in rat hippocampus (CA1) at postnatal day 15 and adult ages: implications for the maturation of synaptic physiology and long-term potentiation. *The Journal of Neuroscience* **12**, 2685 (1992).
118. Nusser, Z. *et al*. Cell type and pathway dependence of synaptic AMPA receptor number and variability in the hippocampus. *Neuron* **21**, 545–559 (1998).
119. Henley, J. M. & Wilkinson, K. A. Synaptic AMPA receptor composition in development, plasticity and disease. *Nature Reviews Neuroscience* **17**, 337–350 (2016).
120. Zhao, Y., Chen, S., Swensen, A. C., Qian, W. J. & Gouaux, E. Architecture and subunit arrangement of native AMPA receptors elucidated by cryo-EM. *Science (New York, N.Y.)* **364**, 355 (2019).
121. Park, P. *et al*. PKA drives an increase in AMPA receptor unitary conductance during LTP in the hippocampus. *Nature Communications* **12**, 413 (2021).
122. Kristensen, A. S. *et al*. Mechanism of CaMKII regulation of AMPA receptor gating. *Nature Neuroscience* **14**, 727 (2011).
123. Lu, W. *et al*. Subunit composition of synaptic AMPA receptors revealed by a single-cell genetic approach. *Neuron* **62**, 254 (2009).
124. Díaz-Alonso, J. & Nicoll, R. A. AMPA receptor trafficking and LTP: Carboxy-termini, amino-termini and TARPs. *Neuropharmacology* **197**, 108710 (2021).
125. Roche, K. W., O'Brien, R. J., Mammen, A. L., Bernhardt, J. & Huganir, R. L. Characterization of multiple phosphorylation sites on the AMPA receptor GluR1 subunit. *Neuron* **16**, 1179–1188 (1996).
126. Diering, G. H. & Huganir, R. L. The AMPA receptor code of synaptic plasticity. *Neuron* **100**, 314 (2018).
127. Diering, G. H., Gustina, A. S. & Huganir, R. L. PKA-GluA1 coupling via AKAP5 controls AMPA receptor phosphorylation and cell-surface targeting during bidirectional homeostatic plasticity. *Neuron* **84**, 790 (2014).
128. Ehlers, M. D. Reinsertion or degradation of AMPA receptors determined by activity-dependent endocytic sorting. *Neuron* **28**, 511–525 (2000).
129. Park, M., Penick, E. C., Edwards, J. G., Kauer, J. A. & Ehlers, M. D. Recycling endosomes supply AMPA receptors for LTP. *Science* **305**, 1972–1975 (2004).

130. Passafaro, M., Piãch, V. & Sheng, M. Subunit-specific temporal and spatial patterns of AMPA receptor exocytosis in hippocampal neurons. *Nature Neuroscience* **4**, 917–926 (2001).
131. Ashby, M. C. *et al*. Removal of AMPA receptors (AMPARs) from synapses is preceded by transient endocytosis of extrasynaptic AMPARs. *Journal of Neuroscience* **24**, 5172–5176 (2004).
132. Tardin, C., Cognet, L., Bats, C., Lounis, B. & Choquet, D. Direct imaging of lateral movements of AMPA receptors inside synapses. *EMBO Journal* **22**, 4656–4665 (2003).
133. Lee, H. K., Barbarosie, M., Kameyama, K., Bear, M. F. & Huganir, R. L. Regulation of distinct AMPA receptor phosphorylation sites during bidirectional synaptic plasticity. *Nature* **405**, 955–959 (2000).
134. Kim, S. & Ziff, E. B. Calcineurin Mediates Synaptic Scaling Via Synaptic Trafficking of Ca2+-Permeable AMPA Receptors. *PLoS Biology* **12**, e1001900 (2014).
135. Matsuda, S., Mikawa, S. & Hirai, H. Phosphorylation of serine-880 in GluR2 by protein kinase C prevents its C terminus from binding with glutamate receptor-interacting protein. *Journal of Neurochemistry* **73**, 1765–1768 (1999).
136. Matsuda, S., Launey, T., Mikawa, S. & Hirai, H. Disruption of AMPA receptor GluR2 clusters following long-term depression induction in cerebellar Purkinje neurons. *The EMBO Journal* **19**, 2765–2774 (2000).
137. Kim, C. H., Hee Jung Chung, Lee, H. K. & Huganir, R. L. Interaction of the AMPA receptor subunit GluR2/3 with PDZ domains regulates hippocampal long-term depression. *Proceedings of the National Academy of Sciences of the United States of America* **98**, 11725 (2001).
138. Hee Jung Chung, Xia, J., Scannevin, R. H., Zhang, X. & Huganir, R. L. Phosphorylation of the AMPA Receptor Subunit GluR2 Differentially Regulates Its Interaction with PDZ Domain-Containing Proteins. *The Journal of Neuroscience* **20**, 7258 (2000).
139. Wu, Z. L. *et al*. Comparative analysis of cortical gene expression in mouse models of Alzheimer's disease. *Neurobiology of Aging* **27**, 377–386 (2006).
140. Ginsberg, S. D., Che, S., Counts, S. E. & Mufson, E. J. Single cell gene expression profiling in Alzheimer's disease. *NeuroRx* **3**, 302 (2012).
141. Yao, P. J. *et al*. Defects in expression of genes related to synaptic vesicle trafficking in frontal cortex of Alzheimer's disease. *Neurobiology of Disease* **12**, 97–109 (2003).
142. Loring, J. F., Wen, X., Lee, J. M., Seilhamer, J. & Somogyi, R. A gene expression profile of Alzheimer's disease. *DNA and Cell Biology* **20**, 683–695 (2001).
143. Dickey, C. A. *et al*. Selectively Reduced Expression of Synaptic Plasticity-Related Genes in Amyloid Precursor Protein + Presenilin-1 Transgenic Mice. *The Journal of Neuroscience* **23**, 5219 (2003).
144. Sze, C. I., Bi, H., Kleinschmidt-Demasters, B. K., Filley, C. M. & Martin, L. J. Selective regional loss of exocytotic presynaptic vesicle proteins in Alzheimer's disease brains. *Journal of the Neurological Sciences* **175**, 81–90 (2000).
145. Blalock, E. M. *et al*. Incipient Alzheimer's disease: Microarray correlation analyses reveal major transcriptional and tumor suppressor responses. *Proceedings of the National Academy of Sciences of the United States of America* **101**, 2173–2178 (2004).
146. Scheff, S. W. *et al*. Synaptic Change in the Posterior Cingulate Gyrus in the Progression of Alzheimer's Disease. *Journal of Alzheimer's disease : JAD* **43**, 1073 (2015).

147. Scheff, S. W., Price, D. A., Schmitt, F. A., Scheff, M. A. & Mufson, E. J. Synaptic Loss in the Inferior Temporal Gyrus in Mild Cognitive Impairment and Alzheimer Disease. *Journal of Alzheimer's disease : JAD* **24**, 547 (2011).
148. Scheff, S. W., Price, D. A., Schmitt, F. A. & Mufson, E. J. Hippocampal synaptic loss in early Alzheimer's disease and mild cognitive impairment. *Neurobiology of Aging* **27**, 1372–1384 (2006).
149. Sze, C. I. *et al*. Loss of the presynaptic vesicle protein synaptophysin in hippocampus correlates with cognitive decline in Alzheimer disease. *Journal of Neuropathology and Experimental Neurology* **56**, 933–944 (1997).
150. Gong, Y. *et al*. Alzheimer's disease-affected brain: Presence of oligomeric Aβ ligands (ADDLs) suggests a molecular basis for reversible memory loss. *Proceedings of the National Academy of Sciences of the United States of America* **100**, 10417 (2003).
151. Lacor, P. N. *et al*. Synaptic Targeting by Alzheimer's-Related Amyloid β Oligomers. *The Journal of Neuroscience* **24**, 10191 (2004).
152. Lacor, P. N. *et al*. Aβ oligomer-induced aberrations in synapse composition, shape, and density provide a molecular basis for loss of connectivity in Alzheimer's disease. *Journal of Neuroscience* **27**, 796–807 (2007).
153. Roselli, F. *et al*. Soluble β-Amyloid1-40 Induces NMDA-Dependent Degradation of Postsynaptic Density-95 at Glutamatergic Synapses. *Journal of Neuroscience* **25**, 11061–11070 (2005).
154. Spires, T. L. *et al*. Dendritic spine abnormalities in amyloid precursor protein transgenic mice demonstrated by gene transfer and intravital multiphoton microscopy. *The Journal of Neuroscience* **25**, 7278–7287 (2005).
155. Scheff, S. Reactive Synaptogenesis in Aging and Alzheimer's Disease: Lessons Learned in the Cotman Laboratory. *Neurochemical Research* **28**, 1625–1630 (2003).
156. Meyer-Luehmann, M. *et al*. Rapid appearance and local toxicity of amyloid-beta plaques in a mouse model of Alzheimer's disease. *Nature* **451**, 720–724 (2008).
157. Zou, C. *et al*. Intraneuronal APP and extracellular Aβ independently cause dendritic spine pathology in transgenic mouse models of Alzheimer's disease. *Acta neuropathologica* **129**, 909–920 (2015).
158. Blazquez-Llorca, L. *et al*. High plasticity of axonal pathology in Alzheimer's disease mouse models. *Acta neuropathologica communications* **5**, 14 (2017).
159. Bittner, T. *et al*. Multiple events lead to dendritic spine loss in triple transgenic Alzheimer's disease mice. *PloS one* **5**, (2010).
160. Tsai, J., Grutzendler, J., Duff, K. & Gan, W. B. Fibrillar amyloid deposition leads to local synaptic abnormalities and breakage of neuronal branches. *Nature Neuroscience* **7**, 1181–1183 (2004).
161. Villa, K. L. *et al*. Inhibitory Synapses Are Repeatedly Assembled and Removed at Persistent Sites In Vivo. *Neuron* **89**, 756–769 (2016).
162. Brawek, B. & Garaschuk, O. Network-wide dysregulation of calcium homeostasis in Alzheimer's disease. *Cell and Tissue Research* **357**, 427–438 (2014).
163. Konur, S. & Ghosh, A. Calcium signaling and the control of dendritic development. *Neuron* **46**, 401–405 (2005).

164. Kuchibhotla, K. V. *et al*. Abeta plaques lead to aberrant regulation of calcium homeostasis in vivo resulting in structural and functional disruption of neuronal networks. *Neuron* **59**, 214–225 (2008).
165. Chang, E. H. *et al*. AMPA receptor downscaling at the onset of Alzheimer's disease pathology in double knockin mice. *Proceedings of the National Academy of Sciences of the United States of America* **103**, 3410 (2006).
166. Hsieh, H. *et al*. AMPAR Removal Underlies Aβ-Induced Synaptic Depression and Dendritic Spine Loss. *Neuron* **52**, 831–843 (2006).
167. Snyder, E. M. *et al*. Regulation of NMDA receptor trafficking by amyloid-β. *Nature Neuroscience* **8**, 1051–1058 (2005).
168. Huang, S. *et al*. Astrocytic glutamatergic transporters are involved in Aβ-induced synaptic dysfunction. *Brain Research* **1678**, 129–137 (2018).
169. Matos, M., Augusto, E., Oliveira, C. R. & Agostinho, P. Amyloid-beta peptide decreases glutamate uptake in cultured astrocytes: Involvement of oxidative stress and mitogen-activated protein kinase cascades. *Neuroscience* **156**, 898–910 (2008).
170. Nimmrich, V. *et al*. Amyloid β Oligomers (Aβ1–42 Globulomer) Suppress Spontaneous Synaptic Activity by Inhibition of P/Q-Type Calcium Currents. *The Journal of Neuroscience* **28**, 788 (2008).
171. Parodi, J. *et al*. β-Amyloid Causes Depletion of Synaptic Vesicles Leading to Neurotransmission Failure. *The Journal of Biological Chemistry* **285**, 2506 (2009).
172. Park, D. & Chang, S. Soluble Aβ1-42 increases the heterogeneity in synaptic vesicle pool size among synapses by suppressing intersynaptic vesicle sharing. *Molecular Brain* **11**, 1–9 (2018).
173. Um, J. W. *et al*. Alzheimer amyloid-β 2 oligomer bound to postsynaptic prion protein activates Fyn to impair neurons. *Nature Neuroscience* **15**, 1227–1235 (2012).
174. Ji, W. U. & Stephen, M. S. Amyloid-β induced signaling by cellular prion protein and Fyn kinase in Alzheimer disease. *Prion* **7**, 37 (2013).
175. Salter, M. W. & Kalia, L. V. SRC kinases: A hub for NMDA receptor regulation. *Nature Reviews Neuroscience* **5**, 317–328 (2004).
176. Liu, L. *et al*. Role of NMDA Receptor Subtypes in Governing the Direction of Hippocampal Synaptic Plasticity. *Science* **304**, 1021–1024 (2004).
177. Li, S. *et al*. Soluble Aβ Oligomers Inhibit Long-Term Potentiation through a Mechanism Involving Excessive Activation of Extrasynaptic NR2B-Containing NMDA Receptors. *Journal of Neuroscience* **31**, 6627–6638 (2011).
178. Bao, Y. *et al*. NMDAR-dependent somatic potentiation of synaptic inputs is correlated with β amyloid-mediated neuronal hyperactivity. *Translational Neurodegeneration* **10**, 1–15 (2021).
179. Sepulveda, F. J., Parodi, J., Peoples, R. W., Opazo, C. & Aguayo, L. G. Synaptotoxicity of Alzheimer Beta Amyloid Can Be Explained by Its Membrane Perforating Property. *PLoS ONE* **5**, 11820 (2010).
180. Varghese, K. *et al*. A New Target for Amyloid Beta Toxicity Validated by Standard and High-Throughput Electrophysiology. *PLOS ONE* **5**, e8643 (2010).
181. Mucke, L. & Selkoe, D. J. Neurotoxicity of Amyloid β-Protein: Synaptic and Network Dysfunction. *Cold Spring Harbor Perspectives in Medicine* **2**, a006338 (2012).

182. Wu, H. Y. & Lynch, D. R. Calpain and synaptic function. *Molecular Neurobiology* **33**, 215–236 (2006).
183. Rami, A. Ischemic neuronal death in the rat hippocampus: The calpain-calpastatin-caspase hypothesis. *Neurobiology of Disease* **13**, 75–88 (2003).
184. Liu, S. J., Gasperini, R., Foa, L. & Small, D. H. Amyloid-β decreases cell-surface AMPA receptors by increasing intracellular calcium and phosphorylation of GluR2. *Journal of Alzheimer's Disease* **21**, 655–666 (2010).
185. Guntupalli, S., Widagdo, J. & Anggono, V. Amyloid-β-Induced Dysregulation of AMPA Receptor Trafficking. *Neural Plasticity* **2016**, 3204519 (2016).
186. Tong, L. *et al*. Brain-Derived Neurotrophic Factor-Dependent Synaptic Plasticity Is Suppressed by Interleukin-1β via p38 Mitogen-Activated Protein Kinase. *The Journal of Neuroscience* **32**, 17714 (2012).
187. Devi, L. & Ohno, M. TrkB reduction exacerbates Alzheimer's disease-like signaling aberrations and memory deficits without affecting β-amyloidosis in 5XFAD mice. *Translational Psychiatry* **5**, e562 (2015).
188. Reddy, P. H. & Beal, M. F. Amyloid beta, mitochondrial dysfunction and synaptic damage: implications for cognitive decline in aging and Alzheimer's disease. *Trends in Molecular Medicine* **14**, 45–53 (2008).
189. Armada-Moreira, A. *et al*. Going the Extra (Synaptic) Mile: Excitotoxicity as the Road Toward Neurodegenerative Diseases. *Frontiers in Cellular Neuroscience* **14**, 521326 (2020).
190. Kamenetz, F. *et al*. APP Processing and Synaptic Function. *Neuron* **37**, 925–937 (2003).
191. Nieweg, K., Andreyeva, A., Van Stegen, B., Tanriöver, G. & Gottmann, K. Alzheimer's disease-related amyloid-β induces synaptotoxicity in human iPS cell-derived neurons. *Cell Death & Disease 2015 6:4* **6**, e1709–e1709 (2015).
192. Ting, J. T., Kelley, B. G., Lambert, T. J., Cook, D. G. & Sullivan, J. M. Amyloid precursor protein overexpression depresses excitatory transmission through both presynaptic and postsynaptic mechanisms. *Proceedings of the National Academy of Sciences of the United States of America* **104**, 353 (2007).
193. Tzioras, M., McGeachan, R. I., Durrant, C. S. & Spires-Jones, T. L. Synaptic degeneration in Alzheimer disease. *Nature Reviews Neurology 2022 19:1* **19**, 19–38 (2022).
194. Birks, J. S. & Harvey, R. J. Donepezil for dementia due to Alzheimer's disease. *Cochrane Database of Systematic Reviews* **2018**, (2018).
195. Rösler, M. *et al*. Efficacy and safety of rivastigmine in patients with Alzheimer's disease: international randomised controlled trial. Commentary: Another piece of the Alzheimer's jigsaw. *BMJ* **318**, 633–640 (1999).
196. Coyle, J. & Kershaw, P. Galantamine, a cholinesterase inhibitor that allosterically modulates nicotinic receptors: Effects on the course of Alzheimer's disease. *Biological Psychiatry* **49**, 289–299 (2001).
197. Russ T. & Morling J. Cholinesterase inhibitors for mild cognitive impairment. *The Cochrane Database of Systematic Reviews* **2012**, (2012).
198. Reisberg, B. *et al*. Memantine in Moderate-to-Severe Alzheimer's Disease. *New England Journal of Medicine* **348**, 1333–1341 (2003).
199. Dhillon, S. Aducanumab: First Approval. *Drugs* **81**, 1437–1443 (2021).
200. Arndt, J. W. *et al*. Structural and kinetic basis for the selectivity of aducanumab for aggregated forms of amyloid-β. *Scientific Reports* **8**, (2018).

201. U.S. Food and Drug Administration (FDA). Combined FDA and Applicant PCNS Drugs Advisory Committee Briefing Document. *Peripheral and Central Nervous System (PCNS) Drugs Advisory Committee Meeting* https://fda.report/media/143503/PCNS-20201106-CombinedFDABiogenBackgrounder_0.pdf (2020).
202. Vaz, M., Silva, V., Monteiro, C. & Silvestre, S. Role of Aducanumab in the Treatment of Alzheimer's Disease: Challenges and Opportunities. *Clinical Interventions in Aging* **17**, 797 (2022).
203. Shcherbinin, S. *et al.* Association of Amyloid Reduction After Donanemab Treatment With Tau Pathology and Clinical Outcomes: The TRAILBLAZER-ALZ Randomized Clinical Trial. *JAMA Neurology* **79**, 1015–1024 (2022).
204. Cohen, S. *et al.* Lecanemab Clarity AD: Quality-of-Life Results from a Randomized, Double-Blind Phase 3 Trial in Early Alzheimer's Disease. *Journal of Prevention of Alzheimer's Disease* **10**, 771–777 (2023).
205. Wang, H. *et al.* Modified titration of donanemab reduces ARIA risk and maintains amyloid reduction. *Alzheimer's and Dementia* **21**, (2025).
206. Goate, A. *et al.* Segregation of a missense mutation in the amyloid precursor protein gene with familial Alzheimer's disease. *Nature* **349**, 704–706 (1991).
207. Levy-Lahad, E. *et al.* Candidate gene for the chromosome 1 familial Alzheimer's disease locus. *Science* **269**, 973–977 (1995).
208. Sherrington, R. *et al.* Cloning of a gene bearing missense mutations in early-onset familial Alzheimer's disease. *Nature* **375**, 754–760 (1995).
209. Dourlen, P., Kilinc, D., Malmanche, N., Chapuis, J. & Lambert, J. C. The new genetic landscape of Alzheimer's disease: from amyloid cascade to genetically driven synaptic failure hypothesis? *Acta Neuropathologica 2019 138:2* **138**, 221–236 (2019).
210. Mendez, M. F. Early-Onset Alzheimer's Disease. *Neurologic clinics* **35**, 263 (2017).
211. Chartier-Harlin, M. C. *et al.* Early-onset Alzheimer's disease caused by mutations at codon 717 of the beta-amyloid precursor protein gene. *Nature* **353**, 844–846 (1991).
212. Murrell, J., Farlow, M., Ghetti, B. & Benson, M. D. A mutation in the amyloid precursor protein associated with hereditary Alzheimer's disease. *Science (New York, N.Y.)* **254**, 97–99 (1991).
213. Muratore, C. R. *et al.* The familial Alzheimer's disease APPV717I mutation alters APP processing and Tau expression in iPSC-derived neurons. *Human Molecular Genetics* **23**, 3523 (2014).
214. Dewachter, I. *et al.* Aging Increased Amyloid Peptide and Caused Amyloid Plaques in Brain of Old APP/V717I Transgenic Mice by a Different Mechanism than Mutant Presenilin1. *Journal of Neuroscience* **20**, 6452–6458 (2000).
215. Suzuki, N. *et al.* An increased percentage of long amyloid beta protein secreted by familial amyloid beta protein precursor (beta APP717) mutants. *Science* **264**, 1336–1340 (1994).
216. Bekris, L. M., Yu, C. E., Bird, T. D. & Tsuang, D. W. Genetics of Alzheimer disease. *Journal of Geriatric Psychiatry and Neurology* **23**, 213–227 (2010).
217. Gatz, M. *et al.* Role of genes and environments for explaining Alzheimer disease. *Archives of General Psychiatry* **63**, 168–174 (2006).
218. Livingston, G. *et al.* Dementia prevention, intervention, and care: 2024 report of the Lancet standing Commission. *The Lancet* **404**, 572–628 (2024).

219. Niu, H., Álvarez-Álvarez, I., Guillén-Grima, F. & Aguinaga-Ontoso, I. Prevalencia e incidencia de la enfermedad de Alzheimer en Europa: metaanálisis. *Neurologia* **32**, 523–532 (2017).
220. Corder, E. H. *et al*. Gene dose of apolipoprotein E type 4 allele and the risk of Alzheimer's disease in late onset families. *Science* **261**, 921–923 (1993).
221. Neu, S. C. *et al*. Apolipoprotein E genotype and sex risk factors for Alzheimer disease: A meta-analysis. *JAMA Neurology* **74**, 1178–1189 (2017).
222. Islam, S., Noorani, A., Sun, Y., Michikawa, M. & Zou, K. Multi-functional role of apolipoprotein E in neurodegenerative diseases. *Frontiers in Aging Neuroscience* **17**, 1535280 (2025).
223. Bertram, L., Lill, C. M. & Tanzi, R. E. The Genetics of Alzheimer Disease: Back to the Future. *Neuron* **68**, 270–281 (2010).
224. Lambert, J. C. *et al*. Genome-wide association study identifies variants at CLU and CR1 associated with Alzheimer's disease. *Nature Genetics 2009 41:10* **41**, 1094–1099 (2009).
225. Harold, D. *et al*. Genome-wide association study identifies variants at CLU and PICALM associated with Alzheimer's disease. *Nature Genetics 2009 41:10* **41**, 1088–1093 (2009).
226. Seshadri, S. *et al*. Genome-wide Analysis of Genetic Loci Associated With Alzheimer Disease. *JAMA* **303**, 1832–1840 (2010).
227. Lambert, J. C. *et al*. Meta-analysis of 74,046 individuals identifies 11 new susceptibility loci for Alzheimer's disease. *Nature genetics* **45**, 1452 (2013).
228. Jonsson, T. *et al*. Variant of TREM2 Associated with the Risk of Alzheimer's Disease. *New England Journal of Medicine* **368**, 107–116 (2013).
229. Guerreiro, R. *et al*. TREM2 Variants in Alzheimer's Disease. *The New England Journal of Medicine* **368**, 117 (2012).
230. Bellenguez, C. *et al*. New insights into the genetic etiology of Alzheimer's disease and related dementias. *Nature Genetics 2022 54:4* **54**, 412–436 (2022).
231. Hardy, J. A. & Higgins, G. A. Alzheimer's disease: The amyloid cascade hypothesis. *Science* **256**, 184–185 (1992).
232. Mormino, E. C. & Papp, K. V. Amyloid accumulation and cognitive decline in clinically normal older individuals: implications for aging and early Alzheimer's disease. *Journal of Alzheimer's Disease* **64**, S633 (2018).
233. Taddei, R. N. & Duff, K. E. Synapse vulnerability and resilience across the clinical spectrum of dementias. *Nature Reviews Neurology 2025 21:7* **21**, 353–369 (2025).
234. Neuhauss, S. C. F. *et al*. Mouse Models of Alzheimer's Disease. *Frontiers in Molecular Neuroscience* **15**, 912995 (2022).
235. Spence, E. F. & Soderling, S. H. Actin Out: Regulation of the Synaptic Cytoskeleton. *Journal of Biological Chemistry* **290**, 28613–28622 (2015).
236. Hotulainen, P. & Hoogenraad, C. C. Actin in dendritic spines: connecting dynamics to function. *Journal of Cell Biology* **189**, 619–629 (2010).
237. Dourlen, P., Chapuis, J. & Lambert, J.-C. Using High-Throughput Animal or Cell-Based Models to Functionally Characterize GWAS Signals. *Current Genetic Medicine Reports* **6**, 107 (2018).
238. Taylor, D. L. Past, present, and future of high content screening and the field of cellomics. *Methods in Molecular Biology* **356**, 3–18 (2007).

239. Coulon, A. *et al*. High-Content Screening of Synaptic Density Modulators in Primary Neuronal Cultures. *Current Protocols* **3**, (2023).
240. Kilinc, D. *et al*. Pyk2 overexpression in postsynaptic neurons blocks amyloid β 1-42-induced synaptotoxicity in microfluidic co-cultures. *Brain Communications* **2**, (2020).
241. Coulon, A. *et al*. Neuronal downregulation of PLCG2 impairs synaptic function and elicits Alzheimer disease hallmarks. *bioRxiv* (2024).
242. Blasiak, A., Lee, G. U. & Kilinc, D. Neuron Subpopulations with Different Elongation Rates and DCC Dynamics Exhibit Distinct Responses to Isolated Netrin-1 Treatment. *ACS Chemical Neuroscience* **6**, 1578–1590 (2015).
243. Guillot-Sestier, M. V. *et al*. α-Secretase-derived Fragment of Cellular Prion, N1, Protects against Monomeric and Oligomeric Amyloid β (Aβ)-associated Cell Death. *The Journal of Biological Chemistry* **287**, 5021 (2012).
244. Lefebvre, C. *et al*. Integration of Microfluidic Devices with Microelectrode Arrays to Functionally Assay Amyloid-β-Induced Synaptotoxicity. *ACS Biomaterials Science and Engineering* **10**, 1856–1868 (2024).
245. Sartori, M. *et al*. BIN1 recovers tauopathy-induced long-term memory deficits in mice and interacts with Tau through Thr 348 phosphorylation. *Acta Neuropathologica* **138**, 631–652 (2019).
246. Eysert, F. *et al*. Alzheimer's genetic risk factor FERMT2 (Kindlin-2) controls axonal growth and synaptic plasticity in an APP-dependent manner. *Molecular Psychiatry* **26**, 5592–5607 (2020).
247. Bassani, S., Folci, A., Zapata, J. & Passafaro, M. AMPAR trafficking in synapse maturation and plasticity. *Cellular and Molecular Life Sciences: CMLS* **70**, 4411 (2013).
248. Hosokawa, T., Mitsushima, D., Kaneko, R. & Hayashi, Y. Stoichiometry and phosphoisotypes of hippocampal AMPA type glutamate receptor phosphorylation. *Neuron* **85**, 60 (2014).
249. Garcia-Alvarez, G. *et al*. STIM2 regulates PKA-dependent phosphorylation and trafficking of AMPARs. *Molecular Biology of the Cell* **26**, 1141–1159 (2015).
250. Song, R. S. *et al*. ERK regulation of phosphodiesterase 4 enhances dopamine-stimulated AMPA receptor membrane insertion. *Proceedings of the National Academy of Sciences of the United States of America* **110**, 15437–15442 (2013).
251. Cummings, K. A. & Popescu, G. K. Glycine-dependent activation of NMDA receptors. *The Journal of General Physiology* **145**, 513 (2015).
252. Lee, H. K., Kameyama, K., Huganir, R. L. & Bear, M. F. NMDA Induces Long-Term Synaptic Depression and Dephosphorylation of the GluR1 Subunit of AMPA Receptors in Hippocampus. *Neuron* **21**, 1151–1162 (1998).
253. Feldman, D. E., Nicoll, R. A., Malenka, R. C. & Isaac, J. T. R. Long-term depression at thalamocortical synapses in developing rat somatosensory cortex. *Neuron* **21**, 347–357 (1998).
254. Frandemiche, M. L. *et al*. Activity-Dependent Tau Protein Translocation to Excitatory Synapse Is Disrupted by Exposure to Amyloid-Beta Oligomers. *The Journal of Neuroscience* **34**, 6084 (2014).
255. Ehrlich, I. & Malinow, R. Postsynaptic Density 95 controls AMPA Receptor Incorporation during Long-Term Potentiation and Experience-Driven Synaptic Plasticity. *The Journal of Neuroscience* **24**, 916 (2004).

256. Lambert, E. *et al*. BIN1 expression in the presynaptic compartment leads to isoform-specific synaptotoxicity. *bioRxiv* (2025).
257. Buccino, A. P. *et al*. Spikeinterface, a unified framework for spike sorting. *eLife* **9**, 1–24 (2020).
258. Yger, P. *et al*. A spike sorting toolbox for up to thousands of electrodes validated with ground truth recordings in vitro and in vivo. *eLife* **7**, (2018).
259. Tropp, J. A. & Gilbert, A. C. Signal recovery from random measurements via orthogonal matching pursuit. *IEEE Transactions on Information Theory* **53**, 4655–4666 (2007).
260. Varol, E. *et al*. Decentralized motion inference and registration of neuropixel data. in *ICASSP, IEEE International Conference on Acoustics, Speech and Signal Processing - Proceedings* vols 2021-June 1085–1089 (Institute of Electrical and Electronics Engineers Inc., 2021).
261. Scopin, M., Spampinato, G. L. B., Marre, O., Garcia, S. & Yger, P. Localization of neurons from extracellular footprints. *Journal of Neuroscience Methods* **412**, (2024).
262. Aertsen, A. M. H. J. & Gerstein, G. L. Evaluation of neuronal connectivity: Sensitivity of cross-correlation. *Brain Research* **340**, 341–354 (1985).
263. Yin, A. *et al*. FAM96A knock-out promotes alternative macrophage polarization and protects mice against sepsis. *Clinical and Experimental Immunology* **203**, 433–447 (2021).
264. Liu, Z. *et al*. Fam96a is essential for the host control of Toxoplasma gondii infection by fine-tuning macrophage polarization via an irondependent mechanism. *PLoS Neglected Tropical Diseases* **18**, (2024).
265. Shin, H. W. *et al*. Roles of ARFRP1 (ADP-ribosylation factor-related protein 1) in post-Golgi membrane trafficking. *Journal of Cell Science* **118**, 4039–4048 (2005).
266. Zahn, C. *et al*. ADP-ribosylation Factor-like GTPase ARFRP1 Is Required for Trans-Golgi to Plasma Membrane Trafficking of E-cadherin. *Journal of Biological Chemistry* **283**, 27179–27188 (2008).
267. Zahn, C. *et al*. Knockout of Arfrp1 leads to disruption of ARF-like1 (ARL1) targeting to the trans-Golgi in mouse embryos and HeLa cells. *Molecular Membrane Biology* **23**, 475–485 (2006).
268. Meyer, D., Bonhoeffer, T. & Scheuss, V. Balance and stability of synaptic structures during synaptic plasticity. *Neuron* **82**, 430–443 (2014).
269. Ivanova, D. & Cousin, M. A. Synaptic Vesicle Recycling and the Endolysosomal System: A Reappraisal of Form and Function. *Frontiers in Synaptic Neuroscience* **14**, 826098 (2022).
270. Fassio, A., Fadda, M. & Benfenati, F. Molecular Machines Determining the Fate of Endocytosed Synaptic Vesicles in Nerve Terminals. *Frontiers in Synaptic Neuroscience* **8**, 10 (2016).
271. Nakai, W. *et al*. ARF1 and ARF4 regulate recycling endosomal morphology and retrograde transport from endosomes to the Golgi apparatus. *Molecular Biology of the Cell* **24**, 2570–2581 (2013).
272. Hausser, A. & Schlett, K. Coordination of AMPA receptor trafficking by Rab GTPases. *Small GTPases* **10**, 419 (2017).
273. Parkinson, G. T. & Hanley, J. G. Mechanisms of AMPA receptor endosomal sorting. *Frontiers in Molecular Neuroscience* **11**, 424290 (2018).
274. Lohmann, C. & Kessels, H. W. The developmental stages of synaptic plasticity. *The Journal of Physiology* **592**, 13 (2013).

275. Bozdagi, O., Shan, W., Tanaka, H., Benson, D. L. & Huntley, G. W. Increasing Numbers of Synaptic Puncta during Late-Phase LTP: N-Cadherin Is Synthesized, Recruited to Synaptic Sites, and Required for Potentiation. *Neuron* **28**, 245–259 (2000).
276. Brain tissue expression of ARFRP1 - Summary - The Human Protein Atlas. https://www.proteinatlas.org/ENSG00000101246-ARFRP1/brain.
277. Harrill, J. A. *et al.* Ontogeny of biochemical, morphological and functional parameters of synaptogenesis in primary cultures of rat hippocampal and cortical neurons. *Molecular Brain* **8**, 1–15 (2015).
278. Plant, K. *et al.* Transient incorporation of native GluR2-lacking AMPA receptors during hippocampal long-term potentiation. *Nature Neuroscience 2006 9:5* **9**, 602–604 (2006).
279. Klinghoffer, R. A. *et al.* Reduced seed region-based off-target activity with lentivirus-mediated RNAi. *RNA* **16**, 879 (2010).
280. Rogers, G. L. *et al.* Innate Immune Responses to AAV Vectors. *Frontiers in Microbiology* **2**, 194 (2011).
281. Pickard, L., Noel, J., Henley, J. M., Collingridge, G. L. & Molnar, E. Developmental Changes in Synaptic AMPA and NMDA Receptor Distribution and AMPA Receptor Subunit Composition in Living Hippocampal Neurons. *Journal of Neuroscience* **20**, 7922–7931 (2000).
282. Wu, Q. L., Gao, Y., Li, J. T., Ma, W. Y. & Chen, N. H. The Role of AMPARs Composition and Trafficking in Synaptic Plasticity and Diseases. *Cellular and Molecular Neurobiology* **42**, 2489 (2021).
283. Schwenk, J. *et al.* Regional Diversity and Developmental Dynamics of the AMPA-Receptor Proteome in the Mammalian Brain. *Neuron* **84**, 41–54 (2014).
284. Boehm, J. *et al.* Synaptic Incorporation of AMPA Receptors during LTP Is Controlled by a PKC Phosphorylation Site on GluR1. *Neuron* **51**, 213–225 (2006).
285. Derkach, V. A., Oh, M. C., Guire, E. S. & Soderling, T. R. Regulatory mechanisms of AMPA receptors in synaptic plasticity. *Nature Reviews Neuroscience* **8**, 101–113 (2007).
286. Tang, A. H. *et al.* A transsynaptic nanocolumn aligns neurotransmitter release to receptors. *Nature* **536**, 210 (2016).
287. Stein, I. S. & Zito, K. Dendritic Spine Elimination: Molecular Mechanisms and Implications. *The Neuroscientist* **25**, 27–47 (2019).
288. Oh, W. C., Parajuli, L. K. & Zito, K. Heterosynaptic structural plasticity on local dendritic segments of hippocampal CA1 neurons. *Cell Reports* **10**, 162 (2014).
289. Bateman, R. J. *et al.* Clinical and Biomarker Changes in Dominantly Inherited Alzheimer's Disease. *New England Journal of Medicine* **367**, 795–804 (2012).
290. Shi, S. H., Hayashi, Y., Esteban, J. A. & Malinow, R. Subunit-specific rules governing AMPA receptor trafficking to synapses in hippocampal pyramidal neurons. *Cell* **105**, 331–343 (2001).
291. Shankar, G. M. *et al.* Natural oligomers of the Alzheimer amyloid-beta protein induce reversible synapse loss by modulating an NMDA-type glutamate receptor-dependent signaling pathway. *The Journal of Neuroscience* **27**, 2866–2875 (2007).
292. Texidó, L., Martín-Satué, M., Alberdi, E., Solsona, C. & Matute, C. Amyloid β peptide oligomers directly activate NMDA receptors. *Cell Calcium* **49**, 184–190 (2011).

293. Kessels, H. W., Nabavi, S. & Malinow, R. Metabotropic NMDA receptor function is required for β-amyloid-induced synaptic depression. *Proceedings of the National Academy of Sciences of the United States of America* **110**, 4033–4038 (2013).
294. Selkoe, D. J. Soluble oligomers of the amyloid beta-protein impair synaptic plasticity and behavior. *Behavioural Brain Research* **192**, 106–113 (2008).
295. Palop, J. J. & Mucke, L. Network abnormalities and interneuron dysfunction in Alzheimer disease. *Nature Reviews Neuroscience 2016 17:12* **17**, 777–792 (2016).
296. Palop, J. J. *et al*. Aberrant excitatory neuronal activity and compensatory remodeling of inhibitory hippocampal circuits in mouse models of Alzheimer's disease. *Neuron* **55**, 697–711 (2007).
297. Minkeviciene, R. *et al*. Amyloid beta-induced neuronal hyperexcitability triggers progressive epilepsy. *The Journal of Neuroscience* **29**, 3453–3462 (2009).
298. Bean, B. P. The action potential in mammalian central neurons. *Nature Reviews Neuroscience* **8**, 451–465 (2007).
299. Obien, M. E. J., Deligkaris, K., Bullmann, T., Bakkum, D. J. & Frey, U. Revealing neuronal function through microelectrode array recordings. *Frontiers in Neuroscience* **9**, 423 (2015).
300. Kim, J. Y., Kim, Y. G. & Lee, G. M. CHO cells in biotechnology for production of recombinant proteins: current state and further potential. *Applied Microbiology and Biotechnology* **93**, 917–930 (2012).
301. Mullan, M. *et al*. A pathogenic mutation for probable Alzheimer's disease in the APP gene at the N-terminus of beta-amyloid. *Nature Genetics* **1**, 345–347 (1992).
302. Welzel, A. T. *et al*. Secreted amyloid β-proteins in a cell culture model include N-terminally extended peptides that impair synaptic plasticity. *Biochemistry* **53**, 3908–3921 (2014).
303. Calabrese, B. *et al*. Rapid, Concurrent Alterations in Pre- and Postsynaptic Structure Induced by Soluble Natural Amyloid-β Protein. *Molecular and Cellular Neurosciences* **35**, 183 (2007).
304. Townsend, M., Shankar, G. M., Mehta, T., Walsh, D. M. & Selkoe, D. J. Effects of secreted oligomers of amyloid β-protein on hippocampal synaptic plasticity: a potent role for trimers. *The Journal of Physiology* **572**, 477 (2006).
305. Kienlen-Campard, P., Miolet, S., Tasiaux, B. & Octave, J. N. Intracellular Amyloid-β1–42, but Not Extracellular Soluble Amyloid-β Peptides, Induces Neuronal Apoptosis. *Journal of Biological Chemistry* **277**, 15666–15670 (2002).
306. Herl, L. *et al*. Mutations in amyloid precursor protein affect its interactions with presenilin/γ-secretase. *Molecular and Cellular Neurosciences* **41**, 166 (2009).
307. Dahodwala, H. & Lee, K. H. The fickle CHO: a review of the causes, implications, and potential alleviation of the CHO cell line instability problem. *Current Opinion in Biotechnology* **60**, 128–137 (2019).
308. Huhn, S. *et al*. Chromosomal instability drives convergent and divergent evolution toward advantageous inherited traits in mammalian CHO bioproduction lineages. *iScience* **25**, 104074 (2022).
309. Carrillo-Cocom, L. M. *et al*. Amino acid consumption in naïve and recombinant CHO cell cultures: producers of a monoclonal antibody. *Cytotechnology* **67**, 809 (2014).
310. Lesné, S. *et al*. A specific amyloid-β protein assembly in the brain impairs memory. *Nature 2006 440:7082* **440**, 352–357 (2006).

311. Fernández-Monreal, M., Brown, T. C., Royo, M. & Esteban, J. A. The Balance between Receptor Recycling and Trafficking toward Lysosomes Determines Synaptic Strength during Long-Term Depression. *The Journal of Neuroscience* **32**, 13200 (2012).
312. Mignogna, M. L. & D'Adamo, P. Critical importance of RAB proteins for synaptic function. *Small GTPases* **9**, 145–157 (2018).
313. Lambert, E. *et al*. The Alzheimer susceptibility gene BIN1 induces isoform-dependent neurotoxicity through early endosome defects. *Acta Neuropathologica Communications* **10**, (2022).
314. Ando, K. *et al*. PICALM and Alzheimer's Disease: An Update and Perspectives. *Cells* **11**, 3994 (2022).
315. Estadella, I. *et al*. Endocytosis: A Turnover Mechanism Controlling Ion Channel Function. *Cells* **9**, (2020).
316. Jensen, C. S. *et al*. Specific Sorting and Post-Golgi Trafficking of Dendritic Potassium Channels in Living Neurons. *The Journal of Biological Chemistry* **289**, 10566 (2014).
317. Tokutake, T. *et al*. Hyperphosphorylation of Tau Induced by Naturally Secreted Amyloid-β at Nanomolar Concentrations Is Modulated by Insulin-dependent Akt-GSK3β Signaling Pathway. *The Journal of Biological Chemistry* **287**, 35222 (2012).
318. Citron, M. *et al*. Inhibition of amyloid β-protein production in neural cells by the serine protease inhibitor AEBSF. *Neuron* **17**, 171–179 (1996).
319. Zheng, T. *et al*. Exosomes Secreted from HEK293-APP Swe/Ind Cells Impair the Hippocampal Neurogenesis. *Neurotoxicity Research* **32**, 82–93 (2017).
320. Choi, S. H. *et al*. A three-dimensional human neural cell culture model of Alzheimer's disease. *Nature* **515**, 274–278 (2014).
321. Gonzalez, C. *et al*. Modeling amyloid beta and tau pathology in human cerebral organoids. *Molecular Psychiatry* **23**, 2363–2374 (2018).
322. Wilson, C. M., Magnaudeix, A., Yardin, C. & Terro, F. DC2 and Keratinocyte-associated Protein 2 (KCP2), Subunits of the Oligosaccharyltransferase Complex, Are Regulators of the γ-Secretase-directed Processing of Amyloid Precursor Protein (APP). *The Journal of Biological Chemistry* **286**, 31080 (2011).
323. Venkataramani, V. *et al*. Histone Deacetylase Inhibitor Valproic Acid Inhibits Cancer Cell Proliferation via Down-regulation of the Alzheimer Amyloid Precursor Protein. *The Journal of Biological Chemistry* **285**, 10678 (2010).
324. Boix, C. P., Lopez-Font, I., Cuchillo-Ibañez, I. & Sáez-Valero, J. Amyloid precursor protein glycosylation is altered in the brain of patients with Alzheimer's disease. *Alzheimer's Research & Therapy* **12**, 96 (2020).
325. Wang, J., Fourriere, L. & Gleeson, P. A. Advances in the cell biology of the trafficking and processing of amyloid precursor protein: impact of familial Alzheimer's disease mutations. *Biochemical Journal* **481**, 1297 (2024).
326. Limone, A. *et al*. Targeting RPSA to modulate endosomal trafficking and amyloidogenesis in genetic Alzheimer's disease. *BBA Molecular Basis of Disease* **1871**, 167753 (2025).